Transactions of the ASME®

Technical Editor
H. L. JULIEN (1998)

Associate Technical Editors
Advanced Energy Systems
M. J. MORAN (1999)
Gas Turbine
D. COOKE (1999)
H. NELSON (1999)
J. PETERS (1999)
J. N. SHINN (1996)
Internal Combustion Engines
D. ASSANIS (1999)
Power
D. LOU (1998)

BOARD ON COMMUNICATIONS
Chairman and Vice President
R. MATES

OFFICERS OF THE ASME
President, KEITH B. THAYER
Executive Director, D. L. BELDEN
Treasurer, J. A. MASON

PUBLISHING STAFF
Managing Director, Engineering
CHARLES W. BEARDSLEY
Director, Technical Publishing
PHILIP DI VIETRO
Managing Editor, Technical Publishing
CYNTHIA B. CLARK
Managing Editor, Transactions
CORNELIA MONAHAN
Production Coordinator
VALERIE WINTERS
Production Assistant
MARISOL ANDINO

Transactions of the ASME, Journal of Engineering for Gas Turbines and Power (ISSN 0742-4795) is published quarterly (Jan., April, July, Oct.) for $195.00 per year by The American Society of Mechanical Engineers, 345 East 47th Street, New York, NY 10017. Periodicals postage paid at New York, NY and additional mailing offices. POSTMASTER: Send address changes to Transactions of the ASME, Journal of Engineering for Gas Turbines and Power, c/o THE AMERICAN SOCIETY OF MECHANICAL ENGINEERS, 22 Law Drive, Box 2300, Fairfield, NJ 07007-2300.
CHANGES OF ADDRESS must be received at Society headquarters seven weeks before they are to be effective. Please send old label and new address.
PRICES: To members, $40.00, annually: to nonmembers, $195.00. Add $30.00 for postage to countries outside the United States and Canada.
STATEMENT from By-Laws. The Society shall not be responsible for statements or opinions advanced in papers or . . . printed in its publications (B7.1, par. 3).

INDEXED by Applied Mechanics Reviews and Engineering Information, Inc. Canadian Goods & Services Tax Registration #126148048

Journal of Engineering for Gas Turbines and Power

Published Quarterly by The American Society of Mechanical Engineers

VOLUME 119 • NUMBER 3 • JULY 1997

TECHNICAL PAPERS

(Contents continued on p. 740)

Fatigue Strength as a Function of Preloading in Dynamic Fatigue Testing of Glass and Ceramics

S. R. Choi
Cleveland State University,
Cleveland, OH 44115;
Senior Resident Research Associate,
NASA Lewis Research Center,
Cleveland, OH 44135

J. P. Gyekenyesi
NASA Lewis Research Center,
Cleveland, OH 44135

The solution of fatigue strength as a function of preloading in dynamic fatigue (constant stress-rate) testing was obtained analytically and numerically. The effect of preloading on dynamic fatigue strength decreases with increasing fatigue parameter (n), and for $n \geq 20$ the effect is negligible up to a preloading of 90 percent. The solution was verified by dynamic fatigue experiments conducted with soda-lime glass and alumina specimens in room-temperature distilled water. This result showed that one can apply a preloading corresponding up to 90 percent of fatigue strength for most glass and ceramic materials, resulting in a dramatic saving of testing time in dynamic fatigue testing. The key feature that makes this technique feasible is that most of the slow crack growth under dynamic fatigue loading occurs close to failure time where the dynamic fatigue strength is defined.

Introduction

Slow crack growth (fatigue) of glass and ceramic materials can be determined by the crack size measurement or strength measurement method. The crack size measurement can be achieved by monitoring crack growth by compliance, optical or electrical techniques, using either precracked fracture toughness test specimens [1–5] or indented flexure beam specimens [5–8]. The strength measurement, on the other hand, is an indirect method, in which slow crack growth is measured via strength degradation due to slow crack growth of test specimens. The strength methods include dynamic, static, and cyclic fatigue testing [9–14].

Dynamic fatigue (constant stress-rate) testing has been used for several decades to characterize fatigue behavior of glass and ceramics materials at both ambient and elevated temperatures. The advantage of dynamic fatigue testing over other methods lies in its simplicity: Strengths are measured in a routine manner at three to four stressing rates by applying constant crosshead speeds or constant loading rates. The fatigue parameters required for design are simply calculated from a relationship between fatigue strength and stressing rate [9]. These merits have prompted an effort to establish an ASTM standard for dynamic fatigue [15].

The testing time, or failure time, in dynamic fatigue testing depends on fatigue strength, stressing rate, and number of test specimens used. For example, if it takes about 6 h at a certain low stressing rate of 2 MPa/min to test one ceramic specimen with a strength of about 700 MPa and if a minimum of 20 specimens is required to obtain reliable statistical data, then the total testing time would be 120 h. If a preload corresponding to 50 percent of the fatigue strength is applied to the specimen prior to testing, 50 percent of the total testing time can be saved as long as the fatigue strength remains unchanged regardless of preloading. In fact, it has been a common, empirical practice in optical fiber testing to apply some preloading (<50 percent), resulting in a considerable saving of testing time.

The purpose of this paper is to study the effect of preloading on dynamic fatigue strength in order to lay a theoretical foundation on such an empirical practice. For this purpose, the analytical and numerical solution of dynamic fatigue strength as a function of preloading was developed for a natural flaw system. To verify the solution, dynamic fatigue testing of glass and ceramic specimens was conducted in a range of preloadings from 0 to 90 percent in room-temperature distilled water. Finally, the testing time as a function of preloading was presented in conjunction with fatigue parameter (n) to give an important implication of the solution established.

Analysis

In this section the analytical and numerical solution of dynamic fatigue strength as a function of preloading is presented. In many cases slow crack growth of glass and ceramics under Mode I loading conditions above the fatigue limit can be described by the following empirical power-law relation:

$$v = \frac{da}{dt} = A\left[\frac{K_I}{K_{IC}}\right]^n \tag{1}$$

where v, a, and t are crack velocity, crack size, and time, respectively. A and n are the material/environment-dependent fatigue parameters. K_I is the Mode I stress intensity factor and K_{IC} is the critical stress intensity factor or fracture toughness of the material under Mode I loading.

Analytical Solution. The corresponding Mode I stress intensity factor for the natural flaw system with no residual contract-stress is

$$K_I = Y\sigma_a a^{1/2} \tag{2}$$

where Y is the crack geometry factor, and σ_a is the applied remote stress. Substituting Eq. (2) into Eq. (i) and solving the differential equation with some manipulations yields [16]

$$S_a^{n-2} = S_i^{n-2} - \frac{1}{B}\int_0^t [\sigma_a(t)]^n dt \tag{3}$$

where S_a is the strength degraded and S_i is the inert strength defined as $S_i = K_{IC}/(Y\sqrt{a_{fi}})$ with a_{fi} being a critical crack size with no slow crack growth. The parameter B is expressed

Contributed by the International Gas Turbine Institute and presented at the 41st International Gas Turbine and Aeroengine Congress and Exhibition, Birmingham, United Kingdom, June 10–13, 1996. Manuscript received at ASME Headquarters February 1996. Paper No. 96-GT-342. Associate Technical Editor: J. N. Shinn.

$$B = \frac{2K_{IC}^2}{AY^2(n-2)} \tag{4}$$

The integral term in Eq. (3) thus represents a strength degradation due to slow crack growth.

In dynamic fatigue testing a constant stressing rate of $\dot{\sigma}$ is employed using either constant displacement rate (position-controlled mode) or constant loading rate (load-controlled mode), as shown in Fig. 1(*a*). The applied stress is

$$\sigma_a(t) = \dot{\sigma}t \tag{5}$$

At fracture, $\sigma_f = \dot{\sigma}t_f$, where σ_f and t_f are fatigue strength and failure time, respectively. Substituting Eq. (5) into Eq. (3) using the relation at fracture, one can obtain the following dynamic fatigue strength as a function of stressing rate [16]

$$\sigma_f = [B(n+1)S_i^{n-2}]^{1/(n+1)}\dot{\sigma}^{1/(n+1)} \tag{6}$$

In deriving Eq. (6), it was assumed that

$$\left(\frac{S_a}{S_i}\right)^{n-2} \ll 1 \tag{7}$$

since $n \geq 10$ for most glass and ceramics. Equation (6) is called a dynamic fatigue equation. The fatigue parameters n and A can be obtained, respectively, from the slope and intercept of a dynamic fatigue curve by a linear regression analysis when $\log \sigma_f$ is plotted as a function of $\log \dot{\sigma}$.

Let us consider a case of preloading as shown in Fig. 1(*b*), where a preloading of σ_o (or P_o) is applied at $t = 0$. The applied stress is then expressed

$$\sigma_a(t) = \dot{\sigma}t + \sigma_o \tag{8}$$

Substituting Eq. (8) into Eq. (3) and solving the integral from $t = 0$ to t_f yields

$$S_a^{n-2} - S_i^{n-2} = -\frac{1}{B(n+1)\dot{\sigma}}(\sigma_{fp}^{n+1} - \sigma_o^{n+1}) \tag{9}$$

where σ_{fp} is the fatigue strength with preloading, corresponding to

$$\sigma_{fp} = \dot{\sigma}t_f + \sigma_o$$

Solving for σ_{fp} in Eq. (9) using the relation of Eq. (7), one can obtain

$$\sigma_{fp} = [B(n+1)\dot{\sigma}S_i^{n-2} + \sigma_o^{n+1}]^{1/(n+1)} \tag{10}$$

But from Eq. (6), $B(n+1)\dot{\sigma}S_i^{n-2} = \sigma_f^{n+1}$, which is the case of zero preloading. Let $\sigma_f \equiv \sigma_{fn}$. Then, Eq. (10) becomes

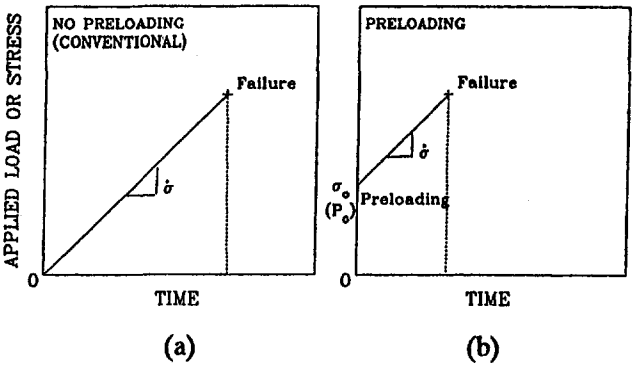

Fig. 1 Mode of loading applied in dynamic fatigue testing: (*a*) without preloading (regular, conventional testing); (*b*) with preloading

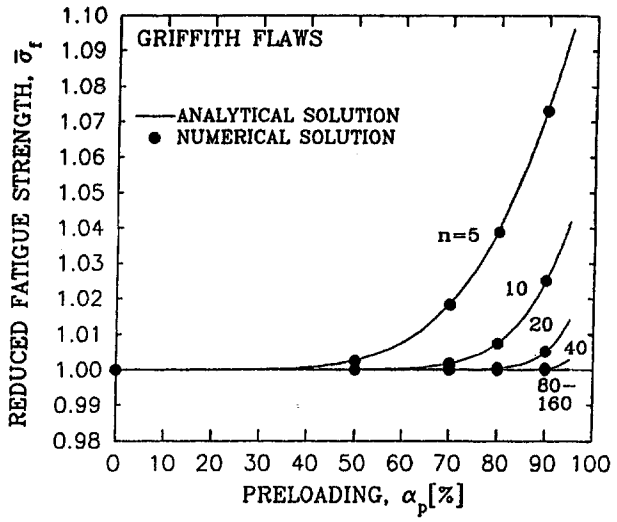

Fig. 2 The solution of reduced fatigue strength ($\bar{\sigma}_f$) as a function of preloading for different n's (solid line: analytical solution; dot: numerical solution)

$$\sigma_{fp} = \sigma_{fn}\left[1 + \left(\frac{\sigma_o}{\sigma_{fn}}\right)^{n+1}\right]^{1/(n+1)} \tag{11}$$

Let

$$\bar{\sigma}_f = \frac{\sigma_{fp}}{\sigma_{fn}}; \quad \alpha_p = \frac{\sigma_o}{\sigma_{fn}} \tag{12}$$

where $\bar{\sigma}_f$ is the "reduced" fatigue strength, in which the fatigue strength with preloading (σ_{fp}) is normalized with respect to the fatigue strength with zero preloading (σ_{fn}). α_p is the preloading factor ($0 \leq \alpha_p < 1$), where the preloading stress σ_o is normalized with respect to the fatigue strength with zero preloading σ_{fn}. Hence, the reduced fatigue strength simply becomes

$$\bar{\sigma}_f = (1 + \alpha_p^{n+1})^{1/(n+1)} \tag{13}$$

When $\alpha_p = 0$, in which no preloading is applied, Eq. (13) reduces to unity, which is the case for Eq. (6). Equation (13) shows that the reduced fatigue strength depends on two variables, fatigue parameter n and preloading factor α_p.

Equation (13) is depicted in Fig. 2. This figure shows that the effect of preloading on the reduced fatigue strength becomes dominant with decreasing fatigue parameter. For example, at a preloading of 90 percent ($\alpha_p = 0.9$), $\bar{\sigma}_f = 1.0736$ and 1.0251, respectively, for $n = 5$ and 10; whereas, $\bar{\sigma}_f = 1.0049$, 1.0001, 1.0000, and 1.0000, respectively, for $n = 20$, 40, 80, and 160. This means that for $n \leq 10$ the effect of preloading on dynamic fatigue strength is not negligible (although small) with an increase in fatigue strength by 7.36 and 2.51 percent, respectively, for $n = 5$ and 10. For $n \geq 20$, the effect is negligible, with a maximum increase by 0.49 percent occurring at $n = 20$. Therefore, a preloading up to 90 percent does not have any significant influence on dynamic fatigue strength of most glass and ceramic materials, since those materials, in general, exhibit $n \geq 20$ at room temperature.

Numerical Solution. The fact that the assumption (Eq. (7)) was made in deriving Eq. (13) and that crack growth as a function of time was not determined easily by the analytical solution prompted the use of numerical procedures to find related exact solutions. The differential equation of slow crack growth, Eq. (1), can be solved numerically to determine the effect of preloading on fatigue strength as well as on crack growth behavior. To minimize having to specify several parameters, it is convenient to utilize a normalization scheme, as used

previously in the fatigue analysis of postthreshold indentation flaws [17] and subthreshold flaws [18]. With reference to the previous studies [17, 18], the normalized variables are introduced as follows:

$$K^* = \frac{K_I}{K_{IC}}; \quad J = \frac{A}{a_{fi}}t; \quad \sigma^* = \frac{\sigma_a}{S_i};$$

$$C^* = \frac{a}{a_{fi}}; \quad \dot{\sigma}^* = \frac{\sigma^*}{J} \tag{14}$$

where K^*, J, σ^*, C^*, and $\dot{\sigma}^*$ are, respectively, normalized stress intensity factor, normalized time, normalized applied stress, normalized crack size, and normalized stressing rate. Using these variables, the power-law crack velocity (Eq. (1)) yields

$$\frac{dC^*}{dJ} = [K^*]^n$$

$$K^* = \sigma^* C^{*1/2}$$

$$\sigma^* = \dot{\sigma}^* J + \sigma_o^* \tag{15}$$

where σ_o^* is the normalized preloading stress, which has the following relation (see also Eq. (12)):

$$\alpha_p = \frac{\sigma_o^*}{\sigma_{fn}^*} \equiv \frac{\sigma_o}{\sigma_{fn}} \tag{16}$$

with σ_{fn}^* being a normalized fatigue strength with zero preloading. A solution of the differential equation in Eq. (15) in terms of the normalized variables such as failure time, fatigue strength, and critical crack size can be obtained by stepwise numerical integration using a fourth-order Runge–Kutta method. The initial condition was taken to be $C^* = 1$ at $J = 0$ and the instability condition was $K^* = 1$ and $dK^*/dC^* > 0$.

The solution procedure was first initiated to determine the normalized fatigue strength with zero preloading (σ_{fn}^*) as a function of normalized stressing rate ($\dot{\sigma}^*$) for the selected values of $n = 5$–160. A range of $\dot{\sigma}^* = 1.0 \times 10^{-2}$ to 1.0×10^{-7} was used. The normalized fatigue strength with preloading (σ_{fp}^*) was then determined for a given n as a function of normalized preloading stress (σ_o^*), ranging from $\alpha_p = 0.5$ to 0.9. This procedure was continued for the values of $n = 5$ to 160. The input variable σ_o^* was calculated using Eq. (16) with the known α_p and σ_{fn}^*.

The result of the numerical solution is shown in Fig. 2 in which the analytical solution is also included. As seen in the figure, excellent agreement is found between the two solutions, confirming the accuracy of each solution. This also indicates that the assumption (Eq. (7)) that was made in deriving both the dynamic fatigue (Eq. (6)) and the preloading (Eq. (13)) equations can be extended to fatigue parameters, $n \geq 5$.

Based on the solution obtained, several conclusions can be drawn. The use of preloading up to 90 percent gives rise to a maximum inaccuracy of 2.5 percent in dynamic fatigue strength for $n \leq 10$. For glass and ceramics that usually exhibit $n \geq 20$, it results in only 0.5 percent. Of course, the less preloading the higher accuracy. The simple analytical solution of Eq. (13) thus provides an excellent tool of dynamic fatigue test methodologies with which a considerable amount of testing time can be saved through an appropriate choice of preloading. Experimental confirmation is needed and will be discussed in the next sections.

Experimental Procedure

Dynamic fatigue (constant stress-rate) experiments were conducted to verify the analytical and numerical solutions. Soda-lime glass slide specimens and alumina flexure beam specimens were tested at room temperature in distilled water. Controlled surface flaws were used for the glass specimens to minimize the ambiguity associated with low Weibull modulus typical of glass. This was achieved by using microindentation flaws produced on specimen surfaces by a Vickers microhardness indenter. The soda-lime glass specimens (Product #2954-F, Erie Scientific Co., Portmouth, NH) measuring 75 mm (length) × 25 mm (width) × 1.2 mm (thickness) were annealed at 520°C in air for 20 h to remove any spurious residual stress. After annealing, the center of the tensile surface of each specimen was indented in air with a Vickers microhardness indenter (Model 3212, Zwick, Germany) for about 15 s with one of the indentation diagonals aligned along the direction of the prospective tensile stress of the specimen. An indentation load of 19.6 N was used.

After indentation the indented specimens were annealed at 520°C in air for 20 h to eliminate residual contact stress produced by indentation [19] and thus to obtain residual stress-free flaw configurations. Dynamic fatigue testing of the indented-and-annealed specimens was carried out using an electromechanical testing machine (Model 8562, Instron Co., Canton, MA) with a four-point bend fixture with 20 mm inner and 40 mm outer spans. Five different actuator speeds from 5 mm/min to 0.0005 mm/min were employed using a position-controlled mode. A total of six specimens were used at each actuator speed. This "regular" dynamic fatigue testing was required to obtain both fatigue parameter n and fatigue strength with zero preloading. Additional dynamic fatigue tests at actuator speeds of 0.05, 0.005, and 0.0005 mm/min were performed to determine the influence of preloading on fatigue strength. Four preloadings of 50, 70, 80, and 90 percent were used at each actuator speed. The magnitudes of preloading at each actuator speed were calculated based on the average fatigue strength with zero preloading obtained for the same actuator speed. Five specimens were used at each preloading condition.

Dynamic fatigue testing was conducted for as-machined 96 wt % alumina flexure beam specimens (ALSIMAG 614, G.E. Ceramics, Laurens, SC) by using a four-point flexure fixture with 20/40 mm spans and using the same testing machine that was used for the glass specimens. The nominal dimensions (width × height × length) of the test specimens were 4 × 3 × 45 mm, respectively. Seven different stressing rates from 0.2 MPa/min to 200,000 MPa/min were applied in a load-controlled mode. A total of ten specimens were used at each stressing rate. Preload tests were conducted at two different stressing rates (0.2 and 2 MPa/min). Five preloads ranging from 50 to 90 percent were used at each stressing rate with a total of four specimens at each preload condition. Since the coefficient of variation in fatigue strength of this material was found to be less than 5 percent, the number of test specimens used in this series of preloading tests was considered to be reasonable for reliable fatigue strength data.

Results and Discussion

Experimental Results

Glass Specimens. The dynamic fatigue results for the indented-and-annealed glass specimens with natural flaw configurations are presented in Fig. 3, where mean fatigue strengths ($\log \sigma_f$) are plotted as a function of applied actuator speed ($\log \dot{x}$) based on Eq. (6). (Note that $\dot{\sigma}$ is a linear function of $\dot{x}$ for an infinite body containing a crack so that the fatigue parameter n remains unchanged, using either $\dot{\sigma}$ or $\dot{x}$). A decrease in fatigue strength with decreasing actuator speed (or stressing rate), which represent fatigue susceptibility, was evident in the range of actuator speeds employed. The fatigue parameter n can be determined from the slope of Fig. 3 by a regression analysis of $\log \sigma_f$ versus $\log \dot{x}$ using Eq. (6). A value of $n = 17.1 \pm 0.5$ was obtained. The correlation coefficient was found to be

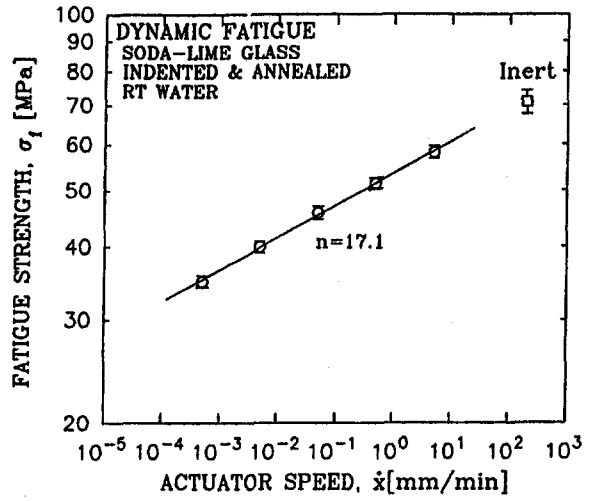

Fig. 3 Dynamic fatigue results of indented-and-annealed soda-lime glass specimens in room-temperature distilled water with zero preloading. The solid line represents the best-fit line based on Eq. (6). Error bar shows one standard deviation.

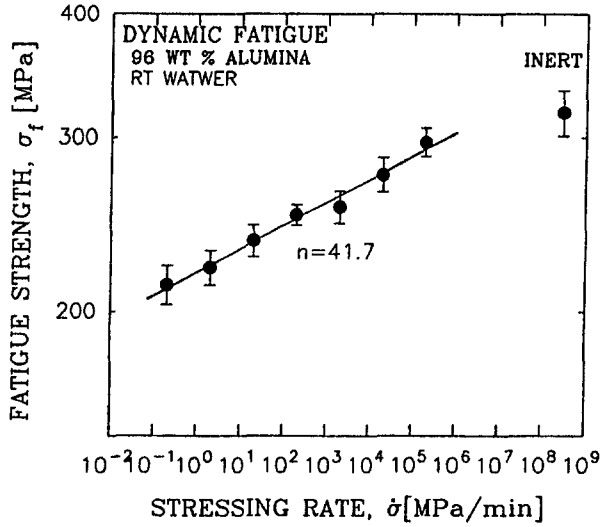

Fig. 5 Dynamic fatigue results of as-machined 96 wt % alumina flexure specimens in room-temperature distilled water with zero preloading. The solid line indicates the best-fit line based on Eq. (6). Error bar represents one standard deviation.

≥ 0.999, showing an excellent data fit to the dynamic fatigue equation.

The influence of preloading on dynamic fatigue strength for the indented-and-annealed specimens is shown in Fig. 4, where dynamic fatigue strength are plotted against preloading (α_p) for three different actuator speeds. The horizontal line represents the dynamic fatigue strength with zero preloading obtained at each actuator speed. No significant variation in fatigue strength with preloading can be found.

96 wt % Alumina Specimens. The dynamic fatigue results for the as-machined 96 wt % alumina specimens are depicted in Fig. 5. A value of $n = 41.7 \pm 2.3$ was obtained with a correlation coefficient of >0.990. The resulting plots of preloading tests are shown in Fig. 6. Similar to the results obtained for the glass specimens, no significant variation in fatigue strength with preload can be observed at both stressing rates studied.

Comparison With Theoretical Solution. A comparison of the solution with the experimental data can be made if dynamic fatigue strength with preloading is normalized with respect to the dynamic fatigue strength without preloading at each actuator speed (or stressing rate), thereby obtaining $\bar{\sigma}_f$ in accordance with Eq. (13) or Fig. 2. The resulting plots for the soda-lime glass and the alumina specimens are presented in Fig. 7. The theoretical line was also included for each material, determined based on Eq. (13) with fatigue parameter n.

The average reduced fatigue strengths obtained from the soda-lime glass and the alumina specimens in a range of preloadings from 50 to 90 percent were $\bar{\sigma}_f = 1.007 \pm 0.023$ and $\bar{\sigma}_f = 1.001 \pm 0.018$, respectively. This indicates that despite a little scatter in the fatigue strength data, preloading did not have any significance influence on dynamic fatigue strength up to a preloading of 90 percent, consistent to the analytical solution. The somewhat higher strength scatter exhibited for the glass specimens, compared with the analytical solution, might be attributed to a change in crack tip morphologies from one configuration to another upon annealing.

Based on the comparison made between the solution and the experimental data, it is concluded that theory agrees very well

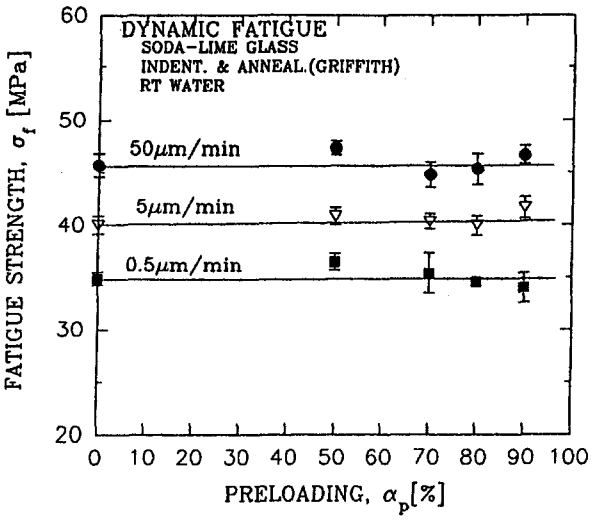

Fig. 4 Dynamic fatigue strength of indented-and-annealed soda-lime glass specimens as a function of preloading for different actuator speeds. Error bar indicates one standard deviation. Each solid line shows the fatigue strength with zero preloading at each actuator speed.

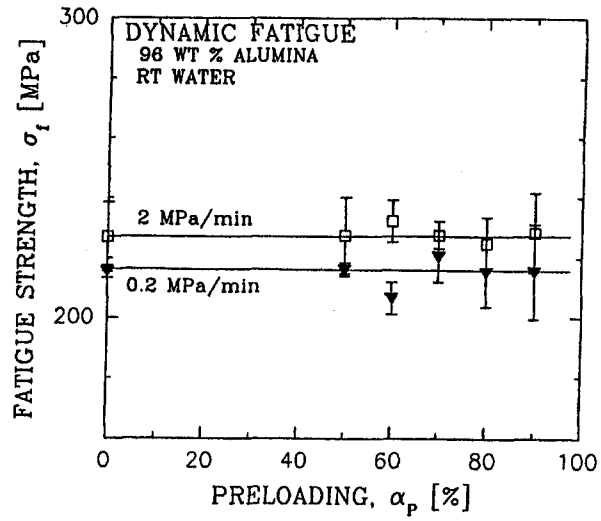

Fig. 6 Dynamic fatigue strength of as-machined 96 wt % alumina flexure specimens as a function of preloading for different stressing rates. Error bar indicates one standard deviation. The solid line represents the fatigue strength with zero preloading.

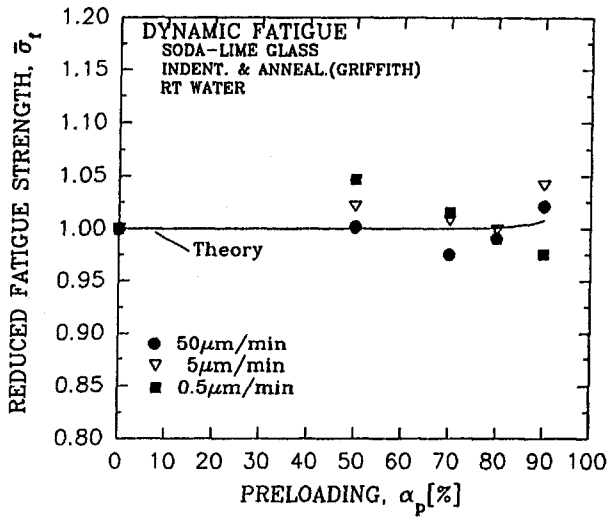

(a)

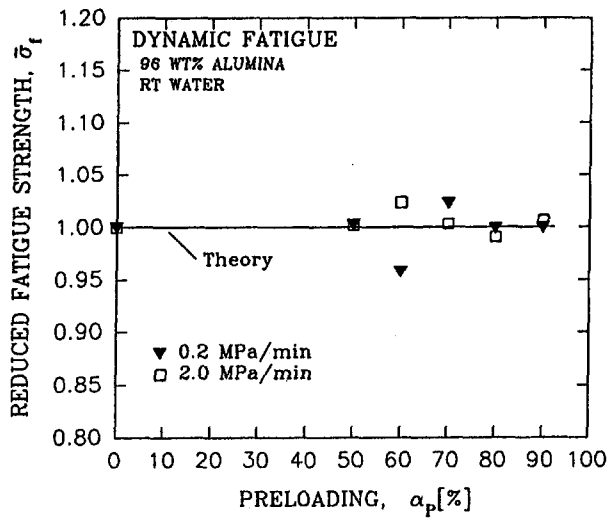

(b)

Fig. 7 "Reduced" fatigue strength (σ_f) as a function of preloading: (*a*) soda-lime glass; (*b*) 96 wt % alumina. Each solid line in the figure represents the analytical solution.

with the experimental data and that the developed theory could be extended to any materials that exhibit slow crack growth as a governing failure mechanism. The reason for the insensitivity of dynamic fatigue strength to preloading can be understood easily if one considers how a crack grows under dynamic fatigue loading conditions.

Crack Growth Behavior. Figure 8 shows the normalized crack size (C^*) as a function of normalized time (J) for the natural flaw system subjected to dynamic fatigue with zero preloading. The data in the figure were obtained numerically for $\dot{\sigma}^* = 1.0 \times 10^{-5}$ with fatigue parameters of $n = 5$ to 80. Due to increased fatigue susceptibility, crack growth is dominant with decreasing n, resulting in shorter failure time and consequently lower fatigue strength. It is very important to note that the initial crack ($C^* = 1.0$) grows very little during most of testing time, but grows instantaneously close to and/or at the failure time at which dynamic fatigue strength is defined. This phenomenon is more enhanced with increasing fatigue parameter, as seen in the figure. Therefore, it is evident that the nature of this *long "incubation" time* of an initial crack is a key aspect that makes the preloading technique feasible in dynamic fatigue.

Implications

The most direct and powerful effect of preloading is the saving of test time. For example, if it takes about 7 h in dynamic fatigue testing at a certain low stressing rate (say, 2 MPa/min) to test one specimen of silicon nitride whose strength is 800 MPa, and if a minimum of 20 specimens is required to obtain reliable statistical data, then the total test time would be 140 h. But if a preloading of 80 percent is applied, the total testing time would be reduced to only 28 h so that 80 percent of the total test time can be saved. And 70 percent saving for a preloading of 70 percent, and so on. This is a tremendous amount of time saving, which gives a great impact on testing economy. The test time, excluding any preparation time, as a function of preloading in conjunction with fatigue parameter (n) is derived as follows.

The dynamic fatigue equation of Eq. (6) is rewritten

$$\sigma_f = \Gamma[\dot{\sigma}]^{1/(n+1)} \tag{17}$$

where

$$\Gamma = [B(n+1)S_i^{n-2}]^{1/(n+1)} \tag{18}$$

At failure ($t = t_f$), the fatigue strength is

$$\sigma_f = t_f \dot{\sigma} \tag{19}$$

Equating these two equations and solving for failure time t_f, one can obtain

$$t_f = \Gamma[\dot{\sigma}]^{-n/(n+1)} \tag{20}$$

It is a general practice to use three to five stressing rates that could be related as follows:

$$\dot{\sigma}_1 = \alpha\dot{\sigma}_2 = \beta\dot{\sigma}_3 = \gamma\dot{\sigma}_4 = \ldots \quad 1 < \alpha < \beta < \gamma < \ldots \tag{21}$$

Then, the total test time (t_{ft}) with several different stressing rates is

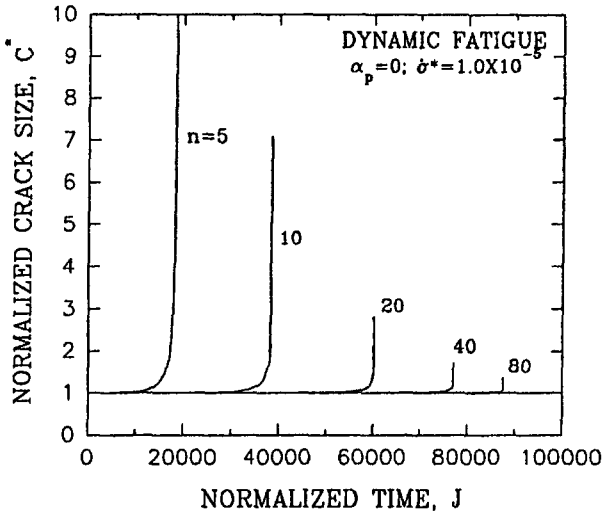

Fig. 8 Numerical solutions of normalized crack size (C^*) as function of normalized time (J) for a normalized stressing rate of $\dot{\sigma}^* = 1.0 \times 10^{-5}$ for different n's

$$t_{ft} = t_{f1} + t_{f2} + t_{f3} + t_{f4} + \ldots$$
$$= \Gamma\dot{\sigma}_1^{-n/(n+1)}\left[1 + \left(\frac{1}{\alpha}\right)^{-n/(n+1)} + \left(\frac{1}{\beta}\right)^{-n/(n+1)} + \left(\frac{1}{\gamma}\right)^{-n/(n+1)} + \ldots\right] \quad (22)$$

For convenience, let $\bar{t}_f \equiv$ normalized total test time, which is defined as:

$$\bar{t}_f = [\dot{\sigma}_1^{n/(n+1)}\Gamma^{-1}]t_{ft} \quad (23)$$

Then, the normalized total test time yields

$$\bar{t}_f = 1 + \left(\frac{1}{\alpha}\right)^{-n/(n+1)} + \left(\frac{1}{\beta}\right)^{-n/(n+1)} + \left(\frac{1}{\gamma}\right)^{-n/(n+1)} + \ldots. \quad (24)$$

Figure 9 shows the normalized test time as a function of fatigue parameter n for four different stressing rates with $\alpha = 10$, $\beta = 100$, and $\gamma = 1000$, which is the general order of magnitudes used in dynamic fatigue testing. For convenience, $\dot{\sigma}_1$ was taken to be unity (=1.0 MPa/min). As seen in the figure, test time depends on both stressing rate and n. The effect of n on total test time is more sensitive at lower fatigue parameters of $n \leq 100$. It is also shown in the figure that most of the test time is consumed at the lowest stressing rate so that the contribution of preloading is maximized when the preload is applied at the lowest stressing rate. Figure 10 shows the plots of normalized total test time as a function of fatigue parameter, n, for different levels of preloads ranging from 50 to 90 percent, where the preload was applied at all four stressing rates. A dramatic time saving corresponding to the applied preloading percentage can be attained.

With the proper use of preloading in conjunction with Eq. (13) (or Fig. 2), a considerable time saving can be achieved. However, it should be noted that an appropriate selection of preloading is also dependent upon the scatter of strength data (Weibull modulus) and that care should be taken particularly for the material with low Weibull modulus ($m \leq 10$) when one intends to use higher preloading ≥85 percent [20]. It is suggested that an approximate average fatigue strength for a given stressing rate be pre-estimated using at least three to five specimens in conjunction with strength scatter (Weibull modulus) to determine the preload value to be used. The technique can also be extended to high-temperature dynamic fatigue testing as far as one governing mechanism, slow crack growth, is associated with failure. Several failure mechanisms such as slow crack growth, creep, and oxidation can occur simultaneously at higher temperatures (≥1200°C) and at lower stressing rates (≤2 MPa/min), which makes it difficult to distinguish the controlling failure mechanism. It has been shown that the application of preloading at high temperatures can give some clues to pinpoint the prevailing mechanism associated with failure [21].

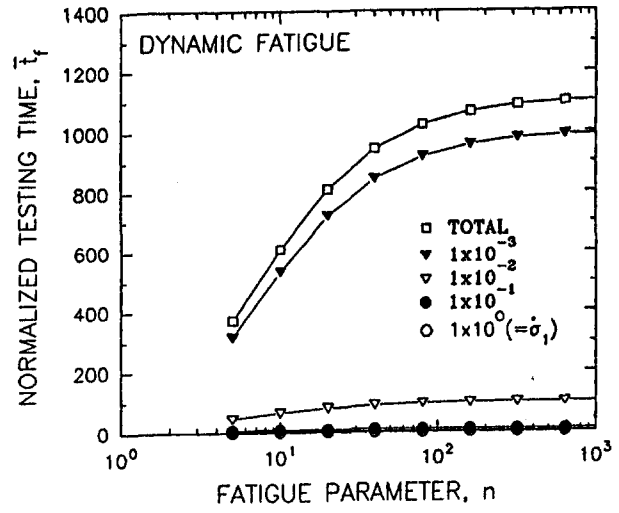

Fig. 9 Normalized testing time ($\bar{t}_f$) as a function of fatigue parameter (n) for four different stressing rates (α = 10; β = 100; γ = 1000; $\dot{\sigma}_1$ = 1 (MPa/min))

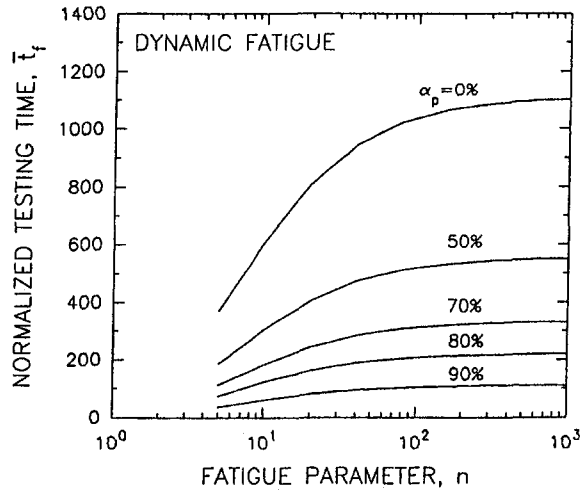

Fig. 10 Normalized total testing time as a function of fatigue parameter (n) for different levels of preloads ranging from 0 to 90 percent (α = 10; β = 100; γ = 1000; $\dot{\sigma}_1$ = 1 (MPa/min))

Conclusions

The analytical and numerical solution of dynamic fatigue strength as a function of preloading was obtained. The effect of preloading on dynamic fatigue strength depends on fatigue parameter (n) and preloading. The effect is diminished for increasing fatigue parameter such that $n \geq 20$. For $n \geq 20$ (common to most of glass and ceramic materials at room temperature) the dynamic fatigue strengths with a preloading of 90 percent resulted in only 0.5 percent higher than that with no preloading. The solution was verified by dynamic fatigue experiments with different preloadings using soda-lime glass and 96 wt % alumina flexure specimens. This indicates that one can apply a preloading up to 90 percent in dynamic fatigue testing for most brittle materials, resulting in a considerable amount of test time saving. The application of preloading technique is feasible due to the fact that most of slow crack growth under dynamic fatigue loading takes place close to failure time where the dynamic fatigue strength is defined.

Acknowledgments

The authors are grateful to R. Pawlik for the experimental work. This work was sponsored in part by the Ceramic Technology Project, DOE Office of Transportation Technologies, under contract DE-AC05-84OR21400 with Martin Marietta Energy System, Inc.

References

1 Wiederhorn, S. M., and Bolz, L. H., "Stress Corrosion and Static Fatigue of Glass," *J. Am. Ceram. Soc.*, Vol. 53, 1970, pp. 543–548.

2 Evans, A. G., and Wiederhorn, S. M., "Crack Propagation and Failure Prediction in Silicon Nitride at Elevated Temperatures," *J. Mater. Sci.*, Vol. 9, 1974, pp. 270–278.

3 Hubner, H., and Jillek, W., "Subcritical Crack Extension and Crack Resistance in Polycrystalline Alumina," *ibid,* Vol. 12, 1977, pp. 117–125.

4 Sakaguchi, S., Sawaki, Y., Abe, Y., and Kawasaki, T., "Delayed Failure in Silica Glass," *ibid,* Vol. 17, 1982, pp. 2878–2886.

5 Dauskardt, R. H., James, M. R., Porter, J. R., and Ritchie, R. O., "Cyclic Fatigue-Crack Growth in SiC-Whisker-Reinforced Alumina Ceramic Composite: Long- and Small-Crack Behavior," *J. Am. Ceram. Soc.,* Vol. 75, 1992, pp. 759–771.

6 Mendiratta, M. G., and Petrovic, J. J., "Slow Crack Growth From Controlled Surface Flaws in Hot-Pressed Si_3N_4," *ibid,* Vol. 61, 1978, pp. 226–230.

7 Henager, C. H., and Jones, R. H., "Environmental Effects on Slow Crack Growth in Silicon Nitride," *Ceram. Eng. Sci. Proc.,* Vol. 9, 1988, pp. 1525–1530.

8 Horibe, S., and Hirahara, R., "Cyclic Fatigue of Ceramic Materials: Influence of Crack Path and Fatigue Mechanisms," *Acta Metall. Mater.,* Vol. 39, 1991, pp. 1309–1317.

9 Ritter, J. E., "Engineering Design and Fatigue Failure of Brittle Materials," in: *Fracture Mechanics of Ceramics,* Vol. 4, Bradt, R. C., Hasselman, D. P. H., and Lange, F. F., eds., Plenum Publishing Co., New York, 1978, pp. 661–686.

10 Trantina, G. G., "Strength and Life Prediction for Hot-Pressed Silicon Nitride," *J. Am. Ceram. Soc.,* Vol. 62, 1979, pp. 377–380.

11 Govila, R. K., "Uniaxial Tensile and Flexural Stress Rupture Strength of Hot-Pressed Si_3N_4," *ibid,* Vol. 65, 1982, pp. 15–21.

12 Quinn, G. D., and Quinn, J. B., "Slow Crack Growth in Hot-Pressed Silicon Nitride," in: *Fracture Mechanics of Ceramics,* Vol. 6, Bradt, R. C., Evans, A. G., Hasselman, D. P. H., and Lange, F. F., eds., Plenum Press, New York, 1983, pp. 603–636.

13 Chuck, L., McCullum, D. E., Hecht, N. L., and Goodrich, S. M., "High Temperature Tension-Tension Cyclic Fatigue for a Hipped Silicon Nitride," *Ceram. Eng. Sci. Proc.,* Vol. 12, 1991, pp. 1509–1523.

14(*a*) Choi, S. R., Salem, J. A., and Palko, J. A., "Comparison of Tension and Flexure to Determine Fatigue Life Prediction Parameters at Elevated Temperatures," in *Life Prediction Methodologies and Data for Ceramic Materials,* ASTM STP 1201, Brinkman, C. R., and Duffy, S. F., eds., ASTM, Philadelphia, 1994, pp. 98–111; (*b*) Choi, S. R., Salem, J. A., Nemeth, N., and Gyekenyesi, J. P., "Elevated Temperature Slow Crack Growth of Silicon Nitride Under Dynamic, Static, and Cyclic Flexural Loading," *Ceram. Eng. Sci. Proc.,* Vol. 15, 1994, pp. 597–604.

15 "Standard Test Method for Determination of Slow Crack Growth Parameters of Advanced Ceramics by Constant Stress-Rate Flexural Testing at Ambient Temperature," in balloting process, ASTM C28 (Advanced Ceramics) Main Committee, American Society for Testing and Materials, Philadelphia, 1997.

16(*a*) Ritter, J. E., Oates, P. B., Fuller, E. R., and Wiederhorn, S. M., "Proof Testing of Ceramics, Part 1 Experiment," *J. Mater. Sci.,* Vol. 15, 1980, pp. 2275–2281; (*b*) Fuller, E. R., Wiederhorn, S. M., Ritter, J. E., and Oates, P. B., "Proof Testing of Ceramics, Part 2 Theory," *ibid,* Vol. 15, 1980, pp. 2282–2295.

17 Lawn, B. R., Marshall, D. B., Anstis, G. R., and Dabbs, T. P., "Fatigue Analysis of Brittle Materials Using Indentation Flaws, Part 1. General Theory," *J. Mater. Sci.,* Vol. 16, 1981, pp. 2846–2854.

18 Choi, S. R., Ritter, J. E., and Jakus, K., "Failure of Glass With Subthreshold Flaws," *J. Am. Ceram. Soc.,* Vol. 73, 1990, pp. 268–274.

19 Marshall, D. B., Lawn, B. R., and Chantikul, P., "Residual Stress Effects in Sharp-Contact Cracking: I," *J. Mater. Sci.,* Vol. 14, 1979, pp. 2001–2012.

20 Choi, S. R., and Salem, J. A., "Preloading Technique in Dynamic Fatigue Testing of Ceramics: Effect of Preloading on Strength Variation," *J. Mater. Sci. Letters,* Vol. 15, 1996, pp. 1963–1965.

21 Choi, S. R., and Salem, J. A., "Effect of Preloading on Fatigue Strength in Dynamic Fatigue Testing of Ceramic Materials at Elevated Temperature," *Ceram. Eng. Sci. Proc.,* Vol. 16, 1995, pp. 87–94.

A Technique to Achieve Uniform Stress Distribution in Compressive Creep Testing of Advanced Ceramics at High Temperatures

K. C. Liu

C. O. Stevens

C. R. Brinkman

Oak Ridge National Laboratory,
Metals and Ceramics Division,
Oak Ridge, TN 37831-6155

N. E. Holshauser
North Carolina A & T State University,
Department of Mechanical Engineering,
Greensboro, NC 27411

A technique to achieve stable and uniform uniaxial compression is offered for creep testing of advanced ceramic materials at elevated temperatures, using an innovative self-aligning load-train assembly. Excellent load-train alignment is attributed to the inherent ability of a unique hydraulic universal coupler to maintain self-aligning. Details of key elements, design concept, and principles of operation of the self-aligning coupler are described. A method of alignment verification using a strain-gaged specimen is then discussed. Results of verification tests indicate that bending below 1.5 percent is routinely achievable with the use of the load-train system. A successful compression creep test is demonstrated using a dumb-bell-shaped silicon nitride specimen tested at 1300°C for a period in excess of 4000 h.

Introduction

Design of ceramic structural components for long-term use at high temperatures requires knowledge of creep behavior in both tension and compression. Because of some experimental difficulties associated with uniaxial testing of brittle materials at elevated temperatures, bend testing methods have been used extensively to investigate mechanical properties of ceramic materials. Lack of appropriate equipment to achieve good load-train alignment, limited research material volume, low specimen cost, and ease of testing are other reasons that made bend testing methods attractive. Drawbacks are that test results do not directly yield intrinsic time-dependent material properties, such as uniaxial data obtained from specimens tested directly in tension and/or in compression. Therefore, data interpretation must be performed based on assumptions to calculate stress and strain which have been shown to be invalid under creep conditions (Anderson et al., 1975; Cohrt and Thuemmler, 1985; Chuang and Wiederhorn, 1988) because the internal stress distribution under bending changes with time, resulting in shifting of the neutral axis plane and skewing of the stress distribution.

Uniaxial tensile creep data are now commonly available, but compressive creep data are still sparse, due to lack of general interest and some experimental difficulties uniquely associated with compressive testing. Compressive specimens are usually small and short to avoid instability. This in turn produces small displacement that demands high resolution from the displacement measurement system. Nonuniform deformation occurring at the ends of the short specimen due to the barreling effect further compounds the problem.

Despite the known problems, the methods used in compressive testing remain elementary, basically using two parallel platens to compress a short cylindrical specimen (Debschütz et al., 1993). This testing method may be acceptable for testing metallic alloys, which are in general ductile. A review of compressive testing methods (Birch et al., 1976; Lankford, 1977; Sines and Adams, 1978; Tracy, 1987) and recent in-house exploratory studies reveal that conventional methods are inappropriate for testing brittle materials because advanced engineering ceramics in general exhibit much higher strength, higher elastic modulus, and lower ductility at high temperatures compared to those of metallic alloys. Therefore, a new testing technique is needed to ensure a high degree of stress uniformity as well as stability.

A new load train for compressive creep testing capable of testing ceramic materials at elevated temperature as high as 1500°C has been developed. Results of verification tests indicate that the self-aligning universal coupler (Liu and Brinkman, 1986) being adopted in the load train was capable of minimizing the deleterious specimen bending below 1.5 percent at the intended maximum loading condition. To complete the high-temperature testing capabilities, a laser-based extensometer was used to measure creep strain directly from the specimen gage section with the aid of two intricate fiducial flags attached to the specimen.

Specimens

Two types of compressive specimen are widely used: (1) a uniform-diameter cylindrical specimen, and (2) a dumb-bell-shaped specimen having a short uniform gage section, as shown in Fig. 1. The diameter of the test section varies nominally from 3 to 6 mm, and the ratio of the height (h) to diameter (d) for the uniform gage section varies also in the range 1.5 to 2.5. The advantages of using straight cylindrical specimens (Fig. 1(a)) are: (1) low cost, (2) small material volume, and (3) no need for special end fixturing. However, this type of specimen can introduce difficulties of alignment when small-diameter specimens are used to minimize applied load for high strength materials. Other problems are buckling when h/d ratio is large and barreling when the ratio is low. A small specimen diameter may indent the platens, resulting in incorrect strain measurement when extensometer rods are attached to the platens. Protective load blocks and pads are inserted between the specimen end and platen to avoid the damage.

The problems associated with cylindrical specimen testing can be overcome by using the dumb-bell-shaped specimen shown in Fig. 1(b). In this case, both ends of a straight cylinder are extended and enlarged. A smooth transition between the

Contributed by the International Gas Turbine Institute and presented at the 41st International Gas Turbine and Aeroengine Congress and Exhibition, Birmingham, United Kingdom, June 10–13. 1996. Manuscript received at ASME Headquarters February 1996. Paper No. 96-GT-341. Associate Technical Editor: J. N. Shinn.

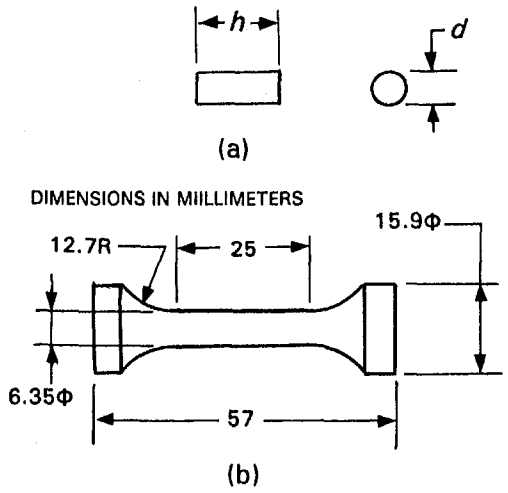

Fig. 1 Specimens used in compressive testing: (*a*) a cylindrical specimen and (*b*) a dumb-bell specimen

gage section and the enlarged end is preferred in order to minimize inherent stress concentration occurring at the end of the gage section. Ideally, a large transition radius is desirable. However, a long specimen is prone to buckling. When a small transition radius is used, the h/d ratio should be increased to ~4 so that the middle section of ~2.5d length remains uniformly stressed. A dumb-bell specimen (Fig. 1(*b*)) having an h/d ratio of 4d, a transition radius of 2d, and an end diameter of 2.5d with a total length of 57 mm (=9d), which is substantially longer than those used by others, have been successfully tested without buckling at 1300°C with an applied stress of 250 MPa. Because of the long uniform gage section, strain can be measured directly from the midportion (3d = 20 mm) of the uniform gage section.

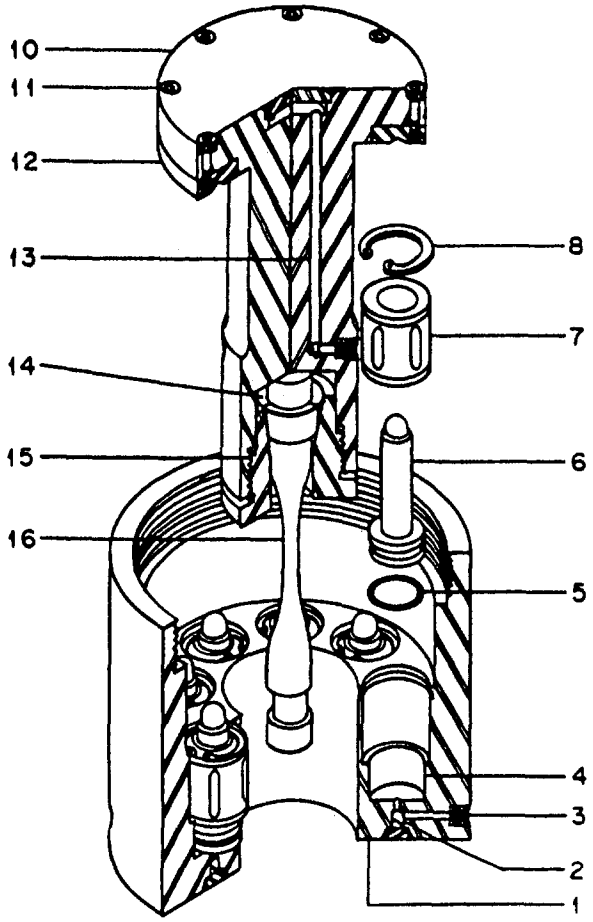

Fig. 2 Details of the self-aligning universal coupler used in tensile testing

Self-Aligned Load Train for Compressive Testing

A self-aligned load train has been successfully developed for uniaxial tensile testing of brittle materials at high temperatures. Key to the successful development is the in-house developed hydraulic universal coupler (Fig. 2), which is capable of self-aligning its central axis unambiguously with the load-train axis. The self-aligning universal coupler is also utilized in the load-train for compression testing. Therefore, a brief description of internal mechanisms, operational features, and principles of operation may facilitate later discussions.

The universal coupler consists basically of two major components: a hydraulic housing assembly (1) and a pull rod assembly (10). The pull rod assembly is turned over in the reversed direction and used as a push rod for compression testing. Inside the housing block (1) are eight built-in miniature hydraulic piston assemblies equally spaced on a circle. The cutout view of a hydraulic piston assembly shows an O-ring seal (5) and a piston (6) with a long stem being guided by a ball-bearing bushing (7). At the bottom of the oil chamber (4) is a vertical hole connected to a manifold (2). The oil chambers are therefore interconnected by the manifold. The piston assembly is secured in place by a snap ring (8), as shown in the front assembly near the lower end of the specimen (16).

For tensile testing, a buttonhead specimen (16) is directly connected to the metal pull rod assembly (10), using tapered split collets (14) and a matching metal plug (15). This gripping method provides good concentricity between the pull rod and specimen and reliable specimen gripping. A concentrically V-grooved circular ring (12) made of tempered steel is attached to the rod side of the disk head (10) by eight small screws (11). The tensile load train is assembled by slipping the pull rod assembly into the center hole of the housing with the grooved ring (12) resting on the piston-rod ends. A cover plate (not shown) completes the assembly. For tensile testing, two couplers are required, one at each end of the specimen.

The universal coupler is designed based on basic principles of hydrostatics and mechanics. To describe the operational principle, a schematic diagram shown in Fig. 3 will be employed. The center arrow "P" represents the specimen load, which is counterbalanced by a circular array of short arrows labeled R_1, R_2, . . . , R_8 symbolizing reacting forces of the eight piston assemblies. Two conditions must be met in order to achieve perfect concentric loading (i.e., zero eccentricity $\delta_x = \delta_y = 0$).

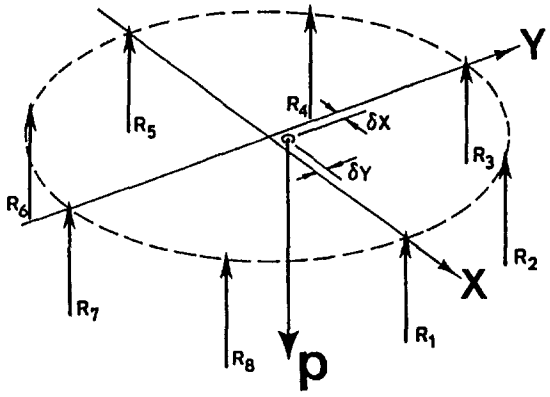

Fig. 3 A schematic diagram illustrating the design concepts of the self-aligning universal coupler shown in Fig. 2

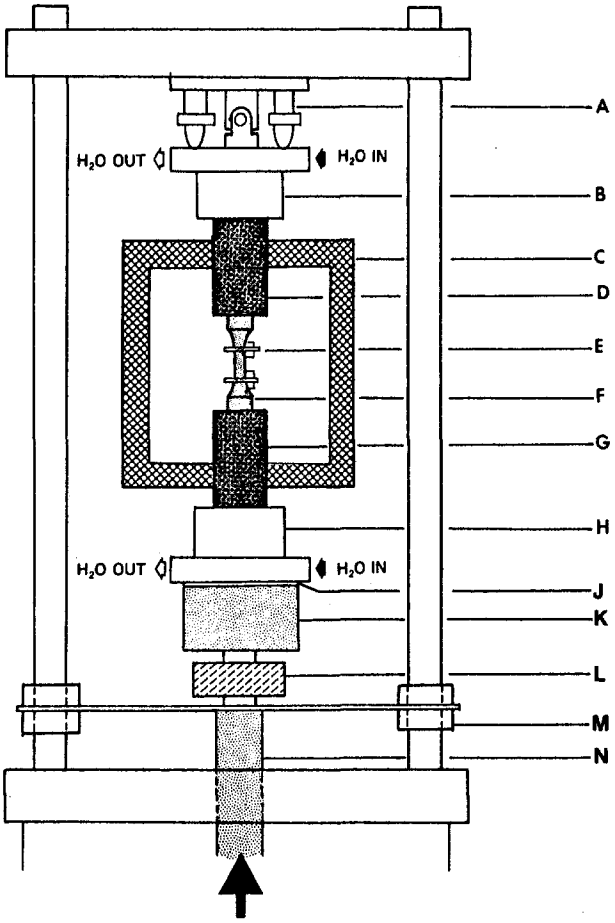

Fig. 4 A schematic diagram of a load-train assembly for compressive testing of ceramic materials at high temperatures

The first condition requires that all reacting forces must be equal in magnitude. Since the pistons are hydraulically interconnected through the manifold, the specimen load "P" must be equally distributed to all of the pistons. The second condition requires that the reaction forces representing the positions of the pistons must be equally spaced on a circle. Any deviations from the ideal conditions result in some eccentricity. A previous evaluation indicated that an eccentricity less than 25 μm can be achieved.

A schematic of a load-train assembly is shown in Fig. 4 (parts identified by letters) for compressive creep testing of ceramic materials at high temperatures. For compression testing, the pull rod assembly (part 10 in Fig. 2) is turned over and used as a push rod. To seat the disk head concentrically on the piston assembly, the V-grooved ring (J, part 12 in Fig. 2) is attached to the flat side of the disk head. For elevated temperature testing use, the long metallic pull rod is shortened almost to the root and used as a compression anvil (H), which secures a ceramic push rod (G) having a diameter of 32 mm.

Only a single universal coupler (K) is used in the load train for compression testing. The universal coupler is directly connected to a load cell (L), which in turn is connected to a ram rod (N). To maintain the axiality of the ram rod, a guide bar (M) is attached directly below the load cell. The guide bar has a teflon bushing at each wing guided by the load posts. The top push rod assembly (B and D) is the same as the bottom assembly, except that the upper compression anvil (B) is connected to the upper platen by a mechanical universal joint and leveled by four turnbuckles (A) spaced equally on a circle. The upper push rod assembly is aligned with the lower assembly with the aid of a strain-gaged dummy specimen. The method of alignment will be discussed later. The compression specimen (F) is seated concentrically with both push rods using a centering cup not shown in Fig. 4. Only the specimen and part of the ceramic push rods are enclosed in the furnace (C), and both of the compression anvils are water-cooled.

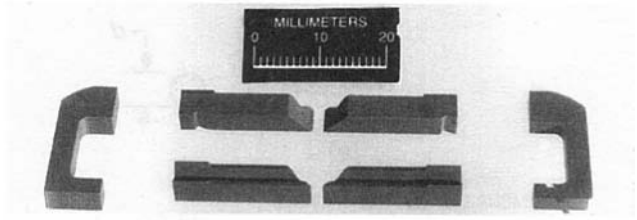

Fig. 5 Disassembled fiducial flags, showing an extra pair of wedge parts for detail

Optical Extensometer

Compression strain is measured using a commercial laser-based optical extensometer (LaserMike Model 162-100) capable of 0.3 μm resolution and accuracy of 1 μm for applications in ambient temperature. However, both the resolution and accuracy degrade as temperature increases in the range above 1000°C. The extensometer measures the clearance between the two fiducial flags (E, short vertical pieces) attached to the side of the gage section and held by a C-shaped clip (E, horizontal piece) visible in Fig. 4. Two pairs of the fiducial flags and a pair of C-clips are shown in Fig. 5. Both the flags and C-clips are preferably made of the specimen material or the same type of ceramic material. One end of the flag is beveled, and the side to be mounted on the specimen is V-grooved, as shown in the bottom set of flags. Ridges on both sides of the groove are ground from the beveled end to ~3 mm from the unbeveled end. The unground section is directly attached to the gage section of the test specimen. With the aid of the V-groove, the flags can be secured rather easily on a curved surface and aligned with the specimen axis. A shallow notch is provided at the back side of the high ridges, visible in the other set of the flags shown in Fig. 5, to facilitate the final step of installation by the C-clip that clamps the flag on the specimen. The distance between the midpoints of the high ridge section is defined as the gage length, and the average strain within the gage section is calculated from the change of the gage length, i.e., the change of the clearance between the flags.

A schematic diagram of a laser-based extensometer is shown in Fig. 6. A light source generates a collimated laser beam, which scans vertically from the bottom up to form a thin ribbon of laser light passing through a slit cut in the furnace wall and then the centerline of the flags. The light passing through the opening between the flags exits through a second slit and falls

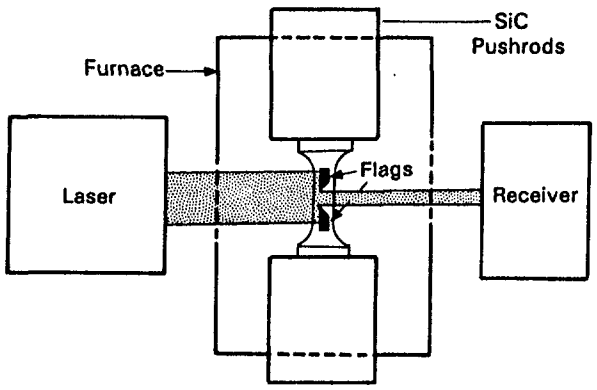

Fig. 6 A schematic diagram of a laser-based optical extensometer

on a photodetector positioned behind the specimen. The time required to sweep across the opening between the two flags and the sweeping speed determine the size of the opening. It must be noted that strain is calculated from the change of the opening size with respect to the gage length defined in the preceding section. Because the strain is measured on one side of the specimen, stringent specimen alignment is required to warrant the accuracy of strain measurement.

Alignment of Load-Train Assembly

Inherent problems associated with compressive testing such as (1) nonparallel specimen ends, (2) nonparallel compression interfaces, (3) off-center specimen seating, and (4) buckling are all related to load-train alignment. Off-center specimen seating can be largely eliminated by the use of a shallow centering cup having a concentric hole in the bottom. The cup fits snugly on the end of the push rod and the center hole seats the specimen. The following procedure is intended to correct the nonparallel compression interfaces in order to avoid specimen bending and eventual buckling failure. The use of a strain-gaged verification specimen with slightly nonparallel ends (or angularity) will be discussed later.

Alignment of the load train was accomplished in two steps. First, preliminary alignment was performed with a short cylindrical block having the same diameter as the ceramic push rods and the same height as a compressive test specimen (32 mm diameter by 32 mm length). With the cylinder being lightly compressed between the two push rods, reasonably good alignment can be achieved by adjusting the four turnbuckles (part A in Fig. 4). Alignment of the push rods was checked with a long steel ruler (~0.5 m long) having a straight edge. At this juncture, the alignment was still coarse and needed improvement. Misalignment was indicated when a light thrust applied to the side of the cylinder caused it to swing out of the load-train assembly. The rotational axis indicated the location of the lowest point between the two compressive interfaces. This information was used to bring the push rods in alignment by adjusting the turnbuckles. The procedure was repeated until the cylinder virtually locked in the center position.

Following the preliminary alignment, a fine alignment must be performed with a strain-gaged dummy specimen. A dummy specimen having the same geometry as the compressive specimen was fabricated from a high-strength 7075-T6 aluminum. Four strain gages were instrumented on the surface of the gage section at the midlength and equally spaced around the circumference.

To minimize the specimen and strain gage biases, the load train is usually aligned and checked with the strain-gaged specimen being rotated through a complete 360 deg cycle at a 90 deg increment, as outlined in ASTM Standard Test Methods C1273-94 (ASTM, 1995). To facilitate the following discussion, four fixed positions were assigned to the upper push rod as "A, B, C, and D." The side facing an observer standing in front of the load train was designated as position A, and the far side from the observer as position C. The side facing toward the right side of the observer was designated as position B, and the opposite side as position D. To avoid confusion, numbers from 1 to 4 were used to designate the strain gages, with No. 1 being selected arbitrarily and the others following the position sequence.

The first alignment verification test was initiated with gage No. 1 at position A, gage No. 2 at position B, and so forth. The dummy specimen was loaded to ~2.2 kN, which was well within the elastic range of the material, and four sets of load-strain data were acquired simultaneously as the specimen was loaded and unloaded. The alignment test was repeated each time the specimen was rotated 90 deg. The acquired data were then analyzed to determine the location where the line of resultant force intersects with the strain gage plane, as shown in Fig. 7.

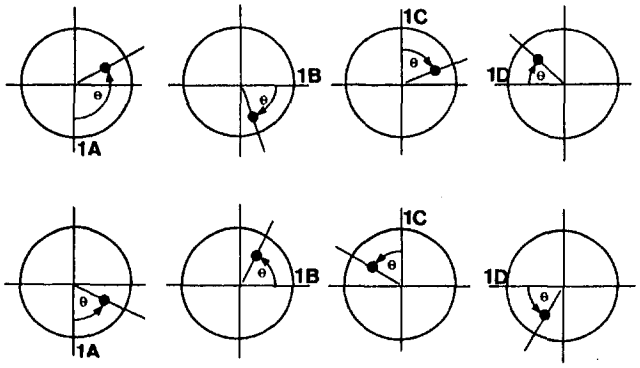

Fig. 7 Top row indicates nonparallel interfaces; bottom row indicates reasonably good parallel interfaces. "1A, 1B, 1C, and 1D" indicate gage No. 1 oriented to positions A, B, C, and D, respectively

The eccentricity, i.e., the distance between the resultant force and the center axis of the specimen (coordinate origin), is exaggerated in Fig. 7 for illustrative purpose.

When the resultant force is located indiscriminately on different quadrants as the alignment specimen rotates, as illustrated in the top row of Fig. 7, the indication is that the load train is not properly aligned. Ideal alignment would be when the resultant force is on the coordinate origin regardless of the specimen orientation. This situation would rarely occur unless the verification specimen is geometrically flawless and the strain gages are identical and bonded precisely 90 deg apart.

The geometric integrity of a verification specimen is often unchecked and used as unblemished. Although extreme care may have been exercised during specimen machining, handling, and inspection, imperfection could remain undetectable by instruments such as a shadowgraph, which has its own limitations in resolution and accuracy. Therefore, it is prudent to assume that an extremely small angularity may exist between the ends of a verification specimen. Despite the defect, it is possible to eliminate the effect of nonparallel specimen ends when the load-train is being aligned.

A personal computer (PC) program capable of data acquisition and alignment analysis has been developed, allowing a user to easily recognize various possible conditions of nonparallel compression interfaces. This program is intended to facilitate identification of the tilt of the upper compression interface and to assist in adjusting the four turnbuckles above the fixed compression anvil. This process is repeated as the specimen is rotated through the four positions. When load-train alignment is completed, the resultant force should locate on each of the four quadrants as illustrated in the bottom row of Fig. 7, showing approximately equal amounts of eccentricity and the same angular position with respect to gage No. 1.

Figure 8 shows the load-strain response curves for the four strain gages with gage No. 1 oriented at position A. All strain readouts were reset to zero at load-free condition. The initial diversion of strain readouts at 0.25 kN indicated that the ends of the verification specimen were slightly nonparallel. The curves beyond 0.75 kN are virtually linear and parallel to each other, indicating that the specimen was uniformly compressed.

Bending strain in terms of percentage of the average strain at each level of loading was calculated and plotted in Fig. 9. Four alignment evaluations were performed with gage No. 1 oriented to four different positions as indicated. A high percentage of bending at low loads is due to the low average strain. Since the amount of eccentricity will cease to increase when both ends of the verification specimen become parallel, the percentage of bending should, in theory, approach a small number as load increases. Figure 9 shows that the percentage of bending decreased to <5 percent as loads exceed 1.75 kN, which meets the condition recommended for uniaxial tensile

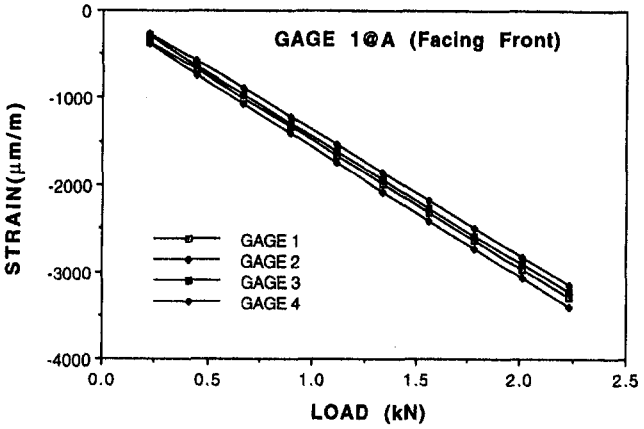

Fig. 8 Load-strain response curves for four strain gages with gage No. 1 oriented toward position A

testing per ASTM-C1273-94. The intrinsic eccentricity that excludes the effects of specimen imperfection was then calculated using linearized test data, which show that the load train is capable of uniform compressive loading with low bending less than 1.5 percent.

Test Results and Discussion

A grade of hot-isostatically-pressed silicon nitride ceramic, engineered and marketed commercially as GN-10 by AlliedSignal Ceramic Components, Torrance, California, was tested in compressive creep. Results of a compressive creep test at 1300°C are shown in Fig. 10, which also shows previously reported tensile creep data (Ding et al., 1994) for comparison. Under an applied stress of 125 MPa, the tensile creep specimen ruptured in 15.2 h of testing with a creep rate of 3.76×10^{-4} h^{-1} shortly before failure. The creep rate under the same stress in compression became reasonably steady after completing ~100 h of testing with a creep rate of 5.33×10^{-7} h^{-1}, which was about three orders of magnitude lower than that under tension. The compressive stress was increased intermittently in steps of 25 MPa each time the specimen completed a period of discernible steady-state creep. The creep behavior during the second leg of testing at −150 MPa was slightly erratic but the trend of creep deformation was discernible. Transient creep was observable following each load increment. Currently, the specimen has just completed a period of ~1500 h of testing at 250 MPa with a creep rate of $\sim 1.07 \times 10^{-6}$ h^{-1}. Cursory examination indicated that the creep rate increased proportionally with the applied stress, suggesting that creep of Si_3N_4 under compression may be promoted by a shearing mechanism. No

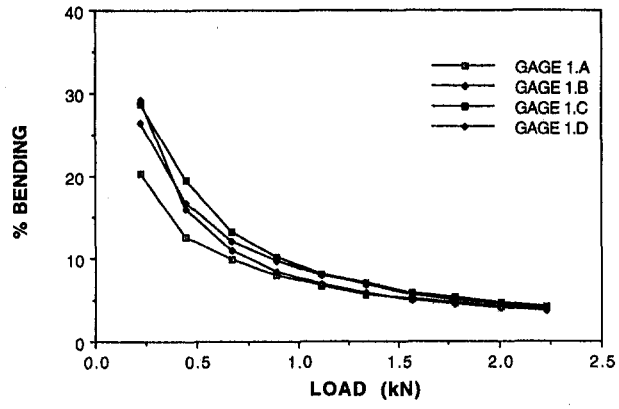

Fig. 9 Percentage of bending strain as a function of load

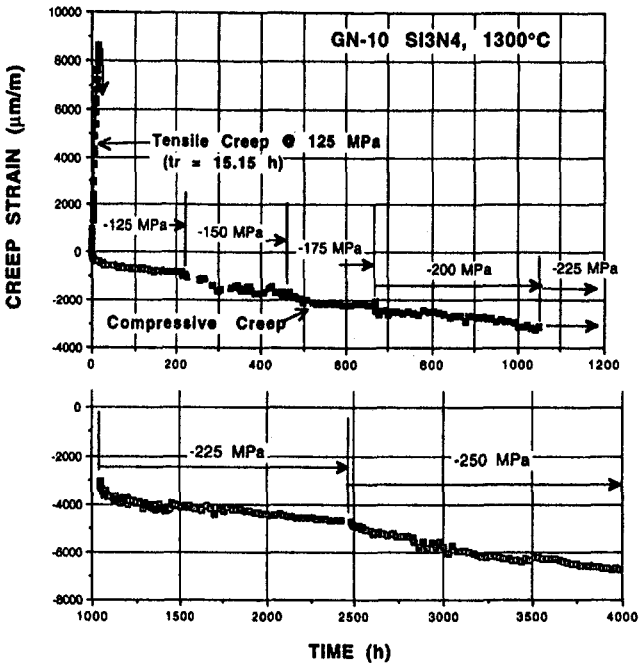

Fig. 10 Creep curves of GN-10 Si_3N_4 specimens tested at 1300°C in tension (ruptured in 15.2 h) and in compression (discontinued at 4200 h).

indication of imminent failure has been observed and the load train appears to be in stable condition.

Summary

A unique load-train assembly was developed for testing a dumb-bell-shaped ceramic specimen in compression at high temperatures. Excellent load-train alignment is attributed to the self-aligning universal coupler, which appears to operate reliably according to the basic design principles warranted by the definitive laws of hydrostatics and mechanics. Results of evaluation tests using a strain-gaged specimen indicated that specimen bending below 1.5 percent is routinely achievable with the use of the self-aligning coupler. A PC software program was developed to facilitate alignment and evaluation. An alignment method was discussed as how to eliminate the effect of using an evaluation specimen with slight inherent imperfections. Meaningful test data were obtained from an actual compressive creep test on a Si_3N_4 ceramic specimen tested at 1300°C for a long period of time in excess of 4000 h, demonstrating high reliability and dependability of the load-train system.

Acknowledgments

The authors thank Drs. A. A. Wereszczak and S. K. Iskander for reviewing the manuscript and providing many valuable suggestions.

This research was sponsored by the U.S. Department of Energy, Assistant Secretary for Energy Efficiency and Renewable Energy, Office of Transportation Technologies, as part of the Ceramic Technology Project of the Propulsion System Materials Program, under contract DE-AC05-96OR22464 with Lockheed Martin Energy Research Corporation.

References

Anderson, C. A., Wei, D. P., and Kossowsky, R., 1975, "Analysis of the Time Dependent Flexural Test," *Deformation of Ceramics*, R. C. Brandt and R. Tressler, eds., Plenum Press, New York, pp. 383–398.

ASTM, 1995, "Standard Practice for Tensile Strength of Monolithic Advanced Ceramics at Ambient Temperatures," C1273–94, *Annual Book of ASTM Standards*, Vol. 15.01, pp. 385–402.

Birch, J. M., Wilshire, B., Owen, D. J. R., and Shantaram, D., 1976, "The Influence of Stress Distribution on the Deformation and Fracture Behaviour of Ceramic Materials Under Compression Creep Conditions," *J. of Materials Science,* Vol. 11, pp. 1817–1825.

Chuang, T. -J., and Wiederhorn, S. M., 1988, "Damage-Enhanced Creep in a Siliconized Silicon Carbide: Mechanics of Deformation," *J. of American Ceramic Society,* Vol. 71, pp. 595–601.

Cohrt, H., and Thuemmler, F., 1985, "Creep of Reaction Bonded, Siliconized Silicon Carbide," *International J. of High Technology Ceramics,* Vol. 1, pp. 87–105.

Debschütz, K. D., Schneider, G. A., and Petzow, G., 1993, "Critical Evaluation of the Compression Creep Test," *J. of American Ceramic Society,* Vol. 76, No. 10, pp. 2468–2474.

Ding, J. L., Liu, K. C., More, K. L., and Brinkman, C. R., 1994, "Creep and Creep Rupture of an Advanced Silicon Nitride Ceramic," *J. of American Ceramic Society,* Vol. 77, No. 4, pp. 867–874.

Lankford, J., 1977, "Compressive Strength and Microplasticity in Polycrystalline Alumina," *J. of Materials Science,* Vol. 12, pp. 791–796.

Liu, K. C., and Brinkman, C. R., 1986, "Tensile Cyclic Fatigue of Structural Ceramics," *Proc. 23rd Automotive Technology Development Contractors' Coordination Meeting,* Dearborn, MI, Oct. 21–24, 1985, SAE, Warrendale, PA, P-165, pp. 279–284.

Sines, G., and Adams, M., 1978, "Compression Testing of Ceramics," *Fracture Mechanics of Ceramics,* R. C. Bradt et al., eds., Plenum Press, New York, Vol. 3, pp. 403–434.

Tracy, C. A., 1987, "A Compression Test for High Strength Ceramics," *J. of Testing and Evaluation,* Vol. 15, No. 1, pp. 14–19.

Structural Design and High-Pressure Test of a Ceramic Combustor for 1500°C Class Industrial Gas Turbine

I. Yuri

T. Hisamatsu

K. Watanabe

Y. Etori

Central Research Institute of Electric Power Industry, Yokosuka, Kanagawa, Japan

A ceramic combustor for a 1500°C, 20 MW class industrial gas turbine was developed and tested. This combustor has a hybrid ceramic/metal structure. To improve the durability of the combustor, the ceramic parts were made of silicon carbide (SiC), which has excellent oxidation resistance under high-temperature conditions as compared to silicon nitride (Si_3N_4), although the fracture toughness of SiC is lower than that of Si_3N_4. Structural improvements to allow the use of materials with low fracture toughness were made to the fastening structure of the ceramic parts. Also, the combustion design of the combustor was improved. Combustor tests using low-Btu gaseous fuel of a composition that simulated coal gas were carried out under high pressure. The test results demonstrated that the structural improvements were effective because the ceramic parts exhibited no damage even in the fuel cutoff tests from rated load conditions. It also indicated that the combustion efficiency was almost 100 percent even under part-load conditions.

Introduction

The development of a high-temperature gas turbine is being carried out to improve the thermal efficiency on IGCC (Integrated coal Gasification Combined Cycle power plant), which is expected to be the thermal power plant of the future. The principal combustible component of coal gasified fuel produced in an air-blown entrained bed coal gasifier is carbon monoxide (CO), and the lower heating value of the fuel is as low as 3.9 MJ/m^3N. Furthermore, if a hot type gas cleaning system is used, ammonia (NH_3) produced in the gasifier is supplied to the gas turbine combustor. Thus, it is important to develop a high-temperature gas turbine combustor that is able to achieve low NO_x and stable combustion of the low-Btu gas, including NH_3.

If ceramic materials, which have excellent heat resistance, are utilized in gas turbine components, it is possible to raise the turbine inlet temperature (T.I.T.) and reduce the amount of cooling air needed for the combustor wall. Consequently, the temperature of the combustor wall reaches above 1000°C and the combustion reaction near the surface of the wall is accelerated. This allows greater freedom in the air distribution design of the combustor. Therefore, it is believed that low NO_x and stable combustion can be achieved with a ceramic combustor more easily than with a conventional metallic one.

Central Research Institute of Electric Power Industry (CRIEPI) has studied the application of ceramics and various structure designs for gas turbine combustor and combustion technology to achieve low NO_x and stable combustion of coal gasified fuel. So far, we have developed a ceramic combustor for a 20 MW, 1300°C class gas turbine using low-Btu gaseous fuel [1, 2]. The combustor has a ceramic/metal hybrid structure. As the result of high-pressure tests, it was clear that the hybrid structure is effective in ensuring the strength reliability for ceramic parts made of Si_3N_4.

When the T.I.T. rises to 1500°C, we have found the application of SiC more efficient because of its excellent oxidation resistance. Although the fracture toughness of SiC is lower than that of Si_3N_4 and the maximum level of thermal stress to SiC ceramic parts is higher than that of Si_3N_4 under the same thermal conditions, the oxidation resistance of SiC is superior to that of Si_3N_4.

This paper describes the application of SiC ceramics to a 1500°C class gas turbine combustor for IGCC. The structure designs for improved strength reliability of ceramic parts and the results of the high pressure combustor tests using low-Btu gaseous fuel are described.

Ceramic Material for 1500°C Class Combustor

Si_3N_4 (which we chose for the 1300°C class ceramic combustor) and SiC are both commonly used in the construction of ceramic gas turbines. They are appropriate for use because they have superior strength at high temperatures and thermal shock resistance. With the rise in the turbine inlet temperature, the durability (i.e., oxidation resistance) of the ceramic materials become important. Si_3N_4 and SiC oxidize at high temperatures, and the reaction accelerates as the temperature rises. Thus, it is necessary to choose the ceramic material that has superior durability at higher temperatures.

The atmospheric oxidation characteristics of Si_3N_4 and SiC at 1500°C in an electric furnace are shown in Fig. 1. This indicates that SiC has excellent oxidation resistance compared to Si_3N_4, and that the oxidation rate of SiC is low because the SiO_2 layer formed on the surface of SiC restrains the diffusion of oxygen. Therefore, to improve the durability of ceramic parts, SiC was chosen as the ceramic material for the 1500°C class combustor.

However, the fracture toughness of SiC is lower than that of Si_3N_4, and the maximum level of thermal stress to SiC ceramic parts is higher than that of Si_3N_4 under the same thermal conditions because of the difference in material properties. Thus, a structural design that allows a low fracture toughness and improves the strength reliability is necessary when applying SiC in a 1500°C class combustor.

Structural and Combustion Design of Ceramic Combustor

Basic Structure of Ceramic Combustor. The basic structure of ceramic combustor for a 20 MW, 1300°C class gas

Contributed by the International Gas Turbine Institute and presented at the 41st International Gas Turbine and Aeroengine Congress and Exhibition, Birmingham, United Kingdom, June 10–13, 1996. Manuscript received at ASME Headquarters February 1996. Paper No. 96-GT-346. Associate Technical Editor: J. N. Shinn.

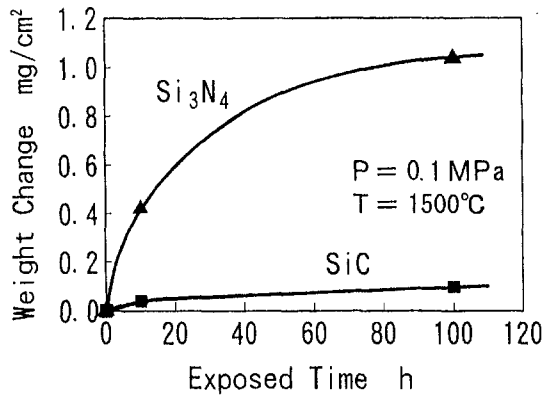

Fig. 1 Atmospheric oxidation characteristic of Si_3N_4 and SiC at 1500°C

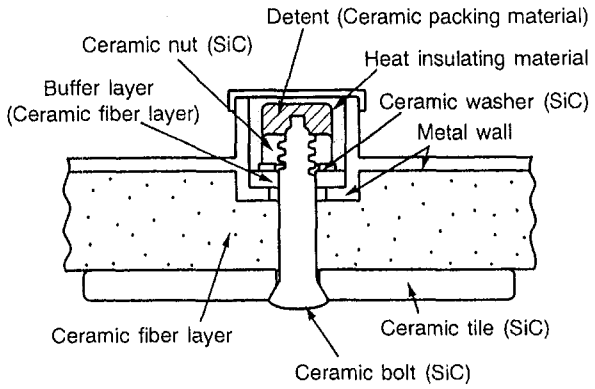

Fig. 3 Structure of nut and bolt fastening part

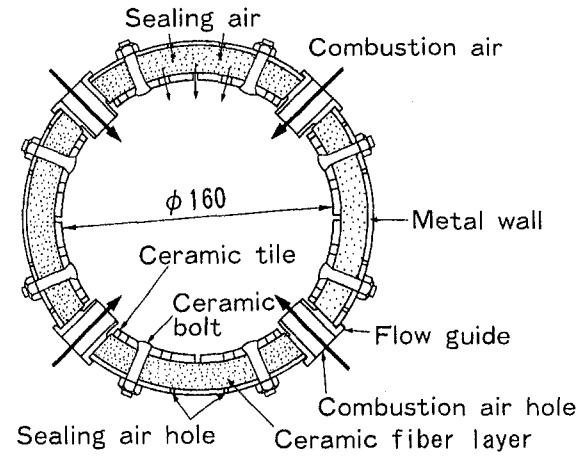

Fig. 2 Basic structure of ceramic combustor for a 1300°C, 20 MW class gas turbine

turbine is shown in Fig. 2. The outer wall is made of metal and inside of the metal wall is covered with ceramic fiber layer. The inner wall of the combustor is lined with ceramic tiles. The structure of the combustor follows the concepts of the structural design for ceramic components [3, 4], which include concepts improving the strength reliability of ceramic components, i.e., a ceramic/metal hybrid structure and the division of ceramic parts. The ceramic fiber layer is protected from high-temperature gas flow by the ceramic tiles. By feeding a small amount of sealing air, which prevents the penetration of high temperature gas into the fiber layer and shields the heat from the ceramic tiles, the temperature of the metal wall is kept at the same level as the combustion air temperature. Simultaneously, the fiber layer functions as a buffer layer to the distortion between the ceramic tiles and the metal wall. Ceramic nuts and bolts are used to fasten the ceramic tiles and the ceramic fiber layer to the metal wall.

Fastening Structure of Ceramic Nut and Bolt. In a ceramic/metal hybrid structure, the device used to fasten the ceramics to the metal is most important. This was achieved by using ceramic nuts and bolts. When applying SiC to the basic structure of the ceramic combustor, a fastening structure, which allows a low fracture toughness of SiC and improves the strength reliability, is necessary. Structural improvements were made as follows and the improved structure is shown in Fig. 3.

1 Heat Insulation at Fastening Part. The ceramic bolt passes from inside of the combustor, whose temperature is over 1000°C, through the metal wall, which is cooled by combustion air. Thus, to reduce the thermal stress of the ceramic bolt, the fastening part of the nut and bolt are insulated.

2 Installation of Buffer Layer. To reduce the stress on the nut and bolt caused by the difference of the thermal expansion between ceramic fiber layer and metal wall, a buffer layer made of ceramic fiber layer was set between the nut and the metal wall.

3 Screw Shape of Nut and Bolt. To improve the strength of the screw thread and prevent stress concentration at the screw of bolt and nut, the shape of the screw was changed from a coarse screw thread, which is applied to a 1300°C class ceramic combustor using Si_3N_4, to a trapezoidal screw thread as shown in Fig. 4.

4 Detent of Ceramic Nut and Bolt. To apply the detent on the ceramic nut and bolt, the tip of the ceramic bolt is flattened and covered with ceramic packing materials. In addition to this improvement of the fastening structure, the following improvement was made.

5 Chamfering Corner of Ceramic Parts. To prevent stress concentration at the corners of ceramic parts, all corners are chamfered and smoothed.

Combustion Design. The basic specifications of the combustor are shown in Table 1. The quantity of air supplied to a 1500°C class combustor is 2.6 kg/s, which is about 1.4 times

Nomenclature

C.R. = conversion ratio (the ratio of measured NO_x concentration to that of 100 percent conversion from NH_3 under the same test condition), percent
Ga = air flow rate, kg/s
G.T.L. = gas turbine load, percent
η = combustion efficiency, percent
L = combustion intensity, $MW/(m^3 \cdot MPa)$
P = pressure, MPa
Pc = combustor outlet pressure, MPa
P.F. = pattern factor = (maximum combustion gas temp. − average combustion gas temp.) × 100/(average combustion gas temp. − combustion air temp.), percent
T = temperature, °C
Ta = combustion air temperature, °C
Tc = ceramic tile ($X \fallingdotseq 180$ mm) temperature, °C
Tg = average gas temperature at combustor outlet, °C
X = axial distance through combustor, mm

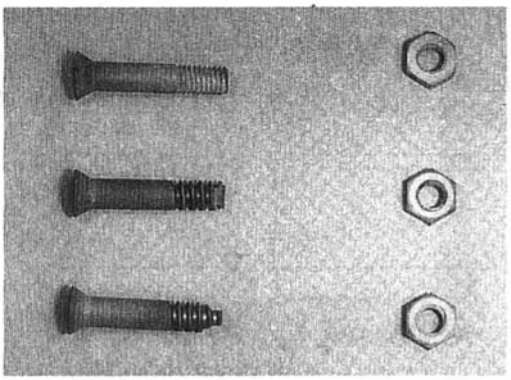

Fig. 4 Shape of ceramic nut and bolt: Upper: Si_3N_4 nut and bolt; Middle and lower: SiC nut and bolt

Table 1 Basic specifications of combustor

Item	Value
Outlet gas temperature	1500°C
Combustor outlet pressure	1.52MPa
Combustion Intensity	360MW/m³·MPa
Inlet air temperature	393°C
Inlet air flow rate	2.6kg/s
Fuel temperature	357°C
Fuel flow rate	2.0kg/s
Low heating value	3.90MJ/m³N
Combustor size	
Liner	
diameter	160mm
length	500mm
Transition piece	
length	360mm

the theoretical quantity of air needed for complete combustion. That quantity corresponds to about 70 percent of the 1300°C class combustor. Therefore the quantity of dilution air that doesn't directly influence combustion reaction and stability was cut to a large degree. About 96 percent is supplied as the combustion air, and about 3 percent supplied as sealing air of the ceramic fabric.

To reduce the conversion ratio from NH_3 to NO_x by applying a rich-lean combustion method, the air ratio in the primary combustion zone is set at less than 0.7.

The appearance of a SiC ceramic combustor for a 20 MW, 1500°C class gas turbine, including structure design to improve strength reliability and combustion design as described above, is shown in Fig. 5.

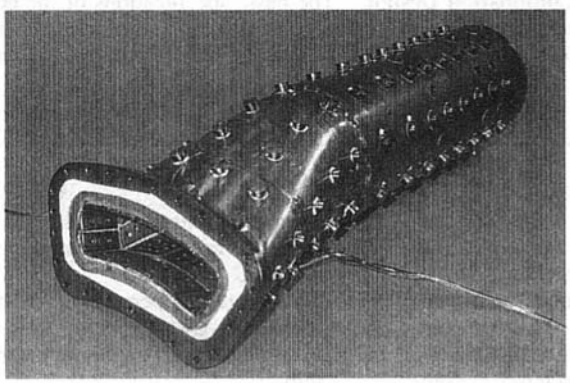

Fig. 5 SiC ceramic combustor for a 1500°C, 20 MW class gas turbine

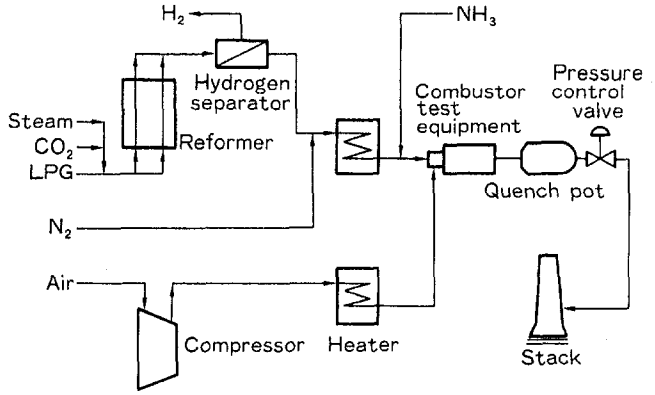

Fig. 6 Schematic of test facility

Test Facility and Test Method

Test Facility. Figure 6 shows the schematic of the test facility. This facility can produce a low-Btu gaseous fuel that simulates the composition of coal gas produced in an air-blown coal gasifier. After the reformed gas, which is made of propane, CO_2 and steam, is adjusted for CO-to-H_2 molar ratio, calorific value, NH_3 concentration, and temperature, it is supplied to the combustor. The combustion air, pressurized by a compressor, is supplied to the combustor after it is heated to about 400°C. The combustion gas is then exhausted through a quench pot and a pressure control valve. The pressure control valve adjusts the combustor outlet pressure.

A sectional view of the combustor test equipment is shown in Fig. 7. The temperature distribution, composition, and total pressure of the combustion gas at the combustor outlet are measured as it passes through a refractory insulated duct. The gas temperature distribution is measured with five pyrometers. Each pyrometer consists of five sheathed type-R thermocouples. The diameter of thermocouple is 1.6 mm. The combustion gas is sampled with two water-cooled probes after passing through the pyrometers, and the CO, CO_2, O_2, NO_x, and THC in it are measured. The water-cooled probes are also used to measure the total pressure of the combustion gas.

To observe the temperature of the combustor components, sheathed type-R thermocouples are set in the ceramic tiles and sheathed type-K thermocouples are set on the metal wall.

Test Method. The combustion tests and the fuel cutoff tests were carried out under high pressure. For the combustion tests, the calorific value of fuel was 3.9 MJ/m³N (LHV), the CO-

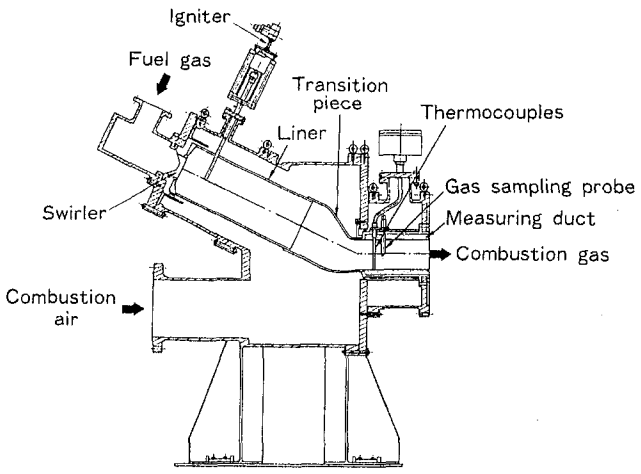

Fig. 7 Sectional view of combustor test equipment

Table 2 Basic conditions of combustion test

Fuel	Low heating value	3.90MJ/m³N
	Composition	
	H_2	6.9vol %
	CO	18.3vol %
	N_2	56.2vol %
	CO_2	13.0vol %
	CH_4	2.5vol %
	H_2O	3.0vol %
	NH_3	1000ppm-vol
	CO/H_2	3
	Temperature	400 ℃
Air temperature		400 ℃

to-H_2 molar ratio 3, and the temperatures of both the fuel and the combustion air about 400°C. Basic conditions of the combustion air and the fuel are as shown in Table 2. We set the average gas temperature at about 1500°C and the outlet air pressure at about 1.52 MPa as the rated load conditions for the combustion tests. In the combustion tests, we changed the outlet gas temperature and pressure of each gas turbine load on the basis of the rated load conditions.

To simulate the conditions in a gas turbine trip from the rated load, the fuel cutoff tests were carried out by rapidly shutting down the fuel cutoff valve. In this test, because we kept the opening of both the combustion air flow control valve and the pressure control valve constant, the changes of the combustion air flow and the combustor outlet pressure are different from those of a usual gas turbine trip, in which both rapidly decrease.

The total time of the combustion test was about 8 hours, of which 2 hours were under the rated load conditions.

Test Results and Discussion

Combustion Characteristics

Combustion Efficiency. Figure 8 shows the relation between the gas turbine load (G.T.L.) and combustion efficiency. Combustion efficiency increases in relation to the G.T.L., and reaches almost 100 percent when the G.T.L. is over 25 percent. Under the rated load conditions, even at the combustion intensity of 360 MW/(m³·MPa), which is higher than that of a conventional metallic combustor, it is possible to achieve stable combustion with almost 100 percent efficiency. This is possible because the combustor inner wall temperature can be kept

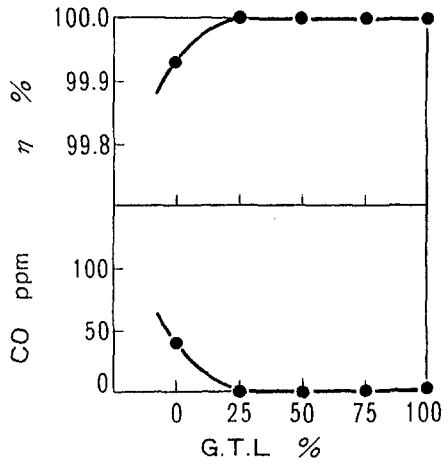

Fig. 8 Relation between gas turbine load and combustion efficiency

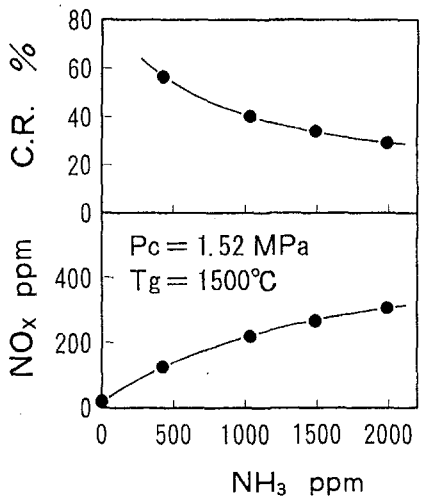

Fig. 9 Effect of NH_3 concentration on NO_x conversion ratio under rated load condition

higher than 1000°C, as shown in the temperature distributions of each component below.

NO_x Emission Characteristics. Figure 9 shows the effect of NH_3 concentration in the fuel on the NO_x emission characteristics and NO_x conversion ratio (conversion ratio from NH_3 in fuel to NO_x) at the combustor outlet under rated load conditions. The NO_x conversion ratio was calculated by ignoring the thermal NO_x, because the thermal NO_x emission level is expected to be low in combustion of low-Btu gaseous fuel with low flame temperature. Actually thermal NO_x emission concentration is 20 ppm. When the NH_3 concentration in the fuel is 1000 ppm, which is a basic condition, the NO_x emission concentration is 213 ppm and a low NO_x combustion is achieved with NO_x conversion ratio of about 40 percent.

Temperature Distributions of Each Component. Figure 10 shows the temperature distribution of each component under rated load conditions. The horizontal axis shows the axial distance through the combustor from the swirler. Since the air ratio in the primary combustion zone is kept low and fuel-rich combustion is carried out there, the ceramic tile temperatures near the swirler is low. However, all ceramic tile temperatures are over 1000°C and the maximum temperature, which exists in the center of the combustor liner, reaches approximately

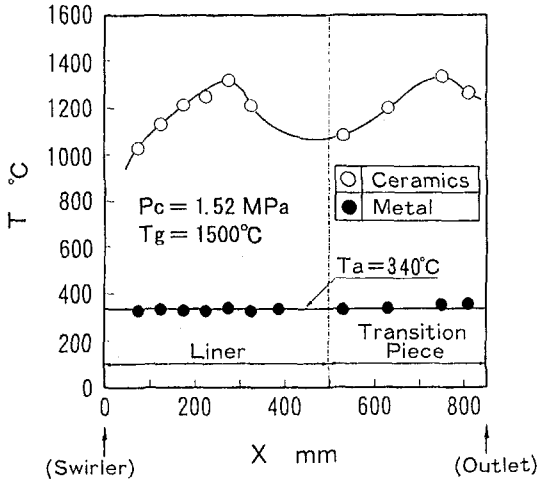

Fig. 10 Temperature distribution of each component under rated load condition

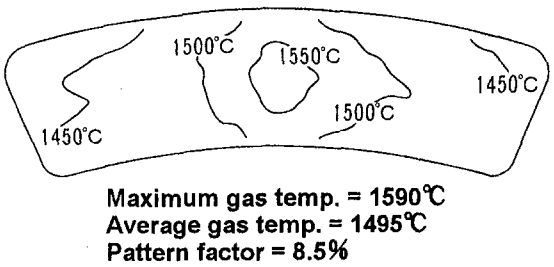

Fig. 11 Example of gas temperature distribution at combustor outlet under rated load condition

1350°C. On the other hand, the metal wall temperatures are kept at the same temperature as that of the combustion air. This shows that the performance of both the insulation and the heat shield are excellent.

Combustion Gas Temperature Distribution. An example of the gas temperature distribution at the combustor outlet under the rated load condition is shown in Fig. 11. The maximum gas temperature, which exists at the center of the combustor outlet, is 1590°C, with an average of 1495°C. The gas temperature distribution at the combustor outlet is almost symmetric and the pattern factor (P.F.), which is an index of uniformity in the combustion gas temperature distribution, is 8.5 percent. This value is less than that of a conventional metallic combustor. It is clear that, by applying ceramics to the combustor, it will be possible to make the gas temperature distribution uniform. This means that a ceramic combustor not only greatly reduces the amount of the cooling air flow, but it also allows the combustor wall temperature to exceed 1000°C. Also we consider that this uniformity of gas temperature distribution reduces the thermal stress on both the ceramic stator vanes and the ceramic rotor blades. It also effectively improves the reliability of a ceramic gas turbine.

Reliability of Ceramic Components. The combustion test was conducted for about 4 hours, 1 hour of which was conducted under the rated load conditions.

After a test under the rated load conditions, chips at the head and cracks at the screw were detected in some ceramic bolts by visual inspection, as shown in Figs. 12 and 13. A total of 16 bolts were damaged. Eight exhibited chipped heads. Three exhibited cracked screws. Five showed damage to both head and screw. The following became clear after a detailed inspection of the damaged parts:

1 The damage was concentrated on the entrance and outlet side of the combustor liner and the transition piece.

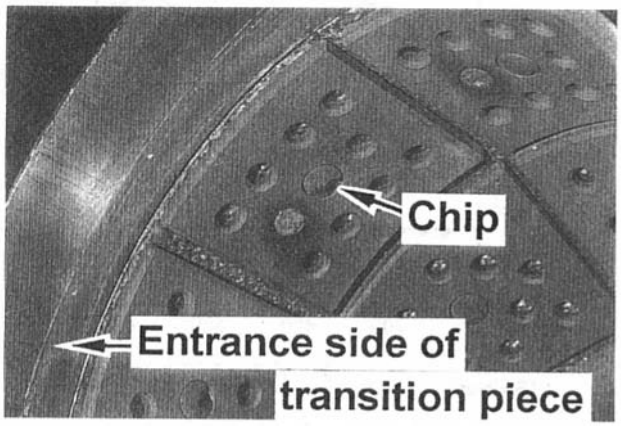

Fig. 12 Chip at head of bolt (entrance side of transition piece)

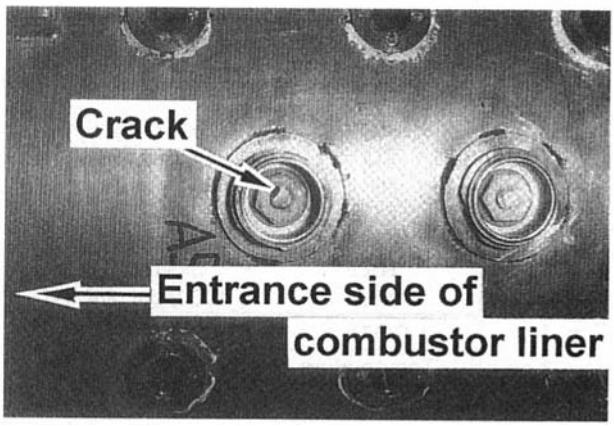

Fig. 13 Crack at screw of bolt (entrance side of combustor liner)

2 The chips at the head of the bolts existed at the far position from the end face of liner and transition piece. For example, at the outlet side of the combustor liner, the chips existed at the entrance side of the liner. On the other hand, at the entrance side of the transition piece, they existed at the outlet side of the transition piece.
3 Conversely, the cracks at the screw of the bolts existed at the near position from the end face of liner and transition piece.

From these inspection results, it is clear that the inclination of bolt occurred from the difference of the thermal expansion between ceramic fiber layer and metal wall. It was presumed that the bolt was damaged because the inclination occurred beyond the limit of the buffer layer.

Improvement of Fastening Structure and Result of Fuel Cutoff Test. Based on these results, a plate spring made of metal was set between the buffer layer and metal wall. The improved fastening structure is shown in Fig. 14.

To examine the strength reliability of the improved ceramic combustor, a combustion test under rated load conditions and a fuel cutoff test, which simulated the conditions in a gas turbine trip from rated load, were conducted. This test was of the same duration as the first test.

Figure 15 shows the changes of the conditions after fuel cutoff. In the actual gas turbine trip, the pressure and the combustion air flow drop rapidly. However, in these tests, the pressure drop was small and the combustion air flow increased after the fuel cutoff, because the opening of the pressure control valve and the combustion air flow control valve were constant. Consequently, the heat transfer coefficient at the surface of the ceramic parts after fuel cutoff would be higher than that in an

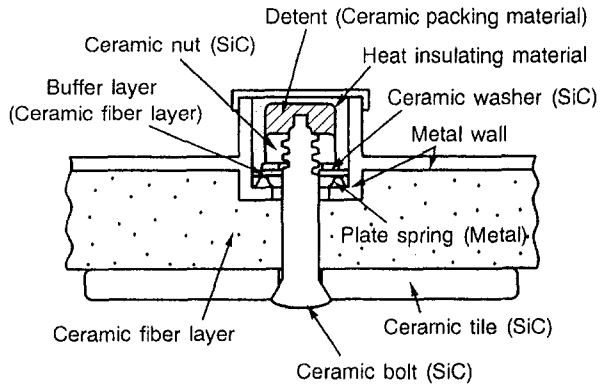

Fig. 14 Structure of nut and bolt fastening part (after improvement)

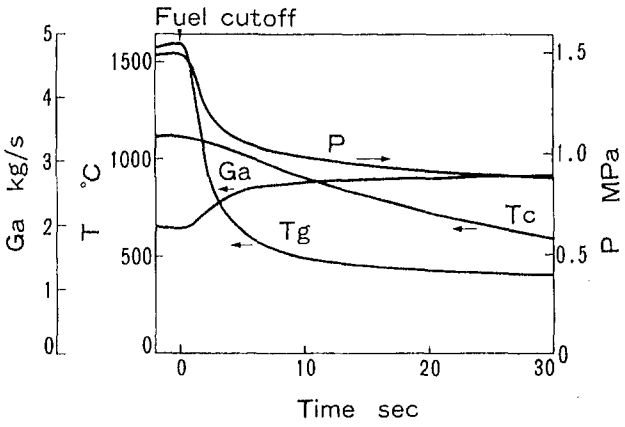

Fig. 15 Changes of conditions after fuel cutoff

actual gas turbine trip, and it is considered that the conditions for the ceramic parts were more severe.

Though the measured maximum drop rate of the gas temperature was about 400°C/s, the actual temperature drop rate was larger because the response time lag of the thermocouples was not compensated. The maximum rate of the change of the ceramic tile temperature was about 50°C/s.

After the fuel cutoff test, a visual inspection was conducted on the ceramic components, especially the fastening parts of ceramic nuts and bolts, and the plate spring. Consequently, no damage was detected in the ceramic components and the plate spring. Therefore, the structural improvement of the nut and bolt fastening part was effective.

Conclusion

In the development of a SiC ceramic combustor for a 20 MW, 1500°C class gas turbine, we found it necessary to study the structural design of the fastening in order to improve the strength reliability of the ceramic parts. Consequently, it was confirmed that by applying this structural design, the brittleness of SiC can be overcome allowing it to be applied as a structural material in a 1500°C class gas turbine combustor.

Furthermore, in the combustion characteristics, it was clear that the stable combustion of coal gasified fuel and uniformity in the combustion gas temperature distribution can be achieved by applying ceramic materials to the gas turbine combustor.

Acknowledgments

We are grateful to Dr. T. Machida, Mr. K. Wada, and Mr. M. Nakayama of Hitachi Ltd. with whom we collaborated on the development of the 1300°C class ceramic combustor. The basic structure of the 1300°C class ceramic combustor was used for our 1500°C class ceramic combustor.

References

1 Mori, N., et al., "High Pressure Test of a Ceramic Combustor for a High Temperature Industrial Gas Turbine," *Proc. Emerging Energy Technology,* ASME PD-Vol. 50, 1993, pp. 95–100.

2 Machida, T., et al., 1990, "Performance Test on Ceramic Combustor for High Temperature Industrial Gas Turbine," *Proc. Fossil Fuel Combustion Symposium 1990,* ASME PD-Vol. 30, 1990, pp. 183–187.

3 Miyata, H., et al., "Application Technology on Ceramics for Structural Components of High-Temperature Machines," *JSME International Journal,* Series I, Vol. 32, No. 4, 1989, pp. 596–604.

4 Hisamatsu, T., et al., "Development of a Ceramic Gas Turbine for an Electric Power Plant," *Trans. Jpn. Soc. Mech. Eng.* [in Japanese], No. 90-0916B, Vol. 57, No. 535, 1990, pp. 819–824.

Structure of Airblast Sprays Under High Ambient Pressure Conditions

Q. P. Zheng

A. K. Jasuja[1]

A. H. Lefebvre

School of Mechanical Engineering,
Cranfield University,
Cranfield, Bedford MK43 0AL
United Kingdom

A single-velocity-component phase Doppler particle analyzer is used to survey and measure local variations in drop-size distributions and drop velocities in the near-nozzle region of a practical, contraswirling, prefilming airblast atomizer. The technique of laser sheet imaging is used to obtain global patterns of the spray. All measurements are taken with a constant pressure drop across the atomizer of 5 percent, at ambient air pressures of 1, 6, and 12 bar. The liquid employed is aviation kerosine at flow rates up to 75 g/s. The results show that increasing the air pressure from 1 to 12 bar at a constant air/fuel ratio causes the initial spray cone angle to widen from 70 to 105 deg. Farther downstream the spray volume remains largely unaffected by variations in atomizer operating conditions. However, the radial distribution of fuel within the spray volume is such that increases in fuel flow rate cause a larger proportion of fuel to be contained in the outer regions of the spray. The effect of ambient pressure on the overall Sauter mean diameter is small. This is attributed to the fact that the rapid disintegration of the fuel sheet produced by the contraswirling air streams ensures that the atomization process is dominated by the "prompt" mechanism. For this mode of liquid breakup, theory predicts that mean drop sizes are independent of air pressure.

Introduction

Originally introduced as a measure to alleviate smoke emissions from turbojet engines, prefilming airblast atomizers are now employed in a wide range of aircraft, industrial, and marine gas turbines. A key feature of all practical prefilming airblast atomizers is that the bulk fuel is first spread into a thin continuous sheet, a process called "prefilming," and then exposed to high-velocity, swirling air streams on both sides of the sheet.

In recent years considerable advances have been made in the development of laser diagnostic techniques for spray characterization. These developments have led to a resurgence of interest in determining the properties of sprays produced in prefilming airblast atomization. Efforts are now under way to gain a better understanding of the basic phenomena occurring within complex practical systems of the types currently in service on advanced turbojet engines. Wang et al. (1992a, 1992b, 1994, 1995) and McDonell et al. (1994) used two-component phase-Doppler interferometry to make detailed measurements in the flows downstream of a SNECMA/General Electric CFM-56 airblast atomizer. In addition to time-averaged properties, transient phenomena were also examined. These studies provided valuable insight into the general structure of the gas phase as well as details regarding the complex behavior of drops. Of special interest from a practical viewpoint is that actual engine hardware was used to examine the sensitivity of the spray structure to scaling and hardware variations. Hebrard et al. (1991, 1993) also used two-component phase-Doppler interferometry to characterize the two-phase flow field generated by an engine airblast atomizer. Their measurements included mean axial and transverse velocities for each phase as well as volume flux and drop size distributions. Wynne and Jasuja (1991) and Jasuja and Lefebvre (1994) used various nonintrusive techniques, including phase-Doppler interferometry, high-intensity spark photography, high-speed cinephotography, video imaging to capture the dynamic and unsteady spray characteristics produced in prefilming airblast atomization. All the injectors used in the program were typical of modern gas turbine practice and differed from each other only with regard to various design details, such as swirler flow area and vane angle. The results obtained showed that the sprays produced by actual engine nozzles exhibit appreciable nonuniformities with regard to droplet trajectories and mass flux distributions. In our 1994 study, all measurements of spray characteristics were carried out at distances of 50 to 70 mm downstream of the fuel nozzle. The objective of the present work is to extend the previous study by carrying out detailed mapping of drop size distributions and drop velocities at higher fuel throughputs and in regions closer to the nozzle. This near-nozzle region is of special importance from a combustion viewpoint because it is the zone in which combustion is initiated and sustained.

Experimental

The test facility for this study is a large cylindrical vessel designed to operate at high pressures in accordance with British Standards specification BS 5500. A flexible optical window arrangement permits the use of nonintrusive diagnostics, including phase-Doppler interferometry and laser sheet imaging. High-pressure air is delivered from a multistage screw-type compressor to the fuel injector, which is located at one end of the test vessel and is arranged to spray horizontally along its major axis, as shown schematically in Fig. 1. The same source of air is used to pressurize the test vessel, the level of pressure being controlled by means of a spill valve, which is located at the downstream end of the vessel.

Atomizer. The fuel injector is essentially a prefilming airblast atomizer of the type shown in Fig. 2 which is representative of the injectors used in many gas turbine combustors. It features a pair of concentric air inlets that generate two separate swirling airflows in opposite directions. Low-velocity fuel is first spread into a thin, circumferentially uniform sheet on an annular surface and then sandwiched between the two swirling

[1] Corresponding author.

Contributed by the International Gas Turbine Institute and presented at the 41st International Gas Turbine and Aeroengine Congress and Exhibition, Birmingham, United Kingdom, June 10–13, 1996. Manuscript received at ASME Headquarters February 1996. Paper No. 96-GT-131. Associate Technical Editor: J. N. Shinn.

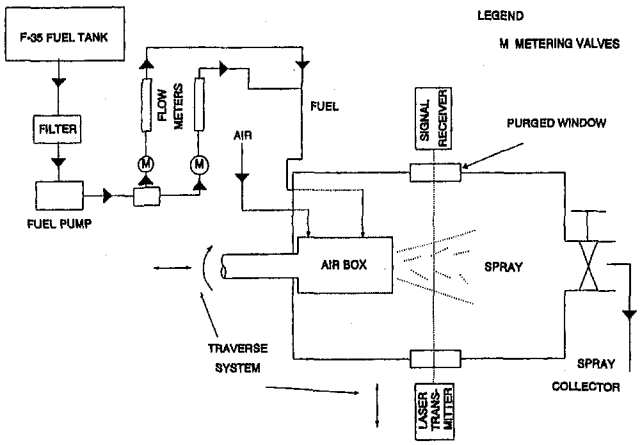

Fig. 1 High-pressure spray facility

air streams. This configuration promotes a high shearing action between the fuel and the atomizing air, which is beneficial to atomization and also helps to match the resulting spray with the combustor air flow pattern. The fuel injector is fitted into a high-pressure air box located inside the test vessel, as shown in Fig. 1.

Two separate and independent traverse systems for the air box–fuel injector assembly are provided. The traverse system for the laser diagnostics is a mechanical one offering three degrees of freedom. Normally, the optical system moves along the horizontal diameter of the pressure vessel. The repeatability of positioning is within 0.25 mm. The second traverse system provides two degrees of freedom for the air box relative to the diagnostics line of sight. The first one is a linear movement along the longitudinal axis of the pressure vessel, while the second is a rotational movement around the axis of the air box. As both of these movements are controlled by a computer-operated stepper motor, very precise and repeatable injector positioning can be achieved.

Optical Diagnostics. Four optical-quality quartz windows provide the desired optical access into the pressure vessel. Each of these large windows has a multipoint purge feed of high velocity air to prevent fuel deposition. A single-component phase-Doppler particle analyzer (PDPA), manufactured by Aerometrics Inc., was used in this study. Its velocity component coincides with the main axis of the conical sprays. The instrument was operated in the forward scattering mode, which is best suited for dense spray measurements. Its argon-ion laser gave a maximum power in the probe volume of around 250 mW at a wavelength of 514.5 nm. During the course of the investigation, special attention was paid to the setting up and operation of the PDPA, in particular, the laser power and the photomultiplier tube (PMT) voltage. The methods employed to optimize data quality have been described in some detail by Jasuja and Lefebvre (1994). The FFT-type signal processor—a Doppler Signal Analyzer (DSA)—used in the measurements is claimed to be capable of processing signals as weak as −5 db (Zhu et al. 1993).

The technique of laser sheet imaging was also applied to obtain global patterns of the spray. With this technique, a pulsed Nd:YAG laser beam is converted into the form of a thin sheet, which illuminates the spray flow field under investigation. The system provides a power density of 27 MW/cm^2 in the laser sheet probing volume. The scattered signals at a wavelength of 532 nm were recorded on black and white film positioned perpendicular to the laser sheet. The laser pulse duration of 15 ns is generally considered short enough to freeze the particle motion. The primary magnification factor (i.e., negative image size to actual object size) is 0.5.

Test Conditions. The test conditions were selected to simulate the air densities encountered in gas turbine combustors when operating at pressures up to 30 bar. All measurements were taken with a pressure drop across the atomizer, $\Delta P/P$, of 0.05, i.e., 5 percent, which is typical of modern combustors. Atomizer air/fuel ratios ranged from 1.1 to 7.8. The ambient air temperature was kept constant at around 323 K. The ambient air pressures employed were 1, 6, and 12 bar. Air flow rates were measured using an orifice plate meter. A rotameter/turbine flow meter combination was used to measure fuel flow rates. At the 12 bar condition, the maximum air and fuel mass flow rates were 0.3 kg/s and 75 g/s, respectively. Aviation kerosine (μ = 0.0013 kg/ms, σ = 0.0277 kg/s^2, and ρ = 784 kg/m^3, all at 288 K) was used throughout the test program. PDPA data were taken at downstream distances from the atomizer exit plane of 27 and 45 mm along radii perpendicular to the spray axis. Due to the signal attenuation associated with high throughput sprays, when operating at a pressure of 12 bar the sample size was reduced from 5000 to around 2000 drops to avoid long run times.

Results

One phase of the test program was devoted to photographic studies using pulsed laser sheet lighting to illuminate the spray. The main objective was to examine the extent to which the overall size and shape of the spray are affected by changes in pressure and fuel flow rate. Such information could lead to a better understanding of the effects of these parameters on various aspects of combustion performance. Knowledge of global spray dimensions over a range of atomizer flow conditions provides useful guidance in determining the optimum locations within the spray (in terms of downstream distance and spray radius) for the measurements of drop size and velocity distributions during the PDPA investigation phase.

Spray Structure. Some of the results of the photographic studies are shown in Figs. 3 and 4. Figure 3 shows how the physical structure of the spray is affected by an increase in ambient air pressure from 1 to 12 bar while maintaining the fuel mass flow, m_F, constant at 5 g/s. These photographs show clearly the heterogeneous nature of the spray, especially at low air pressures.

Inspection of these and other photographs, along with corresponding measurements of drop velocities, suggests that the annular sheet of fuel flowing over the prefilmer lip rapidly disintegrates into droplets, which tend to maintain the general direction imparted to the air by the air swirlers incorporated within the atomizer. However, as the atomizing-air flow field expands downstream of the nozzle, the combined effects of aerodynamic diffusion and external air entrainment cause veloc-

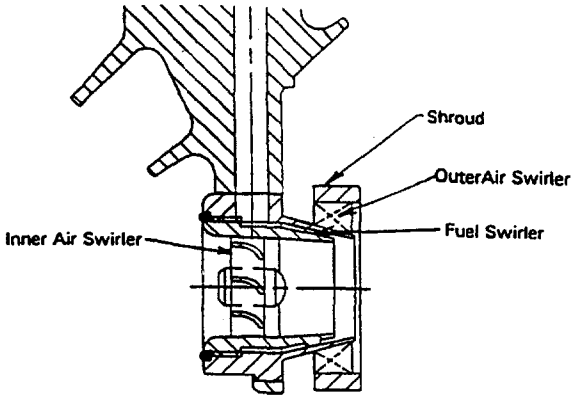

Fig. 2 Schematic diagram of airblast atomizer (courtesy of Parker Hannifin Corp.)

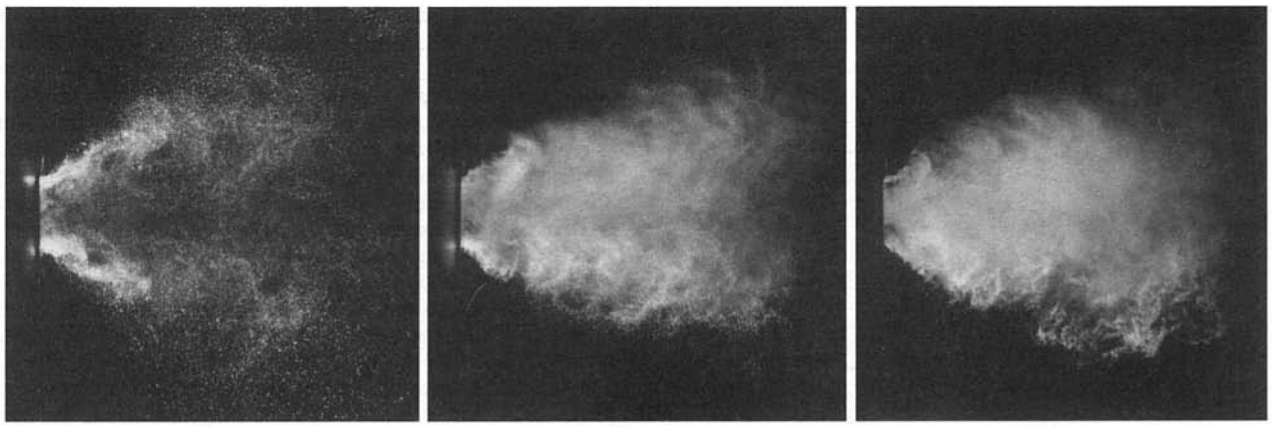

Fig. 3 Influence of air pressure on spray structure for a constant fuel flow; m_F = 5 g/s

ities to decline. This is especially true in the outer regions of the spray where the effects of air entrainment are most pronounced.

In most practical combustors, the fuel flow does not remain constant as pressure is varied, but rather changes in such a manner as to maintain a fairly constant air/fuel ratio (AFR). Figure 4 shows similar photographs to those presented in Fig. 3 except that for these tests the fuel flow was increased along with pressure to provide a constant AFR of 3.9. These photographs show the spray emerging from the nozzle and then expanding radially outward to form a hollow-cone spray. As the droplets move downstream, the spray boundaries, which initially are in the form of a straight cone, start to become curved due to the effects of air interaction, as mentioned earlier. Measurements of spray profiles are made difficult by the fact that the eddies generated by the shearing action of the two contrarotating swirling air flows cause the spray boundaries to fluctuate. Inspection of Figs. 3 and 4 suggests the possible occurrence of periodicity in the flow near the atomizer. Clearly this aspect warrants further investigation, since any pulsatile behavior in this region could give rise to combustion instability, although none has been experienced with this type of atomizer. In this context it is worth recalling that the eddy shedding associated with many types of bluff-body flame holders under cold-flow conditions is no longer observed under burning conditions. By superimposing on each other a number of spray profiles derived from individual high-speed photographs, as illustrated in Fig. 5 for a pressure of 1 bar and an AFR of 3.9, an informative and reasonably accurate "mean" spray profile can be constructed.

The fact that the sprays produced in airblast atomization tend to have curved boundaries creates difficulties in the definition and measurement of cone angle. With pressure-swirl atomizers, this problem is usually resolved by defining the cone angle as the angle formed by two straight lines drawn from the discharge orifice to cut the spray contours at some specified distance from the atomizer face. For prefilming airblast atomizers, an analogous method would be to use straight lines drawn from the prefilming lip to intersect the spray boundaries at some specified distance downstream of the lip. A drawback to this approach, at least in the context of the contraswirler design employed in these experiments, is that the diameter of the spray as it emerges from the nozzle is not only different from that of the prefilmer but also varies with changes in atomizer operating conditions. Measurements of spray diameter just downstream of the nozzle exit plane yielded values of 17.6, 15.5, and 15.7 mm for pressures of 1, 6, and 12 bar, respectively. For these measurements the AFR was held constant at 3.9. The cone angles obtained by drawing straight lines from the spray diameter at the nozzle exit to the mean spray diameter at certain specified distances downstream of the nozzle are presented in Fig. 6. They show that in the "near-nozzle" region, where the influence of the "natural" spray cone angle (i.e., the cone angle without any air flow) is quite strong, the cone angle widens with an increase in air pressure at a constant AFR. This is because the natural cone angle of the spray is wider than the cone angle of the atomizing air and its contribution to the resultant spray angle increases as a result of the increase in fuel/air

Fig. 4 Influence of air pressure on spray structure for a constant air/fuel ratio; AFR = 3.9

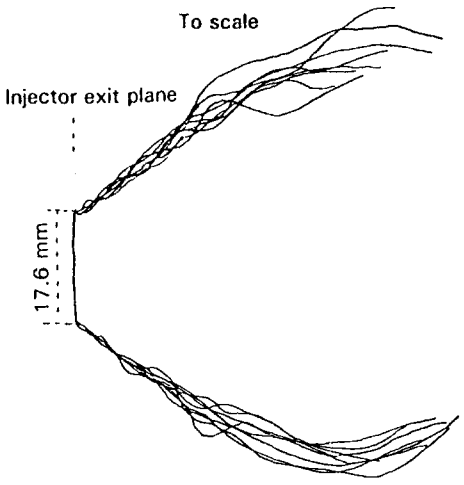

Fig. 5 Spray profiles measured at P = 1 bar and AFR = 3.9

momentum ratio that accompanies an increase in air pressure at constant AFR. Farther downstream, where atomization is complete and the droplets are completely airborne, the spray angle becomes largely independent of pressure. This result is only to be expected since the swirling and recirculating air flow patterns created by the air swirlers are independent of air pressure. However, it is important to recognize that although the overall dimensions of the aerodynamic recirculation zone tend to remain fairly constant with changes in operating conditions, the radial distribution of fuel within the total spray volume does vary with changes in pressure and fuel flow rate. This is illustrated in Fig. 7, which shows that increases in m_F tend to place more fuel in the outer regions of the spray. Photographic images such as those presented in Figs. 3 and 4 provide valuable insight into the prevailing spray structures, but caution must be exercised in their interpretation. For example they do not yield reliable information regarding such important spray properties as the size, velocity, and number density of droplets.

Drop Size and Velocity Distributions. The effects of variations in fuel flow rate on the radial distribution of Sauter mean diameter (SMD) and droplet velocity are demonstrated in Fig. 7 for values of m_F of 35, 50, and 65 g/s at a constant air pressure of 6 bar. As might be expected, increase in fuel flow rate increases both the local values of SMD and the overall spray SMD ($\overline{\text{SMD}}$). The latter was obtained as the mean of all the local measured values after each local value had been corrected using appropriate area and velocity weighting factors to account for the higher flow areas in the outer regions of the spray and the nonuniformity of the radial velocity distribution.

Figure 8 illustrates the results of detailed spray measurements carried out at normal atmospheric pressure. In this figure, local measured values of SMD and mean axial velocity are shown plotted against radial distance from the centreline of the spray. Measurements were carried out in two planes at downstream distances, Z, of 27 and 45 mm. The fuel flow rate was adjusted to maintain a constant AFR of 3.9.

The SMD curves shown in Fig. 8 are typical of all the results obtained at atmospheric pressure. At Z = 27 mm, the SMD initially increases with increase in spray radius up to a maximum value, which usually occurs at about the midradius, and then declines to a fairly constant value of SMD throughout the outer regions of the spray where most of the drops are located. With increase in downstream distance, the flow recirculations and mixing processes evident in Fig. 3 cause the radial distributions of both SMD and axial velocity to become more uniform. Thus, at a downstream distance of 45 mm, the local values of SMD increase gradually and continuously with increase in spray radius, as shown in Fig. 8.

Conversion of the local SMD values in Fig. 8 to $\overline{\text{SMD}}$ data revealed virtually no differences in $\overline{\text{SMD}}$ between the measurements carried out at downstream distances of 27 and 45 mm, being 54 μm in one case and 55 μm in the other. This suggests that the atomization process is virtually complete within a distance of 27 mm from the atomizer exit. It also indicates that in the fairly dilute sprays associated with atomization at low air pressures and low fuel flows rates, the effects of droplet coalescence, if any, are negligibly small. This is supported by the relatively flat droplet size–velocity correlation observed at this condition, thus implying no significant difference between the mean velocities of different drop size classes. The droplet velocities presented in Fig. 8 largely reflect the local values of axial air velocity. Near the spray axis, axial velocities are low and sometimes negative due to reverse flow of air in this region resulting from the large-scale flow recirculations created by the atomizing air. In the outer regions of the spray, the entrainment of surrounding air inevitably leads to a reduction in axial velocity, with the result that droplet velocities tend to be highest at about the midradius of the spray.

Figure 9 shows similar data to those presented in Fig. 8 for a pressure of 6 bar. At this higher ambient pressure the local values of SMD are fairly constant throughout the spray volume, increasing slightly with increase in spray radius. There is also a small rise in $\overline{\text{SMD}}$ from 47 to 50 μm with increase in Z from 27 to 45 mm. Other measurements at 6 bar showed similar small increases in $\overline{\text{SMD}}$ with increase in downstream distance, but the total number of data points obtained was too small to draw any worthwhile conclusions regarding the possible intervention of drop coalescence. Additional measurements at much higher pressures might have proved instructive in this regard. Unfortunately, at a pressure of 12 bar the spray density was usually too high to permit accurate measurements of SMD at Z = 27 mm. Consequently, the only data acquired at this pressure were at a downstream distance of 45 mm.

The influence of ambient air pressure on SMD is shown more directly in Fig. 10. These data indicate that an increase in pressure serves to reduce the $\overline{\text{SMD}}$. The effect is not large. For the test conditions quoted on the figure, $\overline{\text{SMD}}$ is reduced from 55 to 38 μm by an increase in pressure from 1 to 12 bar. Even this small effect of pressure is exaggerated by the fact that in these tests the fuel flow rate was maintained constant at 35 g/s regardless of changes in air pressure. Other tests in which pressure was varied while maintaining a fairly constant AFR, showed a much smaller effect of pressure on $\overline{\text{SMD}}$.

Data Analysis. Analysis of all the experimental data on $\overline{\text{SMD}}$ confirmed that the effect of pressure was small and could be described by the relationship $\overline{\text{SMD}} \propto P^{-0.05}$. The analysis

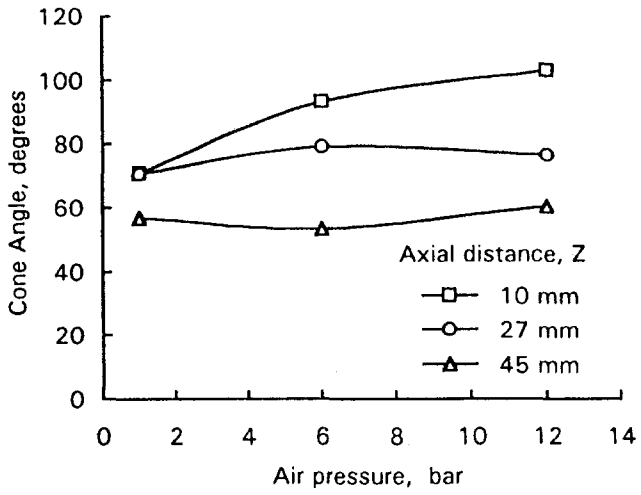

Fig. 6 Influence of pressure on spray cone angle for AFR = 3.9

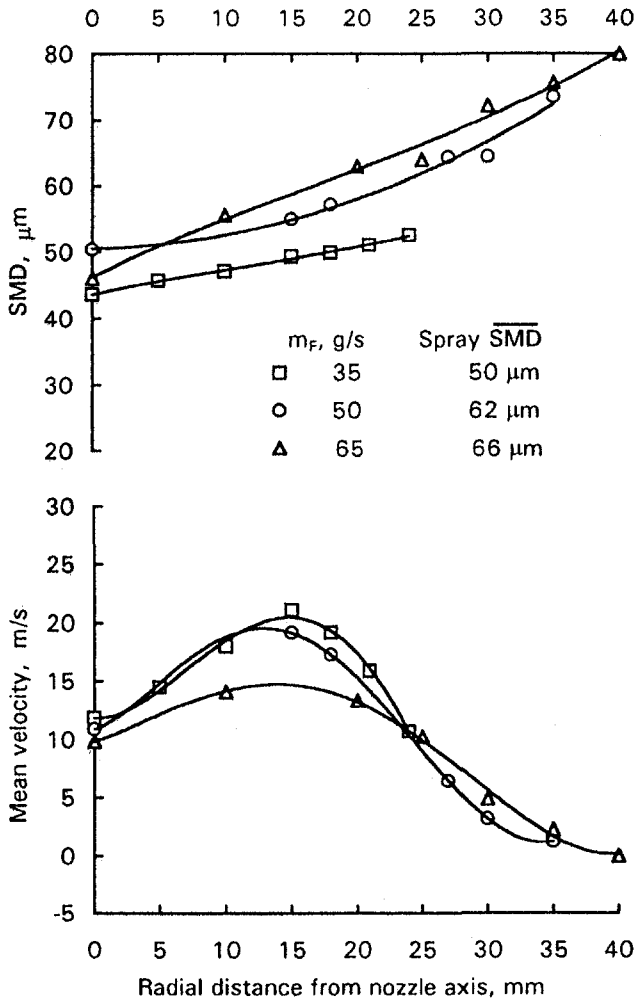

Fig. 7 Influence of fuel flow rate on drop sizes and velocities at P = 6 bar and Z = 45 mm

also indicated that the main factor governing spray $\overline{SMD}$ is air/fuel ratio, as indicated in the following empirical equation for $\overline{SMD}$ used to provide the data correlation shown in Fig. 11:

$$\overline{SMD} = 48\ P^{-0.05}(1 + AFR^{-1})^{0.5}$$

where $\overline{SMD}$ is in microns and P is the ambient air pressure in bar. This equation has no basic significance and is not dimensionally correct but it serves to illustrate the effects on mean drop size of the two main parameters covered in this investigation, namely air/fuel ratio and pressure. The air/fuel ratio term presents no special problems because the relationship $\overline{SMD} \propto (1 + AFR^{-1})^{0.5}$ has been reported by several previous workers, including Wigg (1964) and Jasuja (1979). Of primary concern is the relatively small effect of pressure on $\overline{SMD}$. Previous studies at Cranfield by Jasuja (1981, 1982), El Shanawany and Lefebvre (1980), and Rizk and Lefebvre (1984) yielded pressure exponents ranging from −0.4 to −1.0. A possible explanation for the apparent discrepancy between these results and those obtained in the present investigation is that airblast atomization can occur by one or two different mechanisms, or sometimes by a combination of both. If the atomizing air is flowing in generally the same direction as the fuel, atomization takes place relatively slowly by the classical mechanisms of liquid sheet breakup whereby $\overline{SMD}$ decreases markedly with increase in ambient air pressure (Squire, 1953). However, if sheet breakup occurs rapidly, the flow and surface instabilities that are an essential prerequisite for the classical mechanism of breakup have insufficient time to develop. Instead, the fuel sheet disintegrates into droplets as soon as it encounters the atomizing air. Under these conditions of "prompt" atomization, the $\overline{SMD}$ is predicted to be independent of pressure (Lefebvre, 1992). The importance of these findings in the present context is that the previous Cranfield studies were conducted on airblast atomizers in which the liquid and atomizing air were essentially coflowing. This arrangement is characterized by a relatively small aerodynamic interaction between the fuel and the air in the initial stages of the atomization process, thereby providing ideal conditions for breakup to occur via the classical mechanism. On the other hand, with modern practical atomizers (including the fuel injector used in this test program) the fuel sheet is subjected to the strong shear forces generated at the interface between two contraswirling air streams. Under these conditions the prompt mechanism of atomization must necessarily be dominant. This serves to explain why previous results on comparatively low-shear coflowing devices exhibited a marked dependence of $\overline{SMD}$ on pressure, whereas more recent measurements on modern high-shear practical atomizers generally indicate a much lower dependence of $\overline{SMD}$ on pressure.

Measurements reported by Jasuja and Lefebvre (1994) on a SNECMA prefilming airblast atomizer showed that with this nozzle design the SMD actually increased slightly with increase in pressure. They attributed this result to a combination of several possible effects, all of which are related to the increase in fuel flow rate that accompanies an increase in air pressure at

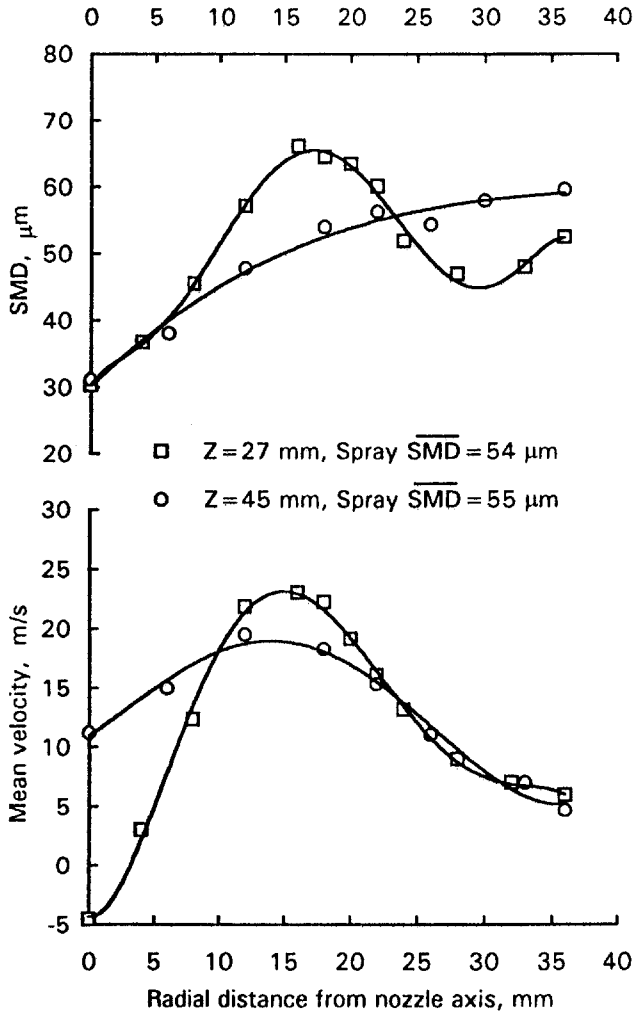

Fig. 8 Influence of downstream distance on drop sizes and velocities; P = 1 bar and AFR = 3.9

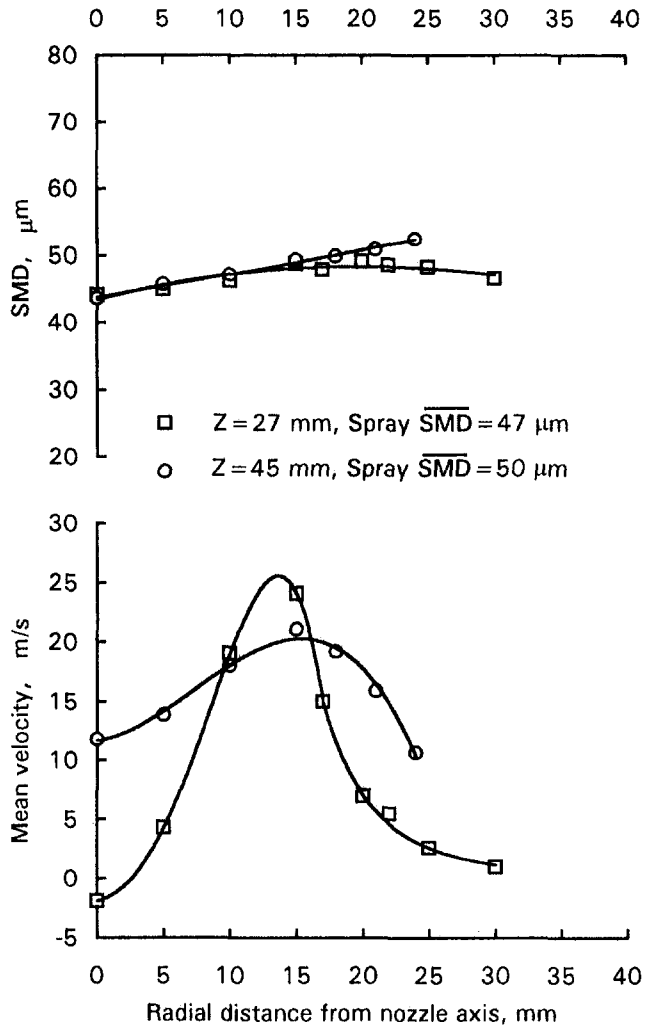

Fig. 9 Influence of downstream distance on drop sizes and velocities; P = 6 bar and AFR = 3.9

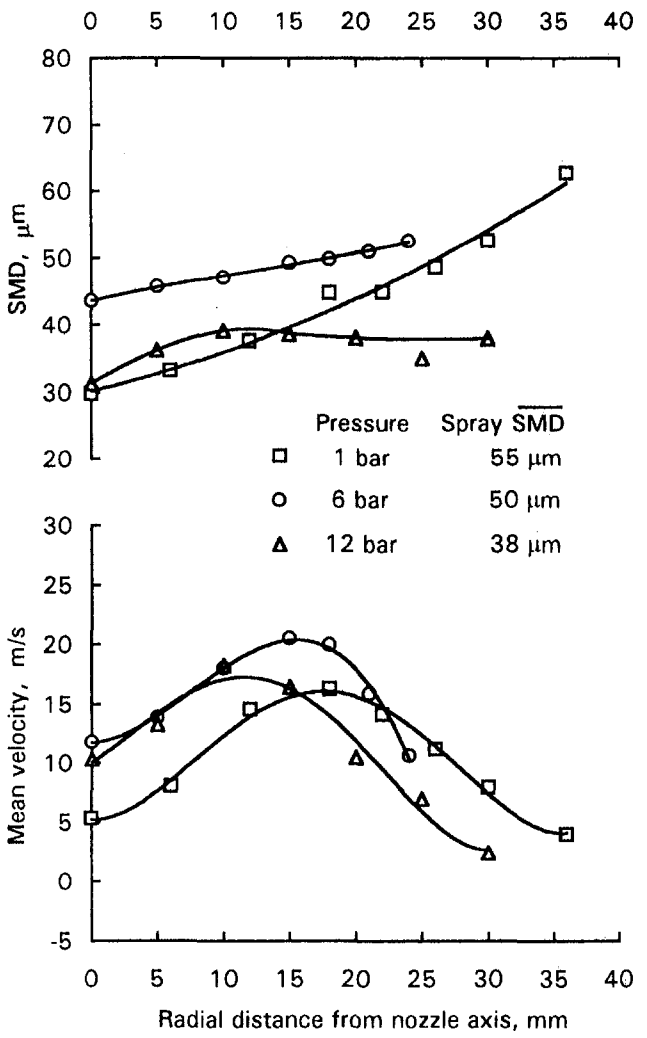

Fig. 10 Influence of air pressure on drop sizes and velocities; Z = 45 mm and m_F = 35 g/s

constant AFR. These include increase in initial film thickness, reduction in relative velocity between the fuel and the atomizing air, increased droplet coalescence, and the lower accessibility of the fuel to the atomizing air.

The fact that some or all of these effects can contribute toward increasing the SMD was confirmed in the present investigation, in which a number of tests were carried out at different levels of pressure while maintaining either a constant fuel flow rate (by allowing the AFR to increase linearly with increase in pressure) or a constant AFR. The purpose of these tests was to enable the effect of fuel flow rate on SMD to be separated from that of pressure. The results showed that increasing the pressure from 1 to 6 and then to 12 bar, while maintaining the fuel flow constant at 35 g/s, caused the measured SMD to decline from 55 to 50 and then to 38 microns, as shown in Fig. 10. This relatively large reduction in SMD ($\overline{SMD} \propto P^{-0.15}$) is due mainly to the increase in AFR that accompanied the increase in pressure. Similar tests over the same range of pressures for a constant AFR of 3.9 revealed a much smaller pressure dependence ($\overline{SMD} \propto P^{-0.05}$). These findings when considered alongside those obtained on a different design of prefilming airblast atomizer by Jasuja and Lefebvre (1994) tend to suggest that for high-shear atomizers the influence of pressure per se on overall Sauter mean diameter is quite small. In practice, increase in pressure may cause the SMD to either increase slightly or decrease slightly, depending on the design of the atomizer that governs the nature of the ensuing interaction between the fuel and the air streams. Clearly, a more systematic investigation is warranted to explore more fully the manner and extent to which various atomizer design features, notably prefilmer and air swirl geometries, govern the influence of air pressure on overall spray mean drop size.

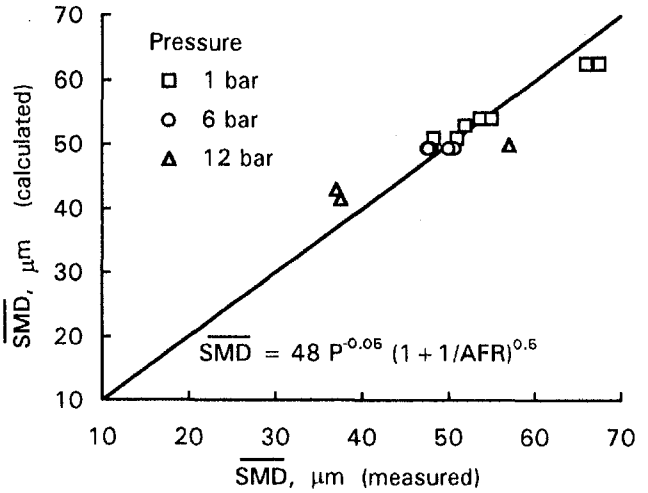

Fig. 11 Correlation of SMD data

Conclusions

From a series of measurements of drop sizes, drop velocities, and spray profiles carried out using kerosine fuel on a modern, practical, prefilming airblast atomizer featuring contraswirling air flows, the following conclusions are drawn:

1 Increase in ambient air pressure at a constant air/fuel ratio causes the initial spray cone angle to widen from 70 deg at 1 bar to around 105 deg at 12 bar. Farther downstream the cone angle and overall dimensions of the spray volume tend to remain fairly constant and independent of pressure.

2 The radial distribution of fuel within the spray volume is such that increase in fuel flow rate and/or decreases in air pressure cause a larger proportion of fuel to be contained in the outer regions of the spray.

3 Near the spray axis, the droplet axial velocities are generally low and sometimes negative. Droplet velocities increase with increase in spray radius, usually attaining their maximum values around the midradius of the spray. Beyond this point, velocities decline with increase in radius, reaching minimum values at the spray boundaries. This decline in axial velocity is attributed to the decelerating effect of air entrainment into the outer regions of the spray.

4 The results of tests carried out over a range of pressures from 1 to 12 bar show that the effect of ambient air pressure on the overall Sauter mean diameter (SMD) of the spray is quite small. This is attributed to the fact that for contraswirling airblast atomizers of the type employed in this investigation, the atomization process is dominated by the prompt mechanism of liquid sheet breakup, which theory indicates should be independent of pressure.

Acknowledgments

The authors gratefully acknowledge the award of a EPSRC-Rolls Royce plc co-funded research grant GR/H82372 entitled "Laser Diagnostics for Characterization of Gas Turbine Sprays under High Air Pressure Conditions." Special thanks are due to Mr. D. Whittington of Cranfield University for his painstaking efforts in regard to the experimental rig organization and running and to Miss B. Wilson for the skillful typing of the paper. The Parker Hannifin Corporation of Cleveland, Ohio, USA is also acknowledged for supplying the fuel injector used in this study.

References

El-Shanawany, M. S. M. R., and Lefebvre, A. H., 1980, "Airblast Atomization: The Effects of Linear Scale on Mean Drop Size," *J. Energy,* Vol. 4, No. 4, pp. 184–189.

Hebrard, P., Trichet, P., and Bardey, X., 1991, "Experimental Investigation of Two-Phase Flow in the Near Field of an Airblast Atomizer," *Fifth International Conference on Liquid Atomization and Spray Systems,* Gaithersberg, MD, pp. 669–678.

Hebrard, P., Lavergne, G., Beard, P., Donnadille, P., and Trichet, P., 1993, "Modelisation de las Phase Liquide dans les Chambres de Combustion," *AGARD Conference Proceedings 536,* pp. 36/1–12.

Jasuja, A. K., 1979, "Atomization of Crude and Residual Fuel Oils," ASME JOURNAL OF ENGINEERING FOR POWER, Vol. 101, No. 2, pp. 250–258.

Jasuja, A. K., 1981, "Airblast Atomization of Alternative Liquid Petroleum Fuels Under High Pressure Conditions," ASME JOURNAL OF ENGINEERING FOR POWER, Vol. 103, pp. 514–518.

Jasuja, A. K., 1982, "Plain-Jet Airblast Atomization of Alternative Liquid Petroleum Fuels Under High Ambient Air Pressure Conditions," ASME Paper 82-GT-32.

Jasuja, A. K., and Lefebvre, A. H., 1994, "Influence of Ambient Pressure on Drop Size and Velocity Distributions in Dense Sprays," *Twenty-Fifth Symposium (International) on Combustion,* The Combustion Institute, Pittsburgh, PA, pp. 345–352.

Lefebvre, A. H., 1992, "Energy Considerations in Twin-Fluid Atomization," ASME JOURNAL OF ENGINEERING FOR GAS TURBINES AND POWER, Vol. 114, No. 1, pp. 89–96.

McDonell, V. G., Seay, J. E., and Samuelsen, G. S., 1994, "Characterization of the Non-Reacting Two-Phase Flow Downstream of an Aero-Engine Combustor Dome Operating at Realistic Conditions," ASME Paper No. 94-GT-263.

Rizk, N. K., and Lefebvre, A. H., 1984, "Spray Characteristics of Plain-Jet Airblast Atomizers," ASME JOURNAL OF ENGINEERING FOR GAS TURBINES AND POWER, Vol. 106, pp. 634–638.

Squire, H. B., 1953, "Investigation of the Instability of a Moving Sheet," *British Journal of Applied Physics,* Vol. 4, pp. 167–169.

Wang, H. Y., McDonell, V. G., and Samuelsen, G. S., 1992a, "The Two-Phase Flow Downstream of a Production Engine Combustor Swirl Cup," *Twenty-Fourth Symposium (International) on Combustion,* The Combustion Institute, Pittsburgh, PA, pp. 1457–1463.

Wang, H. Y., McDonell, V. G., Sowa, W. A., and Samuelsen, G. S., 1992b, "Scaling of the Two-Phase Flow Downstream of a Gas Turbine Combustor Swirl Cup," ASME JOURNAL OF ENGINEERING FOR GAS TURBINES AND POWER, Vol. 115, pp. 453–460.

Wang, H. Y., McDonell, V. G., Sowa, W. A., and Samuelsen, G. S., 1994, "Experimental Study of a Model Gas Turbine Combustor Swirl Cup, Part II: Droplet Dynamics," AIAA *Journal of Propulsion and Power,* Vol. 10, No. 4, pp. 446–452.

Wang, H. Y., McDonell, V. G., and Samuelsen, G. S., 1995, "Influence of Hardware Design on the Flow Field Structures and the Patterns of Droplet Dispersion," ASME JOURNAL OF ENGINEERING FOR GAS TURBINES AND POWER, Vol. 117, pp. 282–289.

Wigg, L. D., 1964, "Drop Size Predictions for Twin-Fluid Atomizers," *J. Inst. Fuel,* Vol. 27, pp. 500–505.

Wynne, A., and Jasuja, A., 1991, "Visualization of Airblast Atomized Spray Structure Under Varying Air Pressure Conditions," AIAA Paper No. 91-2199.

Zhu, J. Y., Bachalo, E. J., Rudoff, R. C and Bachalo, W. D., 1993, "Assessments of a Fourier Transform Doppler Signal Analyser (DSA) and Comparisons With a Time-Domain Counter Processor," 6th ILASS-America.

Coupled Lagrangian Monte Carlo PDF–CFD Computation of Gas Turbine Combustor Flowfields With Finite-Rate Chemistry

A. K. Tolpadi

I. Z. Hu

S. M. Correa

General Electric Research & Development Center, P.O. Box 8, Schenectady, NY 12301

D. L. Burrus

General Electric Aircraft Engines, Mail Drop E404, Cincinnati, OH 45215

A coupled Lagrangian Monte Carlo Probability Density Function (PDF)–Eulerian Computational Fluid Dynamics (CFD) technique is presented for calculating steady three-dimensional turbulent reacting flow in a gas turbine combustor. PDF transport methods model turbulence–combustion interactions more accurately than conventional turbulence models with an assumed shape PDF. The PDF transport equation was solved using a Lagrangian particle tracking Monte Carlo (MC) method. The PDF modeled was over composition only. This MC module has been coupled with CONCERT, which is a fully elliptic three-dimensional body-fitted CFD code based on pressure correction techniques. In an earlier paper (Tolpadi et al., 1995), this computational approach was described, but only fast chemistry calculations were presented in a typical aircraft engine combustor. In the present paper, reduced chemistry schemes were incorporated into the MC module that enabled the modeling of finite rate effects in gas turbine flames and therefore the prediction of CO and NO_x emissions. With the inclusion of these finite rate effects, the gas temperatures obtained were also more realistic. Initially, a two scalar scheme was implemented that allowed validation against Raman data taken in a recirculating bluff body stabilized $CO/H_2/N_2$–air flame. Good agreement of the temperature and major species were obtained. Next, finite rate computations were performed in a single annular aircraft engine combustor by incorporating a simple three scalar reduced chemistry scheme for Jet A fuel. This three scalar scheme was an extension of the two scalar scheme for $CO/H_2/N_2$ fuel. The solutions obtained using the present approach were compared with those obtained using the fast chemistry PDF transport approach (Tolpadi et al., 1995) as well as the presumed shape PDF method. The calculated exhaust gas temperature using the finite rate model showed the best agreement with measurements made by a thermocouple rake. In addition, the CO and NO_x emission indices were also computed and compared with corresponding data.

Introduction

A gas turbine combustor is a complex combustion device within which there exists a wide range of coupled, interacting physical and chemical phenomena. Some of these phenomena are finite-rate chemistry of combustion/NO_x emissions/CO emissions, turbulent transport, two-phase flow, radiation, and particulate behavior. Depending on the specific issues being addressed, models of varying degrees of sophistication have been employed. The level of sophistication in design models has been increasing over the years with improvements in numerical methods, computer capabilities, and physical understanding. Generally speaking, in order to model three-dimensional flows, a compromise has to be made between the complexity of the model and the speed of the available computers.

The calculation of emissions in practical combustors requires the treatment of finite rate kinetics as well as the need to compute the three-dimensional flow field within them (combustors). In order to predict emissions accurately, it is important to account for the effect of turbulent fluctuations. Modeling of combustion with an eddy breakup model is inadequate because it does not contain any information about kinetics and ignores the effect of turbulent fluctuations on the reaction rate. The effect of fluctuations can be modeled using the probability density function (PDF) approach. Current generation CFD models for practical combustors typically employ an assumed shape PDF parameterized by the mean and variance of the mixture fraction (Correa and Shyy, 1987; Shyy et al., 1988; Tolpadi, 1995). Transport equations are solved for each of the mean and variance. The chemistry is assumed to be infinitely fast, although slow reactions can be considered if they are decoupled from the heat release reactions. The density and temperature field are then related to a single conserved scalar. A variety of shapes can be prescribed for the PDF. In the work referenced above, a beta PDF was employed. Such an approach makes reasonable estimates (Gulati et al., 1995) of the combustor exit temperature profile and NO_x emissions as a function of inlet pressure, temperature, fuel–air ratio, etc., in terms of trends. However, it cannot predict CO, UHC, and other important phenomena such as blowout. It is possible to model finite rate kinetics with multidimensional assumed shape PDF's, but it is not very practical since the PDF prescription can become very complex and problem dependent.

A more promising approach for the solution of turbulent flows with finite rate chemistry is the PDF transport method (Pope, 1990). The PDF transport method solves the transport equation for a joint PDF of at least the composition variables. The composition PDF eliminates the need to model the mean reaction rates. The mean value of density, temperature, and the composition can be obtained from the PDF. Models have to be

Contributed by the International Gas Turbine Institute and presented at the 41st International Gas Turbine and Aeroengine Congress and Exhibition, Birmingham, United Kingdom, June 10–13, 1996. Manuscript received at ASME Headquarters February 1996. Paper No. 96-GT-205. Associate Technical Editor: J. N. Shinn.

developed for convection and molecular mixing. The velocity terms can be retained to yield a joint velocity–composition PDF that eliminates the need for gradient transport models, although modeling of the viscous terms and the pressure gradient are required. The mean pressure field can be obtained by solving a Poisson equation for elliptic flows (Anand et al., 1990) or through the solution obtained by a conventional flow solver (Correa and Pope, 1992). The joint velocity–composition PDF approach was used in calculating a recirculating two-dimensional axisymmetric stabilized flame (Pope and Correa, 1986; Correa and Pope, 1992). A review of the pertinent literature was made in Tolpadi et al. (1995).

In the earlier paper (Tolpadi et al., 1995), the development of a Monte Carlo composition PDF module and its coupling with a fully elliptic three-dimensional body-fitted CFD code based on pressure correction techniques (CONCERT-3D) was described. CONCERT-3D has been used extensively to calculate complex single phase (Shyy et al., 1985, 1988) and two-phase (Tolpadi, 1995) three-dimensional flow fields in an aircraft engine combustor. CONCERT calculates the mean velocity and turbulence field (using a standard $k-\epsilon$ turbulence model) that are required by the composition PDF module. The PDF transport equation was solved using a Lagrangian particle tracking Monte Carlo method. By performing ensemble averages of the particles in each computational cell, the mean density field is obtained and supplied to the CONCERT code. In the present paper, reduced chemistry schemes were incorporated into the Monte Carlo module that enabled the modeling of finite rate effects. This, in turn, allows the prediction of CO and NO_x emissions.

Prior to the simulation of the gas turbine flow field, a recirculating bluff body stabilized $CO/H_2/N_2$ flame was modeled (Raman measurements for this flame were made by Correa and Gulati (1992)). A simple two scalar scheme as described by Correa and Pope (1992) was implemented and served as an initial validation of the three-dimensional CFD/finite rate calculation procedure. The computed temperature and major species showed very good agreement with the data. Next, this two scalar scheme was extended to three scalars (Correa, 1995) for Jet A fuel and was used to analyze a three-dimensional single cup section of a modern aircraft engine combustor. Numerical solutions with the present finite rate model were obtained on an HP-735 workstation and compared with those obtained using the fast chemistry PDF transport approach (Tolpadi et al., 1995) as well as the presumed shape PDF method. The predicted exhaust gas temperature contours showed best agreement with measurements (made by a thermocouple rake) with the finite rate chemistry PDF transport approach. In addition, the CO and NO_x emission indices were also computed and compared with exhaust gas sampled data.

Methodology

Monte Carlo/CONCERT Code Structure. The hybrid Monte Carlo/CONCERT CFD code consists of three separate modules that interface and communicate with each other via Fortran common blocks. The three modules are, respectively: (1) the chemistry and mixing module, (2) the particle tracking module, and (3) the gas velocity (i.e., CFD) module. A detailed description of these modules is available from Tolpadi et al. (1995). Only a brief description will be given here. Figure 1 outlines the flow of information between the modules. In the PDF transport method, the scalar PDF is discretized into equal "particles." These particles carry with them a certain number of attributes, which are convected and diffused through the entire computational domain based on the mean gas velocity field and the diffusion parameters. The particle array $\mathbf{f}(\mathbf{n}, \mathbf{m})$ describes the composition completely. In this notation, n is the particle index ($n = 1, 2, \ldots . N_p$ where N_p is the total number of particles) and m is the attribute number given as follows:

m = 1 is the particle density (ϱ)
m = 2 is the cell number of the particle location at a given time
m = 3 is the particle weight that is associated with the mass flux
m = 4, 5, ... $4 + N_s - 1$ are the values of each of the N_s scalars represented by the particle
m = $4 + N_s$, ... $4 + N_s + 2$ are the local coordinates of the particle within a cell

From the list of particles present in a computational cell, the PDF of a particular attribute can be obtained in the cell. Thus, instead of assuming a shape for the PDF, it is actually computed by this method. In what follows, each of these modules together with their functions will be briefly described.

Chemistry/Mixing (CM) Module. The chemistry module is the one that changes the scalar attributes of each particle based on chemistry and mixing. An ordinary differential equation (ODE) is solved for each particle and for each scalar attribute. Turbulent mixing is modeled by the "Interaction by Exchange with the Mean" (IEM) model (Borghi, 1988). The form of the differential equation is given by Tolpadi et al. (1995). In a fast chemistry calculation, the mixture fraction attribute (ξ) of the particle is the only scalar that is computed, and the source term of the corresponding ODE is zero. In the finite rate chemistry model, two more scalars are calculated that represent the fuel mass fraction (Y_f) and a reduced scalar $Y^*_{H_2}$ that comprises a combination of certain species to be described later. The ODEs for these two scalars have nonzero source terms. These three scalars are the main scalars representing the finite rate chemistry for Jet A. (Details of the reduced chemistry scheme will be given later in this section.) In the actual implementation of the finite rate chemistry PDF transport method, five additional scalars are tracked for each particle: temperature (T), source term for the Y_f equation ($\dot{W}_{Y_f}$), source term for the $Y^*_{H_2}$ equation ($\dot{W}_{Y^*_{H_2}}$), source term for the NO_x equation ($\dot{W}_{NO}$, Zeldovich mechanism assumed) and the CO mass fraction (Y_{CO}). Prior to performing any calculations, a thermochemical lookup table is generated that contains ϱ, T, $\dot{W}_{Y_f}$, $\dot{W}_{Y^*_{H_2}}$, $\dot{W}_{NO}$ and Y_{CO} as a function of (ξ, Y_f, and $Y^*_{H_2}$). The table is quite refined with 50 intervals in ξ space, 30 intervals in Y_f space, and 200 intervals in $Y^*_{H_2}$ space. Based on the computed values of the three main scalars for each particle, the values of the other scalars are obtained from the table using a trilinear interpolation procedure. The mean density in each cell is the only scalar that is passed

Nomenclature

d = jet exit diameter (bluff body flame)
D = diffusivity used in the random walk $= 2\mu_T/\bar{\varrho}$
N_p = total number of particles in the computational domain
N_s = number of scalars represented by a particle
t = time coordinate
Δt = time step
x = axial distance downstream from jet (bluff body flame)
Y_f = fuel mass fraction
$Y^*_{H_2}$ = combined reactive scalar (Eq. (9))
ξ = mixture fraction
μ_T = turbulent viscosity (momentum equations)
$\bar{\varrho}$ = mean density calculated for each computational cell

to the CFD module. The CM module works strictly with the list of particles, and does not actually require any information about the geometry (other than the index of the cell in which each particle resides, which is provided by the particle tracking module).

Particle Tracking (PT) Module. The particle tracking module is set up to repetitively do the following prototypical initial value problem: Given the starting particle positions (x_n^0, y_n^0, z_n^0), the size of the time step Δt and the velocity field from the CFD module, it returns the new position (x_n, y_n, z_n) and the corresponding control volume index at the end of the time step. Diffusion of the particles is controlled by the term that models the random walk (stochastic fluctuations) as the particles move through the domain. This walk is random and is assumed to be isotropic possessing a Gaussian probability distribution in the fluctuating displacement. This displacement has a standard deviation given by Brownian motion theory to be $(D\Delta t)^{1/2}$, where $D = 2\mu_T/\bar{\varrho}$ (Pope, 1985). At the inlets, the incoming mass flow is discretized into particles in such a way that the same number of particles enter from each inlet cell but their weights are adjusted to reflect the mass flow. Further details of the PT module are available from Tolpadi et al. (1995).

CFD Module. The gas phase velocity field is computed by the CONCERT-3D CFD code. The standard $k-\epsilon$ turbulence model is used with wall function treatment for near wall regions. The equations of motion solved by CONCERT-3D are continuity, momentum, and turbulence (k and ϵ). The governing equations together with their discretization and the numerical algorithm have been described in detail by Tolpadi and Braaten (1992) and Shyy and Braaten (1986) and will not be repeated here.

Figure 1, as mentioned before, gives a pictorial representation of the communication between the modules. In the serial implementation, the modules are run in the following sequence: The CFD module is run for 100–200 iterations (assuming constant density) that provides a provisional gas velocity field, which is supplied to the particle tracking module. An initial ensemble of particles is specified cell-by-cell with equal number of particles in each cell. The initial scalar attribute of each of these particles is set equal to the initial value of the scalar (which, in fact,

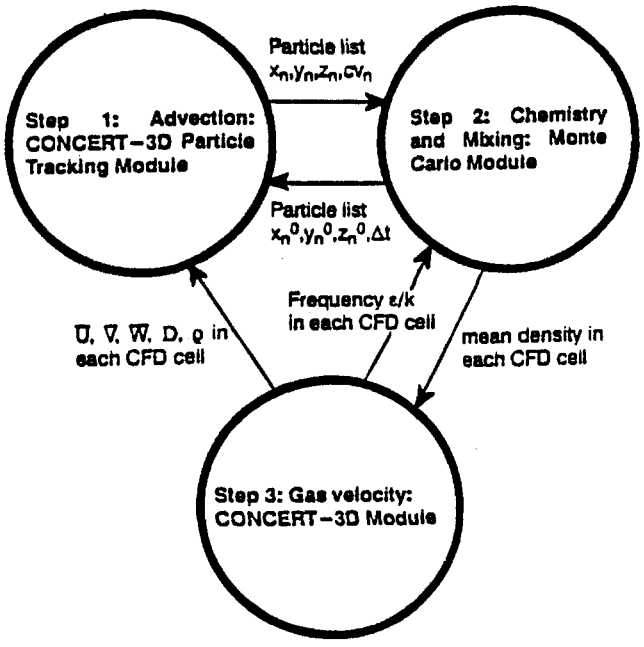

Fig. 1 Schematic of communications within the modules of the hybrid CONCERT/Monte Carlo code

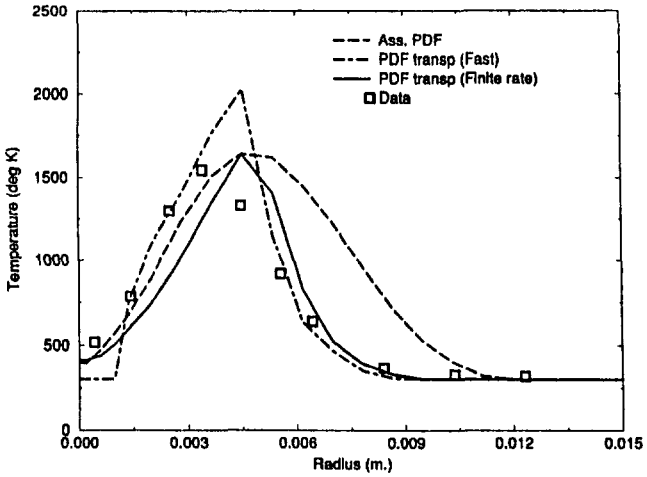

Fig. 2 Predictions of the radial distribution of the temperature at x/d = 10, and compared against data (Correa and Gulati, 1992)

may be zero) in the cell in which the particle resides. The particle tracking and chemistry modules are advanced 20–50 time steps. At each time step, a fixed number of particles enter from the inlets while all the particles within the domain are transported around in both physical and composition space (some particles leave the domain through the exits). At the end of the 20–50 time steps, a new density field is computed. At this point, one cycle of the calculations is complete. At the beginning of the next cycle, this new density field is used by the CFD module to recompute the gas velocity field and the entire process repeats thereon. A stochastic steady-state solution (fixed number of particles in the domain and constant ensemble averages of the attributes) was typically achieved in about 10–25 cycles of the computations.

Finite Rate Chemistry Model. Given the complexity of hydrocarbon chemistry and the cost of PDF transport simulations, a three-scalar reduced kinetic model (Correa, 1995) for Jet-A fuel is adopted to represent the finite-rate chemistry in the present work. In this reduced kinetic model, fuel (C_nH_m, n = 12.5, m = 23 for Jet-A) is pyrolyzed to CO and H_2 in a global step:

$$C_nH_m + \frac{n}{2}O_2 \rightarrow nCO + \frac{m}{2}H_2 \quad (1)$$

and the oxidation of CO and H_2 is described by the following detailed scheme:

$$CO + OH \leftrightarrows CO_2 + H \quad (2)$$

$$H_2 + O \leftrightarrows OH + H \quad (3)$$

$$O_2 + H \leftrightarrows OH + O \quad (4)$$

$$OH + OH \leftrightarrows H_2O + O \quad (5)$$

$$H_2 + M \leftrightarrows H + H + M \quad (6)$$

$$O_2 + M \leftrightarrows O + O + M \quad (7)$$

$$H + OH + M \leftrightarrows H_2O + M \quad (8)$$

where Steps (2)–(5) are shuffle reactions and Steps (6)–(8) are three-body recombination reactions. This reduced scheme contains nine species: C_nH_m, CO, CO_2, H, H_2, H_2O, O, O_2 and OH, which is still a large number for Monte Carlo simulations.

To reduce the number of scalars further, the shuffle reactions are assumed to be fast enough to reach equilibrium state compared to the recombination reactions. With this partial equilibrium assumption, only three independent scalars are needed to

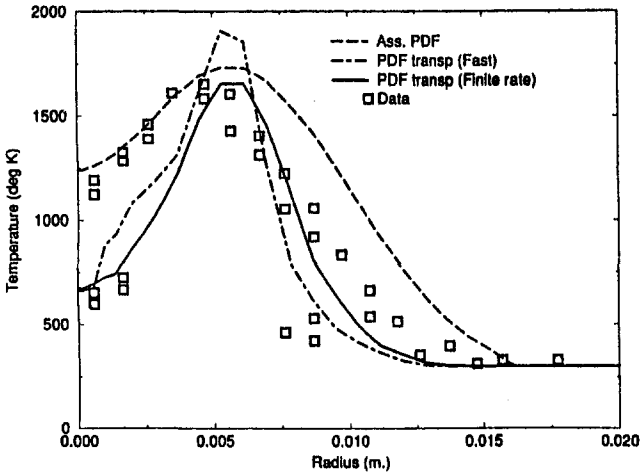

Fig. 3 Predictions of the radial distribution of the temperature at x/d = 20, and compared against data

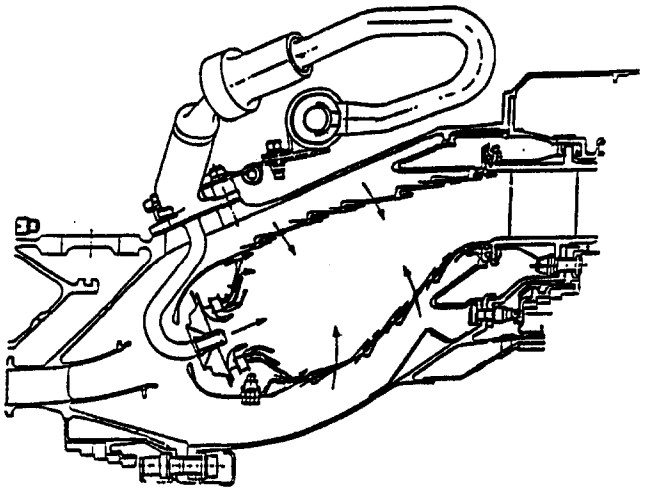

Fig. 5 Geometry of a typical single annular aircraft engine combustor

determine the thermochemical state of the finite-rate chemistry. These three scalars are the mixture fraction ξ, the mass fraction of fuel Y_f and a combined variable $Y^*_{H_2}$, which is defined as

$$Y^*_{H_2} = Y_{H_2} + \tfrac{1}{2}Y_{OH} + Y_O + \tfrac{3}{2}Y_H + Y_{CO} \quad (9)$$

where Y_j (j = H_2, OH, O, H, CO) is mass fraction of species. The ranges of these three scalars are confined within a tetrahedron described by Correa (1995).

Given values of ξ, Y_f, and $Y^*_{H_2}$, the thermochemical properties, such as temperature, density, and species concentrations, are uniquely determined from conservation of elements, conservation of energy, state equation, and relations among species introduced by the equilibrium assumption of Reactions (2)–(5). The reaction rates for Y_f and $Y^*_{H_2}$ are then computed from the species concentrations and temperature.

The reaction rate for the pyrolysis step is expressed in Arrhenius form:

$$\dot{w}_{Y_f} = -A \exp(-T_a/T)[C_nH_m][O_2] \quad (10)$$

where the variables take the units of kmol, m, s, and K. The rate constants A and T_a are obtained by calibrating the autoignition time against the measured data (Spadaccini and TeVelde, 1980) at a series of pressure and inlet temperature of interest. In the present work, $A = 8.04 \times 10^{14}$ m^3/kmol/s, and T_a = 22700 K. The production rate of the combined scalar $Y^*_{H_2}$ can be derived from the net reaction rates of H_2, OH, O, H, and CO, and the result is

$$\dot{w}_{Y^*_{H_2}} = -2(\dot{w}_6 + \dot{w}_7 + \dot{w}_8) \quad (11)$$

where $\dot{w}_6$, $\dot{w}_7$, and $\dot{w}_8$ are the net forward reaction rates of Reactions (6), (7), and (8), respectively. The standard rate constants are used for these three elementary reactions.

To shorten the computing time of the PDF transport simulations, a table containing thermochemical properties, e.g., $T(\xi, Y_f, Y^*_{H_2})$, is generated before the actual calculations begin. The scalars ξ, Y_f, and $Y^*_{H_2}$ are the three independent attributes of each particle in the Monte Carlo simulations. All other attributes of a particle, i.e., temperature, density, CO mass fraction, and the reaction source terms are then obtained by looking up the property table. The mean thermo-chemical properties within a CFD cell are computed by ensemble averaging each attribute over all the particles in that cell.

Results

As stated earlier, initially, the two scalar scheme was implemented for a $CO/H_2/N_2$ fuel. Calculations were performed to

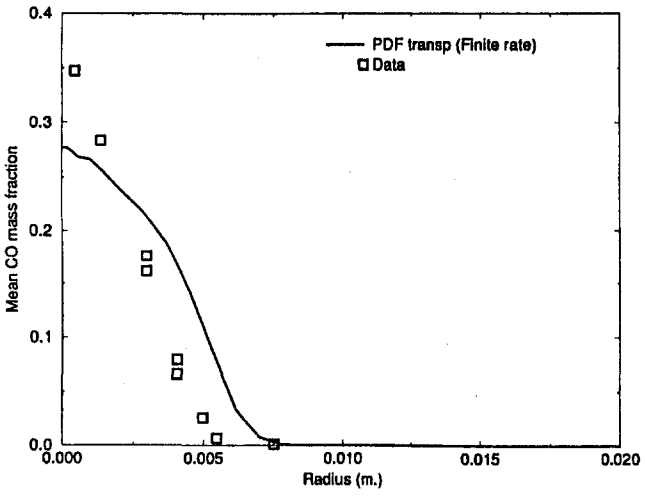

Fig. 4 Predictions of the radial distribution of the CO mass fraction at x/d = 10, and compared against data

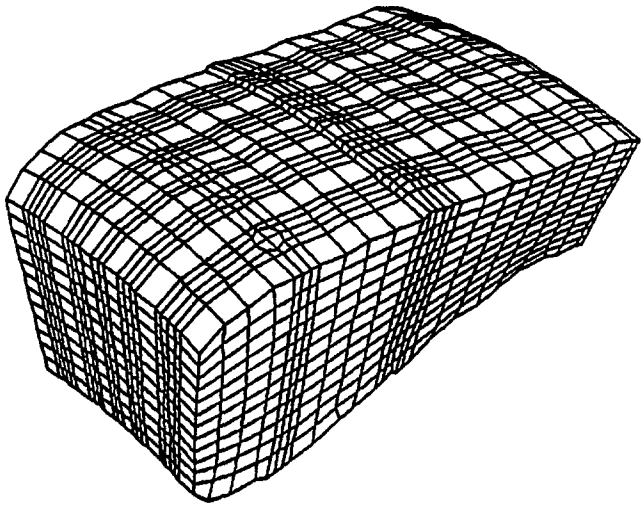

Fig. 6 Three-dimensional view and grid of a single cup sector of an annular combustor

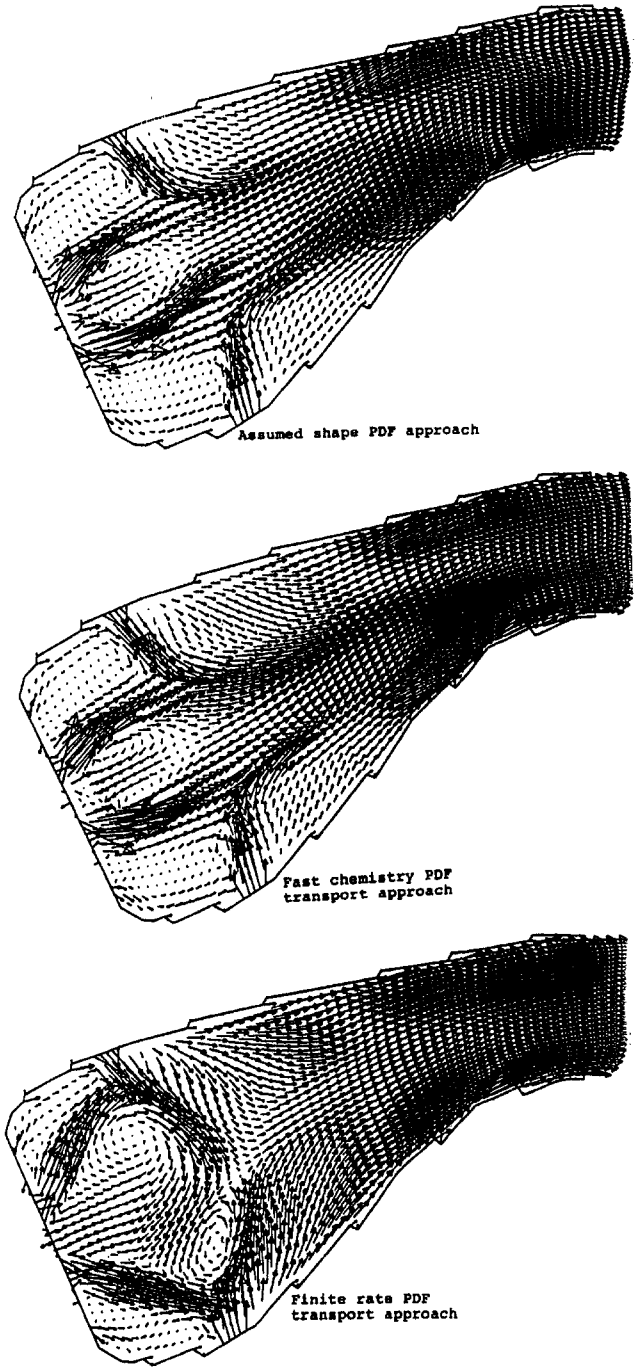

Fig. 7 Projected velocity vectors in a side view through the swirl cup of the engine combustor at high power conditions (assumed shape PDF approach, fast chemistry PDF transport approach, and finite rate PDF transport approach)

predict the flow field in a bluff body stabilized nonpremixed axisymmetric flame with this fuel within which Raman data have been taken by Correa and Gulati (1992). Information about the experimental configuration as well as the computational details are given by Tolpadi et al. (1995) in which fast chemistry PDF transport calculations were reported. Even though the geometry is two-dimensional axisymmetric, the bluff body was modeled as a three-dimensional object (polar grid with 15 deg sector angle) with 75 cells in the axial, 60 cells in the radial, and 3 cells in the angular direction. A total of 17 cycles was required to obtain a converged finite rate solution. Each cycle in this case comprised of 200 CONCERT iterations and 30 time steps through which the PT/CM modules were advanced.

Figure 2 shows the radial temperature distribution at the axial location of $x/d = 10$. This figure displays the result from the present two scalar (finite rate) PDF transport calculation as well as the fast chemistry PDF transport calculation from Tolpadi et al. (1995). Also shown is the result from the assumed shape PDF computation with fast chemistry. The PDF transport solution with fast chemistry predicts a peak temperature of over 2000 K that is much higher than the data, which is due to lack of modeling of the finite rate effects. When the finite rate effects are included via the two scalar model, the peak temperature decreases and the profile shows much better agreement with the data although it appears to be slightly shifted (relative to the data) in the region near the centerline. Interestingly, the assumed shape PDF solution predicts a peak temperature that

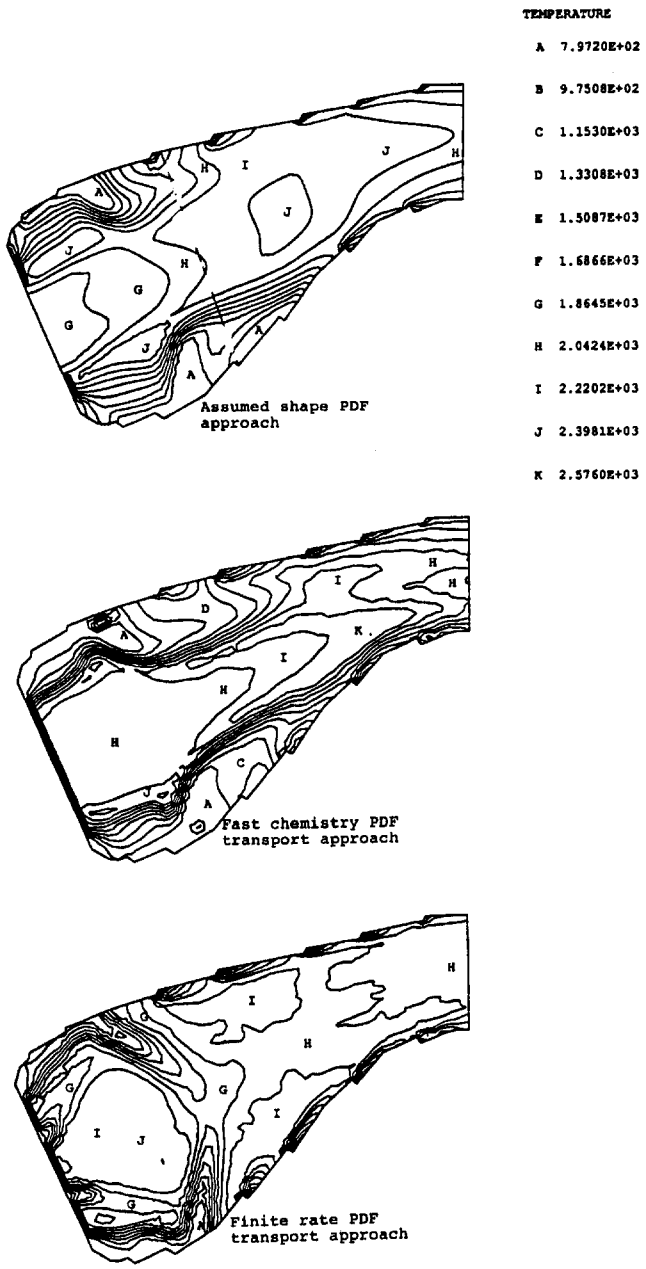

Fig. 8 Calculated temperature contours (K) in a side view through the swirl cup of the engine combustor (assumed shape PDF approach, fast chemistry PDF transport approach, and finite rate PDF transport approach)

is only slightly greater than the data but in regions away from the centerline this temperature is significantly overpredicted. Figure 3 shows the temperature comparisons at $x/d = 20$. The same conclusions can be made at this location as well: The PDF transport solution with the two scalar model shows better agreement with the data than the corresponding fast chemistry calculation while the assumed shape PDF solution overpredicts the far field temperature. Figure 4 shows the comparison of the predicted radial distribution of CO with data. The agreement appears to be quite reasonable with the center peak profile obtained in the calculations, although the CO mass fraction is underpredicted near the centerline and vice-versa away from the centerline. Predictions of H_2, CO_2, and H_2O (although not shown) indicated similarly good agreement with the data.

Figure 5 shows a schematic of a modern aircraft engine combustor that was analyzed earlier (Tolpadi et al., 1995). It is of annular design with 20 swirl cups equally spaced around the circumference. Within a single-cup sector of 18 deg span, there are five dilution holes (two primary and three secondary) on each of the top and bottom surfaces. There are also seven and six film cooling slots on the top and bottom surfaces, respectively. The calculations were conducted in a single cup sector with periodic boundary conditions imposed on the two side planes. The mesh for this combustor has $61 \times 31 \times 31$ grid points (total: 54,000 cells) in the three directions. Figure 6 shows the grid with several grid lines removed to improve clarity. Finite rate calculations using the PDF transport model were performed with Jet A fuel and under full power conditions. There were 4630 incoming particles per time step, 702,000 initial particles in the domain and the time step Δt was 0.1 ms. One complete cycle consisted of 200 CFD iterations and 30 time steps through which the PT/CM modules were advanced. After particle clustering/splitting, the total number of particles in the domain reached a steady number of 1.08 million. A total of 20 cycles were required and the total HP-735 cpu time needed was 85.7 hours with the following distribution: 26.2 hours in the CFD module, 14.9 hours in the CM module, and 44.6 hours in the PT module. This should be compared with the 61.8 hours required for the corresponding fast chemistry PDF transport computation (Tolpadi et al., 1995). This finite rate calculation requires about 39 percent more cpu time, with the table lookup process in the CM module taking up most of the additional time. The turnaround time of these Monte Carlo simulations can be reduced significantly if the particle tracking and interpolation tasks were distributed over a parallel network of workstations/processors. This approach is presently being studied.

Figure 7 shows the velocity vectors in a side view plane in line with the swirl cups. While the flow field as calculated by the PDF transport approach with fast chemistry is very similar to that obtained with the assumed shape PDF, the corresponding vectors are dramatically different with the finite rate model. The primary dilution hole flows from the inner and outer walls interact with each other as well as with the flow from the swirl cups, resulting in the establishment of a recirculation zone for the flame. But this recirculation zone is very small in the first two cases and far more pronounced with the finite rate effects. The recirculation zone fills the head end of the combustor and entrains a significant fraction of the dilution jets issuing from the lower and upper walls. In contrast, the flowfields of Figs. 7(*a*) and 7(*b*) manifest little interaction of the fuel-laden swirl cup flow with either the total volume of the head end or with the dilution jets. Although direct observation of the flame zone of this full power engine condition was not possible, there is indirect but strong evidence supporting the flow structure of Fig. 7(*c*). For example, perfectly stirred reactor calculations using all the swirl cup flow, half the dilution jet flow, and the total volume of the head end agree well with thermal NO_x and flame stability data from a range of engines.

Figure 8 is the temperature field in the same side view plane as obtained by the three methods. As expected, the predicted temperature is lower with the finite rate PDF transport model with the peak values in the region between the inlet and the primary dilution holes. The other two approaches predict the peak temperature to be beyond the primary dilution holes. Figure 9 shows the temperatures in the exit plane together with measured test data acquired from traversing the combustor exit annulus with conventional thermocouple rakes (in Fig. 9(*d*)). The most important point to note in this figure is that the peak temperature decreases by nearly 250 K with the finite rate PDF transport model as compared to the fast chemistry PDF transport

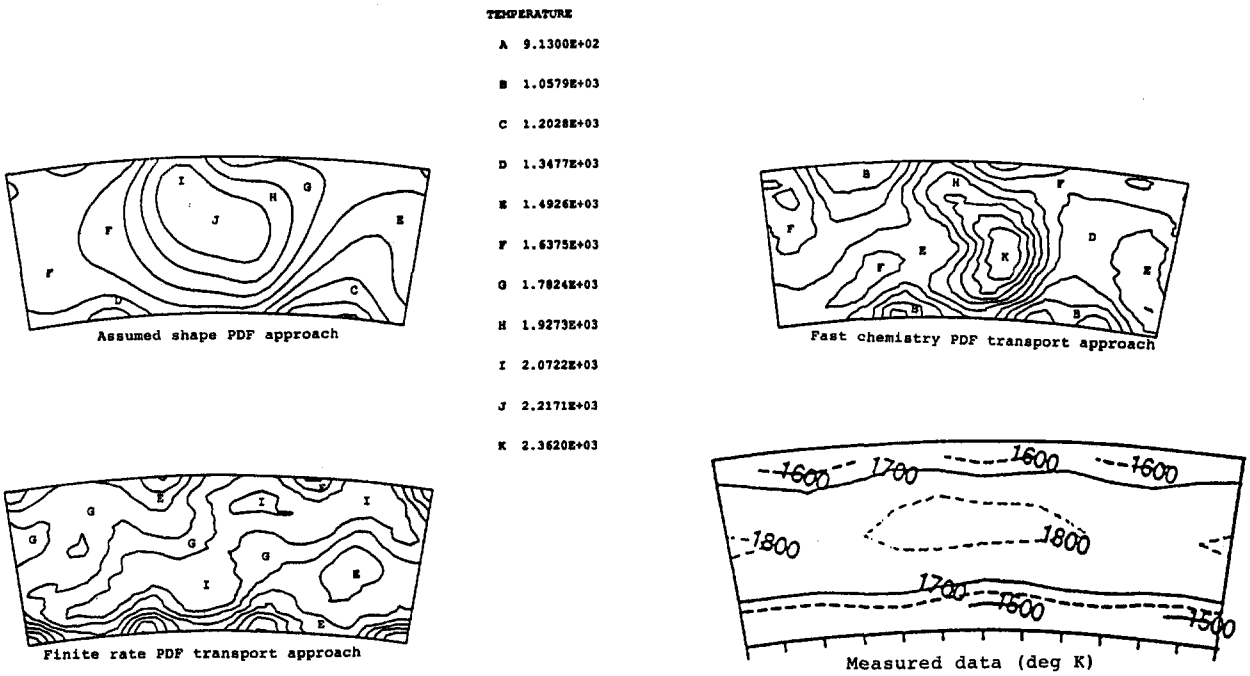

Fig. 9 Calculated temperature contours (K) at the exit of the engine combustor (assumed shape PDF approach, fast chemistry PDF transport approach, finite rate PDF transport approach and measured data)

model. The finite rate prediction of the exit temperatures is also closer to the data. However, the measured exit gas temperature data indicate the peak temperature to be still over 200 K lower than the prediction from the finite rate PDF transport model. The qualitative features of the gas temperature variation displayed as contours appear to be best predicted with the finite rate PDF transport approach.

This finite rate simulation also allowed the calculation of CO emissions. Figure 10 shows the CO mass fraction distribution in the same side view plane in line with the swirl cups. Clearly, a significant amount of CO is formed in the primary reaction zone, which is quickly oxidized in the dilution zone downstream. The field of fuel concentration (not shown here) shows that all the fuel is pyrolyzed to CO and H_2 in the primary zone. The field of the third scalar $Y^*_{H_2}$ shows that the combustion reaches an equilibrium state at the exit plane and explains why only a small amount of CO is observed at the exit. By mass averaging this exit CO, the corresponding emission index (EICO) was computed in terms of gm/kg fuel. The emission index was also obtained from rig tests (based on gas sampling) performed at GE-Aircraft Engines. The following table summarizes the results:

	EICO (predicted)	EICO (measured)	$EINO_x$ (predicted)	$EINO_x$ (measured)
High Power	3.835	0.90	31.8	18.3
Low Power	1.669	34.0	1.656	4.0

The CO emission index at high power operation is predicted to be 3.835 compared to the measured level of 0.90.

In addition to the calculations at high power conditions described so far, simulations were also performed at low power (ground idle). No detailed contour plots for this case will be included here, but the predicted emission indices are also shown in the above table. At low power conditions, the pressure and the fuel inlet temperature were much lower than full power, and the combustor fuel–air ratio was also lower. The CO emission was expected to be much larger than the high-power case, as indicated by the measured data. However, the calculated EICO was 1.669, which again corresponded to the equilibrium state at the exit plane. The prediction of EICO was lower in the low-power case relative to high power because of differences in the equilibrium state at the two corresponding fuel–air ratios.

High CO emissions measured at low power are likely caused by slower vaporization of liquid fuel injected from the swirlers.

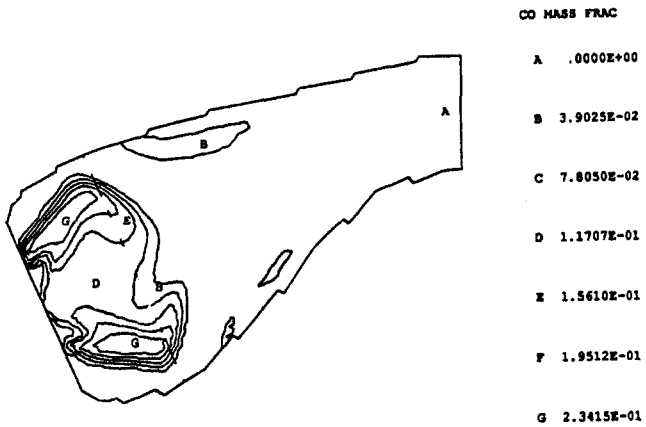

Fig. 10 Calculated CO mass fraction contours in a side view through the swirl cup of the engine combustor (finite rate PDF transport)

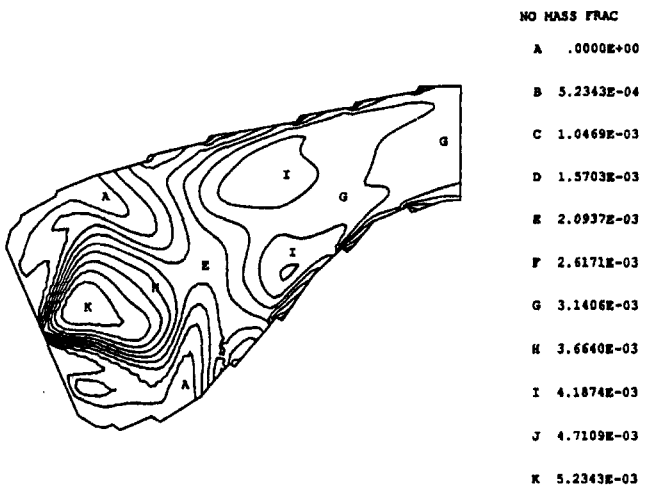

Fig. 11 Calculated NO_x mass fraction contours in a side view through the swirl cup of the engine combustor (finite rate PDF transport)

Liquid droplets were not modeled in the present work to reduce overall computational time requirements. In all of the calculations described in this paper, the fuel injected was assumed to be entirely in the gas phase. It is well known that the liquid phase of the fuel plays an important role in low power emissions (McDonnell et al., 1994). It is expected that predicted CO levels would be significantly higher if the delay of vaporization of the Jet A fuel were included in the PDF transport simulation. Two phase PDF transport calculations would be performed as a next modeling step.

The NO_x emissions (using two reaction Zeldovich mechanism) were also studied at both high and low power by performing post-processing of the solution. Figure 11 shows a side view of the NO_x mass fraction distribution at high power. It may be noted that the NO_x is generated in the high-temperature region and mixes downstream with the dilution flow. The predicted NO_x emission index ($EINO_x$) is also compared with measured data in the above table. The NO_x emissions are predicted to be in better agreement with the measured data. Consistent with the measurements, the calculated NO_x increases from low to high power. The calculations of CO and NO_x are clearly quite preliminary, and a great deal of calibration/validation of the coupled PDF–CFD model (including the kinetics modeling) is still required before the PDF transport approach becomes a reliable design tool for the prediction of emissions in real combustors.

Conclusions and Future Directions

A Lagrangian PDF transport model has been coupled with a three-dimensional body-fitted CFD code (CONCERT-3D). The work done earlier with fast chemistry only (Tolpadi et al., 1995) has been extended in this paper by including finite rate chemistry effects via a multiple scalar scheme for the fuel. The development of the PDF model is highly modular, enabling its interface with any CFD code. The temperature and major species predicted by the model indicated excellent agreement with bluff body reacting flow Raman data. The code was applied to a real piece of combustion hardware by analyzing the three-dimensional flow in a single annular aircraft engine combustor with Jet A fuel. A three scalar reduced kinetic model for Jet A fuel was used in the PDF transport calculations, which enabled the study of the interaction of finite rate chemistry and turbulent mixing. A strong effect of finite rate chemistry was observed in the primary reaction zone. The finite rate PDF transport calculation indicated a significantly different flow field relative to the fast chemistry PDF transport approach or even the assumed shape PDF method: The recirculation region was bigger, thus

providing better flame stabilization. The temperature levels in the entire combustor were predicted to be lower, as expected, with the finite rate PDF transport method. The calculated combustor exit gas temperature distribution agreed reasonably well with engine data.

The finite rate PDF transport approach also enabled the prediction of CO and NO_x emissions, which were compared with gas sampling measurements made in rig tests of the selected combustor. The current model made a reasonable CO prediction at high power, but failed to predict it at low power where vaporization of the liquid fuel is thought to be a predominant factor that was not considered in this paper. The emission index for NO_x indicated closer agreement with the data. In summary, it should be said that for the first time Monte Carlo PDF–CFD simulations were performed in a real engine configuration with finite rate chemistry of Jet A fuel. The results obtained were very encouraging. However, there is a good amount of validation/calibration that still needs to be done in the application of this new method to real combustors to achieve levels of predictive accuracy required by design engineers. The impact of liquid droplet effects will be included in future extensions of this present work.

Acknowledgments

The authors wish to thank GE-Aircraft Engines for sponsoring this work, and for granting permission to publish the same.

References

Anand, M. S., Pope, S. B., and Mongia, H. C., 1990, "Pressure Algorithm for Elliptic Flow Calculations With the PDF Method," CFD Symposium on Aeropropulsion at NASA-Lewis.

Borghi, R., 1988, "Turbulent Combustion Modeling," *Prog. Energy Combust. Sci.*, Vol. 14, pp. 245–292.

Correa, S. M., and Shyy, W., 1987, "Computational Models and Methods for Continuous Gaseous Turbulent Combustion," *Prog. Energy Combust. Sci.*, Vol. 13, pp. 249–292.

Correa, S. M., and Gulati, A., 1992, "Measurements and Modeling of a Bluff Body Stabilized Flame," *Combust. Flame*, Vol. 89, pp. 195–213.

Correa, S. M., and Pope, S. B., 1992, "Comparison of Monte Carlo PDF/Finite Volume Mean Flow Model With Bluff Body Raman Data," *24th Intl. Symp. on Combust.*, pp. 279–285.

Correa, S. M., 1995, "Assessment of a Three-Variable Reduced Kinetic Scheme in Prescribed Turbulence," *AIAA J. Prop. & Power*, Vol. 11, No. 3, pp. 448–455.

Gulati, A., Tolpadi, A. K., VanDeusen, G., and Burrus, D., 1995, "Effect of Dilution Air on Scalar Flowfield at Combustor Sector Exit," *AIAA J. Prop. & Power*, Vol. 11, No. 6, pp. 1162–1169.

McDonell, V. G., Samuelsen, G. S., and Seay, J. E., 1994, "Characterization of the Nonreacting Two Phase Flow Downstream of a Aeroengine Combustor Dome Operating at Realistic Conditions," ASME Paper No. 94-GT-263.

Pope, S. B., 1985, "PDF Methods for Turbulent Reactive Flows," *Prog. Energy Combust. Sci.*, Vol. 11, pp. 119–192.

Pope, S. B., and Correa, S. M., 1986, "Joint PFD Calculations of a Non-equilibrium Turbulent Diffusion Flame," *21st Intl. Symp. on Combust.*, pp. 1341–1348.

Pope, S. B., 1990, "Computations of Turbulent Combustion: Progress and Challenges," *23rd Intl. Symp. on Combust.*, pp. 591–612.

Shyy, W., Tong, S. S., and Correa, S. M., 1985, "Numerical Recirculating Flow Calculations Using a Body-Fitted Coordinate System," *Numer. Heat Trans.*, Vol. 8, pp. 99–113.

Shyy, W., and Braaten, M. E., 1986, "Three-Dimensional Analysis of the Flow in a Curved Hydraulic Turbine Draft Tube," *Intl. J. Numer. Meths. Fluids*, Vol. 6, pp. 861–882.

Shyy, W., Correa, S. M., and Braaten, M. E., 1988, "Computation of Flow in a Gas Turbine Combustor," *Combust. Sci. and Tech.*, Vol. 58, pp. 97–117.

Spadaccini, L. J. and TeVelde, J. A., 1980, "Auto-Ignition Characteristics of Aircraft-Type Fuels," NASA-CR-159886.

Tolpadi, A. K., and Braaten, M. E., 1992, "Study of Branched Turboprop Inlet Ducts Using a Multiple Block Grid Calculation Procedure," ASME *Journal of Fluids Engineering*, Vol. 114, pp. 379–385.

Tolpadi, A. K., 1995, "Calculation of Two-Phase Flow in Gas Turbine Combustors," ASME JOURNAL OF ENGINEERING FOR GAS TURBINES AND POWER, Vol. 117, pp. 695–703.

Tolpadi, A. K., Correa, S. M., Burrus, D. L., and Mongia, H. C., 1997, "Monte Carlo Probability Density Function Method for Gas Turbine Combustor Flowfield Predictions," *AIAA J. Prop. & Power*, Vol. 13, No. 2, pp. 218–225.

Fuel Nozzle Aerodynamic Design Using CFD Analysis

D. S. Crocker

E. J. Fuller

C. E. Smith

CFD Research Corporation,
Huntsville, AL 35805

The aerodynamic design of airflow passages in fuel injection systems can be significantly enhanced by the use of CFD analysis. Attempts to improve the efficiency of the fuel nozzle design process by using CFD analyses have generally been unsuccessful in the past due to the difficulties of modeling swirling flow in complex geometries. Some of the issues that have been obstacles to successful and timely analysis of fuel nozzle aerodynamics include grid generation, turbulence models, and definition of boundary conditions. This study attempts to address these obstacles and demonstrate a CFD methodology capable of modeling swirling flow within the internal air passages of fuel nozzles. The CFD code CFD-ACE was used for the analyses. Results of nonreacting analyses and comparison with experimental data are presented for three different fuel nozzles. The three nozzles have distinctly different designs (including axial and radial inflow swirlers) and thus demonstrate the flexibility of the design methodology. Particular emphasis is given to techniques involved in predicting the effective flow area (ACd) of the nozzles. Good agreement between CFD predictions of the ACd (made prior to experiments) and the measured ACd was obtained. Comparisons between predicted and measured velocity profiles also showed good agreement.

Introduction

The design of the fuel nozzle for gas turbine engines is critical to the performance of the combustor. The fuel spray distribution affects performance parameters including ignition, lean blowout, pattern factor, gaseous and smoke emissions, combustion efficiency, and liner wall temperatures. The air flow through the fuel nozzle and/or dome swirler is at least partially, and often completely, responsible for determining the fuel atomization and distribution in the combustor primary zone. In most combustors, moderate to strongly swirling air is used to maintain a stable flame by creating a central recirculation zone, which entrains hot combustion products and mixes them with unreacted fuel and air. The swirling flow is usually produced by some combination of radial vanes or axial vanes. Radial vanes generally have lower loss and lower manufacturing costs. Axial vanes can usually be packaged in a smaller diameter, and they are necessary if fuel is introduced between two air passages. Specific design details of swirler vanes and downstream air passages vary widely.

This paper addresses the use of CFD as a tool for modeling and increasing understanding of the air flow field through fuel nozzles and in the combustor primary zone. Neither liquid spray nor reacting flow are considered. Demonstrated and consistently accurate modeling of the nonreacting flow field, though less informative than a full reacting model, is still of great use to the fuel nozzle designer. A basic characteristic of a fuel nozzle is its effective flow area (ACd). Accurate prediction of the ACd of a given nozzle geometry can significantly improve design productivity, especially with the advent of lean injection in which a relatively large percentage of the total air flow enters the combustor through the fuel nozzle. It is now possible to produce a fuel nozzle with the correct ACd reasonably quickly using rapid prototyping techniques. Rapid prototyping and simple ACd measurements, however, will provide only limited understanding of the physics of the flow through the nozzle. Accurate CFD modeling can provide the designer with a level of understanding (i.e., the influence of design parameters) that cannot be practically achieved through experimental measurements. Greater understanding will inevitably lead to better designs produced in less time.

Currently, fuel nozzles/air swirlers are designed primarily through a combination of scaling from existing designs, trial and error flow tests, and past experience of the designer. CFD is just beginning to be used as an effective design tool. Numerous studies have been performed in which CFD analyses of fuel nozzles were compared with experimental velocity field data. Most of the work that has been done in modeling fuel nozzles has assumed two-dimensional axisymmetric flow. The quality of the simulations has been inconsistent at best. Mongia (1994), in his review of combustion modeling, admits that qualitative agreement with LDV measurements using simple profile boundary conditions and the standard $k-\epsilon$ model has been "less than successful." One of the most comprehensive studies covering a wide range of axial swirler design parameters was performed by Lilley (1985) and several of his students. Rizk and Chin (1994), Rizk (1994), and Rizk et al. (1997) have analyzed various fuel nozzles. In these studies, the agreement between CFD results and experimental measurements for air flow (without fuel spray) was generally poor. The results were, however, somewhat better when adjustments were made to the air flow rates and/or passage flow splits. Fuller and Smith (1994) showed good agreement with the experimental measurements of McVey et al. (1989) for a research nozzle.

Significant difficulties still remain in the application of CFD to the design of fuel nozzles. The most important of these difficulties are:

1. rapid grid generation for complex passages;
2. timely solution convergence with adequate grid resolution;
3. adequate turbulence models; and
4. definition of boundary conditions.

Grid generation difficulties have been largely overcome with the availability of multidomain topology for structured grids and easy to use graphic interfaces. A quality grid for a geometry with numerous complex passages can usually be generated in at most a few hours. Modified grid meshes for minor model variations can then be generated in minutes. Adequate grid reso-

Contributed by the International Gas Turbine Institute and presented at the 41st International Gas Turbine and Aeroengine Congress and Exhibition, Birmingham, United Kingdom, June 10–13, 1996. Manuscript received at ASME Headquarters February 1996. Paper No. 96-GT-127. Associate Technical Editor: J. N. Shinn.

lution for two-dimensional axisymmetric models usually requires from ten to fifteen thousand cells. Solution convergence for such a model can typically be achieved on state-of-the-art work stations in one or two hours for nonreacting flow. (Reacting flow cases generally require two to ten times more cpu effort, depending on the complexity of the reaction model.)

Two-equation turbulence models such as the standard $k-\epsilon$ model (Launder and Spalding, 1974), which employ an isotropic eddy viscosity, have been demonstrated to be less than completely adequate for swirling flows (Sloan et al., 1985). The turbulence models are most inadequate near the centerline of axisymmetric swirling flows. It is generally observed that the inadequacy of the standard model arises due to the lack of sensitivity of the dissipation rate to extra strains such as swirl. In order to remedy this, Yakhot et al. (1992) proposed a modified $k-\epsilon$ model based on the Renormalization Group (RNG) theory. In their RNG $k-\epsilon$ model, the coefficient of production of dissipation varies as a function of the strain parameter η, which is defined as the ratio of turbulent to mean strain time scales. More advanced turbulence models, such as the Reynolds-stress transport models, have the potential to improve solution accuracy, but have not been demonstrated to justify the associated price of computational effort and convergence difficulty. Poor CFD results are frequently blamed on poor turbulence models and the blame is certainly justified to some extent. On the other hand, one must be careful not to falsely accuse turbulence modeling when other more easily resolved sources of error may exist. The most prevalent source of error in modeling fuel nozzle flows, in the authors' opinion, is inaccurate specification of boundary conditions. The most significant boundary conditions are the flow properties (velocity components and turbulence levels) where the swirler air is introduced to the computational domain, usually at the trailing edge of the swirl vanes. Specification of the velocities is not as easy as it may seem at first glance. The biggest difficulty is determining what percentage of the total flow goes through each passage. Even measurement of ACd for individual passages is generally not adequate since strong interactions between air passages may exist. Determination of flow splits requires accurate prediction of the total pressure drop through each air passage. The pressure drop through the swirl vanes is usually significant. A systematic method for correctly determining swirler boundary conditions is first presented below. Application of the method using the CFD code CFD-ACE is then given for three fuel nozzle designs with substantially different flow characteristics.

Determination of Swirler Boundary Conditions

This discussion of swirler boundary conditions assumes that the computational domain begins at the trailing edge of the swirl vanes or the exit of angled holes or slots and that the CFD analysis is two-dimensional axisymmetric. For a given mass flow through a swirler the velocity normal to the swirler exit plane is determined from continuity as

$$V_n = W_{sw}/(A_{se}\rho) \tag{1}$$

V_n is the axial velocity u for axial swirlers and the radial velocity v for radial swirlers. The velocity normal to the swirler walls (v for axial swirlers and u for radial swirlers) can generally be assumed to be zero. The only case where it might not be zero is when there is a strong gradient in the normal velocity V_n. The simplest way to determine the tangential velocity w is to assume that the flow exiting the swirler has the same angle as the swirl vanes. However, this assumption can lead to significant errors since small changes in the swirl angle of the air can result in large changes in the flow pattern. A better expression for the tangential velocity considers the effects of vane blockage b, slot discharge coefficient Cd_s, and vane turning efficiency η. The tangential velocity is determined from

$$w = \eta V_{ns} \tan \alpha_v \tag{2}$$

where the turning efficiency is given by

$$\eta = \sin \alpha_a / \sin \alpha_v \tag{3}$$

and V_{ns} is the velocity normal to the swirler exit plane just before exiting the swirler:

$$V_{ns} = W_{sw}/(A_{se}\rho Cd_s(1 - b)) \tag{4}$$

The higher value of V_{ns} (compared to V_n) should be used to determine the tangential velocity because the tangential velocity is not significantly affected by the dump at the swirler exit. Halpin (1993) calculated a maximum turning efficiency of 0.92 for radial swirlers and an even lower value when a vane loading parameter was increased. However, the turning efficiency was assumed to be 1.0 for the analyses given in the following sections with no apparent detrimental effect on the results. The vane blockage is typically about 0.1 for axial or radial swirlers with thin vanes. The blockage is sometimes higher for radial swirlers with straight slots or for angled holes. The discharge coefficient can be assumed to be very close to 1.0 when the flow area through the swirler contracts substantially as it does for thin vane swirlers. If constant area holes or slots are used, the discharge coefficient can have a substantial effect. A value for Cd_s of 0.75 to 0.80 is a typical estimate for slots or holes with length/diameter greater than unity (Lichtarowicz et al., 1965). The swirl vane pressure loss discussed below should be set to zero for constant area slots or holes.

This discussion on setting the velocities (or swirl angle) at the computational inlets assumes that the velocities are uniform across the inlet. This will not be the case in general, especially for axial swirlers with a small hub diameter (Lilley, 1985). Even the swirl vane angle is frequently not constant for small hub diameter swirlers. The tangential velocity decreases toward zero as the radius approaches zero. The axial velocity (for axial swirlers) also increases with increasing radius because of the swirl-generated radial pressure gradient. Velocity gradients at the swirler exit are important in some cases, but can often be neglected in practice for two reasons: (1) Radial swirlers and most axial swirlers do not have a small hub diameter relative to the outer diameter; and (2) even when there is a small-diameter axial swirler at the core of the nozzle, its mass flow contribution is generally quite small.

Turbulence levels at the inlet boundaries are generally not known, but they seem to have a relatively small effect if there is a confined passageway that extends for some length down-

Nomenclature

ACd = fuel nozzle effective area
A_{se} = swirler exit area
A_{si} = swirler inlet area
Cd_s = slot or hole discharge coefficient
W_{sw} = swirler mass flow rate
W_{tot} = total fuel nozzle mass flow rate
V_i = velocity normal to swirler inlet plane, upstream of inlet plane
V_n = velocity normal to swirler exit plane, downstream of exit plane
V_{ns} = velocity normal to swirler exit plane, upstream of exit plane
b = vane blockage
u = axial velocity
v = radial velocity
w = tangential velocity
α_a = swirler air flow exit angle
α_v = swirler vane exit angle
ΔP_{sw} = total pressure drop across swirler
ΔP_{tot} = total pressure drop across fuel nozzle
η = vane turning efficiency
ρ = density

stream of the swirler exit. Such is the case for most designs. A turbulence intensity of 10 percent and turbulence length scale of 10 percent and turbulence length scale of 10 percent of the swirl vane height seems to be a reasonable guess.

The mass flow through each swirler is controlled by the total pressure drop through the fuel nozzle. Most of the pressure drop for a well-designed fuel nozzle is a result of accelerating the flow through the nozzle and then dumping into the combustor primary zone. The dump loss is determined from the CFD solution. The loss through the swirl vanes is also usually important and should not be neglected. The loss through swirl vanes can be estimated by the following equations, which approximate the data of Kilik (1976) for vanes with aspect ratio of 0.4 and repeated by Lefebvre (1983):

flat vanes:

$$\Delta P_{sw} = 0.5\rho V_i^2[0.02625\alpha_v^2 - 2.1\alpha_v + 45.5], \quad \alpha_v \geq 40 \text{ deg}$$

$$\Delta P_{sw} = 0.5\rho V_i^2[0.0875\alpha_v], \quad \alpha_v < 40 \text{ deg} \qquad (5)$$

curved vanes:

$$\Delta P_{sw} = 0.5\rho V_i^2[0.0075\alpha_v^2 - 0.6\alpha_v + 12.5], \quad \alpha_v \geq 40 \text{ deg}$$

$$\Delta P_{sw} = 0.5\rho V_i^2[0.0125\alpha_v], \quad \alpha_v < 40 \text{ deg} \qquad (6)$$

These pressure loss curves were generated based on experimental data for axial swirlers, but they should also apply to radial swirlers as long as the ratio of the swirler inner radius to outer radius approaches unity. Equations (5) and (6) account for the minor dump loss that occurs at the swirl vane exit for typical thin vanes. If there is vane blockage much greater than 0.1, the vane exit dump loss may be significant and should be added to the swirler total pressure loss.

The mass flow rate must be determined by an iterative process in which the nozzle dump loss, and any other air passage losses, are calculated by the CFD solution and the swirler loss is calculated by Eq. (5) and (6). The steps of the iterative procedure are as follows:

1 Estimate the flow rates, w_{sw} for each air passage for the overall fuel nozzle total pressure drop, ΔP_{tot}.
2 Use the estimates from Step 1 to calculate the total pressure at the swirler exit (computational domain inlet) for each air passage.
3 Use the flow rate estimates from Step 1 to set the inlet velocities [or use the total pressures from Step 2 and set the inlet total pressures] and obtain a converged CFD solution.
4 Check the calculated total pressure at the swirler exit (CFD inlet) for each air passage and compare with the values calculated from Step 2 [or check the calculated mass flow for each air passage and compare with the values from Step 1].
5 Return to Step 1 and adjust the air flow rates as necessary and repeat until the total pressure from Step 2 and Step 4 agree [or until the mass flows from Step 1 and Step 4 agree].

The *ACd* for the fuel nozzle can be found from

$$ACd = W_{tot}/\sqrt{2\rho\Delta P_{tot}} \qquad (7)$$

The result of the iterative process is an accurate prediction of the total effective flow area and individual passage flow splits for the fuel nozzle. The extra effort required for the iterative process is not excessive since only three or four iterations are usually required and the CFD solutions converge much more quickly after the initial run. Table 1 shows a comparison of the measured and calculated *ACd*'s for several different fuel nozzles with a range of design characteristics and size. In most cases the calculations were performed as part of the design process before the measurements were taken. The Low Emissions-1 and the Integrated Combustor fuel nozzles are discussed below. The Dual-Spray airblast nozzle is described by Smith et al. (1995). The other fuel nozzles are proprietary designs so the details are not published. It is evident from the results shown in Table 1 that it is possible to predict fuel nozzle effective flow area accurately.

Low-Emissions Fuel Nozzle

A low-emissions fuel nozzle with both radial inflow and axial air swirlers was developed by CFDRC for Pratt & Whitney. Experimental tests at ambient conditions using full-scale prototype hardware were conducted by United Technologies Research Center (UTRC). A cross section of the fuel nozzle is shown in Fig. 1. The low-emissions fuel nozzle consisted of a central fuel injector with two axial swirlers. The fuel was injected radially outward through discrete holes and atomized by a combination of fuel pressure and the high velocity air stream. A large percentage of the total air flow (82 percent) entered through the radial inflow swirler. The fuel was injected radially outward to provide better fuel/air uniformity. The radially outward fuel injection was the motivation behind the rather unique fuel nozzle design with the center pintle. Aerodynamically curved vanes with a 50 deg vane exit angle were employed for the radial inflow swirler and the outer axial swirler. The inner swirler had 45 deg straight helical vanes to simplify fabrication. Unswirled air was also admitted through a small gap as indicated in Fig. 1. The diameter of the fuel nozzle at the exit plane to the combustor was 6.6 cm.

The experimental tests and the corresponding CFD analyses were performed for unconfined flow at atmospheric pressure and ambient temperature conditions. The total pressure drop through the fuel nozzle was 1.7 percent. Axial and tangential velocities at a position 0.76 cm downstream of the nozzle exit (the downstream face of the center pintle) were experimentally measured using a laser-Doppler velocimeter (LDV).

A portion of the two-dimensional axisymmetric, multiblock grid used for the CFD analyses is shown in Fig. 2. The remainder of the grid extended 25 cm downstream in the axial direction and 15 cm in the radial direction. The model began at the trailing edge of the swirler vanes. The swirler locations have

Table 1 Comparison of measured and calculated *ACd*'s

Fuel Nozzle	ACd (cm^2)	
	Measured	Calculated
Low Emissions - 1	15.1	15.2
Integrated Combustor	2.45	2.42
Low Emissions - 2	7.2	7.0
Dual-Spray Airblast - 1	0.49	0.48
Dual-Spray Airblast - 2	0.37	0.37
LDI Airblast - 1	7.3	7.4
LDI Airblast - 2	6.8	7.4
LDI Airblast - 3	12.9	12.5
LDI High Shear	14.8	15.3

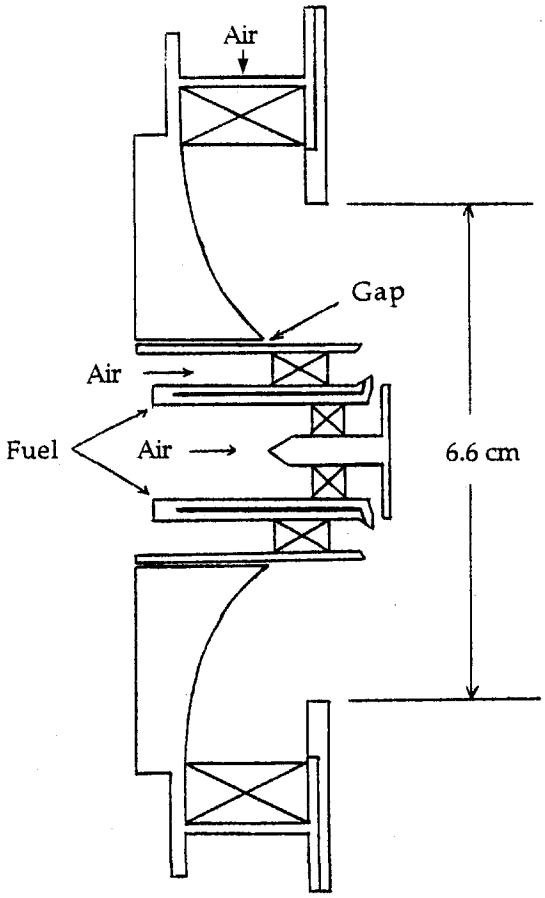

Fig. 1 Low-emissions fuel nozzle cross section

been included in Fig. 2 for clarity. The exit boundary and the outer radial boundary were assumed to be fixed at atmospheric pressure. The swirler inlet boundaries were modeled as fixed mass inlets with air swirl angles of 48.0, 52.8, and 52.9 deg for the inner and outer axial swirlers and the radial inflow swirler, respectively. The mass flow rate for each passage was set using the iterative procedure described in the previous section. The air

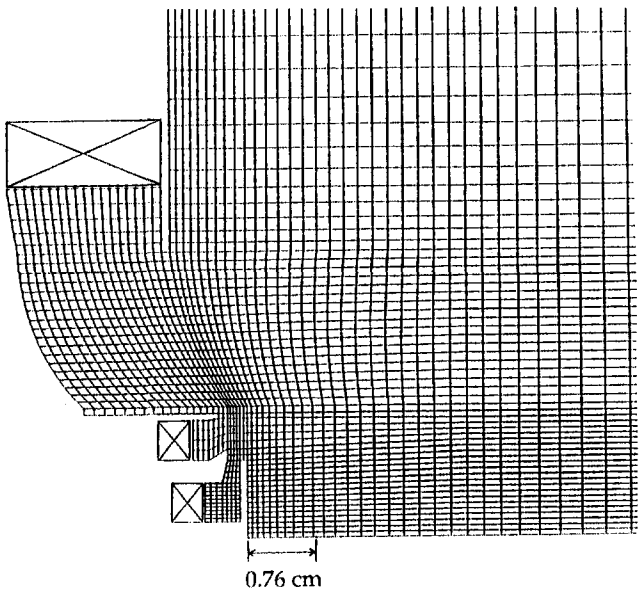

Fig. 2 Partial computational grid for low-emissions fuel nozzle

Table 2 Low-emissions fuel nozzle *ACd* and swirler pressure drop

	Axial, Inner	Axial, Outer	Radial Inflow	Gap*	Total
ACd (cm^2)	0.45	1.74	12.39	0.58	15.2
Swirler $\Delta P/P$ (%)	1.34	0.78	0.16	0.36	---

* pressure drop based on gap length

swirl angles were slightly higher than the vane angles because of the effect of vane blockage. The turbulent intensity was assumed to be 10 percent and the turbulent length scale was assumed to be 10 percent of the swirl vane height.

The predicted *ACd*'s for the fuel nozzle and for each passage individually are shown in Table 2. The predicted *ACd* of 15.2 cm^2 (obtained before experimental measurement was performed) is almost identical to the measured *ACd* of 15.1 cm^2. Table 2 also shows the pressure drop through each swirler. A relatively large fraction of the 1.7 percent total pressure drop occurred in the axial swirlers because they were at a low radius, resulting in a high axial velocity through the swirler. The total pressure drop through the radial inflow swirler, where most of the air is admitted, was quite low.

Four CFD cases were performed and compared with experimental measurements:

Case 1. $k-\epsilon$ turbulence model, upwind differencing;
Case 2. RNG turbulence model, upwind differencing;
Case 3. RNG turbulence model, second-order upwind differencing; and
Case 4. Low Reynolds number turbulence model, upwind differencing.

Streamline contours for Case 3 are shown in Fig. 3. A recirculation zone behind the center pintle is evident. Axial and tangential velocity profiles for each of the four cases are compared with the experimental results in Fig. 4. All of the cases show reasonable agreement with the experimental data. The RNG turbulence model in Case 2 had slightly better agreement with the diameter of the jet (axial velocity near 3 cm radius) and the tangential velocity in the center (near 2 cm radius) of the jet flow. The second-order upwind differencing in Case 3 further improved the prediction of the jet width. All four cases predicted a secondary recirculation zone on the centerline at the face of

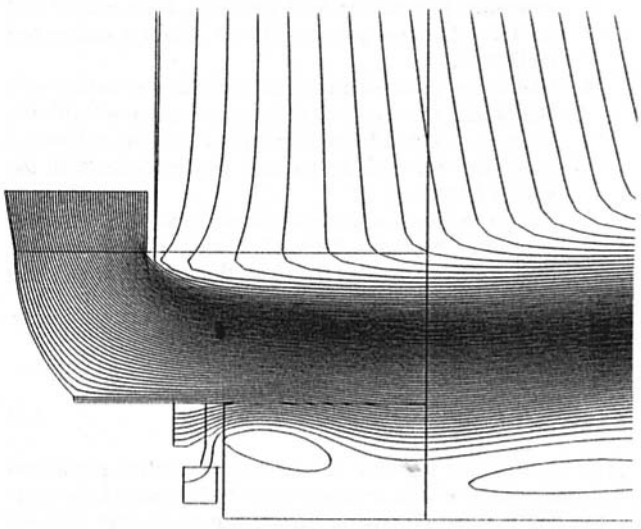

Fig. 3 Streamline contours for low-emissions fuel nozzle discharging into ambient environment—Case 3

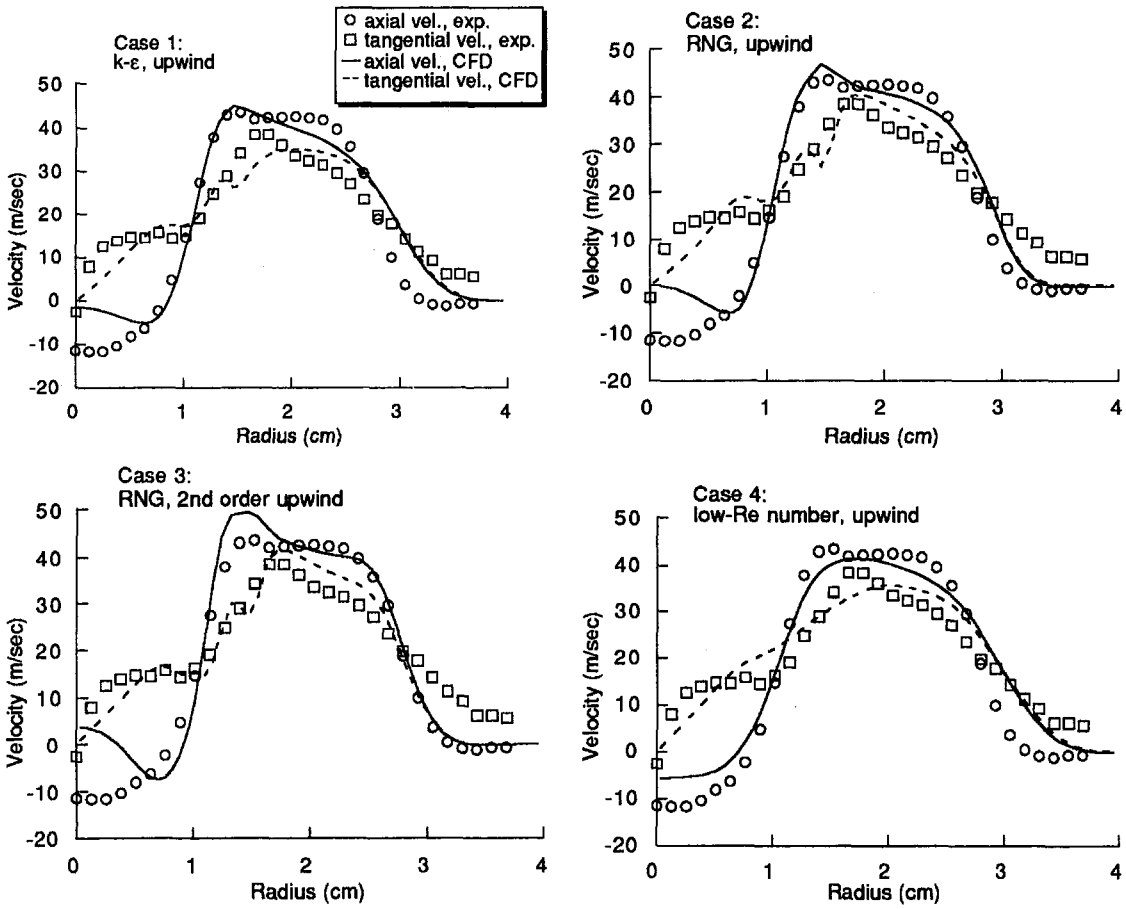

Fig. 4 Velocity profiles at axial location 0.76 cm downstream of pintle face for low-emissions fuel nozzle

the pintle. A secondary recirculation zone streamline is not captured in Fig. 3 because it has a very low flow rate. The size of the secondary recirculation zone is overpredicted by the first three cases as evidenced by the increase in axial velocity near the centerline. The low Reynolds number turbulence model (Case 4) better matches the experimental data near the centerline. The low Reynolds number model (Chien, 1982) avoids difficulties with wall functions by permitting integration of the momentum and $k-\epsilon$ equations all the way to the wall. The low Reynolds number model probably performed better because the grid cells adjacent to the pintle and near the centerline were in the laminar sublayer. The elevated swirl velocity at the outer edge of the jet was also not predicted by any of the cases.

Integrated Combustor Fuel Nozzle

The "integrated combustor" and its associated fuel nozzle were designed and developed at CFD Research Corporation. The integrated combustor was so named because of the manner in which the combustor design and the fuel nozzle design were integrated to achieve optimum performance for a high temperature rise combustor with increased turn-down fuel/air ratio. A description of the concept is given by Fuller and Smith (1994). A cross section of the fuel nozzle is shown in Fig. 5. The fuel nozzle consisted of three axial swirlers with inner, mid, and outer vane angles of 45, 45, and 60 deg, respectively. Vanes for all three swirlers were curved and the inner swirler was counterrotating. The primary fuel circuit consisted of a pressure atomizer located in the center of the nozzle. The secondary fuel was introduced onto a filming surface between the mid and outer air swirlers where it was atomized by the air streams.

The computational grid, shown in Fig. 6, was two-dimensional axisymmetric with nine blocks. The model began at the trailing edge of the swirler vanes and included the combustor liner walls and upstream flowing cooling slots. Air that would normally be injected through primary zone liner holes was added to the liner cooling for this high-temperature-rise com-

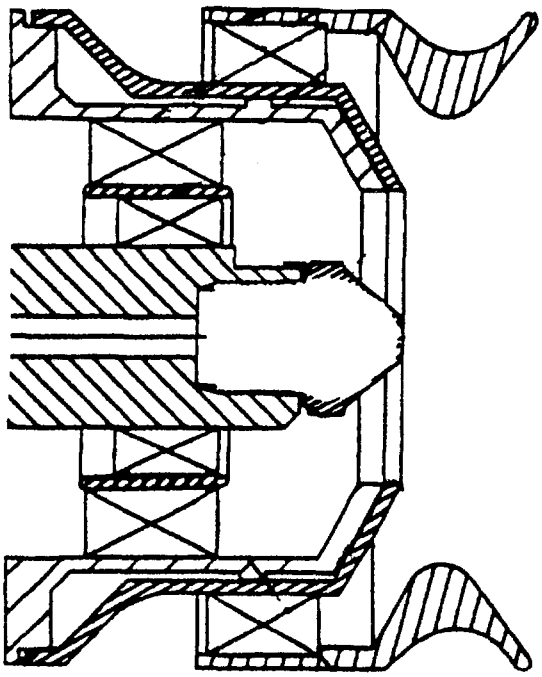

Fig. 5 Integrated combustor fuel nozzle cross section

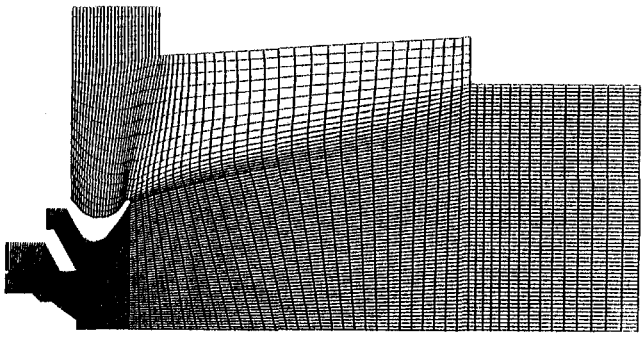

Fig. 6 Computational grid for integrated combustor nozzle

bustor. The upstream direction of the cooling slots causes the large amount of cooling air to be utilized in the primary zone reaction. The swirler inlet boundaries were modeled as fixed mass inlets with mass flow for each swirler determined iteratively as previously discussed. The air flow angles were 48.0, 48.0, and 62.5 deg for the inner, mid, and outer swirlers, respectively. The total pressure drop through the fuel nozzle was 3 percent and the exit boundary was assumed to be fixed pressure. The turbulent intensity was assumed to be 10 percent and the turbulent length scale was assumed to be 10 percent of the swirl vane height. The RNG turbulence model and second-order upwind differencing was used in the calculation.

The fuel nozzle was fabricated and tested at Delavan, Inc. *ACd* measurements and various combustion tests were performed, but air velocity measurements were not made. An *ACd* of 2.42 cm^2 was predicted by the CFD analysis, which was very close to the measured value of 2.45 cm^2. The *ACd* with all passages flowing for the inner, mid, and outer swirlers was calculated as 0.49, 0.92, and 1.01 cm^2, respectively. The pressure drop through the swirlers as a percentage of the overall fuel nozzle total pressure drop was 13 percent for the inner, 8 percent for the mid, and 35 percent for the outer swirler. It is clear that the pressure drop through the swirler cannot be neglected, especially for high vane angles. For the 60 deg outer swirler, the pressure loss was substantial even for curved vanes. Flat vanes would have had a severe impact on the performance of the nozzle. Streamline contours are shown in Fig. 7. A large recirculation zone was generated by a combination of the swirling flow and the expanding nozzle cap. Maintaining a stable flame in the central recirculation zone was particularly challenging for the integrated combustor because of the large amount of cooling air bearing down on the nozzle. CFD analyses contributed significantly to the development of a nozzle cap design that provided good flame stability.

High-Shear Research Nozzles

Pratt & Whitney performed an extensive study of the performance of high-shear fuel injectors for the U.S. Navy, as reported by Smith et al. (1986). Of the numerous configurations investigated in that study, results from the LA and the LE configurations are compared with CFD results here. A cross section of the LA configuration is shown in Fig. 8. Both configurations had a central fuel nozzle that injected fuel onto the inner prefilming surface. The two corotating radial swirlers consisted of constant area slots (see Fig. 8) rather than thin vanes. The angle of the inner and outer slots respectively was 8.3 and 60 deg for configuration LA and 10 and 60 deg for configuration LE. A complete description of other varying slot dimensions for the two configurations is given by Smith et al. (1986).

Experimental velocity measurements and the CFD analyses were performed for unconfined flow at atmospheric pressure and ambient temperature conditions with a total pressure drop of 1.7 percent. Axial and tangential velocities were measured at a position 0.25 cm downstream of the nozzle exit plane.

A portion of the two-dimensional axisymmetric, multiblock grids used for the CFD analyses is shown in Fig. 9. The remainder of the grid extended 15 cm downstream in the axial direction and 7 cm in the radial direction. The model began at the trailing edge of the radial swirler slots. The exit boundary and the outer radial boundary were assumed to be fixed at atmospheric pressure. The swirler boundaries were modeled the same as for

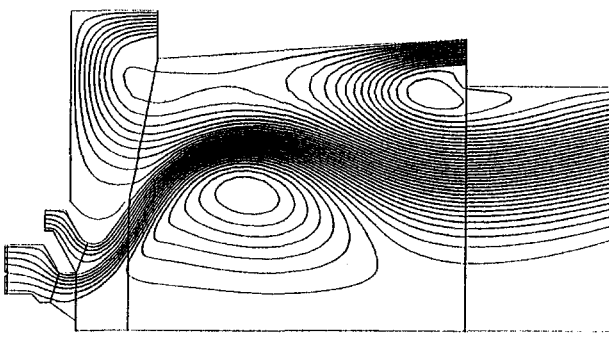

Fig. 7 Streamline contours for the integrated combustor nozzle

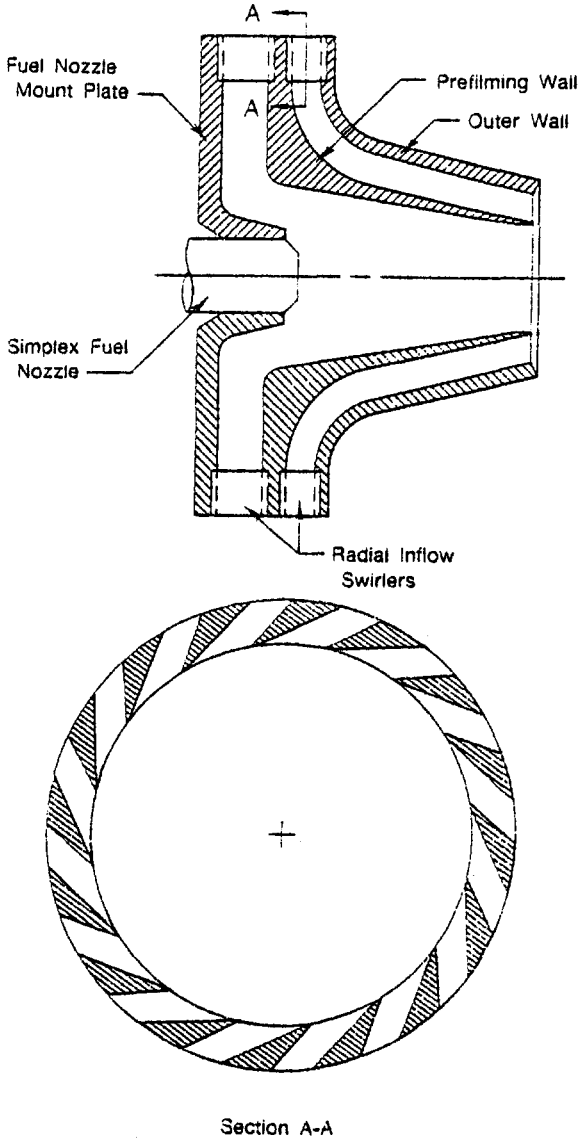

Fig. 8 High-shear nozzle cross section (configuration LA)

previously discussed cases with air flow swirl angles for the inner and outer slots respectively of 47.2 and 69.0 deg for configuration LA and 39.9 and 69.0 deg for configuration LE. The air flow angles are substantially higher than the slot angles because a Cd_s of 0.75 was assumed and because there was significant blockage b by the slot walls at the exit of the swirl slots. In this case it is apparent that setting the air flow angle equal to the slot angle would be a poor assumption. The mass flow rate for each passage was set using the iterative procedure previously described and the turbulent intensity was assumed to be 10 percent and the turbulent length scale was assumed to be 10 percent of the slot height. The RNG turbulence model and first-order upwind differencing were used in the calculation.

The ACd for configuration LA was 1.72 cm^2 and the flow split was 51 percent to the inner passage and 49 percent to the outer passage. The LE configuration had an ACd of 1.64 cm^2 and a flow split of 68 and 32 percent to the inner and outer passages, respectively. The calculated ACd's were within the ACd range measured by Smith et al. (1986), but specific measured ACd's for each configuration were not published. Axial and tangential velocity profiles for the LA and LE configurations are compared with experimental results in Fig. 10. The calculated axial velocities agree very well with the measurements. The shoulder in the velocity profile at a radius of about 0.9 cm is accurately predicted for both configurations. A predicted jet width that is slightly narrower than the measurements is the only deviation between numerical and experimental axial velocities. The predicted tangential velocities are also in reasonable agreement with the measured values, though the predicted peaks are high for the LE configuration.

Conclusions

A CFD modeling methodology for swirling flow in fuel nozzles has been presented. The method focuses on techniques for accurately defining swirler inlet boundary conditions. Pressure drop through the swirl vanes and blockage effects at the swirler exit usually have a significant impact on the effective flow area and the air flow swirl angle of a swirler passage. The method has been successfully used to predict the ACd of numerous fuel nozzles with widely varying design characteristics including both axial and radial swirlers. The ACd was predicted with an average error of 2.6 percent compared with the measured values. In most cases, the predicted ACd was obtained before the experimental measurements were made. Detailed numerical results for three fuel nozzles were presented as further demonstration of the modeling technique. Good agreement between predicted and measured velocity profiles was obtained for each case.

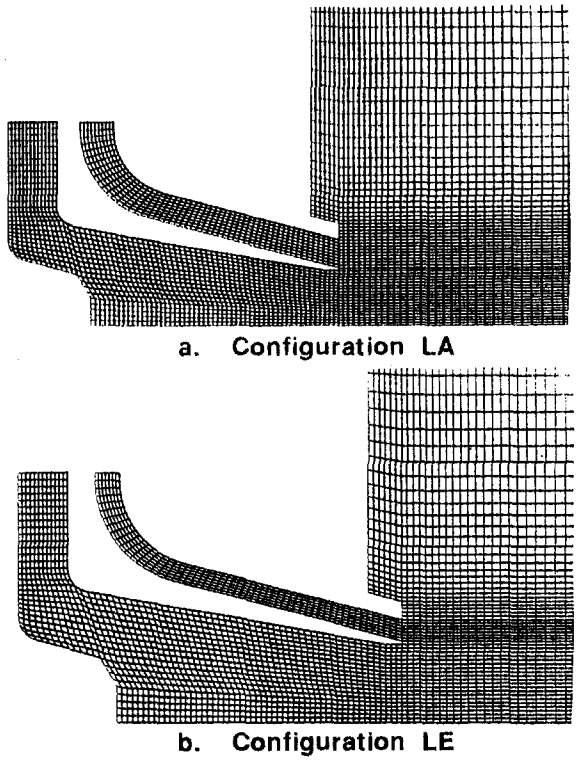

Fig. 9 Partial computational grid for high-shear fuel nozzle (configuration LE)

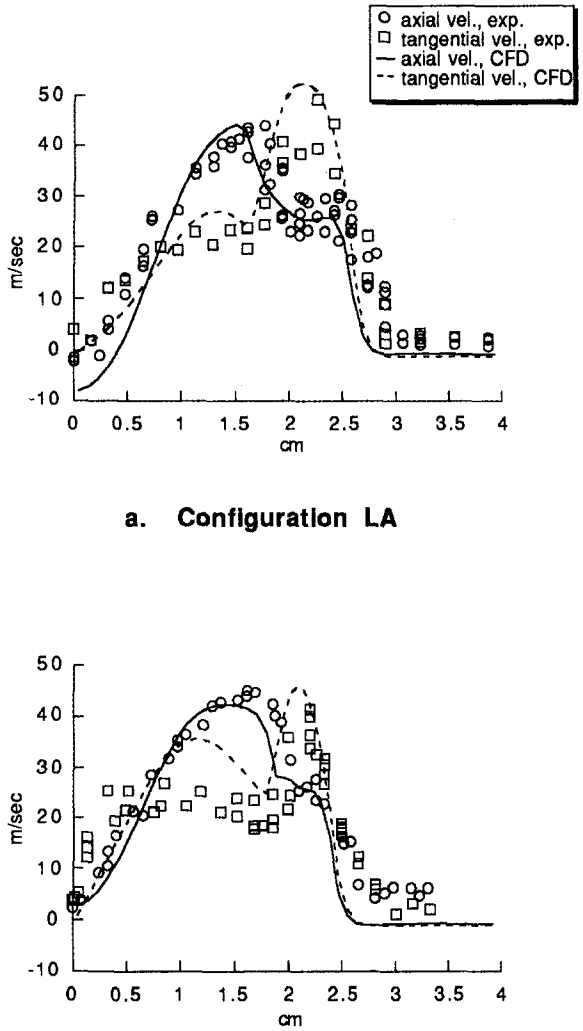

Fig. 10 Velocity profiles at axial location 0.25 cm downstream of nozzle exit plane for high-shear fuel nozzles

Acknowledgments

This paper is derived from a collection of fuel nozzle design and analysis efforts that have been funded in part or in whole by NASA Lewis Research Center, Pratt & Whitney, and CFD Research Corporation. The participation of Jeff Cohen (UTRC) and Qiang Wang (P&W) in fabrication and testing of the low emissions nozzle; and Patrick Riley (Delavan, Inc.) in fabrication and testing of the integrated combustor nozzle is greatly appreciated.

References

Chien, K. Y., 1982, "Predictions of Channel and Boundary-Layer Flows With Low-Reynolds-Number Turbulence Model," *AIAA Journal*, Vol. 20, pp. 33–38.

Fuller, E. J., and Smith, C. E., 1994, "CFD Analysis of a Research Gas Turbine Combustor Primary Zone," Paper No. AIAA-94-2768.

Halpin, J. L., 1993, "Swirl Generation and Recirculation Using Radial Swirl Vanes," ASME Paper No. 93-GT-169.

Kilik, E., 1976, "The Influence of Swirler Design Parameters on the Aerodynamics of the Downstream Recirculation Region," Ph.D. Thesis, School of Mechanical Engineering, Cranfield Inst. of Tech., England.

Launder, B. E., and Spalding, D. B., 1974, *Comp. Methods Appl. Mech. Eng.*, Vol. 3, p. 269.

Lefebvre, A. H., 1983, *Gas Turbine Combustion,* Hemisphere Publishing Corp., New York.

Lichtarowicz, A., Duggins, R. K., and Markland, E., 1965, "Discharge Coefficients for Incompressible Non-cavitating Flow Through Long Orifices," *J. Mechanical Engineering Science,* Vol. 7, No. 2, pp. 210–219.

Lilley, D. G., 1985, "Swirling Flows in Typical Combustor Geometries," Paper No. AIAA-85-0184.

McVey, J. B., Kennedy, J. B., and Russell, S., 1989, "Application of Advanced Diagnostics to Airblast Injector Flows," ASME JOURNAL OF ENGINEERING FOR GAS TURBINES AND POWER, Vol. 111, pp. 53–62.

Mongia, H. C., 1994, "Combustion Modeling in Design Process: Applications and Future Direction," Paper No. AIAA-94-0466.

Rizk, N. K., and Chin, J. S., 1994, "Comprehensive Fuel Nozzle Model," Paper No. AIAA-94-3278.

Rizk, N. K., 1994, "Model for Research Swirl Atomizers," Paper No. AIAA-94-2777.

Rizk, N. K., Chin, J. S., and Razdan, M. K., 1997, "Modeling of Gas Turbine Fuel Nozzle Spray," ASME JOURNAL OF ENGINEERING FOR GAS TURBINES AND POWER, Vol. 119, pp. 34–44.

Sloan, D. G., Smoot, L. D., and Smith, P. J., 1985, "Modeling of Swirl in Turbulent Flow Systems," Central and Western States Sections of the Combustion Institute, 1985 Spring Technical Meeting.

Smith, C. E., Graves, C. B., Johnson, B. V., and Roback, R., 1986, "Advanced Fuel Injector Characterization," Phase I Design Report, U.S. Navy Contract No. N00140-83-C-8899.

Smith, C. E., Fuller, E. J., Crocker, D. S., Mekkes, L. T., and Sheldon, J. C., 1995, "Dual-Spray Airblast Fuel Nozzle for Advanced Small Gas Turbine Combustors," *J. of Propulsion and Power,* Vol. 11, No. 2, pp. 244–251.

Yakhot, V., Orszag, S. A., Thangam, S., Gatski, T. B., and Speziale, C. G., 1992, "Development of Turbulent Models for Shear Flows by a Double-Expansion Technique," *Physics of Fluids,* Vol. 4, pp. 1510–1520.

Anchored CCD for Gas Turbine Combustor Design and Data Correlation

A. M. Danis

D. L. Burrus

H. C. Mongia

Combustion Center of Excellence,
GE Aircraft Engines,
Cincinnati, OH 45215-6301

Correlations based on design database, combined with multidimensional computational combustion dynamics (CCD) models are used in the combustion design process. However, because of limitations in the current turbulent combustion models, numerics, and boundary conditions, CCD has provided mainly qualitative trends for aerothermal performance, emissions, and liner wall temperature levels and gradients. To overcome these deficiencies, hybrid modeling approaches have been proposed to analyze existing combustors. A typical hybrid modeling approach combines empirical and semianalytical correlations with CCD to give quantitatively accurate predictions of NO_x, CO, HC, smoke, lean blowout, ignition, pattern factor, and liner wall temperatures. An alternate approach, anchored CCD, is described in this paper. First, the models were anchored with one of the five modern turbopropulsion engine combustors. The anchored models were then run for the other four combustors. The predicted results correlated well with measured NO_x, CO, HC, LBO, and exit temperature quality data, demonstrating a broader applicability of the anchored method. The models were also used for designing a new combustion concept. The pretest prediction agreed well with sector rig data from development hardware, showing the feasibility of using the anchored methodology as a design tool.

I Introduction

A typical empirical and semi-analytical gas turbine combustion design approach utilizes the design database and empirical experience with current product combustors along with simplified calculations (mostly zero-, one-, and/or quasi-one dimensional including the critical scaling principles), followed by a systematic development effort involving subcomponent, single-module, sector and/or full-scale test rigs, proceeding through engine development and certification activities. This computationally low-power but experimentally intensive approach has been quite successful for developing engine combustors that require taking only evolutionary steps from the field-proven product engine designs. Recognizing the limitation of this approach for developing innovative concepts, the first successful application of an empirical/analytical design methodology involving the use of two- and three-dimensional computational combustion dynamics (CCD) techniques was demonstrated by Mongia et al. (1979). Subsequently over a period of approximately 15 years, the empirical/analytical combustor design techniques have been formulated/adopted, refined, and successfully used by a number of gas turbine companies. As summarized by Mongia (1993), this approach has been used for designing:

(*a*) two low-emissions combustors,
(*b*) five high-temperature rise combustors,
(*c*) four combustors with different cooling schemes,
(*d*) two nonmetallic combustors,
(*e*) four demonstrator engine combustors, and
(*f*) three new centerline product engine combustors.

Over the last 20 years, the empirical/analytical design methodology has also been helpful for providing insight into current engine combustors. However, its impact on derivative-engine combustion products has been less substantial than that on advanced or new centerline engines due mainly to the following reasons.

When designing a combustion system for a growth engine application, the empirical design correlations can be extrapolated with confidence and could achieve the desired level of accuracy. Since the growth engine is based upon a proven design, the combustion designer understands his product well enough not to require any substantial qualitative guidance from CCD. In this situation, state-of-the-art CCD has limited potential for affecting the outcome. The gas turbine combustion modeling process is not developed well enough to give the desired level of accuracy, as listed in Table 1. However, if the fundamental and empirical understanding of the current design is limited, one should make use of CCD to help guide the development effort.

In order to meet the highly aggressive accuracy goals of Table 1 so as to impact development activities for current and growth engine combustors, the combustion research community has been making continuous improvement in measurement technology, physicochemical modeling, and numerical simulation. A number of extensive review articles and books have been published in this area. The following paragraphs give only a brief overview of the evolutionary steps taken by Mongia and co-workers, with the prime objective of explaining the rationale for recommending an anchored CCD approach described in this paper. This work has been influenced by the works of many researchers, some of whom were mentioned in a review article by Mongia (1994) wherein the specific recommendations were made for future research direction from an industry perspective.

Mongia et al. (1979) used a two-step kinetic scheme along with a modified eddy-breakup model to predict the low-power CO and unburned hydrocarbons. Recognizing the limitation of this and the semi-global hydrocarbon/NO_x chemistry, in addition to the computer capabilities in the 70's, Sanborn et al. (1976) demonstrated the feasibility of using a two-step approach combining CCD with two-step/modified eddy breakup with a comprehensive propane kinetic mechanism for predicting performance as well as emissions. An alternate approach, re-

Contributed by the International Gas Turbine Institute and presented at the 41st International Gas Turbine and Aeroengine Congress and Exhibition, Birmingham, United Kingdom, June 10–13, 1996. Manuscript received at ASME Headquarters February 1996. Paper No. 96-GT-143. Associate Technical Editor: J. N. Shinn.

Table 1 Accuracy goals for next-generation gas turbine combustion models

Variable	Predictive accuracy band
NOx	± 5 %
CO and unburned hydrocarbons	± 10 %
Exhaust SAE Smoke Number	± 2
SLS idle lean blowout fuel/air ratio	± 0.001
Pattern factor (Peak Profile Factor)	± 0.03
Average radial profile factor	± 0.015
Maximum liner wall temperature	± 25^0 F
Combustion system pressure drop	± 0.25 (% Pt3)
Diffusion system pressure drop	± 0.125 (% Pt3)
Circumferential location of the liner hot spot	± 0.1 × Nozzle sector
Axial location of the liner hot spot	± 0.01 × Comb. length

ported by Srivatsa (1982), combined CCD with trace species calculations (as a post processor) for NO_x and soot.

None of these approaches were pursued beyond the feasibility demonstration phase due mainly to the conclusion arrived in a NASA HOST sponsored study reported by Srinivasan et al. (1983), namely, the state-of-the-art turbulence models ($k-\epsilon$, algebraic, and full Reynolds stress transport models) were not accurate enough for the complex flow fields relevant to gas turbine combustors; and that there is a need for creating benchmark quality data and undertaking a more extensive effort for the formulation and validation of advanced combustion models.

Until more advanced models and numerics were developed (notwithstanding the uncertainties in specifying the boundary and initial conditions in gas turbine combustors) an alternate approach for current and new product combustors was needed. This led to the formulation of a hybrid modeling approach by Rizk and Mongia (1986). This technique turned out very successful in providing the required degree of accuracy with the database of ten conventional diffusion flame combustors requiring a single set of empirical constants (Rizk and Mongia, 1990, 1991). Rizk and Mongia (1990a, b) successfully extended their hybrid modeling approach to rich-quench-lean, and lean premixed combustors. Unfortunately, they had to use different semi-empirical formulations for NO_x, CO, and unburned hydrocarbons and the corresponding set of empirical constants for these three types of combustors, namely diffusion, lean premixed, and rich-quench-lean combustion concepts. This led to the development of semi-analytical correlations for NO_x, CO, and hydrocarbons for diffusion-flame combustors (Rizk and Mongia, 1993a) and its successful application in the hybrid modeling approach (Rizk and Mongia, 1993). Subsequent activities for formulating a common approach for all the three types of combustors are described by Rizk and Mongia (1993b, 1995). Further work, however, is required to make use of the hybrid modeling approach for designing new product engine combustors.

In parallel with the hybrid combustion modeling activities, Rizk and Mongia (1991) formulated and validated a comprehensive fuel nozzle model that includes simplified process equations for fuel filming, primary and secondary atomization. However, in order to match the measured radial profiles of the gas-phase turbulent kinetic energy, mean axial, radial, and tangential velocity components downstream from the nozzle, they had to assume that the radial velocity component at the nozzle exit plane was zero instead of the negative values given from the fuel nozzle internal flow calculations. With this arbitrary assumption ($v = 0$ at nozzle exit), they were able to achieve good agreement with the measured two-phase flow field indicating that the spray formation processes were reasonably well represented by their formulation. Subsequent attempts without $v = 0$ assumption, see for example Rizk et al. (1997), have provided only qualitative agreement with measurements. In fact, the simplified, semi-analytical nozzle model of Rizk and Mongia (1992), which uses empirical expressions for the gas phase velocity field, gave better correlation with data from several fuel nozzles. This indicates that the prime deficiency in the comprehensive fuel nozzle model of Rizk and Mongia (1991a) might be related to the single-phase calculations, including the use of the $k-\epsilon$ turbulence model.

Other work has also raised questions concerning the accuracy of the turbulence models used for gas turbine applications. So

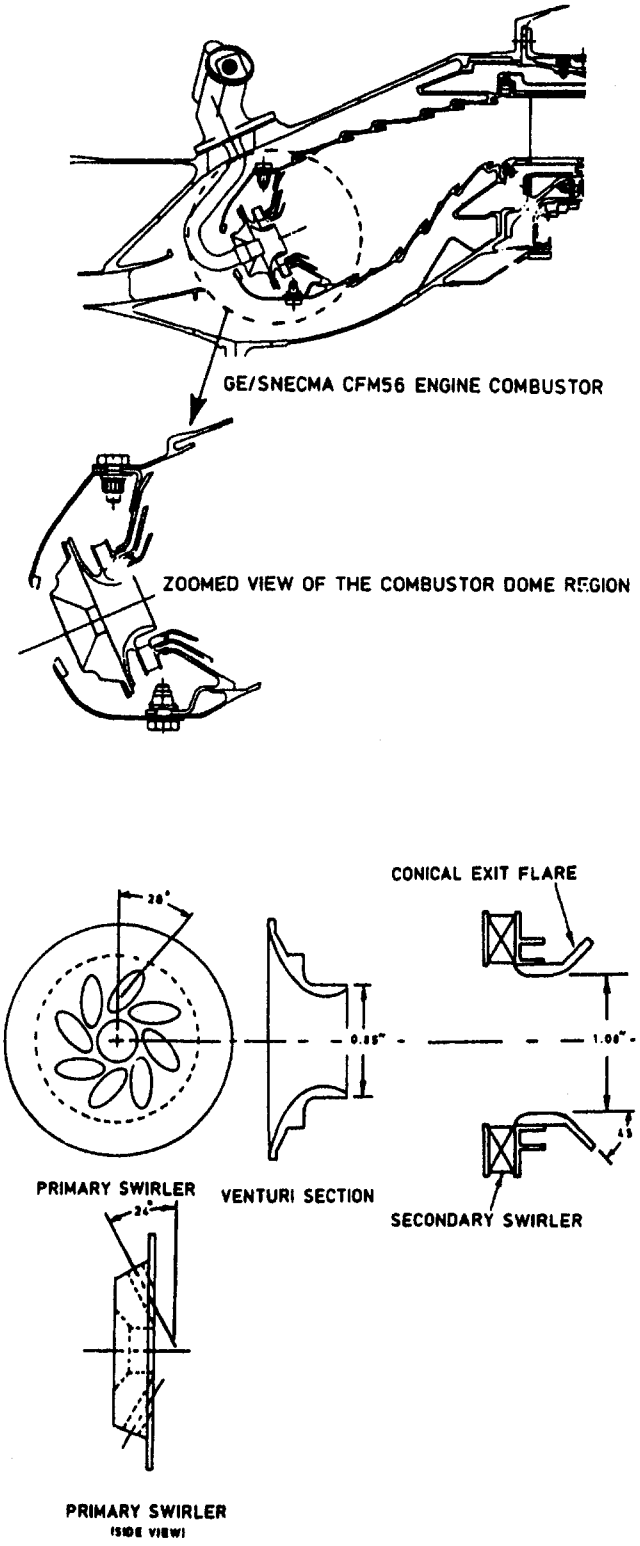

Fig. 1 GE/SNECMA CFM56 engine combustor and details of the swirl cup from Tolpadi et al. (1993)

et al. (1985, 1985a) conducted experimental evaluation of a strongly confined 66-deg axial swirler with a concentric simulated fuel nozzle tube of 8.7 mm diameter. The flow-field generated from this experimental setup is of relevance to that of the many ultralow emissions combustion concepts. Hogg and Leschziner (1989) based on calculations concluded that the boundary conditions had significant impact, and that even though the Reynolds stress model did better than the $k-\epsilon$ model, more work is needed to predict this type of complex flow involving vortex breakdown accurately.

An extensive experimental and analytical investigation by Nikjooy et al. (1993) on the single- and two-phase swirling

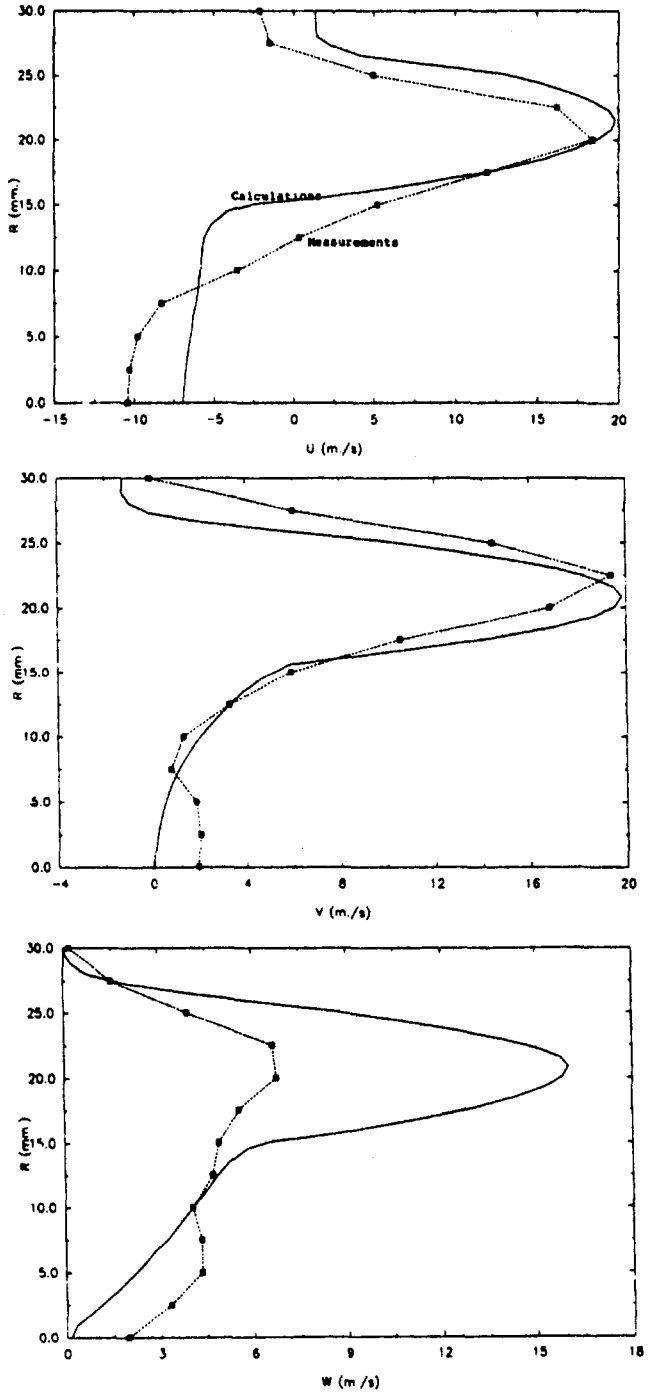

Fig. 2 Comparison between predicted and measured radial profiles of mean axial, radial, and swirl velocity components 17 mm downstream of swirl cup, from Tolpadi et al. (1993)

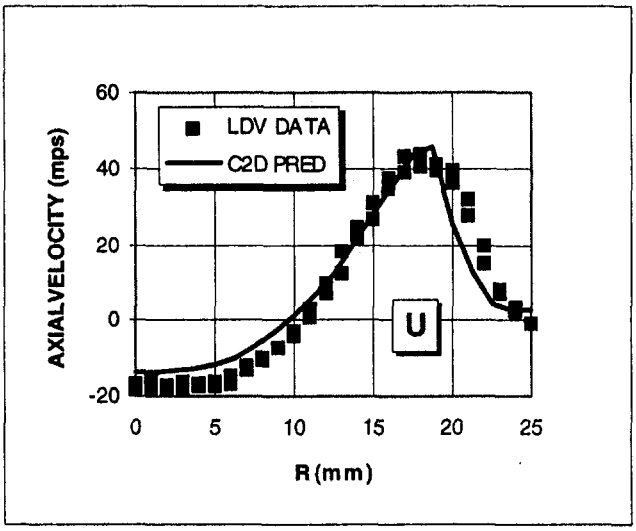

(a)

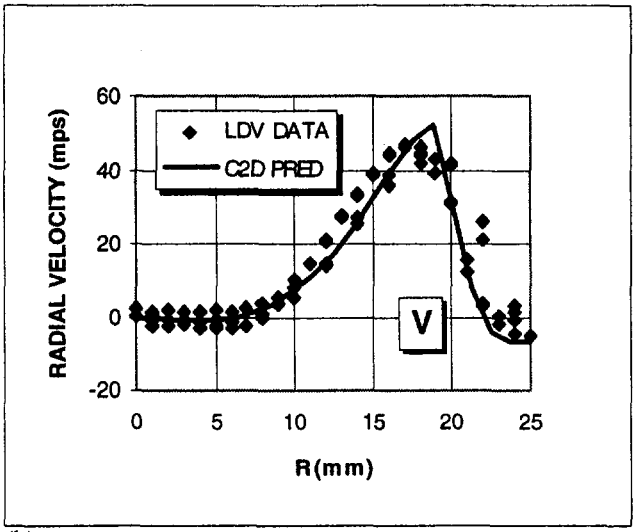

(b)

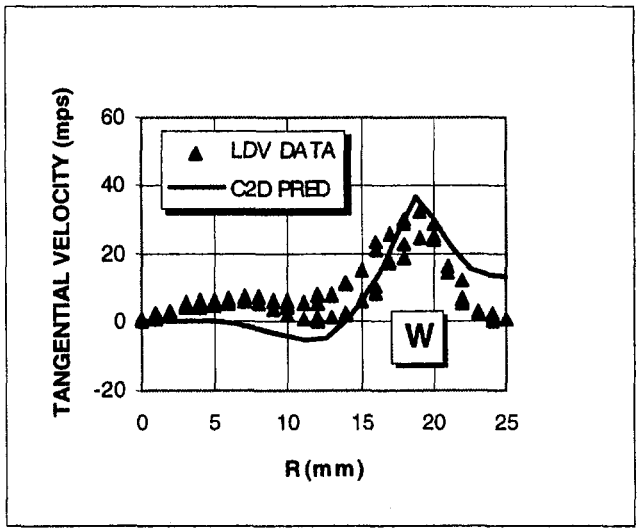

(c)

Fig. 3 Comparison between predicted and measured mean axial, radial, and tangential velocity components 2.0 mm downstream of Combustor 5 swirl cup

flows relevant to gas turbine swirler/fuel nozzle interaction has also clearly established the deficiencies in the state-of-the-art $k-\epsilon$, algebraic, and Reynolds stress transport models.

The dilution jet mixing problem has also been worked on for more than 20 years, as summarized by Holdeman (1993). However, even the simple problem of isothermal jet in crossflow remains an unsolved problem, as demonstrated clearly by Baker and McGuirk (1993).

Based on these demonstrated deficiencies and 20 years of lessons learned from the application of the empirical/analytical combustor design methodology, Mongia (1994) outlined an approach for further improving the gas turbine combustion system models. Under the sponsorship of the AFOSR Focused Research Initiative, a five-year program involving the researchers from GEAE, GECR&D, UCI, UCB, UICU, Penn State, MIT, Georgia Tech, and JPL has been initiated with the prime objective of improving our fundamental understanding of the gas turbine combustion processes, and to develop a significantly more accurate combustion modeling approach with attendant

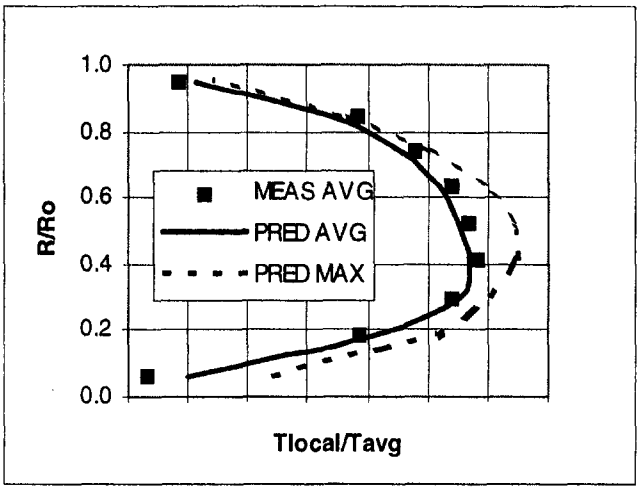

Fig. 5 Comparison between predicted and measured radial profile of exit temperature for Combustor 5

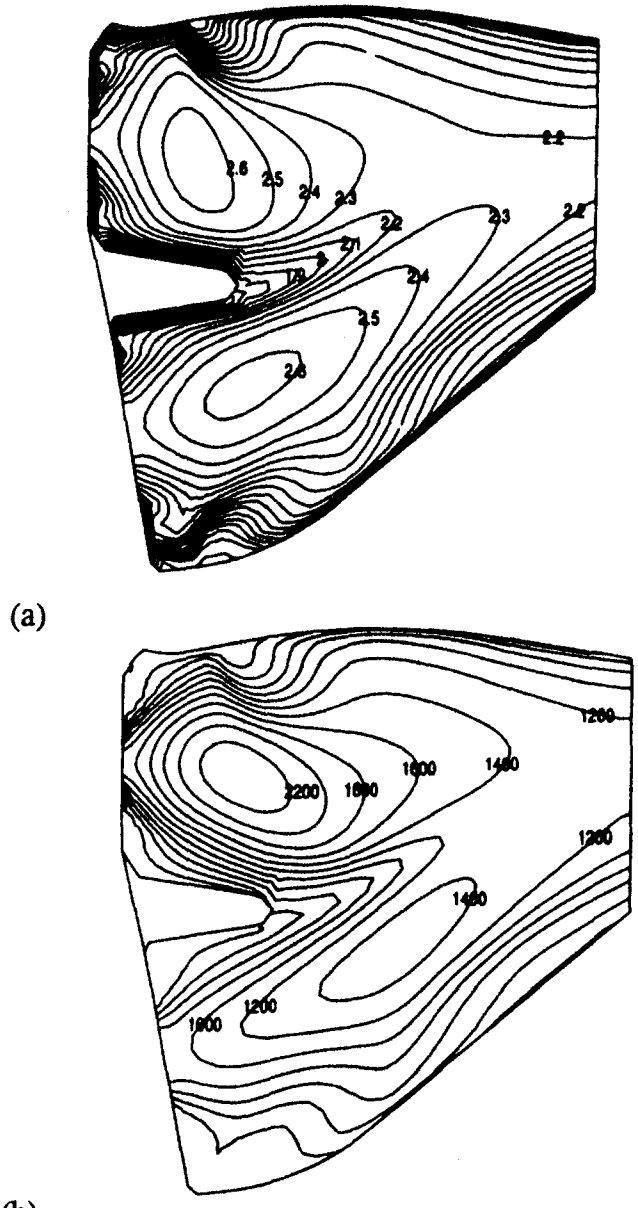

Fig. 4 Predicted isopleths within Combustor 5 liner: (*a*) gas temperatures normalized by combustor inlet temperature, (*b*) NO in ppm

impact on the innovative high-performance, low-emissions combustor design concepts. A multigeneration combustion modeling approach has been planned that includes the following two levels of analyses:

1 A simplified computationally cheap analysis approach that utilizes state-of-the-art empirical, semi-empirical, and semi-analytical understanding of the combustion processes that impact emissions, performance, operability, and life characteristics. The validated correlations are used for preliminary design, trade studies, detail design, *d*ata *r*eduction and *a*nalysis (DRA) of current and future design concepts. The first-generation DRA methodology as described by Danis et al. (1996) is a first step to meeting the accuracy goals of Table 1.

2 Anchored CCD modeling approach based on refined empirical turbulence model constants and boundary conditions targeted for design system applications in current and growth engine combustors, as described in this paper.

II Anchored CCD Methodology

The prime objective of the anchored methodology is to provide qualitatively accurate insight in regard to the combustion system internal flow field, and to give *quantitatively accurate* (ultimately reaching the accuracy levels specified in Table 1) predictions of emissions, performance, operability, liner wall

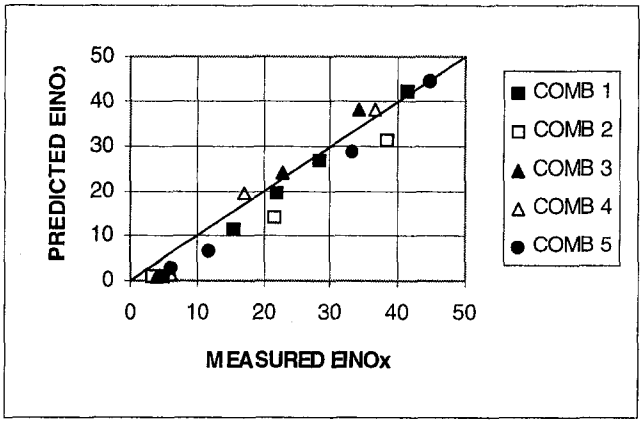

Fig. 6 Comparison between predicted and measured NO_x emissions indices of Combustors 1–5

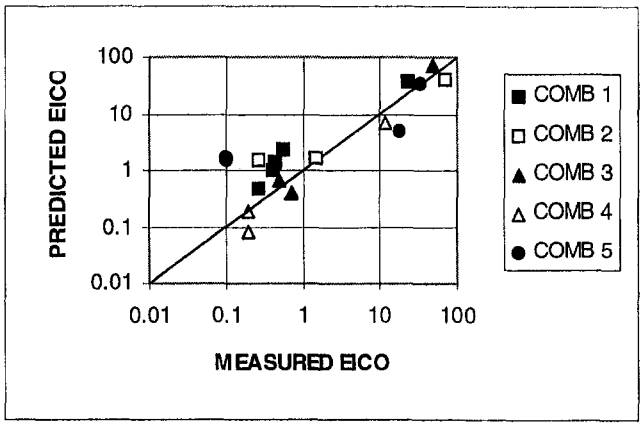

Fig. 7 Comparison between predicted and measured CO emissions indices of Combustors 1–5

temperature, and life characteristics of new product engine combustors. The turbulent combustion modeling will be limited to the use of second-order closure modeling, including realistic finite chemistry/turbulence interactions through the Monte Carlo simulation of multispecies kinetic schemes, e.g., Tolpadi et al. (1995), and Raju (1995).

Tolpadi et al. (1993) reported two-dimensional axisymmetric calculations of a GE/SNECMA CFM56 combustor swirl cup, shown in Fig. 1. A typical comparison between calculated and measured radial profiles of the gas-phase mean axial, radial, and swirl velocity components 17 mm downstream from the primary venturi is shown in Fig. 2. Even though the calculations give qualitatively good trends, the quantitative agreement is not good enough for design substantiation due to problems with the turbulence models and the specification of boundary conditions, as stated earlier.

Shortcomings such as these led to an alternate approach, the formulation and development of an anchored CCD methodology as presented in this paper. The proposed approach uses GEAE's proprietary code CONCERT described by Burrus et al. (1988). An elliptical grid generation procedure coupled with suitable meshing around the internal obstacles, when present, is used to simulate engine combustors, shown typically in Fig. 1. The transport equations for mass, momentum, enthalpy, and species written for the arbitrary curvilinear three-dimensional coordinate system are transformed from physical domain to a rectangular parallelepiped. Hybrid or QUICK differencing approximation along with SIMPLE algorithm are used to solve the finite-difference equations as described by Burrus et al. (1988). Other

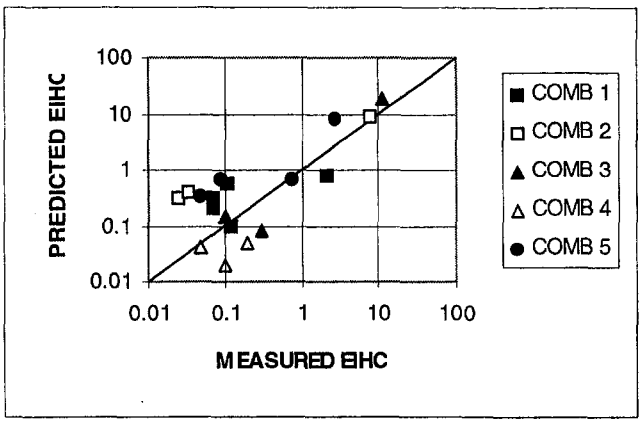

Fig. 8 Comparison between predicted and measured UHC emissions indices of Combustors 1–5

Table 2 Emissions/lbo/exit temperature prediction agreement

	POWER RANGE*	EINOx	EICO	EIHC	LBO	RPF	PTF
Combustor 5	ALL	25%	69%	62%			
ANCHORED	HIGH	8%	1.5 EI	0.4 EI		6%	7%
CONCERT	LOW		4%	65%	10%		
COMB 1-4	ALL	35%	51%	59%			
ANCHORED	HIGH	13%	0.5 EI	0.2 EI		24%	9%
CONCERT	LOW		43%	34%	14%		
Combustor 6	ALL	24%	42%	39%			
ANCHORED	HIGH	12%	0.8 EI	0.2 EI		11%	4%
CONCERT	LOW		7%	10%	N/A		
DRA for Emissions from Danis, Pritchard and Mongia (1996)							
COMB 1-4	ALL	15%	56%	56%			
SINGLE	HIGH	8%	0.85 EI	0.15 EI			
REACTOR	LOW	23%	34%	27%			
* NOTE: HIGH POWER = NOx > 10 EI; LOW = NOx < 10 EI							

details, especially for spray modeling, are given by Tolpadi et al. (1993).

In order to maintain the numerical diffusion as affected by geometry simulation and related matters to "essentially similar levels," a standardized procedure is used for generating grid network, the boundary condition specification, and other things required for CCD calculations. For the high-power simulated engine points, the flow field is calculated by assuming fast-chemistry, and thermal NO_x with an extended Zeldovich mechanism using equilibrium values of N_2, O_2, N, O, and OH. (This NO_x model is limited to combustion regimes in which thermal NO_x is the main contributor.) A two-step kinetic scheme with modified eddy-breakup model is used for calculating CO and unburned hydrocarbons. The pre-exponent and the activation energy for the first step (fuel $\rightarrow$ CO) are 3.162×10^{14} and 54 kcal/g mole, respectively; the corresponding values for the CO oxidation step are 6.026×10^{8} and 25 kcal/g mole.

A fine-grid two-dimensional axisymmetric CONCERT run is made for calculating the flow field coming out of the swirl-cup in accordance with the procedure described by Tolpadi et al. (1993), under properly simulated back-pressure influence caused by the confined flow downstream within the combustor liner. When the elliptic upstream influence of the combustion chamber is included into the swirl cup calculations, one can obtain reasonably good correlation with the measured profiles using the following set of empirical constants, and assumptions about the inlet and boundary conditions:

- accurate cross-sectional geometry maintained
- swirler vane-blockage and Cd accounted for
- inlet velocity/momentum correctly matched
- accurate exit area ratio maintained
- standard $k-\epsilon$ turbulence model constants used
- standard logarithmic law-of-the-wall used
- inlet turbulent energy/length scale set to the computed in-cell values.

Results of a typical "anchored" two-dimensional swirler analysis are shown in Section 3, and generally give better agreement to measured swirler exit velocity profiles then that shown previously (Tolpadi et al., 1993).

The CCD anchoring process can be done in a number of ways. The first approach is to anchor (calibrate) the modeling methodology with one combustor, and then apply it identically to other combustors. If one obtains a reasonably good agreement between data and predictions for the group as a whole, then there is no need for further anchoring the models. The second approach involves a continuous refinement of the global anchoring process as more data become available. The third approach could be called a "local anchoring exercise" wherein one further refines the set of empirical constants along with the appropriate inlet and boundary conditions specific to the particular combustor design.

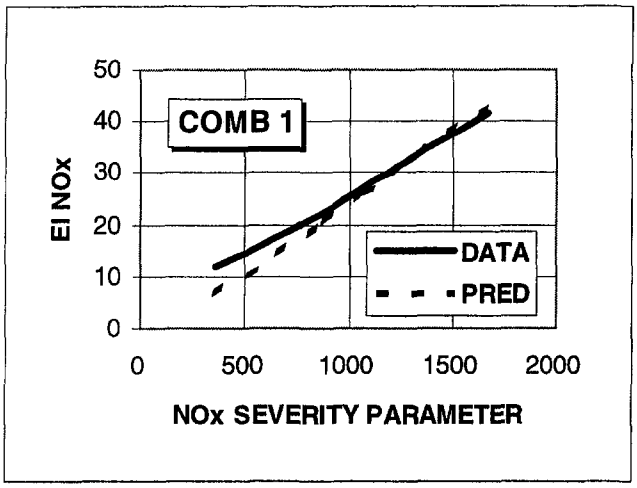

(a)

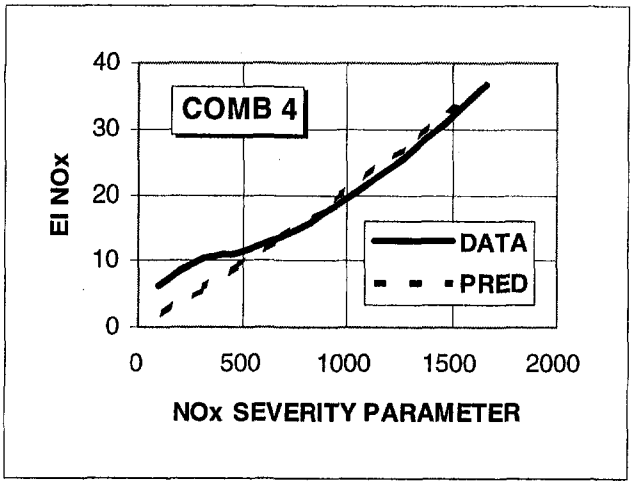

(d)

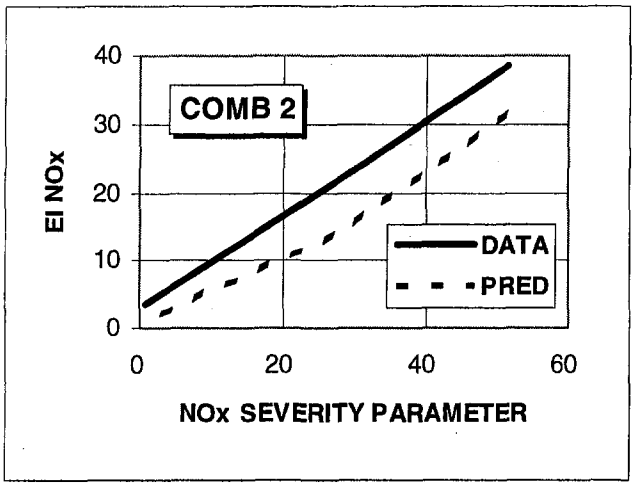

(b)

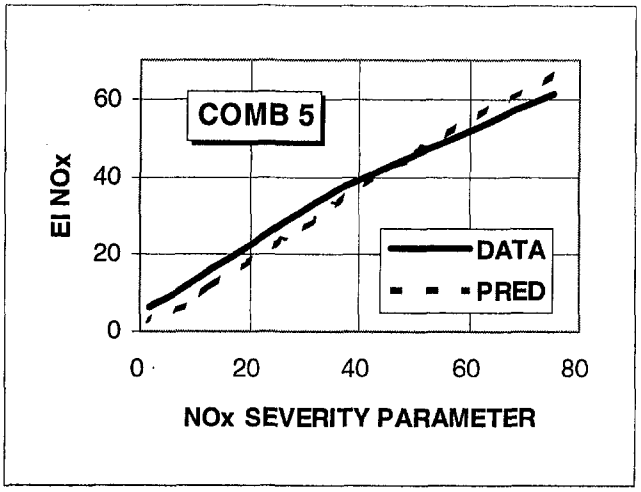

(e)

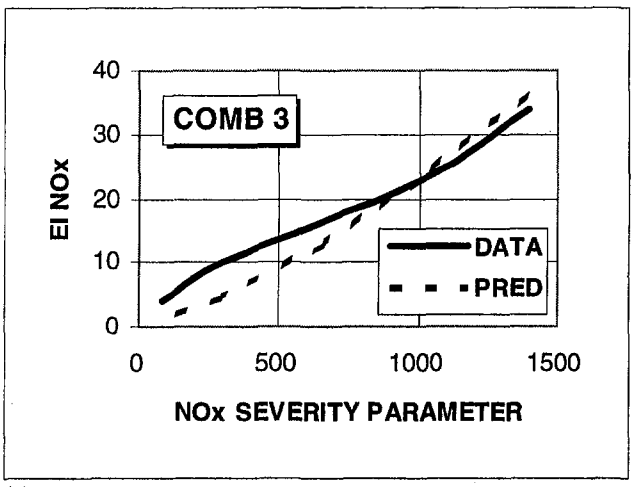

(c)

Fig. 9 Comparison between predicted and measured NO_xEI versus severity parameter for Combustors 1–5

This paper covers only the first approach, summarized as follows. The two-dimensional and three-dimensional CONCERT and heat transfer calculations were first anchored with the available data on emissions, lean blowout (LBO), burner exit temperature quality, and liner and dome wall temperatures from a low-emissions, high pressure ratio, certified product engine dual-annular combustor (DAC) with a "near stoichiometric" short residence time primary zone, identified as Combustor 5. (This combustor was chosen because it was under development at the same time as the process.) The swirl cup was analyzed with CONCERT2-D to provide the inlet conditions required for performing three-dimensional calculations. The three-dimensional model was calibrated (anchored) with measured data on NO_x, CO, HC, lean blowout, and combustor exit temperature profile and pattern factor by suitably modifying the model constants. As shown in Section 3, the predicted values agree well with data from Combustor 5. The anchored CONCERT2/3D was then run for the three single annular combustors (SAC) with "rich" primary zones, identified as Combustors 1, 3, and 4, and another DAC with a "lean" primary zone, Combustor 2. As shown in Section 4, the model predictions agreed well with data from these four combustors indicating a broader applicability of the anchored methodology. The anchored CONCERT modeling technique along with conventional design approach was then used for designing another high pressure development combustor with "rich" dome primary zone, Combustor 6. The pretest predictions of Combustor 6 matched well with a full-scale sector test data as shown in Section 5, indicating the applicability of the anchoring methodology as a design tool.

III Anchoring With Combustor 5

CONCERT2D was used to predict the flow field within the swirl cup and in the x–y region (10 Rp × 5 Rp, where Rp is

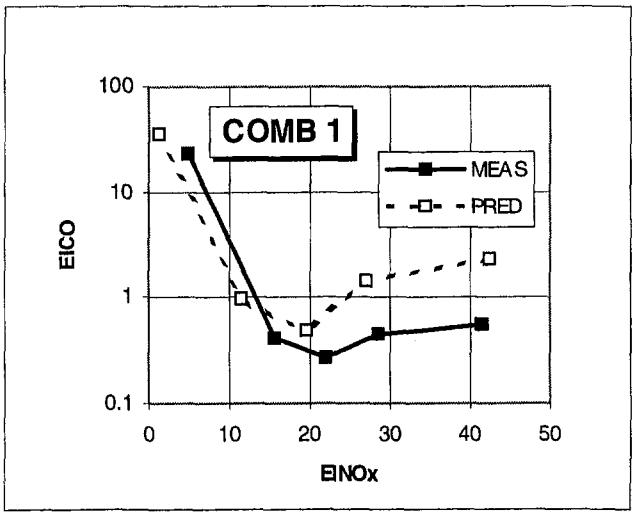

(a)

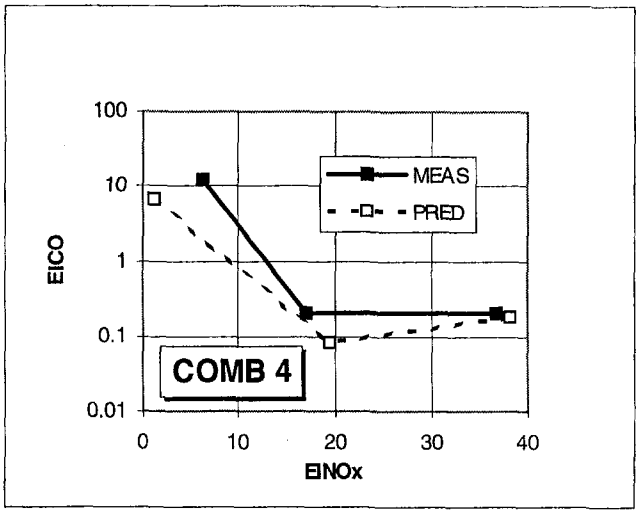

(d)

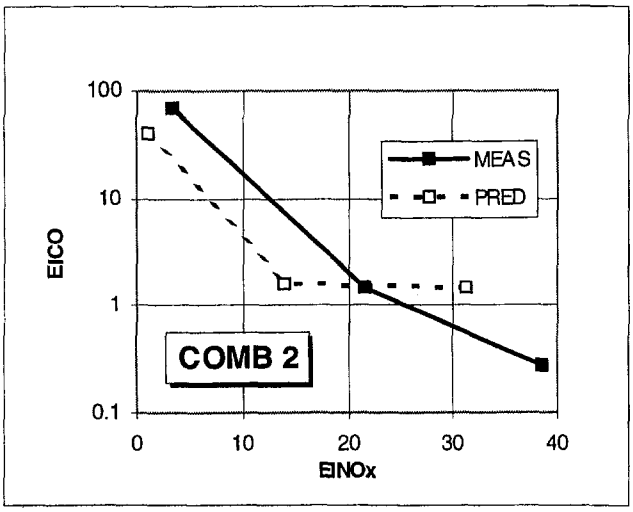

(b)

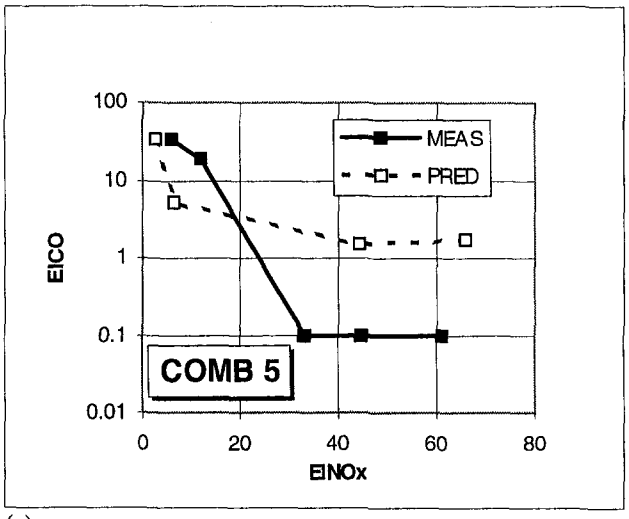

(e)

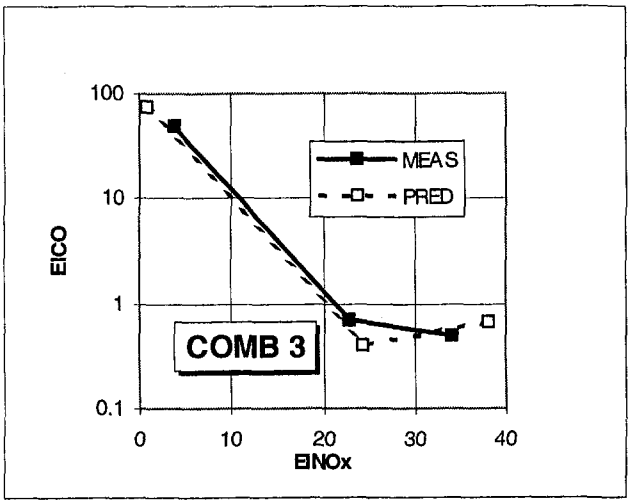

(c)

Fig. 10 Comparison between predicted and measured COEI versus NO_xEI for Combustors 1–5

the primary venturi radius) immediately downstream of the cup for Combustor 5. A nonuniform grid network of 160 × 60 grids was used to simulate closely the geometric features of the swirl cup along with the dome and liner design features downstream of the cup so that the elliptic effects caused by the confining boundaries are included in these calculations. Other details for this type of calculation are given by Tolpadi et al. (1993). Figure 3 shows a typical comparison between predicted and measured radial profiles of the mean axial (U), radial (V), and swirl (W) velocity components 2.0 mm downstream from the swirl cup. The predicted results are in good agreement with the data.

CONCERT2D predicted swirler exit velocity profiles along with measured spray quality were used as the swirl cup inlet conditions for CONCERT3D calculations. Since the two-dimensional axisymmetric model does not include three-dimensional effects, only mean quantities (velocities and fuel concentrations) were carried over to the three-dimensional inlet conditions. Turbulence properties at the swirler exit, which are sensitive to three-dimensional effects, were first estimated based on the two-dimensional results, and then varied (or calibrated) as part of the three-dimensional anchoring process.

The three-dimensional reacting flow calculations were done for the entire combustor, which was simulated by 50 × 50 × 30 nonuniformly spaced grid network. One of the biggest advantages of CCD over the empirical, semi-empirical/analytical correlation approach is in regard to providing detailed information on the combustor internal flow field, which can help the designer to get quick resolution on the conflicting design

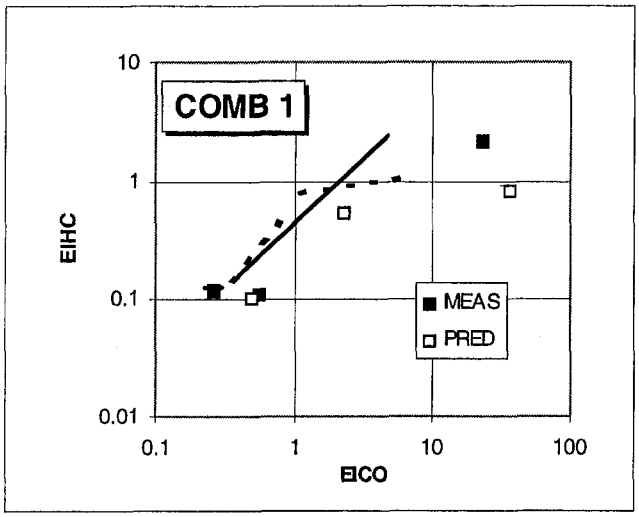

(a)

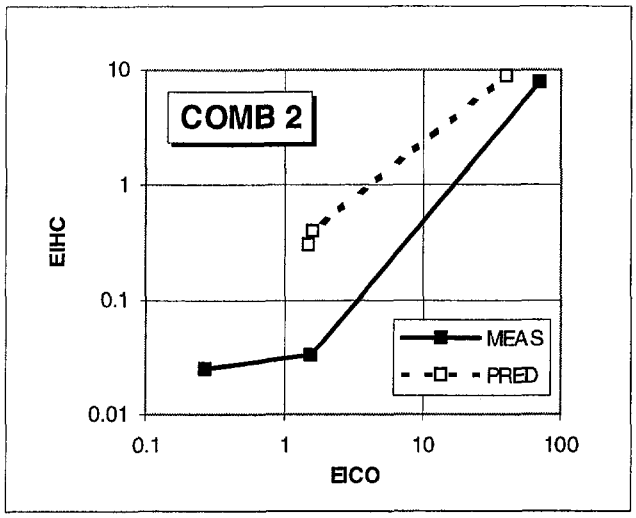

(b)

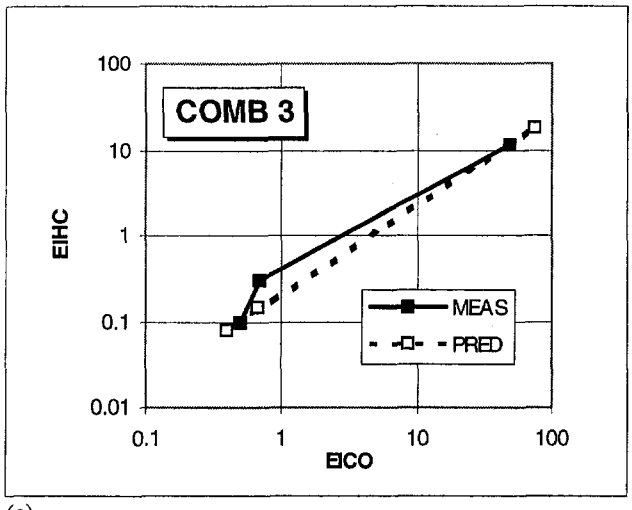

(c)

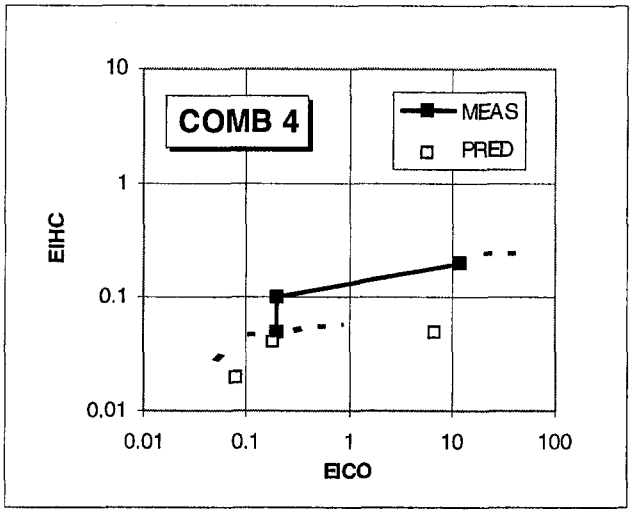

(d)

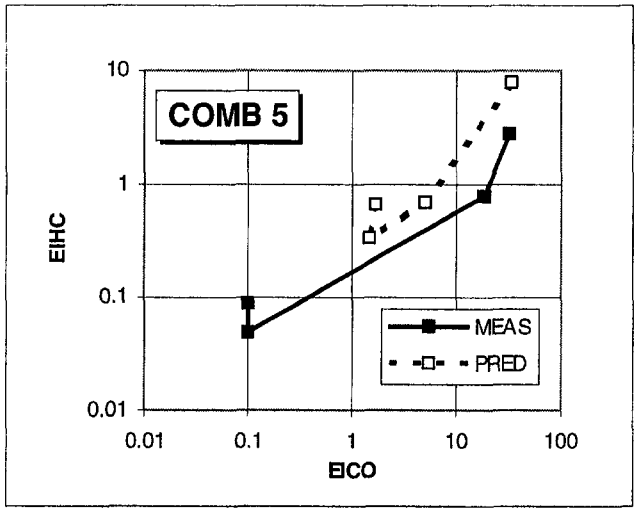

(e)

Fig. 11 Comparison between predicted and measured HCEI versus COEI for Combustors 1–5

requirements with attendant reduction in development cycle time and effort. This is illustrated by Fig. 4. Figure 4(a) shows predicted isopleths of gas temperatures normalized by combustor inlet temperature. For this particular combustor operating condition, one can see that even though the peak temperature levels are approximately the same for both the inner and outer combustion regions, the characteristics are significantly different. This is reflected from the NO isopleths (values in ppm), as shown in Fig. 4(b).

Figure 5 shows the average nondimensional exit temperature profile (T_{local}/T_{avg}) for the same combustor, along with the predicted average and maximum exit profiles. As seen, the CCD anchoring process resulted in good agreement with data.

Figures 6, 7, and 8 show comparison between predicted and measured NO_x, CO, and unburned hydrocarbons emissions indices (g/kg) respectively, for all five combustors. For now, the discussion is limited to Combustor 5. The predicted NO_x for the high-power points matches the data well. However, the model underpredicts NO_xEI at the low power points. The level of agreement between the prediction and data can be described many ways. For example, Table 2 lists the average error, defined as $\sum_n Abs\ (\%\ \text{Error})_i/n$, for the whole power range from maximum to idle. From the first entry in Table 2, one can see that even with anchoring the average errors for the whole power range are 25, 69, and 62 percent for NO, CO, and HC, respectively. Most of the error in NO_x is associated with the low-power range, whereas the errors for CO and HC are very high in the high power range. If high power region is arbitrarily

defined as the region with NO_xEI greater than 10.0 g/kg, then the average error for NO is only 8.0 percent. The corresponding errors for CO and HC are only 1.5 and 0.4 g/kg, respectively. Similarly, for the low-power region where the NO_x contribution to the total emission is not significant, the average error for CO is only 4.0 percent. However, the corresponding error for HC is very high, 65 percent. There are a number of reasons for this. First, the low-power anchoring was done to match CO data, which was considered more important than HC for this particular application. Moreover, the technical challenges for lowering HC are not as demanding as those for CO. It is well recognized that a two-step kinetic scheme coupled with eddy-breakup has not provided good agreement in regard to CO to HC ratio. In addition, unless one develops a suitable comprehensive model for the fuel–air preparation devices including filming, primary and secondary atomization, one might not achieve an equally good level of agreement for both CO and HC even with the "right" kinetic scheme and turbulence/chemistry interaction.

As explained by Danis et al. (1996), empirical assessment of emissions technology can be made by comparing the three sets of plots, namely, NO_xEI as a function of a NO_x severity parameter, COEI versus NO_xEI, and HCEI versus COEI, so-called NO_x–CO–HC plots. Therefore, even though it is a common practice to show a "diagonal plot" of data versus model predictions, more insight into the model deficiency or strength is expected by using NO_x–CO–HC plots, as shown in Figs. 9, 10, and 11. It should be noted that the NO_x severity (correlating) parameters used in Fig. 9 are: $(P_3)^{0.5}$ $\exp(T_3/345)$ $\exp(-0.0027 \text{ Humidity})$ for Combustors 1, 3, and 4, which are "rich dome" stoichiometry; and that same expression times fuel–air ratio for Combustors 2 and 5, which operate with lean to stoichiometric domes (Danis et al., 1996).

Anchoring CCD for lean blowout is more heuristic because the actual process of engine flameout is very complex. One can pursue a number of approaches to match the LBO data. The approach used here is as follows. Get a steady-state CCD solution for the engine condition for which one wants to predict LBO. Reduce the fuel flow rate while maintaining the same P3, Wa3, and T3 until one achieves a predetermined value of combustion efficiency at the burner exit. With this approach, it was possible to good agreement with the data, as shown in Fig. 12, for Combustor 5 at the sea-level idle condition.

IV Comparison With Other Combustors

Section 3 showed that one can use state-of-the-art two-dimensional and three-dimensional CCD to get good agreement with a modern gas turbine combustor (e.g., Combustor 5) in regard to NO_x, CO, HC, LBO, and burner exit temperature quality. It may be recalled that Combustor 5 is a high-pressure dual annular combustor with a "near-stoichiometric" primary zone. If one can use the anchored CCD for correlating data from other combustors, not previously used in the anchoring process, and get good agreement with data, this would be a useful tool for use in the combustion design process. To check the feasibility of this approach, the anchored CCD was used to make predictions for three single annular combustors (Combustors 1, 3, and 4), and a lean dual-annular combustor (Combustor 2). These runs were made with the same procedure, as described in Section 3, and without modifying any of the model constants and/or boundary and inlet conditions established for Combustor 5.

From Figs. 6–12, previously discussed relative to Combustor 5 only, one can see that the models correlated NO_x, CO, and HC emissions data from combustors 1–4 well also, or as well as can be reasonably expected considering the models were calibrated only for Combustor 5. This indicates that if the anchoring methodology is as broad in application as it appears from these five combustors, its use is not limited to analysis and data correlation only. One should also be able to use it as a design tool, as will be demonstrated in Section 5.

The last entry in Table 2 is the corresponding average errors from the semi-empirical "single-reactor" modeling correlation described by Danis et al. (1996). From here it is seen that the original intent of the anchoring CCD has been achieved in that the multidimensional modeling predicts emissions levels with confidence levels comparable with that of the semi-empirical models.

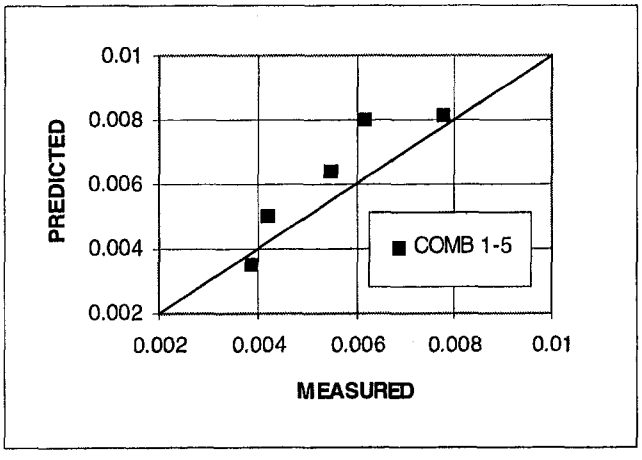

Fig. 12 Comparison between predicted and measured lean blowout fuel–air ratio for Combustors 1–5

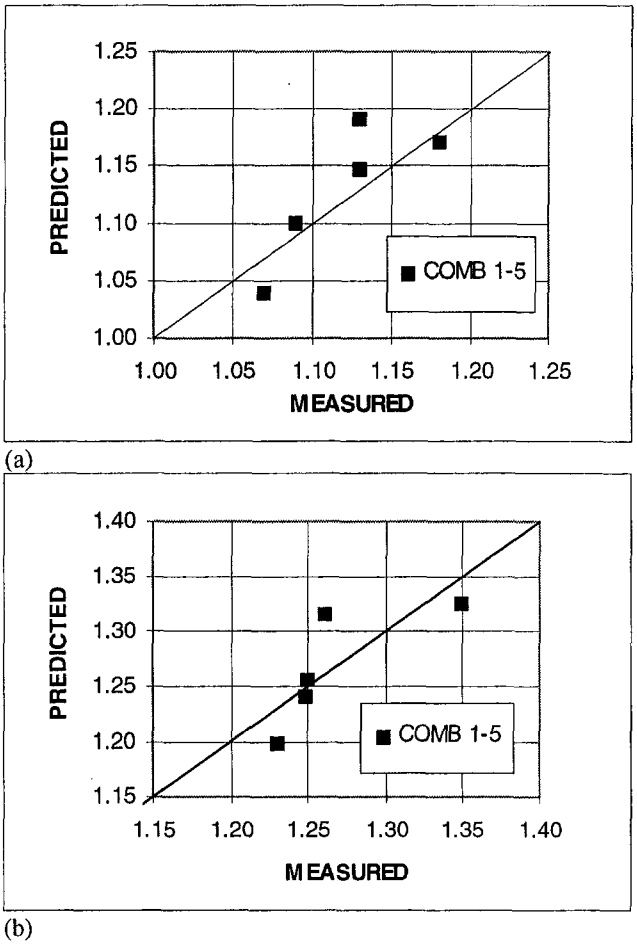

Fig. 13 Comparison between predicted and measured nondimensional burner exit temperature quality; (*a*) average radial profile factor, (*b*) peak temperature factor for Combustors 1–5

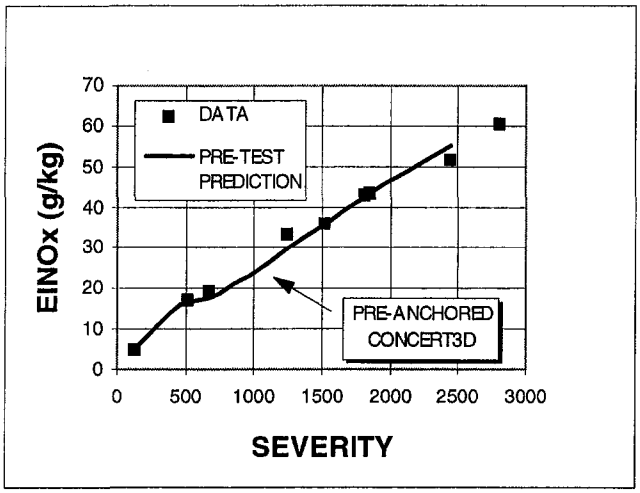

(a)

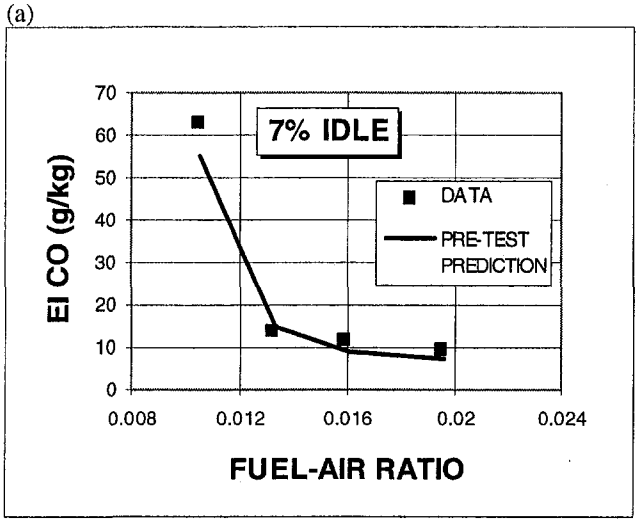

(b)

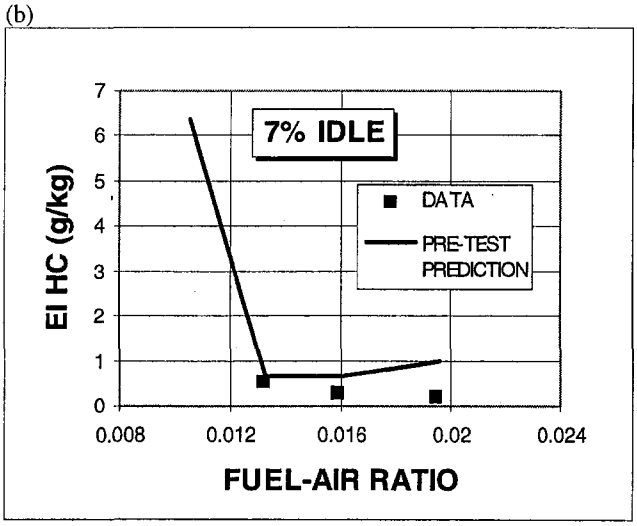

(c)

Fig. 14 Comparison between pretest predictions and measured emissions characteristics of Combustor 6

Figure 12 discussed previously for anchoring the LBO data for Combustor 5 shows that the agreement with data from combustors 1, 2, and 4 is also equally good; it meets the LBO goal of ±0.001, as outlined in Table 1. However, for Combustor 3 the error is 0.002. This is reasonable outcome considering that a simplistic criteria for LBO has been used in this study.

Figures 13(*a*) and 13(*b*) for radial profile factor and pattern factor show that the anchored methodology gives reasonable agreement with exit temperature quality data for a wide range of combustors.

As summarized in Table 2, the anchored CCD methodology gives good agreement in regard to NO_x, burner exit temperature quality at high power, CO, HC, and lean blowout at low power. Further work is however is needed to get good agreement across the whole power range.

V Anchored CCD as a Design Tool

From the previous two sections, it has been shown that once the model had been anchored with a "near-stoichiometric dual-annular combustor (here Combustor 5)," the predicted results agreed well with measured NO_x, CO, HC, LBO, and burner exit temperature quality data from the other four modern combustors. This section illustrates briefly the use of anchored CCD as a design tool.

The application involved the design and analysis of a development combustor concept (identified as Combustor 6) that uses a "rich dome" approach. A number of design iterations were made starting from the baseline concept. These runs were made with the same procedure, as described in Section 3, and without modifying any of the model constants and/or boundary and inlet conditions. The most promising design configuration was fabricated and tested in a full-scale annular sector rig that simulated engine conditions over the operating range from idle to maximum power.

The measured data, including emissions and burner exit plane quality, agreed well with the pretest predictions, with emissions results shown in Fig. 14. Predicted versus measured NO_xEI is plotted as a function of severity parameter in Fig. 14(*a*), and excellent agreement is seen across the entire operating range. Predicted versus measured COEI and HCEI are shown in Figs. 14(*b*) and 14(*c*), respectively, plotted as a function of combustor fuel–air ratio at the 7 percent idle operating condition. Again, the agreement is good across a range of fuel–air ratios for both species. As shown in Table 2, the average errors for Combustor 6 are comparable with those of Combustors 1–4.

VI Summary

Due to limitations of the state-of-the-art turbulent combustion models, and insufficient information about the inlet and boundary conditions required for the CCD analysis of engine combustors, a new approach—anchored CCD—has been formulated. First, the models were anchored with one modern turbopropulsion engine combustor, and then applied to four additional combustors. The anchored models correlated well with measured NO_x, CO, HC, LBO and exit temperature quality, demonstrating a broader applicability of the anchored method. The anchored models were then used for designing a new combustion concept. The pretest prediction agreed well with the sector rig data showing the feasibility of using the anchored methodology as a design tool. Further improvement in the anchored CCD methodology is planned for achieving the ultimate goals listed in Table 1.

References

Baker, S. J., and McGuirk, J. J., 1993, "Multijet Annulus/Core-Flow Mixing—Experiments and Calculations," ASME JOURNAL OF ENGINEERING FOR GAS TURBINES AND POWER, Vol. 115, pp. 473–479.

Burrus, D. L., Shyy, W., and Braaten, M. E., 1988, "Numerical Models for Analytical Predictions of Combustor Aerothermal Performance Characteristics," in: *Combustion and Fuels in Gas Turbine Engines*, AGARD-CP-422, Paper No. 25.

Danis, A. M., Pritchard, B. A., and Mongia H. C., 1996, "Empirical and Semi-empirical Correlation of Emissions Data From Modern Turbopropulsion Gas Turbine Engines," ASME Paper No. 96-GT-86.

Hogg, S., and Leschziner, M. A., 1989, "Computation of Highly Swirling Confined Flow With a Reynolds Stress Turbulence Model," *AIAA J.*, Vol. 27, No. 1, pp. 57–63.

Holdeman, J. D., 1993, "Mixing of Multiple Jets With a Confined Subsonic Crossflow," *Prog. Energy Combust. Sci.,* Vol. 19, pp. 31–70.

Mongia, H. C., Reynolds, R. S., Coleman, E., and Bruce, T. W., 1979, "Combustor Design Criteria Validation. Vol. 2—Development Testing of Two Full-Scale Annular Gas Turbine Combustors," USARTL-TR-78-55B (AD-AO-67689).

Mongia, H. C., 1993, "Application of CFD in Combustor Design Technology," AGARD CP 536, *Fuels and Combustion Technology for Advanced Aircraft Engines,* pp. 12-1 through 12-17.

Mongia, H. C., 1994, "Combustor Modeling in Design Process: Applications and Future Direction," AIAA Paper No. 94-0466.

Nikjooy, M., Mongia, H. C., McDonnell, V. G., and Samuelsen, G. S., 1993, "Fuel Injection-Air Swirl Characterization Aerothermal Modeling. Phase II. Final Report," NASA CR-189193; Paper No. 25, AGARD-CP-422, Combustion and Fuels in Gas Turbine Engines.

Raju, M. S., 1995, "Coupled Monte-Carlo-PDF/Spray/CFD Computations of Swirl-Stabilized Flames," AIAA Paper No. 95-2442.

Rizk, N. K., and Mongia, 1986, "Gas Turbine Combustor Design Methodology," AIAA Paper No. 86-1531.

Rizk, N. K., and Mongia, H. C., 1990, "Three-Dimensional Combustor Performance Validation With High Density Fuels," *J. Propulsion & Power,* Vol. 6, No. 5, pp. 660–667.

Rizk, N. K., and Mongia, H. C., 1990a, "Ultralow NO_x Rich-Lean Combustion," ASME Paper No. 90-GT-87.

Rizk, N. K., and Mongia, H. C., 1990b, "Lean Low NO_x Combustion Concept Evaluation," *23rd Symposium (International) on Combustion,* pp. 1063–1070.

Rizk, N. K., and Mongia, H. C., 1991, "Model for Airblast Atomization," *J. Propulsion & Power,* Vol. 7, No. 3, pp. 305–311.

Rizk, N. K., and Mongia, H. C., 1991a, "Three-Dimensional Analysis of Gas Turbine Combustors," *J. Propulsion & Power,* Vol. 7, No. 3, pp. 445–451.

Rizk, N. K., and Mongia, H. C., 1992, "Calculation Approach Validation for Airblast Atomizers," ASME JOURNAL OF ENGINEERING FOR GAS TURBINES AND POWER, Vol. 114, pp. 386–393.

Rizk, N. K., and Mongia, H. C., 1993, "Three-Dimensional Gas Turbine Combustor Emissions Modeling," ASME JOURNAL OF ENGINEERING FOR GAS TURBINES AND POWER, Vol. 115, pp. 603–611.

Rizk, N. K., and Mongia, H. C., 1993a, "Semianalytical Correlations for NO_x, CO, and UHC Emissions," ASME JOURNAL OF ENGINEERING FOR GAS TURBINES AND POWER, Vol. 115, pp. 612–619.

Rizk, N. K., and Mongia, H. C., 1993b, "Three-Dimensional Emission Modeling for Diffusion Flame, Rich/Lean and Lean Gas Turbine Combustors," AIAA Paper No. 93-2338.

Rizk, N. K., and Mongia, H. C., 1995, "A Semi-Analytical Emission Model for Diffusion Flame, Rich/Lean, and Premixed Lean Combustors," ASME JOURNAL OF ENGINEERING FOR GAS TURBINES AND POWER, Vol. 117, pp. 290–301.

Rizk, N. K., Chin, J. S., and Razdan, M. K., 1997, "Modeling of Gas Turbine Fuel Nozzle Spray," ASME JOURNAL OF ENGINEERING FOR GAS TURBINES AND POWER, Vol. 119, pp. 34–44.

Sanborn, J. W., Reynolds, R. S., and Mongia, H. C., 1976, "A Quasi-Three-Dimensional Calculation Procedure for Predicting the Performance and Gaseous Emissions of Gas Turbine Combustors," AIAA Paper No. 76-682.

So, R. M. C., Ahmed, S. A., and Mongia, H. C., 1985, "Density Effects on Jet Characteristics in Confined Swirling Flow," *Exp. in Fluids,* Vol. 3, pp. 231–238.

So, R. M. C., Ahmed, S. A., and Mongia, H. C., 1985a, "Jet Characteristics in Confined Swirling Flow," *Exp. in Fluids,* Vol. 3, pp. 221–230.

Srinivasan, R., Reynolds, R., Ball, I., Berry, R., Johnson, K., and Mongia, H. C., 1983, "Aerothermal Modeling Program. Phase 1. Final Report," NASA CR-168243.

Srivatsa, S. K., 1982, "Computations of Soot and NO_x Emissions From Gas Turbine Combustors," NASA CR-167930.

Tolpadi, A. K., Burrus, D. L., and Lawson, R. J., 1993, "Study of Two-Phase Flow Downstream of a Gas Turbine Combustor Dome Swirl Cup," ASME Paper No. 93-GT-392.

Tolpadi, A. K., Correa, S. M., Burrus, D. L., and Mongia, H. C., 1995, "A Monte Carlo PDF Method for the Calculation of Gas Turbine Combustor Flow Fields," AIAA Paper No. 95-2443.

Preliminary Gas Turbine Combustor Design Using a Network Approach

P. J. Stuttaford

P. A. Rubini[1]

School of Mechanical Engineering,
Cranfield University,
Cranfield, Bedfordshire, MK43 0AL,
United Kingdom

The preliminary design process of a gas turbine combustor often involves the use of cumbersome, geometry restrictive semi-empirical models. The objective of this analysis is the development of a versatile design tool for gas turbine combustors, able to model all conceivable combustor types. A network approach is developed that divides the flow into a number of independent semi-empirical subflows. A pressure-correction methodology solves the continuity equation and a pressure-drop/flow rate relationship. The development of a full conjugate heat transfer model allows the calculation of flame tube heat loss in the presence of cooling films, annulus heat addition, and flame tube feature heat pick-up. A constrained equilibrium calculation, incorporating mixing and recirculation models, simulates combustion processes. Comparison of airflow results to a well-validated combustor design code showed close agreement. The versatility of the network solver is illustrated with comparisons to experimental data from a reverse flow combustor.

Introduction

The preliminary design of a combustor involves the application of a large pool of knowledge to conceptualize an overall structure, normally requiring the use of cumbersome, geometry restrictive semi-empirical models. The results of such an analysis become the input for more thorough investigations such as computational fluid dynamics (CFD) simulations and rig resting. The cost of rig testing and to a lessor degree CFD prohibits their use. Simple empirical models are therefore optimized as much as possible before further advanced development.

Semi-empirical models have the advantage of rapid execution times, on the order of a few minutes or less. This is an advantage for the design engineer as it allows optimization with relatively little time expenditure. The more accurate this initial design process, the more rapid the following phases of design. The limitations of such tools include their restriction to simple geometries; being cumbersome to set up; and having difficulties with convergence when applied to more irregular flow fields. Network methods have the ability to model complicated and unusual geometries effectively and with little numerical difficulty while retaining the advantage of rapid execution.

A network consists of a number of independent subflows linked together to model a physical process. The method has been used with success in modeling large pipe networks (Greyvenstein and Laurie, 1994). Since the orientations of the subflows are independent, multidimensional features such as total-static fed cooling rings may be modeled with ease. Each subflow is defined by a semi-empirical pressure-drop/flow rate relationship and a heat transfer relationship. A pressure correction methodology is used to solve the continuity equation and a pressure-drop/flow rate relationship.

Gas Turbine Combustor Modeling for Design

Initial gas turbine combustor design procedures are based on overall performance requirements including combustion efficiency, lean lightoff and blowoff limits, exit temperature traverse, and emissions of CO and NO_x.

Mellor and Fritsky (1990) demonstrated the application of a characteristic time model in achieving these goals. The model provided full details of primary and secondary air requirements. Comparisons with rig test data proved reasonably accurate. This form of analysis provides a sound basis for more detailed computations, giving predictions of mass flow splits, pressure loss, and heat transfer. The results allow a fine-tuning procedure, improving upon the initial design. Three-dimensional analysis of the flame tube enables further optimization before undertaking the costly procedure of rig testing.

Empirically based procedures have led to successful evolutionary combustor improvements, but they exhibit shortfalls when significantly different technological designs from those of proven concepts are required. Advances in computational fluid dynamics (CFD) modeling have allowed the successful simulation of gas turbine combustor flows. However, the accuracy of such simulations remains limited by the submodels they employ. CFD computations require the time-consuming procedure of grid generation, boundary condition specification, and obtaining solution convergence.

In combination, these two methodologies have proven a valuable combustor design tool (Holdeman et al., 1989). Examples of the successful application of such a procedure to specific combustors are given by Mongia et al. (1986). Historical trend lines and one-dimensional models were used to develop a preliminary design. A three-dimensional empirical/analytical procedure was employed to augment the basic design, providing a good qualitative analysis, using the submodels of turbulent reactive flow available. Rizk and Mongia (1991) obtained satisfactory agreement with experimental results for a range of combustors under various operating conditions, using a three-dimensional analytical/empirical performance model.

The use of three-dimensional computational models is a time-consuming task, and only undertaken in an attempt to visualize a combustor for which a preliminary design has already been developed. Phenomena displayed by this more complicated analysis may lead to modifications in the design.

A number of empirically based models have been developed in the past. These include turbulent flame speed models, where the effect of turbulence on the combustion is simulated by calculating a turbulent flame speed based on analogy with laminar

[1] Corresponding author.

Contributed by the International Gas Turbine Institute and presented at the 41st International Gas Turbine and Aeroengine Congress and Exhibition, Birmingham, United Kingdom, June 10–13, 1996. Manuscript received at ASME Headquarters February 1996. Paper No. 96-GT-135. Associate Technical Editor: J. N. Shinn.

flame speed; microvolume burning models, where mixing and chemical reaction processes are accounted for in a series of turbulent eddies within small cubes; stirred reactor models, where each zone is assumed to contain a homogeneous reacting mixture (Hammond and Mellor, 1970).

Mellor (1978) in an evaluation of modular gas turbine models found the approach of Mosier et al. (1973), and Mado and Roberts (1974) the most successful. In this model the internal flowfield is approximated by a series of co-annular, one-dimensional reacting streamtubes. A one-dimensional streamtube represents the flow recirculation in the primary zone, i.e., a well-stirred reactor. A procedure was developed whereby the streamtubes exchange mass, momentum, and energy via turbulent mixing. The effects of port and film cooling air injection were modeled semi-empirically. Swithenbank et al. (1973) developed a model containing partially stirred reactors, based on turbulent mixing. The model was shown to predict blow-off stability limits, overall combustion efficiency, combustion intensity, and overall pressure loss. Secondary analysis was able to predict emissions and wall heat transfer. The methodology proved useful in analyzing the effects of design modifications.

One-dimensional models, such as that described by Burrus et al. (1987), have been used successfully for the preliminary design and sizing of a combustor. Given target airflow distributions, the required flow areas could be computed, or given the areas, the various flow splits and pressure drops may be calculated. The one-dimensional models incorporate numerous experimental data, and empirically derived correlations to support the simplified overall governing equations (Mellor, 1990).

A flexible geometry-independent one-dimensional model, while lacking the resolution of the three-dimensional models, is still able to predict reasonably accurate results very rapidly. The flexibility of network analysis allows the simple modeling of complex geometries, and removes many of the restrictions placed upon conventional one-dimensional models. The submodels within these solution procedures, e.g., equilibrium models, film-cooling models, radiation models, etc., continue to be improved upon. The network approach offers a simple procedure of incorporating the latest submodels in an algorithm, enabling the complete modeling of a combustor.

Numerical Algorithm

The domain of interest is modeled by overlaying a network on the system geometry. The network consists of a number of elements and nodes. The elements represent actual physical features in the domain, e.g., duct sections, holes, etc. The nodes join the elements to one another, thus combining independent features into a meaningful overall structure. The overall governing equations are solved within the nodes, while semi-empirical relationships may be employed to describe the flow through an element.

The procedure used for obtaining a solution to the flow equations is the SIMPLE (Patankar, 1980) pressure correction methodology. The one-dimensional flow may be incompressible or compressible.

The overall governing flow equations are the continuity equation, and a pressure-drop/flow rate relationship (Greyvenstein and Laurie, 1994). The continuity equation may be specified as,

$$\sum_{j=1}^{J} \rho_{i,j} Q_{i,j} s_{i,j} = -d_i \quad i = 1, 2, \ldots, J \tag{1}$$

and the pressure-drop/flow-rate relationship as,

$$\Delta P_{i,j} = P_{n_{i,j}} - P_i = s_{i,j} H_{i,j} g_{i,j} f_{i,j} \tag{2}$$

where

$$g_{i,j} = g_{i,j}(\rho_{i,j})$$

$$f_{i,j} = f_{i,j}(|Q_{i,j}|)$$

$$H_{i,j} = \frac{Q_{i,j}}{|Q_{i,j}|}$$

$s_{i,j} = 1$ if the flow is in the positive direction

$s_{i,j} = -1$ if the flow is in the negative direction.

These functional relationships are derived from semi-empirical formulations for combustor features and internal flows. Examples of the formulations, such as the Darcy–Weisbach equation and flow in duct sections, may be found in Jeppson (1977) and Saad (1985). Internal flow effects such as momentum addition and recirculation could be accounted for in the pressure-drop equations, but only from an empirical standpoint. The functional relationships are written as coefficients in the overall solution matrix, and simultaneously solved using the direct method discussed later in this section.

For an ideal gas,

$$\rho_{i,j} = \frac{P_{i,j}}{RT_{i,j}} \quad \text{or} \quad \rho_{i,j} = \frac{P_i + P_{n_{i,j}}}{2RT_{i,j}} \tag{3}$$

Figure 1 shows a section of a typical network. Initially, the temperatures and pressures at the nodes, $T^*_{i,j}$ and P^*_i, are predicted, and if the flow is compressible Eq. (3). Is used to calculate $\rho^*_{i,j}$. Using Eq. (2). a predicted flow-rate, $Q^*_{i,j}$, is calculated.

The predictions are corrected using the following relationships:

$$P = P^* + P'$$

$$Q = Q^* + Q'$$

$$\rho = \rho^* + \rho' \tag{4}$$

To correct these values a relationship between the flow rate and pressure is computed, obtained by differentiating Eq. (2) with respect to $Q_{i,j}$,

Nomenclature

Cp = specific heat at constant pressure
C/H = carbon/hydrogen mass ratio of fuel
d = external mass flow into node
E = energy source term
h = convective heat transfer coefficient
L = luminosity
l_b = mean beam length
$\dot{m}$ = mass flow rate
P = pressure
Q = volumetric flow rate
q = fuel/air ratio
R = gas constant
T = temperature
ϵ = convergence parameter
ϵ_g = gas emissivity
η = film effectiveness
ρ = density

Subscripts

f = film
g = hot gas
i = center node
i, j = branch element
$n_{i,j}$ = branch node
p = adjacent upstream location

Superscripts

* = predicted values
′ = correction values

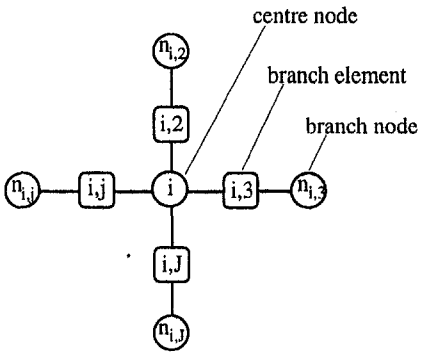

Fig. 1 Network nomenclature

$$Q'_{i,j} = P'_{n_{i,j}}\left[\frac{1}{s_{i,j}g^*_{i,j}f1^*_{i,j}} - \frac{H_{i,j}a_{i,j}f^*_{i,j}g1^*_{i,j}}{g^*_{i,j}f1^*_{i,j}}\right] - P'_i\left[\frac{1}{s_{i,j}g^*_{i,j}f1^*_{i,j}} + \frac{H_{i,j}a_{i,j}f^*_{i,j}g1^*_{i,j}}{g^*_{i,j}f1^*_{i,j}}\right] \quad (5)$$

where

$$a_{i,j} = \frac{1}{2RT_{i,j}}; \quad g1_{i,j} = \frac{\partial g_{i,j}}{\partial \rho_{i,j}}; \quad f1_{i,j} = \frac{\partial f_{i,j}}{\partial |Q_{i,j}|}$$

Substituting Eqs. (4) and (5) into Eq. (1) gives

$$P'_i = \frac{\sum_{j=1}^{J}(c_{i,j}P_{n_{i,j}}) + b_i}{c_{i,i}} \quad (6)$$

where

$$c_{i,i} = \sum_{j=1}^{J}\left[\frac{\rho^*_{i,j}}{g^*_{i,j}f1^*_{i,j}} + s_{i,j}H_{i,j}a_{i,j}\left(\frac{\rho^*_{i,j}f^*_{i,j}g1^*_{i,j}}{g^*_{i,j}f1^*_{i,j}} - |Q^*_{i,j}|\right)\right]$$

$$c_{i,j} = \frac{\rho^*_{i,j}}{g^*_{i,j}f1^*_{i,j}} - s_{i,j}H_{i,j}a_{i,j}\left(\frac{\rho^*_{i,j}f^*_{i,j}g1^*_{i,j}}{g^*_{i,j}f1^*_{i,j}} - |Q^*_{i,j}|\right)$$

$$b_i = d_i + \sum_{j=1}^{J}(\rho^*_{i,j}Q^*_{i,j}s_{i,j})$$

Equation (6) is solved simultaneously for all nodes in the network. Updated values for flow rate, pressure, and density are calculated from Eq. (4). The process is repeated until convergence is achieved. The convergence criterion for the continuity equation is,

$$\epsilon_m < \frac{|h_i|_{\max}}{|\dot{m}|_{\text{mean}}} \quad (7)$$

where,

$$h_i = \sum_{j=1}^{J}(\rho_{i,j}Q_{i,j}s_{i,j}) + d_i$$

and for the pressure-drop equation,

$$\epsilon_p < \sum_{e=1}^{E}\left|\frac{\Delta P_1 - \Delta P_2}{\Delta P_1}\right| \quad (8)$$

where,

ΔP_1 = pressure drop across element from Eq. (2).
ΔP_2 = pressure difference between two nodes associated with element

The envelope method (George and Liu, 1981) is used to solve Eq. (6) exactly. Formerly, this method is identical to the Gaussian elimination method. Essentially the approach allows significant savings in computing time and storage allocation by not computing quantities known in advance to be zero. A further optimization is made by employing the reverse Cuthill–McKee re-ordering algorithm (George and Liu, 1981). An evaluation of this methodology by Greyvenstein and Laurie (1994) illustrated significant improvements on convergence in comparison to other methods, such as the Newton–Raphson scheme.

The energy equation is satisfied by ensuring an enthalpy balance at each node within the network. This may be specified at nodes with branch elements containing mass transfer as,

$$T_i = \frac{\sum_{j=1}^{J}(E_{i,j} + \dot{m}_{i,j}CpT_{n_{i,j}})_{\text{inflow bits}}}{\sum_{j=1}^{J}(\dot{m}_{i,j}Cp)_{\text{inflow bits}}} \quad (9)$$

where

$$E = H - W$$

= (heat transfer to element) − (work done by element)

A semi-implicit formulation is used to compute node temperatures on boundaries or within walls, i.e., at nodes where the branch elements contain no mass flow. On the flow boundaries, where conduction, convection, and radiation are present, this may be expressed as,

$$T_i = \frac{(\sum_{j=1}^{J}R_{i,j}T_{n_{i,j}})_{\text{conduction}} + (\sum_{j=1}^{J}h_{i,j}T_{n_{i,j}})_{\text{convection}} + Q_{\text{radiation}}}{(\sum_{j=1}^{J}R_{i,j})_{\text{conduction}} + (\sum_{j=1}^{J}h_{i,j})_{\text{convection}}} \quad (10)$$

where

R = conductive heat transfer coefficient
Q = heat flux

and within the solid where conduction is the only mode of heat transfer,

$$T_i = \frac{(\sum_{j=1}^{J}R_{i,j}T_{n_{i,j}})_{\text{conduction}}}{(\sum_{j=1}^{J}R_{i,j})_{\text{conduction}}} \quad (11)$$

The heat transfer coefficient terms in Eq. (10) are evaluated using semi-empirical correlations and data for various cooling types found in gas turbine combustors. The effect of film cooling has a significant effect on the wall temperatures, and must be modeled accurately. The calculations take the form of Nusselt number correlations, employing numerous experimental data. A wide range of cooling effects are modeled, including Z-rings, lipped-rings, slots, effusion patches, and transply patches. Examples of such correlations are given in Lefebvre (1983). Heat pick-up by the fluid moving though the flame tube wall is computed. Multiple films at the same location, originating from different features, are accounted for when computing the effective heat transfer coefficient. The effects of adjacent film temperatures and upstream conditions are incorporated using

$$T_f = T_{fp}(\eta_f/\eta_{fp}) + (1 - \eta_f/\eta_{fp})\left(\frac{T_{gp} - T_g}{2}\right) \quad (12)$$

Radiative fluxes may account for over half the total heat flux "seen" by the flame tube walls. A simple empirical model is presently used to account for radiative heat flux (Lefebvre,

1983). The gas emissivity is calculated using a corrected luminosity for gases containing soot clouds,

$$\epsilon_g = 1 - \exp[-290PL(ql_b)^{0.5}T_g^{-1.5}] \quad (13)$$

where

$$\text{luminosity, } L = 7.53(\text{C/H} - 5.5)^{0.84}$$

The accuracy of such a simple model is limited, since in combustors operating at high pressures, luminous emissivity will be highly dependent upon soot formation and oxidation, not simply on fuel type. A more realistic radiation model is being developed, based upon the discrete transfer methodology of Lockwood and Shah (1981).

The Gauss–Seidel iterative technique with successive overrelaxation is used to solve the node temperatures. The convergence criterion for the energy equation is,

$$\epsilon_e > \sum_{i=1}^{N} \left| \frac{T_{i_{\text{old}}} - T_{i_{\text{new}}}}{T_{i_{\text{old}}}} \right| \quad (14)$$

The solution of the flow and energy equations are coupled.

A constrained equilibrium computation (Coupland, 1989) calculates adiabatic flame temperatures from local species concentrations at given fuel/air ratios. The computation is based upon the original chemical equilibrium algorithm developed by Gordon and McBride (1971). During the solution procedure the temperature calculation is performed within specified elements, and the resulting heat release is treated as a source term in the energy equation. The source term from the adiabatic flame temperature calculation is corrected to account for the heat loss within the flame tube.

The equilibrium model constrains certain species concentrations such as CO and CO_2. The model uses these constraints to compute other species concentrations, and hence flame temperature. The constraints are computed by fitting an efficiency curve to the flame tube centreline. This efficiency curve is a function of overall loading, and is correlated for a number of combustor types, thus making allowance for various injectors and fuel types over a range of operating conditions.

The equilibrium point of a system occurs where a combusting fuel/air mixture decomposes into a mixture of chemical species at a specific temperature. The composition of this equilibrium mixture may be described by a minimization of free energy formulation. Gibbs free energy is given by (Gordon and McBride, 1971),

$$g = \sum_{j=1}^{n} \mu_j n_j \quad (15)$$

where

μ_j = chemical potential of species j
n_j = concentration of species j

The minimization of free energy is subject to the following constraint;

$$b_i^0 - b_i = 0 \quad i = 1, 2, \ldots, l \quad (16)$$

where

b_i^o = assigned number of kilogram – atoms of element i per kilogram – mole species j
$b_i = \sum_{j=1}^{n} a_{ij} n_j \quad i = 1, 2, \ldots, l$
a_{ij} = number of kilogram – atoms of element i in species j
l = number of elements
n = number of species

Chemical species do not always attain full equilibrium in practical systems. The gas temperature is highly affected, should

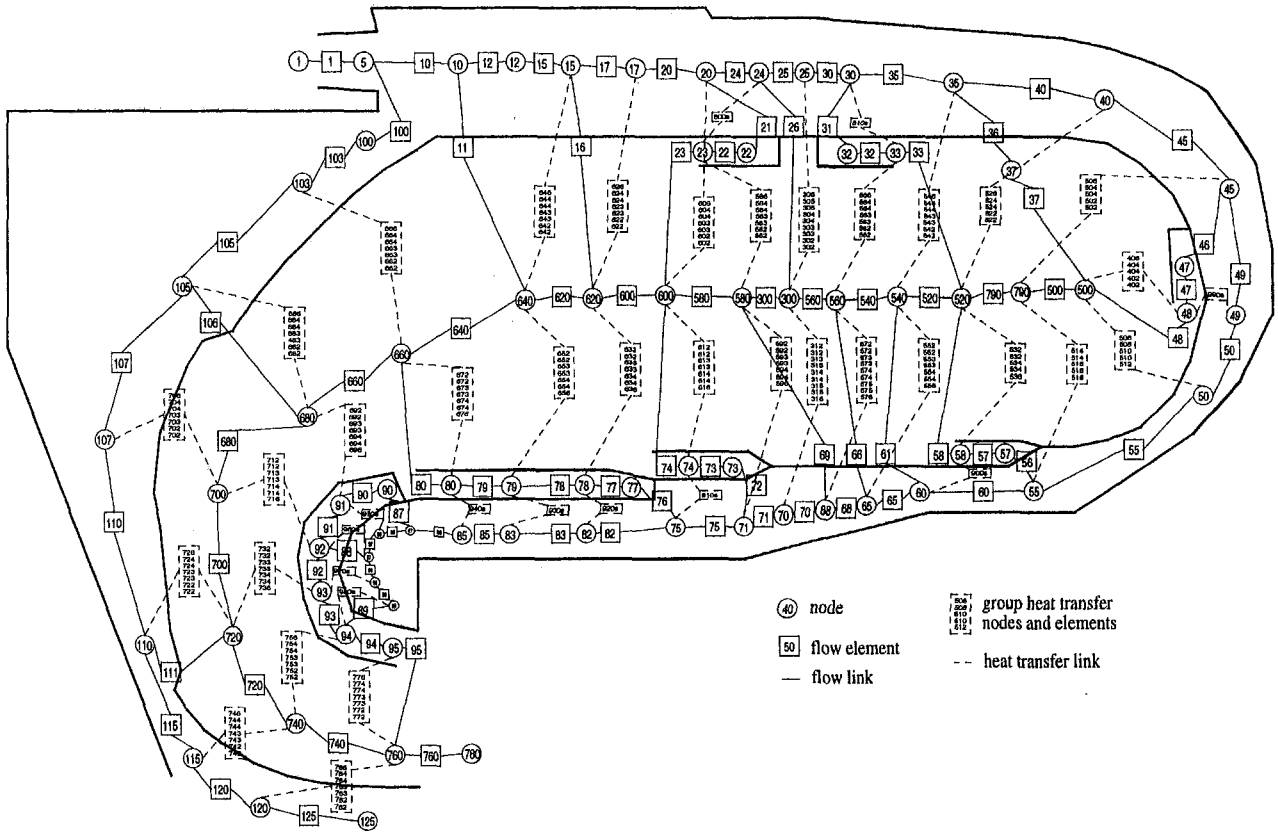

Fig. 2 Network diagram for reverse flow combustor

the fuel/air mixture reach a partial or constrained equilibrium state. This constrained equilibrium may be accounted for by specifying the final concentrations of certain species by setting it as an extra element b_i, thereby increasing the number of constraints that the calculation is subject to by one per constrained species.

Clearly the most important factor in obtaining a realistic flame temperature is the predicted local fuel/air ratio. A mixing/recirculation model was developed to distribute air from flametube ports and cooling features into the combusting flow, based on simple empirically derived rules.

The Combustor Network

A sample combustor network is shown in Fig. 2. The reverse flow combustor selected for discussion exhibits features that conventional one-dimensional models have difficulty simulating. This includes counterflowing air streams, and extensive double skin features on the liner wall. The dark outline is a not-to-scale representation of the combustor general features. The solid network of elements and nodes refers to the flow computational cells, in which the flow and energy equations are solved. The dashed network represents the heat transfer sequence of elements and nodes required to model the overall heat transfer from the flame tube through the liner to the annuli.

Mass flow splits and pressure drops were computed in the flow logic links, and included various correlations for diffuser, liner hole features, and duct flows. The mixing and recirculation models were used to compute local bulk fuel/air ratios, and this in combination with typical efficiency curves was used to compute local adiabatic flame temperatures from the constrained equilibrium model. The species constrained in this analysis were CO and CO_2. The heat transfer logic allows for the effects of film cooling, thermal barrier coating, and liner hole heat pick-up. Heat transfer through the double skin regions was also computed.

No restrictions are placed on the network setup. Networks for annular combustors, or combustors with multiple combustion zones, such as double annular combustors, require no additional effort from the user, and the basic methodology for generating the network is identical.

Results and Discussion

The initial validation of the network solver was undertaken with comparisons to mass flow splits, and pressure drops obtained from a proven industrial one-dimensional combustor code, CODAS (Lowe, 1995), for two annular combustor geometries. The CODAS results generated for these two production combustors have been well validated (Lowe, 1995). The combustors will be simply referred to as Annular Combustor .1 and Annular Combustor .2 for the purposes of this discussion.

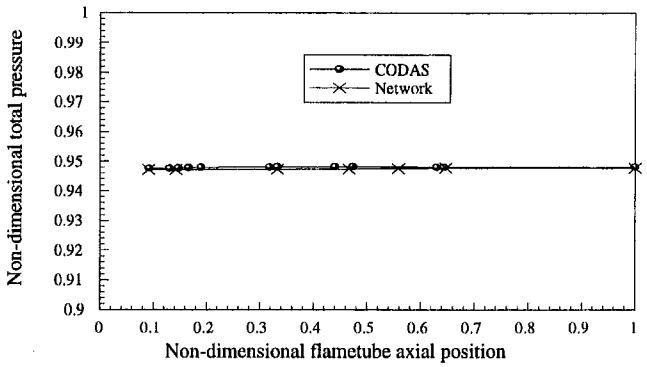

Fig. 4 Annular combustor .1 flame tube total pressure comparison

The mass flow split comparison of Fig. 3 shows the close agreement between CODAS and the network solver. The mass flows are nondimensionalized by the predicted annuli head flows. The liner features through which these flow splits were computed included ports, lipped cooling rings, and effusion patches. Similar methods for the diffuser pressure loss calculation resulted in the close agreement of the head flows. Good agreement was also achieved with the flame tube total pressure profiles shown in Fig. 4. The total pressures include the effects of momentum addition from the liner features. The pressures were nondimensionalized by the combustor total inlet pressure. The difference between the overall pressure loss predicted by the two solvers was within 0.05 percent.

The results for Annular Combustor .2 followed those of the first test case. The results were nondimensionalized as before. Figure 5 shows the close agreement in the annuli mass flow splits. The liner features in this case included ports, lipped rings, total-static-fed slots, static-fed slots, and effusion patches.

The total pressures (see Fig. 6) exhibited close agreement. The baseplate exit pressure differed slightly, resulting in the network solver results being uniformly lower than the CODAS results. The difference was small and resulted from slightly differing treatment of the snout and baseplate region. The pressure rise within the flame tube was in close agreement for the two results. The overall combustor pressure loss differed by 0.2 percent.

The final combustor modeled with the network solver was the reverse flow combustor shown in Fig. 2. The network accounted for momentum addition from the liner features as well as the effects of the radial pressure gradient within the flame tube. The complexity of the reverse flow geometry resulted in only slightly slower convergence than for the annular cases, on the order of a minute on a typical workstation. The airflow

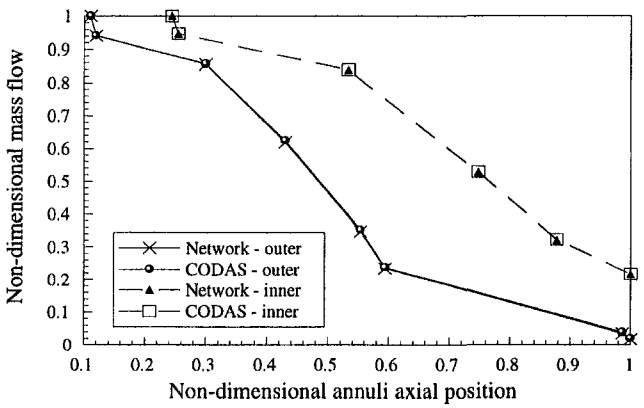

Fig. 3 Annular combustor .1 mass flow split comparison

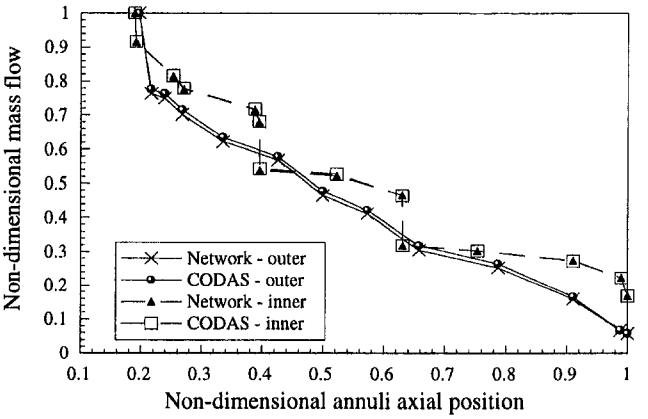

Fig. 5 Annular combustor .2 mass flow split comparison

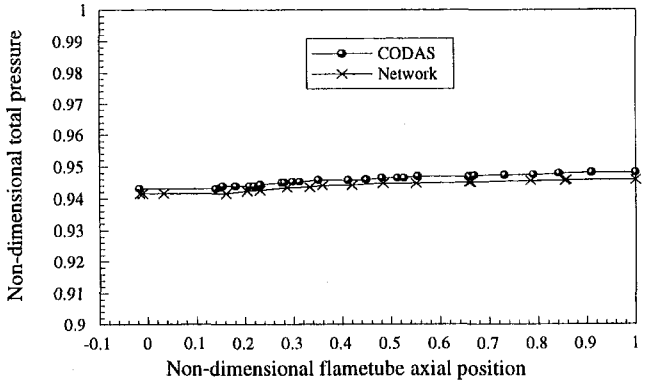

Fig. 6 Annular combustor .2 flame tube total pressure comparison

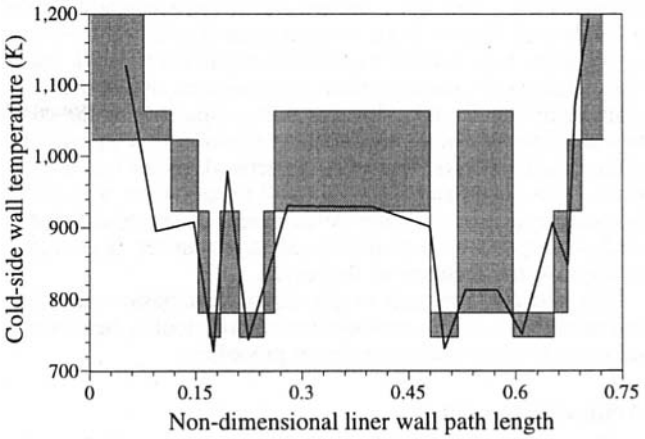

Fig. 8 Clockwise cold-side liner wall temperature comparison

results for this case could not be compared to CODAS values as in the previous two cases since the CODAS algorithm is unable to model the reverse flow geometry. However, some comparisons were made between the network results and a combination of pressure measurements and corresponding manual calculations (Gardiner, 1995). The overall computed and measured combustor pressure loss agreed within 0.1 percent. Typically, the mass flow splits through the various liner features agreed within approximately 5 percent.

A heat transfer analysis was coupled to the airflow analysis as described in the previous section. The results obtained from this computation were compared to thermal paint data obtained during rig tests (Gardiner, 1995). A sample section of the thermal paint data is presented in Fig. 7. The region below the areas marked "G" corresponds to the diffuser exit plane. The clockwise annulus is in the upward direction. The thermal paint photographs were used to generated the temperature band plots shown in Fig. 8. and Fig. 9.

External wall temperature results generated with the network solver were compared to these temperature bands. The solid line represents the computed values and the shaded region represents the temperature bands of the thermal paint data. Figure 8 shows reasonable agreement between the calculated and measured temperatures. Impingement of combustion gases on the upper liner wall from the primary ports (element "66" in Fig. 2) results in a relatively rapid degradation of the film cooling layer developed by the static ring (elements "22" and "23" in Fig. 2). The dilution ports (element "16" in Fig. 2) within the liner wall resulted in the destruction of any remaining film cooling downstream of the ports. These two effects increased the wall temperature in this region, and appear to be captured by the network solver. The effects of static fed slot film cooling, effusion cooling, and double skins were resolved by the network solver. The accuracy of the computation at the head of the flame tube was limited by the range of validity of the heat transfer correlations.

The thermal paint data extended only as far as element "71" in Fig. 2. The effects of the film cooling would become more pronounced as the heat transfer network "density" increases. The resolution could be easily manipulated should more detailed information be required. The predicted metal temperatures reached a peak in the final section of the double skinned annulus region, as might be expected since no film cooling is possible in this region. The anticlockwise annulus was cooled by three Z-rings and thermal barrier coated. Figure 9 shows a comparable trend between the computational and experimental results.

The broad bands of the thermal paint data limit the usefulness of the data in assessing the accuracy of the computed results. However, the effects of the various cooling features were captured by the network algorithm.

Predicted wall temperatures varied with flame tube gas temperature, and hence with the recirculation and mixing predicted within the network model. This proved significant in the treatment of the primary port recirculation. The amount of recirculation was simply estimated based on knowledge of the combustor or an understanding of the flowfield generated within the primary zone, from for example CFD predictions.

Conclusions

A new gas turbine combustor preliminary design methodology has been developed. The network method applied to combustors removes many of the limitations placed upon models by conventional semi-empirical analysis. The network analysis offers versatility as well as computational efficiency for a coupled solution strategy.

Comparisons to a proven airflow analysis code and experimental results have illustrated the ability of the network solver

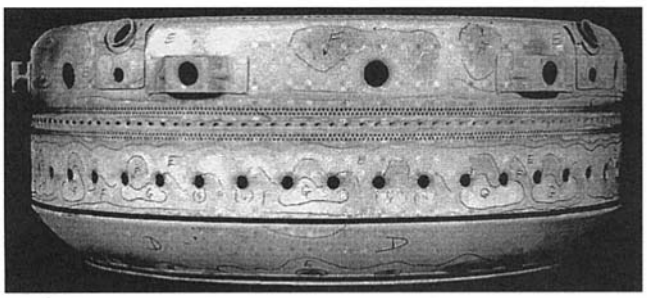

Fig. 7 Sample thermal paint results for reverse flow combustor

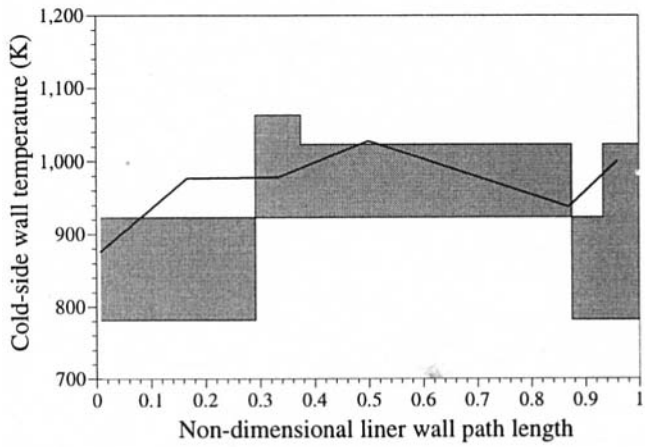

Fig. 9 Anticlockwise cold-side liner wall temperature comparison

to predict mass flow splits and pressure drops accurately within a combustor. Experimental thermal paint results were used to evaluate the heat transfer mechanism within the network code. The nature of the model limited the resolution to assumed circumferential uniformity. The predictive capability of the code was also limited in regions containing significantly varying multidimensional effects. However, the network model was able to predict the trends and ranges of wall temperatures with good qualitative accuracy. Future development of the heat transfer analysis, especially in modeling radiative transfer, is expected to improve the accuracy of the results.

The network approach to gas turbine combustor modeling has been shown to be a versatile and accurate tool in the preliminary gas turbine combustor design procedure.

Acknowledgments

This work was funded by Rolls-Royce plc and the Defence Research Agency, with technical input from both organizations.

References

Burrus, D. L., Shyy, W., and Braaten, M. E., 1987, "Numerical Model for Analytical Predictions of Combustor Aerothermal Performance Characteristics," APGARD CP 422.

Coupland, J., 1989, Rolls-Royce, U.K., Private Communication.

Gardiner, J., 1995, Rolls-Royce, U.K., Private Communication.

George, A., and Liu, J. W., 1981, *Computer Solution of Large Sparse Positive Definate Systems,* Prentice-Hall, Englewood Cliffs.

Gordon, S., and McBride, B. J., 1971, "Computer Program for Calculation of Complex Chemical Equilibrium Compositions, Rocket Performance, Incident and Reflected Shocks, and Chapman-Jouget Detonations," NASA SP-273, U.S.A.

Greyvenstein, G. P., and Laurie, D. P., 1994, "A Segregated CFD Approach to Pipe Network Analysis," *International Journal for Numerical Methods in Engineering,* Vol. 37, pp. 3685–3705.

Hammond, D. C., and Mellor, A. M., 1970, "A Preliminary Investigation of Gas Turbine Combustor Modelling," *Combustion Science and Technology,* Vol. 2, pp. 67–80.

Holdeman, J. D., Mongia, H. C., and Mularz, E. J., 1989, "Assessment, Development, and Application of Combustor Aerothermal Models," NASA TM-4087.

Jeppson, R. W., 1977, *Analysis of Flow in Pipe Networks,* Ann Arbor Science, MI.

Lefebvre, A. H., 1983, *Gas Turbine Combustion,* Hemisphere Publishing Corporation, New York.

Lockwood, F. C., and Shah, N. G., 1981, "A New Radiation Solution Method for Incorporation in General Combustion Prediction Procedures," *Eighteenth Symposium on Combustion,* The Combustion Institute, Pittsburgh, PA.

Lowe, D. R., 1995, Rolls-Royce, U.K., Private Communication.

Mado, R. J., and Roberts, R., 1974, "A Pollutant Emissions Prediction Model for Gas Turbine Combustors," AIAA Paper No. 74-1113.

Mellor, A. M., 1978, "Turbulent-Combustion Interaction Models for Practical High Intensity Combustors," *Seventeenth Symposium on Combustion,* The Combustion Institute, pp. 377–387.

Mellor, A. M., and Fritsky, K. J., 1990, "Turbine Combustor Preliminary Design Approach," *Journal of Propulsion and Power,* Vol. 6, No. 3, pp. 334–343.

Mellor, A. M., ed., 1990, *Design of Modern Turbine Combustors,* Academic Press, New York.

Mongia, H. C., Reynolds, R. S., and Srinivasan, R., 1986, "Multidimensional Gas Turbine Combustion Modelling: Applications and Limitations," *AIAA Journal,* Vol. 24, No. 6, pp. 890–904.

Mosier, S. A., Roberts, R., and Henderson, R. E., 1973, "Development and Verification of an Analytical Model for Predicting Emissions From Gas Turbine Combustors during Low-Power Operations," AGARD-CP-125, United Kingdom, pp. 25-1–25-12.

Patankar, S. V., 1980, *Numerical Heat Transfer and Fluid Flow,* Hemisphere Publishing Corporation, New York.

Rizk, N. K., and Mongia, H. C., 1991, "Three-Dimensional Analysis of Gas Turbine Combustors," *Journal of Propulsion and Power,* Vol. 7, No. 3, pp. 445–451.

Saad, M. A., 1985, *Compressible Fluid Flow,* Prentice-Hall, Englewood Cliffs, NJ.

Swithenbank, J., Poll, I., and Vincent, M. W., 1973, "Combustion Design Fundamentals," *Fourteenth Symposium (International) on Combustion,* The Combustion Institute, Pittsburgh, PA.

K. Döbbeling

A. Eroglu

D. Winkler

T. Sattelmayer

ABB Corporate Research,
Dättwil, Switzerland

W. Keppel

ABB Power Generation,
Mannheim, Federal Republic of Germany

Low NO_x Premixed Combustion of MBtu Fuels in a Research Burner

The paper reports on the development and testing of a premix research burner for MBtu fuels. The burner has a quartz glass annular mixing section and a quartz glass flame tube to allow visualization of the flame. A central lance is used to mount modules for fuel injection, swirl generation, and flame stabilization. This allows a large number of variants with different swirl strength, mixing section length, fuel injection geometry, and flameholder size and shape to be easily tested. Experiments have been performed at atmospheric pressure and under high-pressure conditions (14 bar pressure, 400°C air preheat temperature) for syngas with a H_2/CO ratio of up to 5. In a preliminary study, the mixing quality of the tested variants has been assessed with planar laser-induced fluorescence (LIF). High-pressure combustion tests show that low NO_x (<10 vppmd @ 15 percent O_2) premix combustion of MBtu fuels under industrial GT conditions without dilution is feasible.

Introduction

Low emissions, high efficiency, and reliability are the major requirements for the current power generation market. With the strong increase of natural gas consumption for power generation in combined-cycle gas turbine plants, the future availability and price of sufficient amounts of natural gas are major concerns of the power producers. In comparison to natural gas and oil, the known coal reserves will last about five times longer, based on current consumption rates. About 40 percent of the world-wide electricity production is based on coal. Two methods of utilizing coal in highly efficient, gas turbine combined-cycle plants have been matured to large-scale applications: pressurized fluidized bed coal combustion (PFBC) and integrated coal gasification combined cycle (IGCC). In the IGCC process, no major modifications have to be applied to the gas turbine and the combined-cycle process. However, one of the critical parts of the IGCC plant is the GT combustor, which must be able to burn syngas. For oxygen-blown coal gasifiers, which have already been tested at large scale, the syngas produced is a mixture of H_2 and CO and small amounts of N_2. The major requirements for the combustion technique are: (1) NO_x and CO emissions comparable to or lower than for natural gas, (2) a minimum of design changes for the conversion of a standard NG gas turbine to syngas combustion, (3) the possibility to switch from syngas to a backup fuel, which can be natural gas or oil No. 2. With a properly designed combustion chamber, CO emissions are generally very low, if the combustion temperature and residence time are kept sufficiently high; the larger problem is to achieve low NO_x combustion. NO_x is produced mainly in the flame zone, in regions of locally high temperature. A simple method to lower the NO_x emissions, which is successfully applied for natural gas and oil No. 2 combustion, is the injection of water or steam into the combustion zone to lower peak temperatures. This method can also be applied for syngas applications. The disadvantages of this method are that it uses large amounts of water (especially for syngas combustion) which results in a loss of cycle efficiency (Jury et al., 1992; Döbbeling et al., 1993). A method that avoids those disadvantages is the premix technique. With this technique peak temperatures in the flame zone are avoided by thoroughly mixing fuel and air at a fuel equivalence ratio of approximately 0.5, which restricts the maximum flame temperature to below 1800 K. The latter technique is now widely used for natural gas combustion but is still in the development phase for oil No. 2 combustion in modern high-temperature, high-pressure gas turbines.

The work presented in this paper is a fundamental study on premix combustion of undiluted syngas fuel. As shown in previous work (Döbbeling et al., 1996), a variant of the ABB double cone burner (EV burner) is capable of dry low NO_x combustion of syngas, which has to be diluted to approximately 7.5 MJ/kg for NO_x levels of less than 25 vppmd (@15 percent O_2). In this study generic burner concepts that allow low NO_x operation without any dilution are investigated.

MBtu Fuel Characteristics

The syngas considered in this study has a heating value about $\frac{1}{4}$ to $\frac{1}{3}$ of that of natural gas. For oxygen-blown coal gasification, it consists of about 30 percent H_2, 60 percent CO, and 10 percent N_2 by volume. The laminar flame velocities and adiabatic flame temperatures as a function of the fuel equivalence ratio at gas turbine conditions (compared to natural gas, NG) are plotted in Fig. 1.

The peak laminar flame speed of the syngas occurs at a fuel equivalence ratio of 2, i.e., at fuel-rich conditions. As a consequence, flame stabilization in a syngas air premix burner is most likely to appear in regions close to the fuel injection. The value of the maximum flame speed of syngas–air mixtures at GT conditions is about six times higher as compared to natural gas. To make things worse, the maximum flame temperature (close to stoichiometric conditions) is about 180 K higher than the value for natural gas. The consequences of these laminar fuel characteristics are: (1) Flame stabilization close to the fuel injection in a syngas–air premix burner is more likely to occur for syngas than for natural gas, and (2) if the flame stabilizes close to the fuel injection, the NO_x values produced by such flames are at least two times higher than those produced by a natural gas diffusion flame. However, for lean premixed flames, the laminar flame speed of syngas–air mixtures decreases rapidly with decreasing fuel equivalence ratio.

For perfectly premixed, laminar syngas–air flames, the NO_x production is almost identical to the very low values calculated for natural gas–air flames at equivalent adiabatic flame tempera-

Contributed by the International Gas Turbine Institute and presented at the 41st International Gas Turbine and Aeroengine Congress and Exhibition, Birmingham, United Kingdom, June 10–13, 1996. Manuscript received at ASME Headquarters February 1996. Paper No. 96-GT-126. Associate Technical Editor: J. N. Shinn.

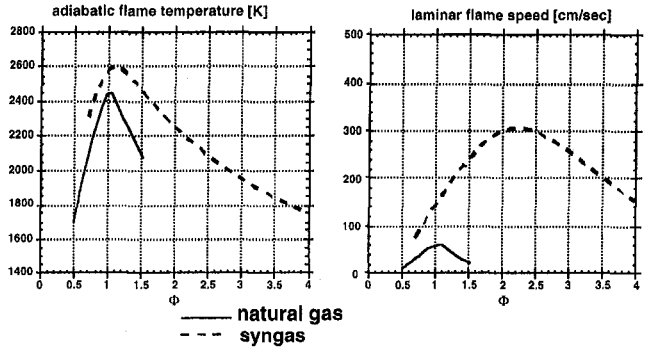

Fig. 1 Syngas flame properties at GT conditions (14.5 bar, 570 K preheat)

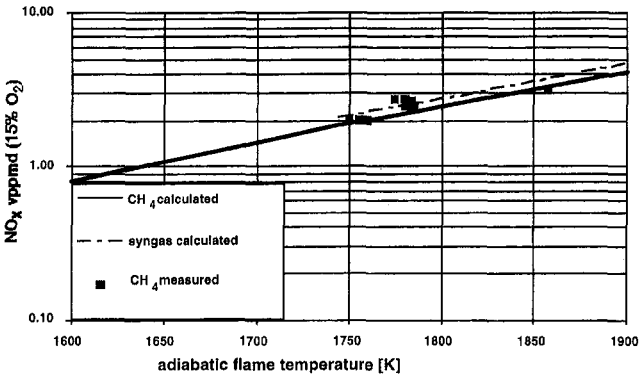

Fig. 2 NO_x emissions in perfectly premixed natural gas and syngas flames. Calculations are done with CHEMKIN (Kee et al., 1992) and the Miller–Bowmann (1989) reaction scheme.

tures (Fig. 2). As a result of these basic considerations, it can be concluded that the design of a reliable syngas air premixer that does not tend to flashback is the key development step of a burner development program for undiluted syngas. If full premixing can be achieved, a very low NO_x concentration will be found in the combustion products and the low lean blowout temperature of syngas flames will lead to a broad operation range of the combustor without staging.

Experimental Facility

To study different premixers and flameholders at realistic GT conditions, a modular burner has been built. It consists of a central lance, which can carry various arrangements of swirl generators, fuel injectors, and flame holders. Both the premixing

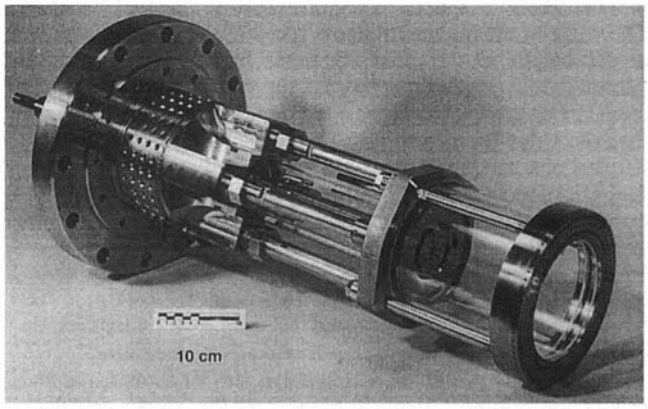

Fig. 3 Modular research burner for premix syngas combustion

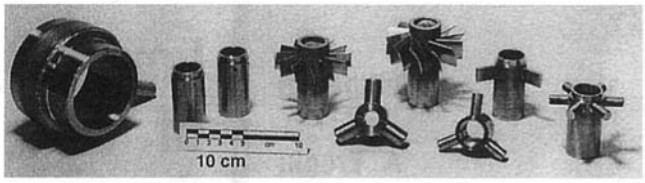

Fig. 4 Burner modules (from left to right): radial outer injection, two radial inner injection modules, 30 and 50 deg swirlers, radial spokes flameholders, and radial spokes injection module

section and the flame tube are assembled with quartz glass tubes in order to allow optical access. Figure 3 shows a photograph of the modular burner. Some of the modular elements that can be used to assemble burners with different premixers and flame stabilization devices are shown in Fig. 4.

The central lance has a diameter of 30 mm, the mixing tube diameter is 68.5 mm, its length is 300 mm, the flame tube inner diameter and length are 130 mm and 180 mm, respectively.

In Figs. 5 and 6 the two main variants selected for the high-pressure tests are shown. A typical configuration relevant to gas turbine applications is the case of fuel injected radially outward through discrete holes on a central fuel lance downstream of a swirl generator, as sketched in Fig. 5. The swirl is beneficial for flame stabilization in the flame tube and it promotes mixing along the mixing section. This specific geometry includes 12 vane-type swirl generators with 30 deg angle and 12 injection holes with 3.3 mm diameter located 25 mm downstream of the trailing edge of the vanes. In order to improve flame stabilization, a central blockage with 50 mm diameter is mounted at the downstream end of the mixing section (50 percent blockage). The ratio of the flame tube cross-sectional area to the mixture outlet cross section is 11.

The second main variant without swirl, which uses radial cylindrical spokes for fuel distribution, is sketched in Fig. 6. The six spokes have an outer diameter of 9 mm and six injection holes perpendicular to the air flow. The hole diameter increases radially outward in order to account for the increased area at larger radii. Again the central blockage is installed at the mixing tube end for better flame stability.

Three different test rigs are used to investigate the modular burner. In a first step, the flow field, pressure drop, and mixing quality are studied in a water channel to screen a number of variants. After a first selection, the flame stability, flash back limits, and the emissions are assessed with atmospheric combustion tests. Since laminar and turbulent flame speed as well as the ignition delay time at GT conditions cannot be simulated in an atmospheric test, full-scale high-pressure testing was carried out in ABB's single-burner high-pressure test rig (see Fig. 7). This rig allows an airflow of approximately 5 kg/s with a preheat temperature of 400°C. Video cameras are used to monitor the premixing section and to observe the flame shape inside the quartz glass flame tube. In addition to the area averaging emission probe at the end of the test rig, a traversable emission

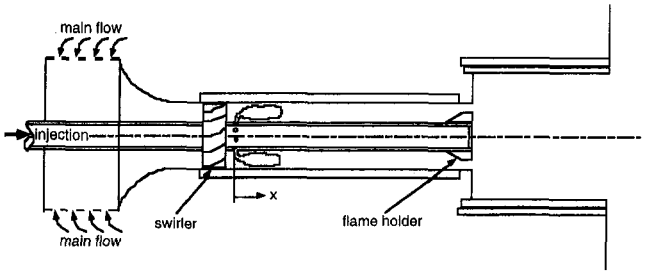

Fig. 5 Burner model with swirl generator, radial injection, and central flame holder

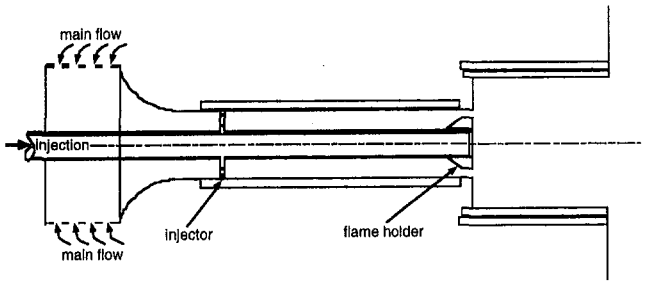

Fig. 6 Burner model with radial-spoke injector and central flame holder

probe immediately downstream of the quartz flame tube was used to determine the radial distribution of the combustion products.

Characterization of Mixing Quality

A Laser-Induced Fluorescence (LIF) technique has been used in water model experiments as the primary tool for assessment of mixing quality. A number of injector and mixer configurations have been tested with this technique in order to determine candidates with the best potential for the combustion tests. The water model facility is shown in Fig. 8. This facility has a vertical test section with a 380 mm by 410 mm cross section and 1400 mm streamwise length. The flow rate can be modulated by a variable frequency drive unit up to a maximum of 60 l/s. The burner model is installed vertically in the test section and the exit of the burner model is mounted on a horizontal plate with a circular hole.

In the LIF technique, the fuel is simulated by a solution of disodium fluorescein in water. This dye fluoresces strongly when illuminated with a wavelength of 488 nm. The light beam from the blue line of an argon-ion laser is transmitted into the test section of the water model through a fiber-optic cable. A cylindrical lens is mounted at the end of the fiber-optic cable to expand the beam into a light sheet of approximately 1 mm thickness and 20 deg spreading angle. This light sheet is traversed via a computer-driven stepping motor along the annular mixing section of the burner model to illuminate selected planes perpendicular to the burner axis.

A monochrome CCD camera (CS8310C from Tokyo Electronic Industry Co.), with 756 (H) × 581 (V) pixel resolution and 11 μm square pixels, is mounted above the water model to allow visualization of the planes illuminated by the light sheet from the downstream end of the burner via a window at the top of the water model. The camera was operated at shutter speeds of 1 and 20 ms. The video signal is processed by an 8 bit frame grabber board (DT 3852-4 from Data Translation) installed on a 100 MHz Pentium computer. Operation of this board is controlled by Global Lab Image software (Data Translation), which permits the selection of gain, offset, and reference settings during image acquisition. Normally, the gain setting of 1.0 is used in order to avoid additional noise associated with amplification. The offset and reference settings, which determine the light intensities assigned to black and white gray levels, are adjusted prior to each acquisition to make full use of the 8-bit (256 gray levels) scale for each picture.

A 90 deg annular segment in each frame is selected as the region of interest in order to keep nonuniformities due to light sheet intensity variation at a low level. The main parameters calculated for the intensity distribution of each picture are mean, standard deviation, minimum, maximum, and the area of the region of interest. In order to quantify the mixing quality, a variation coefficient is defined as the ratio of standard deviation to the mean gray value over the region of interest. This value should approach zero as the mixing progresses. Note that no effort was made to convert the gray scale values to absolute dye concentration with this method. Assigning zero (black) to the pixels where it is known that no dye exists and 255 (white) to the pixels with maximum dye concentration assures that for each plane a mean gray value can be calculated that corresponds to the mean dye concentration for this plane. The only prerequisite is that the dye concentration at each point be low enough so that a linear relationship between locally measured gray value and the actual dye concentration exists. Dye concentration of injected fluid was set to 0.001 g/L prior to each experiment, a low enough value to insure a linear relationship between the fluorescence signal and local dye concentration and yet high

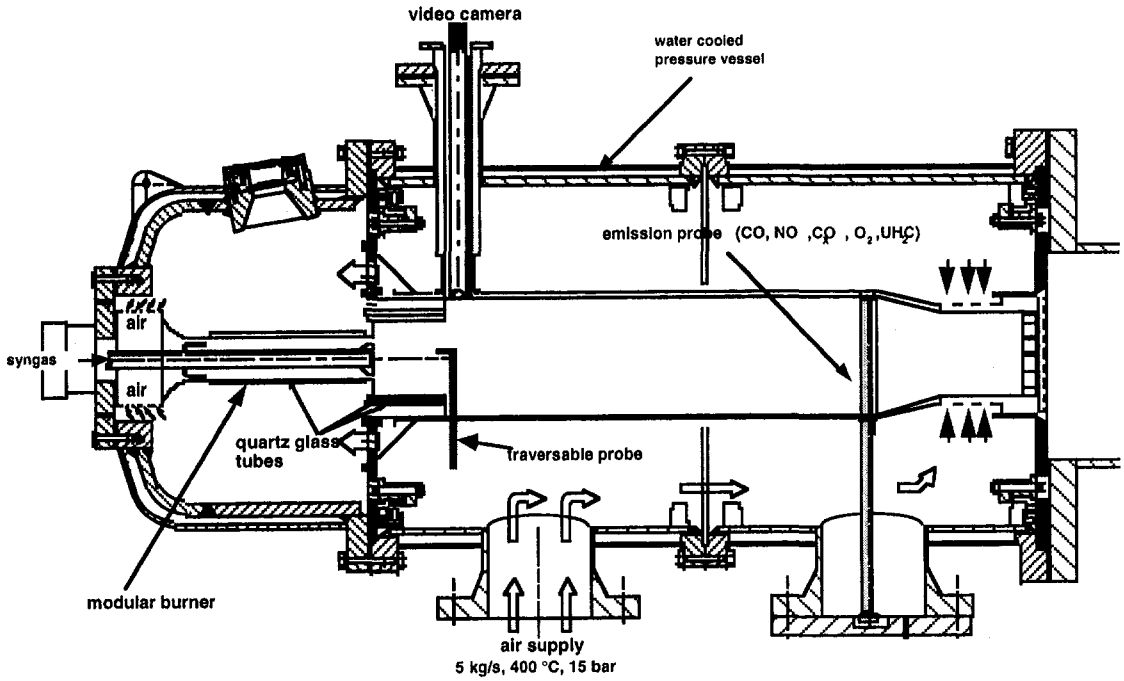

Fig. 7 High-pressure test rig

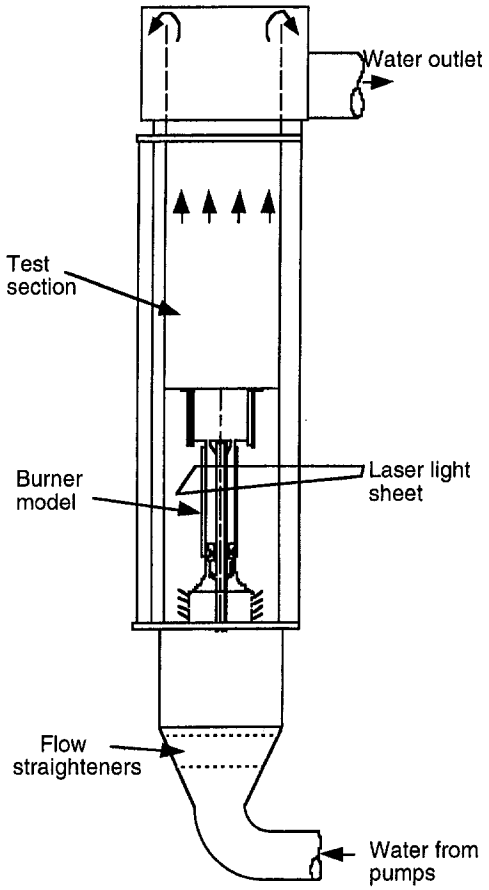

Fig. 8 Water model facility

enough for adequate signal-to-noise ratio even after the injected fluid is diluted more than 10 times upon full mixing. Owing to the small size of the region of interest, no correction is made for signal attenuation due to absorption.

For all tests, the flow speed in the annulus is 3.36 m/s, yielding a Reynolds number of 129,000. The injection mass flow rate is 7 percent of that of the main flow.

LIF mixing studies have been carried out for a number of variants, as an example, the swirl burner configuration of Fig. 5 is discussed here in detail. In this case the jet velocity of the radial outward injection was 6.82 m/s and the injection to mainstream momentum flux ratio 4.12.

A series of LIF pictures for consecutive planes downstream of the injection are presented in Figs. 9 and 10 for shutter speeds of 20 ms and 1 ms, respectively. The dominant features of the mixing behavior are seen clearly in the 20 ms pictures. The integration time of 20 ms is long enough to average over the large-scale structures in the turbulent flow. The initial penetration depth of the individual jets is relatively low, owing to the moderate momentum flux ratio of 4.12. Farther downstream, a shear layer type instability sets in, giving rise to large-scale vortices, which distribute the dye across the full annulus height. Despite this, a clear excess of dye is to be seen at the inner part of the annulus all along the mixing section. The 1 ms shutter time is short enough to resolve spatial structures with a size of 3 mm. The instantaneous mixing pattern can therefore be seen in these pictures. Considering the short reaction times under pressure, the fuel–air mixture fluctuations seen in these short-exposure pictures are more relevant for pollutant formation than the time-averaged pictures.

The calculated statistical values for these pictures are presented in Fig. 11 in terms of variation coefficient; i.e., the ratio of standard deviation to the mean gray value. Consecutive pictures with 20 ms shutter time taken at the same axial location are giving nearly the same variation coefficient, whereas for the 1 ms pictures the variation coefficient of consecutive pictures scatters about 10 percent. One can see a rapid drop in the variation coefficient along the first few annulus heights, indicating a fast mixing progress. After about five annulus heights, the curves level off to a range where the progress is very slow. The two curves for 1 ms and 20 ms exposure times run almost parallel to each other with a large difference in absolute values. This means that although the time-averaged spatial mixing progresses rapidly in the first 80 mm to a variation coefficient of less than 0.2, the instantaneous mixture fluctuations in the small scales still have a high variation coefficient of >0.3, and further fine-scale mixing would require considerable additional mixing length.

Atmospheric and High-Pressure Test Results

Atmospheric burner tests have been performed on natural gas and syngas. In all tests the bulk flow velocity in the mixing section was kept constant at 75 m/s. Without swirl and without flameholder at the end of the mixing section no stable flame could be produced using natural gas, for syngas flame stabilization could only be achieved for high adiabatic flame temperatures (>1800 K). Even at this high flame temperature, a lifted flame was observed (Fig. 12).

Using radial spokes for flame stabilization produces three individual flame brushes in the wakes of the spokes (Fig. 13(a)), whereas the central blockage produced an axisymmetric flame (Fig. 13(b)). Lean blowout on natural gas occurred at approximately 1600 K flame temperature using the central blockage.

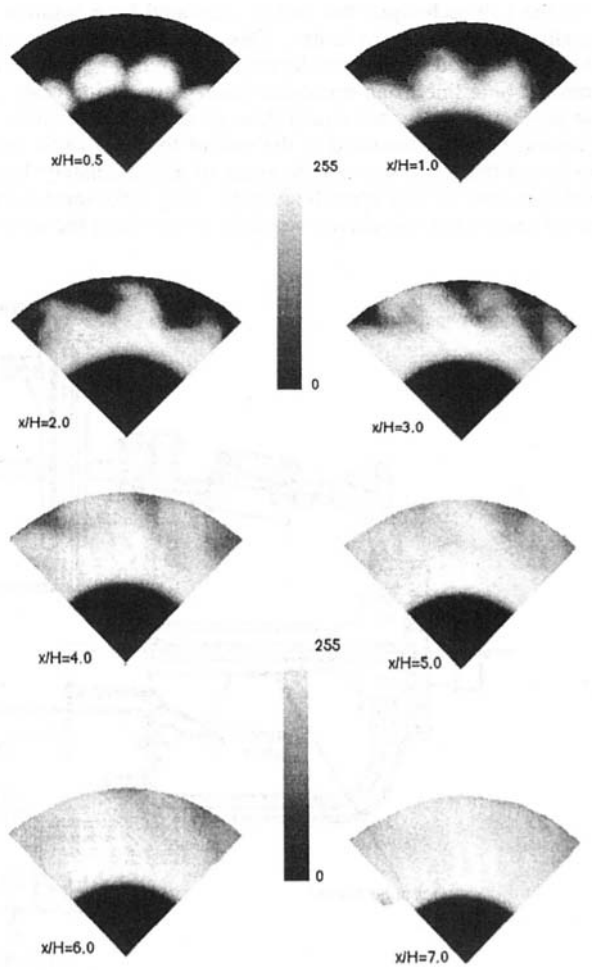

Fig. 9 LIF pictures with 20 ms exposure time

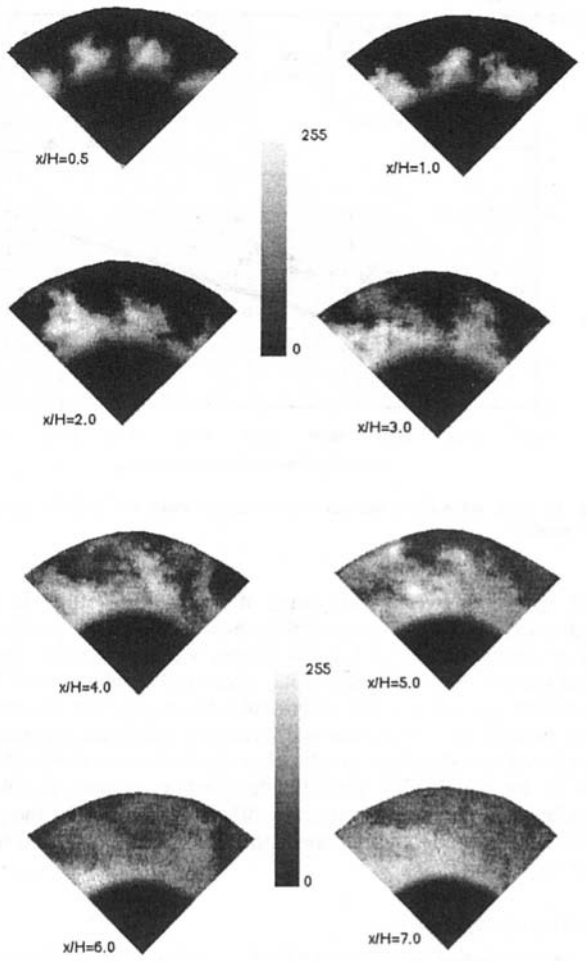

Fig. 10 LIF pictures with 1 ms exposure time

With the 30 deg swirler the flame was considerably shortened; the 50 deg swirler caused the flame to flash back into the mixing section along the boundary layer at the fuel lance.

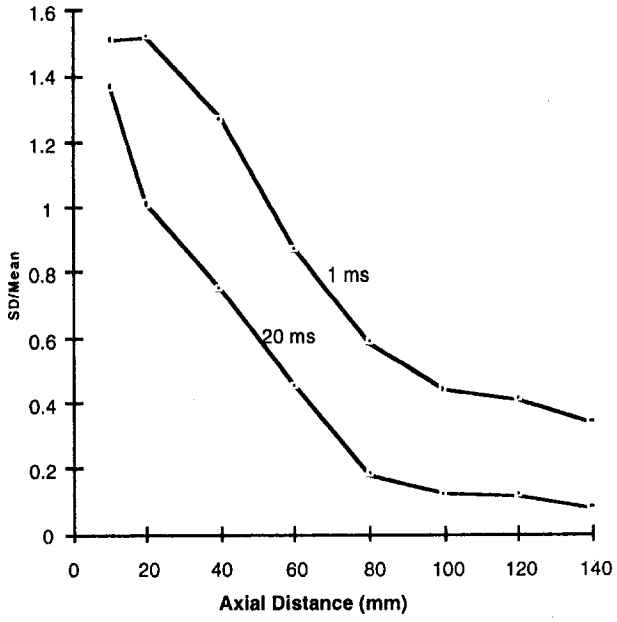

Fig. 11 Variation coefficient versus axial distance for 1 ms and 20 ms LIF pictures

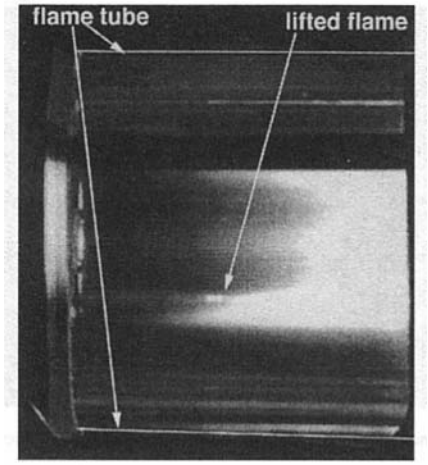

Fig. 12 Atmospheric syngas combustion tests: without stabilization

As a result of the atmospheric testing, a variant with moderate swirl (30 deg swirler) and radial fuel injection as shown in Fig. 5 and a variant without swirl and radial fuel distribution spokes (Fig. 6) were chosen for the high-pressure tests. Both variants used the central blockage as flameholder. The variant with the 30 deg swirler and the central blockage flameholder offered the best flame stability (Fig. 14) without flashback in the atmo-

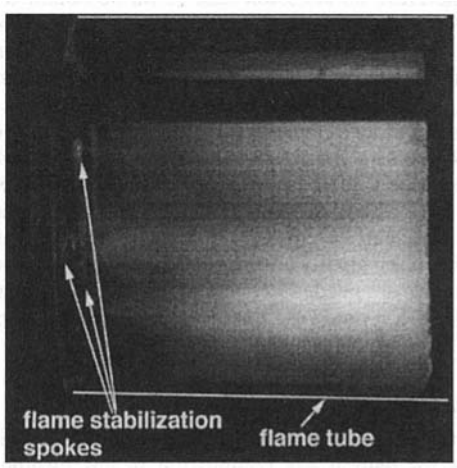

Fig. 13(*a*) Atmospheric syngas combustion tests: radial spokes flame stabilization, no swirl

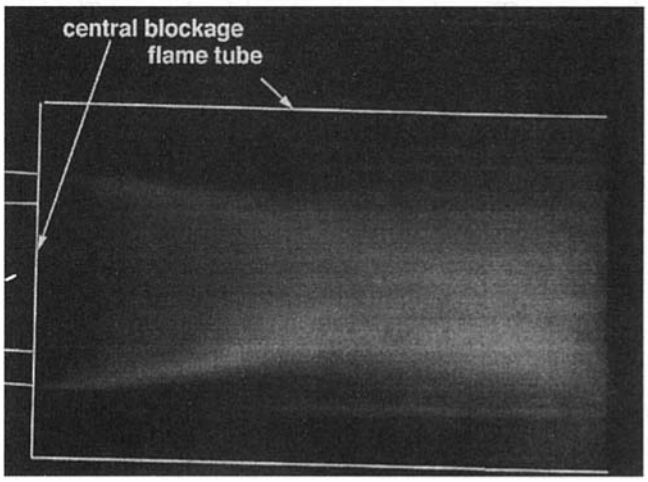

Fig. 13(*b*) Atmospheric syngas combustion tests: central blockage flame stabilization, no swirl

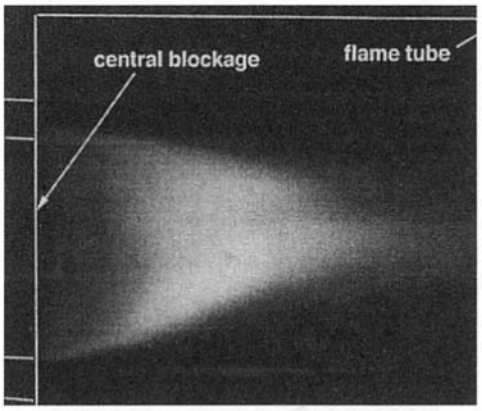

Fig. 14 Atmospheric syngas combustion tests: central blockage and 30 deg swirler

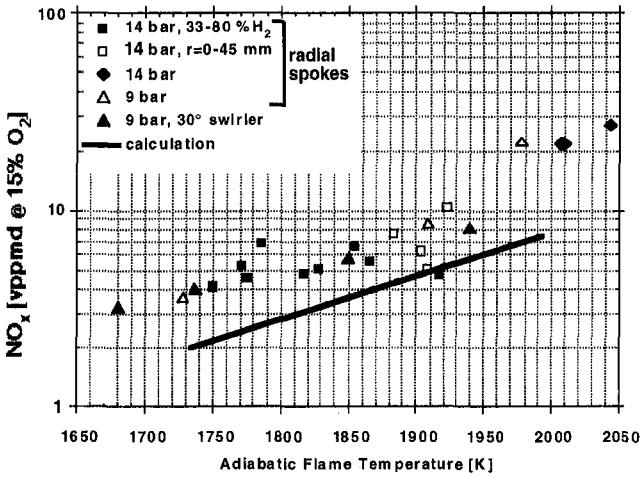

Fig. 15 NO_x emissions versus flame temperature for premix syngas combustion

spheric combustion tests. The radial fuel distribution spokes variant was found to give good mixing even without swirl. This turned out to be the best variant with respect to flashback.

Figure 15 shows the emissions measured in the high-pressure test rig with syngas (30 percent H_2, 60 percent CO, 10 percent N_2 by volume). The 30 deg swirler variant was tested at 9 bar pressure and produced NO_x emissions well below 10 vppmd (@ 15 percent O_2) for flame temperatures in the range of 1680 K to 1940 K. However, at higher pressures flashback was observed; therefore no emission data could be obtained for pressures >9 bar. The radial fuel distribution spokes variant showed similarly low NO_x emissions; even at flame temperatures above 2000 K no flashback occurred. For higher hydrogen content (up to $80\%_{vol.}$ H_2) low NO_x emissions were still measured. This can be interpreted as an indication for sufficient premixing of syngas and air. Traversing the emission probe from its centerline position to larger radii (Fig. 15, open squares) showed a 100 percent variation of NO_x emissions with only small flame temperature changes. This can be caused for instance by a change in the fine-scale mixing quality at different radial positions, but further measurements are needed to clarify this. CO levels were always lower than 100 vppmd (@15 percent O_2) for flame temperatures above 1700 K at 14 bar pressure.

Conclusions

After the successful implementation of the premix burner technique for natural gas combustion in gas turbine burners, extension of this technique to fuels (such as syngas) with high flame speeds and low ignition delay times is the next challenging goal for GT combustor research and development. The work done in this study shows that with the help of modern measurement techniques, burner principles can be identified that are suitable for the combustion of syngases with high amounts of H_2 in a premix flame. Burner configurations selected in water channel and atmospheric tests consistently showed very low NO_x emissions over a wide range of flame temperatures in the high-pressure tests. Values slightly higher than those predicted for perfectly premixed laminar flames were measured. Apart from the very low NO_x emissions, premixed combustion of the undiluted syngas has the additional advantages that the mass flow balance of compressor and turbine is nearly unchanged as compared to natural gas combustion, the fuel mass flow, which has to be handled by the fuel distribution system, is much smaller compared to steam or N_2 diluted systems, and the gas turbine can be operated independently of the air separation unit and the steam cycle.

Acknowledgments

The support of the German "Bundesministerium für Bildung, Wissenschaft, Forschung und Technologie (Förderkennzeichen 314-4003-0326782A)" for this work is gratefully acknowledged. The authors are responsible for the contents of this paper.

References

Döbbeling, K., Knöpfel, H. P., Sattelmayer, T., Müller, P., and Reyser, K., 1993, "ABB's Medium Btu EV Burner for Syngas Applications—Test Results and GCC Integration Concept," presented at the Twelfth EPRI Conference on Coal Gasification Power Plants, San Francisco, CA.

Döbbeling, K., Knöpfel, H. P., Polifke, W., Winkler, D., Steinbach, C., and Sattelmayer, T., 1996, "Low-NO_x Premixed Combustion of MBtu Fuels Using the ABB Double Cone Burner (EV Burner)," ASME JOURNAL OF ENGINEERING FOR GAS TURBINES AND POWER, Vol. 118, pp. 46–53.

Jury, W., Müller, P., and Reyser, K., 1992, "Gas Turbine (GT) Air Separation Unit (ASU) Integration for GCC: A Study Based on ABB EV Burner Technology for Gas Turbines," presented at the EPRI Conference on Clean Coal Combustion Technology, San Francisco, CA.

Kee, R. J., Grcar, J. F., Smooke, M. D., and Miller, J. A., 1992, "A Fortran Program for Modeling Steady Laminar One-Dimensional Premixed Flames," Sandia Report Sand85-8240. UC-401.

Miller, J. A., and Bowmann, C. T., 1989, *Prog. Energy Combustion Sci.*, Vol. 15, p. 287.

NO_x Measurements for Combustor With Acoustically Controlled Primary Zone

P. J. Vermeulen

V. Ramesh

The University of Calgary,
Department of Mechanical Engineering,
2500 University Drive N. W.,
Calgary, Alberta T2N 1N4 Canada

Successful NO_x measurements at the end of the primary zone of a small tubular combustor of conventional gas turbine design, employing acoustically controlled primary zone air-jet mixing processes, have been made at scaled $\frac{1}{4}$ and $\frac{1}{8}$ load operating conditions. Testing at $\frac{1}{8}$ load significantly increased the effective strength of the acoustic drive, which strongly improved the mixing by the acoustically driven primary zone air-jets. The acoustic drive caused partial blockage of the combustor primary zone air flow. This increased the equivalence ratio and the gas temperature, and made the gas temperature distribution more uniform, except for lean conditions at $\frac{1}{8}$ load, in the plane of the NO_x measurements. This explained the measured greater NO_x "with-drive," and the distinctly more uniform NO_x distribution, which confirmed that mixing was acoustically augmented. The acoustically produced changes were greater at $\frac{1}{8}$ load. The acoustic drive significantly changed the combustor operating characteristic so far as mean NO_x was concerned, and under lean conditions at $\frac{1}{8}$ load mean NO_x was reduced, indicating that a value of 10 ppm is possible (a 50 percent reduction).

Introduction

Acceptable gas turbine combustor performance depends critically on good air-jet mixing (Lefebvre, 1983a). In particular in the primary zone, high burning rates, efficient combustion, and minimum soot and nitric oxide formation are attained by good mixing. In the dilution zone the thorough mixing of dilution air and combustion products is necessary for a satisfactory temperature pattern quality at the combustor exit. Acoustically excited jets give enhanced mixing properties over steady jets; therefore, the technique has been applied to the air-jets of the primary zone of a small tubular combustor of conventional gas turbine design because of the potential for control and minimization of NO_x emissions. Furthermore, acoustically driving the primary zone air-jets, Fig. 1, may cause the primary zone to better approximate a well-stirred reactor by virtue of the increased momentum and entrainment of the excited jets. This is an intriguing possibility since Zelina and Ballal (1994a) showed that a WSR has the characteristics of an idealized high-efficiency, low-emissions combustor of the future.

The earliest known work on internally acoustically excited jets is that of Hahnemann and Ehret (1943) who modulated a propane–air mixture flowing to a nozzle burner and showed that the flame shape was strongly modified. The stability of acoustically excited jets was studied by Anderson (1955), Becker and Massaro (1968), Crow and Champagne (1971), and Kibens (1980) who showed there are two main instability modes. In the first mode, the initial thin laminar boundary layer develops waves before rolling up into traveling toroidal vortices on progression along the jet. A turbulent boundary layer cannot sustain oscillations, but the jet column can, and on excitation develops wave motion growing into a train of toroidal vortices as the second mode. At optimum or strong driving conditions the vortices are energetic enough to disintegrate the jet column. Air-jets have been sinusoidally excited up to 20 kHz, up to a Mach number of 0.6, for Reynolds numbers up to 10^6, to establish toroidal vortices, by Sarohia and Massier (1978) and Heavens (1980).

The majority of work on the excited jet has been concerned with jet noise and turbulence and little attention was given to jet mixing. However, from the indirect measurement of integrating velocity profiles Crow and Champagne (1971), Binder and Favre-Marinet (1973), Hill and Greene (1977), Bremhorst and Harch (1978), established that the entrainment rate could be increased by as much as 90 percent. Following on this, Vermeulen et al. (1982, 1987) established that the dilution air jet mixing processes of a small tubular combustor of conventional gas turbine design could be beneficially controlled by acoustic means. This work showed that acoustic excitation of the dilution air jet flows allowed selective and progressive control of the exit plane temperature distribution. In particular, for an already good temperature traverse quality, it was possible to trim the temperature profile. Thus, by these means a desired exit-plane temperature distribution may be achieved. From these results it was inferred that the entrainment rate and mixing of the dilution air jets was increased by the acoustic pulsations. These encouraging results promoted detailed investigations into acoustically pulsed free-jet mixing (Vermeulen and Yu, 1987; Vermeulen et al., 1986, 1992a), and showed that the entrainment and entrainment coefficient of the jet could be considerably increased, by up to six times. Therefore, jet mixing would be improved also, since jet entrainment is responsible for the mixing produced by a jet.

Gas turbine combustor performance depends in particular on the mixing of air-jets with a confined hot crossflow. Therefore, experimental studies were done on an acoustically pulsed air-jet mixing with a confined crossflow (Vermeulen et al., 1990, 1992b), and showed that mixing was significantly greater and penetration at least 100 percent increased. The entraining action of the traveling toroidal vortices is the primary mechanism of the acoustically augmented mixing and penetration processes. The response of the acoustically pulsed jet, as determined from penetration and mixing, was found to be optimum at a Strouhal number of about 0.27.

The novel NO_x measurements for a combustor with acoustically controlled primary zone to be reported were designed to

Contributed by the International Gas Turbine Institute and presented at the 41st International Gas Turbine and Aeroengine Congress and Exhibition, Birmingham, United Kingdom, June 10–13, 1996. Manuscript received at ASME Headquarters February 1996. Paper No. 96-GT-129. Associate Technical Editor: J. N. Shinn.

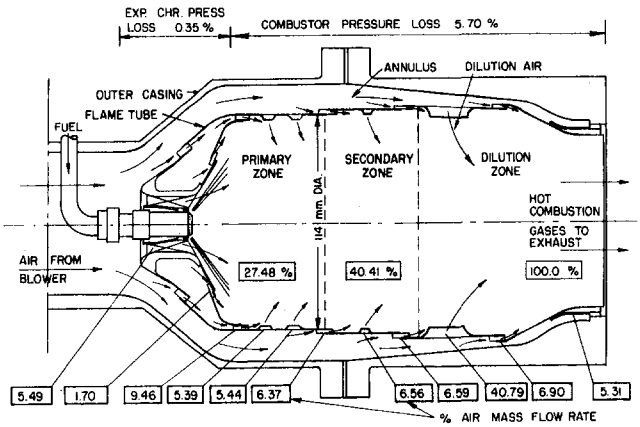

Fig. 1 Cross section through the combustor, unmodified for acoustic control, showing the air distribution

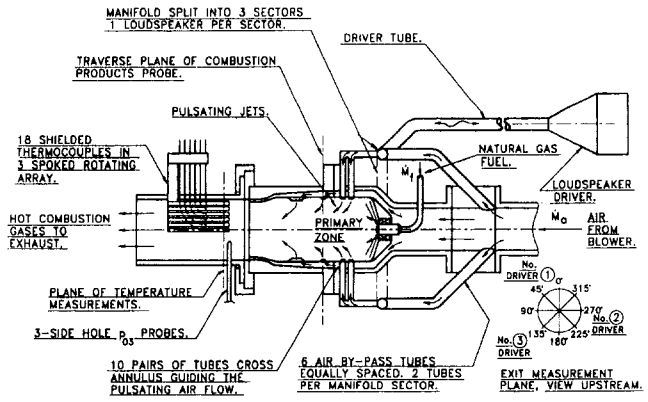

Fig. 2 Acoustic control of combustor primary zone

examine the effectiveness and control by the acoustic drive, by means of NO_x profile measurements at the downstream plane of the primary zone, at $\frac{1}{8}$ and $\frac{1}{4}$ loads for rich to lean conditions, and for the acoustic drivers at 150 W each in order to safeguard the drivers.

Experimental

Combustor With Acoustically Controlled Primary Zone. The apparatus is the same as that described in Vermeulen et al. (1982, 1985). Figure 1 (Vermeulen et al., 1982) shows a cross section of the combustor, unmodified for acoustic control, giving its air distribution and important features. Provision was made for the measurement of air and fuel and mass flow rates and the combustor inlet and exit conditions. Thermocouples measured the combustor exit plane temperature and outside wall temperatures of the flame tube in the primary and dilution zones. NO/NO_x distributions were measured by means of a hot water cooled probe traversed diametrally through a secondary zone air hole, at approximately the 3:30 position looking upstream. To avoid NO_2 loss by water condensing in the gas sample tube to the NO/NO_x analyzer the gas samples were dried by passage through an ice-water-cooled condenser immediately downstream of the probe. However, there was some inevitable loss of NO_2 by dissolving in the water condensate despite restricted contact in the condenser. Thus the measured NO_x magnitudes are deficient by an unknown amount; however, there is in general a large difference between measured NO and NO_x indicating that the lost NO_2 was not seriously large. In order to eliminate the effects of small changes in running condition, values for "no-drive" and "with-drive" conditions at a particular probe position were obtained in pairs. That is, after a no-drive measurement the acoustic drive was turned on, conditions allowed to stabilize and then the with-drive measurement made. The drive was then turned off and the probe moved to the next position followed by stabilization before the measurement procedure was repeated. The pressure and temperature data were processed by a personal computer controlled data logging system, but only sample exit plane temperatures were obtained, sufficient to establish normal operation of the combustor.

Figure 2 illustrates the method for acoustic control of the conventional gas turbine tubular combustor primary zone. The usual liquid fuel atomizer has been replaced by a conical gas injector for the burning of commercial natural gas. The method channels air from upstream of the combustor inlet via six bypass tubes connecting to a three-segment split manifold, which feeds the 20 primary zone air-jet holes in the flame tube. Ten pairs of radial tubes cross the combustor annulus to connect the air holes of the flame tube to the manifold segments surrounding the combustor casing. Each manifold segment is connected by a driver tube to a 300 W loudspeaker, which provides the acoustic driving and control. The strongest acoustic driving mode of the system was found to be at a frequency of 227 Hz by the investigation described in Vermeulen et al. (1995). Because of limited funding, a single two-channel amplifier powered the three loudspeakers, thereby necessitating a parallel connection for two speakers when all three speakers were being used simultaneously. Power at a loudspeaker driver was measured by an A-C voltmeter and ammeter, ignoring the power factor since previous work had shown it to be close to unity (Vermeulen et al., 1986).

Table 1 summarizes the range of test conditions used, where "load" was based upon the reference Mach number aerodynamic scaling factor. As is usual for this type of combustor, M_r

Nomenclature

A/F = overall air/fuel ratio (by mass flow rate)
EI_{NO_x} = emission index, g/kg_f, as NO_2
f = driving frequency
$\dot{M}$ = total mass flow rate
M_r = reference Mach number based on maximum I.D. (inside diameter) of casing
n = number of data points
N = local NO_x concentration in the measurement plane
ND = "no-drive"
NO_x = mixture of NO and NO_2
p = static pressure
p_0 = stagnation pressure
ppm = parts per million by volume
S_N = sample standard deviation, points 1, 14, and 15, neglected because of air dilution error
T = local temperature in the measurement plane
U_j = steady mean jet velocity at the orifice exit plane
W = power at acoustic driver
$\dot{W}_a$ = acoustic power at jet orifice exit plane
WD = "with-drive"
WSR = well-stirred reactor
Δ = change in value = $WD - ND$
ϕ = local equivalence ratio in the measurement plane
ϕ_0 = overall equivalence ratio

Subscripts

a = air
f = fuel
m = mean value
2 = combustor inlet plane (T_2 at centerline)
3 = combustor exit plane

Table 1 NO_x measurements—test conditions

TEST NO.	L_O/A_D	* $\dot{M}_a$ kg/s	A/F	M_r	P_2 kPa	T °C	$P_{02}-P_{03}$ / P_{02} %	f=227 Hz Driver No. & W ① W	② W	③ W
4 ND	1/4	0.0796	57.2	0.0145	89.2	57.1	** 0.69	--	--	--
4 WD		0.0792	57.1	0.0145	89.1	57.7	0.68	142	142	151
5 ND	1/4	0.0798	72.8	0.0146	88.8	56.3	** 0.63	--	--	--
5 WD		0.0774	70.6	0.0141	88.8	56.3	0.66	145	145	154
6 ND	1/4	0.0788	86.4	0.0147	87.0	57.0	0.66	--	--	--
6 WD		0.0782	85.8	0.0146	86.9	57.1	0.68	149	149	157
7 ND	1/4	0.0796	103.3	0.0146	88.3	56.8	0.62	--	--	--
7 WD		0.0781	101.5	0.0144	88.3	56.8	0.67	147	147	157
8 ND	1/8	0.0396	56.6	0.0074	87.6	56.3	0.28	--	--	--
8 WD		0.0370	52.8	0.0069	87.6	56.5	0.30	146	146	157
9 ND	1/8	0.0383	70.0	0.0072	86.9	56.7	0.27	--	--	--
9 WD		0.0399	72.9	0.0075	86.9	56.7	0.30	148	148	156
10 ND	1/8	0.0391	84.8	0.0071	88.8	55.4	0.24	--	--	--
10 WD		0.0384	83.2	0.0070	88.8	55.4	0.28	148	148	157
11 ND	1/8	0.0390	101.5	0.0072	88.0	55.6	0.25	--	--	--
11 WD		0.0402	104.6	0.0074	88.0	55.6	0.28	148	148	158
12 ND	1/8	0.0385	109.0	0.0071	87.6	56.0	0.25	--	--	--
12 WD		0.0380	107.4	0.0070	87.7	56.4	0.27	148	148	158
13 ND	1/8	0.0385	119.2	0.0072	87.5	56.9	0.24	--	--	--
13 WD		0.0380	117.4	0.0071	87.6	56.9	0.27	147	147	157
14 ND	1/8	0.0389	139.8	0.0072	87.5	56.8	0.24	--	--	--
14 WD		0.0382	137.2	0.0071	87.5	56.8	0.25	147	147	158
Theoretical Full-Load Nominal		1.1657	60.4	0.0570	395.4	203	6.05	Standard Combustor		
Stoichiometric			17.16							

* For 1/8 Load Precision Of $\dot{M}_a$ Is Lower Because Of Reduced Magnetude, Thus Some $\dot{M}_a$'s Have Increased "With-Drive" Due To Measurement Inaccuracy. Thus % Pressure Loss Increase Is A Better Indicator Of Blockage Effect.

** For Tests 4 And 5 The Number Of Data Samples For Good Averages Was Low Resulting In Inaccurate % Pressure Loss Values For Test 4.

was calculated at the maximum inside diameter of the casing (142.9 mm).

Combustor Measurements and Accuracy. Oxides of nitrogen samples were measured to within ±1 ppm. All temperatures were measured by chromel-alumel thermocouples accurate to ±2 percent, including random uncertainty, over the experimental range. The fuel mass flow rates were accurate to ±2 percent for both loads. The air mass flow rates were accurate to ±2½ percent and ±4½ percent at ¼ load and ⅛ load, respectively. Individual static and stagnation pressure measurements were accurate to ±0.2 percent, while the hot pressure loss $p_{02} - p_{03}$ was measured to within ±3 percent.

NO_x Measurements and Results. These measurements were made in order to determine for the measurement plane diametral distributions of NO and NO_x and the magnitude of changes caused by acoustic drive. Since the maximum power per acoustic driver was limited to 150 W, and a preliminary test at ¼ load had shown only modest changes in NO_x concentration caused by the acoustic drive, it was decided to also test at ⅛ load in order to make the drive effectively stronger. Thus since Vermeulen et al. (1992a) and Ramesh et al. (1993) had shown that the jet entrainment coefficient was proportional to $(\dot{W}_a/U_j^3)^{1/2}$, for constant jet diameter and density, then for constant acoustic power, testing at ⅛ load halves the jet velocity and should enhance entrainment (also mixing) by a significant factor of 2.8. Furthermore, NO_x concentrations are usually of most interest; therefore the NO data will not be presented.

Figure 3 shows typical NO_x traverses at the end of the combustor primary zone (at the secondary zone air hole) and clearly shows significantly greater NO_x with-drive at ¼ load, and a substantial increase at ⅛ load reflecting the stronger driving at reduced load. The no-drive profiles exhibit a strong bimodal distribution, which for ⅛ load weakens with leaning of the fuel/air ratio. This distribution is no doubt brought about by the core axial recirculatory flow of the bound toroidal vortex of the primary zone (Clarke et al., 1963). The acoustic drive tends to produce a profile of larger mean and somewhat flatter distribution. There is a significant difference between the no-drive profiles for the two loads. These and other features will become more apparent when the data is presented in terms of the NO_x profile's mean N_m and sample standard deviation S_N, where:

$$N_m = \frac{\sum^{n} N}{n} \quad \text{and} \quad S_N = \left[\frac{\sum^{n} (N - N_m)^2}{n-1}\right]^{1/2}$$

Because of dilution by the secondary air jet, data at sample points 1, 14, and 15 have been omitted from the calculation of N_m and S_N, but all data have been included in the calculation of emission index.

Figure 4 presents S_N versus N_m for no-drive at ¼ and ⅛ loads with the overall equivalence ratio indicated for each test point. There was a definite increase in mean NO_x at ⅛ load due to the doubling of residence time, and the range of S_N values was markedly greater. For both loadings N_m was greater, as expected, with richening. The extra test points at leaner values for ⅛ load show a marked reduction in mean NO_x, no doubt due to lower temperatures.

Figures 5 and 6 show the effects of acoustic drive on the S_N versus N_m characteristic for the two loads. At ¼ load all tests show a reduction in S_N with-drive and little or modest increase in N_m. The decrease in S_N was perhaps due to acoustically enhanced mixing. However, at ⅛ load S_N with-drive was larger, except for test 8, which was smaller; the slope of the characteristic was generally less steep than for no-drive. The increase in N_m was greater than at ¼ load, for similar A/F values, due to

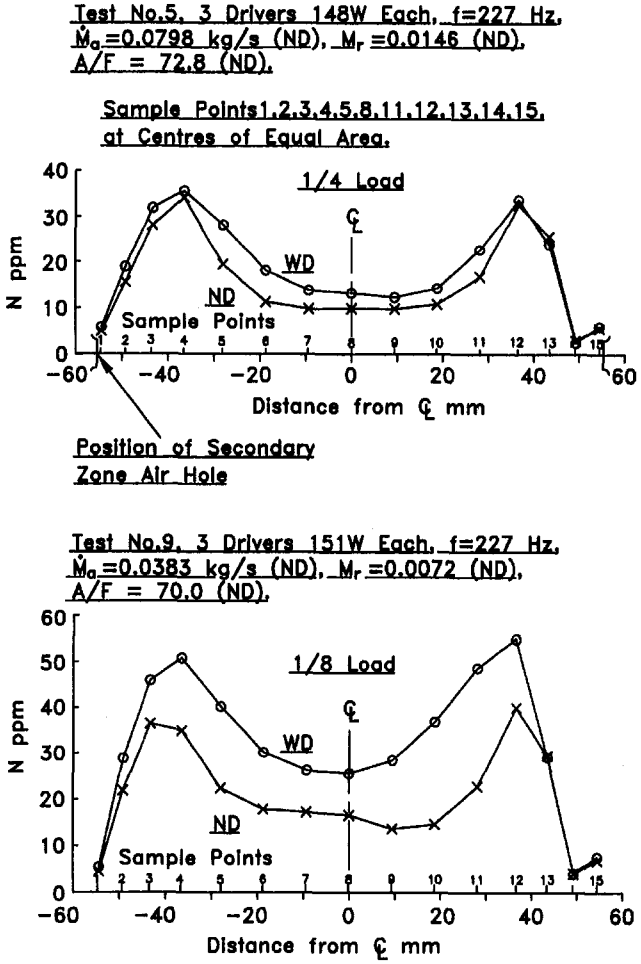

Fig. 3 NO_x traverses at end of combustor primary zone, upper ¼ load, lower ⅛ load

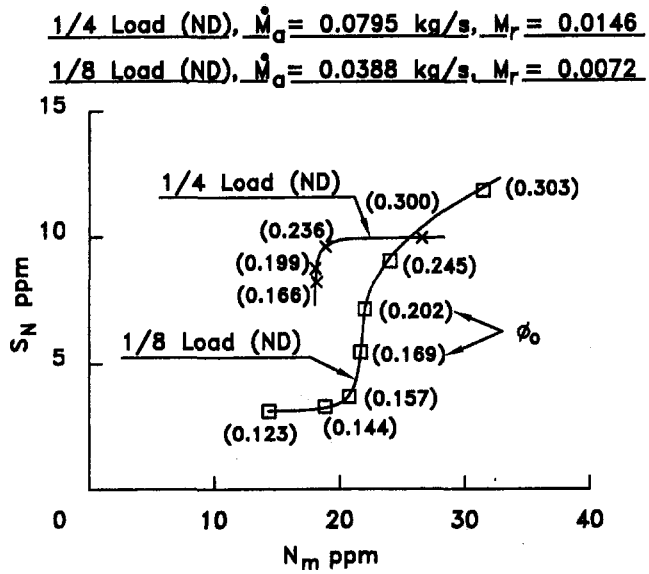

Fig. 4 NO_x standard deviation versus mean for "no-drive"

the stronger acoustic drive, but for the extra tests the increase in N_m became smaller changing to a definite decrease as leaning progressed. This suggests that acoustically increased mixing reduced NO_x and offsets the factors causing an increase.

Discussion

The emission index for NO_x at the combustor exhaust was estimated from the measurement plane data and found to lie between 2.5 to 2.0 g/kg$_f$ (lean to rich) no-drive for $\frac{1}{4}$ load, and from 2.8 to 3.2 to 2.4 g/kg$_f$ no-drive at $\frac{1}{8}$ load. A prediction for thermal NO_x may be made from the equation developed by Pearce et al. (1993), which predicts EI_{NO_x} to lie between 0.9 to 1.1 g/kg$_f$ no-drive for $\frac{1}{4}$ load, and from 1.0 to 1.3 g/kg$_f$ no-drive at $\frac{1}{8}$ load. The agreement is considered to be satisfactory since the experimental scatter about the prediction value is about $+2/-1$ g/kg$_f$ and the data being compared are for a signal diametral traverse at the end of the primary zone. The trend for these estimates of exhaust EI_{NO_x} largely decreasing from lean to rich mixtures instead of the predicted increase is probably due to incomplete chemical reactions for the richer mixtures up

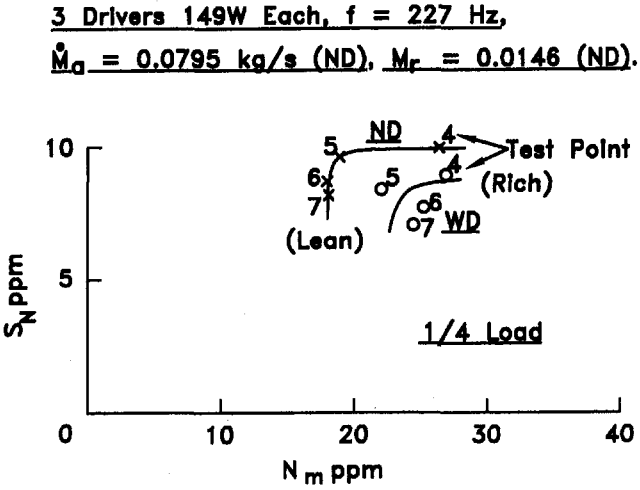

Fig. 5 NO_x standard deviation versus mean, $\frac{1}{4}$ load

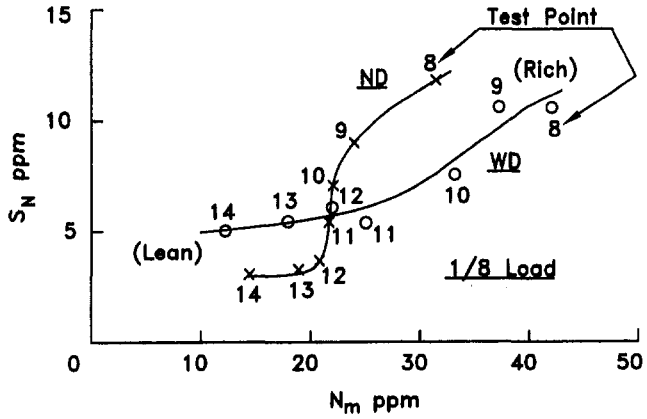

Fig. 6 NO_x standard deviation versus mean, $\frac{1}{8}$ load

to the measurement plane. Overall this indicates that the "no-drive" combustor tested was a normal unit of its type.

Roffe and Venkataramani (1978) show that NO_x is greater for longer residence time and increases exponentially with temperature, peaking on the fuel-lean-side of stoichiometric (Lefebvre, 1983b). Pressure plays a minor role according to the correlation of Pearce et al. (1993), and for these experiments it was not a significant parameter being constant at slightly above ambient pressure, Table 1. Thus the main variables affecting NO_x levels are temperature and residence time, and must be considered when trying to explain the increase with-drive (except for two tests) of these experiments, bearing in mind that improved mixing should reduce NO_x.

The prior work described in Vermeulen et al. (1993, 1995) for this combustor showed that acoustic drive caused partial blockage of the combustor primary zone air flow. This caused average reductions of about 2 and 3 percent in the total air mass flow rate at $\frac{1}{4}$ and $\frac{1}{8}$ loads, respectively. The fuel mass flow rates were unaffected by the acoustic drive since the fuel flow was metered by a choked nozzle. Because of reduced precision of $\dot{M}_a$ measurement at $\frac{1}{8}$ load some tests showed an increase in $\dot{M}_a$ with-drive. However, the percent hot pressure loss showed the expected increase (Table 1) and therefore the inaccurate with-drive $\dot{M}_a$ have been ignored. The partial flow blockage with-drive is due to greater air-jet penetration with enhanced entrainment carrying more material into the combustor core, and also due to the shedding toroidal vortices doubling the diameter of the air-jets (Vermeulen and Yu, 1987). Vermeulen et al. (1993) established data showing that the acoustic drive partial blockage caused a general richening in the equivalence ratio measurements, for the same combustion gas analysis probe traverse diameter as for the NO_x measurements, and also showed that the mean temperature increased (Table 2) and the temperature distribution became more uniform. A new flame tube (our best

Table 2 Combustion analysis data, 0.21 load (Vermeulen et al., 1993)

TEST No.		A/F	ϕ_m	$\Delta\phi_m$%	T_mK
V	ND	55.8	0.617	+9.6	1549
	WD	55.8	0.676		1628
VII	ND	67.5	0.475	+18.7	1357
	WD	67.5	0.564		1477
VI	ND	117.4	0.272	+33.1	1003
	WD	117.4	0.362		1196
Fig.7 was Constructed from the Data of Test VII					

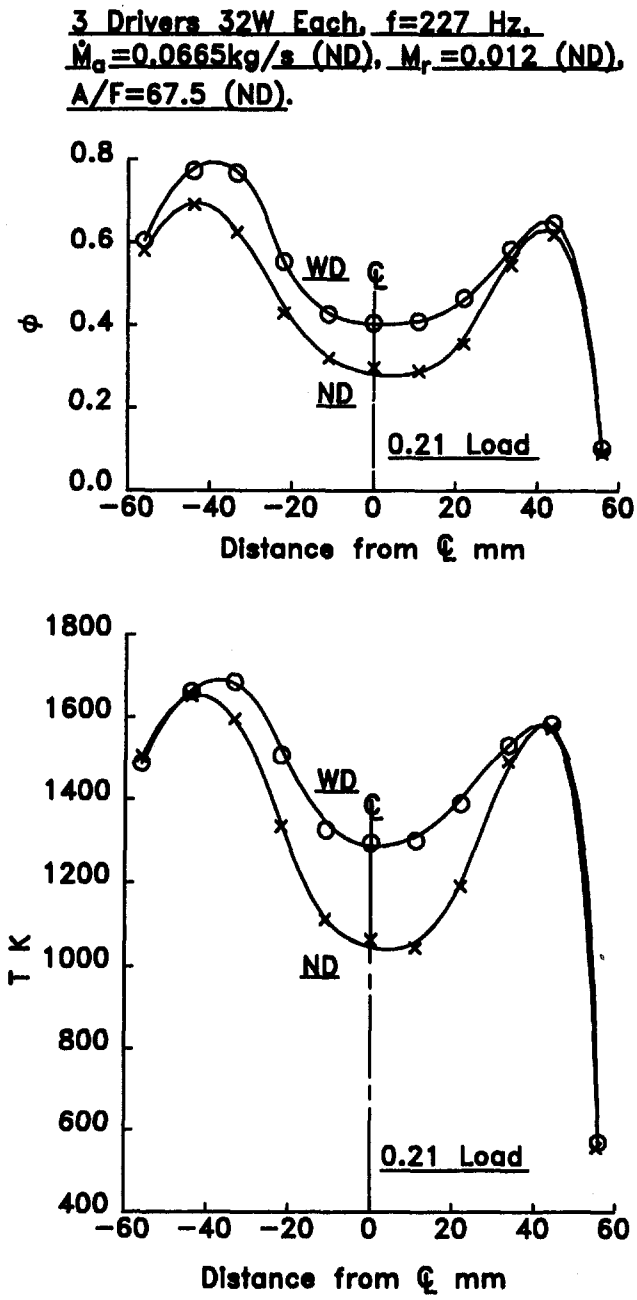

Fig. 7 Representative ϕ, T data, at end of combustor primary zone, 0.21 load, (Vermeulen et al., 1993)

copy) was used for the NO_x measurements, but otherwise the combustor was identical for the two sets of tests. Thus Fig. 7 using the Vermeulen et al. (1993) old data has been selected as representative for these new tests. The loading was 0.21 and acoustic driver power 32 W per driver. Despite the reduced acoustic power, Fig. 7 shows distinct changes with-drive, but, unfortunately, extrapolation to 150 W per driver is not possible because data at other powers were not obtained. The ϕ and T no-drive distributions exhibited a strong core minimum with the leanest condition being not so strongly cored. The temperature distribution obviously governs the no-drive NO_x profile. The ϕ and T profiles were flatter with-drive mainly because of an increase in the core, but at the leanest condition some general increase was present as well. The greater with-drive temperature explains the larger NO_x, keeping in mind the temperatures of Fig. 7 are for the end of the primary zone and will be hotter at the position where the NO_x is initially formed. For these old tests, Fig. 7, the with-drive mean temperature at the measurement plane was increased, and for a flatter distribution which would give a flatter NO_x profile. The with-drive partial blockage lengthens the residence time by up to 29 percent at $\frac{1}{8}$ load, and may be accompanied by a significant change in the primary zone aerodynamics with locally longer residence time effects, thereby increasing NO_x. Zelina and Ballal (1994b) concluded that greater residence time could dramatically increase NO_x production.

The effect of richening (greater temperature) "with-drive" on the measured mean NO_x can be better appreciated by estimating the mean equivalence ratio in the measurement plane. This has been done by assuming that the acoustic drive only reduces the combustor no-drive primary zone airflow of 27.48 percent shown in Fig. 1 by the percent reduction in the total air mass flow rate, i.e., 3 percent at $\frac{1}{8}$ load giving 24.48 percent with-drive for example. The results are presented in Fig. 8, for $\frac{1}{8}$ load, where it will be observed that acoustic drive has markedly changed the relationship between N_m and ϕ_m. Two with-drive characteristics are shown, one for the average blockage increase (3 percent air mass flow reduction) in ϕ_m of 12.3 percent, and the other for the maximum measured blockage change (6.6 percent air mass flow reduction) in ϕ_m of 31.4 percent. A third possibility is according to the variation in ϕ_m from the Vermeulen et al. (1993) old data, shown in Table 2, although these data are for 0.21 load. This gives a steeper characteristic than those shown, but has been omitted for clarity. The change brought about with-drive is most interesting for the leaner ϕ_m values, where the characteristic's slope with-drive is much steeper than for no-drive. Thus operating the combustor leaner with-drive causes the combustor characteristic to cross the no-drive characteristic and produce less NO_x in agreement with Lefebvre (1983c). The variable $\Delta\phi_m$ case implies even less NO_x. Thus an N_m of 10 ppm at $\frac{1}{8}$ load is possible, i.e., approaching that of the WSR of Zelina and Ballal (1994b). Hence it may be concluded that acoustically augmented mixing has improved the combustor operating characteristic so far as mean NO_x is concerned. Also if increased residence time is significant, then eliminating that effect should lower the with-drive characteristic with further improvement in the combustor NO_x performance. For $\frac{1}{4}$ load, the effectively weaker acoustic drive, greater experimental uncertainty and smaller number of test points,

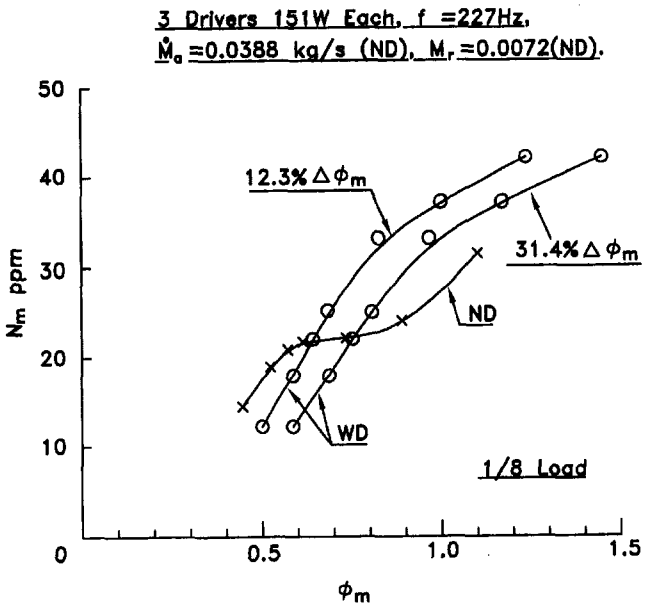

Fig. 8 Mean NO_x versus estimated measurement plane mean equivalence ratio, $\frac{1}{8}$ load

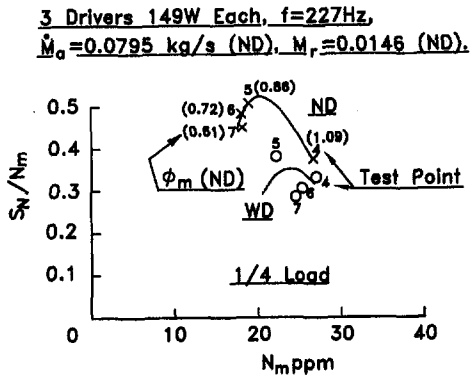

Fig. 9 NO_x profile shape parameter versus mean, $\frac{1}{4}$ load

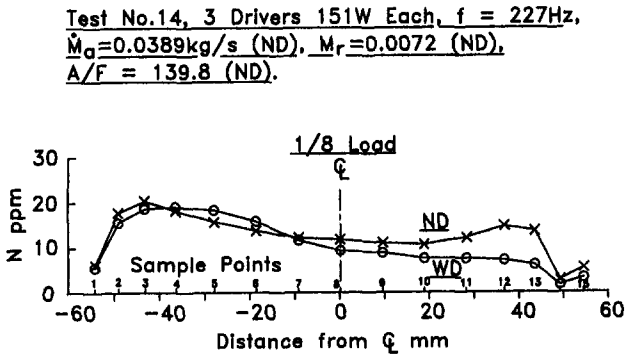

Fig. 11 NO_x traverse at end of combustor primary zone showing asymmetry under lean conditions, $\frac{1}{8}$ load

obscures the behavior, but trends similar to $\frac{1}{8}$ load appear to exist. Presumably by driving the primary zone air-jets strongly enough significantly reduced NO_x at $\frac{1}{4}$ load and even full load, under lean conditions, is possible. However, although the power required at greater load may be scaled from the jet entrainment coefficient being proportional to $(\dot{W}_a/U_j^3)^{1/2}$, it would be a poor estimate since the jet Strouhal number varies with the load and its effect is not quantitatively known.

The ratio S_N/N_m (shape parameter) will tend to be constant for residence time change, will become larger for generally greater temperatures since NO_x increases exponentially with temperature, but will decrease for a flatter temperature profile due to better mixing. Figures 9 and 10 plot S_N/N_m against N_m, with ϕ_m no-drive indicated for each test point, and show significant acoustically produced change. Clearly for $\phi_m \geq 0.61$ no-drive the acoustic drive has reduced the value of S_N/N_m, confirming that mixing has been augmented acoustically. However, for the $\frac{1}{8}$ load leaner extra tests (Fig. 10) the with-drive characteristic crossed the no-drive characteristic, to reach lower mean NO_x values, at the expense of a poorer shape parameter. For the no-drive characteristic the shape parameter was also poorer since the NO_x profile had become asymmetric as shown in Fig. 11. Under with-drive the asymmetry was worse, accounting for the poorer shape parameter and perhaps indicating that the blockage effect had affected the primary zone aerodynamics under these lean conditions. Nevertheless, with-drive there was a reduction in mean NO_x at lean conditions brought about by a combination of an increase through longer residence time, an increase by greater mean temperature and an overriding decrease through improved mixing. The full significance of this is, of course, brought out by Fig. 8. That improved mixing may produce significant reduction in mean NO_x was demonstrated by a calculation for a typical temperature profile, assuming better mixing to a flat profile at the mean temperature, which showed a 40 percent decrease in N_m.

The data show that the acoustic drive has significantly augmented mixing, and under lean conditions at $\frac{1}{8}$ load mean NO_x was reduced indicating that a value of 10 ppm is possible (a 50 percent reduction). It is possible that obviating the acoustic drive richening of the primary zone, with the associated reduction in residence time, may favorably change the with-drive $N_m - \phi_m$ characteristics of Fig. 8. Unfortunately, it was impossible to explore this with the current apparatus.

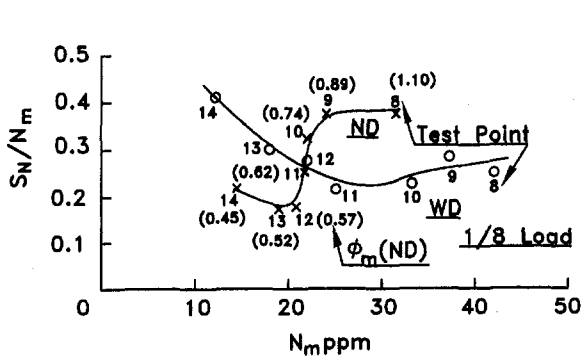

Fig. 10 NO_x profile shape parameter versus mean, $\frac{1}{8}$ load

Conclusions

Successful NO_x measurements at the end of the primary zone of a small tubular combustor of conventional gas turbine design, employing acoustically controlled primary zone air-jet mixing processes, have been made at scaled $\frac{1}{4}$ and $\frac{1}{8}$ load operating conditions. Testing at $\frac{1}{8}$ load significantly increased the effective strength of the acoustic drive, which strongly improved the mixing by the acoustically driven primary zone air-jets. The acoustic drive caused partial blockage of the combustor primary zone air flow, which increased the equivalence ratio and the gas temperature in the plane of the NO_x measurements. The gas temperature distribution was also made more uniform by the acoustically augmented mixing, except for lean conditions at $\frac{1}{8}$ load. This explained the measured greater NO_x with-drive, and the distinctly more uniform NO_x distribution, which confirmed that mixing was acoustically augmented. The acoustically produced changes were greater at $\frac{1}{8}$ load. The acoustic drive significantly changed the combustor operating characteristic so far as mean NO_x was concerned, and under lean conditions at $\frac{1}{8}$ load mean NO_x was reduced indicating that a value of 10 ppm is possible (a 50 percent reduction).

Acknowledgments

The authors are indebted to Mr. R. Bechtold, Chief Technical Supervisor, and to Mr. M. Johnson, Technician, for their expert work in necessary modifications to the test rig. We are also grateful to Mr. A. Moehrle, Research Technician, for invaluable assistance with instrumentation and operational requirements, and to Mr. N. Vogt for the careful production of the manuscript figures. The work was supported financially by the Natural Sciences and Engineering Research Council of Canada, under Grant No. A7801.

References

Anderson, A. B. C., 1955, "Structure and Velocity of the Periodic Vortex-Ring Flow Pattern of a Primary Pfeifenton (Pipe Tone) Jet," *The Journal of the Acoustical Society of America*, Vol. 27, No. 6, pp. 1048–1053.

Becker, H. A., and Massaro, T. A., 1968, "Vortex Evolution in a Round Jet," *Journal of Fluid Mechanics,* Vol. 31, Part 3, pp. 435–448.

Binder, G., and Favre-Marinet, M., 1973, "Mixing Improvement in Pulsating Turbulent Jets," *ASME Symposium on Fluid Mechanics of Mixing,* Georgia Institute of Technology, Atlanta, Georgia, pp. 167–172.

Bremhorst, K., and Harch, W. H., 1978, "The Mechanism of Jet Entrainment," *AIAA Journal,* Vol. 16, No. 10, pp. 1104–1105.

Clarke, A. E., Gerrard, A. J., and Holliday, L. A., 1963, "Some Experiences in Gas Turbine Combustion Chamber Practice Using Water Flow Visualisation Techniques," *Ninth Symposium (International) on Combustion,* The Combustion Institute, Academic Press, pp. 878–891.

Crow, S. C., and Champagne, F. H., 1971, "Orderly Structure in Jet Turbulence," *Journal of Fluid Mechanics,* Vol. 48, pp. 547–591.

Hahnemann, Von H., and Ehret, L., 1943, "Uber den Einfluss Starker Schallwellen auf eine Stationar Brennende Gasflamme," *Zeitschrift für Technisch Physik,* Vol. 24, pp. 228–242.

Heavens, S. N., 1980, "Visualisation of the Acoustic Excitation of a Subsonic Jet," *Journal of Fluid Mechanics,* Vol. 100, Part 1, pp. 185–200.

Hill, W. G., and Greene, P. R., 1977, "Increased Turbulent Jet Mixing Rates Obtained by Self-Excited Acoustic Oscillations," ASME *Journal of Fluids Engineering,* Vol. 99, No. 3, pp. 520–525.

Kibens, V., 1980, "Discrete Noise Spectrum Generated by an Acoustically Excited Jet," *AIAA Journal,* Vol. 18, No. 4, pp. 434–441.

Lefebvre, A. H., 1983a, "Ch. 4 Aerodynamics," *Gas Turbine Combustion,* McGraw-Hill Series in Energy, Combustion, and Environment, New York, pp. 107–155.

Lefebvre, A. H., 1983b, "Ch. 11 Emissions," *Gas Turbine Combustion,* McGraw-Hill Series in Energy, Combustion, and Environment, New York, p. 470.

Lefebvre, A. H., 1983c, "Ch. 11 Emissions," *Gas Turbine Combustion,* McGraw-Hill Series in Energy, Combustion, and Environment, New York, p. 485.

Pearce, G. F., Kretschmer, D., Odgers, J., and Wang, G., 1993, "The Prediction of Thermal NO_x in Gas Turbine Exhausts," *X I International Symposium on Air Breathing Engines,* Tokyo, pp. 1–10.

Ramesh, V., Vermeulen, P. J., and Munjal, M. L., 1993, "Measurement of Acoustic Power for a Tube Air Flow and Correlation With Exit Pulsation Velocity," *Proc. Inter-Noise '93,* Leuven, Belgium, Vol. II, pp. 1227–1230.

Roffe, G., and Venkataramani, K. S., 1978, "Emissions Measurements for Lean Premixed Propane/Air System at Pressures up to 30 Atmospheres," NASA CR-159421.

Sarohia, V., and Massier, P. F., 1978, "Experimental Results of Large-Scale Structures in Jet Flows and Their Relation to Jet Noise Production," *AIAA Journal,* Vol. 16, No. 8, pp. 831–835.

Vermeulen, P. J., Odgers, J., and Ramesh, V., 1982, "Acoustic Control of Dilution-Air Mixing in a Gas Turbine Combustor," ASME JOURNAL OF ENGINEERING FOR POWER, Vol. 104, pp. 844–852.

Vermeulen, P. J., Ramesh, V., and Yu, Wai Keung, 1986, "Measurements of Entrainment by Acoustically Pulsed Axisymmetric Air Jets," ASME JOURNAL OF ENGINEERING FOR GAS TURBINES AND POWER, Vol. 108, pp. 479–484.

Vermeulen, P. J., Odgers, J., and Ramesh, V., 1987, "Full Load Operation of Gas Turbine Combustor With Acoustically Controlled Dilution-Air Mixing," *International Journal of Turbo and Jet Engines,* Vol. 4, Nos. 1–2, pp. 139–147.

Vermeulen, P. J., and Yu, Wai Keung, 1987, "An Experimental Study of the Mixing by an Acoustically Pulsed Axisymmetrical Air-Jet," *International Journal of Turbo and Jet Engines,* Vol. 4, Nos. 3–4, pp. 225–237.

Vermeulen, P. J., Chin, Ching-Fatt, and Yu, Wai Keung, 1990, "Mixing of an Acoustically Pulsed Air Jet with a Confined Crossflow," *AIAA Journal of Propulsion & Power,* Vol. 6, No. 6, pp. 777–783.

Vermeulen, P. J., Rainville, P., and Ramesh, V., 1992a, "Measurements of the Entrainment Coefficient of Acoustically Pulsed Axisymmetric Free Air Jets," ASME JOURNAL OF ENGINEERING FOR GAS TURBINES AND POWER, Vol. 114, No. 2, pp. 409–415.

Vermeulen, P. J., Grabinski, P., and Ramesh, V., 1992b, "Mixing of an Acoustically Excited Air Jet With a Confined Hot Crossflow," ASME JOURNAL OF ENGINEERING FOR GAS TURBINES AND POWER, Vol. 114, pp. 46–54.

Vermeulen, P. J., Ramesh, V., Sanders, B., and Odgers, J., 1993, "Temperature and Combustion Analysis of Combustor With Acoustically Controlled Primary Zone Air-Jet Mixing," AGARD Conference Proceedings 536, NATO. *Fuels and Combustion Technology for Advanced Aircraft Engines,* pp. 43-1 to 43-13.

Vermeulen, P. J., Ramesh, V., Sanders, B., and Odgers, J., 1995, "Acoustic Control of Combustor Primary Zone Air-Jet Mixing," *AIAA Journal of Propulsion & Power,* Vol. 11, No. 2.

Zelina, J., and Ballal, D. R., 1994a, "Combustion and Emissions Studies Using a Well Stirred Reactor," AIAA Paper No. 94-2903.

Zelina, J., and Ballal, D. R., 1994b, "Combustion Studies in a Well Stirred Reactor," AIAA Paper No. 94-0114.

D. Kretschmer
Professor.

J. Odgers
Professor Emeritus.

Département de génie mécanique,
Université Laval,
Québec, QC, Canada G1K 7P4

The Prediction of Laminar Flame Speeds for Weak Mixtures

In a recent publication [3], the authors tentatively explored the prediction of propane flame speeds using the calculated burned gas temperature (T_b) and the predicted flame extinction temperature (T_i). A formula was developed that utilized these temperatures together with correction factors for inlet temperature and the oxygen/inert ratio. The present paper has extended this technique so that data from 20 different fuels have been examined over a range of conditions, which include significant variations of both inlet temperature and pressure. Limitations of the technique are discussed, as are possible related applications to other premixed systems such as laminar flames and well-stirred reactors.

Introduction

Both the measurement and prediction of laminar flame speeds have provided difficulties for workers in the field of combustion. In a simple form Bradley [1] cites the relation between laminar flame speed and reaction rate as

$$S_u = \sqrt{\frac{\bar{\lambda}\bar{W}(T_b - T_i)}{\bar{c}_p \rho_0 n_{\text{mol}} (T_b - T_0)}} \tag{1}$$

To predict S_u, it is necessary to establish values for W and T_i, both of which are very difficult to obtain. Equation (1) had been derived by consideration of the thicknesses of the preheat and reaction zones associated with laminar flames

$$\delta_{pz} = \frac{4.6\bar{\lambda}}{\bar{c}_p \rho_0 S_u} \tag{2}$$

$$\delta_{rz} = \frac{\bar{\lambda}}{\bar{c}_p \rho_0 S_u} \left(\frac{T_b - T_i}{T_i - T_0} \right) \tag{3}$$

Assuming

$$(T - T_0)/(T_i - T_0) = 1/100.$$

It is obvious that the accuracy of Eqs. (1)–(3) will depend upon the values of T_i. Zeldovitch and Frank-Kamenetsky [2] require that T_i be close to T_b and within $\mathbf{R}T_b^2/E$ of it (e.g., 2600 K for T_b = 3000 K and E = 209.5 kJ/mol). In a recent publication by the present authors [3] the value of T_i was assumed to be that of the flame extinction value without heat loss, T_b was taken as the calculated, dissociated flame temperature at the appropriate equivalence ratio and inlet conditions for the mixture. A formula (Eq. (4)) was developed for propane/oxygen/nitrogen mixtures, which utilized these temperatures and which replaced the other terms of Eq. (1) with simple correction factors for inlet temperature and the inerts/oxygen ratio (m):

$$S_u = 0.00903 \left[\frac{T_b - T_i}{F \times m} \right]^{0.715} \tag{4}$$

The inlet temperature correction factor (F) was that used in [4]:

$$F = \exp[1 - T_0/300] \tag{5}$$

The value for T_i was cited as

$$T_i = 1755 + 847 \times \lg(\lg(1000 \times M_f)) - 16.6 \times 10^{-9} \times Q - 98.4 \times \frac{n_C}{n_H + 1} - 8457 \times M_{ox} \tag{6}$$

The resulting predictions of flame speeds were considered satisfactory. For propane/oxygen/nitrogen mixtures, the data in Table 1 appertained.

The objective of the present work is to extend this correlation to cover additional fuel/oxygen/inert mixtures and inlet conditions including pressure. Because of the difficulty in ascribing a correct theoretical temperature to rich mixtures (certainly when $\Phi \geq 1.5$) the present work will be limited to weak mixtures. Because of this, maximum flame speeds will not be treated, although in those cases where the maximum flame speed is given at $\Phi \approx 1.1$, the extrapolation should not be serious.

Experimental Values of Laminar Flame Speed

The experimental data (635 points) were largely taken from Refs. [5–22], but a few isolated points (about 12) were culled from the general literature and reference handbooks. The range of data is summarized in Table 2.

From one extreme to the other there is a factor of not less than 1.3 up to 3.75. Much of the difference may be attributed to the different techniques and the different ways of defining the flame velocity, but the acceptable value is still a "judgment call." As will be seen in the course of the analysis, the work reviewed here confirms that the scatter disclosed in [23] is certainly of the right order. They reviewed the following techniques (which are represented in the present work): (1) tube methods, (2) contained explosions, (3) flame kernel development in slow systems. They concluded that the most accurate technique was, probably, that of double flame kernels.

With such a wide range of variables, it became necessary to establish the accuracy of the experimental data. In 1972 Andrews and Bradley [23] gave a review of the techniques for the determination of burning velocities. For a number of fuel/oxidant mixtures, they selected a value for the flame speed and assessed the variation as a ratio (Table 3).

It follows that any correlation cannot be of a high accuracy since this sort of scatter cannot be reduced by the correlation. In these notes equal credence will be given to all techniques and it would seem likely therefore that the predicted values will represent more of a "true" value than most of the individual determinations.

Correlation Derivation

Conditions across the flame front of a typical laminar flame are illustrated in Fig. 1. The data are taken from [3].

Contributed by the International Gas Turbine Institute and presented at the 41st International Gas Turbine and Aeroengine Congress and Exhibition, Birmingham, United Kingdom, June 10–13, 1996. Manuscript received at ASME Headquarters February 1996. Paper No. 96-GT-142. Associate Technical Editor: J. N. Shinn.

Table 1 Flame speed correlation for propane/oxygen/nitrogen mixtures [3]

Numberof Points	72		
Standard Deviation	13,7 %		
Maximum Deviations	+29 % & -24 %		
Experimental Range			
Φ	0,59 to 1,00	m	1,02 to 5,02
T_0	298 K to 616 K	S_u	0,15 to 2,20 m/s

Table 2 Range of experimental data

Fuels	20	M_f	2 to 114 g/mol
M_{ox}	9 to 39 g/mol	T_0	293 to 720 K
T_i	1045 to 1708 K	T_b	1104 to 3285 K
p_0	0,1 to 100 atm	m	0 to 5
Φ	0,25 to 1,0	S_u	0,035 to 11 m/s
Inerts N_2, Ar, He, H_2O			

Table 3 Variation of maximum burning velocities for different gases (after [23])

Gas Mixture Selected	No. of Points	Selected Gas Velocity m/s	$\frac{S_{u,\,experiment}}{S_{u,\,selected}}$
Methane/Air	17	0,45	0,71 to 1,11
Ethylene/Air	18	0,79	0,72 to 1,02
Acetylene/Air	14	1,58	0,82 to 1,13
Hydrogen/Air	23	3,10	0,65 to 1,35
Methane/Oxygen	15	4,50	0,64 to 1,40
Acetylene/Oxygen	11	11,4	0,36 to 1,35
Hydrogen/Oxygen	12	14,0	0,37 to 1,03

The inner rectangle of Fig. 1 relates to the preheat zone where reactions are very limited and the increase in temperature is largely due to back diffusion of heat and species. At a temperature (here defined as the "instantaneous" spontaneous ignition temperature (T_i) the reaction "takes off" and the fuel is rapidly consumed. It would seem, therefore, that the overall thickness of the flame is controlled by (a) the processes of diffusion (both species and heat transfer) and then by the reaction rate. The first process is slower than the second and hence the first part of the flame is much thicker than the second. In turn, this implies that the factors controlling diffusion might be of greater significance in defining the thickness of the flame front than those controlling reaction rate.

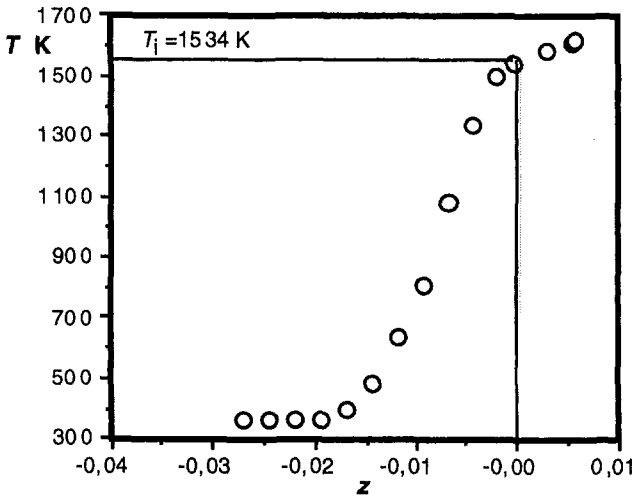

Fig. 1 Measured temperatures within a laminar flame [3]: propane/air, T_0 = 343 K, p = 0.059 atm, Φ = 0.534

Flame Temperature Effects. According to Eqs. (1), (3), and (4), the term $(T_b - T_i)$ should have considerable significance in defining both flame speed and flame thickness. In the past, the difficulty has been to determine the value of T_i. In [3] this problem was considered and a formula was presented for the calculation of T_i (Eq. (6). Figure 2 shows the results for four different fuels tested at atmospheric conditions.

The data for Fig. 2 were selected so as to be representative of both low- and high-energy fuels. The scatter of the data for methane is in accord with that listed in Table 3.

Inlet Temperature Effects. Since publication in 1989 of the correction for inlet temperature, Eq. (5) [3] has proved to be applied to many combustion applications ranging from well-stirred reactors to aircraft combustors.

The equation was used here with the results shown in Fig. 3. Over the range of inlet conditions examined (293 to 720 K) it is quite satisfactory, and the use of F elsewhere suggests that it could be applied to higher inlet temperatures. Also, this would suggest that reaction rates govern the effects of inlet temperature. The inlet temperature data reviewed here do not go below 298 K: Dugger and Heimel [25] measured flame speeds from 141 K to 617 K, but only for maximum flame speeds (i.e., slightly rich mixtures). As an additional test of F, their data have been included in Fig. 3. In this instance the burned gas temperatures were not calculated (dissociated), but the measured values (using the sodium D − line technique) were used instead. The fit of these new data appears to further justify the use of F.

Nomenclature

E = apparent activation energy, J/mol
F = temperature correction factor = $\exp[1 - (T_0/300)]$
M_{ox} = pseudo-molar mass, air + inerts, kg/mol
M_f = molar mass of fuel, kg/mol
m = ratio mol inerts/mol oxygen in mixture
n = apparent overall reaction order
n_{mol} = number of moles consumed in unit time, mol/s
n_H = number of hydrogen atoms in fuel molecule
n_C = number of carbon atoms in fuel molecule
n_O = number of oxygen atoms in fuel molecule
p_0 = inlet pressure of mixture, atm
Q = molal calorific value (net) of fuel, J/mol
R = universal gas constant = 8.3143 J/(mol·K)
S_u = laminar flame speed, m/s
T_b = final burned gas temperature, K
T_i = instantaneous ignition temperature, K
T_0 = inlet gas temperature, K
$\bar{W}$ = mean rate of reaction
$\bar{c}_p$ = mean specific heat, J/kg·K
λ_i = thermal conductivity of inert, W/m·K
$\Delta T = T_b - T_i$, K
δ_{pz} = thickness of flame preheat zone, m
δ_{rz} = thickness of flame reaction zone, m
$\bar{\lambda}$ = mean thermal conductivity, W/(m·K)
ρ_0 = gas density, kg/m^3
Φ = equivalence ratio
$\chi = (n - 2)/n$

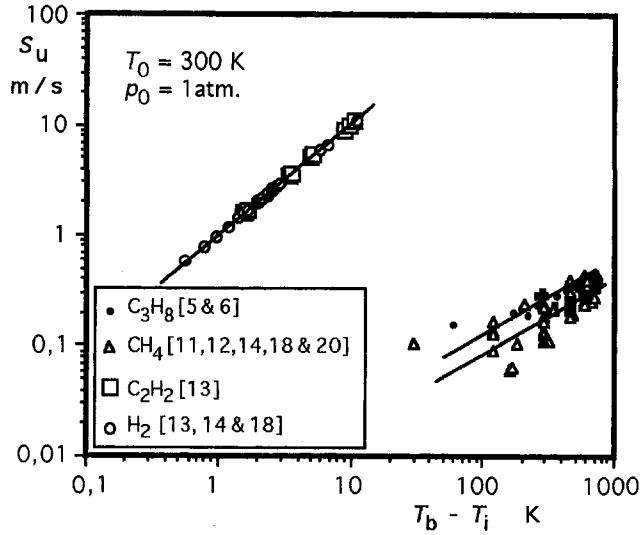

Fig. 2 Effect of $T_b - T_i$ upon S_u: various fuels with air

Several researchers [e.g., 5, 9, 10, 17, 25] give the variation with temperature in the form

$$S_u = A + B\left\{\frac{T_u}{T_0}\right\}^C \tag{7}$$

or

$$S_u(\Phi, T) = S_{u0}(\Phi)\left[\frac{T_u}{T_0}\right]^C \tag{8}$$

For Eq. (7), A seems to range from about 8 to 10, B from about 1.5×10^{-3} to 3.7×10^{-3}, and C from about 1.7 to 2.3, the individual values depending upon the fuel used.

For Eq. (8) C ranges from about 1.5 to 2.0.

For any given fuel the values of Eqs. (8) and (9) are slightly more accurate than the F correction, especially at temperatures well below 0°C. In no case examined to date did the error due to the use of F instead of an individual value yield an error greater than 8 percent in the flame velocity; in most instances the error was 1 percent or less. Based upon these findings it was decided to use F for any general correlation.

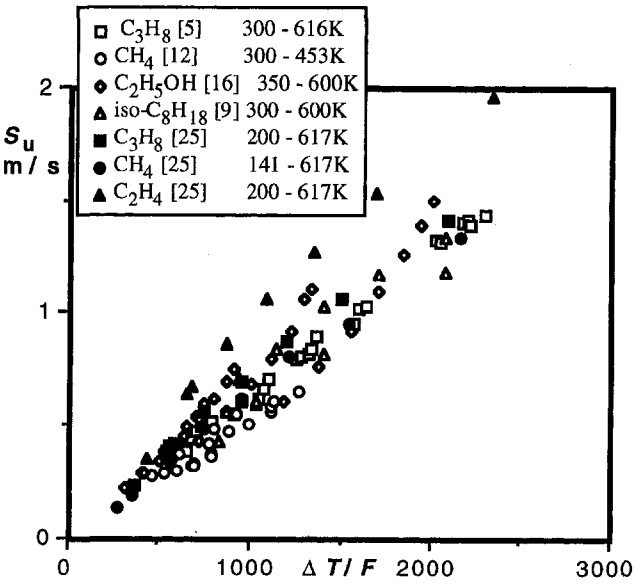

Fig. 3 Effects of inlet temperature upon S_u for fuel/air mixtures at atmospheric pressure

Table 4 Effects of pressure on S_u (near-stoichometric mixtures)

Mixture	Press. atm	(n-2)/2	Ref.
CH_4/air	0,26 to 0,66	-0,5	27
		-0,33	29
	0,7 to 1,0	0	5
	0,33 to 1,0	0	5
		-0,5	10
	0,01 to 3,0	-0,5	18
	0,1 to 95	-0,5	17
	0,5 to 4,0	log p	12
C_3H_8/air	0,33 to 1,0	0	5
		log p	5
	0,5 to 9,0	-0,3	8
C_8H_{18}/air	0,53 to 0,92	-0,39	5
	1 to 8	-0,22	10
CH_3OH/air	1 to 8	$-0{,}2\sqrt{\Phi}$	10
C_2H_2/air	0,26 to 0,66	-0,5	27
	0,01 to 1,0	0	28
		0	29
C_2H_2/O_2		0	29
C_2H_4/air	0,33 to 1,0	log p	5
	0,015 to 1,5	0	5
	0,3 to 0,8	0	5
	0,35 to 1,0	-0,38	5
C_4H_{10}/air		-0,33	27
	0,25 to 1,0	0,17	5
C_7H_{16}/air	0,53 to 1,0	-0,36	5
CO/air		0	5
C_6H_6/air	0,4 to 0,92	-0,33	5
C_2H_5OH/air	1 to 8	$-0{,}2\sqrt{\Phi}$	10

Inlet Pressure Effects. A search through the literature indicates a considerable uncertainty as to the effect of pressure upon laminar flame speed. According to Stambuleanu [26] the theoretical relationship is given by

$$S_u \approx p_0^{(n-2)/2} \tag{9}$$

Most sources agree that the combustion of hydrocarbon fuels at stoichiometric conditions yields a reaction order (n) approximating two. Substituting this value in Eq. (9) yields a pressure exponent of zero. Table 4 gives some relevant experimental data.

As indicated in Table 4, there is some evidence that the pressure exponent alters with equivalence ratio, but there are no general trends, either with fuels or with workers. Some of the variations observed in Table 4 seem to be associated with the pressure range examined. If this was small, the measurements could well be within the experimental scatter referred, say, to the mean pressure. Figure 4 gives some idea of the measured effects of pressure for various fuels. Not all of the data have been recorded in order to preserve some clarity. The slopes of the various data range from about 0.45 (methane) to about 0.2. There is also some evidence that the slope is affected by the equivalence ratio.

Assuming the effects of stoichiometry suggested by some workers (Table 4) it was decided to use a relationship for the hydrogen content developed in a publication on limits of flame propagation [33]

$$y = 2.4570 - 4.9 \times \left|\frac{n_H + n_O}{n_H + n_O + n_C} - 0.63\right|^{1.22} \tag{10}$$

Accounting for the influence of equivalence ratio, the best fit eventually found for the pressure exponent was

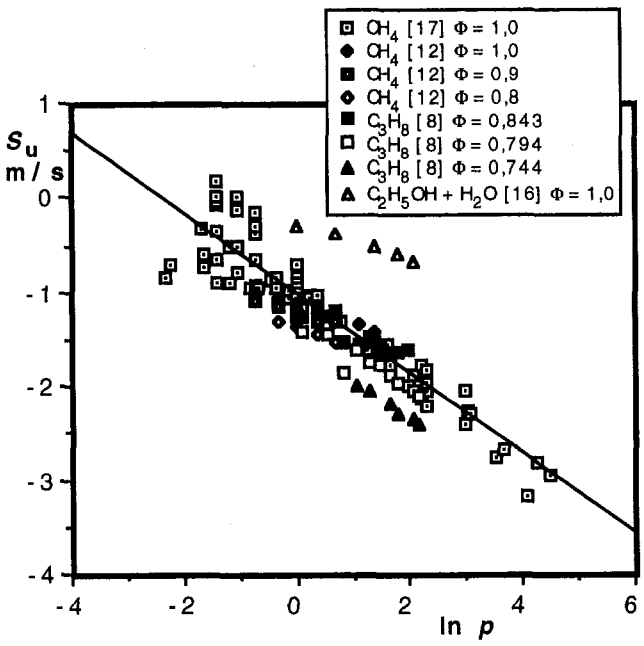

Fig. 4 Effect of pressure upon the flame speeds of several fuel/air mixtures; T_0 = 300 K

$$\frac{n-2}{2} = \frac{y \times \Phi}{4.64} = \chi \tag{11}$$

The Effects of Inerts. Lewis and von Elbe [31] present a series of curves showing the effects of various inert gases. The original work is attributed to Jahn, but the authors claim that the original results are not generally available. Unfortunately the presentation in [31] is not in a form that can be interpreted with accuracy. Table 5 lists the effects of diluents upon the maximum flame speeds of several fuels, and the data have been taken from [5]. The values are relative to nitrogen at the same molar fraction.

The results confirm the thermal effects of the diluents. Helium gives the greatest increase and carbon dioxide the greatest decrease in flame speed. As one would expect, as the oxygen content increases, the effects of the diluents decreases. These thermal effects are emphasized by the data given in [20]. A correction for thermal conductivity of the inert ($\lambda_i^{0.35}$) takes care of the differences between inerts, and Fig. 5 demonstrates this; it gives both the raw data and with the correction. The latter show a significant improvement.

Table 5 Effects of inerts upon maximum flame speeds (after [5])

		Flame Speed Relative to Nitrogen		
Fuel	m	Argon	Helium	Carbon Dioxide
Methane	3,76	2,31	3,27	
	3,76	2,70	3,20	
	3,76	2,31	3,21	
	3,76	1,85	3,00	
	2,33	1,55	2,60	0,24
	1,50	1,40	2,00	0,26
	0,67	1,15	1,50	0,54
	0,25	1,05	1,15	0,76
Propane	3,76	1,80	2,80	
	2,13	1,40	2,35	
	1,38	1,20	1,60	
	0,75	1,10	1,50	
Hydrogen	3,76	1,35	1,35	
	7,33	1,15	2,75	
	3,76			0,50
	2,33			0,68
	1,00			0,85
	0,25			0,96
Acetylene	3,76	1,46	2,25	0,26
	3,76	1,15	2,15	
	7,33	1,90	3,40	

The remaining data used here were restricted to variations of m due to changes in the nitrogen content of the oxidant mixture. Data existed for several workers [5, 7, 13, 20] plus a few scattered data from several sources. Plotted individually the dependence upon m apparently varied from $(m + 1)^2$ to $(m + 1)^{0.84}$. Overall the best fit was obtained with $(m + 1)$.

Correlation Discussion

At this stage a correlation exists that contains components of all the variables. It takes the form

$$S_u = f\left(\frac{\Delta T \lambda^{0.35}}{F p_0^{y \times \Phi/4.64}(m+1)}\right) \tag{12}$$

If the data are plotted, there appears to be some fuel sensitivity. Figure 6 demonstrates this. For clarity, only hydrogen, acetylene, propane, and carbon monoxide are plotted, but similar trends are observed for other fuels. The data at the right of the diagram have been correlated using Eq. (12), hereafter termed "Correlation A." Clearly, the "high-energy" fuels are separated from the propane and carbon monoxide. In an attempt to offset this a new "reaction" term was used, $-E/RT$. The value used for T was T_b, R is the universal gas constant. Values of E were selected from the literature that gave a "best fit" for the data. The effects of this are also shown in Fig. 6 and apparently the correlation is improved. This correlation is termed "B" and has the form

$$S_u = f\left(\frac{\Delta T \lambda^{0.35} e^{-E/RT}}{F p_0^{y \times \Phi/1.9}(m+1)}\right) \tag{13}$$

Actual values of E used ranged from 42,000 (H_2) to 84,000 J/mol (CO).

Since the value of T_b is a function of pressure, the introduction of $-E/RT$ changes the pressure dependence. This was corrected by a change in the constant in χ from 4.64 to 1.9. Figure 7 plots all the data, while Fig. 8 compares the experimental values

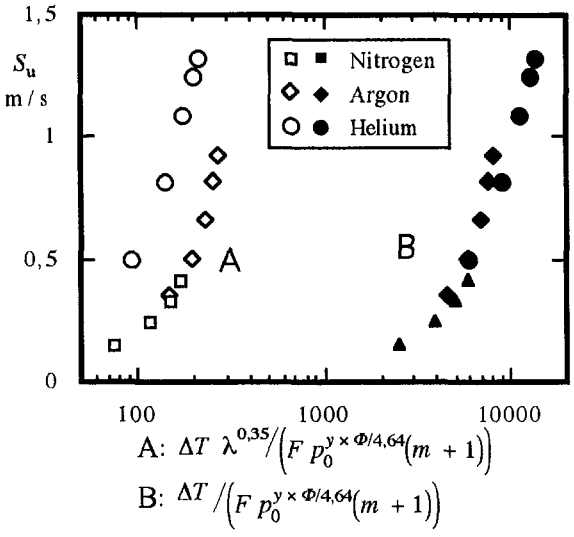

Fig. 5 Effect of inert gases upon the flame speed of methane

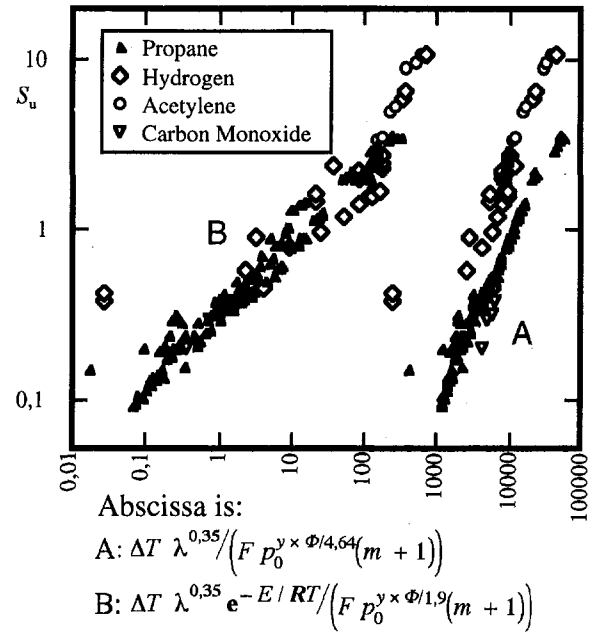

Fig. 6 Two correlations

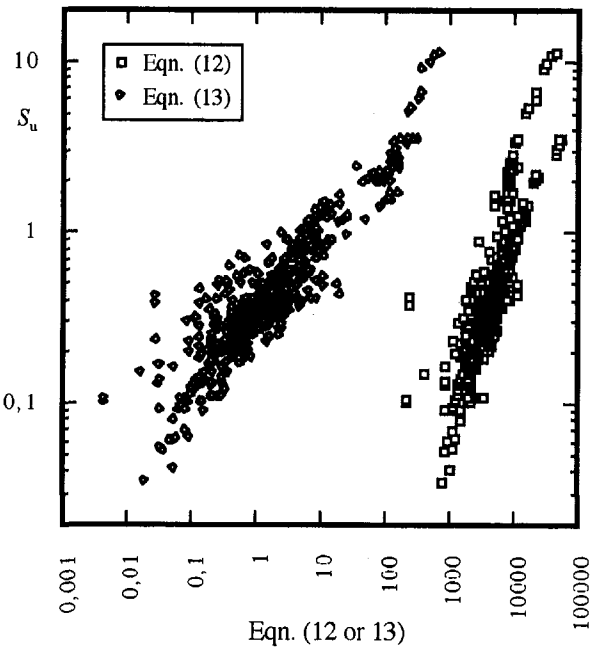

Fig. 7 Two correlations (all data)

of flame speed with those predicted by fitting a straight line through the data in Fig. 7 (Eq. (13).

The final correlation takes the form

$$S_u = 0.337 \times \left(\frac{\Delta T \lambda^{0.35} e^{-E/RT}}{F p_0^{y\times\Phi/1.9}(m+1)}\right)^{0.3951} \quad (14)$$

with a standard deviation of 33.1 percent for 635 points, compared to 36.7 percent for the correlation using Eq. (12), which in its complete form is:

$$S_u = 0.009 \times \left(\frac{\Delta T \lambda^{0.35}}{F p_0^{y\times\Phi/4.64}(m+1)}\right)^{0.978} \quad (15)$$

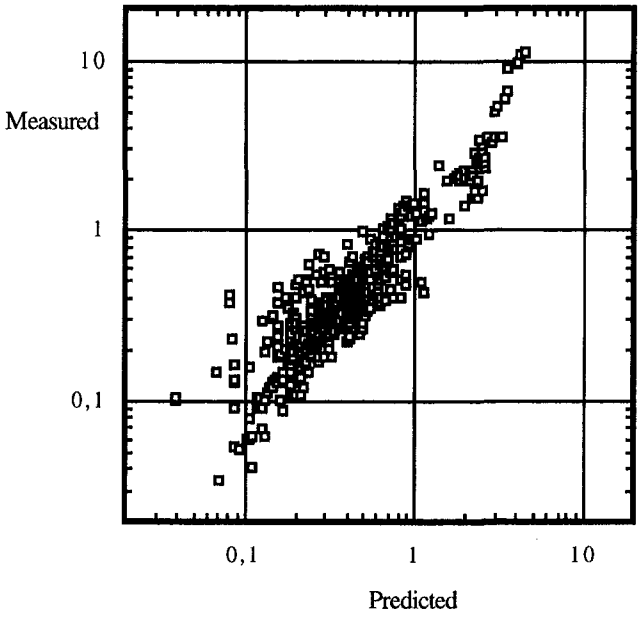

Fig. 8 Predicted and measured flame speeds

Accuracy of the Correlation. For all of the data, the appropriate standard deviation is 33.1 percent. For the correlation A, the value is 34.6 percent. If this value seems excessive, it must be remembered that the experimental variation is often high. For example if the data given by Andrews et al. [17] pertinent to the effect of pressure upon flame speed are examined the data yield: Points 69, Standard Deviation Corr. A 36.8 percent; Corr. B 39.1 percent, Andrews Corr. 42.6 percent.

Limitations of the Correlation

The major limitation is the apparent scatter of the predictions, but as has been pointed out, much of this is attributable to experimental scatter. Of all the data examined, only two points proved to be unpredictable. These were two points in which the combustion temperature was estimated as very slightly above the predicted T_i. This might be attributed to experimental error or to a slight error in the prediction of T_i. Apart from the above, there appear to be few, if any, other limitations. The system is entirely predictive since all of the values of the components of the correlation are calculable or readily available in the published literature.

Some Possible Applications

A simple means of predicting flame speeds is an asset in several fields. In [32] a relationship is given for predicting flame speeds from spherical combustor blow-out data

$$\left[\frac{N}{VP^2}\right]_{\text{Blow out}} = 0.1 S_u^{1.75} \quad (16)$$

This has been used in the past, but it makes no concession to the effects of pressure. For propane/air and iso-octane/air mixtures, Fig. 9 gives a comparison between measured flame speeds and those predicted using Eq. (16) and the present work. The predictions using Eq. (14) are a little better than those using Eq. (16) and they do not require any experimental information and appear to be of general application to hydrocarbon fuels, hydrogen, and carbon monoxide.

Having established a prediction technique for S_u, one possible application is to reverse the process and use the values of S_u to predict the performance of a well-stirred reactor (WSR). In addition since T_i may also be calculated, this may be used for

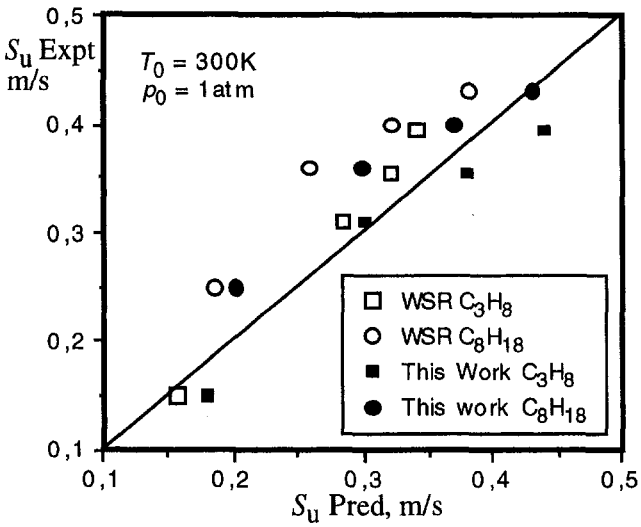

Fig. 9 S_u predictions for this work and for a well-stirred reactor

the blow-out temperature, which to date has not been very well defined in WSR's. In turn, this might also lead to a better definition of the apparent activation energy.

Another possible application that involves both a knowledge of T_i and S_u is the prediction of the temperature distribution across the flame front of premixed flames. This has been done for the flame demonstrated in Fig. 1, and the result of employing the predictions for S_u and T_i, in accord with this work, is given in Fig. 10.

The results are considered to be quite satisfactory and in good agreement with the measured data. Further details are given in [3].

A great deal of attention is still being given to the use of alternative fuels in both spark and compression ignition engines. This correlation offers the opportunity to predict the behavior of new fuels, or even mixtures of fuels. The likelihood that the prediction results would be satisfactory may be gaged from the use of the data from [15, 19], which were taken at enginelike conditions.

Still another application would be to predict the effects of diluent gases upon premixed burner performance; water injection and exhaust gas recirculation are but two possibilities.

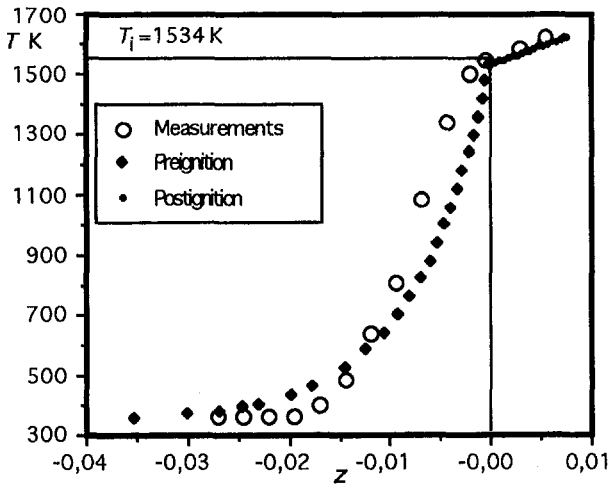

Fig. 10 Temperature within a laminar flame: propane/air, T_0 = 343 K, p = 0.059 atm, Φ = 0.534

Conclusions

A fairly comprehensive review has been made of the measured values of flame speed for many fuels over a wide range of operating conditions. The results have been correlated by

$$S_u = 0.337 \times \left(\frac{\Delta T \lambda^{0.35} e^{-E/RT}}{F p_0^{\gamma \times \Phi / 1.9} (m+1)} \right)^{0.3951}$$

Although the standard deviation of the predictions from the measured data is high (33.1 percent) this is also representative of the variations of the experimental data reported in the literature.

The correlation has been shown to be of application to hydrocarbon fuels, alcohols, hydrogen, carbon monoxide and several other $C_nH_mO_p$ fuels. The range of conditions for which it has been applied is:

Fuels	20	M_f	2 to 114 g/mol
M_{ox}	9 to 39 g/mol		
T_0	293 to 720 K	T_i	1045 to 1708 K
T_b	1104 to 3285 K		
p_0	0.1 to 100 atm	m	0 to 5
Φ	0.25 to 1.0		
S_u	0.035 to 11 m/s	Inerts N_2, Ar, He, H_2O	

Possible applications of the correlation include prediction of WSR performance, temperature distributions in laminar flame fronts, alternative fuel behaviour in SI and Diesel engines and the effects of diluents upon premixed laminar flames.

References

1 Bradley, J. N., *Flame and Combustion Phenomena,* Chapman & Hall Ltd. and Science Paperbacks, 1972, Chap. 3.

2 Zeldovich, Y. B., and Frank-Kamenetsky, D. A., *C. R. Acad. Sci. URSS.,* Vol. 19, 1938, p. 693; and *J. Phs. Chem. USSR,* Vol. 100, 1938.

3 Odgers, J., and Kretschmer, D., "Some Considerations of Weak Blowout and Extinction Limits of Premixed Flames," presented to the XII ISABE, Melbourne, Sept. 10–15, 1995.

4 Kretschmer, D., and Odgers, J., "On the Weak Extinction of Gas Turbine Combustors," presented at the IX ISABE, Athens, Sept. 1989.

5 Barnett, H. C., and Hibbard, R. R., "Basic Considerations in the Combustion of Hydrocarbon Fuels With Air," NACA Report No. 1300, Lewis Flight Propulsion Laboratory, Cleveland, OH, 1957.

6 Harris, M. E., Grumer, J., von Elbe, G., and Lewis, B., *Proc. 3rd Symposium on Combustion and Flames,* Williams and Wilkins, Baltimore, 1949, p. 80.

7 Singer, J. M., Grumer, J., and Cook, E. B., *Proc. of Gas Dynamics Symposium on Aerothermochemistry,* Northwestern University, Evanyson, IL, Aug. 22–24, 1955.

8 Egerton, A. C., and Lefebvre, A. H., "The Effect of Pressure Variation on Burning Velocities," *Proc. Roy. Soc.,* London, Series A, Vol. 222, 1954.

9 Gülder, O. L., "Laminar Burning Velocities of Methanol, iso-Octane and iso-Octane/Methanol Blends," *Combustion Science & Technology,* Vol. 33, 1983.

10 Gülder, O. L., "Correlations for Laminar Burning Data for Alternative S.I. Engine Fuels," SAE Paper No. 841000, 1984.

11 Coward, H. F., and Hartwell, J., *J. Chem. Soc.,* 1932, p. 1996.

12 Sharma, S. P., Agrawal, D. D., and Gupta, C. P., "The Pressure and Temperature Dependence of Burning Velocity in a Spherical Combustor Bomb," *18th Symposium (International) on Combustion,* Combustion Institute, 1981, p. 493.

13 Gaydon, A. G., and Wolfhard, H. G., *Flames, Their Structure and Temperature,* 4th ed., Chapman & Hall, 1979.

14 Pritchard, R., Guy, J. J., and Connor, N. E., *Handbook of Industrial Gas Utilisation,* Van Nostrand, 1977.

15 Al-Himyary, T. J., and Karim, G. A., "A Correlation for the Burning Velocity of Methane–Air Mixtures at High Temperatures and Pressures," ASME Paper No. 87-ICE-6, 1987.

16 Gülder, O. L., "Burning Velocities of Ethanol–Air and Ethanol–Water–Air Mixtures, Dynamics of Flames and Reactive Species," *Progress in Astronautics and Aeronautics,* Vol. 95, 1985.

17 Andrews, G. E., and Bradley, D., "The Burning Velocity of Methane/Air Mixtures," *Combustion & Flame,* Vol. 19, 1972, p. 275.

18 Andrews, G. E., and Bradley, D., "Determination of Burning Velocity by Double Ignition in a Closed Vessel," *Combustion & Flame,* Vol. 20, 1973, p. 77.

19 Halstead, M. P., Pye, D. B., and Quin, C., "Laminar Burning Velocities and Weak Flammability Limits Under Engine-Like Conditions," *Combustion & Flame,* Vol. 22, 1974, p. 89.

20 Clingman, W. H., Brockaw, R. S., and Pease, R. D., *4th Symposium (International) on Combustion,* Combustion Institute, 1953.

21 Glassman, I., *Combustion,* Academic Press, New York, 1977.
22 Kuo, K. K., *Principles of Combustion,* Wiley, New York, 1986.
23 Andrews, G. E., and Bradley, D., "Determination of Burning Velocities; a Critical Review," *Combustion & Flame,* Vol. 18, 1972, p. 133.
24 Friedman, R., and Burke, E., "Measurement of Temperature Distribution in a Low Pressure Flat Flame," *J. Chem. Phys.,* Vol. 22, 1954, p. 824.
25 Dugger, G. L., and Heimel, S., "Flame Speeds of CH_4/Air, C_3H_8/Air and C_2H_4/Air at Low Initial Temperatures," NACA Tech. Note 2624, 1952.
26 Stambuleanu, A., *Combustion Processes in Industry,* Abacus Press, Tunbridge Wells, Kent, 1976, p. 67.
27 Egerton, A., and Sen, D., *4th Symposium (International) on Combustion,* Combustion Institute, 1953, p. 321.
28 Garner, F. H., Ashforth, G. K., and Long, R., *Fuel,* Vol. 30, 1951, p. 17.
29 Gaydon, A. G., and Wolfhard, H. G. M., *Fuel,* Vol. 29, 1960, p. 115.
30 Gilbert, M., *6th Symposium (International) on Combustion,* Combustion Institute, 1957, p. 74.
31 Lewis, B., and von Elbe, B., *Combustion, Flames and Explosions of Gases,* Academic Press Inc. New York, 1961, p. 381 et seq.
32 Clarke, A. E., Odgers, J., Stringer, F. W., and Harrison, A. J., "Combustion Processes in a Spherical Combustor," *10th Symposium (International) on Combustion,* Combustion Institute, 1965.
33 Odgers, J., Kretschmer, D., and Halpin, J., "Weak Limits of Premixed Gases," ASME JOURNAL OF ENGINEERING FOR GAS TURBINES AND POWER, Vol. 107, 1995, pp. 10–17.

Application of Rainbow Thermometry to the Study of Fuel Droplet Heat-Up and Evaporation Characteristics

S. V. Sankar

D. H. Buermann

W. D. Bachalo

Aerometrics, Inc.,
Sunnyvale, CA 94086

Advanced, nonintrusive, laser-based diagnostics are being developed for simultaneously measuring the size, velocity, temperature, and instantaneous regression rates of vaporizing/burning fuel droplets in polydisperse flow environments. The size and velocity of the droplets are measured using a conventional phase Doppler particle analyzer (PDPA), and the droplet temperatures are simultaneously measured with a rainbow thermometer. This integrated diagnostic has been applied to the study of fuel droplet heat-up characteristics in a swirl-stabilized kerosene spray flame. It has also been shown that a novel extension of rainbow thermometry can be used additionally to extract the instantaneous droplet vaporization rate. The feasibility of measuring the instantaneous regression rate has also been demonstrated using controlled experiments with a vaporizing/burning stream of ethanol droplets.

1 Introduction

In order to be able to design and develop efficient and stable spray combustors, it is essential that we first develop a complete understanding of the fundamental phenomena that influence and control the overall spray combustion process. In this regard, advanced diagnostic tools are essential not only for studying fundamental spray combustion processes in ideal laboratory conditions, but also for probing spray flames in realistic environments. Significant advances have been made over the years in the area of laser-based diagnostics for combustion applications (Chigier, 1991; Eckbreth, 1988). Using spectroscopic and nonspectroscopic techniques, it is now possible to measure gas phase velocity, pressure, temperature, and species concentration. However, some of these techniques are so complex that they are not suited for application in actual spray environments.

In the area of fuel droplet characterization, the development of the phase Doppler interferometric technique (Bachalo and Houser, 1984; Bauckhage and Flogel, 1984) has provided the capability for the simultaneous measurement of individual droplet size and velocity in complex reactive and nonreactive sprays. Moreover, with the recent advances in the area of signal processing (Wriedt et al., 1989; Ibrahim et al., 1991), it is now possible to make reliable size and velocity measurements even in extremely noisy situations. The availability of the phase Doppler instrument has permitted simultaneous measurement of droplet size and velocity of fuel droplets in complex spray flames (Edwards and Rudoff, 1990; Presser et al., 1990). These studies have contributed to an increased understanding of the behavior of droplet dynamics and droplet–gas phase interactions in spray flames as well as the effect of fuel properties on the structure of swirling spray flames. However, in order to obtain a better understanding of the droplet heat-up process in spray flames, it would also be advantageous to measure the fuel droplet temperature. Rainbow refractometry/thermometry is an emerging diagnostic technique that has shown potential for the nonintrusive measurement of fuel droplet temperatures. When integrated to a phase Doppler particle analyzer (PDPA), it can be used for simultaneously measuring the size, velocity, and temperature of fuel droplets in a spray flame (Sankar et al., 1993).

Another parameter that is of fundamental interest in the study of spray combustion is the fuel droplet evaporation rate. The study of this parameter is very important for understanding the complex heat transfer process that occurs in spray flames. Also, instantaneous droplet regression data obtained in spray flames can be used to validate currently available spray combustion models (Law, 1982; Sirignano, 1983; Faeth, 1983; Chigier and McCreath, 1974). In spite of these needs, no instrument is currently available for the in-situ measurement of fuel droplet regression rate in spray flames. In the present study, we have not only applied the integrated phase Doppler/rainbow thermometer to the study of fuel droplet heat-up characteristics in a swirl-stabilized kerosene spray flame, but have also demonstrated the feasibility of using a novel extension of rainbow thermometry for the nonintrusive measurement of the fuel droplet regression rates. The feasibility studies were performed with the help of controlled experiments involving streams of burning and nonburning drops. Based on these experiments, it appears that a suitable instrument can be developed for the in-situ measurement of droplet regression rates (in addition to size, velocity, and temperature) in complex spray flames.

2 Measurement Techniques

2.1 Droplet Size and Velocity Measurement Using Phase Doppler Interferometry. The method of particle velocity measurement using a dual-beam laser-Doppler velocimeter (LDV) is over two decades old. However, it continues to be the most robust technique for the nonintrusive measurement of particle and flow-field velocities. Phase Doppler interferometry is an extension of the conventional dual-beam LDV for measuring the diameter of spherical particles in addition to its velocity. Whereas the particle velocity is inferred in LDV by measuring the Doppler difference frequency, in phase Doppler interferometry, the phase difference between two Doppler frequencies recorded at two different spatial locations is used to infer the particle diameter. The phase Doppler technique has matured over the past decade and has now been accepted as a standard diagnostic technique for the nonintrusive and simultaneous measurement of the size and velocity of spherical particles in two-

Contributed by the International Gas Turbine Institute and presented at the 41st International Gas Turbine and Aeroengine Congress and Exhibition, Birmingham, United Kingdom, June 10–13, 1996. Manuscript received at ASME Headquarters February 1996. Paper No. 96-GT-21. Associate Technical Editor: J. N. Shinn.

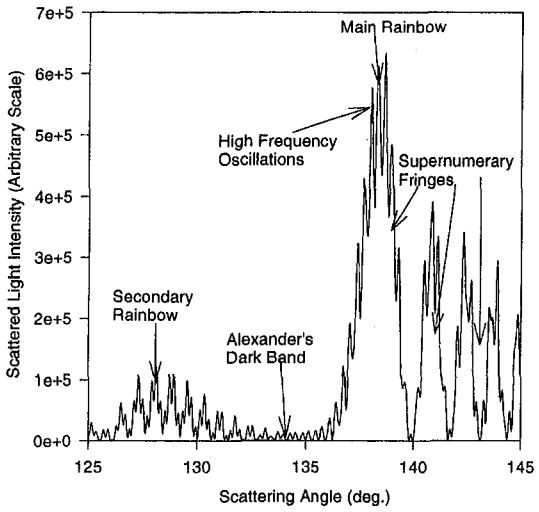

Fig. 1 Computed variation of the scattered light intensity in the neighborhood of the primary and secondary rainbows for a water droplet (m = 1.33) having a diameter of 150 μm and illuminated by a light source having a wavelength of 514.5 nm

phase flow environments. The phase Doppler technique has been demonstrated to be practical for measuring particles as small as 0.3 μm in diameter, and theoretically, there is no upper limit. Under isothermal conditions (no variations in droplet refractive index), measurement uncertainty of the order of about ± 1 percent is possible. The measurement uncertainty is greater in reactive spray flames where there is a large variation in the refractive indices of droplets due to differences in droplet composition and temperature. For example, the temperature effect alone in a kerosene spray flame can give rise to a sizing uncertainty of ± 4 percent when the instrument is set up to measure in the forward scatter angle of 30 deg. Since the phase Doppler response is a function of the scattering angle, the temperature-related measurement uncertainty will also depend upon the chosen optical configuration. The phase Doppler principle is discussed in detail by Bachalo and Houser (1984).

2.2 Rainbow Characteristics. The occurrence of rainbows can be understood with the help of the simple geometric optics based theory proposed by Descartes several hundred years ago. Using geometric optics assumptions, the scattering of light by spherical particles can be described as a combination of diffraction, external reflection, refraction, and refraction occurring after multiple internal reflections. Furthermore, adopting van de Hulst's (1981) notation, $p = 0$ refers to externally reflected light, $p = 1$ refers to refracted rays, $p = 2$ refers to rays that emerge from the droplet after undergoing one internal reflection, and so on. For each order scattered ray, the scattering angle bears a definite relationship to the incident angle. The location of the primary rainbow can then be understood to correspond to that scattering angle at which the angular relationship for $p = 2$ goes through an extremum. At the rainbow angle, the scattered intensity achieves a local maximum. To one side of the rainbow angle is a shadow region into which no rays emerge and to the other side is a lit region. Similarly, the secondary rainbow corresponds to the scattering angle extremum for $p = 3$ rays. For example, for water droplets, the primary and secondary rainbows occur at scattering angles of 137.9 and 128.8 deg, respectively. The dark region between the primary and the secondary rainbow is historically known as Alexander's dark band. Rainbows of order greater than $p = 3$ can also be present, but in general, are very weak in intensity.

Several characteristics of the rainbow cannot be adequately explained with the geometric optics based theory, for example, the presence of supernumerary arcs on the lighted side of the primary and secondary rainbows. They occur as a result of interference between two different rays of the same order emerging in the same direction. Thus, at any given angle slightly greater than the rainbow angle, the scattered light includes rays that have followed two different paths through the droplet. To complicate the situation further, the interference of the internally reflected rays with externally reflected ($p = 0$) rays gives rise to high-frequency intensity oscillations that are superimposed upon the supernumerary fringes. Over the years, several theories have been developed to explain such rainbow characteristics (van de Hulst, 1981). Of these, only the Lorenz–Mie theory provides an exact solution for the scattering of electromagnetic waves by a spherical particle. Figure 1 presents the computed variation of the scattered light intensity in the neighborhood of the primary and secondary rainbows. The computations were performed using the Lorenz–Mie theory for a water droplet (m = 1.33) having a diameter of 150 μm. The wavelength of the illuminating light source was assumed to be 514.5 nm. The important rainbow characteristics such as the locations of the primary and secondary bows, the dark band, the supernumerary fringes, and the high-frequency oscillations that ride on the low-frequency oscillations have been identified in Fig. 1.

2.3 Droplet Temperature Measurement Using Rainbow Thermometry. Rainbow thermometry is a newly emerging diagnostic technique that takes advantage of the fact that the location of the main rainbow (rainbow angle) is a function of the refractive index of the droplet. Therefore, by measuring the rainbow angle with the help of a linear array detector such as a CCD, the refractive index of the droplet can be determined. Since refractive index varies with temperature, the droplet temperature can also be inferred if the relationship between the refractive index and temperature is known a priori. A typical measured (using a linear CCD array) dependence of the rainbow location on the droplet refractive index is presented in Fig. 2.

2.4 Droplet Regression Rate Measurement. In addition to droplet temperature, the instantaneous droplet regression rate is another piece of information that will be useful in the study of fuel droplet heat-up and evaporation characteristics. Anderson and Winter (1992) have used morphology-dependent resonances to measure very small changes (approximately 3 nm) in droplet diameter. With the MDR technique, a dye dissolved

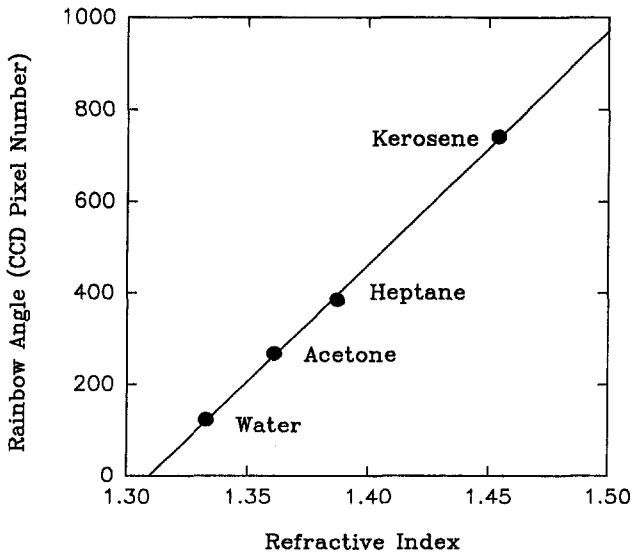

Fig. 2 Calibration of the rainbow refractometer. Droplets (approximately 120 μm in diameter) were generated using a monodisperse droplet generator. The CCD pixel number is a direct measure of the rainbow angle.

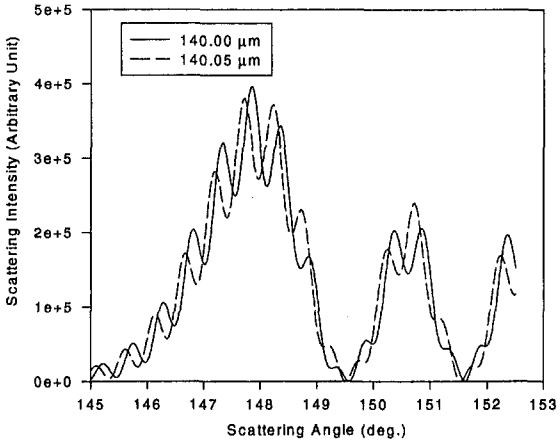

Fig. 3 Computed rainbow signatures for two drops differing in diameter by only 0.05 μm. The refractive index was assumed to be 1.40 and the light wavelength was 514.5 nm.

in the droplet fluid is pumped to an upper electronic state by an external light source. Small droplets of the solvent and dissolved laser dye are illuminated with a high-power pulsed laser. Stimulated emissions from dye molecules just inside the circumference of the droplet are constrained to the inner surface by total internal reflection, effectively producing a spherical ring dye laser. Within the spectral envelope of the dye, frequency modes for which the circumference is an integral number of wavelengths are resonantly enhanced. This information is processed using a spectrometer for extracting the droplet diameter and the change in droplet diameter.

In the present study, we have investigated an alternative approach for droplet regression rate measurement based upon elastic light scattering. This technique removes some of the inherent limitations of MDR, which requires the addition of dopants to the fuel, but at the same time, yields comparable measurement resolution. As mentioned earlier, the interference of internally reflected rays with external reflections occurring in the neighborhood of the rainbow angle gives rise to high-frequency oscillations that are superimposed upon the supernumerary fringes, see Fig. 1. These high-frequency oscillations are extremely sensitive to small changes in the droplet diameter. Therefore, they can be suitably processed to detect ultrasmall changes in the diameter of a regressing fuel droplet and providing a novel way to measure the instantaneous evaporation rate of fuel droplets. However, there are fundamentally two different methods that could be adopted to measure small changes in the diameter of a regressing fuel droplet. We shall refer to these as the *phase* and *frequency* approaches.

In the *phase* approach, the rainbow signature from a single regressing droplet in the spray is recorded at two closely separated (but known) instants of time. Two gated cameras with linear CCD sensors may be required for implementing the *phase* approach. Each camera is used to record one or the other of the two rainbow signatures. Furthermore, the CCD exposure time used in the recording of the individual rainbow signatures will have to be very short (on the order of about 100 ns) for preserving the high-frequency structure of the rainbow signature. Long CCD exposure times will smear out the high-frequency oscillations because of the fuel droplet regression. To handle short exposure times, image intensifiers may also be required. The optimal time interval between the two CCD exposures depends upon various factors including droplet size, regression rate, and droplet velocity. The objective is to capture two rainbow signatures from the same droplet before it leaves the measurement probe volume. Also, the time interval has to be such that the measured phase between the two high-frequency signals does not exceed 360 deg.

Having recorded the rainbow signatures, they can be digitally processed to extract only the high-frequency contributions, and the two high-frequency signals can be correlated to extract the phase difference between them. This phase difference is a measure of the change in droplet diameter. Using simplified geometric optics assumptions, it can be shown that at the rainbow angle this phase difference can be expressed as:

$$\phi = \frac{2\pi D}{\lambda}\left(\cos\theta_0 - \cos\theta_2 + 2m\cos\left(\sin^{-1}\left(\frac{\sin\theta_2}{m}\right)\right)\right) \tag{1}$$

where m is the refractive index of the droplet, λ is the wavelength of light, D is the droplet diameter, and θ_0 and θ_2 are the light incidence angles on the droplet that give rise, respectively, to the externally and internally reflected rays that emerge at the rainbow angle. Relationships describing the dependence of the light incidence angle on the scattering angle for the different order scattering rays have been provided by van de Hulst (1981). Using Eq. (1), the rate of change of phase with diameter can be expressed as:

$$\frac{d\phi}{dD} = \frac{2\pi}{\lambda}\left(\cos\theta_0 - \cos\theta_2 + 2m\cos\left(\sin^{-1}\left(\frac{\sin\theta_2}{m}\right)\right)\right) \tag{2}$$

Equation (2) shows that the phase of the high-frequency oscillations occurring at the rainbow angle is a function only of the droplet refractive index and the light wavelength. It is not dependent on the droplet diameter! This implies that the same measurement resolution can be achieved regardless of the droplet diameter.

A typical example of the high-frequency phase shift resulting from small changes in the droplet diameter is shown in Figs. 3 and 4. The rainbow signatures presented in Figs. 3 and 4 were computed using the Lorenz–Mie light scattering theory for droplet diameters of 140.00 μm and 140.05 μm using a light wavelength of 514.5 nm and a droplet refractive index of m = 1.40. The data presented in Fig. 4 show that a 0.05 μm change in droplet diameter causes a phase shift of approximately 90 deg. Since signals with good SNR can be easily resolved to 1 deg, it is possible to measure droplet diameter changes of the order of 1 nm.

In the *frequency* method, the scattered light intensity is monitored with a very small aperture photodetector located at the rainbow angle. As the fuel droplet regresses, the scattered light

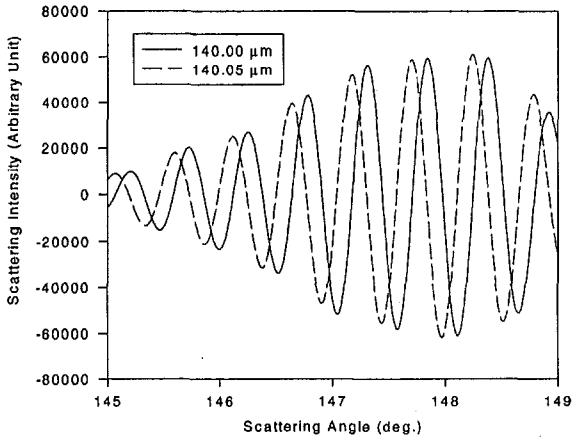

Fig. 4 Computed data showing that the phase shift between the high-frequency oscillations in the neighborhood of the main rainbow resulting from a 0.05 μm change in droplet diameter is approximately 90 deg

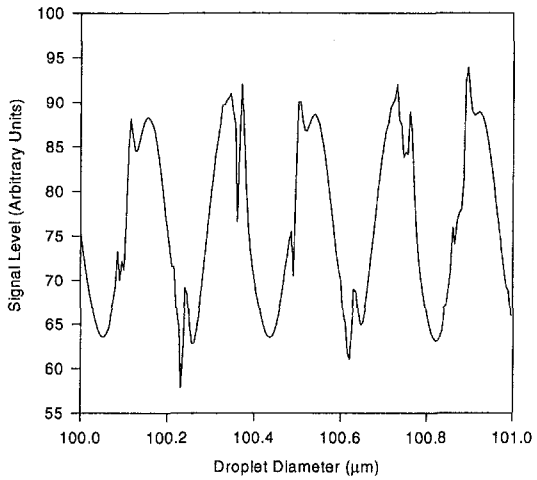

Fig. 5 Computed variation of the scattered light intensity at the rainbow angle (148 deg) for a regressing droplet having an initial diameter of 101.0 μm and a final diameter of 100.0 μm. The refractive index of the droplet was assumed to be m = 1.40 and a laser wavelength was 514.5 nm. The presence of a dominant frequency is obvious in this figure.

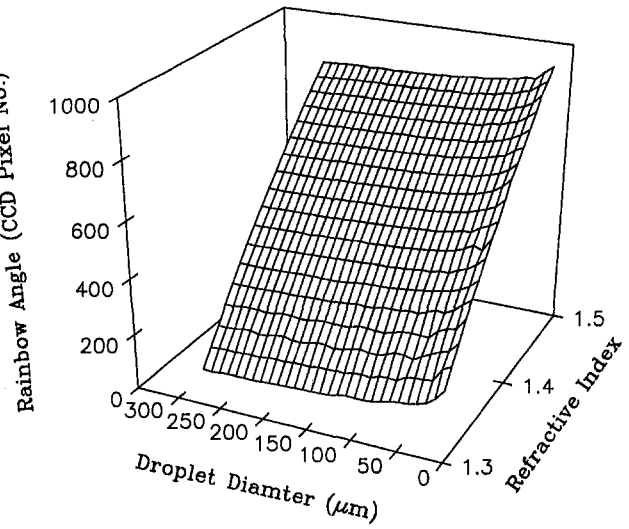

Fig. 6 Computed variation of rainbow angle with droplet size and refractive index

intensity will exhibit an oscillatory resonance characteristic that arises as a result of the phase wrap-around that is implicit in Eq. (1). The droplet regression is monitored continuously during the transit period of the droplet through the measurement probe volume (instead of at two discrete instants of time as in the *phase* method) and this results in an oscillating intensity pattern, the frequency of which can be related to the rate of droplet regression. The computed variation of the scattered light intensities at the rainbow angle (148 deg) for the hypothetical case of a fuel droplet regressing from 101.0 μm to 100.0 μm in diameter is presented in Fig. 5. The data presented in Fig. 5 were computed using the Lorenz–Mie theory assuming a droplet refractive index of m = 1.40 and a laser wavelength of 514.5 nm. The presence of a dominant resonant frequency is obvious in the presented result.

3 Calibration Curves

Droplet size measurement using phase Doppler interferometry, droplet temperature measurement using rainbow thermometry, and droplet regression rate measurement all require the generation of theoretical calibration curves. In general, phase Doppler interferometry requires the computation of the detector phase difference as a function of the particle diameter. In this regard, both geometric optics and Lorenz–Mie theories are used commonly (Sankar and Bachalo, 1991a, b).

For droplet temperature measurement, a curve-fitting technique is used in conjunction with the Lorenz–Mie theory for computing the rainbow angles for several droplets ranging in size from 20 μm to 300 μm and refractive index ranging from 1.30 to 1.50. The computed results are presented in Fig. 6. The data show a linear dependence on refractive index and a quadratic dependence on particle size. The rainbow angle achieves an asymptotic value for particles larger than about 150 μm. A three-dimensional iterative curve fitting algorithm (Marquardt–Levenberg) was also implemented to find a functional form that provides the best fit to the computed data points.

The Lorenz–Mie theory has also been used to generate calibration curves for droplet regression rate measurement. The calibration/response curve for the *frequency* method is presented in Fig. 7, wherein the change in droplet diameter per cycle of intensity oscillation at the rainbow angle is plotted against refractive index. The data presented in Fig. 7 were determined from the computed resonance spectrum for a 51.0 μm droplet regressing to 50.0 μm and a 101.0 μm droplet regressing to 100.0 μm and for a laser wavelength of 514.5 nm. Furthermore, these data have been compared with the geometric optics predictions described by Eq. (2). The geometric optics predictions and the data for the 50.0 μm and 100.0 μm droplets are in excellent agreement, showing that they are independent of the droplet diameter. The data presented in Fig. 7 show a dependence on the droplet refractive index, and furthermore, Eq. (2) suggests an inverse dependence on the laser wavelength. From Fig. 7 it can be observed that the droplet diameter change for every cycle of the intensity oscillation is on the order of about 0.2 μm. Therefore, by measuring the number of cycles in a known time interval, the total change in droplet diameter can be determined, and subsequently, the droplet regression rate can be easily computed.

A typical calibration/response curve for the *phase* method is presented in Fig. 8. In Fig. 8, the computed phase difference between the high-frequency oscillations observable in the spatial rainbow signature is plotted against changes in the droplet diameter. The computations were performed for two hypothetical fuel droplets having a refractive index of 1.40 and regressing in diameter from 50.2 to 50.0 μm and 100.2 to 100.0 μm, respectively. The data presented in Fig. 8 show that the phase change varies linearly with changes in droplet diameter and that

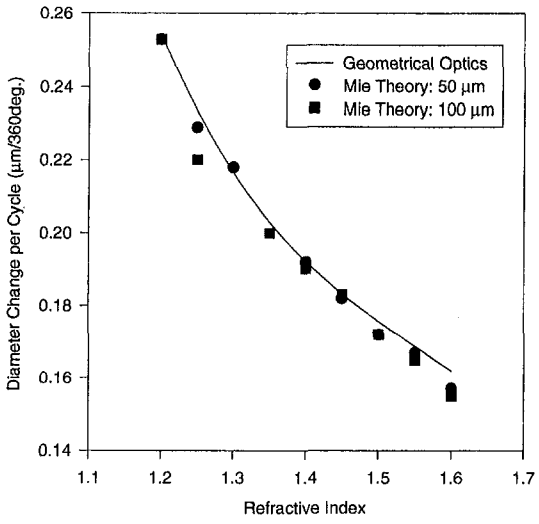

Fig. 7 Computed calibration/response curve for the frequency method

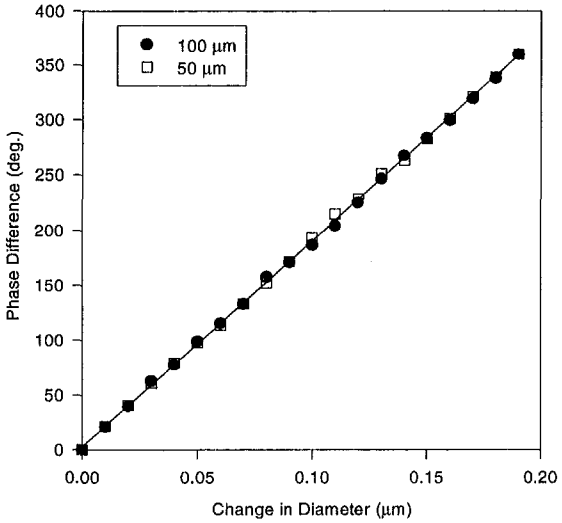

Fig. 8 Computed response curve for the phase method for droplets having a refractive index of 1.40

the response is independent of the droplet diameter, in agreement with the data shown in Fig. 7. From Fig. 8 it can be determined that a change in droplet diameter of approximately 0.19 μm gives rise to a phase change of about 360 deg. This again is in agreement with the data presented in Fig. 7, which show that for $m = 1.40$, the diameter change per cycle of oscillation is approximately 0.19 μm. Therefore, using the *phase* method, droplet diameter changes of the order of 2–5 nm appear to be feasible.

The response curves presented in Figs. 7 and 8 show that both the *frequency* and *phase* methods can be adopted for measuring small changes in the droplet diameter, and hence, the regression rate. However, the *frequency* method is suited for those applications where the droplet regression rate is high enough that several cycles of the intensity oscillations can be observed. On the other hand, if the vaporization or droplet regression rate is not high, the *phase* method can be used to detect ultrasmall changes in the droplet diameter.

4 Integrated Diagnostics

4.1 Optical System. The laser-based, nonintrusive diagnostic instrument developed for the simultaneous measurement of droplet velocity, size, and temperature consists of a rainbow thermometer completely integrated to a phase Doppler particle analyzer. The details of the integrated system have been provided by Sankar et al. (1993). The optical system basically consists of a single transmitting module, a phase Doppler receiver, and a rainbow receiver as shown in Fig. 9. The optical transmitter provides the necessary laser beams for conducting phase Doppler interferometry and rainbow thermometry. For this study, the phase Doppler part of the system was configured to measure only one component of velocity and particle size.

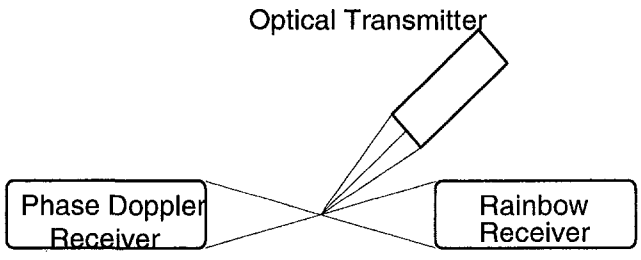

Fig. 9 Optical configuration of the integrated diagnostics

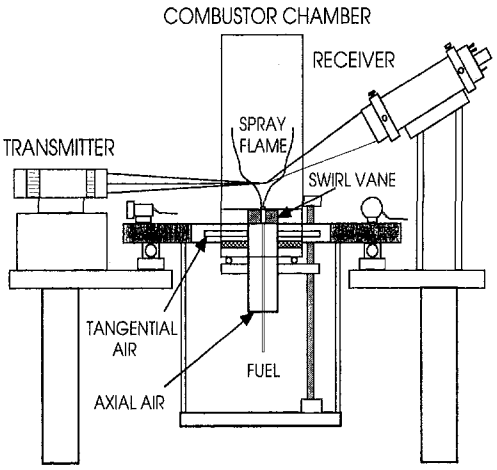

Fig. 10 Schematic of the swirl combustor

The green (514.5 nm) beam from a 5 W argon-ion laser was split into two and used for phase Doppler interferometry, whereas a single blue beam (488.0 nm), lying along the optical axis of the transmitter, was used for rainbow thermometry. The phase Doppler receiver was placed in the forward scatter direction at a scattering angle of 30 deg. The rainbow receiver was placed diametrically opposite to the phase Doppler receiver at a scattering angle of 150 deg. This optical configuration ensures good coincidence between the two receiving systems. The receiver module of the phase Doppler system is identical to that used conventionally. On the other hand, the optical rainbow receiver basically consists of a system of lenses for imaging the rainbow pattern onto a linear CCD array. The optical configuration chosen for the rainbow receiver allows for a temperature measurement range of approximately 300 K (350 K to 650 K) for kerosene droplets. Furthermore, in the current study, the CCD output was used for the *phase* method of droplet regression measurement, and the output of the CCD exposure control PMT was used for the *frequency* method of droplet regression measurement.

4.2 Electronics/Opto-electronics System. The major components of the electronics/opto-electronics system include a CCD based imaging board, a gate control system, data acquisition/signal processing board for processing the rainbow signatures, and a frequency domain based signal processor for processing the Doppler signals. The CCD output is sampled and digitized by a dedicated rainbow signal processor. As discussed earlier, the rainbow signals contain high-frequency components, which would be undesirable if the rainbow peaks are to be determined directly. However, the rainbow signal processor contains a digital filter for minimizing the adverse effects of the high-frequency oscillations. The rainbow peak location and intensity of the rainbow are available for transfer to the data acquisition computer for further analysis and postprocessing. The rainbow signal processor also provides a digital output of each CCD pixel. The digital output can be interfaced to a frame grabber so that large amounts of rainbow signals can be fully digitized and saved for further postprocessing.

5 Experimental Facility

A schematic of the swirl combustor that was used in this study is shown in Fig. 10. It consists of an octagonal combustion chamber having quartz windows. The chamber is 45 cm long and has an inner diameter of 20 cm. The swirler is a typical axial vane type consisting of ten straight vanes welded in place. Three different swirlers are available to provide swirl intensities of $S = 0.48$, 0.63, and 1.172 with swirl angles of 31, 38, and

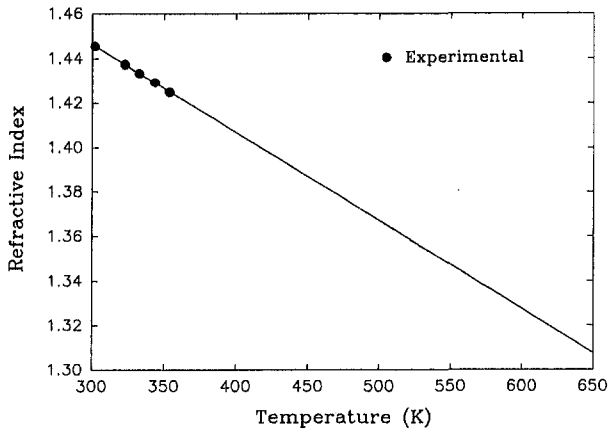

Fig. 11 Experimentally obtained relationship between refractive index and temperature for kerosene

65 deg, respectively. Kerosene is supplied to a Delavan swirl atomization nozzle by means of a bladder-tank system, which permits stable and constant fuel supply. The nozzle cone angle is 30 deg with a semi-hollow cone spray pattern. The combustion chamber is fired with the nozzle spraying vertically upward. The combustion chamber itself is mounted on a three-dimensional traverse system possessing a traversing accuracy of 0.1 mm. For the present study, the kerosene flow rate was set at 0.754 g/s and the swirl air flow rate was 6.54 g/s. This corresponds to an equivalence ratio of about 1.71. It was necessary to operate at this rich condition because the laboratory swirl combustor does not allow for a cool air flow surrounding the nozzle as in practical burners. The swirler with a vane angle of 38 deg and a swirl number of $S = 0.63$ was used.

6 Results

6.1 Droplet Temperature Measurement in a Spray Flame. Detailed LDV characterization of the mean structure and gas-phase aerodynamics of a swirl-stabilized spray flame has been conducted by Edwards and Rudoff (1990) in a combustor similar to that used in the present study. Their study has clearly demonstrated the presence of external and internal recirculation zones. The external recirculation zone is a region outside of the air jet where products are drawn radially inward by entrainment from the main air jet; and the internal recirculation zone is a region of reverse flow induced by the axial pressure gradient of the swirling flow. Although the gas phase aerodynamics has not been explicitly characterized in the present study, it is expected to be similar to that observed by Edwards and Rudoff (1990). Therefore, the emphasis in this study has been to measure the fuel droplet temperatures using the integrated diagnostics.

Before presenting the results of the fuel droplet temperature measurements, it is important that we first recognize that rainbow thermometry assumes that the fuel droplets have a homogeneous temperature. However, in situations where the droplet transient heating time is of the same order of magnitude as the droplet lifetime, the presence of temporally varying radial temperature gradients is possible (Sirignano, 1983). In such situations, rainbow thermometry could give rise to erroneous results. The effect of droplet inhomogeneity on rainbow thermometry has been theoretically studied by Kai et al. (1993) and Schneider et al. (1993). These studies show that radial temperature gradients present during the transient heating of the droplet could lead to erroneous measurement of the droplet temperature as being even below its initial temperature. It is also important to recognize that kerosene is a multicomponent fuel with each of the different components possibly having a different refractive index at the same reference temperature. Therefore, as the droplet evaporates, its composition could also change, and hence, the measured refractive index change cannot solely be attributed to a change in the droplet temperature.

In the present study, droplet heat-up times were first estimated using the approach suggested by Lefebvre (1989). The flame temperature in the spray flame was measured to be approximately 1500 K by means of a Type R Pt-13 percent Rh/Pt thermocouple. For a kerosene droplet having a diameter of 50 μm and an initial temperature of 300 K, the droplet heat-up time (without accounting for convective heating and shear induced internal circulation) was estimated to be approximately 2.0 ms. Furthermore, assuming a typical axial velocity of 10 m/s, it was estimated that the droplet heat-up process is completed at an axial plane of $Z = 2$ cm. Convective heating and shear-induced internal circulation can result in increased heat transfer to the droplets causing them to achieve their wet-bulb or steady-state temperature much earlier. Based on these estimates, rainbow thermometry was applied at three different axial planes in the spray flame, namely $Z = 3$, 4, and 5 cm.

The implementation of rainbow thermometry for fuel droplet temperature measurement requires two functional relationships: a relationship describing the dependence of the rainbow angle on the droplet refractive index and size, and another describing the dependence of the refractive index on temperature for the chosen fuel. The former relationship has been computed using the exact Lorenz–Mie theory, Fig. 6. On the other hand, the refractive index–temperature relationship for kerosene was obtained experimentally, Fig. 11. The refractive index was measured using a Milton Roy Abbe 3-L high resolution refractometer. The temperature of the kerosene sample placed in the refractometer was raised by circulating hot water through the refractometer. Unfortunately, the refractometer is designed to withstand a maximum temperature of only 373 K. Therefore the experimentally obtained data had to be linearly extrapolated for higher liquid temperatures. The slope of 0.0004/K that was obtained from Fig. 11 appears consistent with that available in the literature for kerosene and other liquids.

Typical rainbow signals obtained in the spray flame at an axial location of $Z = 4.0$ cm and a radial location of $r = 2.5$ cm are shown in Figs. 12 and 13. Figure 12 corresponds to a kerosene droplet having a diameter of 118 μm and moving axially at about 17 m/s. This signal is basically free of noise; also, the characteristic high-frequency oscillations is absent from the rainbow signature. This is a direct result of the small changes in droplet diameter that occur due to droplet vaporization. Since the phase of the high-frequency oscillations is very sensitive to changes in droplet diameter, the oscillations tend to be washed out if the exposure time of the CCD camera is sufficiently long. Therefore, rapidly vaporizing or regressing

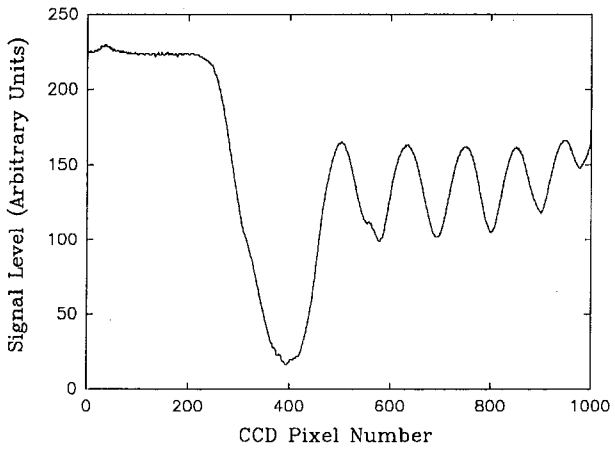

Fig. 12 Typical noise-free rainbow signal

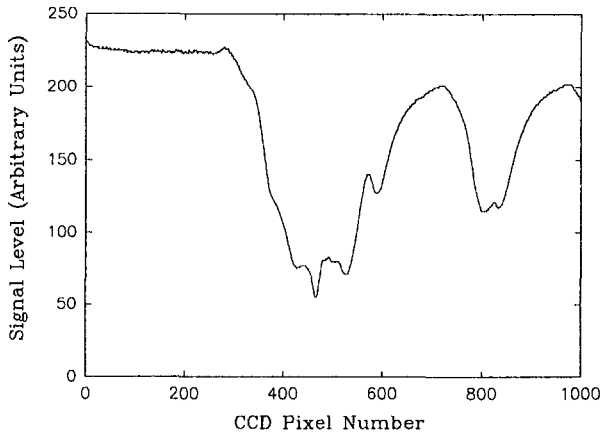

Fig. 13 Typical noisy rainbow signal

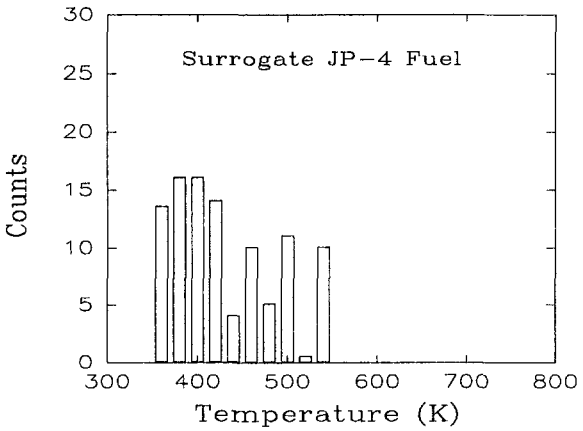

Fig. 15 Expected temperature histogram for a surrogate JP-4 fuel

droplets can help to filter out the high-frequency oscillations from the rainbow signature and improve the droplet temperature measurement accuracy. Figure 13, on the other hand, presents a noisy rainbow signal corresponding to a droplet diameter of 77 μm and an axial velocity of 14 m/s. The presence of high-frequency oscillations, and probably particle obscurations, tends to deteriorate the rainbow signal to some extent. For most effective processing of "bad" rainbow signals, the complete signal will have to be digitized and postprocessed. This will allow for different digital filtering and validation criteria to be implemented as a means of reducing measurement errors. In this study, however, only the peak detection system was used for the droplet temperature measurement.

A typical histogram of the measured droplet temperature at Z = 4.0 cm and r = 2.5 cm in the spray flame is presented in Fig. 14. The histogram exhibits multimodality and also shows a wide range in the measured droplet temperatures (about 400 K to 600 K). This wide range is a direct result of the distillation of kerosene and agrees well with the following specification provided by the manufacturer: initial boiling point of 450 K, 10 percent boil-off at 470 K, 50 percent boil-off at 490 K, 90 percent boil-off at 515 K, and a final boiling point of 550 K. The fact that the maximum droplet temperature is higher than the final boiling point of 550 K can be attributed to various factors including multicomponent fuel and the fact that the peak detection technique that was implemented does not allow for the satisfactory rejection of "bad" measurements.

The multimodality observed in Fig. 14 is believed to arise due to the fact that kerosene is a multicomponent fuel and because the droplet heat transfer process is unsteady (due to turbulence and flame temperature fluctuations). As an illustration, Fig. 15 shows the expected temperature histogram computed for a surrogate JP-4 fuel based upon its composition described by Wood et al. (1989). The theoretical data presented in Fig. 15 are similar to the experimental data shown in Fig. 14, suggesting that the multimodality could indeed be a manifestation of the composition of multicomponent fuels. This explanation is indeed simplistic, for gas phase recirculations, particle dynamics, turbulence, temperature fluctuations, and other complex flow and heat transfer phenomenon could also contribute to a skewing of the measured temperature histogram. For example, the droplet temperatures in the spray flame at this measurement location (Z = 4.0 cm and r = 2.5 cm) were found to exhibit a degree of dependence on the droplet size. The temperature histogram for droplets ranging in size from 45–65 μm is shown in Fig. 16. For this case, the measured temperatures are lower than that in Fig. 14, and the temperature range is much narrower with the mean droplet temperature being around 450 K. Also, the histogram presented in Fig. 16 does not exhibit multimodality. On the other hand, the temperature histogram for droplets ranging in size from 95–115 μm was observed to be similar to that presented in Fig. 14. Interestingly, this implies that the heat transfer to the larger droplets is greater than that to the smaller droplets.

Similarly, it was also observed that slow moving droplets, for example, those moving between 4.0–7.5 m/s, exhibit a temperature histogram almost identical to that shown in Fig. 16, whereas faster moving droplets exhibit a wider range, multimodal histogram such as that shown in Fig. 14. The reason

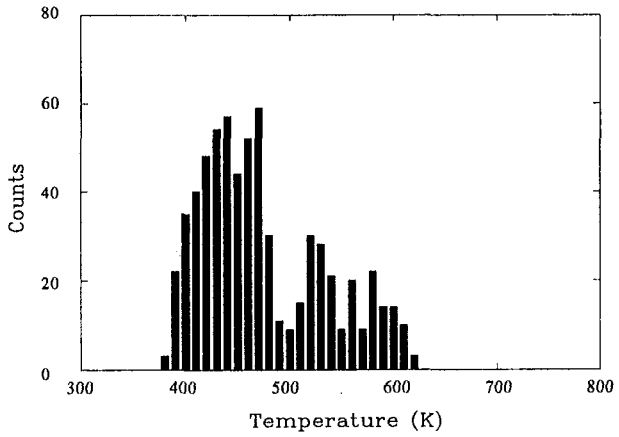

Fig. 14 Measured droplet temperature histogram at Z = 4.0 cm and r = 2.5 cm

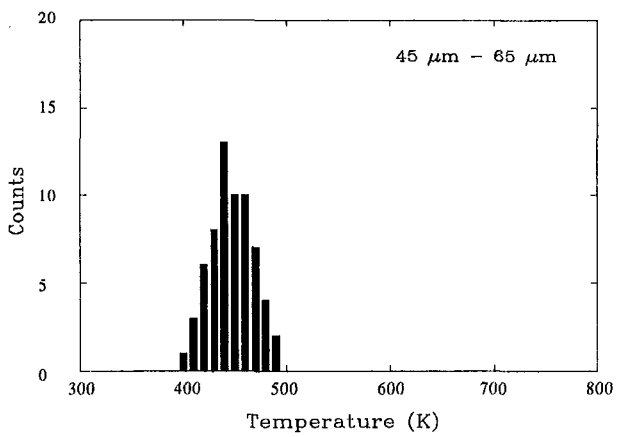

Fig. 16 Measured droplet temperature histogram for droplets having diameters between 45 μm and 65 μm

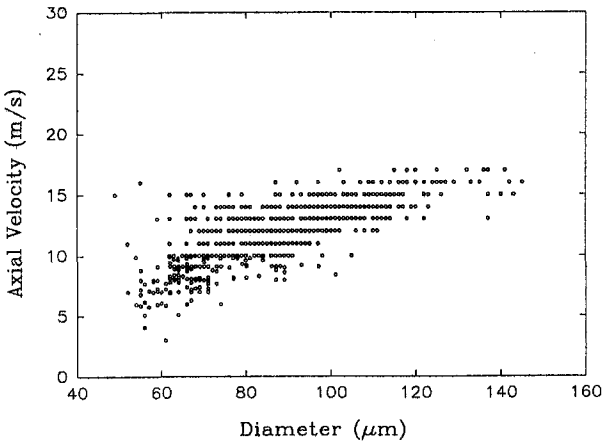

Fig. 17 Measured size–velocity correlation in the spray flame

for this becomes clear by examining a typical droplet size–velocity correlation shown in Fig. 17. This figure shows that the smaller droplets in the spray flame are generally moving at a slower velocity than the larger droplets, which is a typical behavior for pressure atomizers. Furthermore, since the measurement point falls within the gas phase internal recirculation region, the hot gases are moving in a direction opposite to the fuel droplets. Therefore, the velocity differential between the droplet and gas phase motion is greater for the larger drops than the smaller drops. The Reynolds number based upon the relative velocity, droplet diameter, and gas properties is about 4–5 times greater for the larger drops than the smaller drops. As a result, convective heat transfer is greater for the larger particles (Sirignano, 1983). Also, the larger shear forces acting on the liquid surface for the large drops can cause internal circulation within the droplets, thereby enhancing the heating of the larger drops.

The evolution of droplet temperatures in the radial and axial directions is depicted in Fig. 18, which shows the measured temperature histograms for several different points in the radial and axial directions. Only 1000 samples were acquired at each measurement point for this preliminary study. The left column in Fig. 18 corresponds to temperature histograms obtained at an axial location of $Z = 3.0$ cm. From top to bottom, the radial locations where these measurements were made correspond to $r = 1.9$, 2.2, and 3.0 cm, respectively. Similarly, the center and right-most columns correspond to measurements made at $Z = 4.0$ cm and $Z = 5.0$ cm, respectively. For $Z = 4.0$ cm, the radial locations where measurements were made are $r = 2.3$, 2.9, and 3.3 cm and for $Z = 5.0$ cm, the radial locations are $r = 3.3$, 3.7, and 4.1 cm, respectively. The data presented in Fig. 18 show that the droplet temperatures generally decrease with increasing axial and radial positions in the flame. An especially interesting point to note in Fig. 18 is that at the outer edges of the spray the temperature histogram no longer exhibits multimodality. The outer edge of the spray is a region of generally lower gas phase temperature and lower relative velocities between the droplet and gas phase (the gas phase in this region is moving along the same direction as the droplets) and as a result, the convective heating of the droplets is lower.

The axial and radial variation of the mean droplet temperature has been represented in Fig. 19. At $Z = 3.0$ cm, the mean droplet temperature first shows an increase in the radial direction, reaching a maximum at about $r = 2.2$ cm, and then starts decreasing with increasing radial distances. At $Z = 4.0$ cm, the mean droplet temperature decreases with increasing radial distances, and at $Z = 5.0$ cm, the mean droplet temperatures remain fairly constant. Flow visualization experiments using a laser light sheet clearly showed that at $Z = 5.0$ cm, the droplets

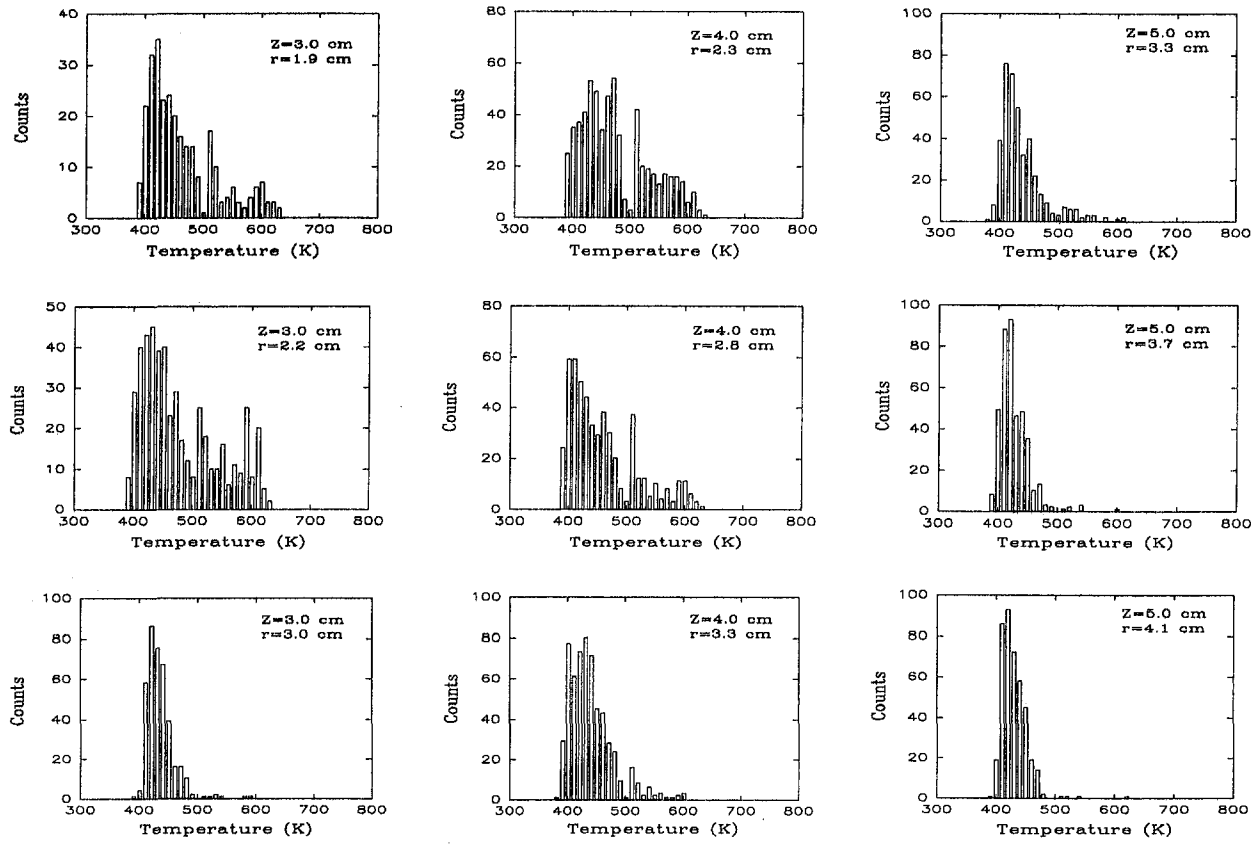

Fig. 18 Measured droplet temperatures at several points in the spray flame depicting the radial and temporal evolution of fuel droplet temperatures

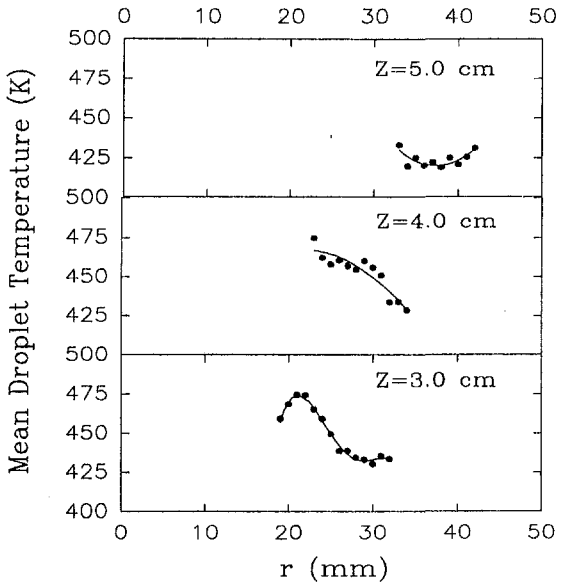

Fig. 19 Measured radial and axial variation of the mean fuel droplet temperature

are completely outside the flame region. This could be the reason for the generally lower droplet temperatures at this measurement plane. An excellent flow visualization photograph showing the penetration of large droplets through a methanol swirl stabilized spray flame has been presented by Presser et al. (1990).

The measured temperature dependence on droplet diameter at several axial and radial locations in the spray flame is presented in Fig. 20. The temperature–diameter correlations shown in Fig. 20 correspond to the temperature histograms shown in Fig. 18. It is interesting to observe that for points lying within the hot gas internal recirculation zone, the mean temperatures for the large droplets are greater than those for the small droplets. This issue has already been discussed earlier in this paper. However, for points on the outer edges of the spray and at increasing axial location, the mean temperature for the smaller droplets is greater than that for the large droplets.

6.2 Droplet Regression Rate Measurement. Measurements were also conducted to examine and demonstrate the feasibility of using the *phase* and *frequency* approaches as sensitive means for measuring small changes in the drop size. For the droplet combustion studies, this information can be used to measure the instantaneous droplet regression rates, and hence, the droplet vaporization rates. Because the implementation of the *phase* approach to regressing fuel droplets requires additional hardware (as explained earlier), we have tried to demonstrate its feasibility by applying it to nonevaporating water droplets generated by an Aerometrics Drop-on-Demand generator that allows for small changes in the droplet diameter. The droplets generated by this unit are highly stable and repeatable. Furthermore, the high voltage applied to the piezo-electric transducer can be varied slightly to cause small changes in the droplet diameter. Therefore, in this study, the high voltage supplied to the droplet generator was slowly varied to examine whether it could produce a measurable change in the high-frequency pattern of the rainbow signature. A high-pass FFT filter was applied to the rainbow signal to extract the high-frequency oscillations from the measured data; see Fig. 21. In Fig. 22, the extracted high-frequency oscillations for two slightly different voltage settings are compared. In order to visually detect any differences in the pattern, we have zoomed into a region in the neighborhood of the main rainbow. The data presented in Fig. 22 show that the two wave patterns are approximately 90 deg out of phase. Using the previously computed calibration/response

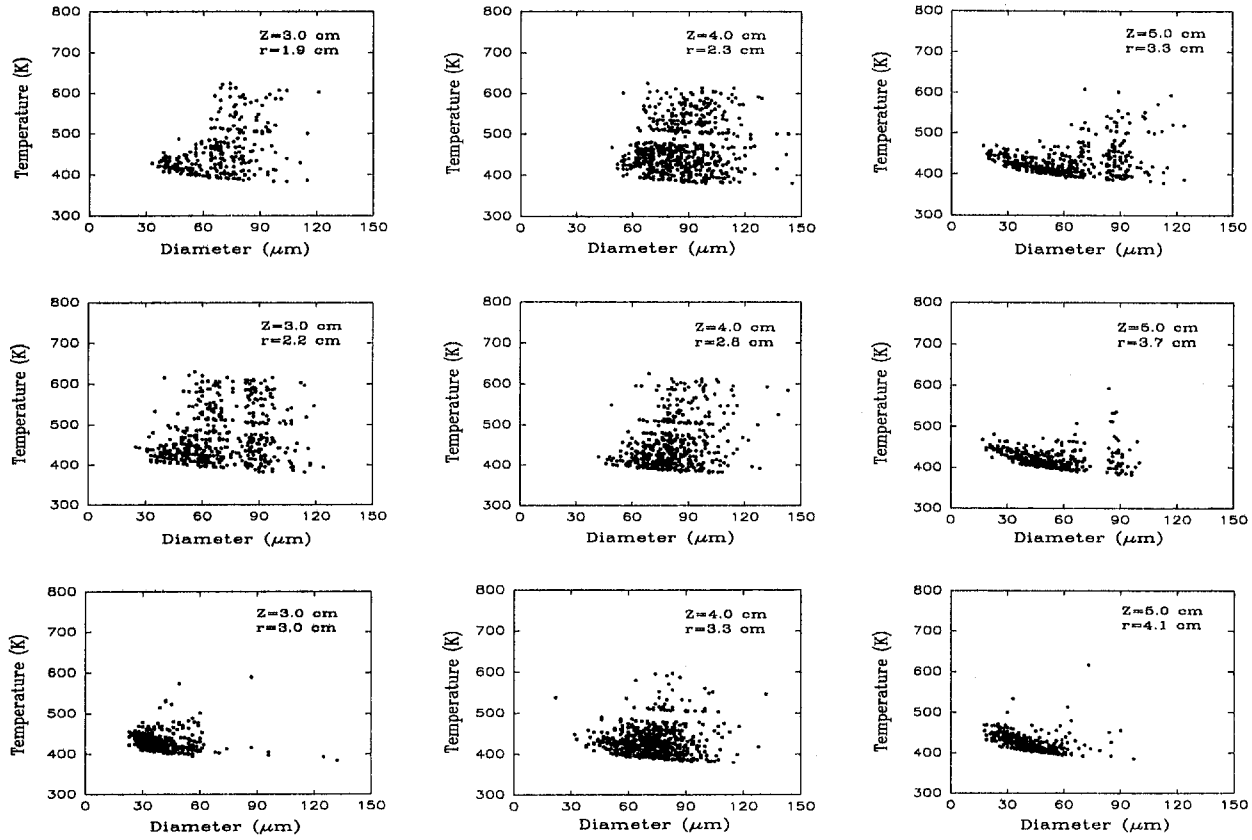

Fig. 20 Measured temperature-diameter correlations at several axial and radial points within the spray flame

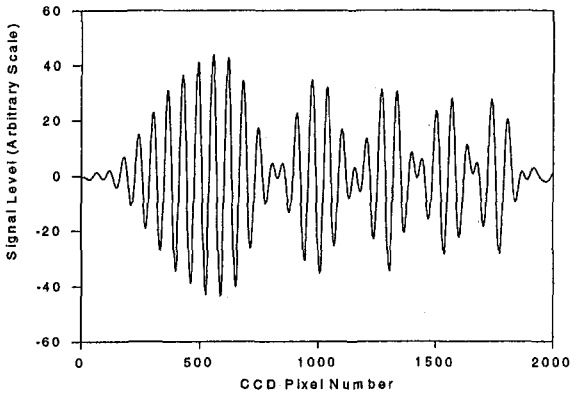

Fig. 21 High pass filtered experimental rainbow signal

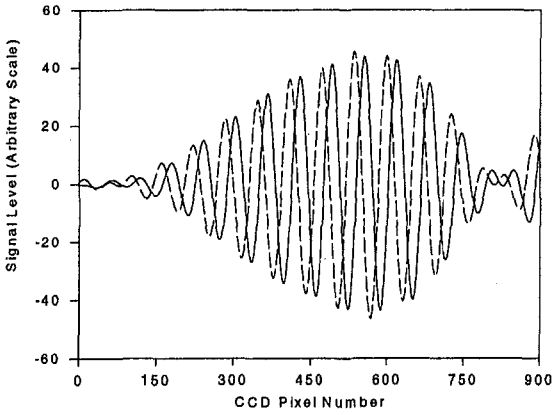

Fig. 22 High pass filtered rainbow signal for two different voltage settings on the drop-on-demand generator

curves, it can determined that this phase shift corresponds to a change in droplet diameter of approximately 0.06 μm. This clearly shows that the high-frequency waveform can be used as a sensitive means of measuring the droplet regression rates in droplet combustion experiments. On the other hand, Fig. 23 compares the low-frequency oscillations for the same two voltage settings. The two patterns are identical, which suggests that the low-frequency oscillations cannot be used to measure small changes in the droplet diameter.

The measured variations in the diameter of the water droplets resulting from continuously increasing the voltage supplied to

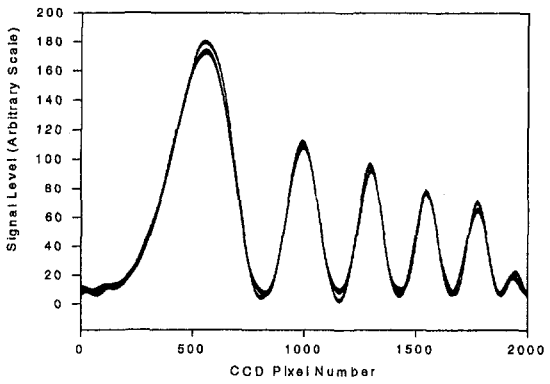

Fig. 23 Low pass filtered rainbow signal for two different voltage settings on the drop-on-demand generator

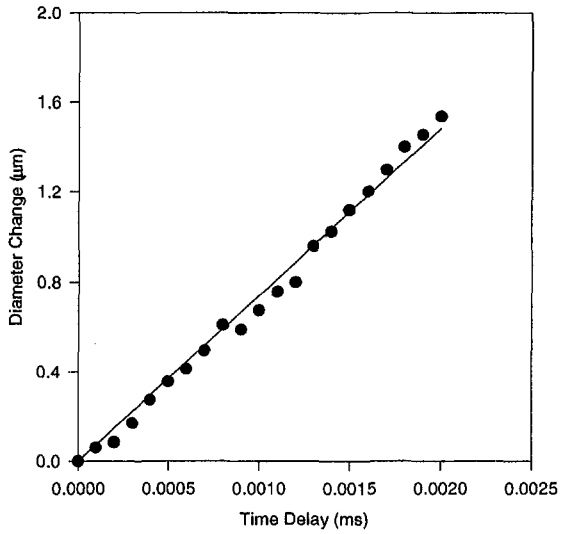

Fig. 24 Measured changes in the droplet diameter as the voltage to the piezo-electric transducer is varied. The time delay is a measure of the voltage applied to the transducer.

the piezo-electric transducer is plotted in Fig. 24. Since the changes in the voltages were so small, they could not be accurately measured. However, changing the voltage slightly also caused a change in the droplet velocity. Therefore, the data in Fig. 24 have been plotted against a time delay that corresponds to the time taken by the droplets to reach the measurement point with reference to the TTL signals supplied to the piezo-electric transducer. A linear variation of the droplet diameter changes with respect to the time delay is observed in Fig. 24. Also, the total change in droplet diameter is about 1.6 μm, which is less than 1 percent of the droplet diameter (180 μm).

The feasibility of using the *frequency* method for droplet regression measurement has also been investigated. For this, measurements were conducted in a burning stream of ethanol droplets generated by a monodisperse droplet generator. A photograph of the burning ethanol droplets is shown in Fig. 25. The droplets are moving vertically upward in this figure. Using the breadboard optical system, rainbow signatures and resonant spectra were obtained at different points within the burning droplet stream. As discussed earlier, the droplet temperature was determined from the digitized rainbow signature and the droplet diameter was measured using phase Doppler interferometry. The resonant spectra were also digitized and processed to determine the frequency of intensity oscillations. This information was used in conjunction with the previously computed response curves to establish the droplet regression rate. From a knowledge of the droplet regression rate and the droplet diameter, the evaporation constant (λ) can be computed as follows:

$$\lambda = 2D\frac{dD}{dt} \tag{3}$$

A typical resonant spectrum that was obtained in the flame zone is shown in Fig. 26. The high-frequency oscillations in the figure correspond directly to changes in the droplet diameter. The low-frequency pedestal is a direct result of the Gaussian incident intensity on the droplet. The corresponding high pass filtered signal is presented in Fig. 27. Table 1 provides a summary of the measured size, temperature, regression rate, and evaporation constant for four different measurement points within the flame zone. The evaporation constant is approximately 0.65 mm^2/s at each measurement point. Furthermore, this value is in good agreement with typical evaporation constants that can be found in the combustion literature. Therefore, this study clearly demonstrates the feasibility of using the reso-

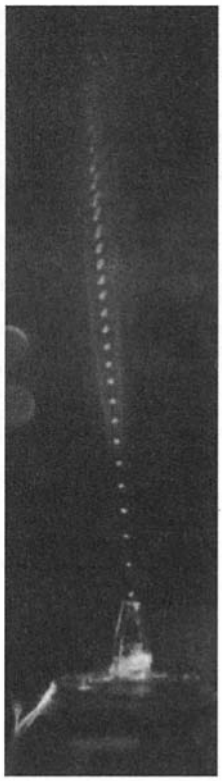

Fig. 25 Photograph of the burning stream of ethanol droplets. The droplets are moving vertically upward.

nant spectrum for measuring the instantaneous droplet regression rates and evaporation constants.

7 Conclusions

The newly integrated phase Doppler interferometer/rainbow thermometer has been successfully applied for studying fuel droplet temperature characteristics in a swirl-stabilized kerosene spray flame. The measured data show that droplet temperatures are dependent upon the droplet size and velocity. Within the hot gas phase internal recirculation region, higher convective heating of the larger droplets causes them to have higher temperatures than the smaller droplets. However, the droplet temperatures generally decrease with increasing radial and axial distance from the nozzle. Also, in the outer regions of the spray, the mean temperature of the smaller droplets is greater than that

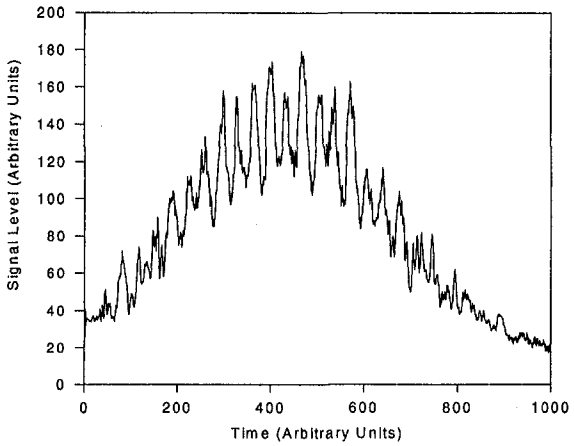

Fig. 26 Experimentally obtained resonant spectrum for a point within the burning zone

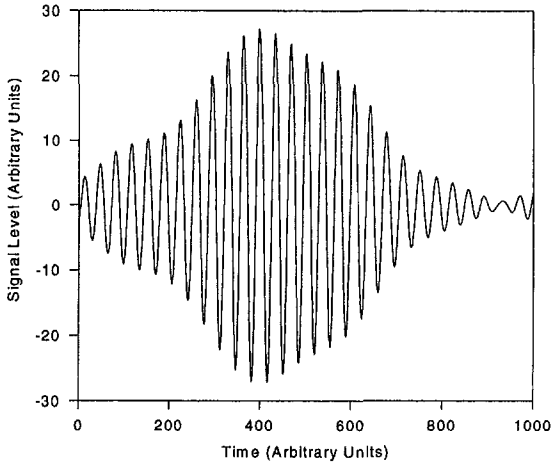

Fig. 27 High pass filter applied to the experimentally obtained resonant spectrum. This signal represents a 5.9 μm change in droplet diameter that occurs over a 2 ms burning period.

Table 1 Measured evaporation constant

No.	Diameter (μm)	Temp. (K)	Regression Rate (mm/s)	Evap. Const. (mm^2/s)
1	110.0	335.0	2.95	0.649
2	95.0	335.0	3.42	0.650
3	80.0	335.0	3.98	0.637
4	65.0	335.0	5.12	0.666

for the large particles. The feasibility of using a novel extension of rainbow thermometry for the instantaneous measurement of fuel droplet regression rates has also been demonstrated.

The final issue pertains to the feasibility of integrating the newly developed droplet regression measurement technique to the PDPA and the rainbow refractometer to yield an integrated diagnostics that can be used for the simultaneous measurement of fuel droplet size, velocity, temperature, and instantaneous regression rate in complex spray flames. The results obtained in this study shows that the addition of droplet regression measurement capability should not pose a significant hurdle. Depending upon whether the *phase* or *frequency* approach is to be used, an additional CCD camera and/or an additional PMT will have to be incorporated into the rainbow receiving optics. Of course, the regular CCD camera may need to be replaced by intensified CCD cameras and the additional PMT might need to be of the multichannel format. The inclusion of these electro-optic components will necessitate a redesign of the optical receiver. Additional electronics to control the multichannel PMT, additional ADCs, and gating circuits to control the intensified camera will need to be developed and incorporated. This is indeed feasible and our future efforts will be directed toward this end.

Acknowledgments

This work has been supported by the NASA Lewis Research Center under Contract No. NAS3-26248 and by the NASA Marshall Space Flight Center under Contract No. NAS8-40503.

References

Anderson, T. J., and Winter, M., 1992, "Measurements of the Effect of Acoustic Disturbances on Droplet Vaporization Rates," presented at the 30th Aerospace Sciences Meeting and Exhibit, Reno, NV, Jan. 6–9.

Bachalo, W. D., and Houser, M. J., 1984, "Phase Doppler Spray Analyzer for Simultaneous Measurements of Drop Size and Velocity Distributions," *Optical Engineering,* Vol. 23, pp. 583–590.

Bauckhage, K., and Flogel, H. H., 1984, "Simultaneous Measurements of Droplet Size and Velocity in Nozzle Sprays," presented at the 2nd Intl. Symp. on Appl. of Laser Anemometry, Lisbon, Portugal.

Chigier, N., and McCreath, C. G., 1974, "Combustion of Droplets in Sprays," *Acta Astronautica,* Vol. 1, pp. 687–710.

Chigier, N., 1991, *Combustion Measurements,* Hemisphere Publishing Co., New York.

Eckbreth, A. C., 1988, *Laser Diagnostics for Combustion Temperature and Species,* Energy and Engineering Science Series, Vol. 7, Abacus Press.

Edwards, C. F., and Rudoff, R. C., 1990, "Structure of a Swirl-Stabilized Spray Flame by Imaging, Laser Doppler Velocimetry, and Phase Doppler Anemometry," *Proc. Twenty-Third Symp. (Intl.) on Combustion,* Orleans, France, The Combustion Institute, pp. 1353–1359.

Faeth, G. M., 1983, "Evaporation and Combustion of Sprays," *Prog. Energy Combustion Science,* Vol. 9, pp. 1–76.

Ibrahim, K. M., Werthimer, G. D., and Bachalo, W. D., 1991, "Signal Processing Consideration for Laser Doppler and Phase Doppler Applications," in: R. J. Adrian, D. F. G. Durao, F. Durst, M. Maeda, and J. H. Whitelaw, eds., *Applications of Laser Techniques to Fluid Mechanics,* Springer-Verlag, Berlin, pp. 291–316.

Kai Li, Massoli, P., and D'Alessio, A., 1993, "Studying Inhomogeneities of Spherical Particles by Light Scattering," *Proc. 3rd Intl. Congress on Optical Particle Sizing,* Yokohama, Japan, pp. 135–143.

Law, C. K., 1982, "Recent Advances in Droplet Vaporization and Combustion," *Prog. Energy Combustion Science,* Vol. 8, pp. 171–201.

Lefebvre, A. H., 1989, *Atomization and Sprays,* Taylor & Francis.

Presser, C., Gupta, A. K., Avedisian, C. T., and Semerjian, H. G., 1990, "Fuel Property Effects on the Structure of Spray Flames," *Proc. Twenty-Third Symp. (Intl.) on Combustion,* Orleans, France, The Combustion Institute, pp. 1361–1367.

Sankar, S. V., and Bachalo, W. D., 1991a, "Response Characteristics of the Phase Doppler Particle Analyzer for Sizing Spherical Particles Larger Than the Light Wavelength," *Applied Optics,* Vol. 30, No. 12, pp. 1487–1496.

Sankar, S. V., and Bachalo, W. D., 1991b, "Sizing Fine Particles With the Phase Doppler Interferometric Technique," *Applied Optics,* Vol. 30, No. 33, pp. 4914–4920.

Sankar, S. V., Ibrahim, K. M., Buermann, D. H., Fidrich, M. J., and Bachalo, W. D., 1993, "An Integrated Phase Doppler/Rainbow Refractometer System for the Simultaneous Measurement of Droplet Size, Velocity, and Refractive Index," presented at the 3rd Intl. Congress on Optical Particle Sizing, Yokohama, Japan.

Schneider, M., Hirleman, E. D., Saleheen, H., Chowdhury, D. Q., and Hill, S. C., 1993, "Rainbows and Radially-Inhomogeneous Droplets," *Proc. 3rd Intl. Congress on Optical Particle Sizing,* Yokohama, Japan, pp. 323–326.

Sirignano, W. A., 1983, "Fuel Droplet Vaporization and Spray Combustion Theory," *Prog. Energy Combustion Science,* Vol. 9, pp. 291–322.

van de Hulst, H. C., 1981, *Light Scattering by Small Particles,* Dover Publications, Inc., New York.

Wood, C. P., McDonell, V. G., Smith, R. A., and Samuelsen, G. S., 1989, "Development and Application of a Surrogate Distillate Fuel," *J. Propulsion and Power,* Vol. 5, No. 4, pp. 399–405.

Wriedt, T., Bauckhage, K. A., and Schone, A., 1989, "Application of the Fourier Analysis to Phase Doppler Signal Correlated by Rough Metal Particles," *IEEE Trans. on Instrumentation and Measurement,* Vol. 38, No. 5, pp. 984–990.

Emissions Characteristics of Liquid-Fueled Pilot Stabilized Lean Premixed Flames in a Tubular Premixer-Combustor

P. Dutta[1]

J. P. Gore

P. E. Sojka

Thermal Sciences and Propulsion Center,
School of Mechanical Engineering,
Purdue University,
West Lafayette, IN 47907

Global emissions of NO_x in a liquid-fueled lean-premixed tubular combustor with a tubular premixer operating under atmospheric pressure are studied experimentally. The effects of equivalence ratio, premixer length, residence time, fuel type, and fuel atomization and dispersion characteristics on NO_x emissions are studied. Measurements of exhaust species concentrations are used as the primary indicator of the effectiveness of premixing-prevaporization upstream of the combustor. Qualitative levels of prevaporization-premixing are determined from Mie-scattering signals measured at the exit of the premixer. Emission measurements show that the equivalence ratio is the dominant operating parameter, with premixing length and residence time being less significant within the present operating range. Ultralow NO_x operation (<10 ppmv @ 15 percent O_2) is feasible for equivalence ratios less than 0.5. More significantly, small drops persist beyond the premixer even for very long premixers, and Mie-scattering measurements show considerable spatial inhomogeneity, while allowing ultralow NO_x operation. One-dimensional evaporation calculations for single drop trajectories confirm that complete evaporation for typical drop size distributions is not possible with reasonable premixer lengths under atmospheric pressure. Fuel dispersion is found to be the most critical parameter for high combustion efficiency, and adverse effects of poor fuel dispersion cannot be overcome by using longer premixers.

Introduction and Background

Reduction of oxides of nitrogen drives a major portion of current gas turbine combustion research. Lean premixed (LP) and catalytically stabilized combustion are the leading technologies available to achieve ultralow NO_x (<10 ppmv @ 15 percent O_2) emissions in future gas turbine combustors (Correa, 1992). However, unresolved issues of catalytic reactor stability and life, and substrate durability in catalytic combustion, make lean-premixed combustion the technology of choice for gas turbine applications in the near term.

Current low NO_x LP gas turbine combustors operate with <25 ppmv NO_x (corrected to 15 percent O_2) in a narrow operating range near full-load conditions using natural gas (e.g., Lovett and Mick, 1995). However, low NO_x operation with liquid fuels (typically No. 2 oil) is a major challenge because of additional complications of liquid atomization, drop dispersion and evaporation, increased auto-ignition problems, and fuel coking. Emissions of NO_x in the 70-90 ppmv (corrected to 15 percent O_2) range at full load conditions are typically achieved. Improved understanding of the physical processes of drop formation, dispersion and evaporation, and premixing of fuel vapor and air prior to flame stabilization is required for designing low NO_x liquid-fueled combustors. Extensive evaluation of lean-premixed-prevaporized (LPP) combustor hardware concepts was conducted as a part of the NASA SCERP program in the '70s and early '80s (e.g., Cooper, 1979; Eckstead and Fear, 1987; Roffe and Ferri, 1975, 1976; Lyons, 1982). Recent environmental concerns about NO_x emissions dictate LPP combustion, and current combustion research focuses on lean-premixed combustion technology.

The success of any lean-premixed combustion system hinges on being able to achieve a uniform fuel–air mixture, so that combustion always occurs at the overall lean equivalence ratio. Some recent studies (e.g., Fric, 1992) address issues of premixing in natural gas fired systems, and indicate that the levels of NO formation are very sensitive to the fuel–air unmixedness. Experimental and computational studies in simple liquid-fueled LPP configurations are useful for analysis of more complex combustion systems. The present work focuses on a simple LPP combustor operating at atmospheric pressure with a pilot stabilized flame, to perform a systematic study of the effects of the variation in global equivalence ratio, premixing lengths, residence time, atomization characteristics, fuel dispersion and fuel property effects on global NO_x emissions. The use of a pilot flame is necessary to avoid a central recirculation zone for flame stabilization, and to keep the flow field relatively simple for computations. Qualitative measurements of premixing-prevaporization are obtained. Evaporation calculations along single drop trajectories under locally laminar flow assumptions are performed to confirm the qualitative observations of fuel vaporization.

Experimental Methods

Apparatus. A schematic of the experimental apparatus is shown in Fig. 1. An atmospheric pressure tubular combustor, supplied with a fuel–air mixture by a tubular premixer (3.8 cm diameter) involving an interchangeable atomizer located upstream of the premixing section is used in the experiments. In an earlier study (Roffe and Ferri, 1976), tubular premixers were found to be less susceptible to problems of auto-ignition and flashback at higher operating pressures. A coflow of preheated air is obtained using electrical immersion heaters. The

[1] Current address: Solar Turbines Inc., 2200 Pacific Highway, P.O. Box 85376, MZ E-4, San Diego, CA 92186-5376.

Contributed by the International Gas Turbine Institute for publication in the JOURNAL OF ENGINEERING FOR GAS TURBINES AND POWER. Manuscript received by the International Gas Turbine Institute November 1, 1996. Associate Technical Editor: J. E. Peters.

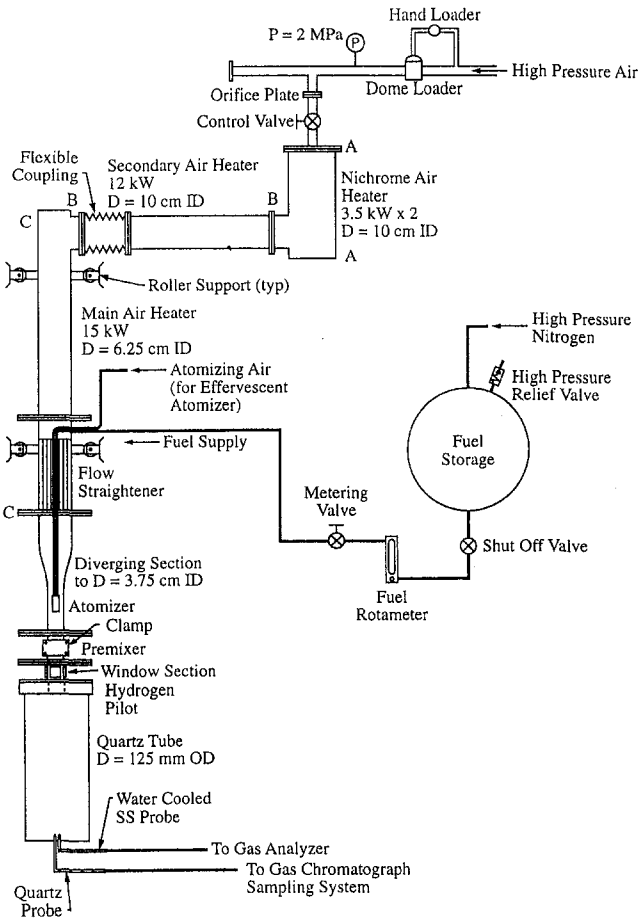

Fig. 1 Schematic of experimental apparatus

fuel spray vaporizes and mixes in the coflowing hot air stream. A pilot ring flame burning very low amounts of hydrogen (about 2 percent by mass of the liquid fuel) is used to stabilize a premixed main flame in a sudden expansion downstream of the premixer. A 125 mm outer diameter, 1-m-long quartz tube contains the flame while allowing visual access. Gas sampling probes mounted at the exit of the quartz tube are used to sample combustion products for analysis using on-line analyzers.

A Mie-scattering apparatus is utilized to measure the scattering signals from the ubiquitous liquid drops, as an indicator of the relative levels of prevaporization-premixing at the premixer exit. A short tubular section with four optical grade quartz windows purged with nitrogen is mounted downstream of the premixer section to allow optical access. In order to accommodate thermal expansion of the test section at elevated air temperatures, a flexible coupling (in section B–B in Fig. 1) and a clamping arrangement are utilized to hold the optical windows in place.

Instrumentation. A water-cooled stainless-steel probe is used to draw samples into the gas analysis system. Species concentrations are measured using a chemiluminescence-based NO/NO_x analyzer, a nondispersive infrared CO_2 analyzer, a gas filter correlation CO analyzer, a flame ionization detector based hydrocarbon analyzer, and a gas-chromatograph with a thermal conductivity detector. The accuracies of the instruments are 1 percent of full-scale for the NO/NO_x measurements, 0.3 percent for the CO_2 measurements, and 0.5 ppm for the CO measurements. A chiller-trap is used to condense out water before the sample enters the NO/NO_x and CO/CO_2 analyzers. The emission measurements reported in the study are based on measurements at the centerline of the flow. However, detailed traverses across the quartz tube cross section were performed to ensure radial uniformity of the measurements and details are available elsewhere (Dutta, 1995).

A 3 W argon-ion laser is used as the light source for the scattering measurements. The scattered light is collected at an angle of 90 deg to the incident beam direction. A 65 mm focal length lens is used to focus the scattered light on to a 1-mm-dia aperture, with a photomultiplier tube (with a 514 nm optical filter) placed behind the aperture. All the receiving optics are mounted on a precision optical jack in order to be able to traverse the entire cross section of the premixer accurately. The incident beam is chopped by an optical chopper at 1000 Hz, and the reference signal is input to a lock-in amplifier. The output of the photomultiplier is band-pass filtered before being input to the lock-in amplifier. The output of the lock-in amplifier is passed through a low-pass anti-aliasing filter set at 400 Hz before being read into a data acquisition program. The background signal is recorded before the fuel flow is started. Once the fuel flow is started, the signal is recorded again. The difference between this signal and the background signal is the scattered signal due to the presence of the fuel–air mixture and the unevaporated drops in the probe volume. Characterization of atomizer performance is conducted under cold flow conditions using a Malvern 2600 series particle sizer, with a 300 mm focal length lens. Details of the operation of the instrument are available elsewhere (Swithenbank et al., 1977). Hot-wire probes (Dantec 55P11) are used to measure mean and rms velocities at the inlet to the premixer under cold flow conditions in the absence of the spray.

Fuel Injection. Standard pressure swirl atomizers (Hago precision burner nozzles) with 30 deg spray cone angles are used for the baseline measurements. However, due to the poor turndown for these atomizers, measurements are limited to a fixed fuel flow rate (close to the rated capacity of the atomizers) so that initial drop size distributions do not change between operating conditions. Thus, changes in equivalence ratio are accompanied by changes in the air flow rate, and hence, a change in the residence time in the premixer and in the flame zone. Effervescent atomizers are used to overcome this limitation due to their excellent turndown characteristics. Two effervescent atomizer designs are used in the experiments. The first design followed the work of Lund et al. (1993) with a single central atomizer discharge orifice, while the second design involved an atomizer similar in concept to the first, but incorporating multiple fuel discharge orifices in order to improve the initial fuel distribution (Fig. 2).

Emissions measurements are conducted with No. 2 oil and *n*-heptane as fuels. The composition of the No. 2 oil used is matched closely to the composition of current gas turbine fuels in terms of the C/H ratio and Fuel-Bound Nitrogen (measured FBN in the fuel ~ 147 ppmv). Measurements with *n*-heptane allow the study of the effects of fuel property variation on emissions. Further details of the experimental apparatus, instrumentation, effervescent atomizer design, and fuel composition have been provided by Dutta (1995).

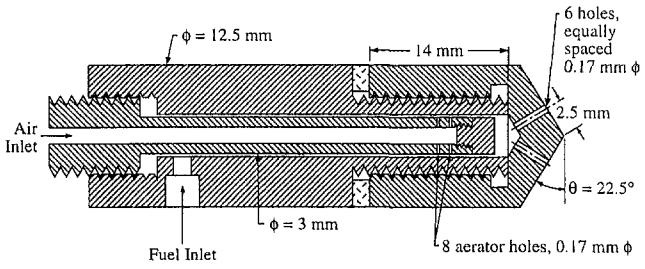

Fig. 2 Schematic of multi-orifice effervescent atomizer

Evaporation Calculations

A simple one-dimensional calculation procedure following Abramzon and Sirignano (1989) is used to obtain estimates of evaporation rates along single one-dimensional trajectories of drops. Mono-dispersed fuel drops are assumed to be uniformly distributed across the constant area tubular premixer, and the number flux of the drops remains unchanged until all drops are completely evaporated simultaneously. Equations for the conservation of mass, energy, and fuel species are solved in conjunction with drop heating and evaporation rates. In order to account for convective effects, the effective evaporation rate at the surface is obtained by using a modified Sherwood number Sh*, so that the surface evaporation rate $\dot{m}''_{Fs}$ is given by:

$$\dot{m}''_{Fs} = \frac{\bar{\rho}_g \bar{\zeta}_g \, \mathrm{Sh}^* \ln\,(1 + B_M)}{D}$$

where the density, $\bar{\rho}_g$, and the diffusion coefficient, $\bar{\zeta}_g$, are evaluated at the reference temperature and mass fraction (Renksizbulut and Haywood, 1988), D is the drop diameter, and B_M is the mass transfer number. The modified Sherwood number is related to the Sherwood number through a correction factor $F(B_M)$, which is a function of the mass transfer number and is estimated from film theory (Abramzon and Sirignano, 1989). Drop heating is accounted for by using an infinite conductivity model, where the drop internal temperature is assumed to be spatially uniform, but temporally varying. The heat transferred into the drop, $\dot{Q}_L$, is given by:

$$\dot{Q}_L = 4\pi r_s^2 \lambda_L \left(\frac{dT_L}{dr}\right)_{r_s}$$

where r_s is the radius of the drop, λ_L is the thermal conductivity of the liquid, and T_L is the drop internal temperature. The heat transferred can be evaluated from the heat transfer number, B_T, and the mass transfer number, B_M.

The equations are solved using a second-order Runge–Kutta method to obtain the drop size, gas and liquid temperature, drop velocity, and the mass fraction of fuel vapor, as a function of the distance from the injection point. Initial conditions for air and liquid mass fluxes, gas and liquid temperatures, fuel mass fraction, drop diameter, and drop velocity are prescribed from experimental conditions. The present laminar one-dimensional calculations provide the length of the trajectory needed for complete drop evaporation. This is an upper bound on the premixer length, since turbulent fluctuations in the gas-phase velocity lead to drop trajectories in the premixer that are longer than the premixer length.

Results

Effective atomization of the fuel is crucial to the prevaporization-premixing process. In order to characterize the performance of the pressure swirl atomizers, drop size measurements were made in a cold spray along the atomizer centerline at a distance of 10 cm downstream of the atomizer exit orifice. Drop size distributions for the four pressure swirl atomizers used in the study (denoted as Nozzles 1, 2, 3, and 4) are shown in Fig. 3. The drop size measurements are made for fuel flow rates of 1.1, 0.9, 0.6, and 0.47 g/s, respectively. The Sauter mean diameter (SMD) varies between 33 and 53 μm for the four atomizers, with most of the drops being below 100 μm for these operating conditions. Measurements of drop size distributions on a single orifice effervescent atomizer similar to the current atomizer produced SMDs between 25 and 45 μm (see Dutta et al., 1994). Other drop size measurements on similar effervescent atomizer designs have been reported by Lund et al. (1993) and their references. In general, the spatial structure of the spray is similar to sprays produced by other twin-fluid atomizers, and shows an increase in SMD with an increase in r/x.

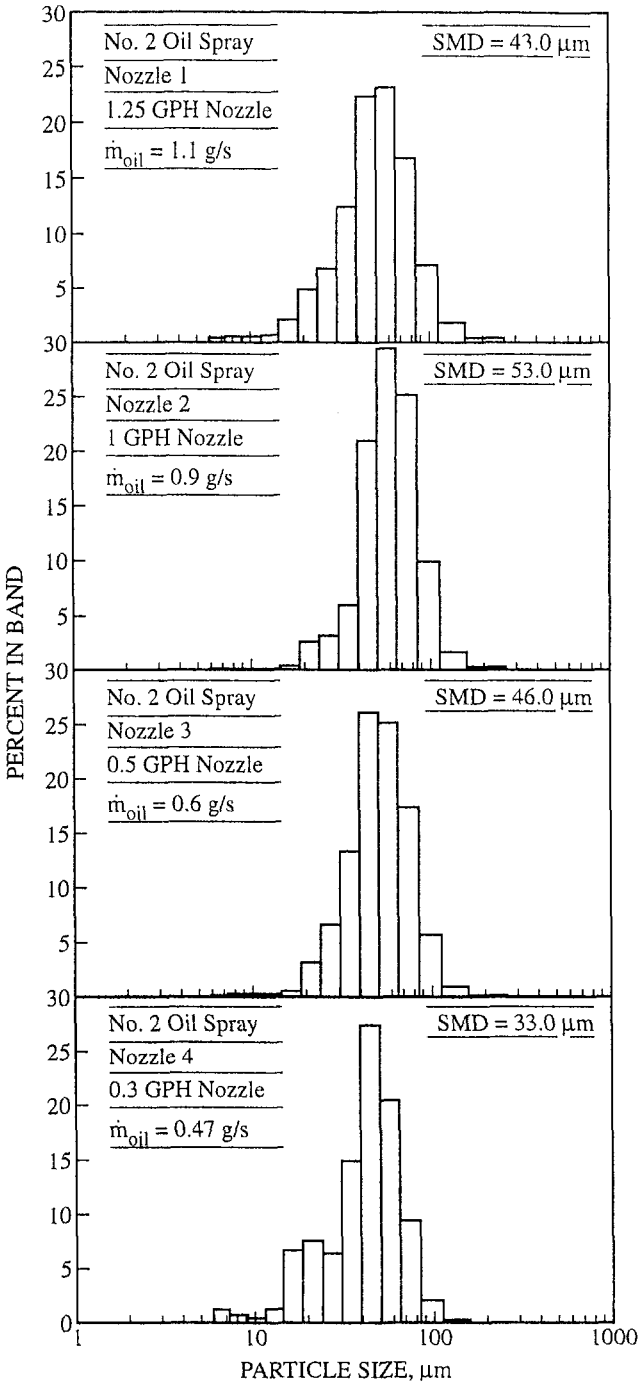

Fig. 3 Drop size distributions for the pressure swirl atomizers using No. 2 oil

Measurements of mean and rms axial velocity at the premixer inlet are shown in Fig. 4. The mean velocity and rms fluctuations in the wake of the injector are low. The intensity of turbulence is relatively high, and the flow field is dominated by the geometry of the atomizer.

Measurements of the concentration of NO_x in the exhaust corrected to 15 percent O_2 for the four pressure swirl atomizers and three premixer lengths (19, 38, and 76 cm) are plotted against equivalence ratio in Fig. 5. These measurements are performed with No. 2 oil, with an air preheat temperature of 400°C. The fuel mass flow rates for the atomizers are identical to the mass flow rates for which drop size measurements are shown in Fig. 3. The emissions measurements are repeatable to within 5 percent. The equivalence ratio based on exhaust CO_2

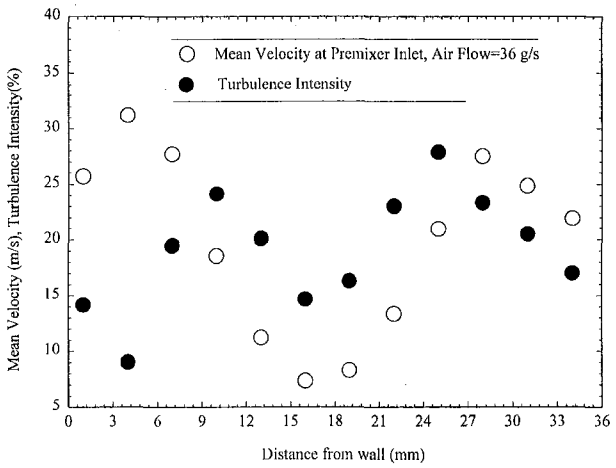

Fig. 4 Mean velocity and turbulence intensity at inlet of premixer for air flow rate of 36 g/s

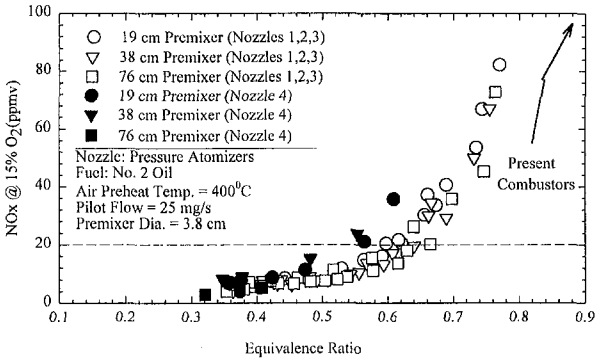

Fig. 5 Measurements of NO_x concentrations @ 15 percent O_2 in exhaust for varying equivalence ratio and premixer length for No. 2 oil

measurements is checked against the equivalence ratio based on the metered air and fuel flow rates to ensure high combustion efficiencies (>99 percent). The trends in the NO_x measurements are similar for all atomizers and all premixer lengths: The equivalence ratio is the dominant variable, while premixing lengths have a less significant effect, especially at lower equivalence ratios. For equivalence ratios less than 0.6, NO_x concentrations are less than 20 ppmv (at 15 percent O_2) for most operating conditions. The NO_x data for Nozzle 4 are somewhat higher than those for the other nozzles due to impingement of the spray on the wall of the premixer at higher equivalence ratios. This was a consequence of keeping the fuel flow constant, and reducing the air flow in order to increase the overall equivalence ratio. The emissions performance of present combustors are also shown in Fig. 5 for comparison. These results show that with the tubular premixer, tubular combustor configuration, ultralow NO_x operation (less than 10 ppmv @ 15 percent O_2) is possible for overall equivalence ratios below 0.5 with No. 2 oil. Assuming the entire FBN is converted to NO under lean burning conditions (Lefebvre, 1983), the contribution of the FBN to the total NO_x is approximately 1 to 2 ppmv (corrected to 15 percent O_2).

Measurements with the pressure swirl atomizers do not allow the separation of effects of changes in equivalence ratio and premixer residence time. This problem is overcome through the use of effervescent atomizers, which allow independent variation of air and fuel flow rates, while maintaining satisfactory atomization. Measurements of the concentration of NO_x in the exhaust, using an effervescent atomizer with six discharge orifices, for the 19 and 38 cm premixers are shown in Figs. 6 and

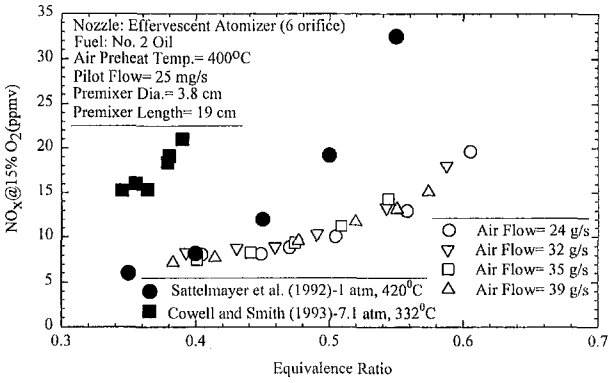

Fig. 6 Measurements of NO_x concentrations @ 15 percent O_2 in exhaust for 19 cm premixer for air flow rates of 24, 32, 35, and 39 g/s using No. 2 oil

7. The expected trends of lower NO_x concentrations at lower equivalence ratios are observed, and again the effect of changing premixer length (within the present range) and residence time is relatively small. Once again, ultralow NO_x operation is feasible for equivalence ratios less than 0.5. A limited amount of lean-premixed emissions data using No. 2 oil has been reported in the literature. The atmospheric pressure data of Sattelmayer et al. (1992) and the high-pressure data of Cowell and Smith (1993) are shown in Figs. 6 and 7 for comparison. There are variations between the two sets of measurements which shows that the NO_x emissions are combustor specific. Indeed, the emissions data of Cowell and Smith (1993) show wide variations for different operating conditions. There are significant differences between the small-scale and large-scale emissions data of Sattelmayer et al. (1992). The present measurements allow low NO_x operation (nominal residence time 3 to 6 ms) over a wider range of equivalence ratios than in the earlier studies.

Measurements are conducted with *n*-heptane to study the effect of fuel property changes on NO_x emissions. Concentrations of NO_x in the exhaust are shown in Fig. 8, and are significantly lower than the measurements with No. 2 oil for similar operating conditions. This is due to a combination of better evaporation characteristics of *n*-heptane, and chemical kinetic effects. Equivalence ratio remains the dominant variable and effect of changing premixer lengths is small. Measurements of CO concentrations for the above operating conditions are shown in Fig. 9. The CO emissions decrease initially with the equivalence ratio, as expected, and then show an increasing trend toward equilibrium concentrations at higher flame temperatures.

Scattering measurements are conducted at the exit of the premixer in order to obtain relative levels of premixing-preva-

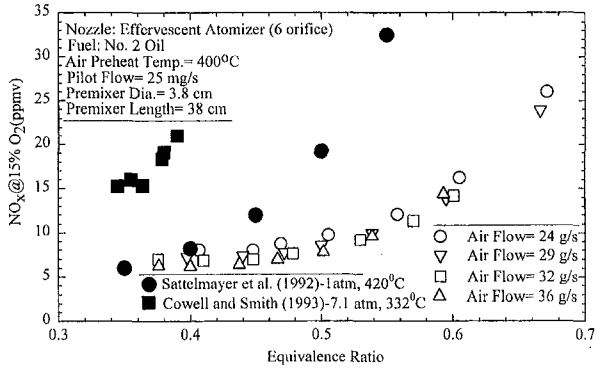

Fig. 7 Measurements of NO_x concentrations @ 15 percent O_2 in exhaust for 38 cm premixer for air flow rates of 24, 29, 32, and 36 g/s using No. 2 oil

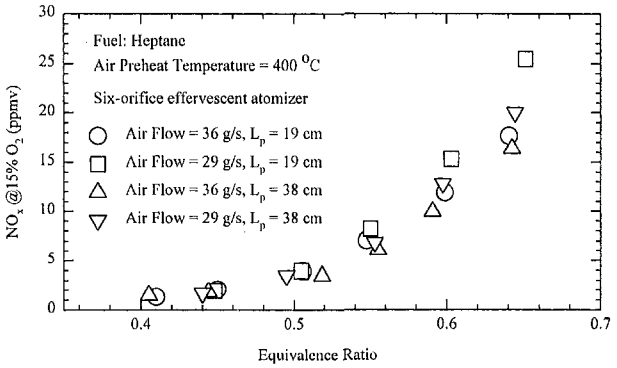

Fig. 8 Measurements of NO_x concentrations in exhaust for 19 and 38 cm premixers for air flow rates of 29 and 36 g/s using heptane

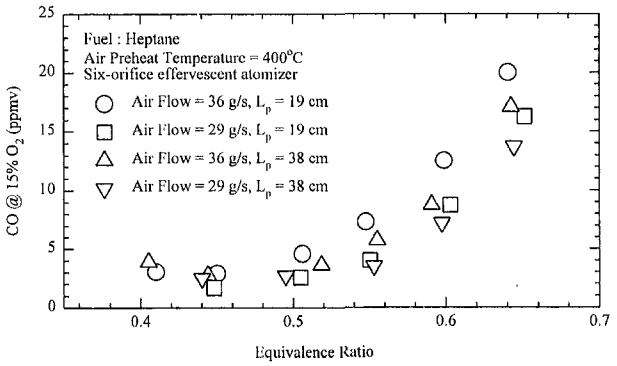

Fig. 9 Measurements of CO concentrations in exhaust for 19 and 38 cm premixers for air flow rates of 29 and 36 g/s using heptane

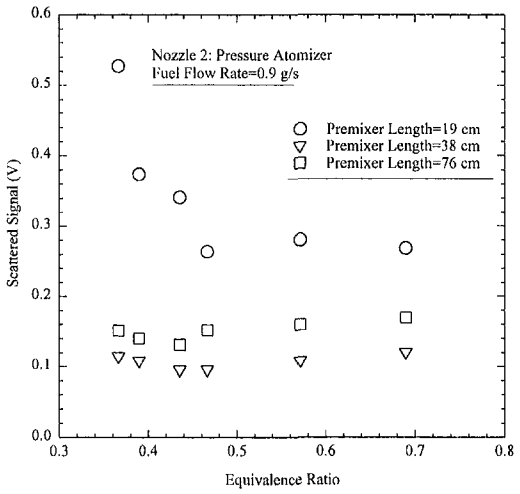

Fig. 10 Scattering signals for 19, 38, and 76 cm premixers at the centerline as a function of equivalence ratio

porization for operating conditions shown in Figs. 5, 6, and 7 for which low NO_x operation was possible. Illumination with a laser sheet shows the persistence of small drops in the optical access section at the exit of the premixer for all operating conditions and all premixer lengths (as long as 76 cm). Figure 10 shows the scattered signal at the centerline of the premixer for the three premixers used in the study using pressure atomizers. The scattered signals are repeatable to within 5–10 percent for most operating conditions, and within 20 percent for all operating conditions. The scattered signal provides a relative indication of the drop sizes and number density at the exit of the premixer. The scattered signals for the 19 cm premixer are higher than those for the 38 and 76 cm premixers, while the differences between the signals for the 38 and 76 cm premixers are relatively small. Measurements at off-centerline locations also show considerable spatial inhomogeneity for all premixers. Local diffusion flames around drops are not observed in the flame region for the data shown in Figs. 5–7. It seems that adequate prevaporization-premixing for low NO_x operation can be achieved for short premixer residence times (3–6 ms), which is encouraging, since at higher operating pressures autoignition delay time is a limiting design constraint.

Evaporation calculations are performed for inlet conditions corresponding to the pressure atomizer experiments. Figure 11 shows evaporation lengths for 50 and 100 μm drops. The initial drop mean velocity is estimated to be 30 m/s based on correlations for pressure swirl atomizers (Lefebvre, 1989). The calculations are performed for n- heptane, since fuel properties for No. 2 oil are not readily available. It is seen that the 50 μm drops evaporate within 9 to 11 diameters from the point of injection (34 to 42 cm downstream from the point of injection), while the evaporation length required for the 100 μm drops is greater than 30 to 40 diameters (110 to 150 cm). The drop size measurements (Fig. 3) show a significant number of drops in the 80–100 μm range, and the evaporation calculations confirm the presence of unevaporated drops at the exit of the premixer. Figure 11 also shows the calculated amount of unevaporated fuel at the exit of the 19, 38, and 76 cm premixers, respectively (for the measured drop size distributions of the pressure swirl atomizer Nozzle 2) using laminar one-dimensional assumptions. These estimates (which are conservative) suggest a significant amount of unevaporated fuel entering the combustor, while allowing ultralow NO_x emissions. It is also possible that the temperature of air near the premixer exit increases significantly due to heat transfer from the flame, causing more rapid evaporation than estimated here.

It was observed that the most critical parameter for high combustion efficiency and low NO_x emissions is fuel dispersion. Standard pressure swirl atomizers used for the baseline measurements, and the multi-orifice effervescent atomizer, provide a well- dispersed initial fuel distribution, and low NO_x operation (and combustion efficiency > 99 percent) is possible (Figs. 5–8). Experiments with the single orifice effervescent atomizer design demonstrate the importance of adequate fuel dispersion. Due to the narrow spray cone angles (~15 deg), most of the drops are concentrated in a narrow region near the center of the premixer, and fail to reach the flame stabilization region. This led to yellow streaks characteristic of diffusion flames, unburned fuel drops exiting the flame zone, and high NO_x emissions (in spite of good atomization). Estimates of the unburned fuel based on exhaust measurements (major species: CO_2, O_2)

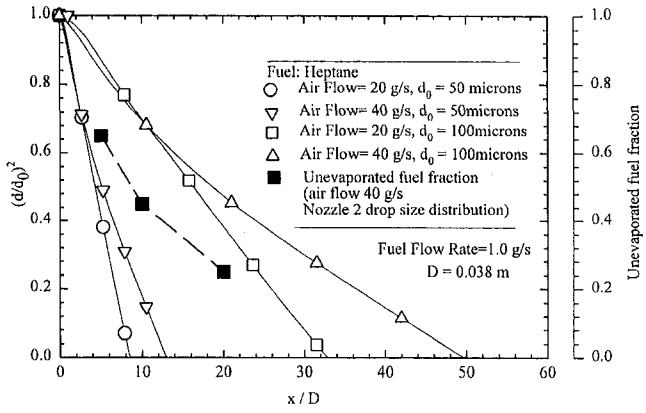

Fig. 11 Variation of drop diameter and fraction of unevaporated fuel as a function of axial position for two air flow rates and two drop sizes

shows that 20–30 percent of the fuel is unburned even for very long premixer lengths (76 cm).

Conclusions

The emissions performance of a liquid-fueled LPP tubular combustor with a tubular premixer is studied experimentally. The conclusions of the study are:

1 Ultralow NO_x operation with liquid fuels (No. 2 oil and heptane) is feasible for equivalence ratios less than 0.5. The equivalence ratio is the dominant variable with premixer lengths and residence times having less significant effects.
2 Ultralow emissions operation is possible for equivalence ratios less than 0.5 even with unevaporated fuel drops exiting the premixer for all operating conditions and premixer lengths, and with measured spatial inhomogeneity.
3 One-dimensional evaporation calculations confirmed that complete evaporation of all drops was not accomplished in the 3–4 ms nominal residence time allowed in the shortest premixer. At gas turbine operating pressures (typically > 10 atm), more complete evaporation can be achieved for similar residence times.
4 Fuel dispersion is the most critical parameter for high combustion efficiency and low NO_x. The fuel injector must be designed to ensure that fuel vapor and unevaporated drops reach the flame stabilization region.

Acknowledgments

This work was supported through a research contract from the Westinghouse Electric Corporation, Orlando, Florida. Many useful discussions with Mr. Dan Thompson, Mr. Dave Amos, and Mr. Rick Antos of Westinghouse Corporation are acknowledged.

References

Abramzon, B., and Sirignano, W. A., 1989, "Droplet Vaporization Model for Spray Combustion Calculations," *Int. J. Heat and Mass Transfer,* Vol. 32, No. 9, pp. 1605–1618.

Cooper, L. P., 1979, "Effect of Degree of Fuel Vaporization Upon Emissions for a Premixed Prevaporized Combustion System," NASA-TM-79154.

Correa, S. M., 1992, "A Review of NO_x Formation Under Gas-Turbine Combustion Conditions," *Combustion Science and Technology,* Vol. 87, pp. 329–362.

Cowell, L. H. and Smith, K. O., 1993, "Development of a Liquid-Fueled Lean-Premixed Gas Turbine Combustor," ASME JOURNAL OF ENGINEERING FOR GAS TURBINES AND POWER, Vol. 115, pp. 554–562.

Dutta, P., Gore, J. P., Sivathanu, Y. R., and Sojka, P. E., 1994, "Global Properties of High Liquid Loading Turbulent Crude Oil + Methane/Air Spray Flames," *Combustion and Flame* ,Vol. 97, pp. 251–260.

Dutta, P., 1995, "A Study of Turbulent Lean Premixed Prevaporized Combustion With Emphasis on Fuel Dispersion," Ph. D. Thesis, Purdue University, West Lafayette, IN.

Eckstead, E. E. and Fear, J. S., 1987, "NASA/GE Advanced Low Emissions Combustor Program," AIAA Paper No. 87-2035.

Fric, T. F., 1992, "Effect of Fuel–Air Unmixedness on NO_x Emissions," AIAA Paper No. 92-3345.

Lefebvre, A. H., 1983, *Gas Turbine Combustion*, Taylor and Francis, New York.

Lefebvre, A. H., 1989, *Atomization and Sprays*, Hemisphere, New York, pp. 105–197.

Lovett, J. A., and Mick, W. J., 1995, "Development of a Swirl and Bluff-Body Stabilized Burner for Low-NO_x Lean-Premixed Combustor," ASME Paper No. 95-GT-166.

Lund, M. T., Sojka, P. E., Lefebvre, A. H., and Gosselin, P. G., 1993, "Effervescent Atomization at Low Mass Flow Rates Part I: The Influence of Surface Tension," *Atomization and Sprays*, Vol. 3, pp. 77–89.

Lyons, V. J., 1982, "Fuel/Air Nonuniformity — Effect on Nitric Oxide Emissions," *AIAA Journal*, Vol. 20, No. 5, pp. 660–665.

Renksizbulut, M., and Haywood, R. J., 1988, "Transient Droplet Evaporation With Variable Properties and Inertial Circulation at Intermediate Reynolds Numbers," *Int. J. Multiphase Flow*, Vol. 14, No. 2, pp. 189–202.

Roffe, G., and Ferri, A., 1975, "Prevaporization and Premixing to Obtain Low Oxides of Nitrogen in Gas Turbine Combustors," NASA CR-2495.

Roffe, G., and Ferri, A., 1976, "Effect of Premixing Quality on Oxides of Nitrogen in Gas Turbine Combustors," NASA CR-2657.

Sattelmayer, T., Felchlin, M. P., Haumann, J., Hellat, J., and Styner, D., 1992, "Second Generation Low-Emission Combustors for ABB Gas Turbines: Burner Development and Tests at Atmospheric Pressure," ASME JOURNAL OF ENGINEERING FOR GAS TURBINES AND POWER, Vol. 114, pp. 118–125.

Swithenbank, J., Beer, J. M., Taylor, D. S., Abbot, D., and McCreath, G. C., 1977, "A Laser Diagnostic Technique for the Measurement of Droplet and Particle Size Distribution, Experimental Diagnostics in Gas Phase Combustion Systems," *Progress in Astronautics and Aeronautics*, Vol. 53, pp. 421–447.

L. D. Hansen

G. D. Kucera

J. S. Clemons

J. Lee

Argo-Tech Corporation,
Cleveland, OH 44117

Aircraft Gas Turbine Engine Fuel Pumping Systems in the 21st Century

Since their introduction, main engine fuel pumping systems for aircraft gas turbine engines have remained relatively unchanged. The main engine fuel pump has been an engine accessory gearbox driven, positive displacement pump (except for the Concorde), until recently when centrifugal pumps were introduced on Pratt-Whitney and General Electric military engines. This paper describes some of the issues that must be addressed as pumping system technology moves into the 21st century and gives a description of two programs that address these issues.

1.0 Typical Gas Turbine Fuel System

A typical commercial gas turbine engine fuel system, as related to the airframe fuel system, is shown in the block diagram in Fig. 1. To be able to evaluate changes to the fuel pumping system, it is necessary to understand the technical requirements of the individual components of the system.

The airframe boost pumps must transfer fuel from the aircraft fuel tanks to the main engine fuel pump at pressures exceeding the fuel true vapor pressure (TVP) + 5.0 psi minimum. There may be several of these pumps in use on a given aircraft, depending on the size of the aircraft, the number of tanks, and the number of engines. Transfer pumps may also be used to move fuel between tanks and for fuel flow to cool airframe accessories.

Fuel delivered by the airframe pumps is introduced to the main engine fuel pump, which generally consists of a low-pressure centrifugal boost stage, an interstage filter, and a high-pressure, positive displacement, main stage. The filter is generally provided with a bypass valve to limit filter pressure drop in the event the filter becomes plugged by contaminant. The main, or high-pressure, stage is also provided with a relief valve to protect the system from overpressurization in the event of a fuel control malfunction. Provisions are also made for connection of one or more heat exchangers, which use fuel to cool engine electronics or engine oil, and the direct mounting or connection of a fuel control unit (FCU), which regulates fuel flow delivery to the gas turbine. Other connections to the pump provide pressure references for the FCU or bypass flow loops to permit the FCU to recirculate excess flow delivered by the positive displacement main stage back into the main engine pump.

The function of the low-pressure boost stage is to pressurize and deliver the flow required to the main stage. The boost stage is generally a two-element centrifugal stage consisting of an inducer and a radial impeller, although in some instances, the inducer may be replaced by a jet pump. The purpose of the inducer is to accept fuel at relatively low pressures, usually TVP + 5 psi minimum from the airframe pump, and to deliver this flow to the impeller in solid liquid form. This must be at a pressure sufficient to fill the impeller entry blading without fluid separation or cavitation. A secondary function of the inducer is to maintain the pumping system, and therefore engine operation, in the event of an airframe pump failure. In the case of such a failure, the inducer design enables it to accept and pressurize fuel with a high vapor to liquid (V/L) ratio, 0.45 to 1.00, or at a low net positive suction pressure (NPSP) of TVP + 1.0 to TVP + 5.0 psi. This high V/L, low NPSP condition is the result of the liberation of air entrained or dissolved in the fuel caused by operation at high altitude, fuel temperature changes, and pressure drops in the fuel supply line as a result of flow-induced pressure losses. The inducer must compress and redissolve the liberated air and at least partially restore pressure before the fluid reaches the impeller to ensure that the impeller can further pressurize the fuel as necessary for main stage filling. These inlet requirements have been steadily increasing as shown in Table 1.

To satisfy the filling requirements of the positive displacement stage, the boost stage centrifugal impeller must develop sufficient pressure to overcome the pressure drops encountered by fuel flow through the filter, external heat exchangers and other internal pump core passages, the vapor pressure changes of the fuel due to temperature changes, and have sufficient excess pressure to fill the gears or other positive displacement main stage pumping elements. With respect to the filter, it is readily apparent that the size of the filter, its micron rating, and the level of contaminant exposure (up to the point the filter bypass valve is caused to open), all influence pressure drop and contribute to the size or pressure rise requirements of the impeller. The effect of fuel vapor pressure on impeller pressure rise requirements and size is also apparent when it is understood that the fuel pressure at the inlet of the main stage must exceed the sum of this vapor pressure and the stage element minimum filling pressure to prevent vapor formation and/or partial filling of the main stage. Under conditions of partial filling, the result is an obvious loss of flow delivery and the substantial risk of cavitation damage to the main stage pumping elements and housings. The size and performance requirements of the boost stage must therefore be determined by consideration of all these factors.

The sizing of the high-pressure positive displacement stage is generally determined by the flow requirement at one or more engine operating conditions and flow margins necessary to satisfy a long service life, typically 15,000 hours, with some flow degradation. Such sizing practices usually result in the pump being oversized for most engine operating conditions. In many cases, the sizing of the pump is determined by engine starting or cranking flow requirements and/or windmill relight flow requirements. In such instances, the operating speed of the pump is very low, causing the normal volumetric efficiency to be adversely affected, and the pump is thus oversized at other flight cycle conditions. The fuel control may require servo flows for auxiliary engine functions, which are in addition to the burn flow required by the engine and add to the pump size. The

Contributed by the International Gas Turbine Institute and presented at the 41st International Gas Turbine and Aeroengine Congress and Exhibition, Birmingham, United Kingdom, June 10–13, 1996. Manuscript received at ASME Headquarters February 1996. Paper No. 96-GT-148. Associate Technical Editor: J. N. Shinn.

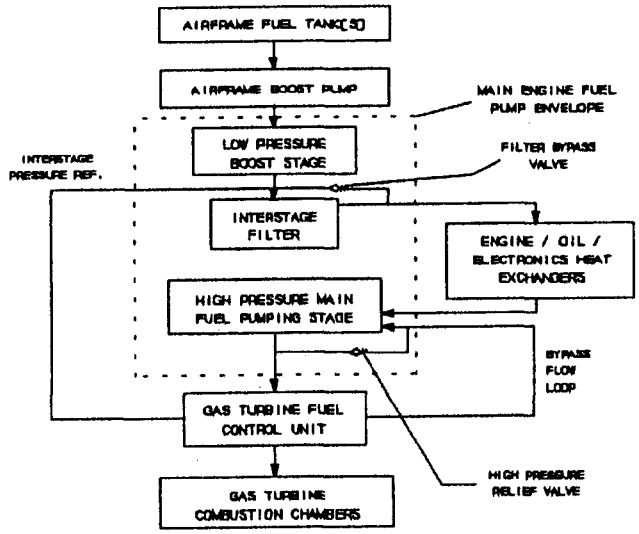

Fig. 1 Gas turbine fuel system block diagram

Table 1 Main engine pump boost stage trends

Decade	70's	80's	90's	Beyond
Design Approach	Conventional -Low Solidity -Low Suction Capacity -Straight Hub -Low Blade Height	Conventional -Med Solidity -Med Suction Capacity -Straight Hub -Med Blade Height	Conventional -High Solidity -High Suction Capacity -Straight Hub -High Blade Height	Innovations such as: -Continuous Bladed Ind/Imp -High Solidity -Curved Hubs -Fwd Swept, Var. Cant Blades -3D Inducer Designs
Performance:				
T'down Ratio	26:1	32:1	57:1	100:1
Efficiency	25%-38%	45%	52%	>60%
NPSP (paid)	TVP+5	TVP+5	TVP+1	<TVP+0.5
Vapor/Liquid	<0.45	0.45	>0.45	>1.0

negative consequences of such oversizing are increased weight, size, and more importantly, increased heat rise or heat input to the fuel system. The engine oil and electronic cooling and resulting heat exchanger systems are adversely affected by this added heat input, reducing the effectiveness of transferring heat into the fuel. The engine and electronic equipment may be required to run at higher temperatures, and the heat exchangers may have to be made larger or supplemented by air/oil or air/fuel coolers, all of which add weight and cost to the system. In some rare instances, engine fuel systems may also be designed with provisions to recirculate some quantity of heated fuel back to the tank to serve as a heat sink. This latter practice has limitations and does not remove the heat from the system. Such practices, if not properly managed, may also lead to pump vapor lock and engine failure caused by fuel boiling as it is moved from the tank and transferred through the pumping system. If the fuel temperature is sufficiently elevated by this heat input and starts to boil, vapor lock or cavitation damage to the pumping system can occur.

2.0 Typical Engine Main Fuel Pump

A typical gas turbine main engine fuel pump is shown in Fig. 2. It is usually gearbox driven, which causes the fuel pump speed to be proportional to the engine speed. The pump drive line incorporates a shaft seal to prevent fuel leakage into the gear box. The splines can be lubricated by one of three means: engine gear box oil, grease packed, or fuel lubricated. The cross section shows only the low-pressure boost stage and the high-pressure gear stage. The fuel control normally mounts to the back of the pump and provides porting for pump discharge and return flows to the pump. The interstage filter is usually a part of the pump housing, along with various other accessories previously mentioned.

Main engine fuel gear pumps are being adversely affected by fuel lubricity issues, higher bearing loads from increased system pressure levels, gear stage cavitation from increased fuel temperatures, and pressure ripple affecting other fuel system components. Material properties must continually be improved to survive in the changing engine environment. The present leaded bronze bearing materials must address higher fuel temperatures, environmental issues concerned with the use of lead, and the loss of lubricity in the fuel ingredients. Engine service use with JP8 + 100 fuels, additives, and higher operating temperatures must also be accomplished for complete acceptance of this fuel.

3.0 Gas Turbine Fuel Pump System Change Issues

For any fuel pump system changes to be accepted by the engine manufacturer and eventually by the airframe customer, certain issues must be addressed at the onset of any fuel pumping technology changes. The normal avenue of introducing technology changes has been the military engine, the traditional proving ground for new technology. This area is presently limited by funding constraints and the lack of government-funded engine programs to use as test vehicles for evaluating new technology. Consequently, the burden is falling back on the engine companies and the fuel pump suppliers.

3.1 Fuel System Reliability. Presently, typical system reliabilities for gas turbine fuel systems operating with positive displacement main engine pumps are achieving mean time between failures (MTBF) of 175,000 hours, mean time between unscheduled removals (MTBUR) of 75,000 hours, in-flight shutdowns related to the main engine fuel pump of less than 0.6 per million flight hours, and service life between overhauls

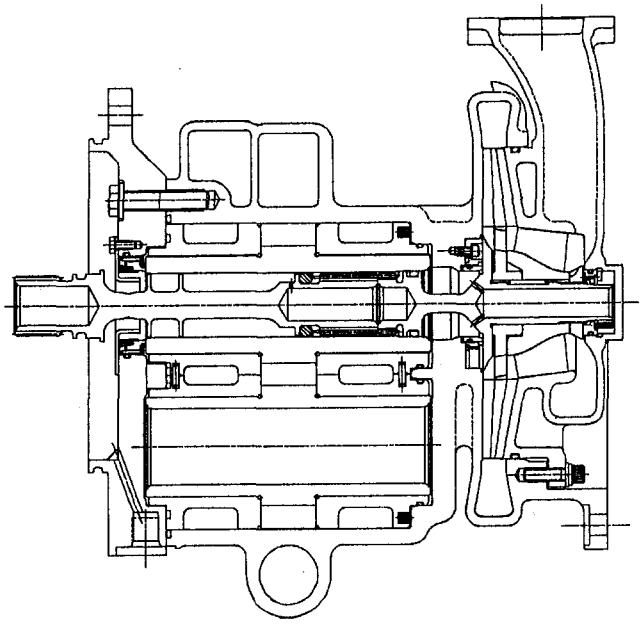

Fig. 2 Gas turbine main engine fuel pump

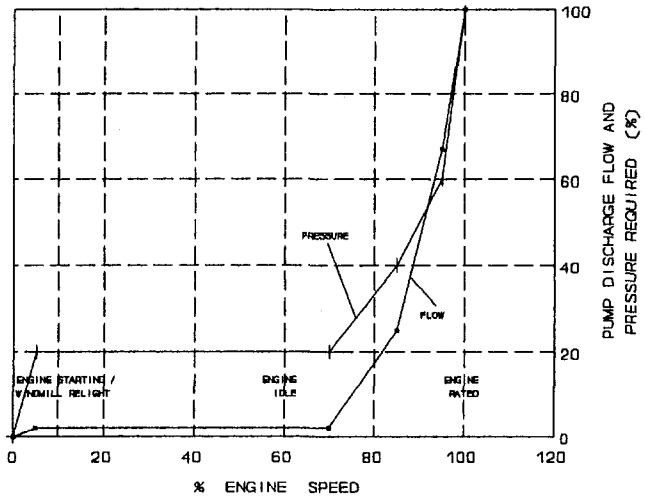

Fig. 3 Gas turbine fuel flow and pressure versus engine speed

of 12,000 to 14,000 hours. Any change to the fuel pumping system in the 21st century must meet or exceed these current values. These criteria are also being steadily improved by pump design technology in newer gas turbine main fuel pumps, which require higher fuel system temperatures (seals, bearing durability), and higher operating pressures (bearing and gear durability, cavitation resistance).

One of the most cherished commodities of any engine and airframe fuel system is certification for Extended Twin Engine Aircraft Operational Procedures (ETOPS). This certification is granted to an aircraft make and model of engine, containing the fuel system, by the Federal Aviation Administration (FAA). This allows for either 120 or 180 minutes of operation over water with one engine out of service on a given twin engine aircraft/engine combination based on number of in-flight shutdowns, aircraft and engine maintenance practices and procedures, and operational history for a given airline with a given aircraft/engine/route system. Any fuel system changes must address the ability of the fuel system to attain this certification, early in the life of the system, to avoid the limitations on the user resulting from the loss of ETOPS certification.

3.2 Cost Advantages. New technology products must address cost impacts, not only to the pumping system itself, but to the total fuel system cost. Not only the initial cost, but the cost of ownership throughout the life of the product are of paramount importance. The product must be capable of being overhauled and serviced economically within the service environment in which it is being used.

The design of the fuel delivery system must be highly reliable and in keeping with the simplification and control capability of Full Authority Digital Engine Controls (FADEC) without affecting the costs of the system. New pumping systems must be capable of being integrated into such a control system while allowing for further simplifications, cost reductions, and operating enhancements of the control system for improved performance and reliability.

The product design should be flexible to enable its use on a number of engine programs to minimize or eliminate the cost of developing not only the pump but the associated engine fuel system and control for the engine and airframe on which it is to be utilized. This would eliminate redundant design, development, qualification, and certification testing associated with new pump designs. Little or no mechanical changes would be required with minimal cost, size, and weight penalties. This might mean that a single pumping system could be utilized on a given family of engines and possibly on a similar competing engine with possible repackaging.

3.3 Lowest Weight Design. The weight of any component in the fuel system is of prime importance to the overall advantage of the engine system in which it is installed. Less weight to the total system means lower fuel consumption, additional range, more passengers, more cargo, and shorter take-off and landing requirements, to mention a few. These weight considerations, however, cannot be limited to the fuel pump but must address the total weight of the fuel system and other components on the engine as the pump will have actuation and electronic features added. The weight savings for the system are dependent on many factors, but one should realize a 10 to 20 percent savings for a total configuration.

3.4 System Heat Load. One of the major drivers to cause the fuel pump in the fuel system to be scrutinized is the allowable temperature rise of the fuel as it travels from the airframe tank to the engine burner fuel nozzles. Boost system inlet temperatures are usually 135°F while the high-pressure discharge temperature at the fuel nozzle is limited to 325°F to prevent coking using today's fuels. Fuels with improved thermal stability and higher operating temperature capabilities such as JP8 + 100 may allow this temperature to be increased. The turndown ratio and the pump's ability to meet the engine's demand for fuel must be addressed by any fuel system changes under any and all operating conditions. It would be ideal, and logically so, for the main engine fuel pump to deliver *only* the flow and pressure required by the engine fuel system. This concept leads to the definition of a "Demand" fuel pump, one that delivers only the required flow at the required pressure to the fuel system.

4.0 Gas Turbine Fuel System Design Constraints

4.1 Fuel Pumping System Issues. Figure 3 shows the typical relationship between engine speed and engine flows/pressures at various operating conditions and altitudes. This engine envelope will vary with the type, size, and use of the engine for various airframes. The trend is for this envelope to be expanded with the newer engine technologies. There are three operating points that normally size the fuel pump; the engine starting condition on the ground, the inflight windmill relight, and the maximum thrust, sea level take-off power, under worst case conditions.

Figure 4 shows a positive displacement pump flow curve placed over the engine operating flow conditions. The closer the pump displacement can be sized to the three critical engine performance conditions, the lower the fuel system turndown

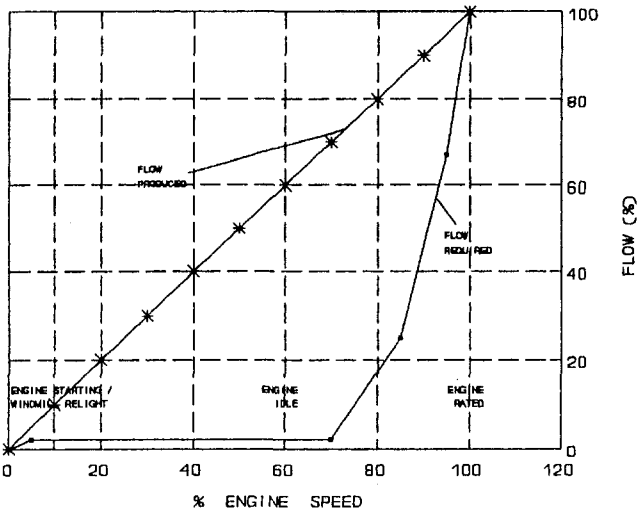

Fig. 4 Gas turbine fuel flow compared to a positive displacement engine pump

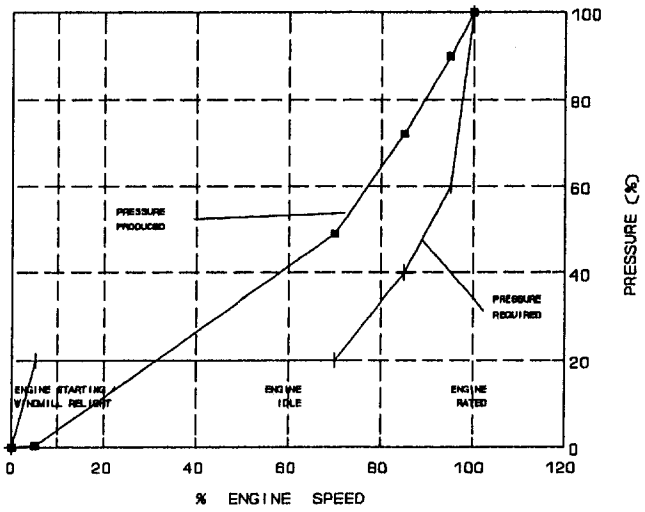

Fig. 5 Gas turbine fuel pressure compared to a centrifugal engine pump

ratio becomes, thus reducing the temperature rise to the fuel system.

Figure 5 shows a centrifugal main engine pump curve criterion placed over the engine operating conditions. In this case, the sizing criterion is usually the maximum thrust, sea level take-off condition. However, it must be noted that most centrifugal pumps, when gearbox driven, do not satisfy the engine starting or relight conditions, or the dry lift and reprime requirements for the fuel system. This issue must be addressed by secondary pumps in the fuel system. On military engines that use centrifugal main engine pumps, the starting and relight roles, as well as the dry lift and reprime needs, are accomplished by the fuel actuator pump. One known commercial engine with a centrifugal main engine pump uses an electric motor driven pump for engine starting.

4.2 Flow/Pressure Stability Range. One of a number of concerns with existing systems is the quality of the fuel delivered to the control components in an engine fuel system. Flow variations, caused by pressure pulses or ripple, can lead to vibratory loads on other system components and must be minimized. Forcing these components to survive in hostile environments in the engine/airframe installation is task enough without adding the effects of adverse flow variations caused by pressure ripples and vibration.

4.3 Fuel Issues. Any considerations to changing the gas turbine fuel pumping system must also include recognition of the ongoing changes affecting the fuel itself. The industry has experienced problems with low-lubricity fuels in various areas causing premature pump wear. Systems that use hydrorefining processes, to achieve better yield from the crude oil, have affected lubricity mechanisms in the fuel. Further oil industry efforts to attain better fuel thermal stability for enhanced engine operation also tend to lower the fuel lubricity. Another factor that must be considered is the use of additives in JP8 to achieve JP8 + 100, which must be fully service evaluated.

4.4 Industry Acceptance of the Pump Technology. The industry, namely the aircraft engine and airframe industry, must be willing to accept new technology and new innovations. Certain types of pumps have, over the years, gained reputations for "catastrophic" failure mechanisms, limited life or reliability, excessive maintenance or acquisition costs, and other perceived limitations of the product. One example of this phenomenon was a variable displacement vane pump on a single engine military aircraft operating at 16,000 rpm with tungsten carbide materials. These issues must be addressed early in the development process for any new fuel pump technology. The materials and designs of choice must function in their intended role in the fuel system without bringing any "unwanted baggage" to the system. Industry acceptance will be gained by design innovations, more robust materials, and extensive (V/L, NPSP) cyclic endurance test to engine operating conditions including fuel temperature changes (thermal effects), inlet conditions, and service type fuels (lubricity and contamination effects).

5.0 Fuel Pumping System Options

5.1 Variable Speed. A brief return to the engine fuel requirements versus speed diagram, utilizing a variable speed pumping system, is shown in Fig. 6. When the pump shaft speed is independent of the engine speed, the use of a centrifugal pumping system becomes acceptable. The speed can be increased to enable the centrifugal pump to provide the required flow at the needed pressure to start the engine, both on the ground and in flight. Technology advances with centrifugal devices may also allow these pumps to provide dry lift and reprime capability with the additional speed available.

However, control of the pump shaft speed can become complicated when it is independent of the accessory gear box shaft speed, which is proportional to the gas turbine speed. One option is to use a variable delivery hydraulic pump to drive a hydraulic motor, which could control the driven component's shaft speed. A similar system is used in constant-speed drives (CSD's) to drive the electrical generator on many commercial and military gas turbine engines. This concept could also be used to drive the fuel pump. Another viable option would be to use a variable speed electric motor, if its reliability could be shown to approach or exceed that of the engine accessory gearbox.

5.2 Variable Displacement (Gearbox Driven). The other option in achieving the ability to match the fuel delivery to engine needs is to use a variable displacement pumping system driven by the current engine accessory gearbox. A brief return to the engine fuel requirements versus speed diagram, utilizing a variable delivery pump in the fuel system, is shown in Fig. 7. When the displacement can be controlled relative to the engine fuel demands, the turndown heat rise to the fuel is eliminated, leaving only the pump efficiency to be included in the heat rise equation.

A review of these engine requirements and the constraints on fuel system pumping technology should lead to this conclusion:

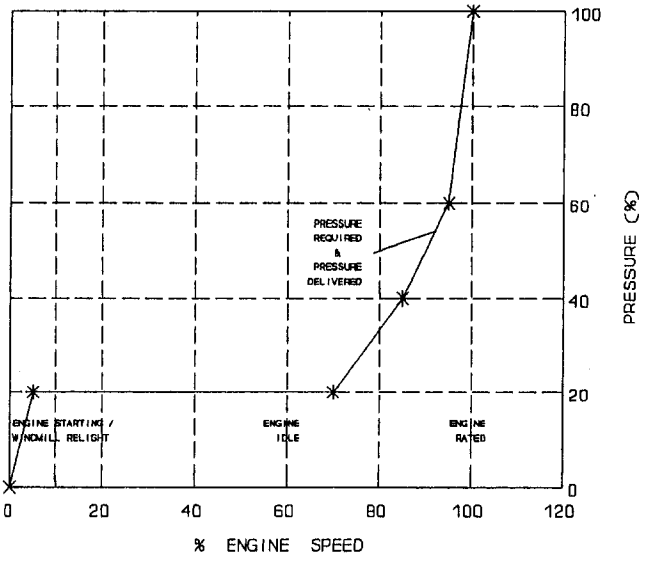

Fig. 6 Gas turbine fuel pressure compared to a variable-speed engine pump

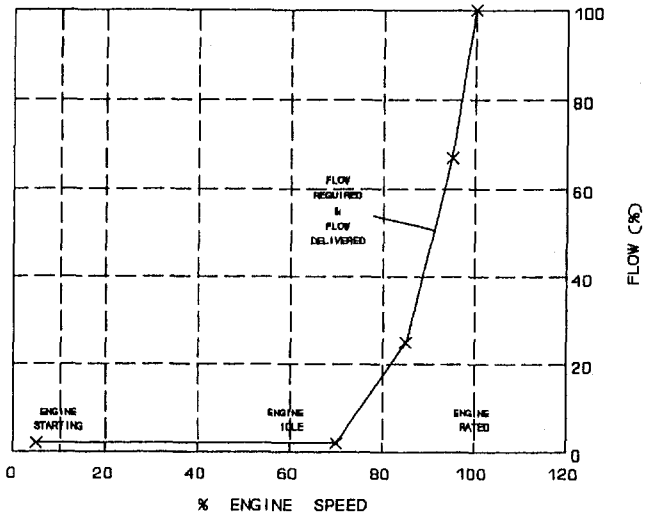

Fig. 7 Gas turbine fuel flow compared to a variable-displacement engine pump

There are two options immediately acknowledged: (1) gain control of the shaft speed of the pumping device, or (2) gain control of the pump displacement to vary fuel flow, in relation to the fuel system requirements, to make major efficiency gains. This conclusion has led one company to assign research and development funds to two potential fuel pumping concepts to address these needs. A brief description of these two advanced conceptual designs and the status of these programs are outlined in the following paragraphs.

6.0 Demand Fuel Systems

6.1 Electric Motor Driven Fuel Pump (Variable Speed)

6.1.1 Design Discussion. Many system changes must be made before this concept can become a viable fuel pumping system. The engine control would differ from conventional propulsion control systems in areas such as active engine rotor clearance control, vehicle power conditioning, and system thermal management. The integration of the electronics and electrical systems on the engine would be a significant issue due to the increased amount of electronics, the physical distribution of the electronics about the engine, and the requirement that all components operate together as a part of the overall engine system. The engine starter/electrical generator power transition and high-temperature miniature electronics that can survive in the engine environment, are just two of the many issues that need to be addressed to enable this technology to emerge on the gas turbine engine.

The electric motor driven fuel pump, referred to as the "Demand Fuel System" (DFS), gains control of the pumping device's shaft speed. Patent and literature searches, internal research and development activities, and contact with various vendors resulted in a design based on meeting the following criteria:

- Develop a variable speed electric motor driven pump with equivalent gear box driven reliability.
- Meet engine fuel demand, with the right flow at the needed pressure, while limiting the heat input to the engine fuel system.
- Evaluate the control system capability with the goal of using the engine Full Authority Digital Engine Control electronic intelligence to control the shaft speed of the motor and engine fuel flow.
- Incorporate high-speed centrifugal impeller technology, with dry lift and reprime capability, in the final design configuration.

The concept designed, fabricated, and under evaluation is shown in Fig. 8. The design utilizes an advanced centrifugal fuel pump driven by a switched reluctance, variable-speed electric motor. The switched reluctance motor concept was selected to enable the use of electronic technology, which would continue to operate even with the loss of one motor winding phase. It also lent itself to potential control logic from the engine FADEC system and permitted the high-speed operation necessary for advanced impeller designs. The configuration would permit the size and weight of the pump and motor to be minimized in the range of horsepower needed for a gas turbine fuel pump using a centrifugal type design. The advanced centrifugal pump design has demonstrated improvements in pressure and flow stability over a wide range of flows necessary for the gas turbine's operating envelope when used as an engine gearbox driven accessory.

The design addressed the operational requirements as shown in paragraphs 6.1.2 and 6.1.3.

6.1.2 System Static Performance

Flow Range	1 to 60 gpm
Discharge Pressure	300 to 1500 psid
Flow Accuracy	±10% of point up to 10 gpm ±1 gpm up to max flow
Flow Hysteresis	0.1%
Fuel Temperature Rise	100°F max @ 1 gpm and 300 psid
Fuel Inlet Temperature	225°F max

6.1.3 System Dynamic Performance

Pump Speed	13,000 to 30,000 rpm
Freq. Response Bandwidth	6.5 Hz (flow control) @ ±625 rpm
Step Response of 2500 rpm	0.100 second max
Open Loop Stability	Gain margin 5.0 dB max phase margin 30° max
Discharge pressure oscillations	4% of point max

The design has been fabricated and is currently undergoing motor characterizations to minimize the heat load to the fuel system and simultaneously meet static and dynamic performance requirements. The unit will undergo evaluation testing to an engine duty cycle for a better understanding of how this mechanism can be designed to the constraints evident for any fuel pumping system technology changes. The unit has shown preliminary characteristics of less than 10°F fuel heating from inlet to discharge at engine flight idle conditions.

The variable-speed, electric motor driven fuel pump's ability to address the four major fuel system change issues depends greatly on the viewpoint taken. Fuel system reliability is the

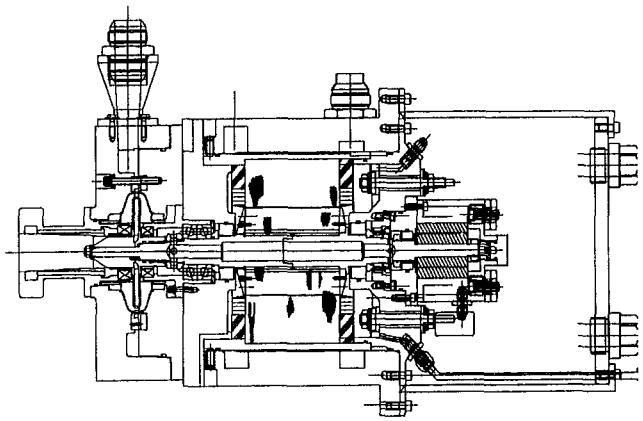

Fig. 8 Variable speed electric motor driven fuel pump

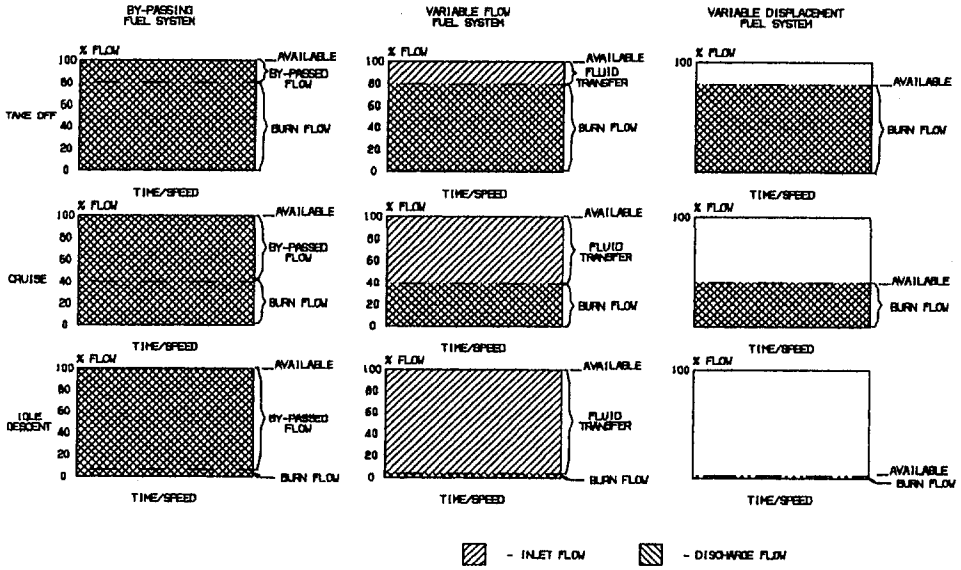

Fig. 9 Variable displacement or variable flow by fluid transfer

question of electric motor drive versus gear box reliability. The cost advantage question depends on the cost for the total engine system rather than the individual components of the system and will have to be decided when the system operates fully and all issues are addressed. The weight will also depend on the total engine configuration rather than that of individual components. Based on initial data, the fuel system heat load appears to be dramatically improved, from 120°F for a conventional system to approximately 10°F for the electric motor driven system. The cost of an electric motor driven pump such as this will depend on the electrical power available on the engine. The test pump operates on 270 volt DC power. The system is flexible for meeting various engine requirements by speed (discharge pressure), flow range (pressure versus flow stability), and can achieve starting and wind-mill relight conditions independent of the former gas turbine engine shaft speed itself.

There are further hurdles to overcome with the concept to enable it to be packaged for operation in the gas turbine engine environment, particularly the electronic controls and power devices required by the design. These issues are to be addressed in subsequent iterations of the design to make it compatible with the total fuel system needs.

6.2 Gearbox Driven Fuel Pump System (Variable Delivery)

6.2.1 Variable Displacement or Variable Flow by Fluid Transfer. In order to discuss the gearbox driven fuel pump system, one area of clarification is necessary; the difference between variable displacement and variable flow by fluid transfer. Figure 9 shows what is meant by these terms. Variable displacement means to change the displaced volume of the pump physically as it rotates, while variable flow by fluid transfer means to limit the amount of pressurized fluid displaced. It is also useful to explain the term "turndown ratio," which is used as a means of quantifying fuel heating. The left-hand column of Fig. 9 shows a fixed displacement type pump in a bypassing fuel system. The displacement had been selected to match the engine's flow demand at some point in its operating envelope, with the excess at other points being bypassed back to pump inlet. Turndown ratio, as shown, is defined to be the total flow capability at a given pump speed divided by the required engine burn flow at that condition.

The middle column shows the ability of the variable flow pumping system to distinguish between the flow needing full pressurization by the system resistance and the total volume, which can be carried back to the pump inlet in an unpressurized condition.

The third column shows that a variable displacement pump would provide only the flow required, producing a turndown ratio of one.

6.2.2 Industry Alternatives. There are basically three types of positive displacement pump available to meet the needs of gas turbine engines; gear, vane, and piston. Two of these, piston and vane pumps, are known to be capable of variable displacement and are in current use in the industry.

There are no known instances of variable displacement spur gear pumps being used in gas turbines or other applications in industry. The standard for the gas turbine industry is the fixed displacement spur gear pump used on the majority of gas turbine powered aircraft applications.

A variable displacement vane pump was used in a gas turbine engine fuel system on one major aircraft engine application. It has been replaced by a spur gear pump for cost and improved reliability. There are, however, several known fixed displacement vane pumps on gas turbine aircraft engines in both commercial and military applications.

The variable displacement piston pump is normally used for air-frame hydraulic applications and has seen limited use for fuel applications, due to the speed, cost, and reliability requirements of gas turbine fuel systems. There are variable displacement piston pumps in use in a gas turbine fuel system for engine actuation systems, one a current military engine and a second being developed. There are some applications in the United Kingdom using variable displacement fuel piston pumps on gas turbine engines.

6.2.3 Variable Delivery Fuel System. After a review of industry patents and known applications, a choice was made to undertake the design of a vane type variable displacement pump. The vane pump offered the following options to provide this capability:

- The vane design offers the highest displacement per pound of any conventional engine fuel pump.
- The vane pump was the first fuel pump to pass full military contamination testing, without the benefit of filtration, by the use of controlled advanced materials.
- The vane mechanism offers a versatile, adaptable design due to the flexibility of the cam ring configuration, namely single or multiple lobes, single or double ramps for inlet

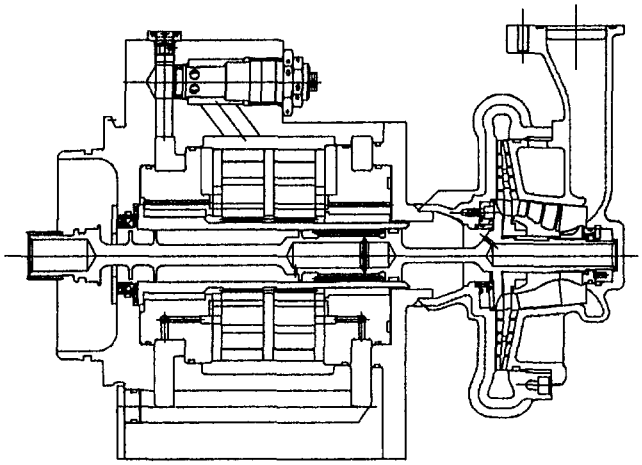

Fig. 10 Variable displacement pump cross section

and discharge chambers, and the ability to provide multiple alternative cam contours.

- Dual lobe designs offer low bearing loads, which aid in addressing fuel lubricity issues.
- The vane pump is lower in cost and complexity than a piston type fuel pump.
- Vane pumps in service have demonstrated over 2,000,000 flight hours with no failures and MTBF's from 30,000 to 45,000 hours on some applications.

As part of the internal research and development program, a trade study of seven concepts was performed before selecting three for design, fabrication, and testing (two variable displacement, one variable flow). Following the initial evaluation of these designs, a configuration was selected for further development based on the following design constraints:

- Variable displacement to minimize fuel system heating.
- Balanced shaft loads to minimize the package size, weight, and bearing requirements.
- Fixed clearance design to enable use of existing vane pump technology.
- Minimize the actuator flow requirements to reduce parasitic flow losses.
- Use existing production relief valve, boost stage, and drive line.
- Meet a current production pump package and performance requirements.
- Provide operation under the following conditions:

Pump Speed	450 to 7250 rpm
Pressure Rise	300 to 1500 psid
Flow Range	1.5 to 120 gpm

The cross section of the variable displacement pump designed and under development is shown in Fig. 10. The section is taken through the boost stage and the high-pressure stage showing the arrangement of the drive line. The design features two side by side vane stages integrated to perform as a single variable displacement pump. The design addresses issues known to exist in previous vane pump designs such as cavitation at engine idle conditions, exposed vane tips passing ports, high vane tip loads, and high bearing loads with single lobe designs. Correcting for these conditions will allow the use of more robust materials in the design. The actuation system and response characteristics are designed to offer the maximum flexibility in the evaluation phase of the program. The pump has been fabricated and is currently undergoing development testing with a fuel control supplier for an engine demonstration test.

The variable displacement pump's ability to address the four major system issues depends on various points of view. Because the design is a limited departure from existing vane pumps in service and incorporates design changes to overcome known industry concerns, the reliability of the concept will depend principally on the actuation system and its integration with the engine FADEC system. The cost issue depends on the ability of the variable displacement pump to simplify the engine control system and the advantages to be gained from the overall engine fuel system. The weight issue is again a system tradeoff of the various components needed in an acceptable engine system. The fuel system thermal heat load will be reduced significantly, tentatively from 120°F for the present system to less than 40°F for the variable displacement system. The design is flexible as the displacement range is a function of the original design process and can be sized effectively to cover various engine requirements and gear box speeds. The cost of the system will be directly dependent on the control aspects of the design, the accuracy, leakage, and response characteristics required to integrate with the engine FADEC system.

Industry acceptance of vane type pumps will require close attention to the pump details and rigid design and material controls to overcome the tarnishing of this pumping concept in the military area, which has spilled over into the commercial area.

7.0 Conclusions

Based on the work completed to date on the two systems discussed, the following conclusions can be drawn:

- The switched reluctance, variable speed motor, with the proper electrical power available, can be developed into a "Demand" fuel pump for gas turbine engine fuel systems.
- The variable displacement pump, using vane pump methodology, can be a "Demand" fuel pump for gear box driven applications. Materials and design technology can make the pump comparable to today's fixed displacement, bypassing fuel systems.
- Gas turbine engine technology is advancing, fuel characteristics are being modified, fuel system reliability must continue to improve, and fuel pumping system technology must advance to address the issues.

What is presented are initiatives by one fuel pump supplier to address fuel system issues. The final solution will be a shared responsibility of the engine, airframe, fuel processing, and fuel system supplier communities.

References

Ervin, J. S., Heneghan, S. P., Martel, C. P., and Williams, T. F., 1996, "Surface Effects on Deposits From Jet Fuels," ASME JOURNAL OF ENGINEERING FOR GAS TURBINES AND POWER, Vol. 118, pp. 278–285.

Ferreira and Richter, 1993, "Detailed Design of a 250 kW Switched Reluctance Starter/Generator for an Aircraft Engine," SAE Paper No. 931389.

Ford, V. C., 1997, "Engine Fuel Systems for Concorde," *Gas Turbine International,* May–June.

Karmel, A. M., 1986, "A Study of the Internal Forces in a Variable Displacement Vane Pump—Part I: A Theortetical Analysis," ASME *Journal of Fluids Engineering,* Vol. 108, p. 227.

Karmel, A. M., 1986, "A Study of the Internal Forces in a Variable Displacement Vane Pump—Part II: A Parametric Study," ASME *Journal of Fluids Engineering,* June, Vol. 108, p. 233.

NACA, 1956, Technical Note 3276, Aug.

Ponnappan, LeLand, and Beam, "Thermal Management Issues of Rotors in Rotating Electric Machines," SAE Paper No. 942184.

Radun and Richter, 1993, "A Detailed Power Inverter Design for a 250 kW Switched Reluctance Aircraft Engine Starter Generator," SAE Paper No. 931388.

SAE, 1900, Aerospace Recommended Practice ARP 492B.

Zabarnick, S., Zelesnik, P., and Grinstead, R. R., 1996, "Jet Fuel Deposition and Oxidation: Dilution, Materials, Oxygen, and Temperature Effects," ASME JOURNAL OF ENGINEERING FOR GAS TURBINES AND POWER, Vol. 118, pp. 271–277.

Investigation of Wedge Probe Wall Proximity Effects: Part 1—Experimental Study

P. D. Smout
Rolls-Royce plc.,
Derby, United Kingdom

P. C. Ivey
School of Mechanical Engineering,
Cranfield University,
Bedford, United Kingdom

Conventional three-hole wedge probes fail to measure the correct static pressure when operating in close proximity to a wall or boundary through which the probe is inserted. The free-stream pressure near the outer wall of a turbomachine may be overindicated by up to 20 percent dynamic head. This paper reports a series of experiments aimed at quantifying this so-called "wall proximity effect." It is shown from a factorial experiment that probe wedge angle, stem design, and free-stream Mach number all have a significant influence. The yaw angle sensitivity of wedge probes is also found to depend on the proximity of the probe to the wall of introduction. Flow visualization studies on large-scale probe models are described, and a qualitative model of the probe local flow structures is developed. This model is used to explain the near-wall characteristics of the actual size wedge probes. In Part 2 of this paper, the experimental data are used to validate CFD calculations of the flow field around a wedge probe. A simple analytical model of the probe/flow interaction is developed from the CFD solutions.

1 Introduction

The three-hole pneumatic wedge probe (Fig. 1) is one of several traverse probe designs used commonly for two-dimensional flow measurements in turbomachinery. Although less compact than alternatives such as the cobra probe, the wedge probe design is inherently robust, and relatively insensitive to changes in the prevailing flow conditions. Time-resolved pressure measurements in unsteady flows have been made successfully using dynamic wedge probe derivatives with miniature pressure transducers installed in the wedge faces (Cook, 1988). Bubeck and Wachter (1987) resolved three-dimensional turbomachinery flows using a wedge probe with a fourth pressure tapping installed on an inclined probe tip.

Despite widespread use in unsteady turbomachinery flows, pneumatic pressure probes are steady-state devices, which indicate an averaged value of the fluctuating pressure. The precise relationship between the probe indicated pressure and the required mean pressure depends on unsteady flow effects around the probe body, and pneumatic averaging in the pipes connecting the probe tappings to remote transducers. Detailed studies have been undertaken by Humm et al. (1995) and others, but the errors associated with measuring unsteady pressures with essentially steady-state probes are not fully understood.

Two further sources of error that occur even under steady flow conditions are discussed in the literature. Wedge-type probes fail to sense the correct static pressure when operating in close proximity to a wall through which the probe is introduced, yet well outside the boundary layer. This phenomenon is termed the "static pressure wall proximity effect" (Smout, 1990), and is illustrated in Fig. 2 (Cook, 1988). Cook calibrated three wedge probes having included angles of 23, 30, and 40 deg, respectively. Each probe was traversed across a 150-mm-dia closed section wind tunnel operating at 0.5 Mach number. Figure 2 shows the variation of static pressure coefficient, B, with immersion from the tunnel wall, where B is defined as the difference between the mean probe indicated static pressure and the true static pressure, normalized by the true dynamic head. All the probes indicated a static pressure near the wall, which was higher than that at larger immersions by an amount that increased as the wedge angle increased.

The second error source relates to the type of facility in which a wedge probe is calibrated. Fransson (1983) reports a cross-calibration exercise of the same 46 deg included angle wedge probe using eleven wind tunnels located throughout Europe. Calibrations at zero incidence over a Mach number range of 0.3 to 1.5 were completed in each facility. In collating the results, Fransson concluded that the probe read a higher static pressure in the free jet than in the closed section type of facility at nominally the same flow condition. From a detailed investigation of pressure probe characteristics, Humm et al. (1995) showed that the apparent sensitivity to yaw angle of a 45 deg wedge probe was higher in a closed section tunnel than in a free jet.

Part 1 of this paper reports a comprehensive series of experiments aimed at quantifying and understanding the wedge probe wall proximity effect and the calibration facility dependence effect over a wide range of representative test conditions. The results are discussed to arrive at a qualitative explanation of the flow mechanisms responsible for the two effects. In part 2 of this paper, the experimental results are used to validate numerical calculations of the flow around a wedge probe geometry. It is shown that the key flow features can be represented analytically to arrive at a simple model for predicting each effect, given a knowledge of the probe geometry and flow conditions.

2 Design of Investigation

The literature showed that the wall proximity effect was influenced by probe shape, by the prevailing flow conditions, and by the way in which the probe was presented to the flow. Because the background information was limited, and because turbomachinery flows are complex, effort was concentrated on establishing the relative importance of variables in a steady flow environment only. Section 3 reports experiments performed with wedge probes typical of those used for turbomachinery flow measurement. A factorial experiment was designed in which the influence of probe wedge angle, stem length, stem shape, flow yaw, and pitch angles on the wall proximity effect were quantified at representative flow Mach numbers and turbulence intensities. This was achieved by traversing wedge probes

Contributed by the International Gas Turbine Institute and presented at the 41st International Gas Turbine and Aeroengine Congress and Exhibition, Birmingham, United Kingdom, June 10–13, 1996. Manuscript received at ASME Headquarters February 1996. Paper No. 96-GT-146. Associate Technical Editor: J. N. Shinn.

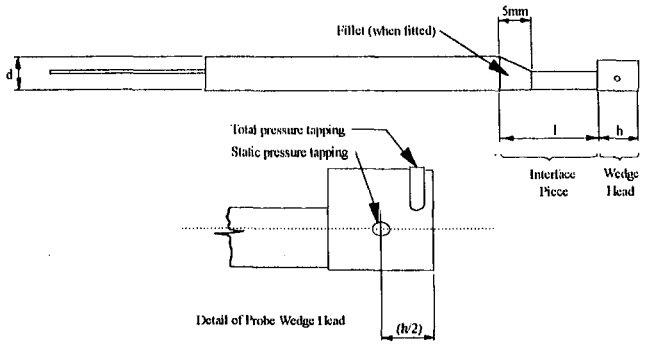

Fig. 1 Wedge-type pneumatic pressure probe

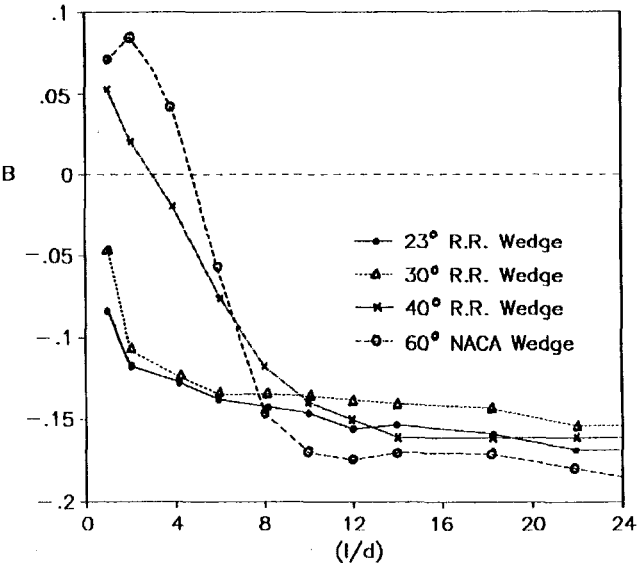

Fig. 2 Wedge probe wall proximity effect (Cook, 1988)

of 6.35 mm diameter in a 200-mm-dia, closed section wind tunnel (section 3.1). A truncated series of traverses was completed with the same probes in a low-speed compressor annulus to determine the influence of casing shape on the wall proximity effect. Section 3.2 describes an experiment to investigate the effect of the wind tunnel wall on probe yaw angle sensitivity. A definitive data set was also required on which to base the investigation of calibration facility dependence. This was established by calibrating four wedge probes in a closed flow and two open jet flows of different size (section 3.3).

The actual probe experiments were essential in quantifying the two effects, but they were not expected to provide much insight into the physical cause. A series of large-scale model tests were arranged for this purpose, and are reported in section 4. Smoke flow visualization tests were completed with various two-dimensional wedge shapes, and with an eight times scale model of a 30 deg included angle wedge probe. Pressure measurements at the probe model surfaces were also made. Results are discussed in section 5.

3 Actual Probe Tests

3.1 Wind Tunnel Factorial Experiment. A 200 mm internal diameter circular section wind tunnel with a bellmouth intake was chosen for the factorial experiment. A centrifugal fan was used to draw air at Mach numbers ranging between 0.1 and 0.8. Free-stream turbulence intensity could be increased from 0.8 to 4.5 percent by introducing a square mesh of circular wires at a plane 168 mm upstream of the traverse plane. To avoid the adverse influence of strong pressure gradients generated by the turbulence grid near the tunnel walls, a verticle plate was installed at the half radius position to act as the probe wall of introduction. The uniformity of the free-stream static pressure profile at the traverse plane was checked and found to differ from the pressures measured at static tappings in the tunnel walls by less than 1 percent dynamic head under all tested flow conditions. Further details of the wind tunnel and of the flow characterization exercise were given by Smout and Ivey (1994).

High and low values of each variable to be used in the factorial experiment were chosen to bracket those typically encountered in turbomachinery rig testing. For example, an included wedge head angle of 24 deg is the smallest that can realistically be achieved, while 60 deg is the largest angle that is normally used to avoid excessive blockage. Table 1 summarizes the high and low values chosen for each variable. Traverses were completed with every combination of high and low values, experiments being conducted in random order to reduce the risk of systematic error.

The results from each experiment were plotted as static pressure coefficient versus normalized probe immersion to give curves that qualitatively resembled the curves in Fig. 2. The area under the curve was computed in each case, and used to indicate the severity of the wall proximity effect in terms of the deviation of static pressure coefficient from the "free-stream" value, and the immersion over which this deviation occurred. Further data reduction was performed using the "Yates" technique (Davies, 1978) for comparing the results of a suitable number of factorial experiments in a sequential manner to quantify the relative effect of each variable, and interactions between variables. Each effect and interaction was tested against criteria based on the uncertainties associated with the experiment to determine its significance.

In brief, it was found that the length, l, of the interface piece had a strong influence on the wall proximity effect, where moving the wedge head away from the circular stem by increasing l gave a marked reduction in wall proximity effect. This is illustrated in Fig. 3, where the wall proximity curves for 24 deg probes with long and short interface piece lengths are overlayed. All other conditions between these two experiments were identical. A difference in static pressure coefficient (B) values for the two probes was also observed (see Fig. 3), where increasing the interface piece length from 6 mm to 20 mm raised B from -0.16 to -0.07 respectively. Three further variables of significance were wedge head included angle, Mach number, and pitch angle, where an increase in any one variable accentuated the wall proximity effect. Less significant were the effects of a stem

Nomenclature

B = probe static pressure coefficient = $(Sm - p_s)/(p_t - p_s)$
$B2$ = B based on $S2$
$B3$ = B based on $S3$
C_{yaw} = probe yaw angle coefficient = $(S2 - S3)/(p_t - p_s)$
d = probe stem diameter
I = probe immersion from wall of introduction
l = length of probe interface piece
p = pressure measured in calibration tunnel
$S2$ = pressure indicated by probe left-hand static tapping
$S3$ = pressure indicated by probe right-hand static tapping
Sm = $(S2 + S3)/2$

Subscripts

s = static value
t = total value

Table 1 High and low values of each variable used in factorial experiment

VARIABLE	HIGH VALUE	LOW VALUE
Wedge Angle	60°	24°
Interface Piece Length	20mm	6mm
Fillet	Fitted	Not fitted
Mach Number	0.75	0.35
Turbulence Intensity	4.5%	0.8%
Yaw Angle	+10°	0°
Pitch Angle	-10°	0°

fillet and the free-stream turbulence intensity, and probe yaw angle had no detectable effect. A fuller discussion of the results from this experiment is given by Smout and Ivey (1994).

To check that the wall proximity effect was independent of the precise geometry of flow ducting, the 24 deg wedge probes were traversed radially at the I.G.V. inlet plane of the Cranfield University low-speed, four-stage compressor rig (Howard et al., 1994). The compressor rig results agreed with the wind tunnel results to within the limits of experimental uncertainty for all tested conditions.

3.2 Near-Wall Yaw Angle Calibrations. The effect of yaw angle on the wall proximity effect was shown from the factorial experiment to be insignificant, but it was observed by Morris (1961) that wedge probe yaw angle *sensitivity* could be influenced by the close proximity of a wall. Yaw sensitivity is the per degree change in yaw coefficient, C_{yaw}, where C_{yaw} is defined as the difference between the probe static tapping readings, normalized by the true dynamic head. The influence of the wall on yaw angle sensitivity was investigated by calibrating wedge probes against yaw angle at four probe immersions. In general, C_{yaw} was directly proportional to yaw angle over ± 8 deg of yaw, beyond which the change in C_{yaw} was nonlinear but still monotonic with yaw angle increasing up to at least ± 20 deg of yaw. A marked difference between the four calibrations was apparent outside the linear region.

The slope of the linear region between ± 8 deg yaw (i.e., the probe yaw sensitivity) is plotted against immersion in Fig. 4, where yaw sensitivity is seen to increase by 12 percent between 15 mm and 60 mm immersion. Also plotted in Fig. 4 is the wall proximity effect curve for the same probe; yaw angle sensitivity is apparently affected over a similar immersion range to static pressure. Assuming that the calibration values at 60 mm were applied in analyzing radial traverse data from a turbomachine, at 0.1 Mach number and a probe setting angle of 5 deg relative to the flow, a near-wall measurement error of +0.7 deg would result from this yaw-angle wall proximity effect.

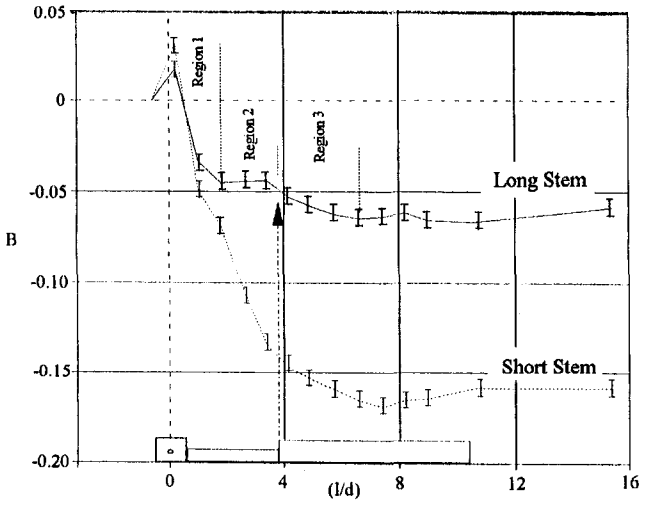

Fig. 3 Influence of interface piece length on wall proximity effect

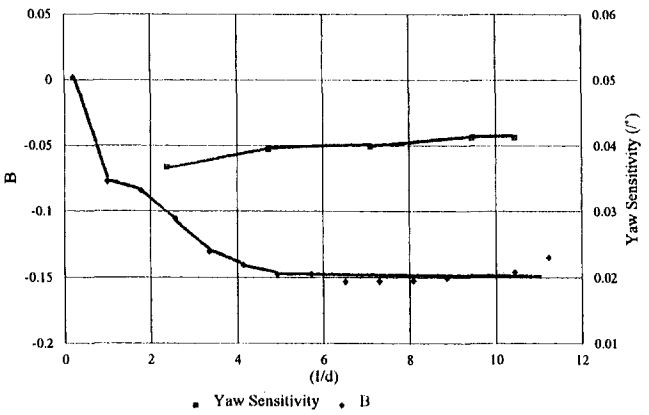

Fig. 4 30 deg wedge probe calibration against immersion at 0.1Mn

3.3 Calibration Facility Dependence. From the literature, it was known that calibrations of static pressure coefficient versus Mach number for a given wedge probe depended on whether a closed duct or a free-jet calibration flow was used (Fransson, 1983), and also possibly on the free-jet diameter (Shreeve, 1976). No information on the influence of probe geometry or incidence angle could be found. An experiment was designed in which the four wedge probes used in the factorial experiment (section 3.1) were calibrated in two open jets of different cross-sectional area, and in the closed section wind tunnel described in section 3.1. The general arrangement of the two open jet facilities was similar, the smaller facility (Jet 1) having a 50 mm by 30 mm rectangular section nozzle, and the larger facility (Jet 2) an octagonal section nozzle 102 mm across flats. Both flows were characterized to ensure uniformity of static pressure at the traverse plane.

Individual calibrations of each probe were completed in each facility at Mach numbers of 0.10 and 0.35. Probes were positioned in the open jets such that the plane of static tappings lay on the jet centerline, and at 100 mm immersion in the closed wind tunnel to avoid wall proximity effects. Yaw angle sensitivities were derived for each probe from the C_{yaw} characteristics, for yaw angle ranges of 0 to 10 deg and 0 to 20 deg. Values obtained at each Mach number and in the three facilities were grouped together under probe type and plotted in bar chart form, as shown in Fig. 5 for the short interface piece 24 deg probe. Static pressure coefficient values at zero yaw were grouped as a function of the probe included wedge angle; a bar chart summary of the 24 deg probe data is given in Fig. 6. For both yaw sensitivity and static pressure coefficient, substantial differences, particularly between the closed tunnel and open jet, but also between the two open jet calibrations, were observed.

4 Model Probe Tests

4.1 Two-Dimensional Models. The flow over various large-scale, two-dimensional wedge shapes was studied in a smoke flow visualization tunnel at the Cranfield University College of Aeronautics. This tunnel conforms with the general guidelines for smoke flow tunnel design given by Mueller (1983); flow is accelerated from the inlet settling chamber through a two-dimensional contraction of 8:1 into the working section, and a multipoint smoke rake mounted vertically in the contraction can be moved radially and laterally to align smoke

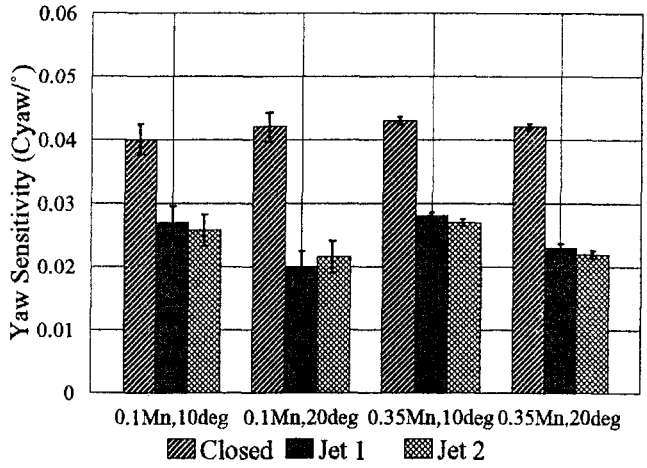

Fig. 5 Comparison between yaw sensitivities of short, 24 deg probe in open and closed flows

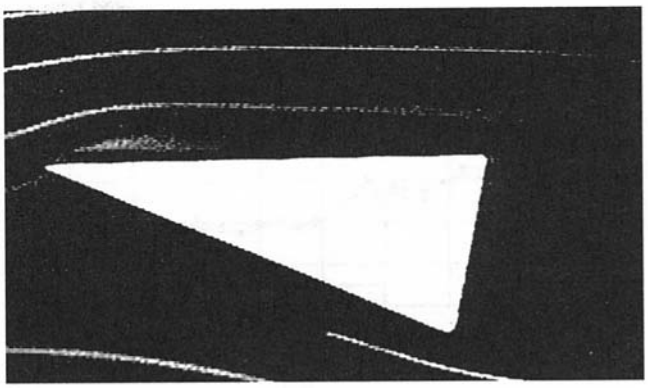

Fig. 7 Visualization of flow over 2-D 24 deg wedge model at 8 deg yaw and 5.2 × 10^4 Re

filaments with features of interest on the model. Stable, dense smoke filaments can be sustained at velocities between 2 and 10 m/s.

Wedges with included angles of 24 and 60 deg were constructed to simulate the actual probes tested in the factorial design experiment. A ×30 scaling factor was used to give turbomachinery representative Reynolds numbers (based on wedge chord) of up to 11 × 10^4, although representative Mach numbers could not be reproduced due to the velocity limit imposed by the smoke flow technique. The wedge leading edges were made detachable at a transverse line 10 percent chord back from the wedge apex, such that rounded leading edges could be substituted. Wedges were mounted in turn onto a disk in the tunnel back wall, and rotated to present the model at any required angle to the flow. Smoke flow patterns were recorded using video and still photography.

Figure 7 shows the flow around the sharp-nosed 24 deg wedge model inclined at 8 deg to the flow, at a Reynolds number of 5.2 × 10^4. Well-defined, laminar smoke filaments were observed in the free-stream flow away from the model, and near the model pressure surface. Although some detail of the suction surface flow was obscured by shadow, the flow lifted noticeably immediately downstream of the leading edge before moving back toward the wedge face further downstream. Diffusion of the same suction surface smoke filament just downstream of the leading edge was apparent from the corresponding video film, indicative of a suction surface separation bubble in the leading edge region at yaw angles of 8 deg and above.

As the yaw angle of the 24 deg probe was increased beyond 8 deg, the reattachment point moved progressively further back along the wedge suction surface until complete separation without re-attachment occurred at 20 deg yaw. A stagnation point was observed on the pressure surface, just downstream of the leading edge, about which the flow divided. This stagnation point migrated away from the leading edge as yaw angle was increased. Generally similar results were recorded for the 60 deg wedge model, with suction surface flow separation beginning at 18 deg yaw, followed by complete separation without re-attachment at 30 deg yaw. Radiusing the leading edge of the 24 deg wedge made little observable difference over the whole yaw angle range, but the suction surface separation bubble on the blunt nosed wedge formed at a lower yaw angle of 4 deg. Fitting a rounded leading edge to the 60 deg wedge had more effect, and delayed the onset of transition and complete separation without re-attachment to higher yaw angles. As with the 24 deg wedge, suction surface separation was evident in the blunt-nosed 60 deg model at 4 deg yaw. Although variations in the size and structure of the separation bubble might have been expected as a function of Reynolds number, the suction surface flow was not visualized in sufficient detail to detect any such changes.

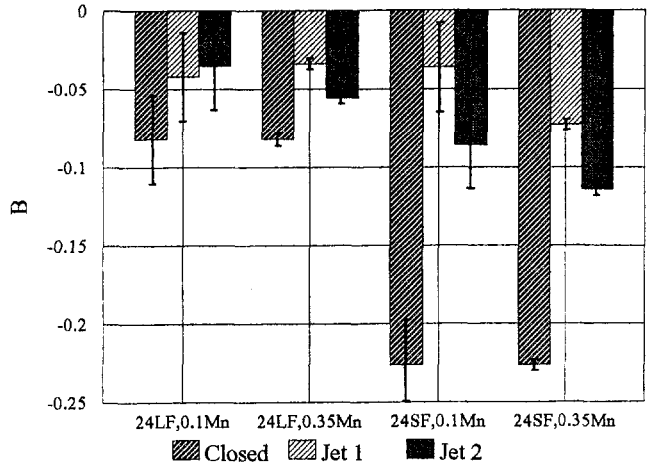

Fig. 6 Comparison between *B* values for 24 deg probes in open and closed flows

4.2 Three-Dimensional Models. A 0.61 m square section wind tunnel at Sheffield University was used for smoke flow visualization experiments on a ×8 scale model of a 30 deg wedge probe. The wind tunnel was similar to the Cranfield tunnel in layout, but with an 18:1 three-dimensional contraction from the inlet to the working section. Optical access was available from each side and through the tunnel roof at the working section. A flat plate was installed 100 mm in from one verticle wall to replicate the environment in which the actual probe factorial experiments were conducted. The static pressure profile at the traverse plane was found to vary by less than ±1.5 percent dynamic head at all flow conditions.

The choice of a ×8 scaling factor for the model probe gave a traverse distance from wall to wall of ten probe stem diameters, sufficient to cover the extent of static pressure wall proximity effects observed in the factorial experiment. The model was fabricated in stainless steel with static pressure tappings incorporated at various locations over the wedge faces and in the stem leading and trailing edge regions (see Figs. 8 and 9). These were intended for mapping the probe surface static pressure distribution as a function of probe immersion, yaw angle and flow condition.

4.2.1 Pressure Measurements. To establish whether this low-speed experiment was representative of the actual scale probe factorial experiment, a series of large-scale probe tra-

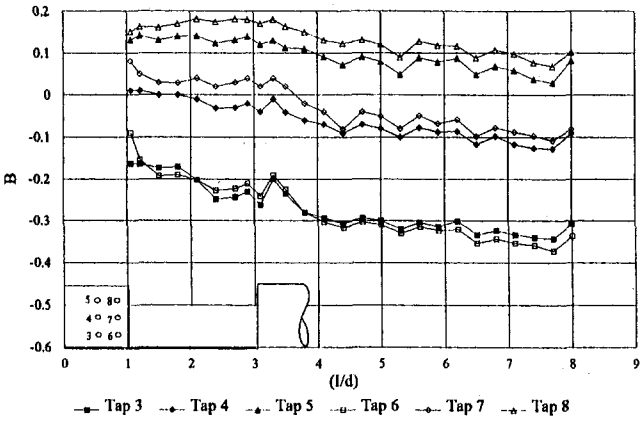

Fig. 8 Large-scale wedge probe radial traverse at 25 m/s (taps 3 to 8)

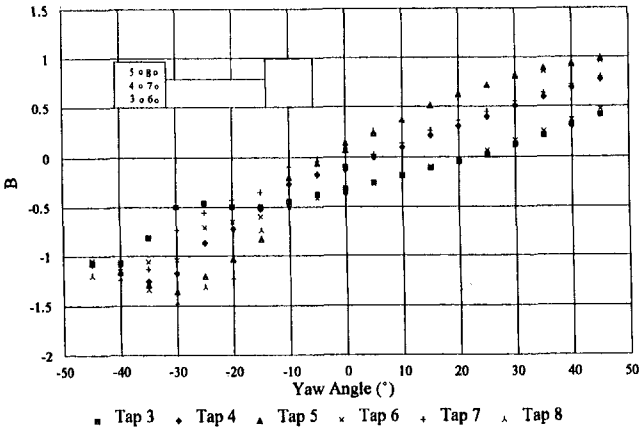

Fig. 10 Large-scale wedge probe calibration against yaw angle at 25 m/s

verses were conducted at 0 deg yaw, and at Reynolds numbers between 1.7×10^4 and 11.3×10^4. Water manometers were used to measure the pressure at each probe surface pressure tapping simultaneously. As in the factorial experiment, the tunnel speed was adjusted at each immersion to retain a constant dynamic head throughout the traverse, thus compensating for probe blockage effects. Calibrations against yaw angle were conducted at an immersion of eight times the probe stem diameter to avoid wall proximity effects.

In Fig. 8, B for six of the wedge face static tappings is plotted against the normalized probe immersion (l/d), for a Reynolds number of 8.3×10^4. The probe is drawn to scale against the abscissa of this plot such that the correspondence between a set of data points and the probe position relative to the flat plate can be visualized. (For example, at $2d$ immersion, the probe wedge head and half of the interface piece were immersed in the flow, etc.). Tapping No. 4 is the closest in position to the static tappings of the actual probes used in the factorial experiment; this tapping indicates a fall in static pressure with increasing immersion, which is characteristic of the wall proximity effect, and of a similar magnitude. Similar behavior is observed with the other tappings, the magnitude of change in B depending primarily on the distance back from the leading edge, and to a lesser extent on the stemwise displacement of the tapping from the probe tip. A discontinuity in the curves for tappings 3 and 6 at three stem diameters immersion is observed, and corresponds with the emergence of the circular probe stem into the flow. The variation of static pressure at the back of the probe as a function of probe immersion at a Reynolds number of 8.3×10^4 is plotted in Fig. 9. The beginning of each curve corresponds with the emergence of each successive pressure tapping.

In Fig. 10, B values for six of the wedge face static pressure tappings are plotted against yaw angle. The curves bunch together in three groups at positive incidence, the lower group comprising the curves for the two rear most tappings (3 and 6), and the upper group the curves for the two near-most leading edge tappings (5 and 8). This grouping is lost at negative incidence where the instrumented wedge face becomes the wedge suction surface, and the variation of B with yaw angle is no longer monotonic. It can be infered from Fig. 10 that probe sensitivity to yaw angle increases as the static pressure tappings are moved toward the wedge leading edge, as previously shown by Ferguson and Al-Shamma (1967) and others. Broadly similar calibrations and traverse results were recorded at the other flow conditions.

4.2.2 Smoke Flow Visualization. The large-scale probe was set to the required immersion at a given flow condition, and a single point smoke wand traversed upstream and in the plane of the probe. Good quality flow patterns were recorded onto video at Reynolds numbers of upto 2.0×10^4, but flow features, particularly in the probe wake, became less well defined at higher Reynolds numbers.

Key features of the visualized flow patterns are sketched in Fig. 11. At $2d$ immersion, a recirculation at the upstream lip of the probe hole of introduction, and a second, stable recirculatory region at the probe tip, in the wake of the wedge head and in the plane of the probe were observed. It was noted that the size

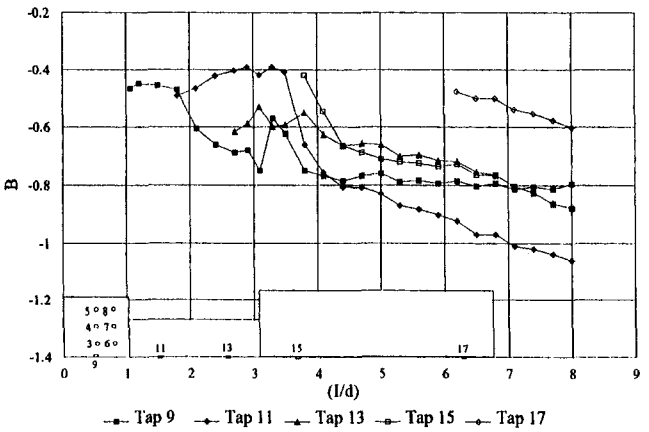

Fig. 9 Large scale wedge probe radial traverse at 25 m/s (taps 9 to 17)

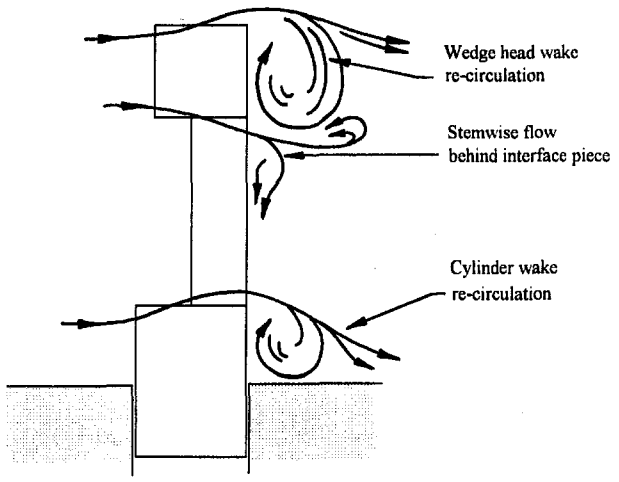

Fig. 11 Sketch of three-dimensional flow versus results: probe at 4*d* immersion

of this second recirculation increased as the probe was traversed out from the wall, before attaining a stable size at approximately $2d$ immersion. Faint traces of smoke in the wake of the interface piece suggested flow out of the bottom of the wedge tip recirculation and down the back of the probe toward the wall. The tip recirculation could be visualized by aligning the smoke probe with either the top or bottom end of the wedge head, indicating that flow was sucked in to the wedge wake region from both the free and supported ends.

By $4d$ immersion, whilst the wedge head wake recirculation remained at its equilibrium diameter, a recirculatory flow structure at the base of the cylindrical stem and in the plane of the probe had also formed, and the stemwise flow along the back of the probe had intensified. As the probe immersion was increased further, the recirculation in the wake of the cylinder continued to grow until stabilizing at a constant diameter of approximately $4d$ at $7d$ immersion. Beyond this immersion, the structure of the recirculatory regions in the wake of the wedge head and the cylindrical stem showed little change, but remained locked to the probe with a continual transfer of fluid from the former to the latter along the back of the interface piece.

Flow over the central part of the wedge head was visualized in a plane perpendicular to the probe as the probe yaw angle was varied. At 0 deg yaw angle, a pair of contrarotating vortices were observed in the wake of the wedge head, which extended downstream from the base of the wedge by approximately 0.75 wedge chord. As yaw angle was increased, the wake flow became more obviously three dimensional, with flow from the wedge pressure surface spiraling over the top of that leaving the suction surface. This observation agreed qualitatively with the two-dimensional wedge model flow visualization experiments. Smoke particles were also observed passing over the tip of the probe from pressure surface to suction surface, but the video image was not sufficiently well resolved to confirm the formation of a separation bubble in the leading edge region of the wedge suction surface at yaw angles greater than 8 deg, as noted in the two-dimensional model studies.

5 Discussion

Considering first the flow visualization results, the coherent, stable recirculatory region identified in the probe wake gives a link between probe immersion and the probe's characteristics. The recirculation is the result of viscous deceleration of fast-moving fluid just downstream of the probe tip, and causes a stemwise velocity component immediately adjacent to the wedge rear face, and toward the probe free end. An associated pressure drop is to be expected, of a magnitude depending on the size and structure of the recirculation and hence on the probe immersion. From Fig. 9, the fall in static pressure at the back of the wedge indicated by tapping No. 9 is 25 percent dynamic head for immersions between $1d$ and $3d$. By conservation of energy, this reduced base pressure must be accompanied by flow acceleration over the wedge faces, resulting in a reduced pressure at the wedge face static pressure tappings consistent with the wall proximity effect.

Close inspection of the wall proximity curve for the long interface piece, actual size probe (Fig. 3), shows that B falls through the immersion range defined as region 1 in a manner consistent with the model described above. The equilibrium state reached in region 2 indicates that the wedge head is now sufficiently immersed to be free from any influence of the eddy at the hole of introduction, and that the recirculation in the wedge head wake has attained an equilibrium diameter with a constant associated wedge base pressure. This is consistent with the flow visualization results in section 4.

The equilibrium state is upset at the beginning of region 3, which corresponds with the emergence of the circular stem through the wall. It is proposed that the recirculating region established in the wake of the cylinder causes a reduction in the static pressure in this region below that which would be expected for an infinitely long (two-dimensional) cylindrical element. This proposition is suggested by the flow visualization study results, and supported by experimental data in Fig. 9, where tappings 15 and 17 positioned in the cylinder trailing edge both indicate a monotonically decreasing pressure with increasing immersion. For this to cause the reduction in indicated static pressure observed through region 3 implies some interaction between the two recirculating regions. An interaction was apparent in the flow visualization studies, where stemwise flow down the back of the probe from the wedge recirculation toward the base of the cylinder was observed. The result is to modify the wedge head wake recirculation and further increase the momentum of fluid near the wedge faces, thus reducing the wedge face static pressure further. In the flow visualization studies, the cylinder wake recirculation reached an equilibrium diameter at a given immersion beyond which no further growth occurred. This is consistent with the second plateau in the wall proximity curve at the end of region 3 in Fig. 3.

Developing this argument, a reduction in the length of the interface piece effectively moves the recirculations behind the wedge and the cylinder closer together. This intensifies the stemwise static pressure gradient, and modifies the wedge wake recirculation, which in turn governs the flow over the wedge faces. A greater wall proximity effect might be expected, and was observed experimentally (Fig. 3). It follows that the different static pressure coefficients associated with the long and short interface piece probes are determined by the relative strengths of these recirculations. Much wedge probe research has been conducted by previous investigators using two-dimensional wedge shapes to determine characteristics, which are then assumed to hold for three-dimensional probes (Ferguson and Al-Shamma, 1967 for example). The validity of this approach must be in doubt, since the recirculations are not established with two-dimensional shapes. If the recirculating regions were influenced by highly turbulent or periodically unsteady flow typical of turbomachinery, it also follows that the static pressure coefficient would differ from that determined in a steady calibration flow.

This previously unreported idea of probe characteristics being governed by interacting regions of recirculating flow in the probe wake is useful in explaining other results from the factorial experiment in section 3.1. For example, changing the pitch angle from 0 to -10 deg resulted in a significant increase in wall proximity effect, which is consistent with the probe wake recirculation model. Introducing negative pitch effectively reduces the separation between the two discrete recirculations, and is analogous to reducing the interface piece length. Inclining the probe also axially displaces the two recirculations relative to each other, which may again influence the interaction between them. Increasing free-stream Mach number also resulted in a significant increase in wall proximity effect. It is well known that the pressure drag coefficient for two-dimensional wedge shapes and cylinders increases with increasing Mach number. Because the wall proximity effect depends directly on the wedge base pressure, and indirectly on the pressure at the back of the cylindrical stem, a more severe wall proximity effect is to be expected at higher Mach numbers.

The model is also of use in understanding results from the facility dependence experiments in section 3.2. Figure 6 shows that the static pressure coefficients at zero yaw obtained in the closed tunnel were always lower (more negative) than the values obtained in the free jet facilities, by up to 18 percent dynamic head in the worst case. From the flow visualization studies, it is estimated that the two probe wake recirculations span a stemwise distance from the probe tip of 51 mm for the long interface piece probe, and 37 mm for the short interface piece probe. Comparing these values with the jet dimensions, the recirculation in the cylindrical stem wake would have been influenced by the interface between the free jet and the sur-

rounding stationary air for both probes calibrated in the smaller jet 1, and for the longer probe in jet 2. Assuming that turbulent flow at the free jet boundary dissipates the recirculating motion behind the cylinder, the probe wake recirculation model predicts a higher value of probe indicated static pressure than that in a larger diameter jet flow where both recirculations were fully developed. This was the case for both the 24 and 60 deg included angle wedge probes.

Extending the probe wake recirculation model to explain the various wedge probe yaw characteristics reported in sections 3.2 and 3.3 is difficult, given the limited flow visualization data at other than 0 deg yaw. Three ways in which the model could be altered to explain these results are offered, but further work is required in this area:

(*i*) The recirculating region in the wake of the wedge head may be sucked into the suction surface region of the wake flow when the probe is operated at incidence, and generate a pressure gradient at the base of the wedge with a minimum at the suction surface corner. As immersion is increased, so the recirculation grows, reducing the base pressure differentially so as to accelerate the flow more rapidly over the suction surface than the pressure surface.

(*ii*) Flow migration over the free end of the wedge head from pressure to suction surface was observed during the flow visualization studies. Over-tip leakage flow may roll up into a tip vortex with its origin at the suction surface trailing edge. The axial velocity associated with such a vortex may locally amplify the recirculation in the suction surface region of the wedge wake and preferentially accelerate the suction surface flow as before.

(*iii*) It was shown from the two-dimensional wedge flow visualisation studies (section 4.1) that a separation bubble forms in the leading edge region of the wedge suction surface at yaw angles of 8 deg and above, and that the re-attachment point moves downstream with increasing yaw angle. Points (*i*) and (*ii*) imply alterations to the suction surface flow that may influence the formation and growth of the separation bubble, and change the static pressure profiles over the wedge faces in consequence.

Each of points (*i*) to (*iii*) links probe yaw measurement characteristics to the probe wake recirculations. For this link to be valid, yaw sensitivity must be influenced under similar circumstances to probe indicated static pressure. In section 3.2 it was shown that the "yaw angle wall proximity effect" occurred over a similar immersion range to the static pressure wall proximity effect (Fig. 4). Considering the calibration facility dependence of yaw angle sensitivity reported in section 3.3, values obtained from the two free-jet facilities agreed with each other within the limits of experimental uncertainty, but were substantially lower than values obtained in the closed tunnel. Hence, although the flow structures local to a yawed probe have not been fully resolved, there is strong experimental evidence to link the yaw angle measurement characteristics of a wedge probe to the recirculations that occur in the probe wake. As with static pressure coefficient, this raises the concern that steady flow probe calibrations against yaw angle may be invalid under unsteady flow conditions.

6 Conclusions

A series of experiments with actual sized wedge probes has been completed to quantify the near-wall characteristics of these instruments more fully. From a factorial experiment in which the effect of seven variables was investigated, it was found that increasing the length of the interface piece between the probe head and stem gave a significant reduction in near-wall static pressure measurement errors. Three further variables of significance were wedge head included angle, Mach number, and pitch angle, where an increase in any one resulted in an accentuated static pressure wall proximity effect. Significantly different calibrations of the same probe were obtained between a closed tunnel and open jet facilities, where static pressure coefficient and yaw angle sensitivity were most altered.

Insight into the physical cause of these effects was gained from flow visualization experiments around large-scale models. Two distinct regions of recirculating flow were identified in the probe wake, and a link between these and the flow over the wedge faces has been demonstrated. It is shown that any alteration to the recirculations, by operating the probe near to the wall or in a free jet, will alter the static pressure and yaw angle measurement characteristics of a wedge probe. Probe calibrations obtained in steady flow may not be valid under unsteady flow conditions for similar reasons.

Acknowledgments

The authors wish to thank Rolls-Royce plc for financially supporting the work described. The views expressed are those of the authors and are not necessarily shared by the company.

References

Bubeck, H., and Wachter, Y., 1987, "Development and Application of a High Frequency Wedge Probe," ASME Paper No. 87-GT-216.

Cook, S. C. P., 1988, "Measurement Techniques for Unsteady Turbomachinery Flows," PhD Thesis, Cranfield University, Bedford, England.

Davies, O. L., 1978, *The Design and Analysis of Industrial Experiments,* 2nd ed., Longman Group Ltd., London, England.

Ferguson, T. B., and Al-Shamma, K. A., 1967, "Wedge Type Pitot-Static Probes," *BHRA SP919,* 9th Members Conference, British Hydromechanics Research Association, Cranfield, England.

Fransson, T., 1983, "Aerodynamic Probe Calibrations—Results From the Workshop on Probe Calibrations, 1981–1983," *Proc. 7th Symp. on Measuring Techniques for Transonic and Supersonic Flows in Cascades and Turbomachines,* Aachen, Germany.

Howard, M., et al., 1994, "Endwall Effects at Two Tip Clearances in a Multistage Axial Flow Compressor With Controlled Diffusion Blading," ASME JOURNAL OF ENGINEERING FOR GAS TURBINES AND POWER, Vol. 116, pp. 635–647.

Humm, H. J., et al., 1995, "On Fast-Response Probes: Part 2—Aerodynamic Probe Design Studies," ASME JOURNAL OF ENGINEERING FOR GAS TURBINES AND POWER, Vol. 117, pp. 618–624.

Morris, R. E., 1961, "Multiple Head Instrument for Aerodynamic Measurements," *The Engineer.*

Mueller, T. J., 1983, "Smoke Visualisation in Wind Tunnels," *Astronautics and Aeronautics,* January ed.

Shreeve, R. P., 1976, "Calibration and Application of Multiple Sensor Pneumatic Probes for Velocity Determination, With Corrections for Boundary Effects," AIAA Paper No. 76-373.

Smout, P. D., 1990, "The Problem of Static Pressure Measurement in Turbomachinery Annuli Using Traversable Instrumentation," *Proc. 10th Symp. Measuring Techniques for Transonic and Supersonic Flow in Cascades and Turbomachines,* VKI, Brussels, Belgium.

Smout, P. D., and Ivey, P. C., 1994, "Wall Proximity Effects in Pneumatic Measurement of Turbomachinery Flows," ASME Paper No. 94-GT-116.

Smout, P. D., and Ivey, P. C., 1997, "Investigation of Wedge Probe Wall Proximity Effects: Part 2—Numerical and Analytical Modeling," ASME JOURNAL OF ENGINEERING FOR GAS TURBINES AND POWER, Vol. 119, this issue, pp. 605–611.

Investigation of Wedge Probe Wall Proximity Effects: Part 2—Numerical and Analytical Modeling

P. D. Smout
Rolls-Royce plc.,
Derby, United Kingdom

P. C. Ivey
School of Mechanical Engineering,
Cranfield University,
Bedford, United Kingdom

An experimental study of wedge probe wall proximity effects is described in Part 1 of this paper. Actual size and large-scale model probes were tested to understand the mechanisms responsible for this effect, by which free-stream pressure near the outer wall of a turbomachine may be overindicated by up to 20 percent dynamic head. CFD calculations of the flow over two-dimensional wedge shapes and a three-dimensional wedge probe were made in support of the experiments, and are reported in this paper. Key flow structures in the probe wake were identified that control the pressures indicated by the probe in a given environment. It is shown that probe aerodynamic characteristics will change if the wake flow structures are modified, for example by traversing close to the wall, or by calibrating the probe in an open jet rather than in a closed section wind tunnel. A simple analytical model of the probe local flows was derived from the CFD results. It is shown by comparison with experiment that this model captures the dominant flow features.

1 Introduction

It is known that wedge-type probes fail to sense the correct static pressure when operating in close proximity to a wall through which the probe is introduced, and that static pressure measurement errors of up to 20 percent dynamic head may occur (Smout and Ivey, 1994). It is also known that the aerodynamic calibration of a given wedge probe performed in a closed-section wind tunnel may differ significantly from that conducted in an open jet. A detailed experimental investigation of both these effects is reported in Part 1 of this paper (Smout and Ivey, 1997). Insight into the physical cause of each effect was gained from flow visualization experiments around large-scale models. Two distinct regions of recirculating flow were identified in the probe wake, and it was shown how these flow features might govern the aerodynamic characteristics of the probe.

The numerical modeling content of this wedge probe investigation was included to complement the experimental work. The ultimate aim was to compute the three-dimensional flow field around a wedge probe immersed by differing amounts from the wall of introduction, to compare the predictions with the flow-visualization pictures qualitatively, and to validate the predictions quantitatively against the factorial experiment results. The intention was then to examine the computed whole flow field solution to understand more fully the flow mechanisms responsible for the wall proximity effect.

The use of computational fluid dynamics (CFD) codes to model the response of a narrow angle wedge probe to periodically unsteady flow at nominally 10 deg incidence is reported by Ainsworth and Stickland (1992). They used a fully viscous, unsteady version of the two-dimensional "UNSFLO" code developed by Giles and Haimes (1991), and resolved a region of separated flow in the suction surface leading edge region. The extent of separation varied periodically with changing flow condition. Depolt and Koschel (1992) used a three-dimensional panel numerical method to investigate the facility dependence of wedge probe calibrations. Although the characteristics of various pressure probes were predicted, the facility dependence was not resolved. No other attempts at numerically modeling the steady flow behavior of pressure probes are found in the literature.

Moore's Elliptic Flow Program (MEFP) pressure correction code was chosen for this study, and is described in section 2. To check the suitability of the code, the two-dimensional flow visualization experiments described in part 1 were simulated by modeling the flow around a 24 deg wedge shape at three yaw angles (section 3). Predictions of the flow around a fully three-dimensional model of a 30 deg probe at three immersions were completed and are reported in section 4. Comparisons with experimental results are included to show the extent to which the predictions can be relied upon. In section 5, the key features of the flow field are identified from the CFD solutions, and modeled analytically. The ability of this analytical model to predict the wall proximity characteristics of a given wedge probe is discussed with reference to experimental results in section 6. Concluding remarks are given in section 7.

2 CFD Code Selection and Description

For the purposes of wedge probe modeling, a pressure correction code was considered more appropriate than time-marching methods, given that the turbomachinery environments in which probes operate are generally subsonic. From the large-scale probe flow visualization studies, it was known that flows local to the probe were highly three-dimensional and potentially unsteady. The complex wedge probe geometry also demanded that a code with sufficiently flexible grid point structuring and classification be chosen. The UNSFLO code is capable of resolving time-dependent fluctuations, but was not available as a three-dimensional flow solver at the time of the investigation. Given that at least the recirculatory regions in the wake of the probe appeared from the flow visualization experiments to be stable, the risks involved in using a steady flow code were judged to be acceptable, and MEFP was selected as best meeting the remaining criteria.

MEFP is a fully three-dimensional, steady flow solver for compressible or incompressible, inviscid, laminar or turbulent

Contributed by the International Gas Turbine Institute and presented at the 41st International Gas Turbine and Aeroengine Congress and Exhibition, Birmingham, United Kingdom, June 10–13, 1996. Manuscript received at ASME Headquarters February 1996. Paper No. 96-GT-147. Associate Technical Editor: J. N. Shinn.

flows with or without heat transfer. It was originally written to calculate flows in turbomachinery blade rows, and has since been used for modeling flows in internal cooling passages, disk cavities, particle separators, and centrifugal impellers (Northall, 1993). A structured, three-dimensional grid is used, the location of each grid point being specified in Cartesian or cylindrical coordinates. Grid points are assigned a type depending on whether they lie in the flow, within the solid body, or on the body surface. This approach permits a grid to pass unaltered through a solid object as well as the flow field, and is particularly amenable to modeling complex geometries. Local mesh embedding is also available, where a fine mesh is incorporated locally into a coarser, structured mesh to better define regions of interest.

The code is based on the steady Reynolds-averaged conservation equations in a rotating coordinate system. (The speed of rotation was set to zero in this case.) Turbulence modeling is achieved using a Prandtl mixing-length model to calculate the turbulent viscosity. This is combined with the laminar flow viscosity, in a way that depends on the proximity to a fluid boundary, to give an effective viscosity for use in the momentum equation. Transition points can be specified by defining arrays that modify the laminar and turbulent viscosities.

The governing equations are discretised on the basis of upwinded control volumes, to achieve a second-order accurate scheme independent of cell Reynolds number (Moore, 1985). This approach avoids the stability difficulties that arise from accurately evaluating absolute values for a given transported variable at the faces of a non-upwinded control volume, and ensures unconditional, second-order accuracy of the convection and diffusion terms in the conservation equations.

The per iteration change in each flow variable may be tuned by the user, but is generally large to give convergence in a relatively small number of iterations. MEFP does not have a built in convergence criterion, but relies on the user to review the results after a certain number of passes, and to run more passes as required. The rms change in static pressure decreases as the calculation converges, and should ultimately reduce to a small fraction of the variation in static pressure across the flow domain. Two orders of magnitude reduction in static pressure change was taken as a good indication of convergence.

3 Modeling of Two-Dimensional Wedge Flows

The flows around a two-dimensional, 24 deg wedge shape inclined at yaw angles of 0, 4 and 8 deg were calculated to assess the suitability of the code for modeling more complex three-dimensional probe geometries. This study was also an opportunity to investigate the separation bubble observed on the suction side of the 24 deg included angle wedge model at 8 deg yaw in the two-dimensional flow visualization experiments (Part 1, section 4.1).

3.1 Mesh Generation. The two-dimensional flow visualization experiment described in Part 1 was simulated by basing the master grid geometry on the wedge model dimensions. The area of the flow domain was made equal to the flow visualization wind tunnel window. A structured grid of coarsely distributed I and J grid lines was introduced over the entire flow domain using mesh manipulation software. More tightly packed lines through the wedge itself were flared to improve cell aspect ratios, and to reduce the skewness of cells near the wedge face corners. A limited amount of embedded mesh was introduced using automated embedding routines described by Lapworth (1993). This improved the grid resolution, particularly in the nose and trailing edge regions, where significant flow activity was expected. The resulting mesh (Fig. 1) was filed as a datum and used as the basis for all subsequent calculations of wedge flows.

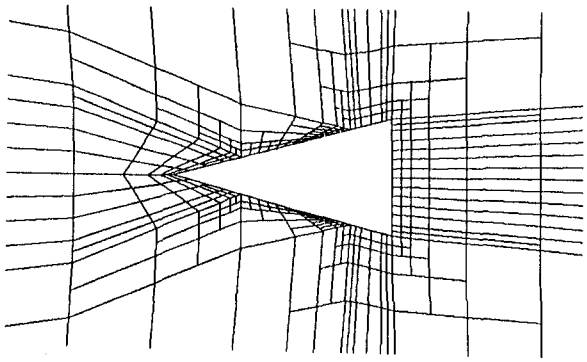

Fig. 1 Datum grid for two-dimensional wedge

3.2 Solutions for 0 deg Incidence. A free-stream velocity of 4.3 m/s was set to give a Reynolds number based on wedge chord of 5.2×10^4. An initial, numerical instability in the highly skewed cells at the wedge leading edge was overcome by applying explicit smoothing to the static pressure in a localized region adjacent to the wedge apex. A converged solution was achieved that showed the expected decrease in static pressure with increasing distance back from the wedge apex. A concentration of concentric contours at the base of the wedge implied a closed wake comprising two symmetric eddies. While the calculated flow was well behaved through the highly skewed cells near the grid corner regions, the jagged nature of the static pressure contours downstream of the wedge indicated some grid dependency in the solution.

To minimize grid dependency, and to improve flow definition in the wake region, the mesh was automatically adapted using an option within the mesh embedding software (Lapworth, 1993). The first-order difference of velocity, du, was used as the criterion for subdividing sufficiently large cells in which du was greater than the rms value of du. A converged solution for the adapted mesh was calculated, and velocity vectors for the final solution are plotted in Fig. 2. Significantly improved definition, particularly of the wake flow structure was achieved as a result of the adaption. From Fig. 2, the length of the recirculat-

Nomenclature

B = static pressure coefficient = $(p_p - p_s)/(p_t - p_s)$
C = speed of sound in air
d = probe stem diameter
I = probe immersion from wall of introduction
L = length of wedge face
p = pressure
q = equilibrium value of forced vortex tangential velocity
r = distance from center of forced vortex
v = forced vortex tangential velocity
w = forced vortex rotational speed
x = distance back from wedge leading edge

Subscripts

b = at base of wedge or cylinder
c = related to cylinder
e = equilibrium value
o = free-stream value
p = predicted
s = static value
t = total value

Superscripts

$'$ = modified once
$''$ = modified twice

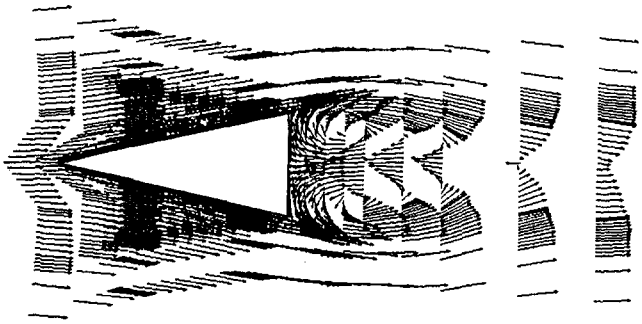

Fig. 2 Velocity vector representation of flow around two-dimensional wedge at 0 deg yaw (after mesh adaption)

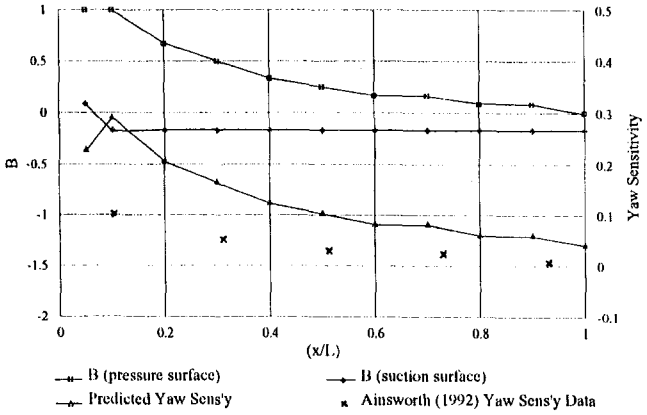

Fig. 3 Predicted 24 deg wedge face static pressure distribution at 4 deg yaw (5.2×10^4 Re)

ing wake region is approximately one wedge chord, in good agreement with the experimental observations. No attempt was made to force symmetry in the solution, and some regions of asymmetric flow are evident, probably due to numeric rounding errors. Further attempts at adapting the grid were largely unsuccessful, the tendency being to concentrate the mesh in these areas and to amplify the asymmetry.

Comparison of the wedge face static pressure distribution with that determined experimentally by Ferguson and Al-Shamma (1967) was made to check the absolute accuracy of the calculation. Static pressure coefficient, B, at various positions, x, downstream from the wedge leading edge was derived from the solution for the adapted mesh. The static pressure profiles agree to within ± 6 percent dynamic head over the range of x/L for which experimental data were available.

3.3 Solutions for 4 and 8 deg Incidence. Yawed flow onto the datum wedge mesh was simulated by defining i and j-direction velocity components to give a resultant of 4.3 m/s positively inclined by 4 or 8 deg to the horizontal. Grid refinement using the adaption and manual embedding methods was required to achieve converged solutions for both cases. In the solution for 4 deg yaw, the flow accelerated over the wedge faces before separating at the rear corners as in the 0 deg yaw case. The contrarotating vortex pair was still apparent in the wake region, but the vortex corresponding to the leeward wedge face had considerably outgrown the other, to increase the closed wake length to approximately two wedge chords. This resulted in higher momentum fluid leaving the pressure surface than the suction surface, causing an asymmetric velocity distribution in the wake further downstream. These trends were also observed experimentally, but because the computation was purely two dimensional and steady, the swirling motion visualized in the wake of the two-dimensional wedge shapes could not be modeled.

The static pressure variation over the wedge faces is shown in Fig. 3, where static pressure coefficient, B, is plotted against x/L. A static pressure coefficient of unity was predicted on the pressure surface for x/L values less than 0.1 and indicates a stagnation point at 5 percent chord back from the pressure surface leading edge position. The flat static pressure profile indicated for the suction surface implies that any variation in static pressure was less than the contour intervals of the plot from which the data were taken, i.e., less than ± 4.5 percent dynamic head.

Yaw sensitivity was computed from the wedge face pressure profiles, and is also plotted against (x/L) in Fig. 3. Experimental data presented by Ainsworth and Stickland (1992) for a $\times 50$ scale, 20 deg wedge at 4.0×10^4 Reynolds number are included for comparison. Both experiment and prediction follow the expected trend of decreasing yaw sensitivity with increasing distance back from the wedge apex. The generally higher level of yaw sensitivity predicted for the 24 deg wedge is to be expected, given that the experimental data relate to a wedge shape of smaller included angle.

In the 8 deg yaw solution, the contrarotating vortex nature of the wake was replaced by a single vortex emanating from the suction surface flow, succeeded downstream by a complex series of eddies. Although generally well converged, some instability was observed in the solution of the wake flow. This was indicative of an unsteady wake, as visualized in the two-dimensional wedge experiments at yaw angles greater than 7 deg. Velocity vectors in the leading edge region are plotted in Fig. 4(a). Flow divides about a stagnation point on the pressure

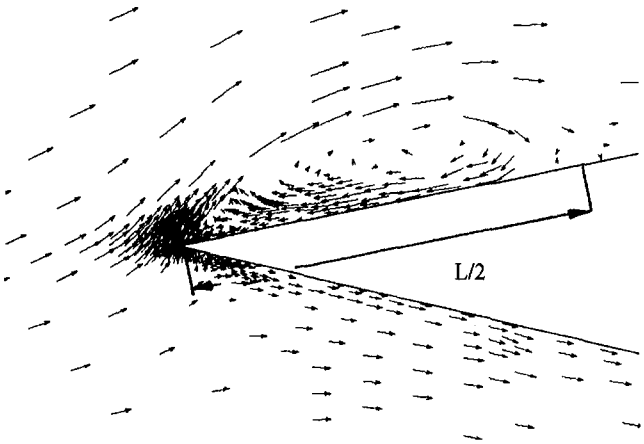

Fig. 4(a) Separation bubble in suction surface leading edge region at 8 deg yaw

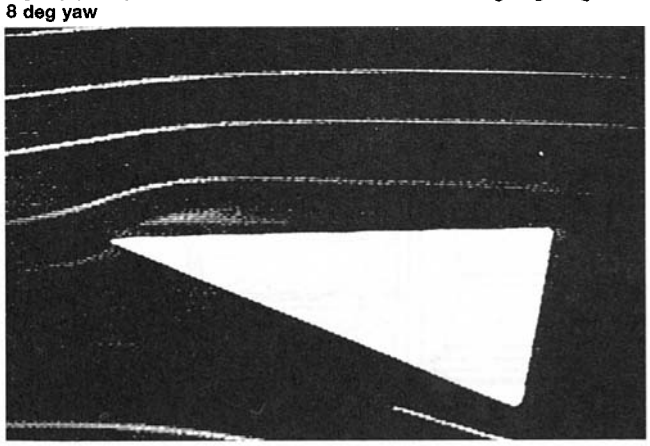

Fig. 4(b) Visualization of flow over two-dimensional 24 deg wedge model at 8 deg yaw and 5.2×10^4 Re

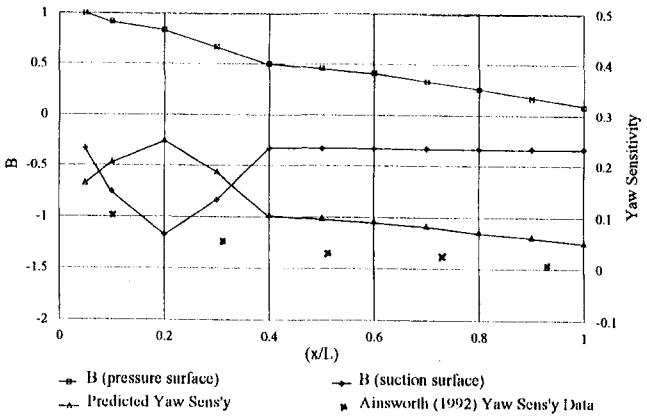

Fig. 5 Predicted 24 deg wedge face static pressure distribution at 8 deg yaw (5.2×10^4 Re)

surface as in the 4 deg yaw case, but then separates at the wedge apex to form a closed recirculation or separation bubble extending half a wedge chord along the suction surface. The prediction of a separation bubble is in excellent qualitative agreement with the two-dimensional flow visualization studies (Fig. 4(*b*)).

The variation of static pressure over the wedge faces at 8 deg yaw is plotted in Fig. 5. A minimum turning point occurs in the suction surface pressure profile at 0.2 (x/L), and corresponds with the center of the separation bubble. The influence of this on the predicted yaw sensitivity is to move the position of maximum sensitivity back from 0.1 (x/L) at 4 deg yaw, to 0.2 (x/L). The experimental data were not sufficiently well resolved in the leading edge region to capture this trend, although the predicted and experimental data show similar trends at greater (x/L) values.

The level of qualitative and quantitative agreement between experiment and numerical prediction was encouraging, particularly the resolution of the suction surface separation bubble at the higher yaw angle setting. As well as providing experience in mesh generation techniques, the two-dimensional wedge shape modeling effectively demonstrated the suitability of MEFP for more ambitious three-dimensional modeling.

4 Modeling of Three-Dimensional Probes

The aim of modeling a complete wedge probe in three dimensions was to determine how the local flow field was altered by inserting the probe to various immersions. The 30 deg included angle wedge probe reported in Part 1 of this paper was modeled, such that predictions could be validated against experimental data. A converged solution for this geometry in a 25 m/s flow was achieved for an immersion of $4d$ from a solid wall. The mesh generation procedure and a sample of results are

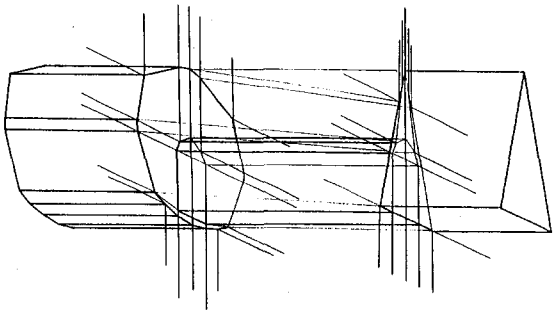

Fig. 6 Datum grid for three-dimensional probe

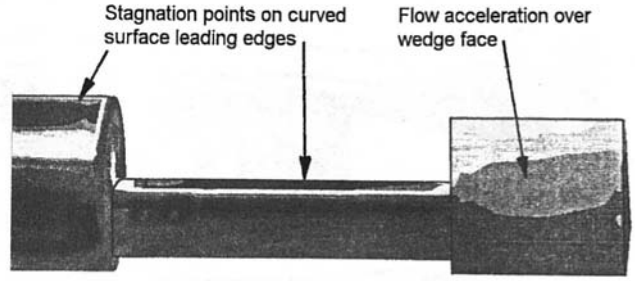

Fig. 7 Surface static pressure variation for solution of 4*d* immersion case at 8.3×10^4 Re

presented below, with reference to further solutions at $1d$ and $2d$ immersion.

4.1 Mesh Generation. To model the $4d$ immersion case, a grid defining the wedge head, all of the interface piece, and a 50 mm length of the cylindrical stem was required. A topology common to the wedge and the cylinder was devised that incorporated the U-shaped interface piece (Fig. 6). The curved surfaces of the interface piece leading edge and the cylindrical stem were defined using nonuniform rational Bezier splines (Versprille, 1975). Corresponding nodes on the wedge and cylinder topologies were linked by skewing grid lines in the k-direction along the length of the interface piece. Fine mesh was embedded as economically as possible to limit the mesh to a manageable 45,790 grid points.

4.2 Solution. The solution was run to the point where per iteration adjustments in static pressure were less than 4 percent dynamic head, the largest changes being in the probe wake region. Convergence could probably have been improved by increasing the mesh density in this area, but the finite time available in the project plan precluded this option. The results presented below must be interpreted accordingly.

The static pressure variation over the probe surface is indicated in Fig. 7 by 25, 40 Pa contour bands spanning a pressure range of 100 kPa to 99 kPa. A uniform decrease in static pressure is observed over the wedge face, which is indicative of gradually accelerating flow from leading to trailing edge. The contours are inclined slightly to the verticle, suggesting that the wedge face flow lifts toward the rear tip of the probe. Static pressure falls rapidly on either side of stagnation points on the interface piece and cylinder leading edges as expected. The prediction is compared with experiment in Fig. 8, where numerically predicted static pressure coefficients at positions corresponding to tappings 3, 4, and 5 on the wedge face are plotted with the corresponding experimental data at $4d$ immersion. Also

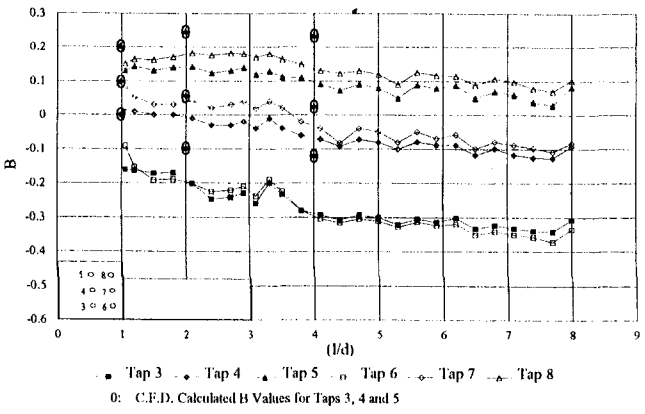

Fig. 8 Comparison of CFD and experimentally determined B values: large-scale probe

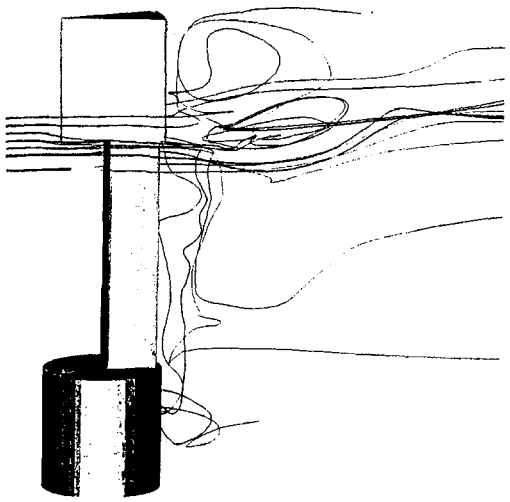

Fig. 9 Streakline representation of calculated flow at 4*d* immersion (8.3×10^4 Re)

shown are the static pressure coefficients corresponding to the same tapping positions, but for probe immersions of $1d$ and $2d$. Agreement between prediction and experiment is within 10 percent dynamic head for the lesser immersions, although less good at $4d$ immersion. The significant feature of this plot is that a trend consistent with the wall proximity effect had been predicted numerically.

The predicted flow field local to the probe is visualized in the streakline representation in Fig. 9. Flow over the lower part of the wedge faces is drawn into a distinct recirculating flow region immediately behind the wedge head. The recirculation is bounded by flow leaving from slightly higher up the wedge faces. A stemwise flow component along the back of the probe toward the wall is apparent, in excellent agreement with the flow visualization in Part 1 of this paper. Flow at the rear of the interface piece is bounded by fluid, which divides about the interface piece leading edge. Figure 10 shows the velocity vectors plotted on a vertical plane through the probe centerline; the recirculatory region in the wake of the wedge head is clearly resolved, and is apparently fed from both ends of the wedge head. The flow lifts at the wedge apex near the tip, and more distinctly at the free end of the cylindrical stem. There is some evidence of recirculatory flow in the wake of the cylinder, although the structure is less coherent than that observed experimentally.

5 Analytical Modeling

Key features of the flow had been identified from the experimental and numerical study of wall proximity effects, which seemed to link the probe immersion to its aerodynamic characteristics. These features were a recirculating flow region in the wake of the wedge head, a recirculating flow region in the wake of the cylindrical stem, and stemwise transfer of fluid between the two recirculations such that changes to one could influence the other. In Part 1 of this paper, it was proposed that the recirculating flow features modified the pressure at the base of the wedge head, and that this in turn influenced the wedge face pressures. This mechanism was identified among a complex flow structure local to the probe; it was required to confirm that the identified features were dominant in controlling the probe near-wall characteristics, and to check that key features had not been neglected.

Simple analytical models of each feature were combined to provide a means of predicting the static pressure wall proximity characteristic of a wedge probe of known geometry. The CFD solution for the $4d$ probe immersion case (Fig. 10) was used to establish a suitable model for the wedge recirculation. It was found that the product $(r \cdot v)$ was almost constant over the majority of the recirculation, where r is the distance from the centre of the recirculation to a tangential velocity vector v. This implied that the wedge wake recirculation could be approximated to a forced vortex. The tangential velocity of the fully developed vortex approximates to the free-stream velocity, v_o (Fig. 10). Taking r_{we} as the equilibrium radius of this vortex, the rotational speed, w, is given by (v_o/r_{we}). At immersions less than r_{we} where the vortex size is restricted by the wall, it was assumed that w remained constant such that the tangential velocity of the vortex, q_w, was reduced in accordance with:

$$q_w = (v_o \cdot r_w)/r_{we} \tag{1}$$

Expressions were derived for the vortex radius as a function of probe immersion, and for the variation of v_o through the boundary layer. These were based on information on the vortex growth from the CFD modeling. It appeared from the flow visualization that the vortex equilibrium radius was reached once the supported end of the wedge head had moved through the boundary layer into the free stream. This was taken to be the case initially, but tested against experimental data as discussed in section 6.

The pressure drag coefficient for an infinitely long element of wedge-shaped cross section was used to give an initial estimate of static pressure at the base of the wedge head for a given flow condition. By the probe wake recirculation model proposed in Part 1 of this paper, the wedge base pressure, p_{bw}, is reduced for actual probes by the stemwise velocity associated with the forced vortex in the wedge wake. It was assumed that the ratio of p_{bw} to the reduced base pressure p'_{bw} was related to the tangential velocity of the forced vortex by the isentropic flow equation:

$$(p_{bw}/p'_{bw}) = \left\{1 + \left(\frac{\gamma - 1}{2}\right)\left(\frac{q_w}{C}\right)^2\right\}^{\gamma/(\gamma-1)} \tag{2}$$

where C is the local speed of sound, and q_w is determined from Eq. (1). The static pressure gradient over the wedge faces was calculated by linearly interpolating between the static pressure just downstream of the leading edge and the modified wedge base pressure at a plane through the static pressure tappings. Results from the CFD modeling were used to support the approximation to a linear pressure gradient over the wedge faces, and to justify setting the wedge trailing edge pressure equal to the modified base pressure, p'_{bw}.

A similar procedure was used in modeling the recirculation in the wake of the cylinder. The CFD calculation of the flow

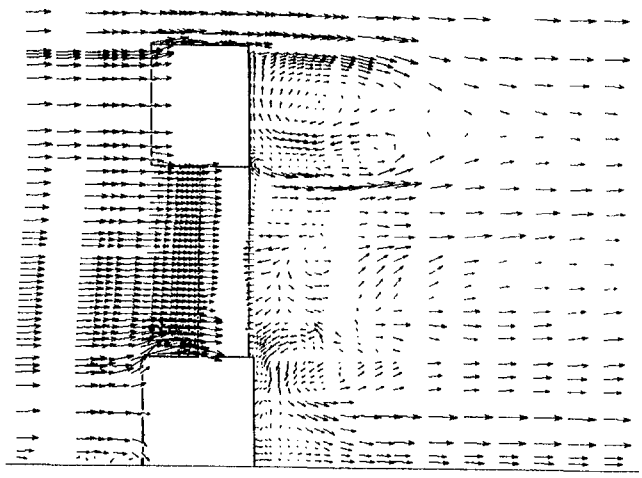

Fig. 10 Velocity vectors for solution of 4*d*

structure in this region was not sufficiently well resolved to verify the assumption of a forced vortex. However, the recirculation observed experimentally in the wake of the cylinder showed good qualitative agreement with that in the wake of the wedge, and a forced vortex structure was assumed on this basis. The radius, r_c, of this vortex was set to half the immersion of the cylindrical stem, and the tangential velocity, q_c, at a given immersion calculated from:

$$q_c = (v_o \cdot r_c)/r_{ce} \tag{3}$$

where r_{ce} was defined as the vortex equilibrium radius. The absolute value of r_{ce} was determined from the flow visualization data (see section 6). The base pressure calculated for a cylindrical element was then modified to account for the forced vortex using the method outlined for the wedge wake recirculation. This gave a modified cylinder base pressure, p'_c.

A complex interaction between the wedge head and cylindrical stem wake vortices involving the stemwise transfer of fluid along the rear of the interface piece toward the cylindrical stem was noted in the flow visualization studies. This implied that the modified base pressure at the base of the cylinder was less than that at the base of the wedge. In deriving a simple model to describe the effect of this interaction, it was assumed that the pressure at the base of the wedge adjacent to the probe tip remained equal to the modified wedge base pressure p'_{bw} regardless of any interaction between the two vortices. The wedge base pressure in the plane of the static pressure tappings was then modified a second time by linearly interpolating between p'_{bw} at the probe tip, and p'_{bc} at a plane through the cylindrical stem coincident with the center of the vortex, to give a new value of wedge base pressure, p''_{bw}.

This was used in recalculating the wedge face static pressure profile with the circular stem immersed into the flow. The success of the model in predicting the wall proximity effect for narrow angle wedge probes typical of those applied in turbomachinery is discussed in the following section.

6 Discussion

6.1 Validation of Analytical Model. Calculated static pressure coefficients were plotted against immersion to give the conventional form of wall proximity curve, which was compared with the corresponding, experimentally determined curve in order to assess the prediction accuracy. The model was optimized against experimental data from the long interface piece, 24 deg probe described in Part 1. A wedge head vortex diameter of 8.5 mm, equal to the sum of the wedge head length and the boundary layer thickness, was used initially. A better fit to the experimental data was achieved using a vortex diameter of 12 mm. This discrepancy may be attributable to the influence of

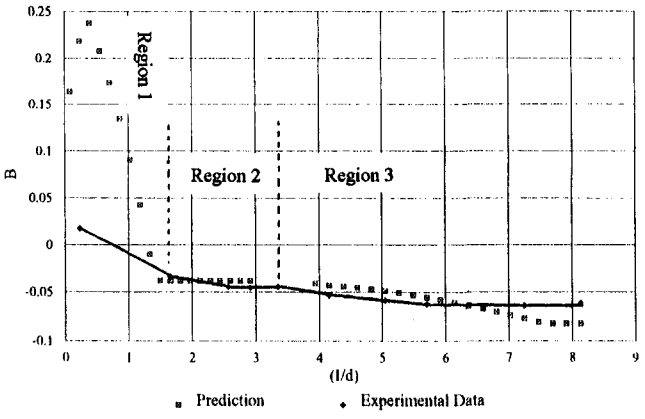

Fig. 11 Comparison between analytically predicted and experimentally determined wall proximity curves

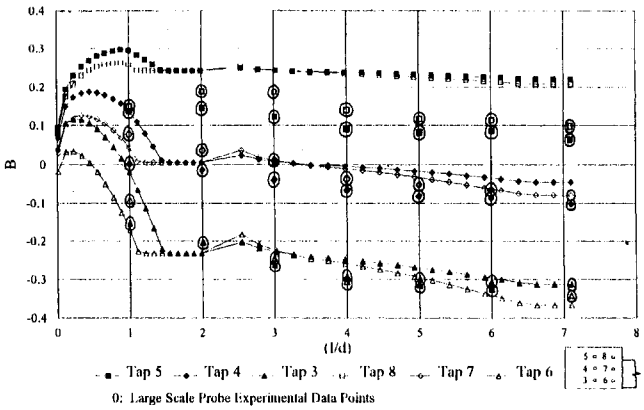

Fig. 12 Comparison between analytically predicted and experimentally determined wall proximity curve for large-scale probe

the hole of introduction, which was not accounted for in the probe vortex model, although a degree of discrepancy is inevitable given the use of simple vortex theory to model a complex flow structure. Best agreement between experiment and prediction was achieved by setting the diameter of the vortex in the wake of the cylindrical stem to 25 mm, or $4d$.

The predicted and experimentally determined wall proximity effect curves for this probe at 0.35 Mach number are plotted in Fig. 11. In general, the predicted curve follows the same trends as the experimental curve through each of the distinct regions labeled 1, 2, and 3. Static pressure coefficient is considerably overestimated near the wall. This may be indicative of the influence of the hole of introduction, but is more probably related to the assumption of a forced vortex to model the wedge head wake recirculation. Agreement between the two curves is within 1 percent throughout the plateau defined as region 2. The second drop in static pressure coefficient corresponding to the emergence of the cylindrical stem is slightly overestimated in magnitude, but occurs over the correct immersion range. Overall, the prediction is seen to be accurate to within ±2.5 percent for immersions greater than 1.3 probe stem diameters.

In the factorial experiment reported in Part 1, the probe interface piece length and the flow Mach number were the two most significant variables tested. To check the general applicability of the optimised probe vortex model, a scaled-down factorial experiment, in which interface piece length and Mach number were tested at the same high and low values as in the full experiment, was conducted using the model to predict the wall proximity curve. For each combination of interface piece length and Mach number, the predicted wall proximity curve agreed with experiment to within ±2.5 percent for immersions of 8 mm or more.

The model was also adjusted to calculate the wedge face static pressure at positions on the wedge face corresponding to the large scale probe model static pressure tapping positions. Prediction and experiment are compared in Fig. 12. Again, the trend through each of the three characteristic regions of the wall proximity curve was well predicted. A significant observation from this plot was the decrease in gradient of the wall proximity curves for tappings close to the wedge leading edge. Physically, this relates to the fact that the forward tappings are furthest removed from any influence that changes in the wedge base pressure may have. A good probe design rule would be to position the tappings as far forward on the wedge faces as possible at least from the point of view of minimizing wall proximity effects.

6.2 Discussion of Facility Dependence Results. In Part 1 of this paper, differences between the static pressure coefficients obtained in open jet and closed tunnel calibration facilities for

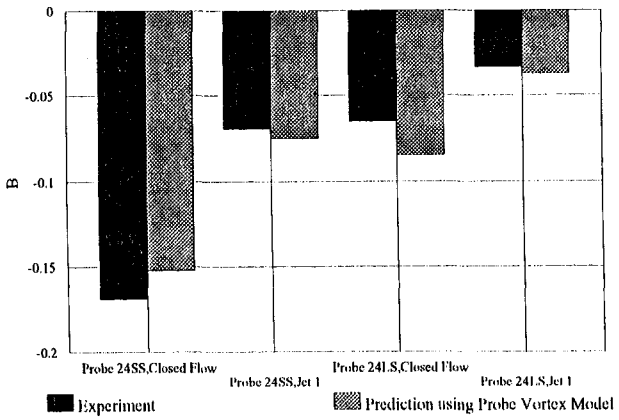

Fig. 13 Comparison between analytically predicted and experimentally determined B values for 24 deg probes at 0.35 Mn

the same probe were reported. It was suggested that the recirculating flow region downstream of the cylinder was destroyed in some cases by the turbulent interface between the jet and the surrounding still air. In Fig. 13, experimentally determined static pressure coefficients are compared with values predicted using the probe vortex model, for both short and long interface piece 24 deg probes in a closed suction tunnel and in a free jet, at 0.35 Mach number. The calibration in the closed tunnel was predicted using the full probe vortex model described in section 5. The model was modified by omitting any contribution from the cylindrical stem recirculation in the prediction of the open jet calibrations. In each case, agreement between experimentally determined and predicted static pressure coefficients is within ±2 percent. This substantiates the suggestion that the action of turbulent, largely inviscid flow at the free jet boundary is responsible for dissipating the circular stem wake vortex and influencing the probe static pressure calibration accordingly.

7 Conclusions

The pressure correction code MEFP has been applied in calculating flows around two-dimensional wedges and a three-dimensional probe. Mesh embedding and automated mesh adaption software was used successfully to optimize the CFD solutions. Key flow features identified from the experimental study reported in Part 1 of this paper were reproduced in the CFD prediction. These included a separation bubble in the suction surface, leading edge region of a 24 deg wedge run at 8 deg yaw, and a recirculating flow region behind the wedge head of the three-dimensional probe. The wall proximity effect was also reproduced in the three-dimensional numerical model.

The CFD calculations supported the idea that recirculations in the probe wake might change the wedge head base pressure and hence the pressure profile over the wedge faces. A simple analytical model was derived by modeling the two recirculations as forced vortices. This model was used to demonstrate that the recirculations, and the interaction between them, govern the probe static pressure measuring characteristics. As concluded from the experimental study, modifications to the probe wake structure, from whatever source, can be expected to influence the aerodynamic characteristics of wedge probes.

Acknowledgments

The authors wish to thank Rolls-Royce plc for financially supporting the work described. The views expressed are those of the authors and are not necessarily shared by the company.

References

Ainsworth, R. W., and Stickland, A. D., 1992, "Experimenting With Fast Response Aerodynamic Probe Geometries," *Proc. 11th Symp. Measuring Techniques for Transonic and Supersonic Flow in Cascades and Turbomachines,* Munich, Germany.

Depolt, Th., and Koschel, W., 1992, "Theoretical Determination of the Characteristics of Multi-hole Pressure Probes Using Panel Methods," *Proc. 11th Symp. Measuring Techniques for Transonic and Supersonic Flow in Cascades and Turbomachines,* Munich, Germany.

Ferguson, T. B., and Al-Shamma, K. A., 1967, "Wedge Type Pitot-Static Probes," *BHRA SP919,* 9th Members Conference, British Hydromechanics Research Association, Cranfield, England.

Giles, M. B., and Haimes, R., 1991, "Validation of a Numerical Method for Unsteady Flow Calculations," ASME Paper No. 91-GT-271; ASME *Journal of Turbomachinery,* Vol. 115, 1993, pp. 110–117.

Lapworth, L., 1993, "Three-Dimensional Mesh Embedding for the Navier Stokes Equations Using Upwind Control Volumes," *Int. J. for Numerical Methods in Fluids,* Vol. 17, pp. 195–220.

Moore, J. G., 1985, "Calculation of 3-D Flow Without Numerical Mixing," AGARD Lecture Series No. 140, *3-D Computational Techniques Applied to Internal Flows in Propulsion Systems.*

Northall, J. D., 1993, "Introduction to the Computational Fluid Dynamics System (CFDS)," Rolls-Royce Internal Report, TSG0689.

Smout, P. D., and Ivey, P. C., 1994, "Wall Proximity Effects in Pneumatic Measurement of Turbomachinery Flows," ASME Paper No. 94-GT-116.

Smout, P. D., and Ivey, P. C., 1997, "Investigation of Wedge Probe Wall Proximity Effects: Part 1—Experimental Study," ASME JOURNAL OF ENGINEERING FOR GAS TURBINES AND POWER, Vol. 119, this issue, pp. 598–604.

Versprille, K. J., 1975, "Computer Aided Design Applications of the Rational B-Spline Approximation Form," Dissertation, Syracuse University.

A Semiclosed-Cycle Gas Turbine With Carbon Dioxide–Argon as Working Fluid

I. Ulizar
Industria de Turbopropulsores-Ajalvir,
Torrejon de Ardoz,
Madrid, Spain

P. Pilidis
School of Mechanical Engineering,
Cranfield University,
Cranfield, Bedford, United Kingdom

This paper describes the performance analysis of a semiclosed-cycle gas turbine. The working fluid is carbon dioxide and the fuel is low heating value gas synthesized from coal. The objective of the machine is to produce clean electricity with the smallest efficiency penalty. First, the thermodynamic properties of the gases in the cycle were obtained as a function of temperature and pressure. Then two performance simulation codes were developed. These have the ability of simulating different configurations of open, closed, and semiclosed cycles. The first code was used for cycle optimization and the second for off-design studies. The design and off-design performances of the machine are predicted. The production of clean electricity will be at the expense of a lower efficiency compared with current equipment. Finally, some critical issues for the development of such a gas turbine are identified.

Introduction

The continuing concern over the emission of greenhouse gases, coupled with the ever-increasing demand for electrical energy, poses a very difficult challenge to power engineers. One possible solution to these conflicting requirements, if solid fossil fuels are to be employed, is to collect and dispose of the emissions in a controlled way.

For example, an internal combustion semiclosed power cycle, where the working fluid is carbon dioxide, with oxygen and fuel injected into the combustion chamber and excess carbon dioxide collected at the outlet, seems to be a very attractive environmental proposition. Such a cycle has a dual advantage. By collecting and storing the excess carbon dioxide safely, the emission of greenhouse gases is controlled. By having a clean fuel and no air in the working fluid, there are no emissions of oxides of sulfur and nitrogen. This proposition becomes particularly attractive when coal is considered. This fuel is in plentiful supply and when gasified it can be a very clean source of energy. The major drawbacks of such a cycle are the complexity of the equipment and the significant reduction in efficiency caused by the need to produce pure oxygen.

The Engine

This paper describes an internal combustion turbine where the working fluid is carbon dioxide, the main mass of which is recirculated in the engine. The choice of working fluid is dictated by the fuel, based on coal, and the requirement to make carbon dioxide collection an easy process.

Heat addition is achieved by injecting oxygen and coal gas fuel in the combustion chamber. To keep a constant mass flow through the device, water is collected at the outlet of the cooler and some carbon dioxide is extracted at the HPC delivery. This gas is compressed to at least 60 atm for efficient collection. All calculations include this compression work.

Figure 1 shows the engine selected and described in the paper, a two-spool gas generator with an independent power turbine. It was selected between several alternatives with core cycles, incorporating a variety of additional components, such as intercoolers and heat exchangers.

Contributed by the International Gas Turbine Institute and presented at the 41st International Gas Turbine and Aeroengine Congress and Exhibition, Birmingham, United Kingdom, June 10–13, 1996. Manuscript received at ASME Headquarters February 1996. Paper No. 96-GT-345. Associate Technical Editor: J. N. Shinn.

Two development options are available. The first one is to use existing equipment; the second is to design a new engine. The first option will be cheaper to develop while the second will have better performance.

Properties of the Gases in the Cycle

The thermodynamic properties of the gases in this cycle, as well as others that could be introduced to enhance the performance of the power plant, were investigated [3]. Carbon dioxide, carbon monoxide, water vapor, argon, oxygen, helium, nitrogen, hydrogen and air are the gases considered in the study [2]. In this paper, only the results for carbon dioxide are reported.

The working fluid includes, in the turbine, any water produced in the combustion process. A small amount of argon is also present because it is much cheaper to leave this gas in the oxygen stream fed to the combustor than to separate it. Its presence has a minor effect on the performance of the cycle.

The gas properties required are enthalpy, entropy, and constant pressure specific heat. Usually they are correlated as a function of temperature, while the effect of pressure is assumed to be negligible. However, this assumption is not valid in high-pressure and low-temperature cases. This situation could arise in the cycle under investigation, so real gas analysis was employed where both pressure and temperature were used as correlation parameters. For example Fig. 2 shows the specific heat at constant pressure (C_p) of carbon dioxide, and Fig. 3 shows when it behaves as an ideal or real gas.

Gas Turbine Overview

To select the main cycle parameters, it was necessary to have an overview of gas turbine current practice. To achieve this, information was obtained on more than 500 different models of open cycle gas turbines and combined cycles, from over 40 manufacturers. The efficiency and power output of these gas turbines, without bottoming cycles, are shown in Fig. 4. Several observations can be made.

Most gas turbines are of the simple cycle type and only a few are recuperative or intercooled. A low-cost option with high efficiency is steam injection, which is also employed for emissions abatement.

With the passage of time, turbine entry temperatures have increased continuously (Fig. 5). In order to increase the life of the components and improve engine reliability and avail-

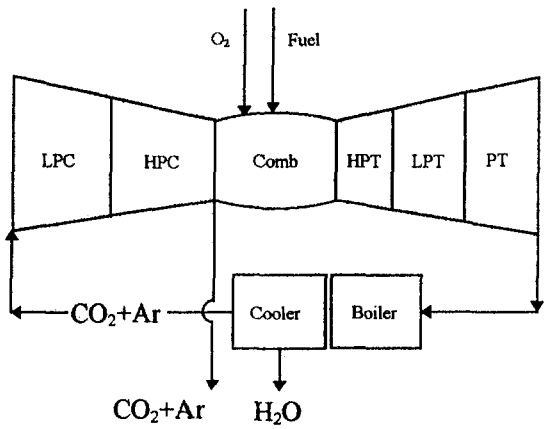

Fig. 1 Diagram of the semiclosed-cycle engine

ability, these temperatures are kept 200–300°C below the maximum temperatures employed in advanced aeroengines. However, they are well over the maximum metal temperature, represented by the continuous line in Fig. 5. Hence, special attention is always paid to blade cooling, one of the critical areas in a new gas turbine development, and to the materials employed.

In the most advanced gas turbines, a mass flow as high as 20 percent of the main flow is used for blade cooling. It must also be pointed out that although heat-resistant materials represent only 2 percent of the cost of an advanced combined-cycle power plant, they play an extremely important role by enabling high operating temperatures.

The most common closed cycle is the regenerative type, many engines incorporating intercooling. The intercooler increases the specific power of an engine and it makes the regenerator more useful, because the compressor discharge temperature is reduced. Closed-cycle turbine entry temperatures are approximately 1100 K, much lower than those employed in open cycles. This is due to the use of a heat exchanger as the source of heat addition. This low temperature coupled with the use of the regenerator results in gas turbines with low pressure ratio. The penalty arising from these characteristics can be partly overcome by employing a working fluid with properties better suited to that design. This can be either a pure substance or a mixture of different gases.

Baseline Cycle Parameters

In the semiclosed cycle, heat addition takes place using a combustor, hence the temperature will be similar to those employed in conventional open cycles. The working fluid is imposed by the characteristics inherent to the cycle, and the fuel is a low heating value gas obtained from coal.

Initially a turbine inlet temperature of 1473 K was selected. This temperature may be considered as a peak temperature. For base load 1300/1350 K seems more reasonable. This is low, for a new gas turbine, when compared to those shown in Fig. 5, but the temperatures illustrated here apply to natural gas or clean distillate fuels. In the case investigated here, allowances have to be made for the use of a lower quality fuel in the interest of longer time between overhauls.

Once the turbine entry temperature has been selected, the rest of the parameters of the cycle are typical of the state of the art in gas turbines: low-pressure compressor polytropic efficiency 90 percent, high-pressure compressor polytropic efficiency 89 percent, combustor efficiency 99.9 percent, combustor pressure losses 5 percent, high-pressure turbine polytropic efficiency 87 percent, low-pressure turbine polytropic efficiency 87 percent, free power turbine polytropic efficiency 87 percent. The regenerator effectiveness is 80 percent. The pressure losses of the heat exchangers, ducts, etc. are: 0.5 percent inlet, 3 percent each side of the regenerator, 5 percent the bottoming cycle heat exchanger, and 2 percent the precooler. A customer bleed of 1 percent is considered, as well as shaft friction losses of 0.5 percent, and a power turbine loss of 2 percent. For combined cycles the discharge temperature of the heat recovery boiler is 420 K, in line with current practice.

With the parameters selected above, the design performance of a gas turbine fitted with an optimized simple steam turbine cycle was calculated in two situations: with pure oxygen as an oxidizer and with oxygen and argon (95/5 percent). As stated before, the small amount of argon is a result of using the cheaper separation process because the cryogenic air separation plant operates at a higher temperature. The presence of argon makes a very minor difference to the performance of the engine. Therefore, the only results shown are those with argon in the working fluid.

The performance prediction can be subdivided into two parts: cycle optimization plus selection and off-design behavior. For this purpose, a program working on the basic principles of TURBOMATCH [4], the Cranfield gas turbine performance simulation software, was generated.

Design Performance of the Cycle

The efficiency of the four gas turbine cycles considered here is shown in the combined gas and steam cycle form. They are: the engine with a simple cycle gas turbine (Fig. 6), intercooled

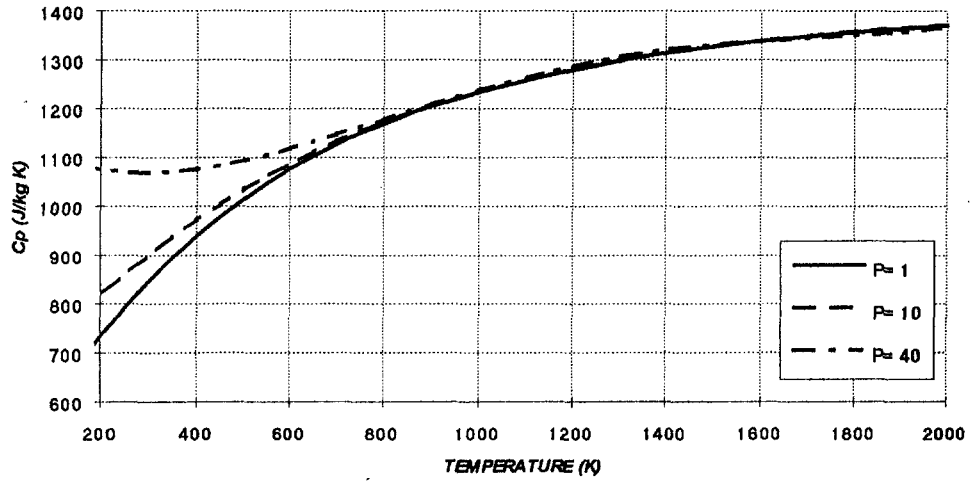

Fig. 2 Constant-pressure specific heat of carbon dioxide; pressures are in atm

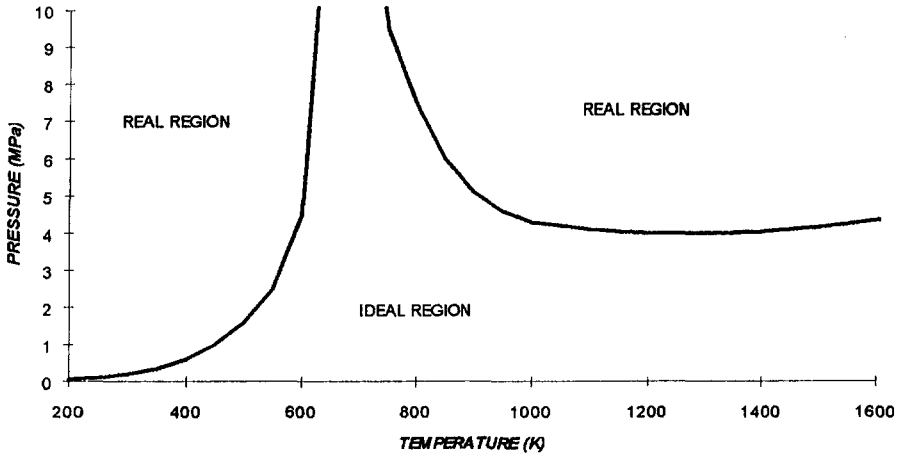

Fig. 3 Ideal and real regions for carbon dioxide

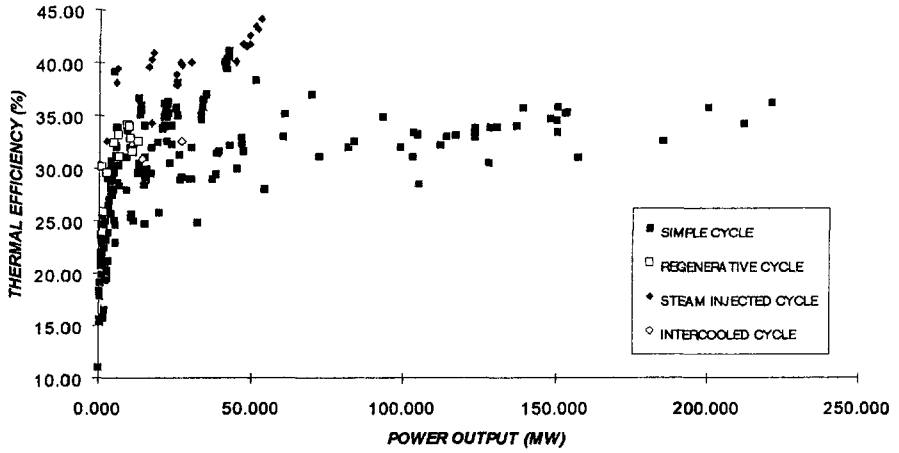

Fig. 4 Thermal efficiency and power of gas turbine cycles

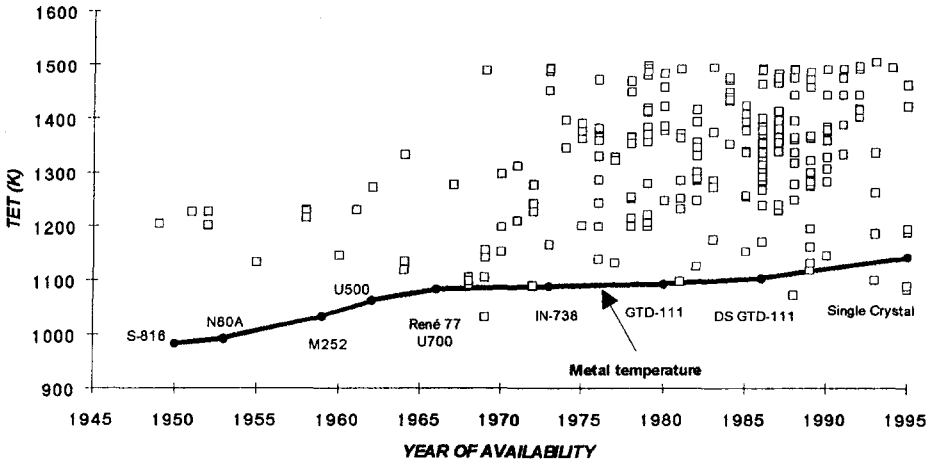

Fig. 5 Turbine entry temperature and metal temperature of gas turbines

(Fig. 7), regenerative (Fig. 8), and regenerative and intercooled cycle (Fig. 9). They all employ advanced full-coverage film cooling in the turbine vanes and blades.

The best efficiencies of the semiclosed cycles fitted with a steam bottoming cycle are of the order of 43–46 percent. Conventional combined cycles, shown in Fig. 10, currently achieve thermal efficiencies well in excess of 50 percent. This difference of the order of 10 percent is mainly due to the large quantity of energy required by the oxygen separation process. Another, smaller, penalty is that due to the higher compressor inlet temperature applicable to closed and semiclosed cycles. Low overall pressure ratio semiclosed cycles are further penalized by the power needed to compress the excess CO_2 to the disposal pressure of at least 60 bar.

The reheat cycle has not been considered here because of the uncertainties and the complexity a second combustor would

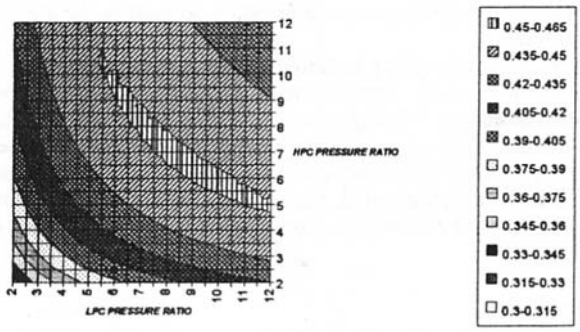

Fig. 6 Thermal efficiency of combined semiclosed-cycle gas turbine

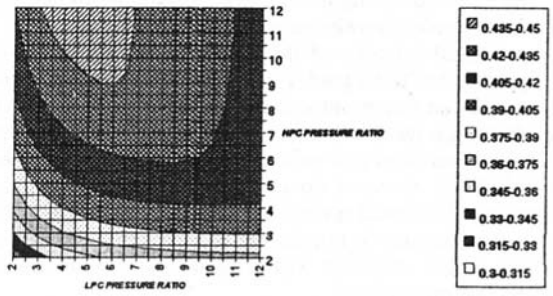

Fig. 7 Thermal efficiency of combined and intercooled semiclosed-cycle gas turbine

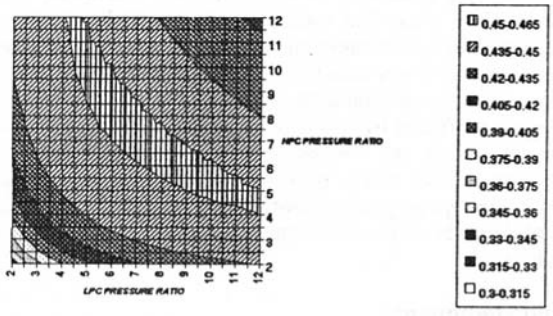

Fig. 8 Thermal efficiency of combined and regenerated semiclosed-cycle gas turbine

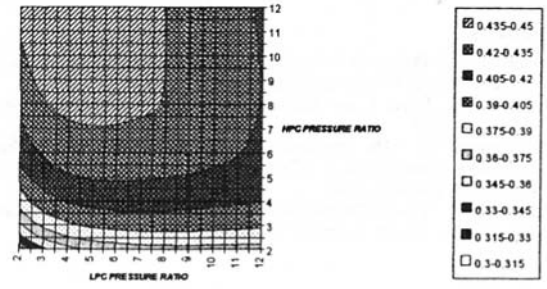

Fig. 9 Thermal efficiency of combined and intercooled and regenerated semiclosed-cycle gas turbine

introduce to the design. Another feature is that all turbomachinery is specifically designed for carbon dioxide. Early in the analysis it became clear that the efficiency penalty associated with using existing turbomachinery was of the order of 10 percent [3]. This was deemed to be unacceptable.

The reason for showing only the performance of the combined cycles, and not just the gas turbine, is that this is the most attractive option for electricity generation. If the interest was

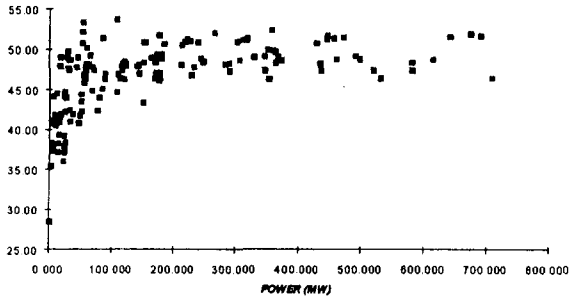

Fig. 10 Thermal efficiency and power of conventional combined cycle gas turbine

in cogeneration, a single cycle gas turbine will be the choice. Due to the very high temperature found at the exit of power turbine, the cycle presented here can be used for industries where the power to heat ratio is low.

The design point analysis carried out indicated that the best efficiencies are achieved with the simple cycle and the regenerated cycle. The cycle selected is therefore the simple cycle with LPC and HPC pressure ratios of 6 and 8, respectively. This engine is the subject of the off-design analysis described in the next section.

The high pressure ratios required by the carbon dioxide cycle indicate a requirement for a two-spool gas generator.

Off-Design Performance of the Cycle

The off-design performance of a semiclosed cycle combines the features of the off-design performance of an open cycle and a closed cycle. Theoretically the compressor inlet pressure can be varied. However, because water must be removed as a liquid before the compressor inlet, changes in this pressure are very limited. The compressor inlet temperature is limited by the precooler water temperature. Hence the main control parameter is the turbine temperature. Nevertheless the limited control in compressor inlet pressure will allow small changes in power output without significant changes in efficiency.

In Table 1, the performance of a two-spool gas generator with an independent power turbine is presented. These results show that the efficiency reduction at part load is larger than would be expected from a conventional open cycle gas turbine.

It is important to note that the high pressure ratios required for a good CO_2 cycle will cause off-design problems, specially in compressor handling. Splitting up the gas generator into two spools will alleviate but not remove these problems.

The handling of an open-cycle gas turbine was compared to that of a semiclosed-cycle one, both using a high heating value fuel and with the same compressor pressure ratios. The low-pressure compressor (LPC) surge margin of the first one fell from 25 to 9 percent when the high-pressure shaft speed fell

Table 1 Semiclosed-cycle performance (simple and combined cycle)

Mass Flow (%)	100.00	93.01	84.13	74.74	65.94	58.40	51.47
LPC P.Ratio	6.00	5.70	5.27	4.80	4.35	3.96	3.57
HPC P.Ratio	8.00	7.70	7.39	7.07	6.75	6.45	6.17
LPC RPM (%)	100.0	96.8	93.3	90.0	87.2	84.7	81.8
HPC RPM (%)	100.0	98.1	96.2	94.0	92.0	90.2	88.4
TET (K)	1473	1423	1373	1323	1273	1223	1173
Fuel (Kg / s)	10.48	9.18	7.81	6.50	5.36	4.41	3.62
η_{SC} (%)	26.22	25.38	23.84	21.73	19.12	16.43	13.43
η_{CC} (%)	47.26	45.82	43.49	40.75	37.63	34.22	30.41

from 100 to 90 percent, while the second one crossed the LPC surge line at a high-pressure shaft speed of 90.75 percent.

This handling problem can be avoided by using variable stators. This is preferred to bleed valves discharging to the exhaust because the high design pressure ratios mean that they will have to be used at high power. If there is a requirement to operate at part load, the consequent efficiency penalty cannot be accepted. The present design, however, will probably need to incorporate bleed valves for starting purposes.

The nature of the compressor design, subsonic or transonic, will have a great influence in the surge margin at part load. Initially both low-pressure compressor and high-pressure compressor were subsonic, the initial turbomachinery design being described in [1]. Then the LPC was changed to an advanced transonic compressor, with a large pressure ratio per stage. The LPC surge margin in this case decreased much more. Real maps for a CO_2 compressor should be obtained by experiment to evaluate, more accurately, the real behavior of the machine. In the simulations presented here the maps employed were the same for air and for carbon dioxide; naturally, the correct nondimensional numbers were used.

The handling issues and the less attractive off-design efficiency require further study. These features do not seem to present any insuperable problems.

Development Issues

A major factor that will affect the development of the engine is the lack of a suitable knowledge database. Air is the working fluid of almost all existing gas turbines. Knowledge of operation with different working fluids is very limited. Several closed cycles have been in operation, some with air, others with helium, mixtures of helium and xenon, etc. However, the total experience accumulated after some 50 years in base-load power generation is around one million hours. This appears to be a large number, but it is very small compared with operational experience of some existing gas turbine models, many having operated for tens of millions of hours.

There will be three major areas of risk in the gas turbine: the aerodynamic design, the combustor design, and blade cooling. The development of an extensive theoretical and experimental knowledge database will be necessary to support the development of these designs. Improvement and validation of Computational Fluid Dynamic codes will be necessary to handle suitable gases and their mixtures. Some basic design criteria will also need updating, due to the different gas properties. Expensive compressor cascade rigs, and at a later stage compressor test stands will be required to examine aerofoil performance in exotic fluids. In particular in the hot section, it is probable that new materials and coatings will be required to cope with the idiosyncracies of the working fluid and the fuel employed.

A similar lack of experience will make the development of the combustor a high risk item. There is no expertise in burning a low heating value gas with pure oxygen in a CO_2 environment. With the high temperatures expected, and a requirement for combustion efficiency of 100 percent, extensive tests must be carried out to ensure proper combustion, as well as the absence of pollutants.

In the case of cooling technology, the current state of the art is also based on the large number of experiments carried out, in other words, on existing experience. In existing closed cycles, where different gases were employed, no cooling was used, because turbine inlet temperatures were low. If a competitive machine is to be designed, temperatures will need to be high to achieve good efficiencies. Therefore blade cooling cannot be avoided.

Conclusion

This paper describes the preliminary performance analysis of a semiclosed-cycle gas turbine. The working fluid is carbon dioxide and the fuel is low heating value gas synthesized from coal. The selected configuration is a two-spool gas generator with an independent power turbine.

The predicted behavior of this engine indicates that an efficiency penalty has to be paid if improved environment friendliness becomes an important criterion when a plant is selected. Some off-design features are not so attractive as those of conventional gas turbines and some handling problems have been identified. These, however, do not appear to present insurmountable barriers. Rotational speeds and size also do not present any extraordinary features. It is therefore expected that the mechanical design of this machine will offer no more problems than that of a conventional one.

The main issue will be an economic one. It is very difficult at this stage to make a realistic estimation of the cost of a power plant of this type. The uncertainties in the development budget, the number of machines to be built, etc., contribute to this difficulty. It is clear that such a machine will be much more expensive than a conventional one. In the balance will be its higher cost and lower efficiency against its ability to use coal and its attractive environment features.

The prize offered by this type of engine is clean electricity. Many difficulties are envisaged in the development of such a machine. Furthermore, its efficiency will be lower than a conventional open-cycle combined-cycle gas turbine. Its development depends on the willingness to pay a premium for clean electricity.

Acknowledgments

The authors are grateful to the C.E.C. for the financial support for this task and to their colleagues in I.T.P. and Cranfield for their support and encouragement.

References

1 Hunter, I. H., "Design of Turbomachinery for Closed and Semiclosed Gas Turbine Cycles," M.Sc. Thesis, Cranfield University, 1994.

2 Keenan, J. H., Kaye, J., and Chao, J., *Gas Tables, International Version*, 2nd ed., SI Units, 1983.

3 Navaratnam, M., "The Investigation of an Aeroderivative Gas Turbine Using Alternative Working Fluids in Closed and Semiclosed Cycles," M.Sc. Thesis, Cranfield University, 1994.

4 Palmer, J. R., "The TURBOMATCH Scheme for Gas Turbine Performance Calculations," Users' Guide, Cranfield Institute of Technology, 1983.

M. Sato

Y. Kobayashi

H. Matsuzaki

Tohoku Electric Power Co., Inc.,
Sendai, Japan

S. Aoki

Y. Tsukuda

E. Akita

Takasago Machinery Works,
Mitsubishi Heavy Industries, Ltd.,
Takasago, Japan

Final Report of the Key Technology Development Program for a Next-Generation High-Temperature Gas Turbine

There is a strong demand for efficient and clean power-generating systems to meet recent energy-saving requirements and environmental regulations. A combined cycle power plant is one of the best solutions to the above [1]. Tohoku Electric Power Co., Inc., and Mitsubishi Heavy Industries, Ltd., have jointly developed three key technologies for a next-generation 1500°C class gas turbine. The three key technologies consist of: (1) high-temperature low-NO_x combustion system, (2) row 1 turbine vane and blade with advanced cooling schemes, and (3) advanced heat-resistant materials; (2) and (3) were verified by HTDU (High Temperature Demonstration Unit). This paper describes the results of the above-mentioned six-year joint development.

Introduction

After the severe oil crises in the 1970's, Japan has striven to mitigate its oil dependency by developing ways to utilize other natural energy resources, such as atomic energy, natural gas, and coal, which will ensure its future energy supply. In addition, environmental issues such as global warming, acid rain, and destruction of the ozone layer have emerged as urgent and difficult problems to solve.

Under these circumstances, a combined cycle power plant is one of the best solutions to resolve the situation, at present, since it is the most efficient way to utilize natural gas, the cleanest fossil fuel, for a current 1350°C class gas turbine with approximately 10 percent higher thermal efficiency against a 1150°C class gas turbine and 20 percent higher when compared to the conventional power plants. Therefore, electric utilities in Japan are promoting combined cycle power plants as their base load or middle load power plants.

Based on the fact that combined cycle efficiency is very dependent on gas turbine firing temperature, Tohoku Electric Power Co., Inc., and Mitsubishi Heavy Industries, Ltd., started a joint investigation on the required key technologies for development of a next-generation gas turbine with a firing temperature of 1500°C, which achieves over 50 percent (HHV) combined cycle thermal efficiency [2].

These key technologies consist of (1) high-temperature low-NO_x combustion system, (2) row 1 turbine vane and blade with advanced cooling schemes, and (3) advanced heat-resistant materials; (2) and (3) were verified by HTDU (High Temperature Demonstration Unit).

Development of High-Temperature Low-NO_x Combustion System

The most important basic technologies required to realize high-temperature low-NO_x combustion systems are shown in Fig. 1 [3]:

1 Multi-premixing nozzle
   - to produce a uniform fuel–air mixture with ease
   - to make fuel staging possible for low-load operation
2 Air bypassing
   - to make air staging possible for low-load operation
3 Use of steam to cool the combustor wall
   - to make a lean fuel–air mixture with same level of lower flame temperature as the 1350°C class gas turbine

Here the steam that cools the combustor is drawn from the Heat Recovery Steam Generator and is exhausted in the steam cycle at a location selected based on optimal cycle performance. Since reduced steam flow may cause an overheat of the combustor wall, appropriate gas turbine control measures are to be used to circumvent such an event.

In order to develop these basic technologies, the following tests and analyses were conducted.

1 Optimization of Multi-Premixing Nozzle. The LNG fuel was injected into air from small holes in the center of the nozzle.

Mixing characteristics of the nozzle were examined using an air flow test device. The combinations of air swirl strength and fuel injection holes configuration were investigated and optimized. Mixing characteristics were obtained by using air, which was added to NO gas instead of using fuel as a tracer, measuring the concentration of NO at each measuring point. Figure 2 shows the mixing characteristics in the case where the swirl angle was changed. The more swirl is strengthened by increasing the swirl angle, the better the mixing characteristics become.

However, the results of the flow analysis using CFD indicate that a stronger swirl produces a lower flow velocity zone or recirculating flow zone in the central portion of the main premix nozzle. In order to prevent dangerous flashback in these regions, it was necessary to select the most suitable swirl angle and fuel injection configuration.

Meanwhile, it is most important to stabilize the low-temperature flame to maintain the low-NO_x combustion. The recirculat-

Contributed by the International Gas Turbine Institute and presented at the 40th International Gas Turbine and Aeroengine Congress and Exhibition, Houston, Texas, June 5–8, 1995. Manuscript received by the International Gas Turbine Institute March 2, 1995. Paper No. 95-GT-407. Associate Technical Editor: C. J. Russo.

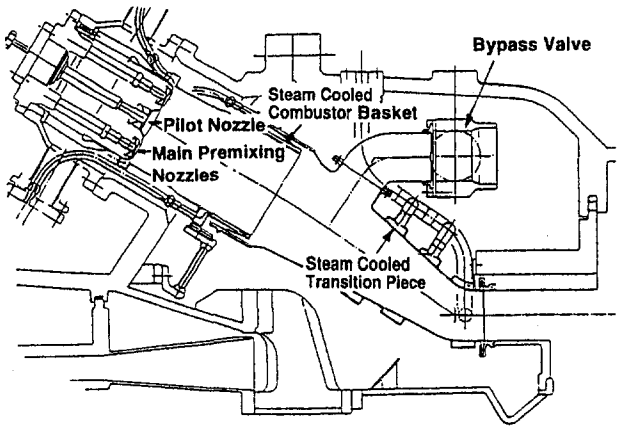

Fig. 1 Conception of 1500°C low-NO_x combustion system

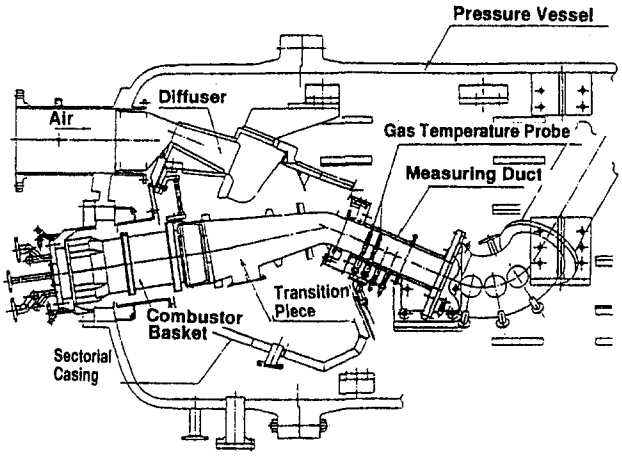

Fig. 3 High-pressure test rig

ing flow of downstream hot gas is the ignition source of the fresh mixture from premix nozzles. Therefore, cold flow tests were conducted and axial flow velocity distribution was measured in the vicinity of the nozzle inside the combustor using two-component laser anemometry. The measurement indicated a center recirculation zone established just downstream from the main nozzles.

2 High-Pressure Combustion Test. Prior to the high-pressure combustion tests, atmospheric pressure combustion tests were conducted in order to investigate basic characteristics such as ignition, flame stability, and emissions. Since low-NO_x emissions were obtained due to both good mixing of the fuel with air flow and a well-stabilized recirculation zone, high-pressure combustion tests were carried out to verify the performance under design conditions using a high-pressure test rig shown in Fig. 3.

Measured NO_x emissions at full-load condition (T_{IT} = 1500°C), corrected according to the square root pressure increase law from high-pressure test condition to the actual machine condition, was less than 50 ppm at 16 percent O_2, and lower NO_x levels could be attained with decreasing pilot fuel ratio. CO and UHC emissions were very low (less than 10 ppm).

3 Further Low-NO_x Program. In order to achieve much lower NO_x, one of the potential solutions is decreasing the NO_x generated from the pilot zone. Figure 4 shows NO_x emissions and gas temperature distribution, which were measured under low-pressure test conditions using a fine wire thermocouple supported by a water-cooled tube and water-cooled sampling probe. It appeared that the high-temperature central region downstream of the pilot nozzle generated the higher NO_x emissions.

To decrease pilot zone NO_x emissions, a premixed pilot nozzle in which almost perfect premixed fuel and air are supplied from outside the combustor, was investigated.

Test results using a middle pressure test rig are shown in Fig. 5 and indicate that the premix pilot is capable of decreasing NO_x emissions under the same pilot fuel ratio as the diffusion pilot.

Development of Advanced Cooled Turbine Vane and Blade

Hot cascade tests were conducted to confirm the cooling effectiveness of the full-coverage film cooled turbine vane and blade for a next-generation 1500°C class gas turbine [4]. Impingement cooling by three inserts and FCFC (Full-Coverage Film Cooling) were adopted for the first-stage vane. On the other hand, three serpentine flow passages with angled turbulator and FCFC were applied to the first-stage blade.

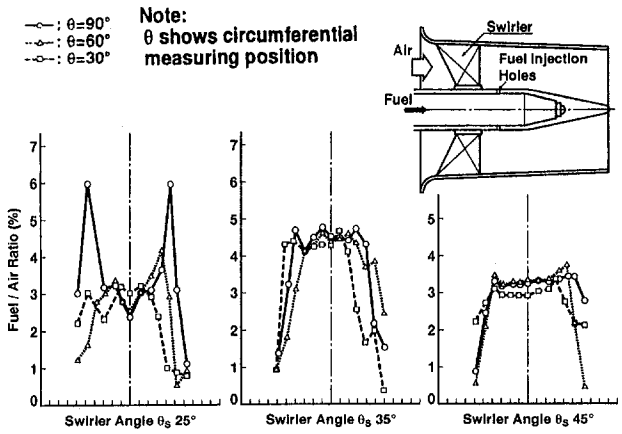

Fig. 2 Mixing characteristic test results of main premix nozzle

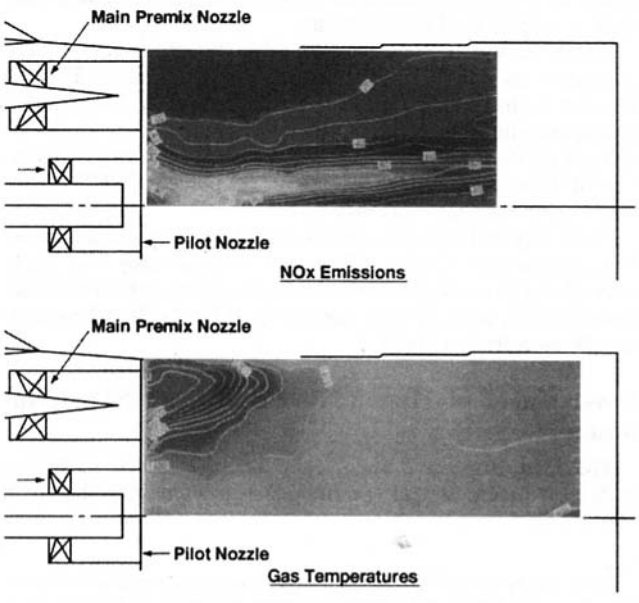

Fig. 4 Gas temperature and NO_x emissions distribution inside combustor

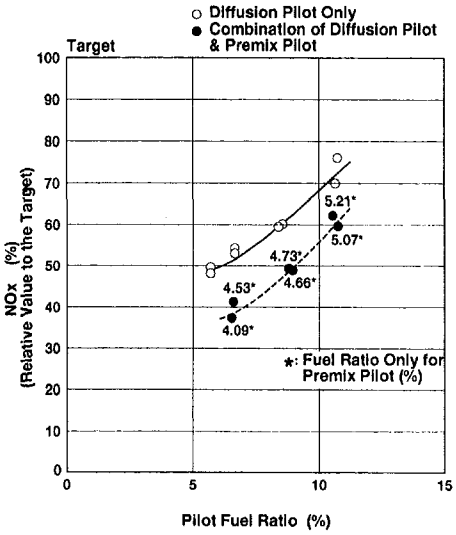

Fig. 5 Effect of premix pilot on NO_x emissions

1 Model Vane and Blade. An air-cooled model turbine vane and blade whose cooling scheme will be applicable for the 1500°C class gas turbine have been designed by optimizing the heat transfer characteristics including FCFC efficiency, impingement cooling heat transfer, and turbulator heat transfer coefficient on serpentine flow passages. The first-stage vane model was manufactured by nickel brazing the vane airfoil and shroud. The finished vane is shown in Fig. 6. The first-stage blade was made by integrated casting. The film cooling holes of the vanes and blades were made by EDM (Electric Discharge Machining).

2 Hot Cascade Test Facility. Hot cascade tests in sector form were conducted using five vanes and blades. A high-temperature, middle-pressure turbine test facility, shown in Fig. 7, was used. The main specifications of the facility were that maximum air flow rate is 15 kg/s, maximum pressure is 6 kgf/cm^2 abs. (0.59 MPa), and maximum average temperature of the combustion gas is 1500°C (1773 K). Gas temperature distribution at the cascade inlet was measured with three total temperature probes mounted in the section connecting the combustor transition piece and the five vanes or blades. These temperature probes were installed at three different circumferential locations and measured temperature at five radially different points by platinum–rhodium thermocouples. The metal temperature of central vane and blade at 50 percent height was measured by grooving them by electric discharge machining and then embedding chromel-alumel thermocouples with inconel sheaths of 1.0 mm OD in nickel-based plasma coating material.

3 Hot Cascade Test Results. The test was conducted over a range of average inlet temperatures for the first-stage vane from 1000°C (1273 K) to 1500°C (1773 K) with the cooling flow

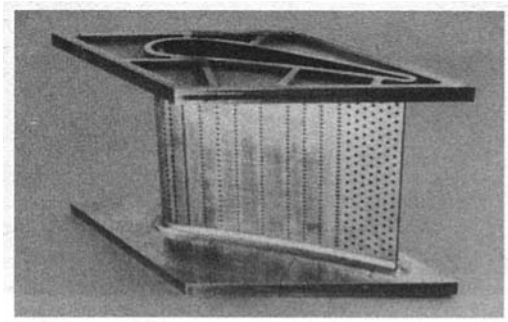

Fig. 6 FCFC first vane

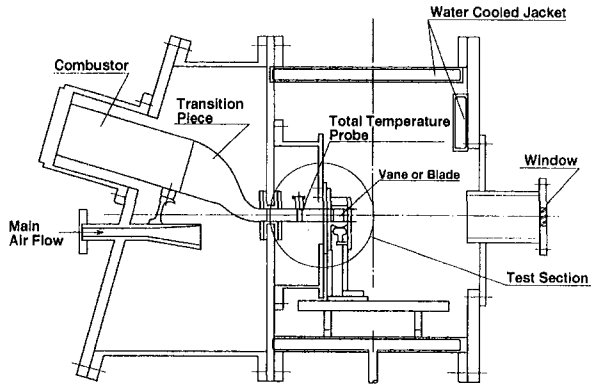

Fig. 7 Hot cascade test facility

rate (Ga/Gg = mass flow of cooling air/mass flow of hot gas) varying from about 6 to 8 percent. The typical hot cascade test condition of the first-stage vane is shown in Table 1.

The measured gas temperature distribution just before the instrumented vane at 50 percent height section was exposed to over 1550°C (1823 K) gas temperature. Figure 8 shows an experimental midspan chordwise metal temperature distribution. This temperature distribution exhibits uniform metal temperature distribution on the pressure surface because of adoption of FCFC and relatively lower metal temperature on the suction surface because of high film cooling efficiency. It is clear that the well-cooled vane was obtained by the combination of FCFC, impingement, and pin fin cooling, and also there is more potential to reduce the cooling air flow rate.

Cooling effectiveness (η) defined by Eq. (1) was calculated by using the average metal temperature of the measured midchord, and is shown in Fig. 9:

$$\eta = \frac{T_g - \bar{T}_m}{T_g - T_a} \tag{1}$$

Table 1 Example of hot cascade test condition of the first-stage vane

Average Inlet Gas Temperature	1,456°C	(1,729 K)
Inlet Gas Pressure	3.99 kgf/cm^{2}Abs.	(0.391MPa)
Exit Gas Pressure	2.78 kgf/cm^{2}Abs.	(0.273MPa)
Main Flow Pressure Ratio	1.44	
Cooling Air Temperature	398°C	(671 K)
Cooling Air Flow Rate (Ga/Gg)	parameter	

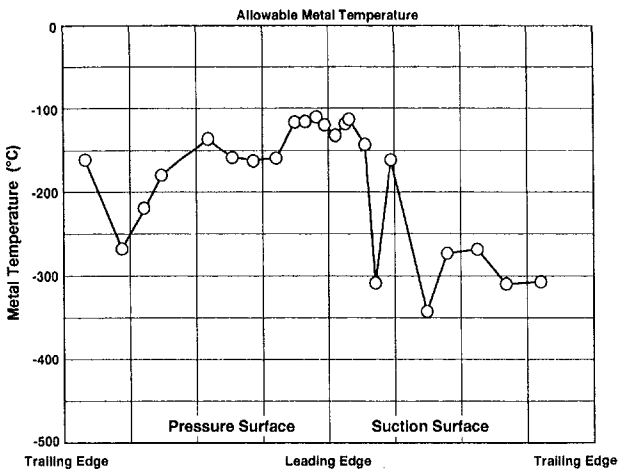

Fig. 8 Metal temperature distribution of the first vane

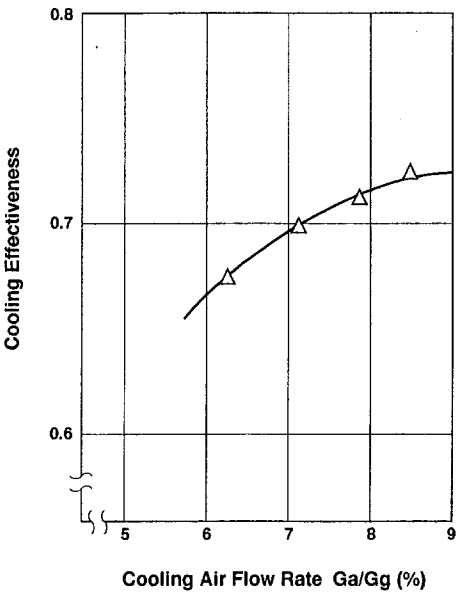

Fig. 9 Cooling effectiveness of the first vane

Table 2 Example of hot cascade test condition of the first-stage blade

Average Inlet Gas Temperature	1,315°C	(1,588 K)
Inlet Gas Pressure	4.33 kgf/cm²Abs.(0.425MPa)	
Exit Gas Pressure	3.06 kgf/cm²Abs.(0.300MPa)	
Main Flow Pressure Ratio	1.42	
Cooling Air Temperature	250°C	(523 K)
Cooling Air Flow Rate (Ga/Gg)	parameter	

T_g = gas temperature
T_m = average metal temperature
T_a = cooling air temperature

It was confirmed that the high cooling effectiveness was attained by using FCFC.

The aerodynamic conditions of the first-stage blade hot cascade test at 50 percent height section simulated the actual engine conditions. The tests were conducted over a range of relative inlet total temperatures for the first-stage blade from 1000°C (1273 K) to 1350°C (1623 K) with the cooling air flow rate (Ga/Gg) varying from about 2.5 to 3.5 percent. The typical test condition of the first-stage blade is shown in Table 2.

Figure 10 shows the experimental midspan chordwise temperature distribution of the first-stage blade. The metal temperature distribution was very uniform except for the film-cooled region on pressure surface near the trailing edge. Film cooling should also be applied at the trailing edge on the pressure surface. A high-reliability, high-efficiency air-cooled first-stage blade was developed by optimizing the cooling air flow passage, angled turbulator dimensions, and FCFC holes.

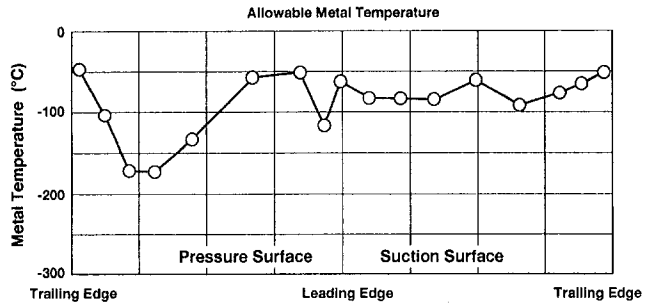

Fig. 10 Metal temperature distribution of the first blade

Table 3 Chemical composition of tested materials (wt%)

Purpose	Alloy	Cr	Co	Mo	W	Ta	Ti	Al	C	B	Zr	Hf	Y_2O_3	Ni
DS	CM247LC	8.20	9.29	0.49	9.50	3.27	0.67	5.68	0.07	0.018	0.010	1.42	—	Bal.
SC	CMSX-2	7.90	4.60	0.60	8.01	6.04	1.01	5.61	—	—	—	—	—	Bal.
ODS	MA754	19.9	—	—	—	—	0.45	0.31	0.06	—	—	—	0.60	Bal.

Development of Advanced Heat-Resistant Materials

The development of the next-generation 1500°C class gas turbine requires materials of excellent high-temperature properties in addition to the technologies of advanced cooling systems for hot parts.

For this purpose, some advanced materials for turbine blades and vanes were investigated.

As a result, Directionally Solidified (DS) blades and vanes with thermal barrier coating (TBC) seem to be the most reliable technology choice [3].

DS blades and vanes improved about 50°C (50 K) of creep rupture strength and 10 times thermal fatigue life against Conventional Casting (CC) materials. TBC reduces metal temperature about 70°C (70 K). Moreover, Single Crystal (SC) blades and Oxide Dispersion Strengthening (ODS) alloys for blades and vanes are being developed for use in the near future.

In this paper the above-mentioned development of DS vanes and SC blades and research of ODS alloys are described.

Chemical compositions of the evaluated advanced materials are shown in Table 3.

1 Trial Cast and Evaluation of DS Vane. DS vane of CM247LC alloy was trial-cast and evaluated. Figure 11 shows a DS trial-cast vane for 230 MW class industrial gas turbine. Airfoil columnar grains have grown in the direction of the airfoil height, which is good morphology. The shroud area was also directionally cast separately from the airfoil because of the direction of high thermal stress. The airfoil and the shroud were joined by diffusion bond.

A metallurgical test, tensile test, stress rupture test, and the characteristics of the bonded area were evaluated. Good property results were observed on each test. For example, Fig. 12 shows stress rupture test results that were evaluated from test specimens taken in the direction of airfoil height. It was confirmed that stress rupture properties of the DS airfoil were similar to CTS (Cast-to-Size) in the 0 deg direction (columnar grain grown direction).

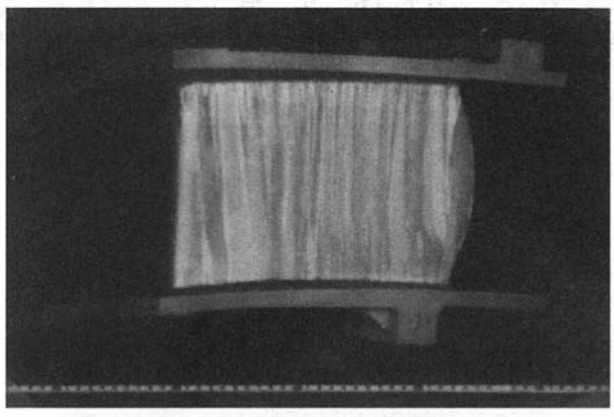

Fig. 11 Macro-structure of trial-manufactured DS vane of 230 MW class gas turbine

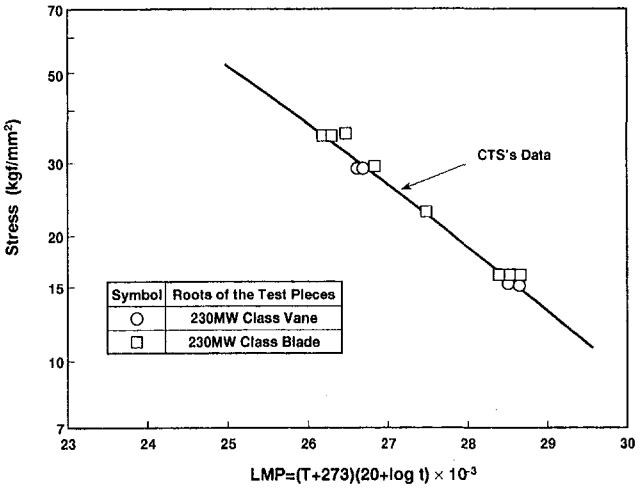

Fig. 12 Creep rupture strength of the test specimens machined from trial manufactured DS vane

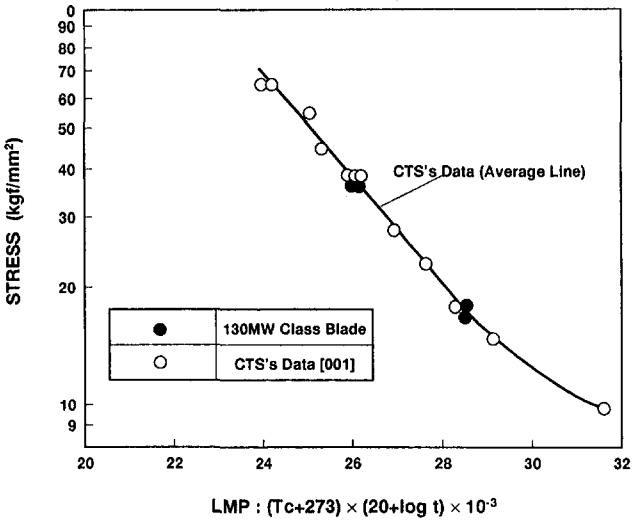

Fig. 14 Creep rupture strength of test specimens machined from trial manufactured SC blade

2 Trial Cast and Evaluation of SC Blade. CMSX-2 material data for the SC blade design were generated and the large-scale SC blades for industrial gas turbine were trial-cast. From the amount of eutectic γ' phase precipitation, morphology of cooling γ' precipitation, and the property of creep rupture life, the heat treatment condition was optimized. (1280°C × 2 hr/ArC + 1305°C × 2 hr/ArC + 1080°C × 4 hr/N_2C + 870°C × 20 hr/N_2C was adopted.)

Mechanical strength (tensile, creep rupture, high cycle fatigue, low cycle fatigue, etc.) and physical properties (Young's modulus, thermal expansion, thermal conductivity, specific heat, etc.) of the CMSX-2 with the optimized heat treatment were tested. Test coupons were machined along the three principal directions of [001], [111], and [011].

As shown in Fig. 13, this SC blade has the acceptable macrostructure with no casting defect of equiaxed grain or freckle indications. The crystal direction of this blade to [001] was 4.5 deg.

The results of tensile test and creep rupture test, using the test coupons machined from the actual blade, showed the blade had satisfactory strength equal to the data of CTS (Fig. 14).

3 ODS Alloy Material Data. MA754 material data for ODS alloy vane designing were generated. Thermal fatigue strength of the ODS alloy is unisotropic as shown in Fig. 15. Rolled direction values surpass the vertical direction values for thermal fatigue strength. The reason for this is that the microstructure grains are extended in the rolling direction. The unisotropic characteristic is also observed in tensile strength, creep rupture strength, Young's modulus, specific heat, and thermal conductivity.

HTDU Test

The final phase in the development of the next-generation 1500°C class gas turbine is the testing of new designs at full engine temperature conditions using HTDU (High Temperature Demonstration Unit) [5]. HTDU is a special core engine with scaled-down turbine blades and vanes of the advanced gas turbine for demonstrating the key technologies mentioned above.

The test was conducted at the gas turbine test facility in Takasago Machinery Works, Mitsubishi Heavy Industries, Ltd. Figure 16 shows a cross-sectional view of the HTDU. The HTDU was originally constructed to demonstrate high-temperature technology applied to the 701F. The turbine is a 0.5 scale of the first stage of the 701F. The HTDU consists of 16 can type combustors, a single-stage turbine (32 vanes and 72 blades), etc. The turbine extracted power output is absorbed by a water brake.

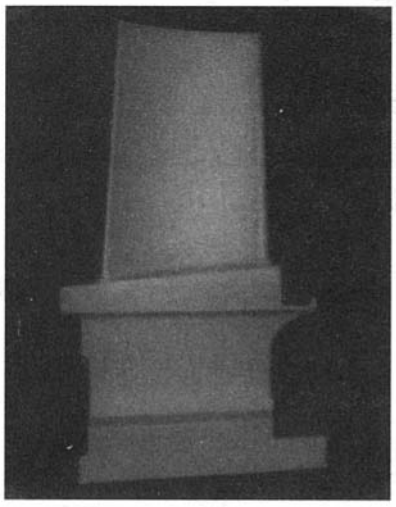

Fig. 13 Macrostructure of trial manufactured SC blade of 130 MW class gas turbine

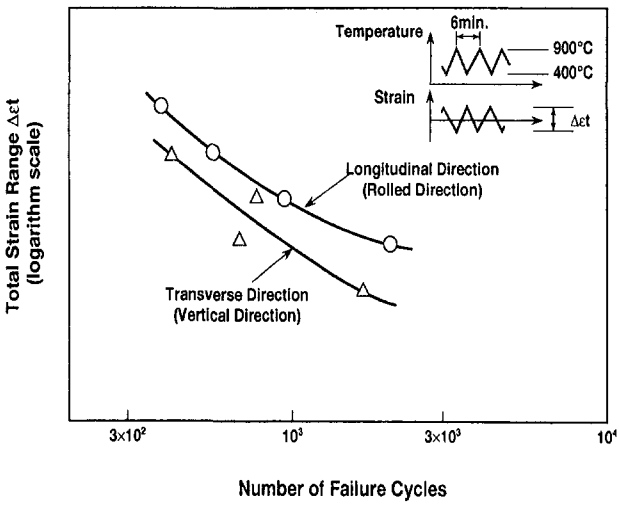

Fig. 15 Thermal fatigue strength of ODS alloy MA754

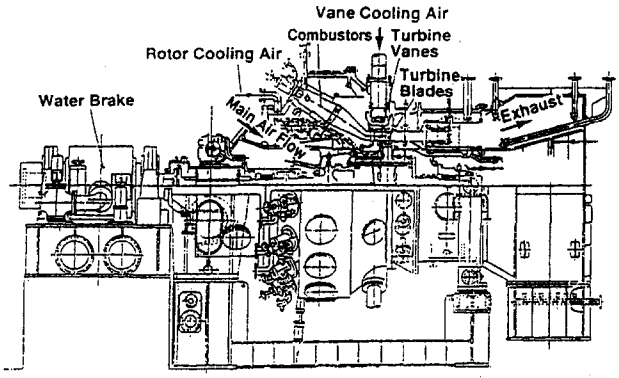

Fig. 16 Cross-sectional view of HTDU

Table 4 Typical test condition

Firing Temperature	1,500°C (1,773K)
Speed	6,000rpm
Main Flow	30kg/s
Power Output	7,000kW
Inlet Total Pressure	3.4kgf/cm^{2}Abs. (3.3MPa)
Turbine Pressure Ratio	1.8

Main and cooling air flow rates and rotor cooling air temperature can be adjusted to the required value by control valves or an air-cooler.

A typical test condition is shown in Table 4. These numbers are set to be the equivalent operating condition of the 1500°C class advanced gas turbine (AGT). The vanes and the blades of the current HTDU are 0.6 scale of those of the first-stage of the 501F/701F. In order to investigate the cooling effectiveness of the advanced cooling, some of the vanes and blades are to be replaced with those that have the cooling scheme of the AGT. Figure 17 shows the comparison of cooling schemes of the AGT and current F series film-cooled vanes/blades.

The first-stage vane of the AGT has three cavities with impingement cooling augmented by film cooling. For the pressure surface, FCFC (Full-Coverage Film Cooling) is applied to improve the cooling effectiveness. At the pin fin region of the trailing edge, cooling air from the afterward cavity is supplied and the cooling air is discharged from the trailing edge.

Table 5 Detail of tested row 1 vanes and blades

Row 1 Vane

NUM. OF VANES	COOLING SCHEME	MATERIAL	CASTING
1	FCFC	E-CY768	CC
2	FCFC + TBC	E-CY768	CC
1	FCFC + TBC	CM247LC	DS
28	FILM + TBC	E-CY768	CC

Row 1 Blade

NUM. OF BLADES	COOLING SCHEME	MATERIAL	CASTING
2	FCFC	IN-738LC	CC
1	FCFC + TBC	IN-738LC	CC
1	FCFC + TBC	CM247LC	CC
2	FCFC + TBC	CM247LC	DS
1	FCFC	CM247LC	DS
65	FILM + TBC	IN-738LC	CC

The first-stage blade of the AGT has three passages. One is a straight passage with film cooling at the leading edge. The second is a serpentine flow passage augmented by suction surface film cooling. The FCFC is also applied for the pressure surface cooling. The third is a cooling flow passage with pin fin rows in the trailing edge region. Air from the third flow passage is supplied for the pressure surface film cooling and the trailing edge cooling. The cooling air for the blade is cooled by the air-cooler before feeding.

The test was conducted utilizing various kinds of blade to verify the cooling effectiveness of the FCFC, heat shield performance of TBC, and the mechanical characteristics of the DS blade. Table 5 shows the various kinds of vanes and blades used for this HTDU test.

Tests are now being carried out for various firing temperatures. Figure 18 shows measuring points of temperature and pressure.

The maximum vibratory stresses were within the allowable stress for each material.

The results obtained here will be used for the actual gas turbine design.

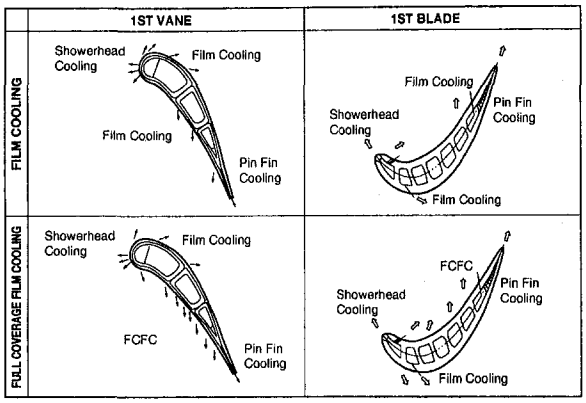

Fig. 17 Cooling scheme for HTDU

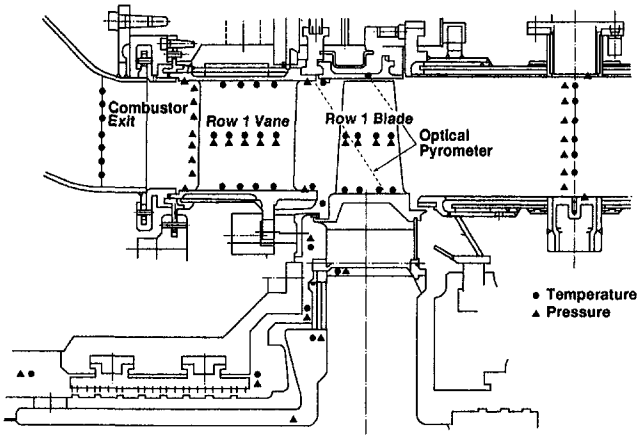

Fig. 18 Instrumentation for vanes and blades

Conclusion

Tohoku Electric Power Co., Inc., and Mitsubishi Heavy Industries, Ltd., have successfully conducted a six-year joint program on key technology development of the 1500°C class next-generation gas turbine for an advanced combined cycle.

Accomplishment of this program is believed to contribute to the realization of this gas turbine for the next-generation advanced combined cycle.

References

1 Hori et al., "Outline of Plan for Advanced Research Gas Turbine," ASME Paper No. 81-GT-28, ASME JOURNAL OF ENGINEERING FOR POWER, Vol. 103, Oct. 1981.

2 Kano et al., "Development Study of 1500°C Class High Temperature Gas Turbine," ASME Paper No. 91-GT-297.

3 Matsuzaki et al., "Investigation of Combustion Structure Inside Low NO_x Combustors for a 1500°C-Class Gas Turbine," ASME Paper No. 92-GT-123.

4 Amagasa et al., "Study on the Turbine Vane and Blade for a 1500°C Class Industrial Gas Turbine," ASME Paper No. 93-GT-414. ASME JOURNAL OF ENGINEERING FOR GAS TURBINES AND POWER, Vol. 116, 1994, pp. 597–604.

5 Sato et al., "High Temperature Demonstration Unit for a 1500°C Class Gas Turbine," ASME Paper No. 94-GT-412.

H. Nomoto

A. Koga

S. Ito

Heavy Apparatus Engineering Lab,
Toshiba Corporation,
Yokohama, Japan

Y. Fukuyama

F. Otomo

Research and Development Center,
Toshiba Corporation,
Kawasaki, Japan

S. Shibuya

Thermal Power Plant Eng. Dept.,
Toshiba Corporation,
Yokohama, Japan

M. Sato

Y. Kobayashi

H. Matsuzaki

Tohoku Electric Power Co., Inc.,
Sendai, Japan

The Advanced Cooling Technology for the 1500°C Class Gas Turbines: Steam-Cooled Vanes and Air-Cooled Blades

It is very essential to raise the thermal efficiency of combined cycle plants from the viewpoint of energy saving and environmental protection. Tohoku Electric Power Co., Inc., and Toshiba Corporation in Japan have jointly studied the next generation of combined cycle systems using 1500°C class gas turbine. A promising cooling technology for the vanes using steam was developed. The blades are cooled by air, adopting the impingement cooling, film cooling, and so on. The cooling effectiveness was confirmed both for the vanes and the blades using a hot wind tunnel. This paper describes the design features of the vanes and the blades, and the results of the verification tests using the hot wind tunnel.

Introduction

There is a global demand to save energy and protect the environment. Especially, recent discussions about acid rain, the destruction of the ozone layer, and the heating of seawater have accelerated the development of the power plants with higher efficiency and lower emissions. At present, the combined cycle is the most prominent solution to these problems due to its potential for high thermal efficiency. The increase of thermal efficiency of the combined cycle has been and will be achieved by raising the inlet temperature of the gas turbine. Tohoku Electric Power Co., Inc. and Toshiba Corporation have been studying 1500°C class gas turbines. Apparently, the key technology to achieve the higher inlet temperature is to maintain the metal temperatures of the vanes and the blades below the allowable limits. Most of the gas turbines have used air as a coolant for vanes and blades in the past. However, there are some studies on alternative coolants such as water (Blazek et al., 1981; Fukuyama and Araki, 1989) and steam. Recently, there have been some papers on gas turbines with steam cooling (Corman, 1995, Fukue, 1995). Although they discuss the advantages of steam cooling and cycle efficiency, etc., the papers do not include any experimental results.

In this study, steam was selected as a coolant of the vanes, taking account of its high heat transfer capability. The blades are made of single crystal alloy, and cooled by air, adopting three independent cooling channels, the impingement cooling, and the film cooling. Basic ideas such as the cycle optimization, the scale model gas turbine, the concept of cooling design both for the vanes and the blades, and the candidate materials have already been discussed (Matsuzaki et al., 1992). The design of the vanes and blades was completed through some analyses and component tests discussed in this paper. Recently, the hot wind tunnel tests were conducted both for the vanes and the blades to confirm the cooling effectiveness, the flow characteristics, and the metal temperature. This paper describes the cooling technology for 1500°C class gas turbine, mainly focusing on the design features and the results of the hot wind tunnel tests for both the vanes and the blades.

Cycle

Figure 1 shows an example of the combined cycle with the steam cooling, and Table 1 shows its specifications. The heat recovery steam generator has three drums, and the inlet temperature of the gas turbine is as high as 1450°C. The cycle efficiency is expected to achieve more than 55 percent (LHV). As is

Contributed by the International Gas Turbine Institute and presented at the 41st International Gas Turbine and Aeroengine Congress and Exhibition, Birmingham, United Kingdom, June 10–13, 1996. Manuscript received at ASME Headquarters February 1996. Paper No. 96-GT-16. Associate Technical Editor: J. N. Shinn.

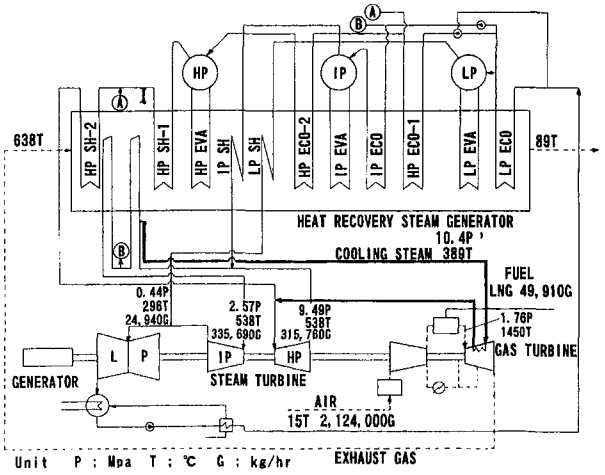

Fig. 1 Diagram of steam-cooled combined cycle

shown in Fig. 1, the cooling steam for the vanes is extracted from the superheater of the heat recovery steam generator. After cooling the gas turbine vanes, the steam is returned to the high-pressure steam turbine, which efficiently recovers the energy obtained by cooling the vanes. Since the coolant steam is not ejected into the gas path due to the closed-loop design, the temperature drop of the hot gas at the vanes is minimized. This makes the higher firing temperature at the first stage rotor inlet possible, causing higher efficiency, and hence makes the lower combustion flame temperature possible, thus decreasing NO_x emission.

Scale-Model Gas Turbine

Although the cycle study was conducted for the large-scale combined cycle, the scale model gas turbine of 60 MW was chosen for the verification of key components such as the first-stage vanes and the first-stage blades. The size of the key components is approximately half of the large-scale machine.

Figure 2 shows the cross section of the turbine. The compressor has 17 stages, and its pressure ratio to the atmosphere is 18. The transonic blades are used for the first and second stages. A variable inlet guide vane and the first-stage vane enable the surge control for the start-up, as well as the improvement of the partial load performance.

The Dry Low NO_x Combustor (DLNC) is used for NO_x emission control. The turbine has three stages, and cooling is employed in the vanes and the blades, except the last-stage blades. The first-stage vanes are cooled by steam with slight film air ejection. The second-stage and third-stage vanes are cooled by air, which is extracted from the midstages of the compressor. The cooling air for the first-stage and second-stage blades is extracted from the compressor discharge, and it is led to the external air cooler before being supplied to the blades.

Design Features of the Steam-Cooled Vanes

Design Features for the High Pressure Steam. The design specifications of the vanes and the blades were determined by the feasibility study of the cycle and the model gas turbine, and Table 2 summarizes the specifications of the cooling design for the first stage vanes. The following points should be kept in mind in order to design the steam-cooled vanes.

- The embodiment of the closed loop
- Optimum flow direction of the coolant steam
- Pressure difference between the steam and the gas
- Thermal stress

Table 1 Specifications of 1500°C class combined cycle

Gas Turbine Output	246 MW
SteamTurbine Output	140 MW
Heat Recovery SteamGenerator	Three Drum Type
Fuel	Liquid Natural Gas
Inlet Temperature of Gas Turbine	1450 ° C
Cycle Efficiency	56.8 % (LHV)

The cross section of the steam-cooled vane is shown in Fig. 3(a) and its configuration is schematically described in Fig. 3(b). The chord length is about 117 mm and the span height is about 92 mm. When the high-pressure steam is adopted as a coolant, it is very important to take the pressure difference between the cooling steam and outer gas pressure into account; in other words, the cooling steam with high pressure should be confined to a small area. Therefore, a straight circular hole configuration, which is similar to the water-cooled vanes, is adopted. The diameter of the circular hole is about 2 mm, and more than 30 holes are arranged in the vanes. The pitches of the holes are designed to make the metal temperature as uniform as possible.

Due to high specific heat, density, and thermal conductivity of the high-pressure steam, the inner convection cooling without impingement achieves enough cooling effectiveness, thus making the cooling path design rather simple.

It should be emphasized that the cooling path design such as the flow direction, the sizes and the pitches of the cooling path, etc., are optimized considering the distribution of the outer heat transfer. Especially, the flow direction of the cooling steam is important since the temperature of the steam increases due to the heat exchange. The areas that should be efficiently cooled are the suction side, the pressure side, the leading edge, the outer end wall, and the inner end wall.

First, the cooling steam is supplied to the suction side, and flows from the tip area to the root area through the straight circular cooling paths. This is because the heat transfer coefficient of the hot gas flow is relatively high in the suction side. This requires that the fresh cooling steam with low temperature should be supplied to the suction side. Second, the cooling steam is collected in the root area after cooling the suction side, and flows in the inner end wall through a couple of cooling paths. Next, the cooling steam returns from the root area to the tip area through the leading edge, the pressure side, and the trailing edge. Finally, the steam is collected again in the tip area, cooling the outer end wall, and then it flows back to the recovery pipe. Thus, the steam flows in a closed loop. Although

Nomenclature

M_s = mass flow rate of cooling steam
M_g = mass flow rate of hot gas
M_c = mass flow rate of cooling air for blades
M_f = mass flow rate of film air for vanes
M_a = outlet Mach number of hot gas
P_g = pressure of hot gas
P_s = pressure of cooling steam
ΔP_s = pressure drop of cooling steam
Re_g = outlet Reynolds number of hot gas
T_g = temperature of hot gas
T_s = temperature of cooling steam
T_c = temperature of cooling air
T_{mo} = outer metal temperature of blades and vanes
$T_{m\text{-}bulk}$ = average metal temperature of blades
η = local cooling effectiveness
$= (T_g - T_{mo})/(T_g - T_s)$ for vanes
$= (T_g - T_{mo})/(T_g - T_c)$ for blades
ρ_s = density of cooling steam

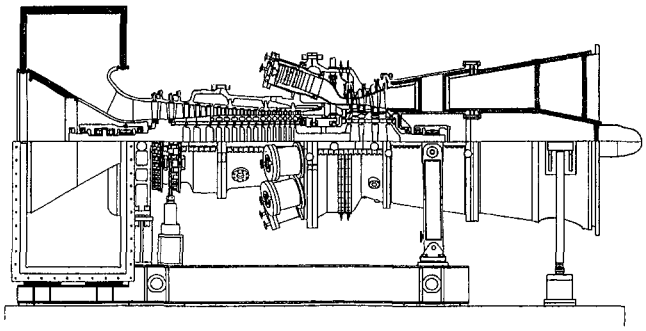

Fig. 2 Cross section of 1500°C class gas turbine

the cooling effectiveness of the steam is excellent, it causes thermal stress due to the steep temperature gradient. According to the stress analysis, it was found that the suction side in the vicinity of the leading edge has high thermal stress. There are two countermeasures to the high thermal stress. One is to eject cooling film on the outer surface of the vane, and the other is to add the thermal barrier coating (TBC). Film cooling decreases the temperature of the hot gas in the vicinity of the vane surface, and thermal barrier coating reduces temperature gradient in the vane due to small heat conductivity. Taking the long-term reliability into account, film cooling is adopted. However, its flow rate is kept as small as possible in order to minimize the temperature decrease of the hot gas at the vane. In fact, the number of film rows is only two, and their location is limited to the suction side of the vane in the vicinity of the leading edge, as is shown in Fig. 3(*a*). The mass flow rate of the film air is given in Table 2, and it is apparently much smaller than an ordinary air-cooled vane. This film air is effective enough to reduce temperature gradient and thermal stress on the suction side near leading edge.

Component Test. In the design process, the following tests and measurements were conducted to obtain the design data:

- Measurement of the pressure drop in the cooling path
- Flow visualization test in the cooling path
- Measurement of mass flow distribution in each cooling path
- Measurement of the film effectiveness

Figure 4 is the photograph of the flow visualization model. Water with small bubbles was used in order to visualize the flow, and static pressure along the steam path was measured. The model was large enough to make the Reynolds number equivalent to the design value. It was confirmed that the flow was smooth in all the cooling paths, showing no large stagnation or inverse flow in the steam path.

Film effectiveness was measured in a two-dimensional model vane (Fukuyama et al., 1994, 1995). First, the test was conducted under the condition of single ejection from each film row. Next, air was ejected from the both film rows; that is, the condition of double ejection. The superimposed film effectiveness from single ejection was compared with that of double

Table 2 Specifications of the cooling design for the vanes

Total Temperature of Hot Gas	Tg	1450 °C
Total Pressure of Hot Gas	Pg	1.8 MPa
Temperature of Coolant Steam	Ts	435 °C
Pressure of Coolant Steam	Ps	10.3 MPa
Non-dimensional Mass Flow Rate of Coolant Steam	Ms/Mg	6.3 %
Non-dimensional Mass Flow Rate of Film Air	Mf/Mg	1.9 %

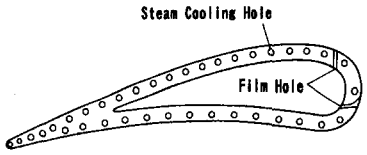

Fig. 3(*a*) Cross section of the steam-cooled vanes

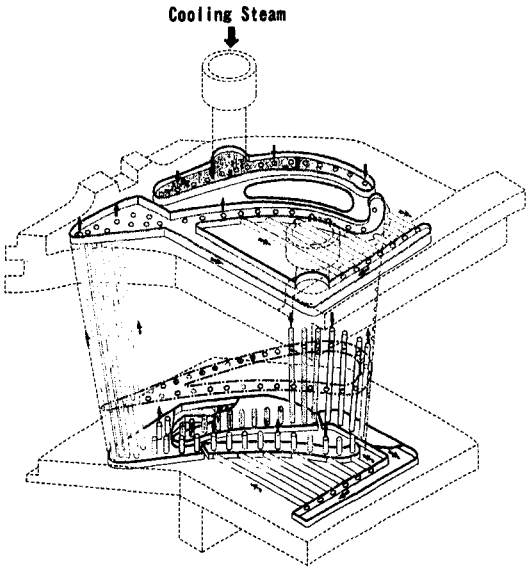

Fig. 3(*b*) Schematic view of the steam-cooled vanes

ejection, and they are in good agreement with each other in a wide range of nondimensional arc length as shown in Fig. 5. The film hole configuration was also studied. The diffusion hole showed higher film effectiveness than the circular hole, but caused higher total pressure loss in the gas path. By considering the results, the diffusion-shaped hole is applied to the first row, while the second row is the circular hole. The distance between the two rows is designed to be optimum based on the measured film effectiveness.

Feasibility Study for Intermediate Pressure Steam. Not only the high-pressure steam but also the intermediate pressure steam can be available to cool the vanes. In this case, the coolant steam can be extracted from the intermediate pressure drum, from the reheater, or from the exhaust of the high-pressure steam turbine. The coolant steam is sent to the reheater or to the intermediate steam turbine, which effectively recovers the

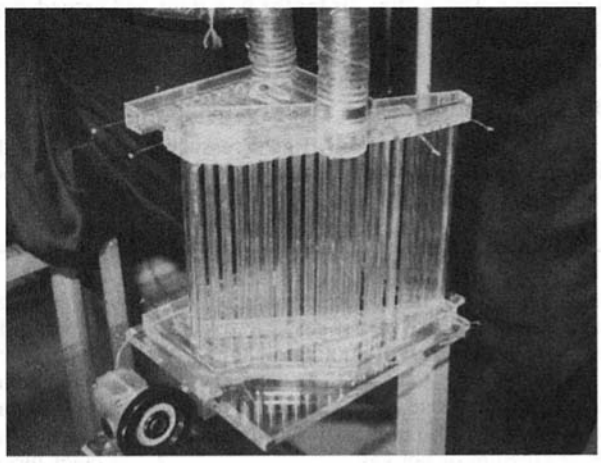

Fig. 4 Flow visualization model

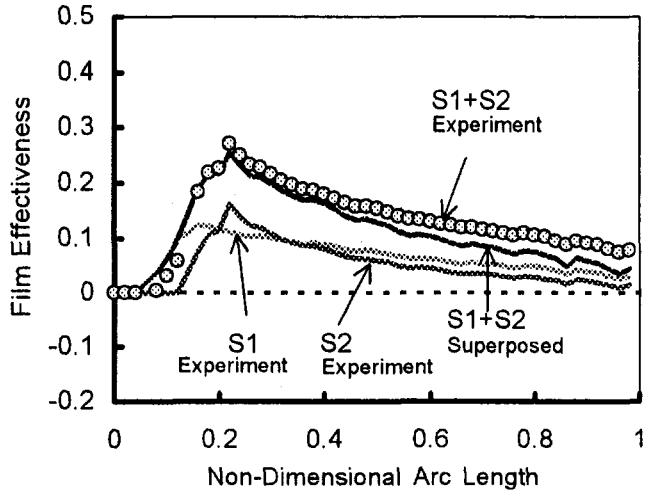

Fig. 5 Film effectiveness for the vanes

energy as well. The feasibility study using the intermediate pressure steam was also conducted (Amagasa et al., 1991), and the design of the vanes is shown in Fig. 6. It is similar to the air-cooled vanes, employing the insert core and the impingement cooling. The steam is supplied from tip area to the insert core of the leading edge, and it is collected in the root area. Then, the steam flows back to the insert core of the midchord and is recovered from the tip area. The trailing edge area is cooled by air with film cooling and the blow-off holes at the trailing edge. The cooling effectiveness was measured by installing a two-dimensional model vanes in a hot wind tunnel, and the results showed that the average cooling effectiveness is about 5 percent higher than for the air-cooled vane.

Design Features of the Air-Cooled Blades

The specifications of the cooling design for the blades are summarized in Table 3. Although the ambient gas temperature is high, the nondimensional mass flow rate of the cooling air is only 4.2 percent, due to the advanced cooling configuration and the use of external cooling of the air.

Figure 7 shows the configuration of the air-cooled blades. The cooling air is supplied from the root area through three independent channels; that is the leading edge side channel, the midchord channel, and the trailing edge channel. The leading edge side channel supplies the cooling air solely to the leading edge. The impingement cooling on the inner surface of the

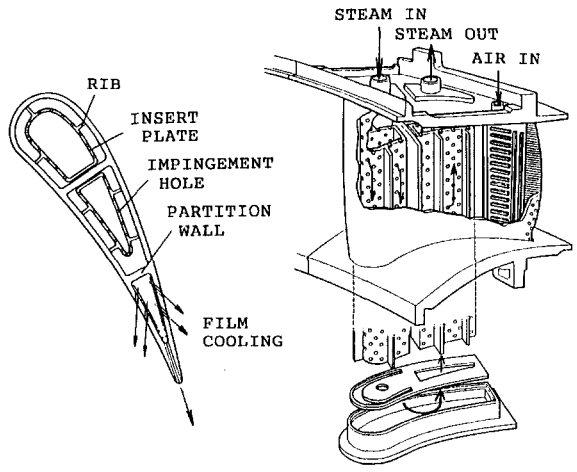

Fig. 6 Steam-cooled vanes by the intermediate pressure steam

Table 3 Specifications of the cooling design of the blades

Total Temperature of Hot Gas	Tg	1266 ° C *
Total Pressure of Hot Gas	Pg	1.11 MPa **
Temperature of Coolant Air	Tc	410 ° C
Non-dimensional Mass Flow Rate of Coolant Air	Mc/Mg	4.2 %

*Relative Total Temperature
**Relative Total Pressure

leading edge is adopted for this channel, and the air flows out of the leading edge through the showerhead. The midchord channel is five-pass serpentine, which enhances the inner convection heat transfer. The trailing edge side channel is three-pass serpentine, and the air flows out of small ejection holes into the gas path. Turbulence promoters in the serpentine channel are leaned toward the air flow direction in order to obtain high inner heat transfer. As far as the ejection holes of the cooling air are concerned, there are four staggered rows for the showerhead on the leading edge, two rows of film holes on the pressure surface, three rows on the suction surface, and ejection holes on the trailing edge. The pitches of all holes are designed to be optimum along the spanwise direction according to the temperature distribution of the hot gas.

Figure 8 shows the calculated temperature distribution of the blade metal and the film air. The ordinate is the temperature divided by the average bulk temperature of the blade. The hatched zone for the film, the exterior surface, and the interior surface, respectively, show the temperature range in the spanwise direction. The temperature distributions of the blade metal and the cooling air are calculated simultaneously taking account of the outer heat transfer, the film effectiveness, the inner heat transfer, and the heat conduction in the vane metal. As far as the outer heat transfer is concerned, the compressible nonviscous

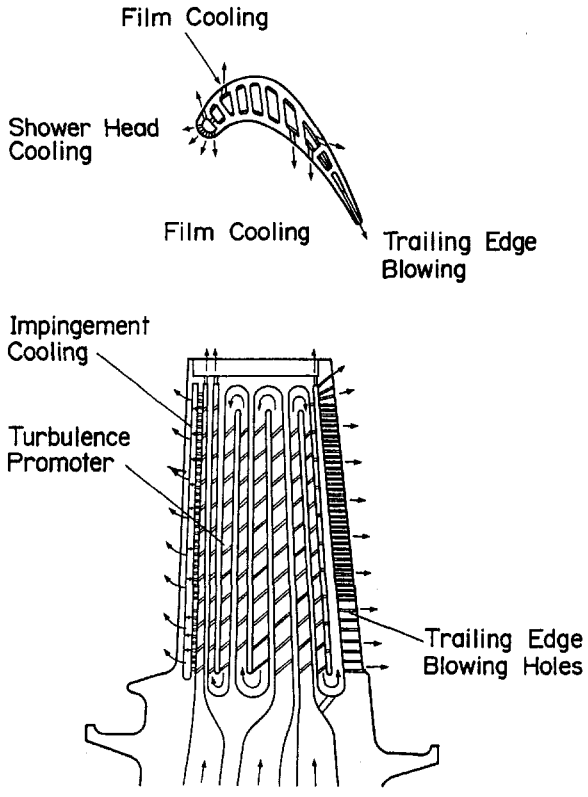

Fig. 7 Cross section of air-cooled blades

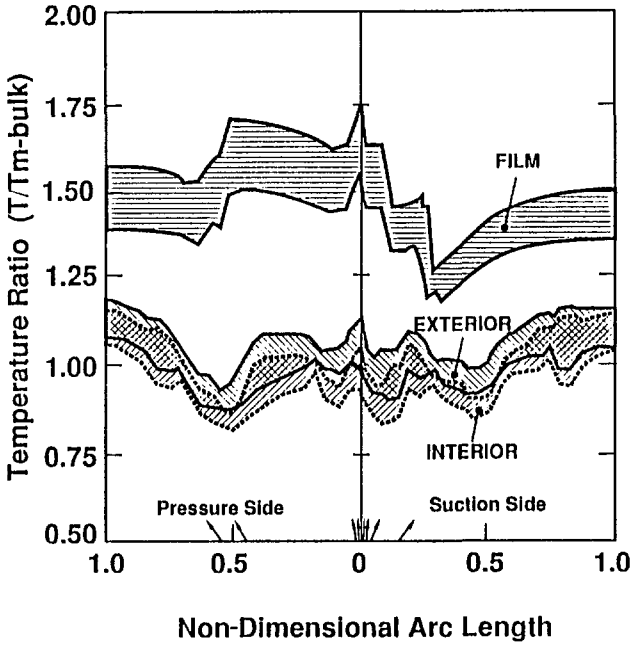

Fig. 8 Predicted temperature distribution of the blades

calculation (Denton's method) and the boundary layer calculation with $k-\epsilon$ model are used (Biswas and Fukuyama, 1994).

Manufacturing Procedure of the Vanes and the Blades

The vanes are made of Co-base superalloy and manufactured by precision casting, including the inner and the outer end walls. The cooling holes are machined by electro-discharge-machining. The cover plate, the supply pipe, and the recovery pipe are welded after machining the cooling holes. Figure 9 shows the appearance of the vanes after machining.

Figure 10 shows the outer appearance and the inner configuration of the blades. The blades are also manufactured by precision casting, and Ni-base single crystal superalloy is adopted from the viewpoint of high-temperature strength. The dovetail area and the shank area are machined after the precision casting, and the film holes are machined by electro-discharge-machining as well. The material specifications including the chemical composition and its casting process are discussed in detail by Yamamoto et al. (1995).

Experimental Apparatus of the Vanes

The hot wind tunnel test was conducted in order to confirm the cooling effectiveness. Figure 11 describes the total system

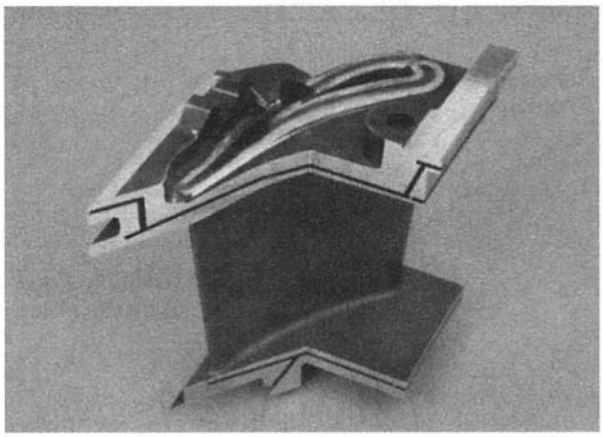

Fig. 9 Steam-cooled vanes after machining

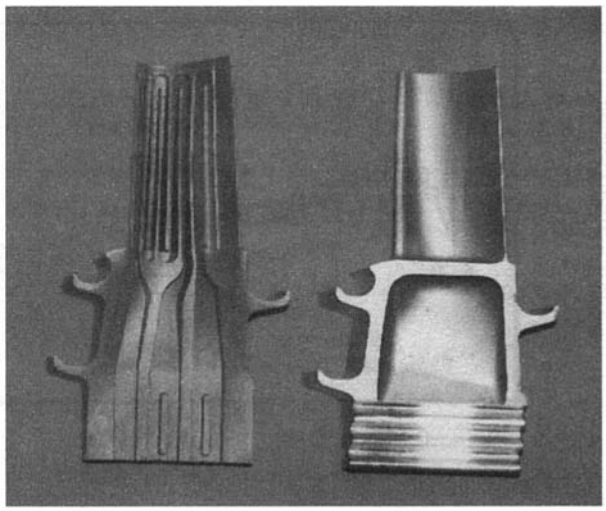

Fig. 10 Air-cooled blades

of the experimental apparatus for the vanes. The test apparatus is designed to simulate the actual conditions as precisely as possible. As is shown in Fig. 11, the test apparatus consists of a gas turbine, a compressor, a heat recovery steam generator, a test rig, a condenser, a stack, etc.

The compressor is driven by the gas turbine, and air is supplied to the test rig from the compressor. The film air is also supplied from the compressor as is the case for the actual plant. The exhaust gas of the gas turbine is sent to the heat recovery steam generator, from which the cooling steam can be supplied to the test rig. The flow rates of the hot gas, the fuel, the cooling steam, and the film air are measured at each supply line. There are a couple of measuring taps for pressure and temperature to monitor the test conditions.

Figure 12 is the photograph of the test rig, and Fig. 13 is its cross section.

As is shown in Fig. 13, a dry low NO_x combustor with 1500°C burner outlet temperature, which was developed for this experiment, is installed in the test rig. Five test vanes are installed in the test rig, with the center vane used for most of the temperature measurements.

A total of 15 temperature probes are installed at the inlet of the vanes. They are arranged at three different circumferential positions and five spanwise positions to measure the temperature distribution of the gas. Three total pressure probes are installed at the vane inlet, and they are located at three different

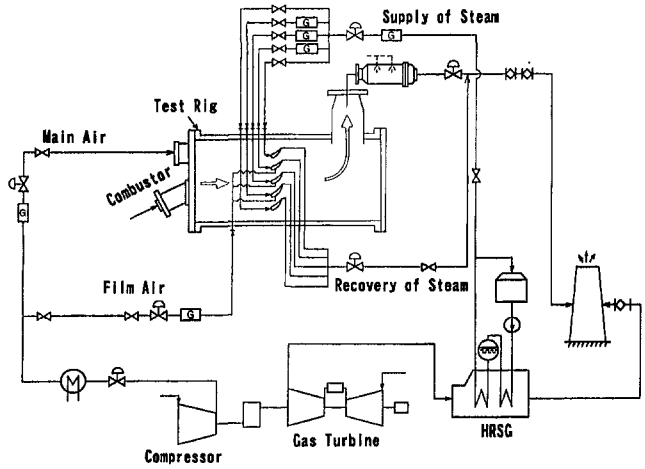

Fig. 11 Diagram of the test apparatus for the vanes

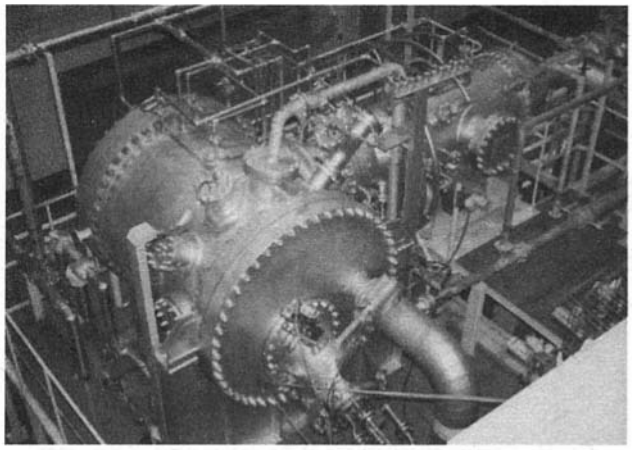

Fig. 12 Test rig for the vanes

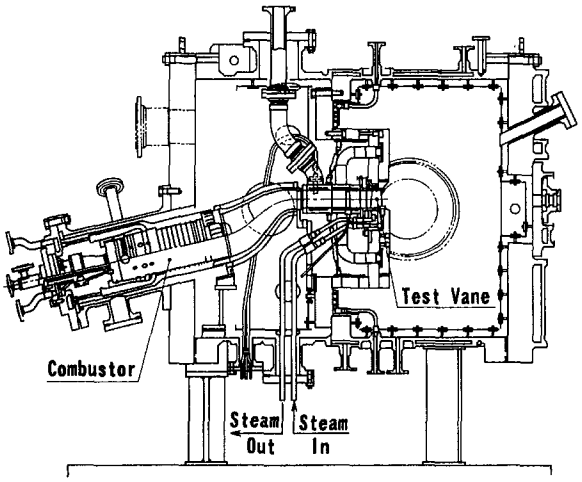

Fig. 13 Cross section of the test rig for the vanes

circumferential positions at mid span. As far as the metal temperature is concerned, thermocouples are installed on outer surface of the vanes. Figure 14 shows the location of the thermocouples installed at the midspan of the vane.

Experimental Results and Discussion for the Vanes

Experimental Conditions of the Vanes. The experiment was conducted in order to verify the local cooling effectiveness defined by the outer metal temperature. Table 4 explains the test range comparing the design points of the scale-model gas turbine. The Reynolds number is defined at the exit of the vane, and its length scale is based on the chord length. The important parameters that affect the local cooling effectiveness were changed systematically. They were: the hot gas temperature, the mass flow rate of the steam and the film air, the Reynolds

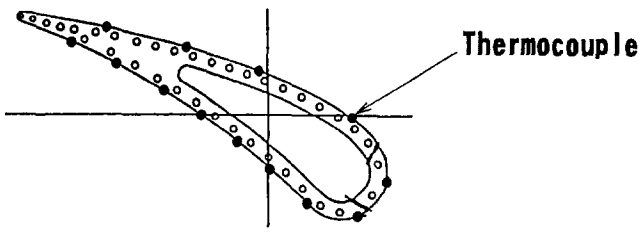

Fig. 14 Locations of the thermocouples of the vane

Table 4 Test range for the vanes

		Test Range	Design Point
Total Temperature of Hot Gas	Tg	Min. 750 ° C Max. 1450 ° C	1450 ° C
Non-dimensional Mass Flow Rate of Steam	Ms/Mg	Min. 3.4 % Max. 7.0 %	6.3 %
Non-dimensional Mass Flow Rate of Film Air	Mf/Mg	Min. 1.6 % Max. 3.0 %	1.9 %
Reynolds Number of Hot Gas	Reg	Min. 0.63×10^6 Max. 2.61×10^6	3.5×10^6
Mach Number of Hot Gas	Ma	0.94	0.95

number of the hot gas, etc. The test conditions include the design point except for the Reynolds number. The pressure of the hot gas is lower than the design point due to the limitation of the test apparatus, and this makes the Reynolds number smaller. However, the effect of the Reynolds number was extrapolated to the design point, and it was compared with analytical results.

Effect of Cooling Steam Flow Rate. It is very important to find the optimum flow rate of the cooling steam. Figure 15 shows the distribution of the cooling effectiveness expressed by Eq. (1). As is in Eq. (1), the outer metal temperature is used to define the cooling effectiveness:

$$\eta = (T_g - T_{mo})/(T_g - T_s) \quad (1)$$

In this series of tests, the hot gas temperature at the inlet of the vane T_g is 1000°C, the Reynolds number of the hot gas, Re_g, is 2.0×10^6, the nondimensional mass flow rate of film air, M_f/M_g, is 1.9 percent. The nondimensional flow rate of the cooling steam, M_s/M_g, is changed from 3.4 to 7.0 percent, including the design point of 6.3 percent. When the flow rate of the cooling steam is increased, the cooling effectiveness naturally increases. However, it is important to emphasize that there is very small change of the cooling effectiveness even with the cooling flow rate increased from 6.6 to 7.0 percent. Therefore, it can be concluded that the design flow rate of 6.3 percent is near the optimum point.

Effect of Film Air Flow Rate. The second series of the test was conducted by changing the film flow rate, while keeping the other parameters constant. Figure 16 describes the variation of the cooling effectiveness when the nondimensional film air flow rate, M_f/M_g, is changed from 1.55 to 3.03 percent. The cooling effectiveness on the pressure side shows little difference since no film air is supplied to the pressure side. On the contrary, there is some difference on the suction side, especially near the leading edge. The cooling effectiveness at the point between two film rows shows very typical behavior due to the film flow

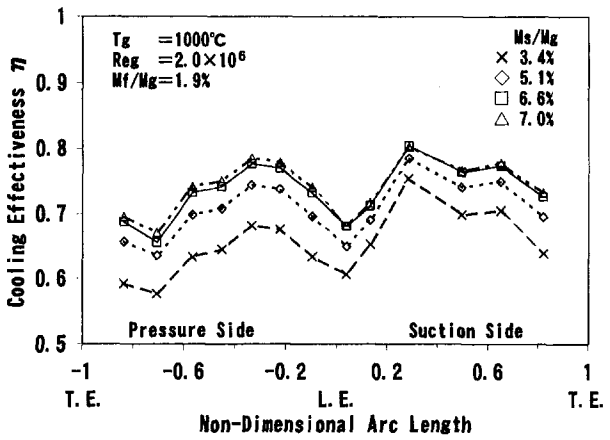

Fig. 15 Effect of cooling steam flow rate for the vanes

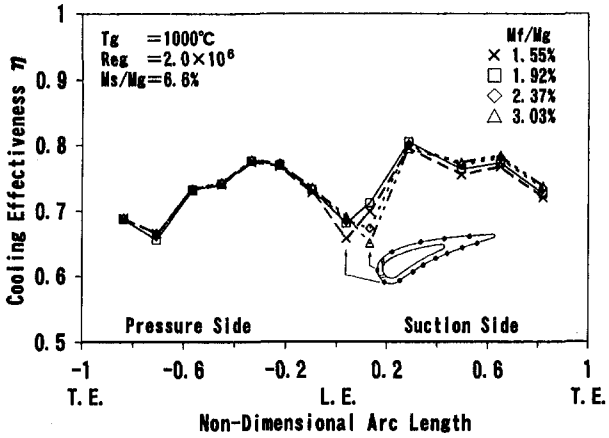

Fig. 16 Effect of film air flow rate for the vanes

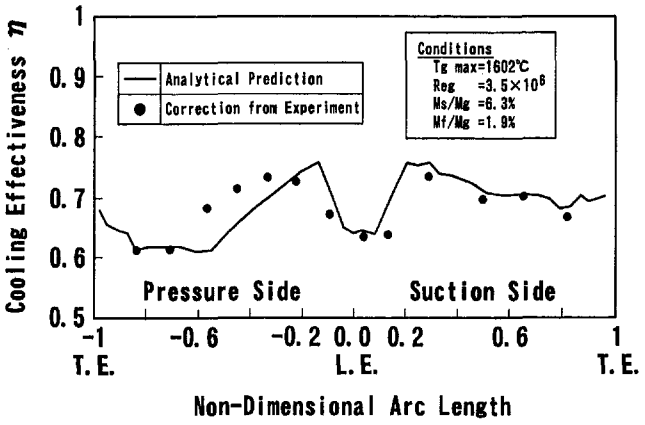

Fig. 18 Cooling effectiveness at the design point of the vanes

rate. When the film flow rate is increased from 1.55 to 1.92 percent, the effectiveness at this point increases. However, when the flow rate is increased further, the effectiveness decreases. This is probably because the film jet penetrates into the hot gas flow due to the higher momentum ratio of the film, and the film jet cores are lifted up. It is generally known that the lifting off and the separation of the jet core from the metal surface cause deterioration of the cooling effectiveness. Thus, the design flow rate of 1.9 percent can be interpreted as optimum.

Effect of Reynolds Number. The effect of the hot gas Reynolds number is plotted in Fig. 17. The tendency is different depending on the nondimensional arc location. For example, the cooling effectiveness generally decreases with higher hot gas Reynolds number in the suction side area, and in the trailing edge area, on the contrary, it increases on the pressure side. It should be noted that not only the hot gas Reynolds number but also the coolant Reynolds number is changed because nondimensional mass flow rate of the coolant is constant. Then, both the heat transfer coefficients of the outer surface and the inner surface become higher when the hot gas Reynolds number is increased. If the dependence of the outer heat transfer coefficient on Reynolds number is higher than that of the inner heat transfer coefficient, the cooling effectiveness decreases for higher Reynolds number and vice versa. Even though dependence of the cooling effectiveness on the hot gas Reynolds number is rather complicated, it has enough accuracy to predict the design condition since its tendency is consistent depending on the nondimensional arc position.

Estimation of Cooling Effectiveness. It is important to predict the cooling effectiveness under the design point both from the experiment and from the analysis. The test was conducted with the hot gas temperature of 1450°C. Other parameters such as the nondimensional mass flow rate of steam and film air are almost equal to the design values, but the Reynolds number of the hot gas was 1.92×10^6. The data can be properly corrected to the design point since the effects of other parameters are clarified by each series of tests.

The corrected result is plotted in Fig. 18, and the analytical prediction is also shown in the figure. The analytical prediction is obtained by the similar method discussed in the design features of air cooled blades. The cooling effectiveness is excellent, considering the fact that it is defined by outer metal temperature. The experimental effectiveness corrected to the design point and the analytical effectiveness agreed well.

Flow Characteristics of the Steam. Although the test range covers the design point of nondimensional flow rate of steam, its absolute value is smaller than the design point. This is because the Reynolds number of the hot gas, in other words the mass flow rate of the hot gas, is lower than the design point. Figure 19 is the comparison of the mass flow rate of the steam with the design point. A good linear correlation was obtained and the measured data can be extrapolated to the design point with good accuracy, showing the flow characteristic of steam path agrees well with the design prediction.

Experimental Results and Discussion for the Blades

Experimental Conditions of the Blades. Table 5 shows the test range of the hot wind tunnel for the blades. The blades are not rotated. The main parameters such as the temperature of the gas, the mass flow rate of coolant air, Reynolds number of the gas, and so on were changed. The Reynolds number is defined at the exit of the blade, and its length scale is based on the chord length.

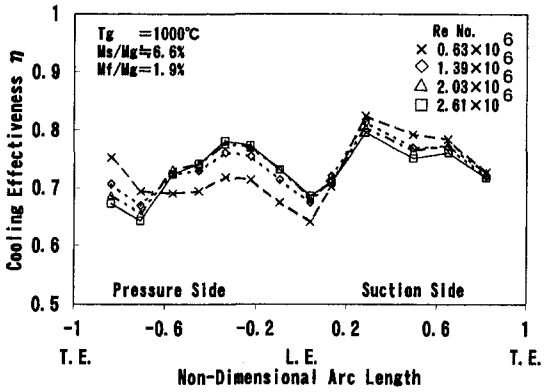

Fig. 17 Effect of Reynolds number for the vanes

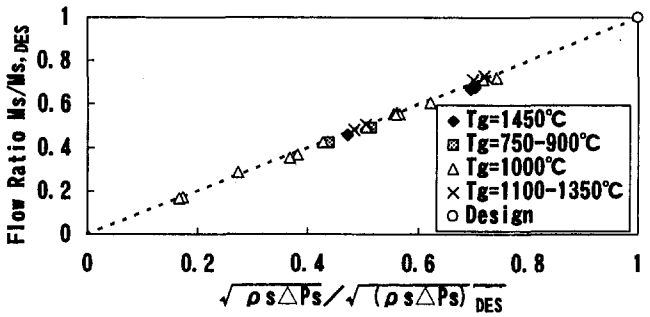

Fig. 19 Characteristics of steam flow

Table 5 Test range for the blades

		Test Range		Design Point
Total Temperature of Hot Gas	Tg	Min.	800 ° C	
		Max.	1480 ° C	1266 ° C
Non-dimensional Mass Flow Rate of Coolant Air	Mc/Mg	Min.	3.6 %	
		Max.	6.2 %	4.2 %
Reynolds Number of of Hot Gas	Reg	Min.	0.21×10^6	
		Max.	0.54×10^6	1.01×10^6
Mach Number of Hot Gas	Ma		0.71	0.71

Effect of Cooling Air Flow Rate. Figure 20 shows the cooling effectiveness when the mass flow rate of cooling air is changed. The local cooling effectiveness is also defined by the outer metal temperature, and is expressed by:

$$\eta = (T_g - T_{mo})/(T_g - T_c) \quad (2)$$

The cooling effectiveness increases almost linearly when the cooling flow rate is increased in this range of test. Generally speaking, it is uniform without any singular point of low effectiveness. But the cooling effectiveness near the leading edge is low when the mass flow rate of cooling air is 3.6 percent. This is probably because the showerhead at the leading edge is not effective enough if the flow rate is less than 4.2 percent.

Effect of Reynolds Number. The effect of Reynolds number is shown in Fig. 21. The cooling effectiveness increases monotonically with the Reynolds number. This can be explained by the test range. The hot gas Reynolds number for the blades test is less than 1×10^6. It is generally known that Nusselt number of the hot gas is proportional to 0.5th power, or at most 0.7th power of Reynolds number since the flow is not in the fully turbulent region. On the other hand, the Nusselt number of the cooling air is supposed to be proportional to 0.8th power of the Reynolds number of the cooling air since it is fully developed turbulent flow. When the Reynolds number of the hot gas is increased, that of the cooling air is also increased because the nondimensional mass flow rate is kept constant in this series of tests. Though there is some scatter band of the hot gas temperature, the variations of thermal conductivity and Prandtl number are small, thus it can be interpreted that the tendency of Nusselt number is equal to that of convective heat transfer. Therefore, the inner heat transfer increases more than the outer heat transfer, resulting in higher cooling effectiveness when Reynolds number becomes high.

Effect of Hot Gas Temperature. Figure 22 describes the cooling effectiveness when the gas temperature is changed. Even if other parameters are kept almost constant, the effectiveness becomes lower for higher hot gas temperature. Although the Reynolds number is not exactly constant, its scatter band does not explain the variation of the cooling effectiveness. The tendency of the cooling effectiveness can be explained by the thermal conductivity of the hot gas. The variations of Nusselt number and Prandtl number in this series of test are small. However, when the hot gas temperature becomes higher, it raises thermal conductivity of the hot gas. Higher thermal conductivity of the hot gas causes higher convective heat transfer. Then, the heat flux from the hot gas increases, resulting in lower cooling effectiveness.

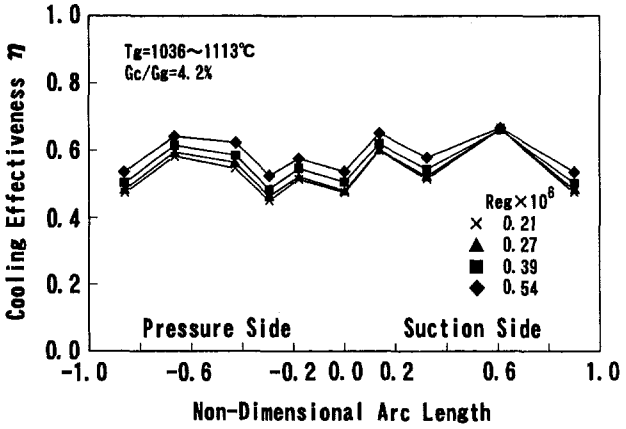

Fig. 21 Effect of Reynolds number for the blades

Estimated Cooling Effectiveness of the Blade. Although the test condition is not exactly equal to the design point, it is possible to make a correction from the obtained test data. Figure 23 shows a comparison of the cooling effectiveness between the analytical prediction and the corrected experimental data. The difference of the cooling effectiveness between them is within −0.04 to 0.1, showing good agreement.

Conclusions

The design features of the vanes and the blades for 1500°C class gas turbine have been discussed. The vanes are cooled by the steam extracted from the heat recovery steam generator, and the blades are cooled by the air extracted from the compressor. The results of the hot wind tunnel tests show they have excellent cooling effectiveness, and the analytical predictions agreed well with the experimental results.

From these results, the key technology for the next generation of 1500°C class gas turbine has been verified. Especially, it is

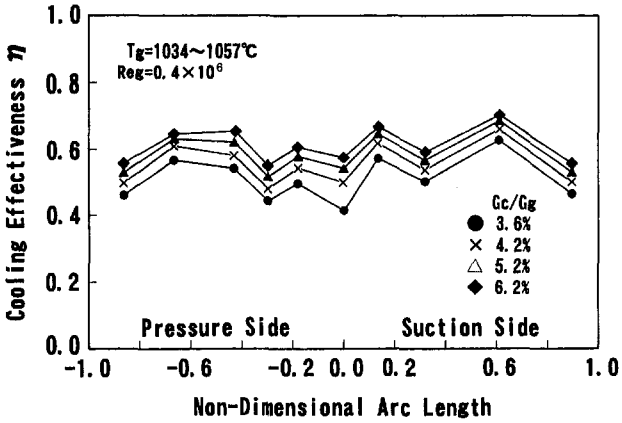

Fig. 20 Effect of cooling air flow rate for the blades

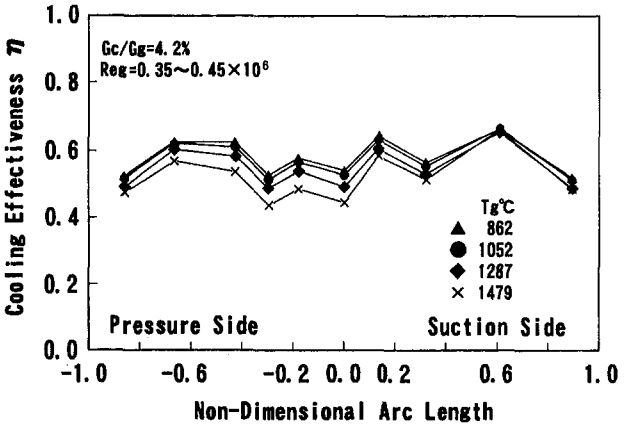

Fig. 22 Effect of hot gas temperature for the blades

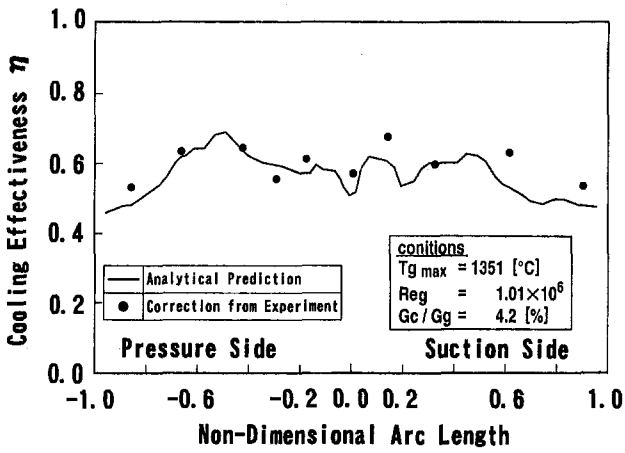

Fig. 23 Estimated cooling effectiveness of the blades

shown that the steam is a promising coolant for the combined cycle of the next generation.

References

Amagasa, S., Otomo, F., Fukuyama, Y., et al., 1991, "Testing for a Steam Cooling Gas Turbine Nozzle," JSME Annual Conf. No. 920-17B, pp. 408–410 [in Japanese].

Biswas, D., and Fukuyama, Y., 1994, "Calculation of Transitional Boundary Layers With an Improved Low-Reynolds-Number Version of the $k-\epsilon$ Turbulence Model," ASME *Journal of Turbomachinery,* Vol. 116, pp. 765–773.

Blazek, W. S., Schiling, W. F., and Schilke, P. W., 1981, "Water-Cooled Gas Turbine Monometallic Nozzle Development," ASME JOURNAL OF ENGINEERING FOR POWER, Vol. 103, No. 4.

Corman, J. C., 1995, "H Gas Turbine Combined Cycle Power Generation System for the Future," *Proc. Yokohama Gas Turbine Congress.*

Fukue, I., 1995, "A New Generation of Advanced Gas Turbine," *Proc. Yokohama Gas Turbine Congress.*

Fukuyama, Y., and Araki, T., 1989, "Testing of Water-Cooled Nozzle for High Temperature Gas Turbine," *Experimental Heat Transfer, Fluid Mechanics, and Thermodynamics,* pp. 1019–1026.

Fukuyama, Y., Otomo, F., et al., 1994, "Experiments on the Film Cooling Effectiveness of Bluff Head Gas Turbine Vane," *Proc. 22nd Annual Gas Turbine Conf.,* pp. 55–62 [in Japanese].

Fukuyama, Y., Otomo, F., et al., 1995, "Prediction of Vane Surface Film Cooling Effectiveness Using Compressible Navier-Stokes Procedure and K-ϵ Turbulence Model With Wall Function," ASME Paper No. 95-GT-25.

Matsuzaki, H., et al., 1992, "New Advanced Cooling Technology and Materials of the 1500°C Class Gas Turbine," ASME Paper No. 92-GT-240.

Yamamoto, H., Yamamoto, K., et al., 1995, "Material Evaluation of Large Single Crystal and Directionally Solidified Bucket Castings for Advanced Land-Based Gas Turbines," ASME Paper No. 95-GT-449.

Design and Test of a New Axial Compressor for the Nuovo Pignone Heavy-Duty Gas Turbines

Erio Benvenuti
Nuovo Pignone S.P.A.,
Firenze, Italy

This axial compressor design was primarily focused to increase the power rating of the current Nuovo Pignone PGT10 Heavy-Duty gas turbine by 10 percent. In addition, the new 11-stage design favorably compares with the existing 17-stage compressor in terms of simplicity and cost. By scaling the flowpath and blade geometry, the new aerodynamic design can be applied to gas turbines with different power ratings as well. The reduction in the stage number was achieved primarily through the meridional flowpath redesign. The resulting higher blade peripheral speeds achieve larger stage pressure ratios without increasing the aerodynamic loadings. Wide chord blades keep the overall length unchanged thus assuring easy integration with other existing components. The compressor performance map was extensively checked over the speed range required for two-shaft gas turbines. The prototype unit was installed on a special PGT10 gas turbine setup, that permitted the control of pressure ratio independently from the turbine matching requirements. The flowpath instrumentation included strain gages, dynamic pressure transducers, and stator vane leading edge aerodynamic probes to determine individual stage characteristics. The general blading vibratory behavior was proved fully satisfactory. With minor adjustments to the variable stator settings, the front stage aerodynamic matching was optimized and the design performance was achieved.

Introduction

The development of this axial compressor was undertaken to create a state-of-the-art design component for current and future Nuovo Pignone industrial gas turbine models. The first application was intended to provide the 10.5 MW PGT10 gas turbine with a higher flow compressor to assure a 10 percent increase in the rated power. At the same time, with the optimization of the blading flowpath and the use of advanced aerodesign techniques, a substantial reduction in the stage and total blade number was sought, to simplify the general layout and reduce costs. The design objectives resulted in an 11-stage axial compressor, Fig. 1, with wide-chord, high-strength blades, that fits the existing gas turbine layout with only minor changes in the interfaces with other components and auxiliaries.

The reference for the new design was the existing PGT10 compressor, and the target was to increase the mass flow by approximately 10 percent without substantially altering the interfaces with the rest of the existing equipment. The design of the present PGT10 compressor, Fig. 2, was started in 1984 as a larger flow version of the 5 MW MS1002 gas turbine 15-stage compressor, with the addition of three transonic front stages and the removal of the last stage (see Benvenuti et al., 1988). To match the existing blading, the three new front stages had to be designed with a constant hub diameter and conically tapered outer casing. To maintain the integral rotor construction, the new stage rotor blades were made of titanium to limit stresses on the tangential root dovetails. To avoid stall during startup and at reduced operating speeds, five rows of variable stators, from the inlet guide vanes through the stage 4 stator row, were incorporated into the design. The design mass flow was set equal to 41.2 kg/s at a pressure ratio of 14:1.

Contributed by the International Gas Turbine Institute and presented at the 41st International Gas Turbine and Aeroengine Congress and Exhibition, Birmingham, United Kingdom, June 10–13, 1996. Manuscript received at ASME Headquarters February 1996. Paper No. 96-GT-145. Associate Technical Editor: J. N. Shinn.

For the new compressor, a 10 percent increase in the design flow was set as the target, to get a correspondingly higher gas turbine shaft power for the same firing temperature. With the turbine first-stage nozzle area left unchanged, this increase requires a 10 percent higher pressure ratio. For the new design mass flow of 44.5 kg/s the pressure ratio results 15.4:1.

The geometric design constraints were imposed by interface requirements with the existing hardware; the principal consequences on the blading design were:

- maintain first-stage inlet hub diameter unchanged to make it compatible with existing bearing number one sizes
- make the exit flowpath diameters compatible with the existing combustor–turbine transition piece
- assure compatibility of the overall compressor length with the existing baseplate and general accessory layout.

The requirement of keeping the overall length substantially unchanged with a smaller number of stages made it possible to increase the airfoil chords, thus achieving a further reduction in the total blade number and assuring an increased mechanical strength.

Structurally, the solid rotor construction was changed into a bolted disk assembly for the first six stages, while the integral structure was maintained for the rotor rear end. The front-end disk construction with axial blade dovetails provided a much larger blade centrifugal force carrying capability, so that use of titanium was unnecessary. High-strength 17-4-PH steel was therefore used on the initial three stages, while 13 percent chromium steel was left unchanged on the rest.

Variable stators were foreseen on the initial stages to prevent stall and surge during startup and at reduced operating speeds. On the prototype compressor, four rows of adjustable vanes were provided (inlet guide vanes and stage 1–3 stators). However, after the initial tests, the fourth adjustable row was fixed with no appreciable change in the measured startup dynamic

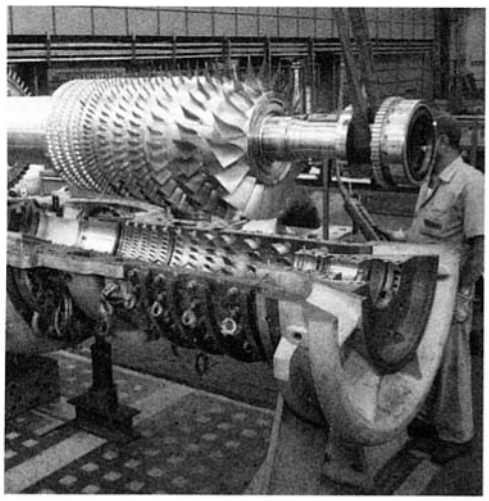

Fig. 1 Eleven-stage compressor assembly

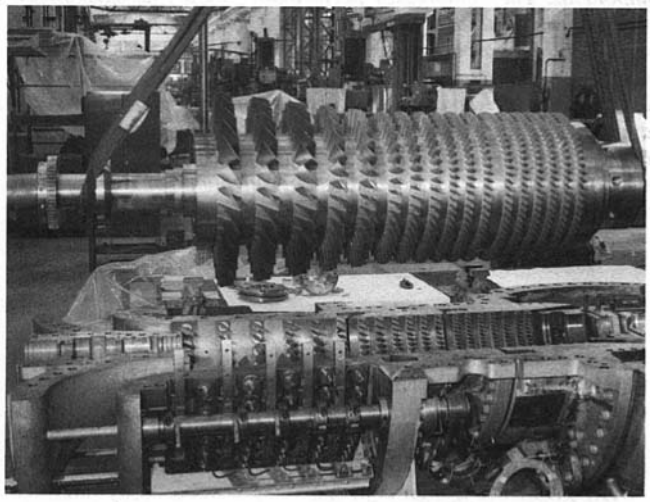

Fig. 2 PGT10 17-stage compressor

stresses and in the flow control for power turndown. Therefore, the production units are being foreseen with only three continuously adjustable rows.

In addition to the increase in the blade chords, the space made available by the stage number reduction was used also to design a new inlet plenum and bellmouth assembly. The new design's aerodynamic performance was experimentally checked on a 1:2 scale model. Very detailed flow surveys on the IGV inlet plane showed an average total pressure drop from the inlet flange lower than 0.5 percent, with swirl angles not exceeding 10 deg. Measured total pressure drop and swirl angle circumferential distributions at IGV midspan can be seen in Fig. 3, where losses and swirls appear significant behind the support struts and almost nonexistent elsewhere.

Blading Aeromechanical Design

Meridional Flowpath Layout. The major difference between the new and the existing compressor design is in the meridional flowpath shape. On the present production compressor, the initial four stages have a constant hub diameter, as a result of the original design requirement of matching the existing MS1002 compressor. In the new design, without such a constraint, the hub diameter could be increased right from the first stage, and kept growing up to a maximum compatible with the allowable hub/tip diameter ratio limit. This difference resulted in substantially higher blade peripheral speeds, with increased work and pressure ratio capability per stage without having to increase the aerodynamic loading coefficients substantially. The differences between the two meridional flowpaths can be seen in Fig. 4. The original flowpath design aim was to keep the outer diameter constant on all the stages. The final outer shape was instead tapered, starting from the fourth stage, to keep the maximum hub/tip diameter ratio within 0.92, beyond which secondary flow losses were expected to increase substantially. The blading exit annulus sizes were also checked for the requirement of matching the existing downstream components. The first-stage inlet hub diameter was kept unchanged for compatibility with bearing number one size requirements. The outer diameter corresponds to a 7 percent increase in the annulus area with respect to the existing compressor, so that the blading inlet axial Mach number is slightly higher to achieve the 10 percent design flow uprate.

The required number of stages was evaluated with the aim of not substantially changing the aerodynamic loading parameters, primarily the stage work coefficients ψ at the hub sections. With the new meridional contour the average hub peripheral speed

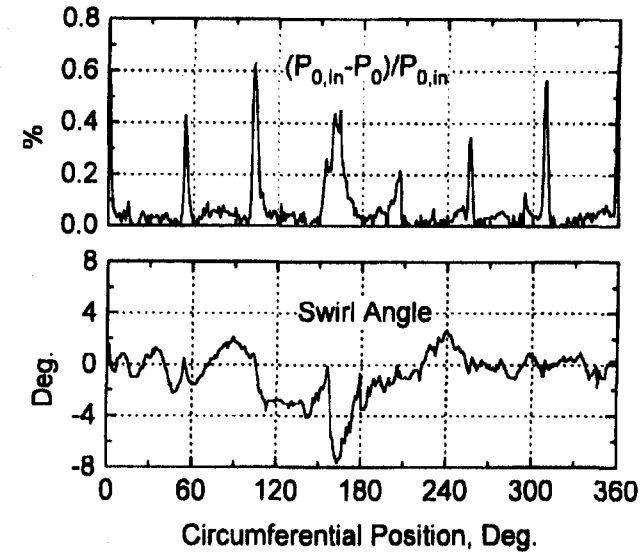

Fig. 3 Inlet duct model performance—IGV midspan

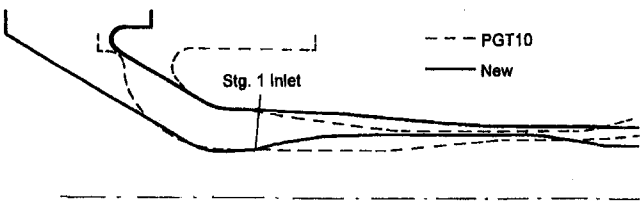

Fig. 4 Meridional flowpaths

Nomenclature

H = stage enthalpy drop, kJ/kg
U = blade peripheral speed, m/s
V_A = flow axial velocity, m/s
ϕ = stage flow coefficient = V_A/U
ψ = stage work coefficient = H/U^2

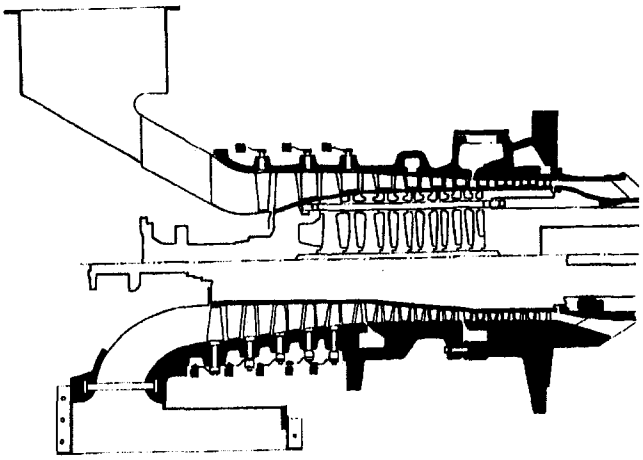

Fig. 5 New (top) and PGT10 (bottom) compressors

U is 1.25 times higher than in the existing compressor. Therefore, the stages can provide a 1.56 times higher specific work H without increasing the hub loadings. Theoretically, the number of required stages is therefore 17/1.56 = 10.9, to be raised to 11.4 to account for a 4.5 percent total work increase required by the higher design pressure ratio. The stage number was actually set at 11, with the small difference being absorbed by a more even loading distribution throughout the entire compressor.

The larger blading exit annulus diameters made it necessary to shape the exit diffuser appropriately to match the existing downstream component sizes. A contour with a constant outer wall diameter and a curved, decreasing diameter inner wall was selected. The design was developed with the aid of a three-dimensional viscous flow analysis code, with a computational grid including the blading exit guide vanes for appropriately setting the diffuser inlet boundary conditions.

As for the existing compressor, two bleed ports are present along the flowpath. The stage four bleed is used for cooling and buffering low-pressure components, while the stage seven bleed is used for start-up and is closed during operation.

The overall bladed flowpath and diffuser length, Fig. 5, is shorter than that in the existing compressor. The remaining length accommodates the new, longer bellmouth, while the slight plenum rearward extension is still compatible with the existing baseplate design with minor modifications.

Aerodynamic Design. The reduced number of stages along with the above-mentioned overall length requirements led to design of wide chord airfoils to fit the available space. Additional benefits resulting from this feature were a further reduction in the overall blade number and a higher mechanical strength. Furthermore, the associated lower airfoil aspect ratios, ranging from 1.1 for the first-stage rotor blade to slightly below 1 for the last stage, can provide wider stage characteristic curves. The number of blades for each row was selected to achieve sufficiently high solidities to keep the diffusion factors below 0.5 on all sections, as for the existing compressor. The inlet guide vane exit swirl angle was set to achieve a first rotor tip relative Mach number between 1.15 and 1.20. Use of multiple circular arc airfoils versus the double circular arc type present on the PGT10 compressor was shown to be adequate by detailed viscous Navier–Stokes blade-to-blade analysis to limit shock losses in the supersonic region. The subsonic rear stage rotor blades and all the stator vanes were designed with standard NACA65 series airfoils.

A further reduction in the airfoil number was achieved at the rear end, where the existing final stage double-row stator and exit guide vane assembly was replaced by a single-row, high solidity and turning cascade. To keep the fluid turning close to 40 deg in this single-row exit guide vane, the rear end stage design flow coefficients were increased by 20 percent with respect to the existing compressor to reduce the rotor blade exit swirls. The potential penalty associated with the higher blading exit axial Mach number was offset by the diffuser design, with increased length and shape optimized with accurate viscous flow analysis calculations. The high-turning exit guide vane airfoil was designed with a special, analytically custom-tailored shape with surface Mach number distributions approaching those found on conventional airfoils with smaller flow turnings. The reduction in the overall stage number, the use of a single exit vane row as well as the low aspect ratio design led to the decrease in the total blade number to below 60 percent of those needed on the existing compressor.

Stationary and Dynamic Stress Analysis. Low-aspect-ratio blades, although providing benefits in terms of increased mechanical strength, entail strongly three-dimensional airfoil shapes with complex steady stress distributions and vibratory mode shapes. For the steady stress analysis, very detailed finite-element models were built and used to evaluate secondary stresses due to three-dimensional effects and to compensate them with appropriate airfoil section stacking. In the dynamic analysis, particular attention was paid to predicting all the natural frequencies accurately, and to interpreting the high-order complex mode shapes typical of wide chord, thin airfoils. Among these high-order modes, those with one or more node lines running almost parallel to the edges may be of concern due to the associated vibratory stresses. In fact, the thin airfoil "Stripes" bound by these lines and the edges can vibrate like independent airfoil portions with high dynamic stresses at the nodes. Nodal lines of the first "Stripe" mode at 2769 Hz for stage one rotor blades are shown in Fig. 6. To check the Stripe mode stresses, the finite-element modal strain analysis was further utilized to assess the appropriate number of strain gage locations on the test compressor and to analyze the stress measurements, as will be described below.

Compressor Test Setup and Instrumentation

Testing of a full-scale compressor of this kind as an independent machine over the speed range typical of a two-shaft gas turbine would require a 15 to 20 MW power variable-speed driver. This could be achieved, for example, by using a production gas turbine, but would be very expensive due to the complexity of the setup and due to the costs associated with keeping an expensive commercial unit unavailable for sale during the entire test program. It was therefore decided to use a test methodology experienced almost at the same time for the new General Electric MS9001EC, 159.5 MW gas turbine compressor mapping test (Mezzedimi et al., 1996). According to this con-

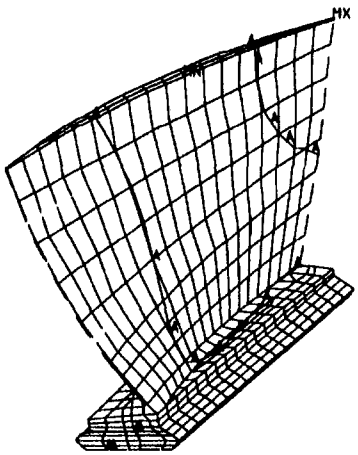

Fig. 6 Stage 1 rotor blade ANSYS modal analysis

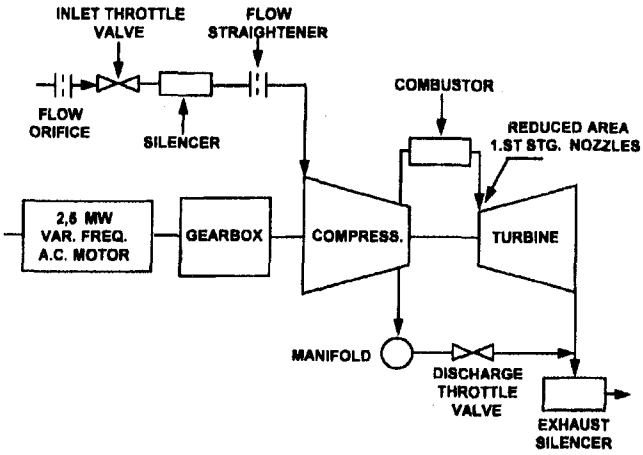

Fig. 7 Layout of the compressor test facility

cept, the compressor itself was made part of a complete PGT10 gas turbine engine, so that it could be driven by its own internal turbine without requiring an external driver.

To explore the performance map extensively, it was necessary to provide a means for controlling the compressor back pressure well away from the turbine matching line. For this purpose, the turbine was modified and a special external flow control valve and piping layout was set up, Fig. 7. To test the performance in the low-pressure-ratio range, special bleed ports with control valves were provided at the compressor discharge. They made it possible to decrease the pressure ratio down to the turbine no-load line. To achieve the high-pressure-ratio range, the standard turbine first-stage nozzle throat area was decreased by modifying the airfoils in the trailing edge area. This throat area restriction was calibrated in order to achieve a pressure ratio midway between design and surge with the compressor discharge valves completely closed. To reach the surge conditions, the back pressure was further raised through the firing temperature increase produced by throttling the compressor suction. In this way the surge pressure levels could be lowered, thus reducing risk of damage to the special flowpath sensors and instrumentation. Because of turbine first-stage nozzle area reduction, to avoid surge during startup, substantial compressor discharge bleed was needed. To compensate for the large energy loss due to such a bleed, the regular starting motor had to be replaced with a 2.5 MW AC motor connected to a variable frequency grid.

Flowpath Aerodynamic Instrumentation. Correct stage aerodynamic matching is a key factor in the development of a high-pressure-ratio compressor of this kind, and must be ultimately checked in actual operation. Therefore, the prototype compressor flowpath was extensively instrumented to determine the individual stage characteristics. Interstage conditions were measured by means of multiple total pressure and temperature probes, Fig. 8, installed in the leading edge of two stator vanes on each stage. Static pressures were measured along the casing at the leading and trailing edge planes of all the stator vanes. To measure average static pressure values, two groups of five equally spaced taps were provided at each plane. In turn, each group was located on the line connecting the edges of two adjacent vanes. The five taps were manifolded under the vane platforms, so that only one averaged pressure signal was sent to the acquisition system. A row-to-row data reduction program was used to calculate the individual stage characteristics in terms of flow, pressure, and work coefficients and efficiency. To detect the approach or onset of nonstationary phenomena like rotating stalls and surge, casing dynamic pressure sensors were provided on a number of stages, including those adjacent to bleed locations.

Blade Strain Gages. Dynamic strain gages were provided for all stator and rotor rows on two blades per row. Particular care was taken to evaluate strain gage position and orientation on low-aspect-ratio airfoils for which high-frequency, complex modes had to be checked. A general rule for strain gage positioning was that of making each individual sensor capable of measuring dynamic stresses associated with more than one mode to keep the total number of strain gages to an acceptable level. Thus it was not necessary to measure the full stress amplitudes, but only relative values to be corrected via suitable calibration factors. These factors were evaluated by means of the relative strain maps provided by the ANSYS dynamic analysis for each mode. Each map made it possible to calculate the ratio between the local and the maximum strain on the airfoil for any position on the airfoil surface. Therefore, it was not necessary to place each strain gage at the point where the maximum strain for a particular mode was expected, but its position could be offset to measure relative stress values of multiple modes. This maximum offset was limited to avoid use of overly large correction factors with a consequent loss in the measurement accuracy. To find the optimum strain gage location for multiple modes, an iterative process was employed, consisting in the computerized scanning of the ANSYS relative dynamic strain maps and in their interpolation over a great number of positions for all the modes of interest for each strain gage. The optimum strain gage location was then considered that for which all the "Transfer Factor," i.e., the ratios between maximum and local strains of each mode, were closest to a minimum. As a general rule, all the rotor and stator blades were provided with strain gages close to the airfoil roots to measure the low-order pure flexural and torsion mode stresses. For the high-order modes, the choice was made selectively on the basis of the anticipated importance of dynamic stresses associated with each mode. As an example, Fig. 9 shows two strain gages provided on the first-stage rotor blade to measure strains for the first stripe mode shown in Fig. 6 and for the third flexural mode.

Compressor Tests

The compressor was extensively tested utilizing the particular layout schematically shown in Fig. 7, with the actual setup shown in Fig. 10. By suitably controlling the compressor discharge valve during acceleration to compensate for the turbine first-stage nozzle area reduction, the regular startup matching line could be closely reproduced.

In the first test runs, all four available variable stator rows were made continuously adjustable for startup, to increase the stall safety margins before some knowledge of the actual limits had been gained. After several successful tests, the fourth adjust-

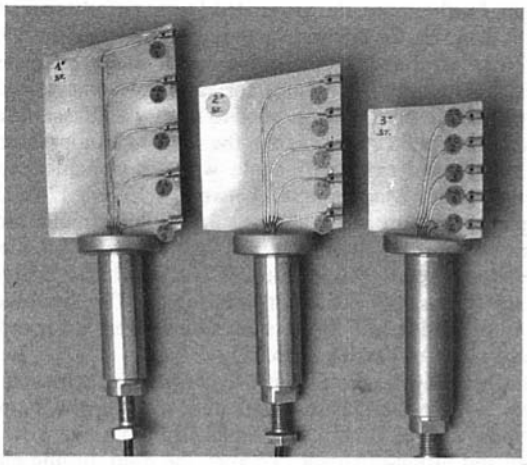

Fig. 8 Stage 1–3 stator vanes instrumented with total pressure probes

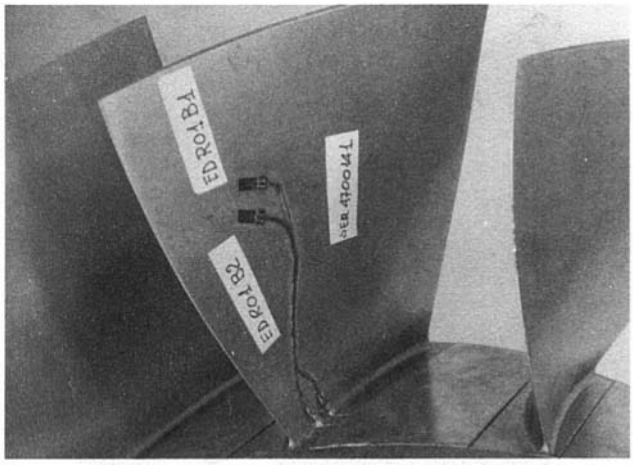

Fig. 9 First-stage rotor blade straingages for high-order modes

able row was fixed in the design position, with no appreciable changes in the blade dynamic stress measurements during the following startups. Therefore, only three rows were finally left variable, according to the design intent.

The performance map was checked at variable corrected speeds from 85 to 110 percent of design speed. For each speed, the pressure ratio ranged from the turbine no-load lineup to an upper limit set by the appearance of marked increases in the dynamic pressure transducer signals indicating the approach of stall. Actual surge points were checked at the very end of the test program to avoid possible premature damage to internal instrumentation, particularly strain gages.

Blade Aeromechanical Behavior. The overall aeromechanical behavior in the startup speed range was in general excellent, with blade vibrations showing appreciable amplitudes only at resonances with low inlet flow harmonics or with upstream/downstream blade passing frequencies. The strain gage location strategy proved very useful in detecting the dynamic stresses for all the modes involved, including high-order, complex modes. Measured natural frequencies in operation were in general within 5 percent of predictions, with the exception of few, high-order, complex modes on the very short rear-end stage blades and not affected by resonances in the operating range. Therefore, no unexpected resonances in the operating range were detected, so that no changes to passing frequencies or to blade natural frequencies were necessary. As an example, the experimental Campbell diagram of the stage 1 rotor blade

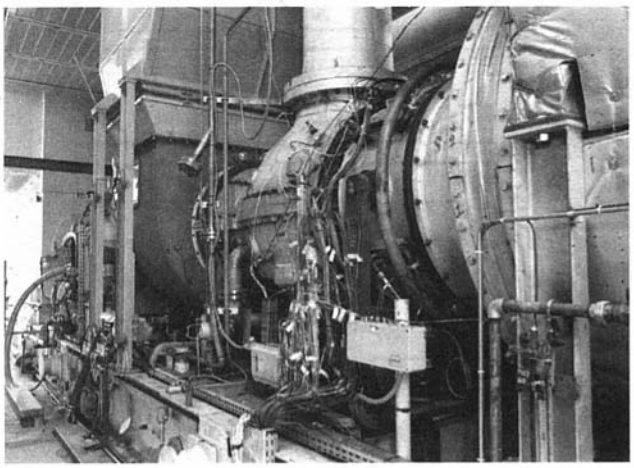

Fig. 10 Compressor-turbine test setup assembly

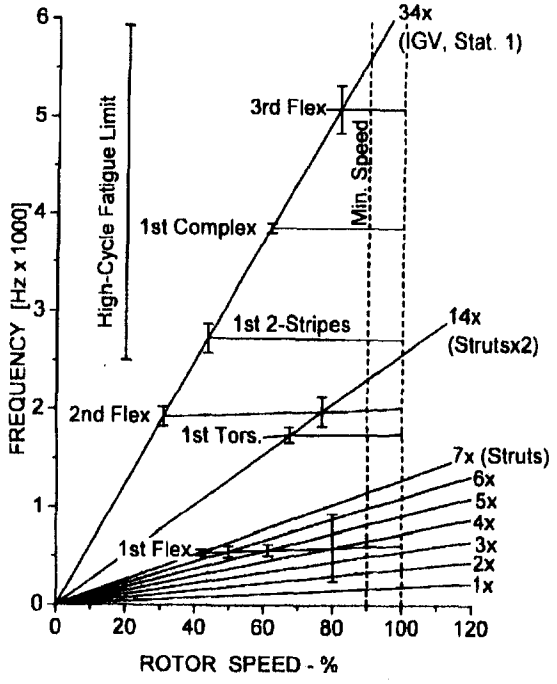

Fig. 11 Stage 1 rotor blade Campbell diagram

is shown in Fig. 11. The 90–100 percent speed range shown is related to normal compressor operation on a two-shaft gas turbine like the PGT10, equipped with variable power turbine inlet nozzles that are used to control the gas generator rotor speed. The vertical bars represent the dynamic stress amplitudes referred to the material high-cycle fatigue limit, shown at the same scale on the diagram. Only stresses for which the Fourier straingage signal analysis showed amplitudes worth noting are represented. The dynamic stress levels did not exceed 25 percent of the high-cycle fatigue endurance limit in the low-speed range. The stresses related to the two-stripe mode detected are low, and this mode is out of resonance with any identified excitation source in the operating range. The stress amplitudes at resonances with low-order harmonics due to inlet distortions and to the strut wakes are very low, and confirm the good quality of the flow at the blading inlet. Similar dynamic stress levels and relationships with upstream and downstream blade passing frequencies were observed on the subsequent stage blades.

Blade Aerodynamics and Performance. Interstage total pressure and temperature measurements made with the stator leading edge instrumentation, associated with three-dimensional flow analysis tools, were extensively utilized in correcting some stage flow mismatchings and to bring the overall performance to the design target. By an appropriate selection of the test point matrix, it was possible to determine the complete characteristic lines of each individual stage, from choke to near-stall conditions. The stage work coefficients and efficiencies were calculated between consecutive total pressure and temperature measuring stations. Therefore, each stage was considered to consist of the upstream stage stator (or IGV for the first stage) and the following rotor blade. The stage flow coefficient was in turn calculated at the rotor blade inlet utilizing the measured wall static pressure at the upstream stator exit.

The flow coefficients corresponding to design conditions were not located at the maximum efficiency points on some stages, thus resulting in an overall performance penalty. Fortunately, these mismatchings appeared to be concentrated in the front-end stages provided with variable stators, that could be easily restaggered to shift the flow coefficients as needed. As an example, the second-stage experimental work coefficient and

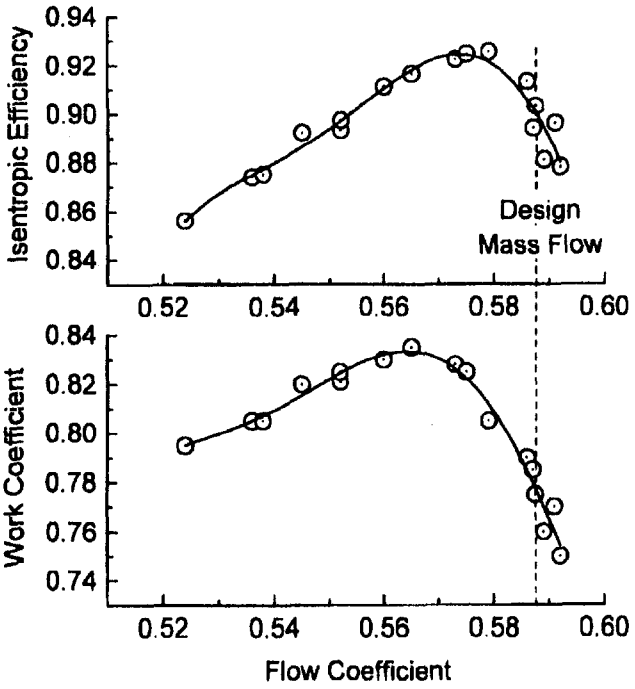

Fig. 12 Stage 2 measured performance curves

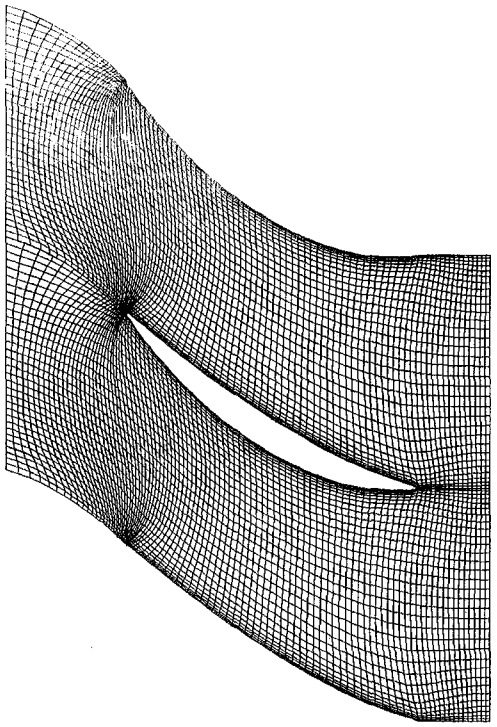

Fig. 13 Rotor 1 blade hub three-dimensional computational mesh

efficiency curves for the stator design settings, Fig. 12, show a 2 percent efficiency loss due to mismatching. A 1 percent loss due to a similar mismatching was observed on both stages 3 and 4. The associated penalty in the overall efficiency was close to 0.5 percent in total.

A study of stator setting changes suitable to rematch the flow coefficients was performed analytically utilizing a three-dimensional viscous flow Navier–Stokes solver with multigrid capability for handling multiple rows simultaneously (Arnone et al., 1993; Arnone and Benvenuti, 1994). The number of rows depends on available workstation RAM and on the grid size. Typically, with a 250 MB RAM, up to five rows can be handled with a number of mesh points sufficient to achieve good accuracy for performance predictions. Figure 13 shows an example of the computational grid used for the first-stage rotor airfoil on the hub surface. The inlet boundary conditions for the next row grid are automatically calculated by the code after completion of each iteration on the upstream row. In the meridional plane near the walls, the grid continues inside the blade tip clearance space in order to model the gap flows and losses finely, thus providing a detailed flowfield description right up to the endwalls.

Before using the computational tool to assess the effects of stator restagger on stage flow coefficients and performance, a number of runs were made to validate the code capabilities versus detailed blade flow measurements. A typical analysis and test data match at the stage 2 stator leading edge for a test point very near to the design conditions is shown in Fig. 14. The calculated back pressure was imposed to reproduce the test mass flow. With this condition, the calculated rotor 2 average exit total pressure and temperature profiles agree very well with measurements. Worth noting is the good reproduction of the radial total temperature profile, which shows the capability of faithfully modeling the end wall and tip clearance effects.

After the code check with the test data match, successive analyses with modified stage 1, 2, and 3 stator vane settings were performed to evaluate the effects on stage flow coefficients and efficiencies. Modified stator settings to bring each stage to operate at maximum efficiency without any need for airfoil design changes were finally identified. Final tests with the new nominal stator settings showed a recovery of the efficiency losses attributed to front-end stage flow coefficient mismatchings.

With the performance finally achieved, the application of this compressor to the PGT10 gas turbine permits a shaft power increase of 1 MW over the present rating, corresponding to the compressor design target.

Concluding Remarks

The approach followed in the development of a new, high-pressure-ratio compressor with a relatively small number of

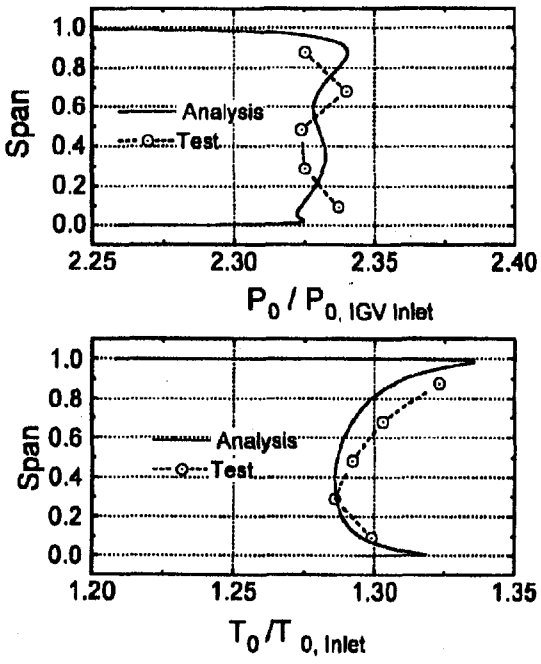

Fig. 14 Three-dimensional analysis and test data match at rotor 2 exit

stages has proven successful in achieving the design targets with moderate tuning efforts. An important contribution to this result was given by the particular test methodology that made it possible to check directly the entire, full-scale compressor over the complete operating map in the actual gas turbine environment. The design strategy, aimed to achieve high-stage pressure ratios without exceeding the existing PGT10 gas turbine compressor aerodynamic loadings, proved effective in terms of reaching comparable performance with a greatly reduced total blade number. The use of low-aspect-ratio, wide chord blade airfoils proved very effective in terms of dynamic response to aerodynamic excitations both in the startup and normal operating ranges.

The flowpath instrumentation layout was conceived for directly interfacing measurements with the structural and flow analysis computer codes. This concept helped to understand fully the blade mechanical and aerodynamic behavior without needing a very large amount of instrumentation, particularly strain gages. As a major result of the measurement and fluid-dynamic computer code integration, stage characteristics could be quickly and accurately rematched to achieve the overall performance target. This result also shows that these sophisticated codes are rapidly progressing toward application as regular tools in the design process.

References

Arnone, A., Liou, M. S., and Povinelli, L. A., 1993, "Multigrid Calculation of Three-Dimensional Viscous Cascade Flows," *Journal of Propulsion and Power*, Vol. 9, No. 4, July-Aug., pp. 605–614.

Arnone, A., and Benvenuti, E., 1994, "Three-Dimensional Navier–Stokes Analysis of a Two-Stage Gas Turbine," ASME Paper No. 94-GT-88.

Benvenuti, E., Bianchi, D., Gusso, R., and Sabella, D., 1988, "The PGT10 Heavy-Duty Gas Turbine," ASME Paper No. 88-GT-319.

Dally, J. W., and Riley, W. F., 1978, *Experimental Stress Analysis*, 2nd ed., McGraw-Hill, New York.

Mezzedimi, V., Nava, P., and Hamilla, D., 1996, "CTV—A New Method for Mapping a Full-Scale Prototype of an Axial Compressor," ASME Paper No. 96-GT-535.

An Improved Epicyclic Gearbox for Reduced and Controllable Subsynchronous Vibrations in Gas Turbogenerator Applications

A. K. Rakhit
Solar Turbines Incorporated,
San Diego, CA

An improvement is made to the design of an epicyclic gearbox that limits the dynamic eccentricities of gearbox components. Gearboxes were manufactured to the new design and tested, showed reduced levels of subsynchronous vibrations at the turbine bearings. The in-situ balancing feature of the gearbox is also found to be very effective in reducing these vibrations further. The improved gearboxes not only assured the service life of the turbine bearings, but also increased the success rate of package testing the first time with substantial cost savings.

Introduction

In gas turbine driven generators (5000 to 25,000 hp), the power turbine speed is reduced to the desired generator rotor speed with a suitable gear speed reducer. Of the various gear arrangements used in these applications, a simple star epicyclic gearbox of Stoeckicht design offers the optimum design for reduction ratios as high as 10:1. For higher ratios, compound star epicyclics are preferred. In the present investigation, a simple star epicyclic gearbox was used to reduce the turbine speed of 8625 rpm to the generator rotor speed of 1500 rpm. Figure 1 shows a sectional view of this gearbox.

In contrast to an ideal Stoeckicht design, the arrangement as depicted in Fig. 1 was developed by Allen Gears Ltd. of England (Yates and Lack, 1992) in which both the radial and axial forces generated at the gear teeth are balanced by the reaction forces. The toroidal couple is balanced by the tooth separating forces acting on each ring gear, thus eliminating any deformation of the teeth. Figure 2 illustrates the basic differences between an ideal Stoeckicht and the alternate design by Allen Gears.

Nevertheless, in gas turbogenerator applications, star epicyclic gearboxes with either Allen or Stoeckicht design seem to induce, besides mesh frequency vibrations, some low-frequency vibrations known as subsynchronous vibrations (SSV), the synchronous ones being at the turbine rotor frequency. When these low-frequency vibrations get transmitted to the turbine rotor bearings, they cause severe damage that reduces their expected service life of 100,000 hours. The present investigation was directed, first, to determine the causes of these undesirable SSV, and then to develop an improved gearbox for reduced vibration levels at the turbine rotor bearings.

Gearbox Vibrations and the Life of Turbine Rotor Bearings

In a gearbox, vibrations can occur at many different frequencies. The most common of these are found at the gear tooth mesh and their harmonics, which are generally high compared to the shaft rotational frequencies. The primary cause of such vibrations is attributed to the transmission error of gear teeth. Several investigators (Smith, 1983; Niemann and Winter, 1983; Tavakoli and Houser, 1986; Umezawa et al., 1986) have carried out a great deal of research on this subject. They have shown how each elemental gear tooth error (profile, lead, and spacing) influences such vibrations. At high acceleration level (above 10 g), these vibrations are quite detrimental to gear life. For an acceptable gear service life of 100,000 hours required in gas turbogenerator applications, experimental investigations and field experience support to limit the acceleration (A) due to gear mesh vibrations and the shaft displacement (d) by the following relationships:

$$A = 0.356 f^{0.32}, \quad g\text{'s (rms)} \tag{1}$$

where

f = gear mesh frequency, Hz
g = acceleration due to gravity

and

$$d = \left(\frac{200}{N}\right)^{0.5} \times 10^{-3} \text{ in. P-P} \tag{2}$$

with the maximum value of $d = 0.002$ in. P-P, where

N = operating speed in cycles/sec.

In most gear applications, these limits are usually achieved with (1) a good design practice, (2) proper selection of gear tooth geometry, and (3) its quality. On the other hand, in epicyclic gearboxes of star configuration, besides mesh frequency vibrations, low-frequency (below the turbine rotor rotational frequency) SSV are also predominant. Package testing of various gas turbogenerators shows that these low-frequency vibrations are due to an unbalance caused by dynamic eccentricities of the gearbox low-speed components (Yanabe and Yoshino, 1994; Cornejo, 1992). In star epicyclics, besides the output shaft, the ring gears and the splined coupling between the ring gears and the output shaft are the primary low-speed components. Splined coupling is used for equal load sharing by the ring gears. Vibrations of this type were also reported to be induced by an index error of ring gear teeth (Rakhit, 1992). In any case, these low-frequency vibrations do not negatively affect the life of gear teeth, and hence no major effort is put in designing a gearbox to minimize such vibrations.

In gas turbogenerator applications, however, when these vibrations are transmitted to the turbine rotor, the life of the babbitted sleeve bearings supporting the rotor is very much reduced. This is particularly applicable to tilt-pad sleeve bear-

Contributed by the International Gas Turbine Institute and presented at the 41st International Gas Turbine and Aeroengine Congress and Exhibition, Birmingham, United Kingdom, June 10–13, 1996. Manuscript received at ASME Headquarters February 1996. Paper No. 96-GT-19. Associate Technical Editor: J. N. Shinn.

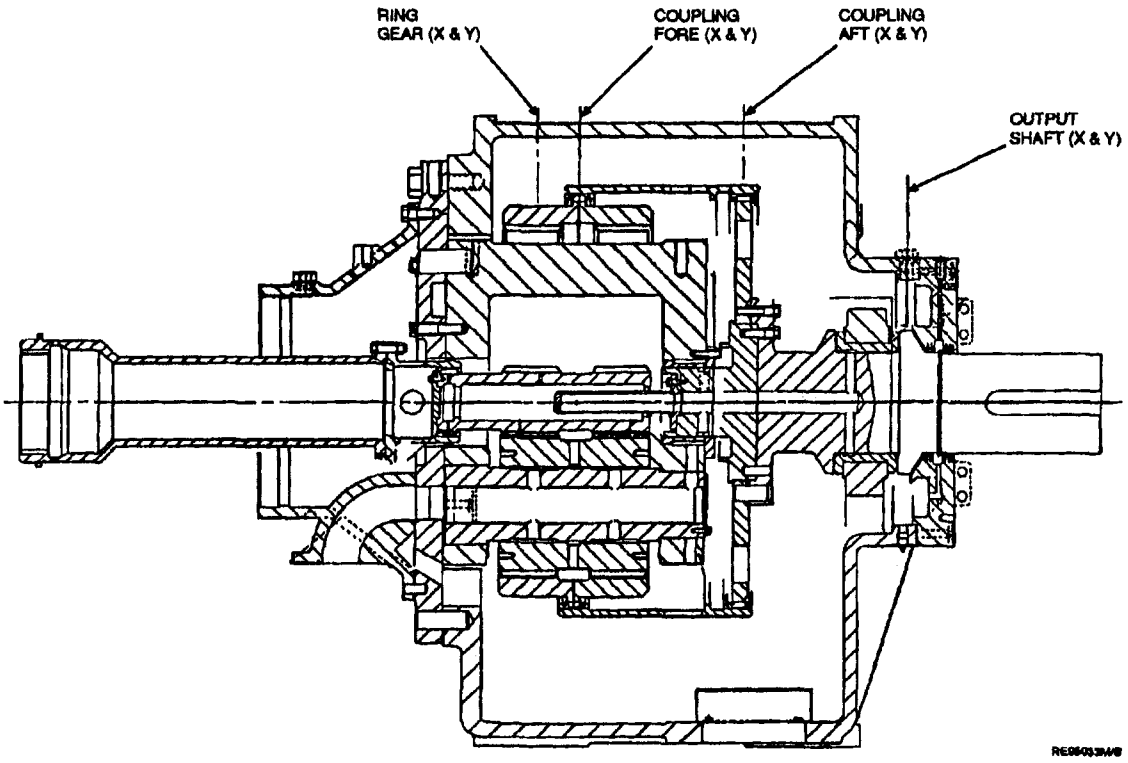

Fig. 1 Sectional view of a simple star gearbox (Allen gear design)

ings, which are predominantly used in modern gas turbines because of their inherent stability characteristics. From an extensive field experience of subsynchronous vibration levels and the life of tilt-pad babbitted sleeve bearings in Solar gas turbine (Mars®) generator sets (50 Hz and 60 Hz), it was recommended to limit the amplitude level of these vibrations to 0.4 mil P-P (peak-to-peak); 1 mil P-P = 0.001 inch P-P. As a result, a great deal of difficulty was always experienced during package testing in meeting this desired vibration level at the turbine rotor bearings with the present gearbox design.

A preliminary analysis of the vibration spectra taken at the bearings showed the frequencies of vibrations with high amplitudes were at the rotational frequency of the ring gears, coupling and the output shaft of the gearbox. Based on this information it was decided that an elaborate testing of some of the packages with special instrumentation to record and analyze vibrations of the gearbox components and turbine rotor bearings would be conducted.

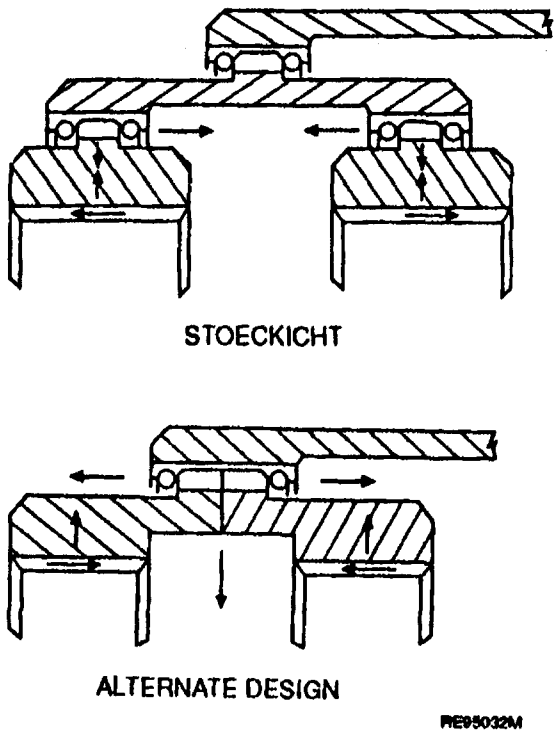

Fig. 2 Principles of Stoeckicht and alternate (Allen gears) star epicyclic designs

Package Testing

A pictorial view of a typical package is shown in Fig. 3(*a*) with a schematic of the test setup in Fig. 3(*b*). Turbogenerator sets used in this investigation were rated ISO 14000 hp. The rating of the gearbox (Rakhit, 1995a) designed and built by Allen Gears was 16,500 hp with an output speed of 1500 rpm. To record vibrations of the ring gears and coupling (fore and aft ends) proximity probes, one vertically and the other horizontally (x and y) at each position, were mounted on the gearbox housing as depicted in Fig. 1. Special care was taken to ensure proper alignment of the turbine rotor, gearbox, low-speed coupling, and the generator shaft. To ensure that SSV induced by gearbox components are least influenced by torsional and lateral critical speeds of the power train, the mass elastic properties of the turbine, gearbox, low-speed coupling, and the generator need to be carefully selected so that the system critical speeds are separated from the gearbox output-generator rotor speed, by a margin of at least ±10 percent. Such a margin can be accomplished with various combinations of mass elastic characteristics of the equipment. Because a turbomachinery manufacturer has a turbine and gearbox already designed and developed, their mass elastic data cannot be easily altered and hence are taken to be fixed as shown in Fig. 3(*b*). A generator manufacturer, on the other hand, has a series of generators with similar

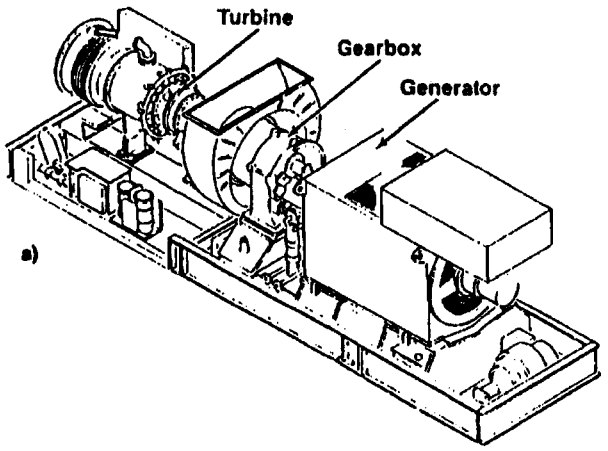

System Schematic and Mass Elastic Data

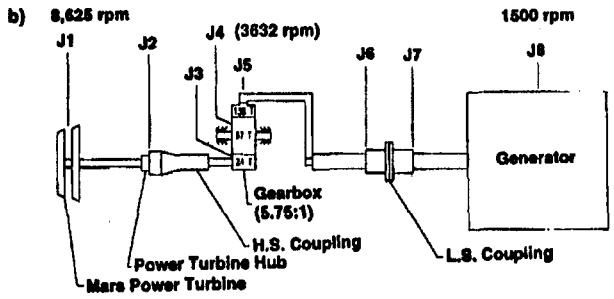

MASSES J, lbf-in-sec²		SPRINGS K, lbf-in/rad x 10⁶	
J1	1173.93	K 1-2	15.20
J2	24.872	K 2-3	19.85
J3	3.681		
J4	68.25	K 5-6	703.4
J5	1146.1	K 6-7	201.0
J6	30.17	K 7-8	—
J7	30.17		
J8	—		

Fig. 3 Turbogenerator test setup

electrical capacity but with different rotor stiffness and inertia. Thus, the selection of a particular generator can be optimized through proper design of the low-speed coupling and its mass elastic data. In designing a coupling it is also important to consider its torque capacity under generator short circuit conditions during which the momentary torque may be as high as six times the nominal torque. Under all of these constraints, a coupling was then designed with K_t(stiffness) = 201 × 10^6 lb·in/rad and WR^2(inertia) = 23,300 lb·in^2. These allowed the use of a generator with K_t = 196.83 × 10^6 lb·in/rad and WR^2 = 20,260 lb·ft^2, which resulted in an 11 percent separation of torsional critical speeds with the generator rotor speed as depicted in Fig. 4. Thus, it was assumed torsional critical speeds of the system had negligible influence on the response of the gearbox output shaft-generator rotor. Similar analysis carried out for lateral critical speeds showed a wider margin of separation. Before any vibration records were taken, each package was subjected to a full heat soak cycle (approximately 3 to 4 hours at full load and speed) to allow for thermal growth of various components in establishing their relative operational positions.

During testing at no load, a high level of low-frequency SSV was noticed at the ring gears, coupling, and also at the turbine bearings. This was attributed to the eccentricities of ring gears and coupling with respect to the gearbox rotational axis. The eccentricities, in this case, were composed of the various clearances in the mating splines, gear teeth, and the bearings. Under load, the applied torque lifts the geometric axes of the ring gears and the coupling to the rotational axis of the gearbox. In this investigation, the minimum torque (T_{min}) needed to raise the geometric axes of ring gears and coupling to the gearbox rotational axis was calculated from the following equation (Kirk et al., 1983):

$$T_{min} = (M \cdot e \cdot \omega^2 \cdot D)/4 \text{ lb} \cdot \text{in.} \quad (3)$$

where:

M = mass of the rotating components, lb·sec^2/in.
e = eccentricity of mass of these components, in.
ω = angular velocity of components, rad/s
D = pitch diameter of components, in.

To measure "e" for the ring gears and coupling, a static lift test was performed before package testing, with the upper half of the gearbox housing removed and a metal chain placed around the coupling to lift it until it could not be raised further without lifting the complete gearbox. One half of this measurement was taken to be the eccentricity of ring gears and coupling with respect to the rotational axis of the gearbox and was found to be 0.03 in. This value of "e" was also verified during the package test by a dc gap measurement with proximity probes.

For the gearboxes used in this investigation,

M = 2.106 lb·sec^2/in.
ω = 157 rad/sec
and
D = 37.0 in.

Substituting these values into Eq. (3) yields:

$$T_{min} = 14{,}409 \text{ lb} \cdot \text{in.}$$

This is equivalent to 342 hp@1500 rpm.

Tests were then continued with the turbogenerator packages for performance acceptance under full speed (8625 rpm) and various loads: 2, 4, 6, and 9.5 MW (full load). For each load, vibration records were taken at the turbine bearings, ring gears, coupling (fore and aft locations), and output shaft. Among the turbine bearings, No. 5 (being closest to the gearbox) showed

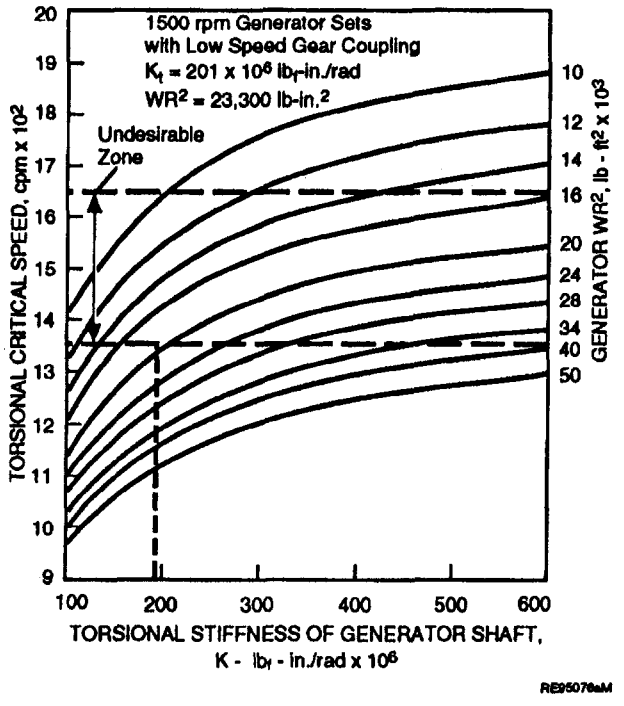

Fig. 4 Torsional critical speeds of the system for different generator mass elastic data

the highest level of low-frequency SSV. Thus, vibration levels at this bearing were of primary concern. A typical vibration spectrum of No. 5 bearing taken at full load with an amplitude of 0.779 mil P-P at 25 Hz is shown in Fig. 5. Also recorded were the dynamic eccentricities of the ring gears and coupling: 21.27 mils P-P for the ring gear and 19.83 mils P-P for the coupling. No significant vibrations were noticed at the gearbox output shaft. Figure 6 illustrates some typical orbital movements of the ring gears, coupling, and the No. 5 turbine rotor bearing.

Analysis of Vibration Records

As mentioned earlier, the minimum power required to lift the geometric axis of the ring gears and coupling to the gearbox rotational axis is 342 hp@1500 rpm. This is significantly lower than the power applied during the performance test. Thus, it can be assumed that there were no low-frequency SSV induced by the ring gears and coupling not being lifted to the gearbox rotational axis. On the other hand, the analysis of No. 5 bearing vibration spectra indicated that the vibration levels that exceeded 0.4 mil P-P were still at the rotational frequency of the ring gears and coupling. Also, phase measurements showed very little phase difference between the vibrations at the bearings and those at the ring gears and coupling. This further identified the bearing vibrations to be of the forced nature and could only be excited by the gearbox components (ring gears and coupling), which obviously did not self-center completely with the gearbox rotational axis.

An investigation into the gearbox manufacturer's specifications showed that all of the rotating components were precisely balanced individually with a residual unbalance of less than the acceptable level of $(4\ W)/N$ oz. in. per API (American Petroleum Institute) specification, where W is the weight of a component (lb) and N is the speed (rpm). The problem is, even in a precisely balanced assembly, a certain amount of unbalance is bound to exist, particularly if the components have splines or gear teeth. Furthermore, to ensure the required balancing accuracy of a splined component, it is essential that balancing is done in a torque load condition. Also, the balancing accuracy of assembled splined components is dependent on the orientation of the mating splines. Thus, in practice, where torque and spline orientation of assembled components could vary, there will always be some residual unbalance that causes dynamic eccentricity of these components. This was quite evident from the orbital excursion records of the coupling and ring gears. The frequency of this orbital motion was the rotational frequency of the coupling and ring gears.

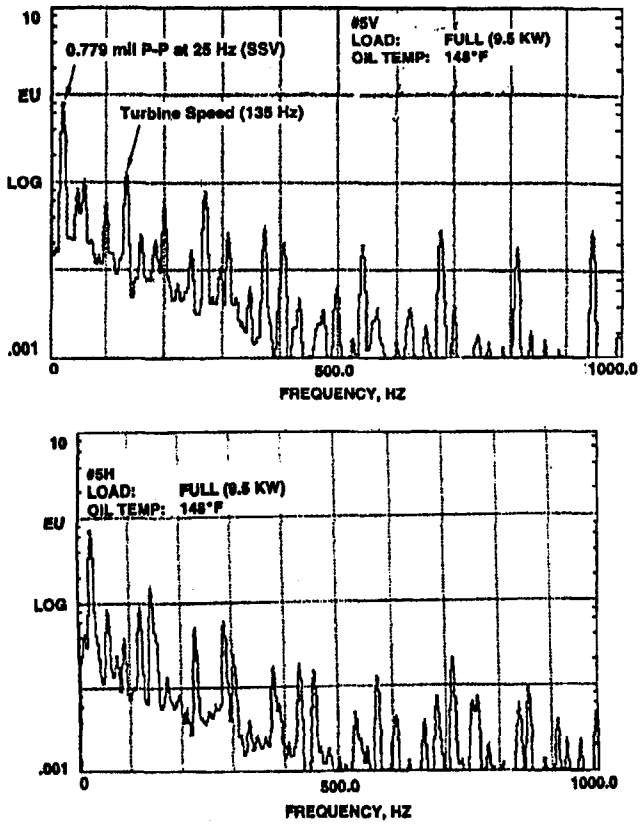

Fig. 5 Vibration spectra at No. 5 bearing with splined coupling in the gearbox

An analysis of vibration records indicates that there was a definite relationship between the amplitude of vibrations at the No. 5 bearing with the dynamic eccentricities of the gearbox coupling and ring gears. The higher these eccentricities, the higher were the vibration amplitudes at the turbine bearings. From the records of various packages tested, an approximate vibration transmission factor of 25:1 was calculated. This means that for every 25 mils P-P of dynamic eccentricity of ring gears or coupling, SSV amplitudes at the No. 5 bearing may be as high as 1 mil P-P. It was thus apparent that the dynamic eccentricity of either the ring gears or the coupling could not be allowed to exceed 10 mil P-P for an acceptable SSV amplitude (0.4 mil P-P) at the bearings. Unfortunately, it was quite difficult to control this eccentricity to the desired limit with the current design of the gearbox. Thus, a number of gearboxes were rejected during package testing because of high SSV at the turbine bearings.

Gearboxes that did not pass package testing standards were removed and disassembled for possible rework of the coupling and ring gears. Sometimes, when these components were reassembled with phasing of splines at 90 deg to the previous orientation, vibration levels were found to be reduced to the acceptable limit. In many instances, it took several teardowns and testings before an acceptable vibration level at the bearings was achieved. To eliminate such costly teardowns and ensure allowable SSV at the turbine bearings, it was obvious that the best possible way to solve this vibration problem was to improve the epicyclic gearbox design (Rakhit, 1995b).

Design of an Improved Epicyclic Gearbox

One of the important features of epicyclic gearbox design is to ensure equal load distribution among the planets and ring gears. To accomplish this in a star epicyclic gear reducer, the sun pinion is supported at the mesh points by the planets at one end, while the other is kept free, so that the pinion can adjust its position axially and radially. Also, in a Stoeckicht or Allen Gears design of star epicyclics, the two ring gears with opposite handed helices are connected to the output shaft by a splined coupling. In this way, the ring gears are free to float relative to the planets, ensuring equal load sharing.

Gearboxes designed and built to these principles were used frequently in turbogenerator sets. The equal load sharing was verified by measuring the load on each planet and ring gear by several manufacturers. The test results were then correlated with the planet and ring gear tooth contact patterns. A gear tooth contact pattern is considered good with a contact area of about 80 percent along the tooth face width, 90 percent along the tooth height, and well centered. In the present investigation, gearboxes that did and did not meet the acceptable vibration level at the turbine bearings were all found to have good tooth contact patterns indicating there was equal load sharing among the planets and ring gears. This focused the improvement of the gearbox design to limit the dynamic eccentricity of coupling and ring gears that would still ensure equal load sharing among the planets and ring gears.

Of the various concepts considered, the one with limited floating feature instead of the present fully floating coupling

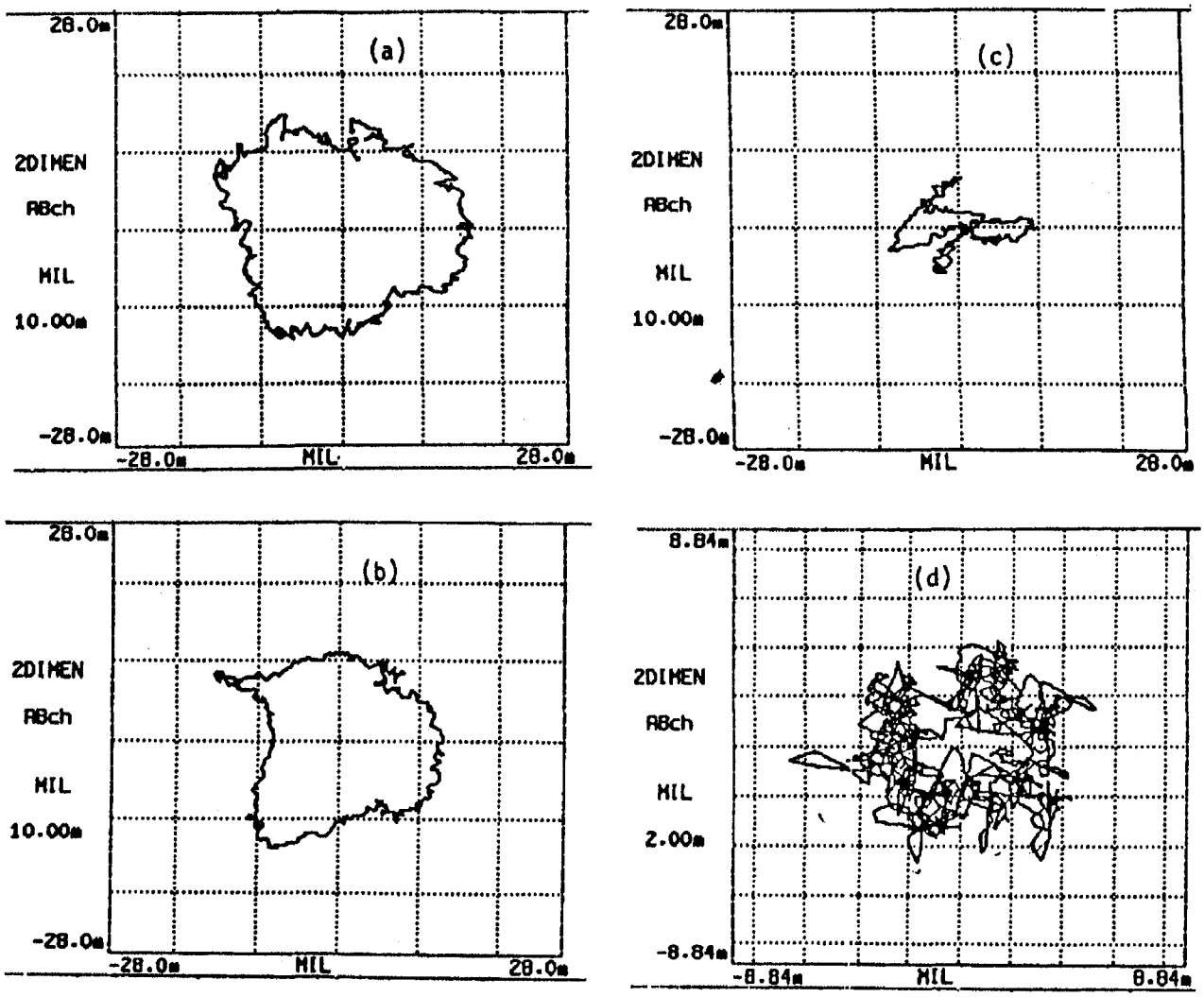

(A) Ring Gear; (B) Coupling (fore end); (C) Coupling (aft end); (D) Turbine Rotor in No.5 Bearing

Fig. 6 Typical vibration orbits: (A) ring gear; (B) coupling (fore end); (C) coupling (aft end); (D) turbine rotor in No. 5 bearing

offered the best solution. This was achieved by eliminating the splines at the aft end with a 12-bolt connection to the output shaft hub, as illustrated in Fig. 7. In addition, the class and fit of all the remaining splines (coupling fore end and ring gears) were changed for reduced clearances, which also contributed in limiting the dynamic eccentricities of these parts. The quality of planet and ring gear teeth was improved from AGMA Class 10 to Class 12 to reduce ring gear pitch diameter variability and run out. Attention was also paid to proper selection of hardware (uniform weight) to maintain the balancing accuracy of the assembly. Furthermore, the new design is equipped with a trim balancing feature.

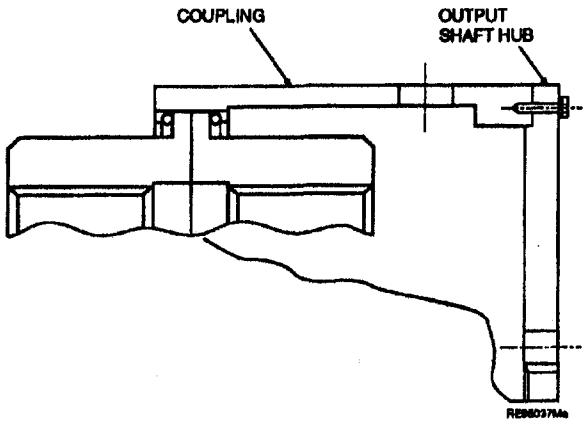

Fig. 7 Outer coupling: bolted design

Trim Balancing

This feature allows in-situ balancing of the low-speed components for which the gearbox housing was modified with access port holes. Figure 8 shows pictorial views of this modification. Among the low-speed components, the coupling was considered to be suitable for adding balance weights because of its large diameter and accessibility. To mount balance weights at desired planes, a number of holes were drilled and tapped on the face of the fore end of the coupling (Fig. 9(a)). To determine the planes at which balance weights (Fig. 9(b)) were to be mounted on the coupling, a key phasor on the output shaft was used as a reference. Ideally, to balance a component "couple balancing" is required in two planes, one at each end of the part and perpendicular to its axis. Because the aft end of the coupling is not easily accessible in this case, the balancing could only be performed at a single plane, fore end.

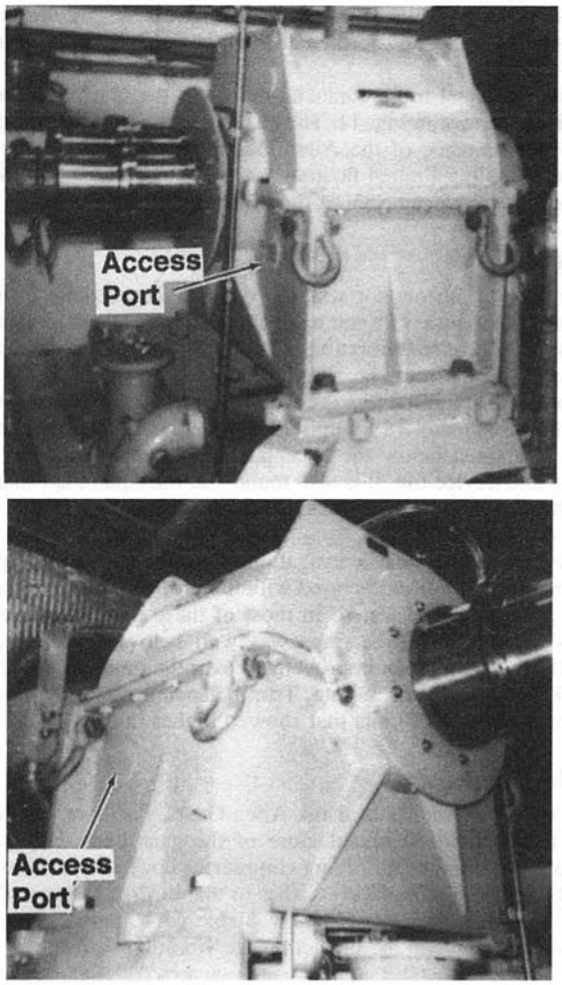

Fig. 8 Pictorial view of the gearbox housing modification with access ports for trim balancing

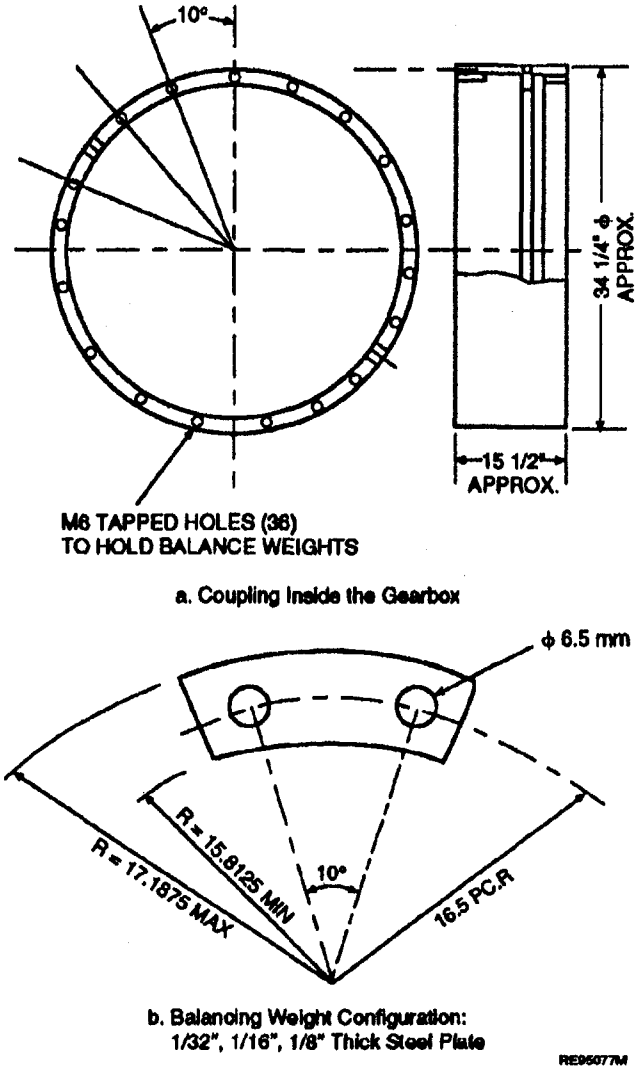

Fig. 9 Modified coupling for trim balancing and balance weights

Nevertheless, with such an in-situ balancing capability, it is expected that the coupling can be fine tuned for an additional reduction of SSV levels at the turbine rotor bearings.

Test Results

With all the proposed design and quality improvements, two gearboxes of Allen design were built for test. At the manufacturer's plant, both the gearboxes were first tested at no load and full speed. Then the load was gradually increased to about 1200 hp, the maximum capacity of the dynamometer available. This power was above the minimum that is required to lift the geometric axes of rotating parts to the rotational axis of the gearbox. The results indicated lower dynamic eccentricities of the ring gears and coupling for the new design compared to gearboxes with splines at both ends of the coupling.

The two gearboxes were then brought to the turbine manufacturer's plant for full-load testing with turbogenerator packages. The vibration levels at the turbine bearings were found to be significantly lower in these packages. Figure 10 depicts a typical vibration spectrum at the No. 5 bearing with an amplitude level of only 0.117 mil P-P for one of the gearboxes. With the second gearbox it was 0.3 mil P-P. Vibrations (dynamic eccentricities) at the ring gears and the coupling were found to be about 7.5 mil P-P in both the gearboxes.

Because the subsynchronous vibration levels recorded at the turbine bearings of both the test packages were below 0.4 mil P-P, no in-situ balancing was considered necessary. To investigate the effectiveness of the proposed in-situ balancing arrangement, a 60 Hz turbogenerator package with improved gearbox that still showed 30 Hz SSV, just above the acceptable limit at No. 5 bearing, was selected. An analysis of vibration spectra taken during the test showed a strong in-phase relationship of the vibrations at the bearing with those at the ring gears and coupling. This indicated the suitability of trim balancing the

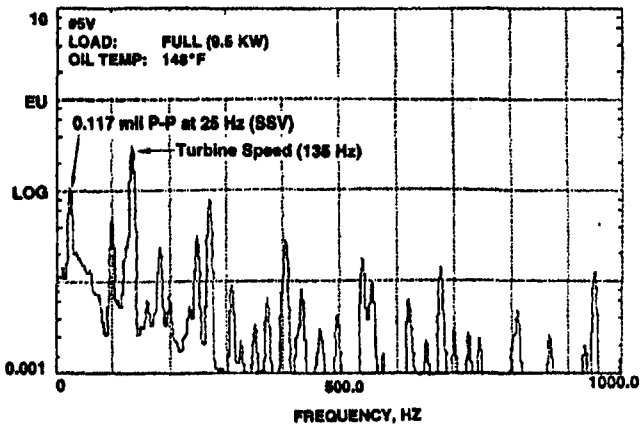

Fig. 10 Vibration spectrum at No. 5 bearing with gearbox coupling bolted at aft end

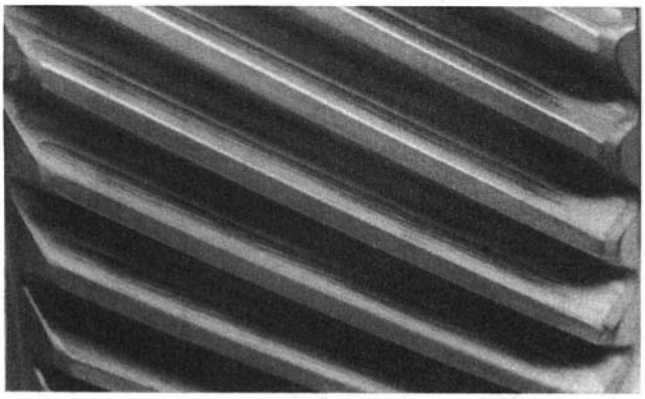

Starwheel 3C R.H. Sun working Flank

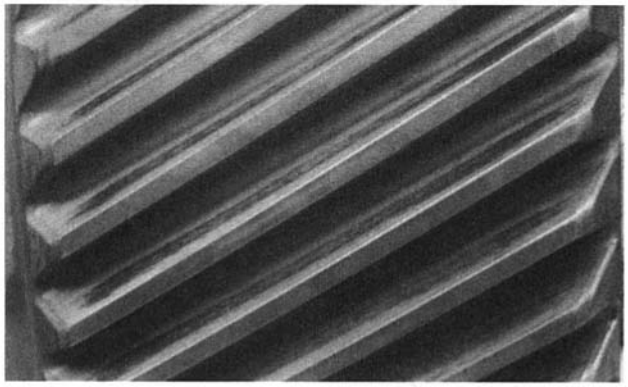

Starwheel 3C L.H. Ann Working Flank

Fig. 11 Gear teeth contact patterns with improved gearbox

coupling to reduce vibration levels further at the bearing. Using the computer program developed at Solar Turbines Incorporated for trim balancing, a weight of 4.65 oz (131.7 gs) was selected for mounting to the coupling at 169 deg to the key phasor. A subsequent retest of this package showed a significant reduction of 30 Hz SSV at No. 5 bearing from 0.56 mil P-P before balancing to 0.32 mil P-P after balancing. This definitely proved the effectiveness of trim balancing feature in the new design of the gearbox.

Design Assessment

The question remains as to whether the new design with limited floating coupling will adversely affect gear life. To properly evaluate, it requires a back-to-back test of the gearboxes under full load and speed. This was beyond the scope of this investigation. On the other hand, if it can be shown that the new design of the coupling does not significantly affect equal load sharing among the planets and ring gears, it will be safe to assume that the gear life is not affected. The most practical way to determine equal load sharing by the planets and ring gears is to compare the tooth contact patterns of all the planets and ring gears as already discussed. Consequently, both of the modified gearboxes were disassembled after full-load and speed package testing. Tooth contact patterns of all the gears were then examined. It was quite encouraging to find the contact patterns very similar to those obtained with the old design of gearboxes, indicating acceptable load sharing among the planets and ring gears.

Some typical tooth contact patterns of the planets and ring gears are shown in Fig. 11. The results definitely prove satisfactory performance of the Allen Gears design of star epicyclic gearbox with a limited floating arrangement of coupling to reduce low-frequency SSV at the turbine rotor bearings.

Conclusions

In gas turbogenerator sets, the dynamic eccentricity of low-speed components of a star epicyclic gearbox is the major cause of subsynchronous vibrations that reduce the life of babbitted tilt-pad turbine rotor bearings. When these gearboxes are designed with a limited floating arrangement of these components, the low-frequency SSV amplitudes at the turbine bearings could be maintained below the acceptable limit of 0.4 mil P-P for their full service life. It is also found that the equal load sharing of the planets and ring gears is not affected ensuring full service life of gears.

Subsequent to this investigation, a number of star epicyclic gearboxes were manufactured with the proposed improvements and then packaged tested. In most of these units, the level of SSV at the turbine bearings was well below the acceptable limit. This is quite an improvement over the previous first-time package testing success rate. Trim balancing was only used in a small number of units that showed higher initial SSV.

Acknowledgments

The author wishes to thank Allen Gears, Pershore, England, for the design and manufacture of the gearboxes, and many helpful discussions in solving complex turbogenerator vibration problems. The author also wishes to thank Mr. Guillermo Cornejo of Solar Turbines for his valuable contribution in setting up the experiment and collecting the vibration data.

References

Cornejo, G., 1992, "Allen Epicyclic Gearbox Vibrations: Splined vs. Bolted Coupling," an Internal Engineering Report, Solar Turbines Incorporated.

Kirk, R., Mondy, R., and Murphy, R., 1983, "Theory and Guidelines to Proper Coupling Design for Rotor Dynamics Considerations," ASME Paper No. 83-DET-93.

Niemann, G., and Winter, H., 1983, *Maschinenelemente,* Vol. II, Springer-Verlag, Berlin.

Rakhit, A., 1992, "Effect of Index Variation Form of Epicyclic Gear Reducer Teeth on Turbo-generator Set Vibrations," *Proc. 6th ASME International Power Transmission and Gearing Conference,* Phoenix, AZ, Vol. 1, pp. 19–28.

Rakhit, A., 1995a, "Development of an Epicyclic Gearbox for Reduced Subsynchronous Vibrations in Gas Turbogenerator Sets," presented at the AGMA Fall Technical Meeting, Paper No. 6.

Rakhit, A., 1995b, "A Realistic Method to Establish the Required Gearbox Rating for a Gas Turbine Application," ASME Paper No. 95-GT-141.

Smith, J. D., 1983, *Gears and Their Vibrations: A Basic Approach to Understanding Gear Noise,* Marcel Dekker, Inc., New York.

Tavakoli, MS., and Houser, D. R., 1986, "Optimum Profile Modifications for the Minimization of Static Transmission Errors of Spur Gears," ASME *J. of Mechanism, Transmissions, and Automation in Design,* Vol. 108, No. 1, pp. 86–95.

Umezawa, K., Suzuki, T., Houjoh, H., and Bagiasna, K., 1986, "Influence of Misalignment on Vibration of Helical Gears," *Proc. 2nd World Congress on Gearing,* Paris.

Yanabe, S., and Yoshino, M., 1994, "Abnormal Vibration and Self-Centering Function of Sun Shaft in Planetary Gear Train," *Proc. 4th International Conference on Rotor Dynamics,* Chicago, pp. 243–248.

Yates, D. E., and Lack, G. J., 1992, "Development Testing of Epicyclic Gearing," ASME JOURNAL OF ENGINEERING FOR GAS TURBINES AND POWER, Vol. 114, pp. 328–333.

A Normalized Modal Eigenvalue Approach for Resolving Modal Interaction

M.-T. Yang

J. H. Griffin

Department of Mechanical Engineering,
Carnegie Mellon University,
Pittsburgh, PA 15213

Modal interaction refers to the way that the modes of a structure interact when its geometry and material properties are perturbed. The amount of interaction between the neighboring modes depends on the closeness of the natural frequencies, the mode shapes, and the magnitude and distribution of the perturbation. By formulating the structural eigenvalue problem as a normalized modal eigenvalue problem, it is shown that the amount of interaction in two modes can be simply characterized by six normalized modal parameters and the difference between the normalized frequencies. In this paper, the statistical behaviors of the normalized frequencies and modes are investigated based on a perturbation analysis. The results are independently verified by Monte Carlo simulations.

Introduction

Variations in manufacturing, measurement, and material properties always cause engineering structures to vary a certain amount from their nominal design. Whether this variation significantly affects the structure's dynamic response depends on the magnitude of the variation and the characteristics of the original design. For systems with well-separated natural frequencies, first-order perturbation theory (Fox and Kapoor, 1968) shows that the changes in natural frequencies and modes are small if the variation is small. The statistical behavior of the frequencies and modes of systems with well-separated natural frequencies have been extensively studied, for example, by Collins and Thomson (1969) and Kiefling (1970). However, it is not unusual for a two- or three-dimensional structure to have closely spaced natural frequencies. In this case, simple perturbation theory indicates that the contributions from the unperturbed neighboring modes to a perturbed mode are significant and can result in large variations in the actual mode shapes.

This result has practical implications to gas turbine blading. Modern low aspect ratio blades often have natural frequencies that are close together. As a result, the modal stress fields of these modes could be highly variable from one blade to the next. This has clear implications to vibration testing and fatigue prediction. If the modal stress fields are highly variable, then it becomes more difficult to characterize the stress ratios for a blade, more strain gages may be required, and it may be necessary to test more blades to assess scatter. For engineers encountering systems with frequencies that are close together, an important concern is how close the frequencies have to be before the modes become highly sensitive to structural variations. This concern provides the motivation for this study.

Papers by Sobczyk (1972) and Schiff and Bogdanoff (1972a, b) addressed the issue of predicting the frequency variation that occurs when the structure is perturbed, but did not discuss the variation in the mode shapes. More recently, the Stochastic Finite Element Method has been widely applied to this class of problems, for example refer to Vanmarcke and Grigoriu (1983), Shinozuka and Yamazaki (1988), or Ramu and Ganesan (1993). The drawbacks of this method are that it is computationally intensive and case specific. Consequently, the results of an analysis on one structure cannot be readily transferred to another.

In this paper, the problem of modal interaction is formulated in terms of a normalized modal eigenvalue problem. A first-order perturbation solution is presented for the case of two modes. The statistical behaviors of the normalized frequencies and modes are then determined from the results of the perturbation analysis. The range of validity of the perturbation solution is then examined by independent Monte Carlo simulations.

Normalized Modal Eigenvalue Problem

Consider the structural eigenvalue problem for an unperturbed system,

$$K^o\Phi^o = M^o\Phi^o\Omega^{o^2} \tag{1}$$

where K^o and M^o are the stiffness and mass matrices. If ϕ_i^o and ω_i^o are the ith mode shape and natural frequency of the unperturbed system, then Φ^o and Ω^o are the unperturbed modal and frequency matrices defined as:

$$\Phi^o = [\phi_1^o\phi_2^o \ldots \phi_N^o] \tag{2}$$

$$\Omega^o = \text{diag}\,(\omega_1^o\omega_2^o \ldots \omega_N^o) \tag{3}$$

where N is the number of degrees of freedom of the system. When the system is perturbed by variations in its structural properties, the stiffness and mass matrices are assumed to change by ΔK and ΔM, respectively. The perturbed structural eigenvalue problem can then be written as

$$(K^o + \Delta K)\Phi = (M^o + \Delta M)\Phi\Omega^2 \tag{4}$$

where Φ and Ω are the modal and the frequency matrices of the perturbed system with the following expressions,

$$\Phi = [\phi_1\phi_2 \ldots \phi_N] \tag{5}$$

$$\Omega = \text{diag}\,(\omega_1\omega_2 \ldots \omega_3) \tag{6}$$

where ϕ_i and ω_i are the ith perturbed mode and its associated natural frequency. Since the unperturbed modes form a complete basis, it is possible to express the perturbed mode ϕ_j in terms of the unperturbed modes ϕ_i^o,

$$\phi_j = \sum_i \phi_i^o\alpha_{ij} \tag{7}$$

where α_{ij} is the component of the ith unperturbed mode in the jth perturbed mode. By substituting Eq. (7) in Eq. (4) and

Contributed by the International Gas Turbine Institute and presented at the 41st International Gas Turbine and Aeroengine Congress and Exhibition, Birmingham, United Kingdom, June 10–13, 1996. Manuscript received at ASME Headquarters February 1996. Paper No. 96-GT-111. Associate Technical Editor: J. N. Shinn.

premultiplying Eq. (4) by Φ^{o^T}, Eq. (4) implies, because of the orthogonality of modes,

$$\Omega^o(I + \Delta I_k)\Omega^o C_\alpha = (I + \Delta I_m)C_\alpha\Omega^2 \tag{8}$$

where $C_\alpha = (\alpha_{ij})$ is the coefficient matrix of α's. Under the assumption of unit modal mass, the perturbations in the normalized modal stiffness and mass matrices are

$$\Delta I_k = \Omega^{o^{-1}}\Phi^{o^T}\Delta K\Phi^o\Omega^{o^{-1}} \tag{9}$$

$$\Delta I_m = \Phi^{o^T}\Delta M\Phi^o \tag{10}$$

Now, if the normalized frequency matrix is defined as

$$\Gamma = \frac{1}{\bar{\omega}}\Omega \tag{11}$$

where $\bar{\omega}$ is a frequency reference, $\Gamma = \text{diag}\,(\gamma_1\gamma_2 \ldots \gamma_N)$, and $\gamma_i = \omega_i/\bar{\omega}$, then, by combining Eqs. (11) and (8), the normalized modal eigenvalue problem is formulated as

$$\Gamma^o(I + \Delta I_k)\Gamma^o C_\alpha = (I + \Delta I_m)C_\alpha\Gamma^2 \tag{12}$$

It should be noted that, in the case of zero perturbations, that is, when ΔI_k and ΔI_m are zero, the eigensolution for Eq. (12) is

$$\Gamma = \Gamma^o \quad \text{and} \quad C_\alpha = C_\alpha^o = I \tag{13}$$

which means that the natural frequencies remain the same and each "perturbed" mode has only the component of the corresponding unperturbed mode. In general, when ΔI_k and ΔI_m are nonzero, the coefficient matrix C_α will not be a diagonal matrix. This indicates that the perturbed modes have nonzero components from several unperturbed modes. Clearly, the amount of modal interaction depends on how the coefficient matrix C_α changes. Note that C_α is only dependent on the perturbations in the normalized modal matrices (ΔI_k and ΔI_m) and on the distribution of the normalized frequencies Γ^o. As a result, Eq. (12) has resulted in isolating the issue of how close the unperturbed frequencies must be to have significant modal interaction from the effect of the perturbations in the modal stiffness ΔI_k and the modal mass ΔI_m.

Perturbation Analysis

In order to gain better insight into the modal interaction problem, consider the case of a system that consists of two closely spaced modes. Assume the two modes have unperturbed natural frequencies ω_1^o and ω_2^o. Then, by letting

$$\bar{\omega} = \tfrac{1}{2}(\omega_1^o + \omega_2^o) \tag{14}$$

$$\delta = \frac{1}{2\bar{\omega}}\,|\omega_1^o - \omega_2^o| \tag{15}$$

$$\Delta I_k = \begin{bmatrix} k_{11} & k_{12} \\ k_{12} & k_{22} \end{bmatrix} \tag{16}$$

$$\Delta I_m = \begin{bmatrix} m_{11} & m_{12} \\ m_{12} & m_{22} \end{bmatrix} \tag{17}$$

the normalized modal eigenvalue problem can be written as

$$\begin{bmatrix} 1-\delta & 0 \\ 0 & 1+\delta \end{bmatrix}\begin{bmatrix} 1+k_{11} & k_{12} \\ k_{12} & 1+k_{22} \end{bmatrix}\begin{bmatrix} 1-\delta & 0 \\ 0 & 1+\delta \end{bmatrix}\begin{Bmatrix} \alpha_{1j} \\ \alpha_{2j} \end{Bmatrix}$$

$$= \gamma_j^2\begin{bmatrix} 1+m_{11} & m_{12} \\ m_{12} & 1+m_{22} \end{bmatrix}\begin{Bmatrix} \alpha_{1j} \\ \alpha_{2j} \end{Bmatrix} \tag{18}$$

where γ_j and $[\alpha_{1j}\alpha_{2j}]^T$ are the jth normalized frequency and mode shape of the perturbed system. Assuming that k_{ij} and m_{ij} are small quantities and neglecting higher order terms in k_{ij} and m_{ij}, the solution for Eq. (18) is

$$\gamma_1 \cong (1-\delta)\left(1 + \frac{k_{11}}{2} - \frac{m_{11}}{2}\right) \tag{19}$$

$$\gamma_2 \cong (1+\delta)\left(1 + \frac{k_{22}}{2} - \frac{m_{22}}{2}\right) \tag{20}$$

$$\begin{bmatrix} \alpha_{11} & \alpha_{12} \\ \alpha_{21} & \alpha_{22} \end{bmatrix} = \begin{bmatrix} 1 & \dfrac{(1-\delta^2)k_{12} - (1+\delta)^2 m_{12}}{4\delta} \\ -\dfrac{(1-\delta^2)k_{12} - (1-\delta)^2 m_{12}}{4\delta} & 1 \end{bmatrix} \tag{21}$$

where γ_1 and γ_2 are the perturbed frequencies, α_{21} is the component of the second unperturbed mode in the first perturbed mode, and α_{12} is the component of the first unperturbed mode in the second perturbed mode. Note that when δ is small, Eq. (21) implies that the interaction between neighboring modes can be quite large, even though the structural perturbations are small.

Once the expressions in Eqs. (19)–(21) were developed, it was possible to define the statistical behaviors of γ_1, γ_2, α_{21}, and α_{12}. Assume that the small quantities k_{ij} and m_{ij} are normally distributed about their mean values $\bar{k}_{ij}$ and $\bar{m}_{ij}$ with standard deviations $\sigma_{k_{ij}}$ and $\sigma_{m_{ij}}$, respectively. The mean values for the frequencies and the amount of modal interaction can be obtained by simply substituting k_{ij} and m_{ij} in Eqs. (19)–(21) by $\bar{k}_{ij}$ and $\bar{m}_{ij}$. By applying basic multivariate statistical analysis, the standard deviations of γ_1, γ_2, α_{21}, and α_{12} are

$$\sigma_{\gamma_1} = \frac{(1-\delta)}{2}\sqrt{\sigma_{k_{11}}^2 + \sigma_{m_{11}}^2 - 2\,\text{cov}\,(k_{11}, m_{11})} \tag{22}$$

$$\sigma_{\gamma_2} = \frac{(1+\delta)}{2}\sqrt{\sigma_{k_{22}}^2 + \sigma_{m_{22}}^2 - 2\,\text{cov}\,(k_{22}, m_{22})} \tag{23}$$

$$\sigma_{\alpha_{21}} = \frac{1}{4\delta}[(1-\delta^2)^2\sigma_{k_{12}}^2 + (1-\delta)^4\sigma_{m_{12}}^2 - 2(1-\delta^2)(1-\delta)^2\,\text{cov}\,(k_{12}, m_{12})]^{1/2} \tag{24}$$

$$\sigma_{\alpha_{12}} = \frac{1}{4\delta}[(1-\delta^2)^2\sigma_{k_{12}}^2 + (1+\delta)^4\sigma_{m_{12}}^2 - 2(1-\delta^2)(1+\delta)^2\,\text{cov}\,(k_{12}, m_{12})]^{1/2} \tag{25}$$

Equations (22)–(25) give a simple way of calculating the standard deviations of the normalized natural frequencies γ_1 and γ_2 and the amounts of the modal interaction α_{21} and α_{12} for a given frequency difference 2δ when the standard deviations and covariances of the six normalized modal perturbations are small.

Monte Carlo Simulation

Two-Mode Case Study. In order to explore the limitations of the perturbation analysis, a Monte Carlo simulation is conducted for the normalized modal eigenvalue problem defined by Eq. (18). The mean values and the covariances of the normalized modal perturbations are assumed to be zero. The mass

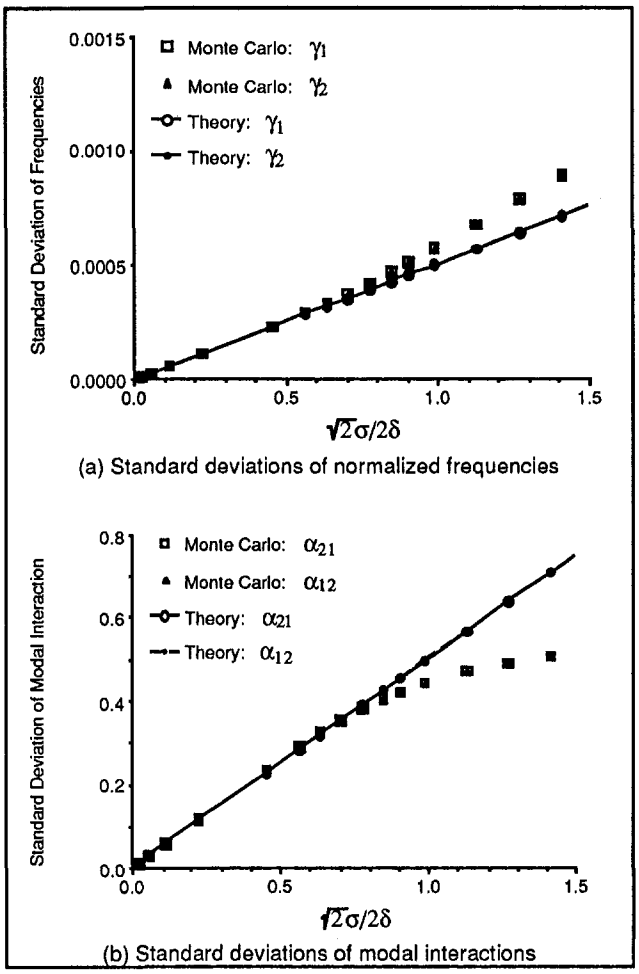

Fig. 1 Two mode case study: $\delta = 0.0005$, σ varies

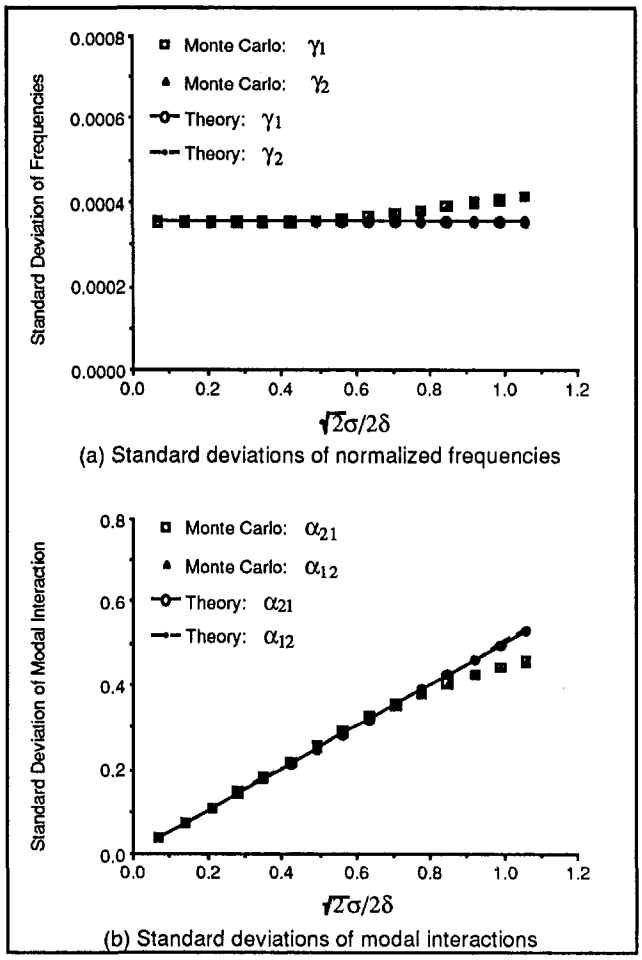

Fig. 2 Two mode case study: δ varies, $\sigma = 0.0005$

and stiffness standard deviations are assumed to be the same, that is,

$$\sigma \equiv \sigma_{k_{ij}} = \sigma_{m_{ij}} \quad \forall i, j \tag{26}$$

Since the case of closely spaced modes is of primary interest, the frequency difference 2δ will be assigned values significantly less than one. The results of the Monte Carlo simulation will be compared with that predicted by Eqs. (22)–(25). Under these assumptions, Eqs. (22)–(25) may be simplified to:

$$\sigma_{\gamma_1} = \sigma_{\gamma_2} = \tfrac{1}{2}(\sqrt{2}\sigma) \tag{27}$$

$$\sigma_{\alpha_{21}} = \sigma_{\alpha_{12}} = \frac{1}{2}\left(\frac{\sqrt{2}\sigma}{2\delta}\right) \tag{28}$$

Equations (27) and (28) imply that the standard deviation in the natural frequencies and in the modal interactions should increase linearly with σ when δ is fixed. Monte Carlo results[1] depicted in Figs. 1(*a*) and 1(*b*) show the linear relationship holds reasonably well for $\sqrt{2}\sigma/2\delta$ less than 0.8. Note from Fig. 1(*b*) that the linear relationship holds for values of $\sigma_{\alpha_{12}}$ up to 0.4 and, consequently, can be used to predict relatively large amounts of modal interaction. The Monte Carlo simulations confirm that the perturbation results also hold when δ is varied and σ is held fixed, Figs. 2(*a*) and 2(*b*). From Fig. 2(*a*) the standard deviation in the frequency is relatively independent of δ when δ is small—a result consistent with Eq. (27). Similarly, from Fig. 2(*b*) it can be seen that $\sigma_{\alpha_{12}}$ is linearly proportional to $\sqrt{2}\sigma/2\delta$, which is consistent with Eq. (28).

Four-Mode Case Study. A practical concern is to what extent the perturbation results developed for the two mode case can be applied to a system that has more than two modes that are close together. This concern is investigated by performing a Monte Carlo simulation of a system with four closely spaced modes. Figure 3 indicates the spacing of the unperturbed frequencies. This study concentrates on the representative case of the interaction between the second and the third modes and how it is affected by the closeness of the first and fourth modes. The selection of the normalized modal parameters is essentially the same as in the two-mode case study. In addition, it is assumed

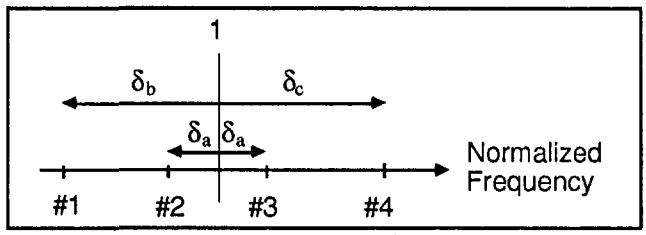

Fig. 3 Frequencies of the four mode case

[1] Based on 10,000 simulations.

that the standard deviations $\sigma_{k_{ij}}$ and $\sigma_{m_{ij}}$ associated with the first and fourth modes are the same as those of the two center modes.

Representative results from the Monte Carlo simulation are depicted in Figs. 4(a) and 4(b). The results in Fig. 4(a) indicate that the standard deviations in the second and third frequencies are essentially independent of the distance, δ_c. This is not surprising since this result is consistent with the two mode case (Fig. 2(a)) and the behavior predicted by Eqs. (22) and (23). Figure 4(b) indicates that the Monte Carlo generated σ_αs agree reasonably well with the theory (Eqs. (24) and (25)) when the interaction between the third and fourth modes is small. Figure 4(b) also indicates that there is some deviation from the two-mode theory when the third and fourth modes are sufficiently close together.

Consequently, the results of the four mode Monte Carlo simulation appear to imply that the perturbation result developed for the two mode case is applicable to structures where several modes have frequencies that are close together, provided that the neighboring modes do not significantly interact with the center modes. This result significantly simplifies the determination of the likelihood of modal interaction in a complex structure since it means that modes can be dealt with a pair at a time.

Conclusions

In this paper the perturbed structural eigenvalue problem is formulated as a normalized modal eigenvalue problem. The advantage of this formulation is that it more clearly separates frequency and structural effects in the modal interaction problem. As a result, a perturbation analysis of the normalized problem yields the results that the standard deviation in the interaction between two modes is approximately given by:

$$\sigma_{\alpha_{ij}} = \frac{1}{4\delta}\sqrt{2}\sigma \tag{29}$$

where δ characterizes the closeness of the frequencies ($\Delta f/\bar{f}$) for the nominal geometry and σ characterizes the variation in the structural properties that corresponds to the modes in question. Thus, for example, if an engineer wants to insure that a perturbed mode will contain no more than 10 percent of an unperturbed neighboring mode, then $\sigma_{\alpha_{ij}}$ could be limited to a third of that value, i.e., 0.0333. The frequency parameter δ could be determined from the natural frequencies of the nominal geometry using a standard finite element analysis. Then Eq. (29) would yield a maximum allowable value of σ.

The structural parameter σ depends on the mode shapes of the specific modes of interest, as well as the amount of variability that occurs in the geometry and in the material properties. It may be possible to develop estimates of σ for certain classes of problems (cast compressor blades, for example) in which the types of structures, modes, and manufacturing processes are limited. This will be the next area of research in this research program. If it is possible to establish estimates for σ, then Eq. (29) and the natural frequencies of the nominal geometry could be used to determine quickly which modes would be likely to have high variability.

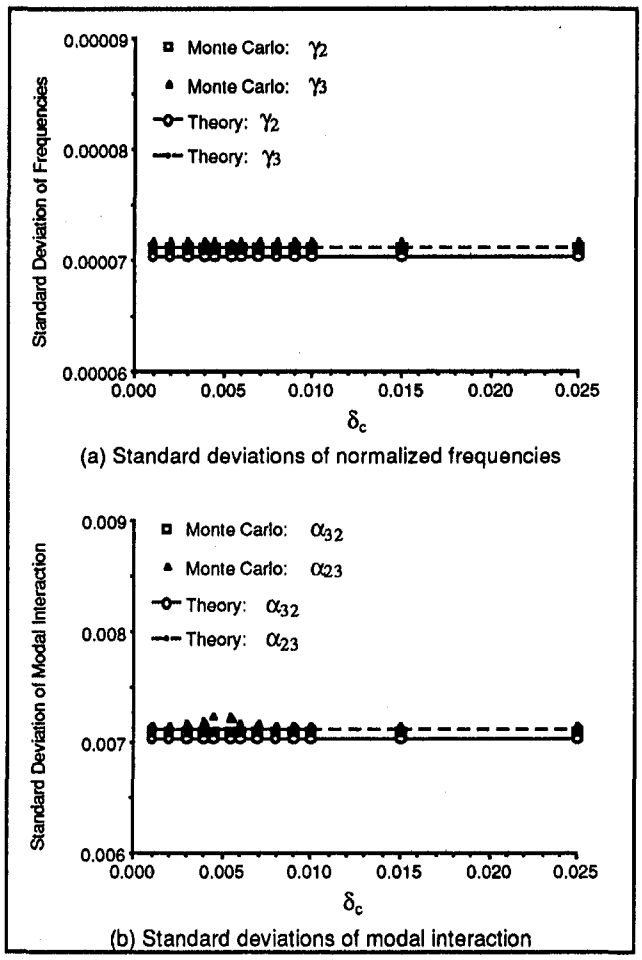

Fig. 4 Four mode case study: δ_a = 0.005, δ_b = 0.010, δ_c varies, σ = 0.0001

Acknowledgments

This work was supported by the GUIde Consortium on the Forced Response of Bladed Disks. Support for the Consortium is provided by its industrial members: AlliedSignal Engines, Allison Engine Company, General Electric Aircraft Engines, Pratt & Whitney, Westinghouse Electric Corporation, NASA, and the U.S. Air Force. Special acknowledgment is given to the members of the Steering Committee for their suggestions and practical knowledge of the problem discussed.

References

Collins, J. D., and Thomson, W. T., 1969, "The Eigenvalue Problem for Structural Systems With Statistical Properties," *AIAA Journal,* Vol. 7, No. 4, pp. 642–648.

Fox, R. L., and Kapoor, M. P., 1968, "Rates of Change of Eigenvalues and Eigenvectors," *AIAA Journal,* Vol. 6, No. 12, pp. 2426–2429.

Kiefling, L. A., 1970, "Comment on 'The Eigenvalue Problem for Structural Systems With Statistical Properties'," *AIAA Journal,* Vol. 8, No. 7, pp. 1371–1372.

Schiff, A. J., and Bogdanoff, J. L., 1972a, "An Estimator for the Standard Deviation of a Natural Frequency—Part 1," ASME *Journal of Applied Mechanics,* Vol. 39, pp. 535–538.

Schiff, A. J., and Bogdanoff, J. L., 1972b, "An Estimator for the Standard Deviation of a Natural Frequency—Part 2," ASME *Journal of Applied Mechanics,* Vol. 39, pp. 539–544.

Shinozuka, M., and Yamazaki, F., 1988, "Stochastic Finite Element Analysis: An Introduction," *Stochastic Structural Dynamics—Progress in Theory and Applications,* Elsevier, New York, pp. 241–291.

Sobczyk, K., 1972, "Free Vibrations of Elastic Plate With Random Properties—The Eigenvalue Problem," *Journal of Sound and Vibration,* Vol. 22, No. 1, pp. 33–39.

Ramu, S. A., and Ganesan, R., 1993, "A Galerkin Finite Element Technique for Stochastic Field Problems," *Computer Methods in Applied Mechanics and Engineering,* Vol. 105, pp. 315–331.

Vanmarcke, E., and Grigoriu, M., 1983, "Stochastic Finite Element Analysis of Simple Beams," *Journal of Engineering Mechanics,* Vol. 109, No. 5, pp. 1203–1214.

A Pump Instability Theory Using an Acoustic Feedback Mechanism

J. E. Corley[1]
The MITRE Corporation,
McLean, VA 22102

A subsynchronous vibration problem with a large water injection pump was solved in 1974 by modifying the discharge piping transition to a long taper configuration. This paper describes a quantitative theory based upon the dynamic modeling of the pump rotor and piping system. The model successfully duplicates the experimental results of the pump instability and reproduces the subsynchronous vibration described in the original paper. The analysis results in a log decrement of the system that is dependent upon the time delay of the acoustic pulsation. It shows that the system can be driven unstable for acoustic path lengths that are much less than the quarter wavelength. The analysis also shows the log decrement is minimized when the time delay is equivalent to exactly that of one eighth wavelength of the resonant frequency of the pump.

Introduction

In the early 1970s, a large oil company in the Middle East began using water injection for secondary recovery. This water injection system utilized very large horizontal split case pumps that were driven by 26,000 hp gas turbines. After less than one year of operation, several of the shipper pumps developed severe and unusual vibrations. The vibration was at a subsynchronous frequency with over 50 mm/s (2 ips) on the bearing caps and 0.64 mm (25 mils) of shaft displacement. The vibration was predominately in a frequency range of 10 to 20 percent below the running speed of the pump. Although the amplitude of the vibration was a strong function of pump speed, the frequency of the vibration was only weakly related to speed. The original problem and its solution were reported in detail in a paper presented to the 7th Turbomachinery Symposium (Corley, 1978).

It was suspected that the pump instability was related to an acoustic feedback phenomenon. The energy of the reflected pressure pulsation is fed back to the resonant member and drives the instability (Benade, 1973). In the pump problem, the rotor acted as the resonant member, which modulated the leakage flow through the wear rings of the pump. This produced a small pressure pulsation, 34.4 kPa (5 psi), at the frequency of the rotor resonance that traveled out to the discharge and was reflected back from the abrupt piping transition. The pressure pulsation produced a strong forcing function when imposed upon the cross-sectional area of the impeller. If the work performed upon the rotor was greater than the damping of the system, the system was driven into a self-sustained instability at the resonant frequency of the rotor. This hypothesized acoustic feedback system is diagrammed in Fig. 1.

The practical solution to the problem was to modify the discharge piping by replacing the abrupt transition piece with a long tapered section. The long taper has less of an impedance mismatch to the acoustic wave and thus reflects less energy back into the system. Although this modification worked, the exact physics behind the solution remained unclear. The acoustic reflection of the transition acted in a similar manner to that of an "organ pipe" type resonance that is common to pump and piping systems (Schwartz and Nelson, 1984; Sparks and Wachel, 1976). However, the hydraulic distance between the wear rings and the piping transition was considerably shorter than the quarter and half acoustic wavelengths that are normally associated with acoustic resonance problems. The purpose of this paper is to follow up the original experimental paper with a mathematical treatment of the system which not only explains the experimental results but also demonstrates that exact quarter or half acoustic wavelength paths are not necessary to produce the instability.

An additional contributing factor to the onset of instability seemed to be an increased clearance in the impeller wear rings. Pumps with design clearances of 0.635 mm (0.025 in.) in the wear rings did not exhibit a subsynchronous vibration. However, three pumps with excess clearances on the order of 1.27 mm (0.05 in.) showed evidence of the problem. It was believed at the time that excess wear ring clearance contributed to the problem in two ways. The larger clearance would have less damping and the increased leakage flow would produce a greater pressure modulation.

Pump Design

The water injection shipper pump is a large, two-stage, double suction, volute pump. The shipper and booster pumps are directly driven by a two-shaft combustion gas turbine. The 16 × 16 × 20 DVMF pump has a pressure dam and babbitted sleeve bearings to suppress oil whirl. Wear rings for the pump are of conventional design with a stellite overlay and API clearances of 0.53 to 0.635 mm (0.021 to 0.025 in.). The couplings on the train were gear-type couplings and the seals were grooved throttle bushings. The pump used aquifer water with a high salinity of 5000 ppm and contained some formation sand. The sand in the water caused erosion and wear in the wear rings and seemed to be a factor in the problem.

Vibration Tests

A few months after startup of the water injection facility in 1973, the shipper pump developed what was thought at the time to be either unbalance or misalignment problems. Because of the size, speed, and prototype nature of the unit, it was not considered unusual for problems of this type to be experienced.

[1] At the time he authored this paper, Mr. Corley was an employee of The MITRE Corporation. Mr. Corley has since retired, and continues to serve as an independent consultant to Mitretek Systems, Inc., an independent company unaffiliated with The Mitre Corporation.

Contributed by the International Gas Turbine Institute and presented at the 39th International Gas Turbine and Aeroengine Congress and Exposition, The Hague, The Netherlands, June 13–16, 1994. Manuscript received by the International Gas Turbine Institute February 4, 1994. Paper No. 94-GT-30. Associate Technical Editor: E. M. Greitzer.

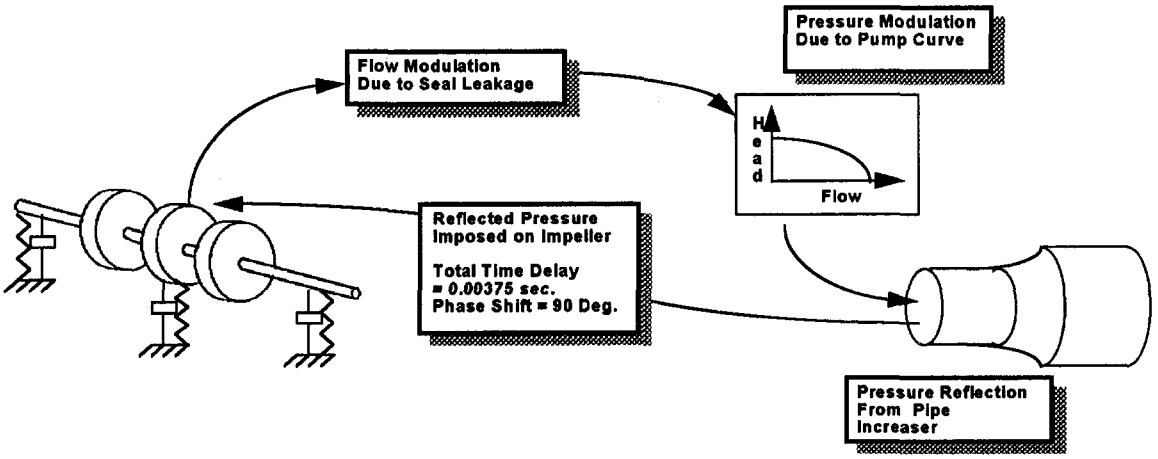

Fig. 1 Diagram of pump: piping acoustic feedback system

The vibration analysis instrumentation available consisted of a simple hand tunable meter with a 3 percent frequency resolution. Although the vibration seemed to be at or near running speed, the vibration meter did not totally agree with the running speed of the pump. This was attributed to a lack of calibration in the meter. During operation, a loud pervasive beat frequency could be heard throughout the facility. Hindsight proved this to be the beating of the subsynchronous vibration with the running speed of the pump.

After many unsuccessful attempts to correct a "mechanical" problem with the pump by sending it to the shop, it was decided to instrument the unit with shaft proximity probes in an attempt to better understand and define the problem. Two proximity probes were installed on each end of the pump shaft near the bearing. When the unit reached a speed of about 3750 rpm, the oscilloscope display of the shaft displacement showed a beat frequency pattern indicative of two closely spaced frequencies. As the speed of the train was increased, the frequencies could be separated with the vibration meter. A plot of the spectrum as a function of speed is shown in Fig. 2. This figure, which was constructed from a tunable filter meter readings, shows that the subsynchronous peak separates from the running speed peak at about 3750 rpm. The frequency of the instability increased somewhat with speed but lagged behind the running speed of the pump. At the pump design speed of 4700 rpm, the subsynchronous vibration peak was at approximately 62.5 Hz (3750 cpm). However, the amplitude of the peak had increased dramatically to approximately 0.51 mm (20 mils) shaft displacement. The running speed peak remained at normal levels throughout the test, as did the 2X component. The running speed vibration did reach a maximum of about 0.127 mm (5 mils) at a speed of 2800 rpm, indicating that the unit had gone through a resonance or critical speed.

During the test, dynamic pressure measurements were made on the discharge piping. These data indicated that a small 34 kPa (5 psi) component existed at the same frequency as the subsynchronous vibration. By comparison, the pressure pulsation at vane passing or 5X running speed was over 344 kPa (50 psi) with a pump discharge pressure level of over 11,000 kPa (1600 psi). However, the relatively small amplitude of the subsynchronous pressure peak belies its effects on the pump's rotor dynamics. If the pressure is applied to the developed cross section area of an impeller the resultant force is large. When this force is at the resonant frequency of the rotor and has a phase that opposes the damping force, extraordinarily high shaft amplitudes will result.

Problem Solution

It was first thought that the problem was a bearing whirl and attempts were made to suppress the "whirl" by installing elliptical bearings. This had no effect on the vibration. Elements of the pump, turbine, and gear box were also reviewed and it was determined that there were no forcing functions at the required frequency anywhere in the machinery train. However, the pump manufacturer's representative had observed that the problem seemed to correlate with the configuration of the suction and/or discharge piping. It was noticed that pumps with very abrupt expansion cones on the discharge pipe seemed to be more susceptible to the subsynchronous problem than ones with a more gentle taper. This suggested a similar mechanism to that described by the article on the physics of brass musical instruments. The test pump had a transition from 0.406 m (16 in.) to 0.609 m (24 in.) over a span of 0.51 m (20 in.). To test this hypothesis, a long tapered transition piece was fabricated for both the suction and discharge piping. At the time it was not certain which direction the pressure wave was transmitted. The new taper had an 8 deg included angle based upon the pipe internal diameter. This angle was selected to prevent flow separation in the increaser. The long tapered transition pieces for the schedule 120 pipe were fabricated by cutting wedges and welding up the cuts to form the taper.

Although the mechanism of the pump instability resembled that of an acoustic pipe resonance, the location of the pipe transition did not correspond to that of a quarter or half acoustic wavelength that was thought to be necessary for this type of

Nomenclature

A = cross-sectional area of pipe
C = damping coefficient
K = shaft stiffness
M = impeller/shaft mass
Q = flow through seal
$\Re$ = reflection coefficient
X = displacement of rotor
Z = impedance of pipe
a = amplitude of vibration
c = acoustic velocity
n = number of vibration cycles
Δ = log decrement
ρ = density of fluid

Subscripts

j = junction
th = throat
1 = small pipe, first cycle, number of mass
2 = large pipe, number of mass
3 = number of mass

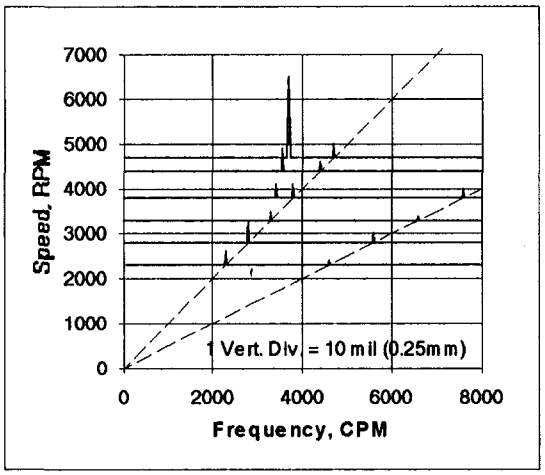

Fig. 2 Pump vibration as a function of running speed for horizontal inboard bearing position

problem. At a frequency of 62.5 Hz (3750 cpm) and a acoustic velocity of 1468 m/s (4800 ft/s), a quarter wave length would be approximately 5.94 m (19.2 ft) (Sparks and Wachel, 1976). The hydraulic distance from the pumps volute to the pipe transition was estimated to be approximately 2.74 m (9 ft) or nearly one eighth wavelength.

With the installation of the piping change, the pump was retested under similar conditions. The pump displayed none of the subsynchronous vibration characteristics over its entire speed range. Because of the success of the piping modification, similar transition pieces were fabricated for the suction and discharge piping for all large water injection pumps. The instability problem was never observed again on an injection pump.

Mathematical Model of System

The explanation of the solution to the problem was qualitative rather than quantitative, with a certain degree of "hand waving." To place the theory of the instability on a firmer analytical basis, a mathematical model of the pump and piping system has been constructed. The model is based upon the use of a dynamic simulation program, which can represent all of the elements thought to be pertinent to the problem (Tutsim). This PC-based program simulates dynamic parameters as block elements in a manner similar to that used in analog computers. The program is easy to use and has all of the block elements necessary to model most dynamic problems. The model is constructed using a built-in CAD system. Figure 3 illustrates the model used for this study. In the model, the three masses that represent the rotor are represented by integration blocks and the damping, spring elements and flow/pressure effects are represented by gain blocks. The time required for an acoustic wave to travel between the pump and the pipe expansion and return is represented by two time delay blocks.

Rotor Dynamic Model. The rotor assembly of the pump was modeled as a simple three-degree-of-freedom spring-mass-dash pot system. The actual pump rotor was tested in the shop by performing an impact test of the rotor placed in "V" blocks and the resonant frequency was observed to be approximately 3200 cpm. In the running machine, a resonance peak was observed at approximately 2800 rpm. The decrease was due to the compliant effect of the oil film bearings. At higher pump speeds, the stiffening effects of the wear rings raised the first mode resonance to the frequency seen in the instability. In the simple rotor model used for this study, the rotor mass, shaft, and bearing stiffness values were adjusted to yield the observed frequencies. The damping and stiffness values of the wear ring seals were input as separate blocks as discussed below. It is recognized that the rotor model is very simplistic, but the results to matched the observed rotor behavior over the limited speed range under investigation.

Wear Ring Model. The wear ring flow, stiffness, and damping characteristics were estimated from the theory developed for a straight, concentric, turbulent seal (Childs, 1983). The values used in the model are given in Table 1.

An estimate of the turbulent flow for an eccentric seal is given by Tao and Donovan (1955). The flow, Q, for an eccentric seal is given relative to that of a concentric seal, Q_0, is shown in Fig. 5.

In theory, it is the change of flow through the seal as a function of rotor displacement that is significant and not the flow itself. For this reason, the derivative of flow with displacement, dQ/dX, is needed. This parameter is obtained by differentiating the curve in Fig. 5. If the rotor centerline is assumed to have an eccentricity greater than about 0.4, the slope of the curve is a constant and the change of flow with a change of displacement is a constant. The values of dQ/dX for the conditions of speed of 3750 and 4700 rpm and 0.635 mm (0.025 in.) and 1.27 mm (0.05 in.) diametrical clearance are given in Table 1. Because the positive flow out of the seals represents a decrease in flow in the pump, the sign of dQ/dX is changed. This value is used in the gain block #19 in Fig. 3. For the purpose of the analysis, only the leakage flow across the four high-pressure wear rings was considered. The flow modulation across the four low-pressure wear rings and shaft bushing seals was ignored for simplicity.

Flow to Pressure Model. The detailed hydraulic modeling of the pump internals is beyond the scope of this paper. Using a simplified analysis, the change of pressure to change of flow is obtained by differentiating the pump performance curve with respect to flow. The pump curves for the two conditions of speed are given in Fig. 6. The derivatives of these curves are shown in Fig. 7. To obtain the parameters needed for this analysis, the derivative is evaluated at the design condition for each speed. For 3750 rpm, the pressure fluctuation is 1,137 Pa/m^3/s (0.045 psi/gpm) and for 4700 rpm it is 1390 Pa/m^3/s (0.055 psi/gpm). These values are used in gain block #20 in Fig. 3.

Acoustic Reflection. A major aspect of the feedback instability theory is the reflection of the pressure wave due to the impedance mismatch at the sudden expansion of the piping. The pressure-amplitude reflection coefficient, $\Re$, is the ratio of the amplitude of the reflected wave to the original wave. It is given by Pierce (1989) as:

$$\Re = \frac{Z_j + \rho c A_2 - \rho c A_1}{Z_j + \rho c A_2 + \rho c A_1} \tag{1}$$

For frequencies less than $(cA_2^2/A_1^3)/2p$. or 254 Hz and abrupt expansions, the impedance of the junction, Z_j, can be neglected and Eq. (1) reduces to

$$\Re = \frac{A_1 - A_2}{A_1 + A_2} \tag{2}$$

or $\Re = -0.385$.

The negative sign on the reflection coefficient indicates that a rarefaction wave is produced by the pipe expansion. In the mathematical model shown in Fig. 3, this value is used in gain block #22 for the original piping configuration:

$$\Re = \frac{Z_{th} - \rho c A_1}{Z_{th} + \rho c A_1} \tag{3}$$

For a conical transition in which the cross-sectional area changes slowly with length and the expansion is long relative to the radius of the pipe, the transition can be represented as a

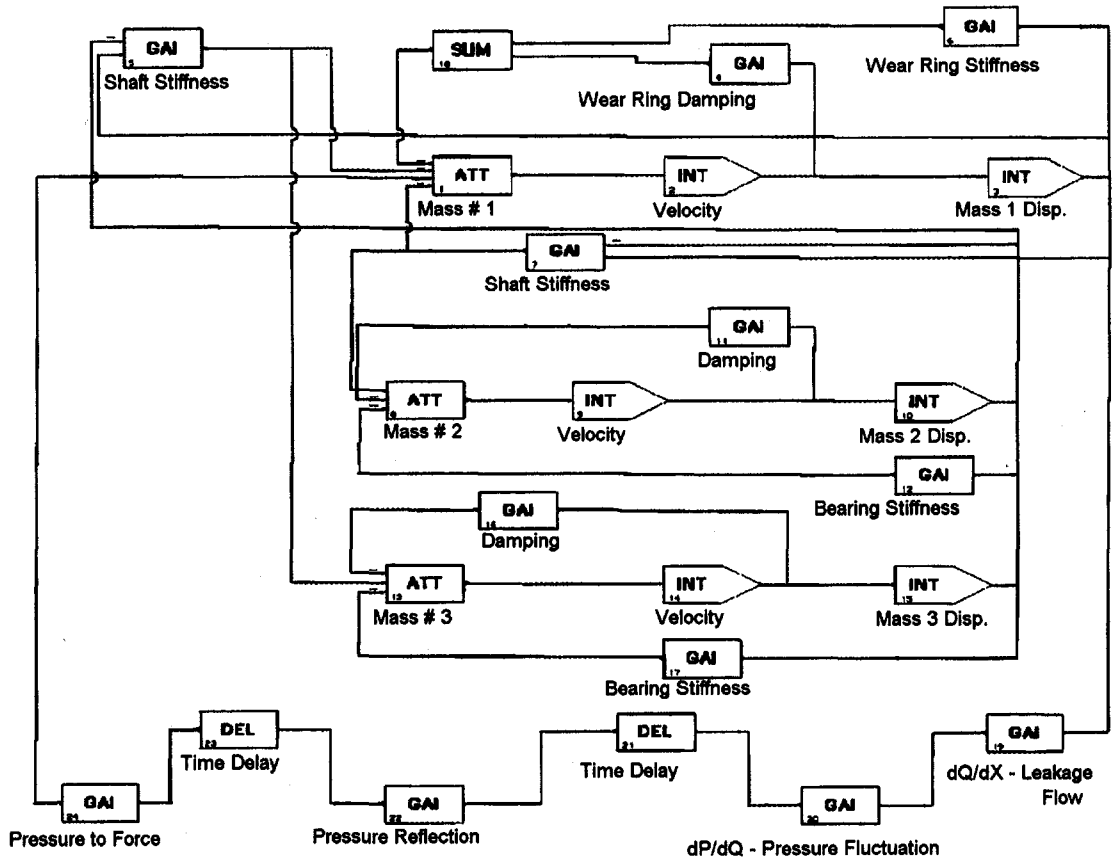

Fig. 3 Block diagram for mathematical model

member of the Salmon's family of horns. The impedance Z_{th} is approximately $\rho c/A_1$ (Pierce, 1989). Equation (3) then reduces to:

$$\Re \approx \frac{A_1 - A_1}{2A_1} \tag{4}$$

or $\Re \approx 0$.

For the case of the modified piping with the long tapered section, this value is used in block #22.

Time Delay. The stability of the system was investigated by varying the time delay that resulted from the acoustic velocity of the pressure pulsation traveling out the discharge piping and reflecting back into the pump. The value of the time delay in seconds was input in the model in two blocks, #21 and #23. Block #21 represented the time required for the pressure wave to transit to the reflector and Block #23 was the time to return to the impeller. For practical purposes in running the model, ease of inputting changes and presenting results, these values could be summed together as one block. Although the model was studied by considering time delays from 0.0 seconds to 0.18 seconds, the total time delay with the actual pump was estimated as 0.0038 seconds. This corresponded to an acoustic length in the pump and piping of approximately 2.74 m (9 ft) and an acoustic velocity of 1463 m/s (4800 ft/s). For a rotor resonance of 62.5 Hz (3750 cpm), this time delay represented

Table 1 Model properties

Pump Speed - Rpm	3750	3750	4700	4700
Wear Ring Clearance -mm	0.635	1.27	0.635	1.275
C_1,C_2,C_3 -Wear Ring Damping -N s/m	299.5	199.6	390.5	257.5
K_1 - Wear Ring Stiffness - N/m	2.4E+05	7.88E+04	3.83E+05	1.24E+5
Wear Ring Flow - m^3/s	2.51E-2	5.78E-2	3.24E-2	7.41E-2
Derivative of Wear Ring Flow, Q/dX -$m^3/s/m$	-5.51E+01	-1.27E+02	-1.42E+02	-1.63E+02
Derivative of Pump Curve - dP/dQ $Pa/m^3/s$	-4.91E6	-4.91E6	-6.01E6	-6.01E6
K_2, K_3 - Shaft Stiffness - N /m	9.54E5	9.54E5	9.54E5	9.54E5
K_4, K_5 - Bearing Stiffness -N/m	3.5E6	3.5E6	3.5E6	3.5E6
M_1 - Shaft/Impeller Weight - Kg	1.27E3	1.27E3	1.27E3	1.27E3
M_2, M_3 - Shaft Weight - Kg.	9.07E1	9.07E1	9.07E1	9.07E1
Reflection Coefficient	-0.385	-0.385	-0.385	-0.385

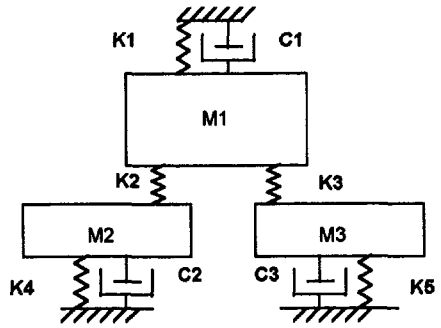

K1 - Wear ring Stiffness
K2 - Shaft Stiffness
K3 - Shaft Stiffness
K4 - Bearing Stiffness
K5 - Bearing Stiffness

C1 - Wear ring Damping
C2 - Wear ring Damping
C3 - Wear ring Damping

M1 - Shaft Mass
M2 - Shaft Mass
M3 - Shaft Mass

Fig. 4 Rotor model represented by a three-mass system

a phase shift of the returning wave of 86 degs. In other words, the pressure wave generated by the rotor movement returns to hit the impeller after it has rotated almost 90 deg. This force counteracts the inherent system damping force at 90 deg and thus contributes to decreasing the stability of the system. It will be shown that the stability of the system is minimized when the time delay corresponds to a rotation of exactly 90 deg of the rotor.

Pressure Forcing Function. It is assumed that the pressure pulsation returning from the piping is applied to the developed area of the impeller and produces a force that drives the rotor. The developed area of the impeller is estimated to be 0.08395 square meters (130 square inches) and is used in gain block #24 of the model.

Model Results

The model was analyzed by varying the total time delay as a parameter and studying its effect on the system stability. Four cases were considered; the pump with original piping running with design wear ring clearances at 4700 rpm, the pump with original piping with excessive wear ring clearances at 3750 rpm and 4700 rpm, and the pump with modified piping running with excessive wear ring clearances at 4700 rpm.

Original Piping. The computer program produces time-dependent plots of the parameter of interest, in this case the amplitude of the rotor. A typical amplitude-time plot is shown in Fig. 8. This particular plot is for the 4700 rpm, 1.25 mm (0.050 in.) clearance case with a total time delay of 0.0038 seconds. It shows the increasing amplitude of the rotor with

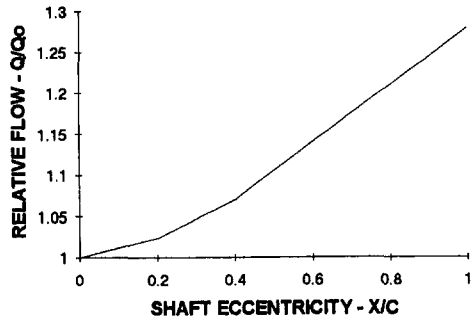

Fig. 5 Flow of an eccentric seal relative to a concentric seal

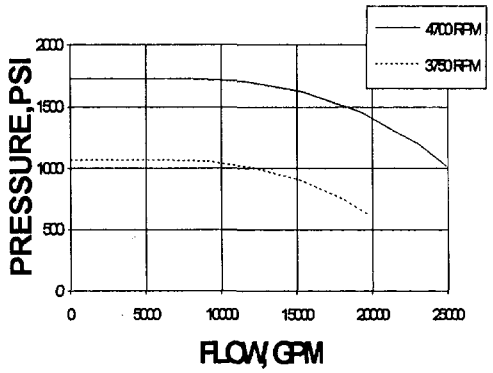

Fig. 6 Pump performance curves for speeds of 3750 and 4700 rpm

time that is indicative of an instability. From the plot, the logarithmic decrement can be determined from the formula:

$$\Delta = \frac{1}{n}\left(\ln \frac{a_n}{a_1}\right) \tag{5}$$

The frequency of the vibration shown in Fig. 8 is 60 Hz (3600 cpm) and corresponds to the resonant frequency of the rotor for that particular condition.

For the unstable condition in the math model, the rotor amplitude increases without limit, unlike that of the actual machine. In the real pump, nonlinearities in the damping and stiffness parameters limit the maximum vibration amplitude. Although the simulation software can handle nonlinear parameters with a curve fit routine, this was not incorporated into the model since the degree of nonlinearity was unknown.

Effects of Pump Speed and Time Delay. In Fig. 9 the log decrement for the system is plotted as a function of total time delay for 3750 and 4700 rpm and a wear ring clearance of 1.25 mm (0.050 in.). This figure shows that for zero time delay, the system is stable, but as the time delay increases the system tends toward instability. The figure indicates that for the 3750 rpm case the pump is marginally unstable at a time delay of 0.004 seconds, which corresponds to the delay produced by the pipe expansion at a hydraulic distance of 2.74 m (9 ft). For the 4700 rpm case, the system is less stable. In the physical system, this is caused by the greater flow and pressure forces that are developed from the increased head produced by the pump.

The figure indicates that a maximum log decrement, minimum stability point is reached at a total time delay of approximately 0.004 seconds. This corresponds to a quarter of a cycle for a rotor resonance of 62.5 Hz (3750 cpm). A distance corresponding to the maximum log decrement is 2.93 m (9.6 ft), which is equivalent to an eighth of an acoustical wavelength. The physical explanation of the instability is that the returning pressure wave is 90 deg out of phase with the rotor displacement and tends to cancel the inherent system damping of the bearings

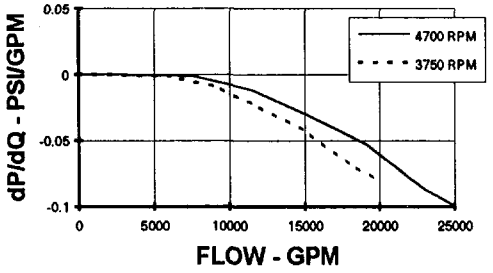

Fig. 7 Derivative of the pump performance curves

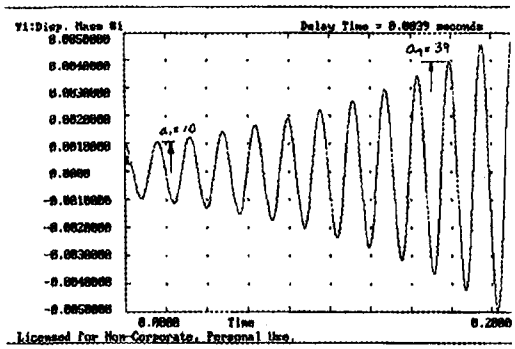

Fig. 8 Time amplitude plot of rotor displacement

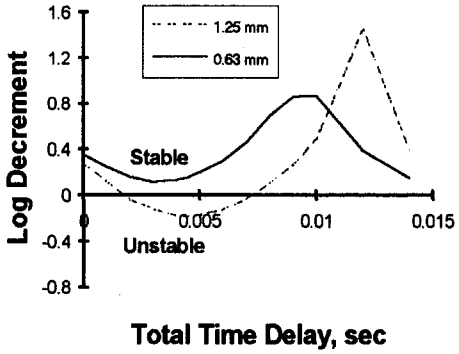

Fig. 10 Stability plot with wear ring clearance as a parameter: original piping

and wear rings. As seen in Fig. 9, there is a wide range of time delays, 0.0018 to 0.0072 seconds, that will produce an unstable system response.

Another interesting observation of Fig. 9 is the increase in stability of the system at time delays on the order of 0.012 seconds. This delay, which represents a phase shift of 270 deg in rotor movement, causes the reflected pressure force to be in-phase with the damping force and results in a significant increase in system damping. This characteristic raises the possibility of maximizing system damping by the judicious tuning of the piping configuration. For example, by replacing the an expansion with a contraction section, the rarefaction pressure wave is replaced with a compression wave and the system is highly damped. As seen in Fig. 11, the system becomes unstable again for time delays greater than approximately 0.017 seconds.

Effects of Wear Ring Clearance. The system stability was also analyzed for a wear ring clearance of 0.63 mm (0.025 in.). The results for the two cases of wear ring clearances for 4700 rpm are shown in Fig. 10. This figure indicates that the system with the design clearance is stable for all speed conditions, as was true in the actual machine. Also seen in the figure are the effects of increased stiffness of the closer clearance wear rings. The higher stiffness increases the resonance of the rotor and shifts the minimum of the log decrement curve to lower time delays, further evidence that it is the mechanical resonance and not the acoustic resonance that modulates the system.

Effects on Rotor System Stiffness. The analysis showed unexpected effect of the time delay on the resonant frequency of the rotor. In Fig. 11, the rotor frequency is shown to vary significantly with no other change except that of the time delay (phase shift) of the returning pressure wave. As well as offsetting the damping term, the force seems to be acting as a variable stiffness component that changes the effective stiffness of the rotor system. Depending on the phase shift, the pressure force can act as either a positive or negative spring. In addition, the damping term probably affects the critical speed and may account for the asymmetric shape of the curve in Fig. 11. At the maximum effective system damping, the critical damping is estimated to be 23 percent. This would shift the resonant frequency approximately 3 percent.

The significance of these effects is not pursued in this paper, but the magnitude of the shift in resonant frequency may have consequences in other systems.

Modified Piping. With the reflection coefficient set to zero for the case of the modified piping, the system is stable for all cases. As would be expected with zero reflection, the log decrement and resonant frequency of the system remains unchanged for all conditions of time lag. This matches the experience found in the field on the real pump.

Extension to Other Instability Problems

In addition to the pump problem described above, the author has observed several other instability cases that appear to be somewhat similar. These are described briefly to demonstrate the range of problems that may be due to this type of feedback mechanism.

Butane Pump. A small, multistage, 3600 rpm butane pump developed a subsynchronous vibration after the balance piston clearance was increased. The vibration was over 25.4 mm/s (1 ips) at 46.6 Hz (2800 cpm). It was suspected that the pressure pulsation through the balance piston was transmitted through the balance line and was driving the rotor at its first resonance. The pump was scrapped before the problem could be corrected.

Water Injection Pump. A large water injection pump developed a subsynchronous vibration at 70 percent of running speed after the pump was reinstalled after a shop overhaul. The

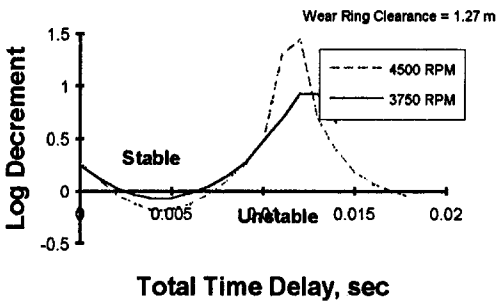

Fig. 9 Stability plot with pump speed as a parameter: original piping

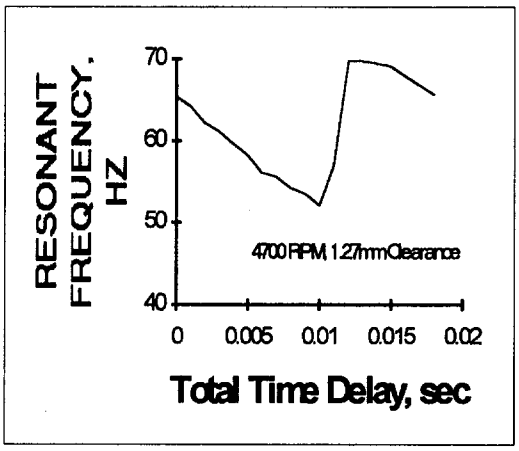

Fig. 11 Effects of time delay on rotor resonant frequency: original piping

problem was observed only during periods when the pump was run on full recycle during start-up. A close inspection of the machine found that the coupling was binding due to a coupling bolt pushing on the end of the pump shaft. In light of the current theory, the coupling lock-up probably changed the rotor dynamics and shifted the resonant frequency into a range where the pressure pulsation feedback through the recycle line could excite the system.

Steam Turbine. A small single-stage steam turbine developed a very high frequency vibration at 2.5 kHz. The vibration was over 50.8 mm/s (2 ips) and the frequency was independent of the turbine speed. Using a model analysis, the frequency was determined to be a higher mode of the turbine wheel. It was theorized that the vibration of the wheel was transmitted through the casing and produced a modulation of the steam valve position. The resulting pressure pulsation of the steam was fed back to the turbine wheel and created the instability. A math model similar to that described here predicted the instability and verified the importance of the time delay, feedback mechanism. The contribution of the steam valve to the problem was demonstrated by tightening the packing on the valve, which decreased the amplitude by 30 percent. A modified valve was proposed but was never installed, and the problem still exists.

Conclusions

A theory of energy feedback has been shown to predict all of the characteristics found in a subsynchronous pump vibration problem. A time delay of the energy feedback was found to be important in offsetting the inherent damping in the system and produces a system that is unstable. The theory indicates that a resonating mechanical member of the system can modulate the energy transport. The mechanism does not preclude a vibration at any frequency. The frequency is determined only by the resonant frequency of any mechanical component that can modulate the energy feedback.

The acoustic transmission path is important in supplying the necessary time delay (phase shift) properties and feedback loop, but unlike the "organ pipe" problem it, does not control the frequency. The model demonstrates that piping can play an important part in the overall dynamics of the machinery, It can produce forces on a rotor that modify both the damping and the stiffness parameters that are normally considered in the machine design.

References

Benade, A. H., 1973, "The Physics of Brasses," *Scientific American,* Vol. 229, No. 1.

Bolleter, U., Buehlmann, E., Eberl, J., and Stirnemann, A., 1992, "Hydraulic and Mechanical Interactions of Feedpump Systems," TR-100990, Research Project 1884-10, Electric Power Research Institute.

Childs, D. W., 1983, "Dynamic Analysis of Turbulent Annular Seals Based on Hirs' Lubrication Equation," ASME *Journal of Lubrication Technology,* Vol. 105, pp. 00–00.

Corley, J. E., 1978, "Subsynchronous Vibration in a Large Water Flood Pump," *Proc. 7th Turbomachinery Symposium,* Texas A&M University, College Station, TX.

Pierce, A., 1989, *Acoustics—An Introduction to Its Physical Principles and Applications,* Acoustical Society of America.

Schwartz, R. E., and Nelson, R. M., 1984, "Acoustic Resonance Phenomena in High Energy Variable Speed Centrifugal Pumps," *Proc. 1st International Pump Symposium,* Texas A&M University, College Station, TX.

Sparks, C. R., and Wachel, J. C., 1976, "Pulsations in Liquid Pumps and Piping Systems," *Proc. 5th Turbomachinery Symposium,* Texas A&M University, College Station, TX.

Tao, L. N., and Donovan, W. F., 1955, "Through-flow in Concentric and Eccentric Annuli of Fine Clearance With and Without Relative Motion of the Boundaries," *Transactions of the ASME,* Vol. 77.

"TUTSIM™ Block Diagram Simulation Language," 1999, Tutsim Products, Palo Alto, CA.

PI Control of HSFDs for Active Control of Rotor-Bearing Systems

J. P. Hathout

A. El-Shafei

Department of Mechanical Design and Production, Faculty of Engineering, Cairo University, Giza, Egypt

This paper describes the proportional integral (PI) control of hybrid squeeze film dampers (HSFDs) for active control of rotor vibrations. Recently it was shown that the automatically controlled HSFD based on feedback of rotor speed can be a very efficient device for active control of rotor vibration when passing through critical speeds. Although considerable effort has been put into the study of steady-state vibration control, there are few methods in the literature applicable to transient vibration control of rotor-bearing systems. Rotating machinery may experience dangerously high dynamic loading due to the sudden mass unbalance that could be associated with blade loss. Transient run-up and coast down through critical speeds when starting up or shutting down rotating machinery induces excessive bearing loads at criticals. In this paper, PI control is proposed as a regulator for the HSFD system to attenuate transient vibration for both sudden unbalance and transient run-up through critical speeds. A complete mathematical model of this closed-loop system is simulated on a digital computer. Results show an overall enhanced behavior for the closed-loop rotor system. Gain scheduling of both the integral gain and the reference input is incorporated into the closed-loop system with the PI regulator and results in an enhanced behavior of the controlled system.

Introduction

Significant efforts have been made to apply active vibration control devices to rotating machinery such as aircraft jet engines, rocket turbopumps, and high-speed compressors. Implementing active vibration control on rotating machinery is expected to give advantages such as the adaptability of the controller to a myriad of load conditions, the attenuation of vibration amplitude during run-up and coast down through the critical speeds, and the reaction of the controller to minimize sudden transient vibration such as sudden unbalance, e.g., through blade loss.

Active vibration control of rotors has been studied using different devices such as electromagnetic bearings and lateral force actuators. In the majority of the active control strategies research for vibration control mentioned in the literature, electromagnetic bearings have the largest share. Schweitzer (1985) and Ulbricht and Anton (1984) examined the stability and observability of rotor-bearing systems with active vibration control. Weise (1985) proposed a proportional, integral, derivative (PID) control of rotor vibrations using magnetic bearings, which force the rotor to spin about its inertial axis. Keith et al. (1988) and Allaire et al. (1988) have implemented analog and digital PD controllers with magnetic bearings. Zhu et al. (1989) proposed the use of optimal control strategies for magnetic bearings. Several efforts using optimal control methods were also investigated for lateral force actuators (Palazzolo et al., 1989a, 1991).

Hybrid squeeze film dampers (HSFDs) were proposed by El-Shafei (1991b, 1993) for active vibration control of rotors. The HSFD is a damper that has the ability to change from a short damper to a long damper and vice versa depending on the position of movable end seals. It was shown that using HSFDs is much more effective in controlling rotor vibrations than previous methods of controlling the pressure in a conventional SFD (Burrows et al., 1983; Adams and Zahloul, 1987).

As a first attempt for active control of rotors using HSFDs, El-Shafei and Hathout (1995) proposed an on-off control algorithm based on feedback of rotor speed and it was shown by simulation to be quite powerful in controlling rotor vibrations while passing through a critical speed. The same algorithm based on feedback of rotor speed was tested experimentally and was shown to be quite successful (El-Shafei and El-Hakim, 1995). Moreover, this algorithm was shown by simulation to be quite effective in suppressing multimodes of more complicated rotor models incorporating fluid inertia effects (Hathout et al., 1997). The feedback on rotor speed is quite attractive for its simplicity and efficiency, but it requires a pre-knowledge of the system critical speeds, which are usually known beforehand while the rotor is designed. This feedback on rotor speed algorithm will not be able to compensate for sudden rotor unbalance. The current goal is to design an active controller capable of overcoming such sudden transient behavior and in addition capable of reacting while passing through critical speeds.

This paper presents the development of a proportional, integral (PI) controller for actively controlling HSFDs. PID controllers in general can handle many simple control problems, provided that the requirements are well defined. This is the reason PID control was chosen to be investigated on this system before testing more advanced control theories (Hathout, 1995). The integral action resulted in giving a well-behaved control performance while the derivative action caused chattering of the sealing rings of the HSFD and thus destabilized the closed-loop behavior. This is due to the anticipatory nature of the derivative control, which in effect anticipates the damping need based on trends, rather than actual needs, resulting in the chattering action. In this case, a PI controller was sufficient to give satisfactory results in suppressing both critical speed vibration and sudden unbalance. Furthermore, the gain scheduling technique is investigated and both the integral gain and the reference input are scheduled with respect to the rotor speed. The gain scheduling enhanced the rotor run-up behavior while maintaining the well-behaved response for sudden unbalance.

Contributed by the International Gas Turbine Institute and presented at the 41st International Gas Turbine and Aeroengine Congress and Exhibition, Birmingham, United Kingdom, June 10–13, 1996. Manuscript received at ASME Headquarters February 1996. Paper No. 96-GT-123. Associate Technical Editor: J. N. Shinn.

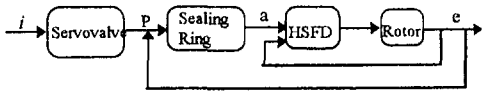

Fig. 1 Block diagram

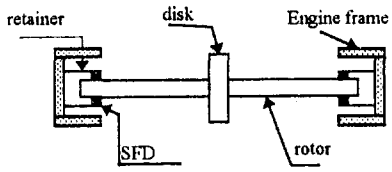

Fig. 2 Jeffcott rotor

Development of a Model for the HSFD-Rotor-Control System

The HSFD-rotor-control system consists of a pressure control servovalve, the HSFD, and the rotor (El-Shafei and Hathout, 1995). The system can be considered as an open-loop system, where the current i actuates the servovalve, which in turn controls the pressure in the sealing chamber p, thus controlling the position of the sealing rings a, and thus giving the amount of damping applied to the rotor. It should be emphasized that the HSFD-rotor-control system is nonlinear in nature because of the nonlinearity of the SFDs, and that the whole system is coupled as shown in the block diagram of Fig. 1.

It is desirable to use a simple model for the investigation of the control algorithm that grasps the basic physics of the problem. Simplicity is needed for designing a robust control algorithm and for ease of simulating our control system on a digital computer. The nondimensionalized model proposed by El-Shafei and Hathout (1995) is used in this work for the development of a PI controller. The model consists of uncavitated HSFDs incorporated on a Jeffcott rotor exhibiting two modes due to the mass of the disk and the additional journal mass included in the model. Cavitation has already been introduced in recent models (El-Shafei et al., 1994) and the dynamics of the rotor showed very slight differences in comparison to the uncavitated case except for jump resonance at high levels of unbalance (El-Shafei, 1990). Thus, an uncavitated damper model is used with linearized damper coefficients. This simple model is quite adequate for the purpose of investigating new control algorithms for the HSFDs.

Figure 2 shows the Jeffcott rotor mounted on two identical ball bearings, each of which is surrounded by an HSFD. The outer race of each ball bearing, which is assumed rigid and massless, is constrained from rotating by a retainer spring of stiffness Kr, which also acts to center the journal in the clearance of the oil film. The rotor is assumed massless with a stiffness of $2K$, the disk is assumed rigid with mass $2m$, and the damping acting at the rotor center has a damping coefficient of $2C$.

The equations of motion of the center of the disk S, in nondimensional form (El-Shafei and Hathout, 1995), are:

$$\bar{x}_s'' + \eta\bar{x}_s' + K^*(\bar{x}_s - \bar{x}_g) = \Omega^{*2}U\cos\Omega^*\tau - \alpha^*U\sin\Omega^*\tau \quad (1)$$

$$\bar{y}_s'' + \eta\bar{y}_s' + K^*(\bar{y}_s - \bar{y}_g) = \Omega^{*2}U\cos\Omega^*\tau + \alpha^*U\sin\Omega^*\tau \quad (2)$$

Assuming that the rotor journal has mass m_b, the equations of motion of the journal center E in nondimensional form (El-Shafei and Hathout, 1995) are:

$$\bar{x}_E'' + m_o\bar{C}_{xx}\bar{x}_E' + m_oC_{xy}\bar{y}_E' + m_oK^*(\bar{x}_E - \bar{x}_s) + m_oK_r^*\bar{x}_E = 0 \quad (3)$$

$$\bar{y}_s'' + m_o\bar{C}_{yz}\bar{x}_g' + m_oC_{yy}\bar{y}_g' + m_oK^*(\bar{y}_g - \bar{y}_s) + m_oK_r^*\bar{y}_g = 0 \quad (4)$$

Again here it should be emphasized that an uncavitated damper

Nomenclature

a = distance of sealing ring from the end of the journal, m
c = radial clearance of damper, m
C_{ij} = damping coefficients, i and j take the values of x and y, Ns/m
$\bar{C}_{ij}$ = nondimensional damping coefficients
$\bar{C}_{ijS}$ = nondimensional short damper coefficient
ΔC = damping increase, Ns/m
ΔC = damping increase
$e = \sqrt{x_g^2 + y_g^2}$ = damper eccentricity, m
F = transmitted damping force, defined as the ratio of the damping to the unbalance force
i = current supplied to servovalve, mA
$i_{\max}$ = maximum current input to the servovalve $\cong$ 10 mA
$i_o = i/i_{\max}$ = nondimensional current
k_i = integral controller gain
k_p = proportional controller gain
K = half rotor stiffness, N/m
K_r = retainer spring stiffness, N/m
$K^* = K/m\omega_n^2$ = nondimensional rotor stiffness
K_1^* = nondimensional valve gain
$K_r^* = K_r/m\omega_n^2$ = nondimensional retainer spring stiffness
K_s^* = spring stiffness, N/m
m = half disk mass, kg
m_b = rotor journal mass, kg
$m_o = m/mb$ = mass ratio
m_r = mass of sealing ring, kg
p = pressure in sealing chamber, N/m^2
p^* = nondimensional pressure in sealing chamber
$r = \sqrt{x_s^2 + y_s^2}/c$ = the vibration amplitude at rotor center
s = Laplace operator
t = time, s
u = nondimensional control input
$U = un/c$ = nondimensional unbalance
un = unbalance, m
x_i = x displacement at the journal center E ($i = E$), or at the disk center S ($i = S$), m
y_i = y displacement at the journal center E ($i = E$), or at the disk center S ($i = S$), m
$\bar{x}_i = x_i/c$ = nondimensional x displacement
$\bar{y}_i = y_i/c$ = nondimensional y displacement
α^* = nondimensional rotor acceleration
$\epsilon = e/c$ = eccentricity ratio
ϵ_r = eccentricity reference input
η = rotor loss factor
η_1 = sealing ring loss factor
$\lambda = a/c$ = measure of the finiteness of the HSFD
$\tau = \omega_n t$ = nondimensional time; a unity is equivalent to 5.3 ms
ω_n = first natural frequency of the rotor, rad/s
ω_r^* = valve natural frequency
ζ_1 = valve damping ratio
Ω = rotor speed, rad/s
$\Omega^* = \Omega/\omega_n$ = nondimensional rotor speed
$(\ )'$ = denotes differentiation with respect to τ

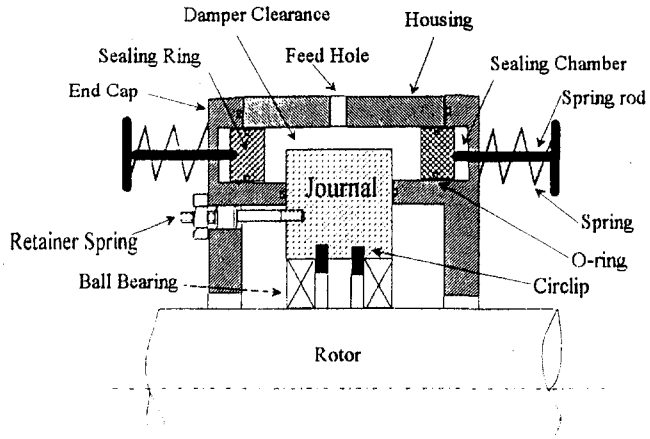

Fig. 3 Schematic of the HSFD

is assumed. At the test rig developed for testing the HSFD at Cairo University (El-Shafei and El-Hakim, 1995), no evidence of cavitation was observed. In addition, cavitation has minimal effect on the dynamics of the rotor except in severe conditions (El-Shafei, 1990) where the nonlinearity becomes profound. For the control development it is desirable to avoid the unwarranted complications afforded by the introduction of cavitation in the model, and the basic objective of developing the PI control algorithm can be sufficiently served by the assumption of the uncavitated damper.

The control input for attenuating rotor vibrations in this system consists of the damping provided by the HSFD according to the position of the sealing rings. The damping coefficients for the HSFD should reduce to those of the short damper at one extreme and to those of the long damper at the other extreme. To incorporate the effect of a finite damper in the HSFD model, a model that consists of a linear combination of the short damper and the long damper damping coefficients is used (Holmes and Dogan, 1985):

$$C = \lambda C_s + (1 - \lambda) C_l \tag{5}$$

where C_s and C_l represent, respectively, the short and the long damping coefficients for the coefficients C_{xx}, C_{xy}, C_{yy}, and C_{yx} in either the short damper or the long damper modes (El-Shafei and Hathout, 1995). λ is a measure of the finiteness of the damper, in the sense that if $\lambda = 1$, at one extreme, the damper behaves as a short damper, and if $\lambda = 0$, at the other extreme, the damper behaves as a long damper. Nevertheless, λ can take any value between 0 and 1 with the help of a spring connected to the sealing ring, as shown in Fig. 3, which will counteract the sealing chamber pressure force exerted on the sealing ring, thus it will behave as a finite damper. Holmes and Dogan (1985) experimentally obtained the appropriate value of λ for the damper they were studying, and they were able to show that a damper with an end seal at a distance from the end equal to the radial clearance c approaches the short damper, and a damper with a closed end will approach the long damper. Thus, in the model, the factor λ is taken to be equal to the ratio a/c, where a is the distance of the sealing ring from the end of the damper. The HSFD dimensions were designed to give a long damper that will be effective in suppressing high vibration, and for the same dimensions, a short damper that induces considerably less damping to the rotor system. This resulted in quite a large clearance for the damper and thus allows the HSFD to behave as a high load damper too.

To model the sealing ring dynamics, the forces acting on the sealing ring are considered. These are the pressure force in the sealing chamber, the pressure at the journal end, the spring stiffness, and the friction acting on the sealing ring. The governing equation for the sealing ring in nondimensional form (El-Shafei and Hathout, 1995) is

$$\lambda'' + \eta_1 \lambda' + K_s^*(\lambda - 1) = F_d^* - p^* \tag{6}$$

where η_1 is a loss factor incorporating all damping effects acting on the sealing ring, including friction with close clearance surfaces and damping forces due to the pressure at the journal end. This is an estimated loss factor, which will be used until further experimental investigations reveal the actual loss factor in the test rig at Cairo University (El-Shafei and El-Hakim, 1995). It should be noted that in the long damper case, the sealing ring is in contact with the damper journal end. Investigation has shown that the effect of friction between the metallic sealing ring and the journal is minimal and can be neglected (El-Shafei and Hathout, 1995). It should be clear that in the HSFD design the contact between the sealing rig and the end damper is allowed and occurs in the long damper mode as described in the experimental investigation of El-Shafei and El-Hakim (1995)!

Finally, to complete the model, the servovalve dynamics are governed by the nondimensional second-order equation

$$p^{*\prime\prime} + 2\zeta_1 \omega_r^* p^* + \omega_r^{*2} p^* = \omega_r^{*2} K_1^* i_o \tag{7}$$

as described in the model of El-Shafei and Hathout (1995).

To develop the control action, it should be clear that the system is chosen to behave in the short damper mode in its normal condition, which gives the least amount of damping to the rotor in the system, and any deviation of λ from the short damper mode position (i.e., $\lambda = 1$) toward the long damper mode position would translate into an increase in the damping of the HSFD. This increase in damping ΔC is the effective control input to the rotor. Thus the controlled damping ΔC becomes

$$\Delta C = (1 - \lambda)(C_s - C_l) \tag{8}$$

and hence the equations of motion of the journal center in both x and y directions can be changed in the form shown below where the right-hand side represents the effective control input to the system, i.e., the damping force causes the increase of damping to the system ΔC. In nondimensional form, Eqs. (3) and (4) reduce to:

$$\bar{x}_g'' + m_o \bar{C}_{xxs} \bar{x}_g' + m_o K^*(\bar{x}_g - \bar{x}_s) + m_o K_r^* \bar{x}_g = -m_o \Delta \bar{C} \bar{x}_g' \tag{9}$$

$$\bar{y}_E'' + m_o \bar{C}_{yys} \bar{y}_E' + m_o K^*(\bar{y}_E - \bar{y}_S) + m_o K_r^* \bar{y}_E = -m_o \Delta \bar{C} \bar{y}_E' \tag{10}$$

Equations (1), (2), and (6)–(10) constitute the complete system equations, which are transformed to the Laplace domain, and put in a block diagram format. Figure 4 shows the block diagram of the open-loop plant consisting of the servovalve transfer function, the sealing ring dynamics, the HSFD, and the rotor dynamics in both the x and y directions. The servovalve reacts to the input current i, and causes an increase in the sealing chamber pressure P, which pushes the sealing ring to move with a displacement λ and hence controls the amount of damping input ΔC to the rotordynamics of the system as shown in Fig. 4(a). All parameters shown in the block diagram of Fig. 4 are taken as for the system of El-Shafei and Hathout (1995). To further explain Fig. 4(b), the damping input ΔC acts on the journal as described by Eqs. (9) and (10). Furthermore, Eqs. (9) and (10) are coupled with the disk Eqs. (1) and (2), with the final output from these four equations being the eccentricity of the journal $\epsilon = \sqrt{\bar{x}_g^2 + \bar{y}_g^2}$, the displacement of the center of the disk $r = \sqrt{\bar{x}_s^2 + \bar{y}_s^2}$, and the force in the damper $F = \sqrt{F_x^2 + F_y^2}$. The closed-loop control system with PI controller added to the plant is illustrated in Fig. 5. The eccentricity

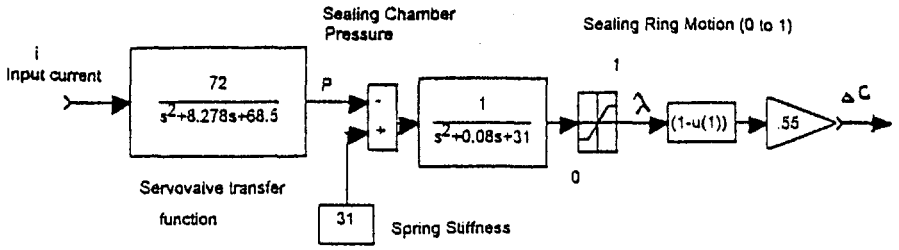

(a) Sealing Rings Dynamics

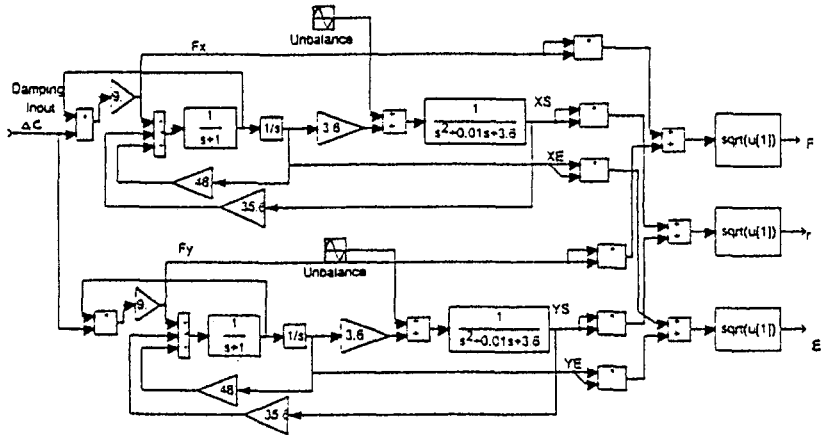

(b) Rotordynamics in both X and Y directions

Fig. 4 Block diagram of the open-loop plant

ratio ϵ at the journal was chosen to be fed back; hence the control input to the servovalve is given by

$$u = \left(k_p + \frac{k_i}{s}\right)(\epsilon_r - \epsilon) \tag{11}$$

where u is the control input, k_p is the proportional gain, k_i is the integral gain, ϵ_r is the reference input, and $(\epsilon_r - \epsilon)$ is the error to be regulated. The system shown in Fig. 5 is simulated in the next section.

Design of the PI Control System

The proportional gain k_p and the integral gain k_i have to be tuned to give the performance sought after. The main objective for controller gain tuning is to find the appropriate gains that would both reduce the high amplitudes of vibration at critical speeds and dampen sudden unbalance, in addition to reducing the transmitted forces away from critical speeds.

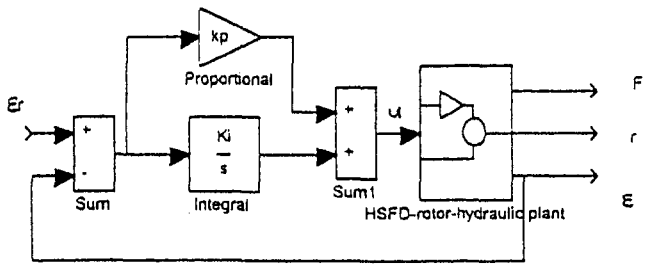

Fig. 5 Block diagram of closed-loop system, PI controller and plant

The design process of the PID control system for this nonlinear system was multilayered. First, a set of trial and error attempts were made, guided by locations of the roots of the open-loop system, with the objective of selecting the appropriate control strategy. This stage led us to conclude that PI control is the appropriate control algorithm for this system. The second stage was to use a well-known tuning method to estimate the PI controller gains. The third step was to fine tune the controller gains by simulation on MATLAB.

In the first step, many trials were done by changing the gains and studying their influence on the roots of the system. Figures 6(a) and 6(b) show the pole-zero mapping for the open-loop and the closed-loop systems, respectively. It should be clear that derivative feedback was first investigated but resulted in severe chattering of the sealing rings. The system would lose its effective control input with the inaccurate positioning and the chattering behavior of the sealing rings, which are the means of providing the necessary amount of damping to the system. Thus, we concluded that the behavior of the system is unsatisfactory with the slightest derivative gain. This is because the derivative control component responds to the rate of change of the error, and hence gives a stronger control signal when the error changes faster and thus it anticipates large errors, and attempts corrective actions before they occur with high control signals. Such high signals cause the chattering of the sealing rings and tend to destabilize the behavior of the system.

On the other hand, the integral control component is commonly used in process control where certain levels must be maintained for the control variables despite disturbances and parameter variations. Integral control tends to reduce steady-state error to zero. Our goal is to position the sealing rings accurately with minimum transient oscillations to give zero steady-state error of the output controlled variable. The integral

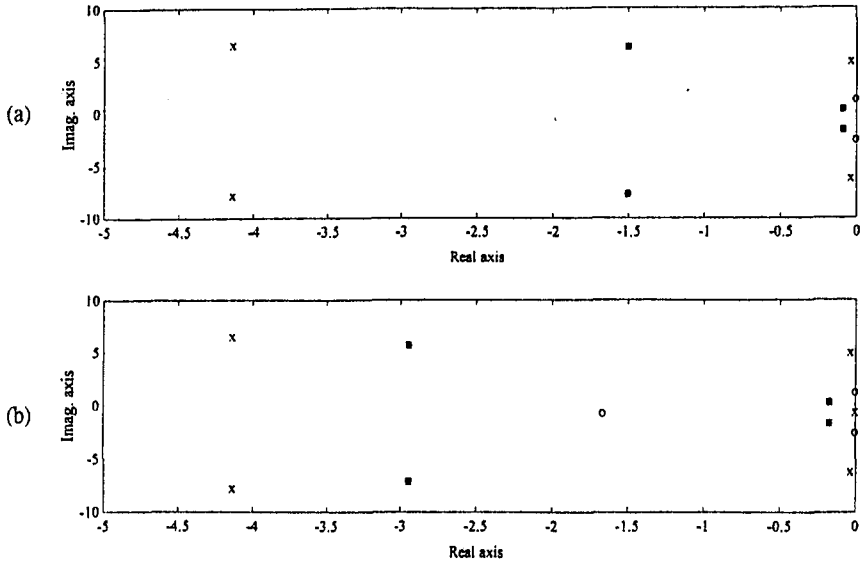

Fig. 6 Pole-zero mapping for the uncontrolled (*a*) and controlled (*b*) systems; X pole; O zero

action is quite appropriate since its control signals are lower and slower than the derivative signals, hence accurate positioning of the sealing rings without severe chattering is possible. The performance of the PI control is quite adequate for controlling our plant if the reference allowable vibration level to be maintained despite disturbances is selected; thus the controller will reduce the error to zero. The only drawback of a PI controller in our case is that it reacts quite slowly to errors and hence gives quite large overshoots especially in the unbalance control and in attenuating the first critical speed during the rotor run-up.

The second step in the controller design process was to use the Ziegler–Nichols tuning method (Astrom and Wittenmark, 1989) in selecting the PI controller gains. The Ziegler–Nichols tuning method assumes that the system behaves as a first-order system with delay, and the controller gains are chosen as a function of the time delay, time constant, and open-loop gain. This tuning method resulted in determining the gains k_p and k_i with acceptable system performance. The third and last stage was to fine tune these gains by trial and error to achieve the stated objectives of the controlled system. This final design stage resulted in $k_p = 3$ and $k_i = 5$, which give satisfactory results as discussed below.

Simulation of the Behavior of the Closed-Loop Control System

To simulate the behavior of the closed-loop system, the block diagram developed in the previous section describing the dynamics of the complete closed-loop system is implemented on a digital computer. The block diagram is manipulated on SIMULAB™ and MATLAB™ to permit the simulation of a nonlinear system in the Laplace domain. In order to simulate this model, the most convenient and robust integration technique was the Adams–Gear method (MATLAB, 1991).

(a) Control of Transient Run-up Through Critical Speeds. The uncontrolled system is speeded up linearly from rest to a nondimensional rotational speed Ω^* of 12 (equivalent to 21,590 rpm approximately) in a nondimensional time $\tau = 1200$ and equivalent to about 7 seconds approximately. The uncontrolled run-up of the rotor, i.e., while the HSFD behaves in the short damper mode, is shown in Fig. 7 for a nondimensional unbalance $U = 0.1$. The eccentricity ratio ϵ, the vibration amplitude of the rotor center r, and the transmitted damper force F are studied versus the nondimensional run-up time τ. It can be clearly seen from Fig. 7(*a*) that the short damper mode exhibits mainly two modes at speeds of $\Omega^* = 1$ and 7 approximately. The first and second modes are quite accentuated and some transient oscillations persist after the first mode is surpassed. Figure 7(*b*) shows that the second mode is well damped for the vibration amplitude of the rotor center r.

The reference input of the controlled system is chosen to be $\epsilon_r = 0.3$. The same run-up discussed above is used and the behavior of the controlled system is shown in Fig. 8. Figures 8(*a*) and 8(*b*) show that the eccentricity ratio exceeds the reference input at the first critical speed, but still the overall behavior while passing through the critical speed is enhanced. The amplitude of vibration is lowered, and the transient oscillations are eliminated. The control action for the first critical speed is slow and the error is quite large. This is caused from the slow reaction of the integral control component to a vibration amplitude peak, which builds up very rapidly; the integral action

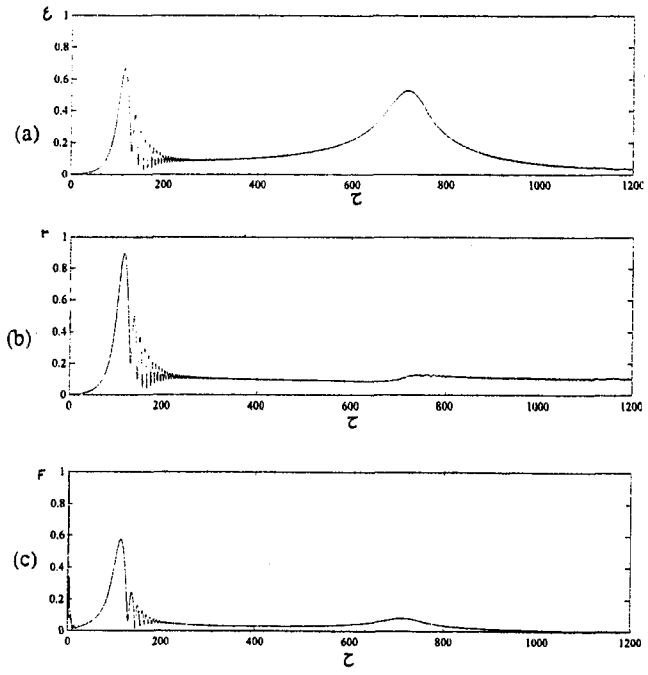

Fig. 7 Transient run-up of the controlled system

needs more time to react. This fact is clear while the system overcomes the second peak, which is less accentuated and takes quite a larger time to build up; the integral action is more efficient and the reference input is respected. Some transient oscillations persist for about 0.2 seconds, then the behavior is improved. These transient oscillations can be explained from Fig. 8(d), which describes the motion of the sealing ring λ. The amount of damping to the system relies on the position of the sealing rings. The controller signal forced the sealing rings to reach a value $\lambda = 0.5$ approximately to dampen the second peak; this finite positioning of the sealing ring between $\lambda = 1$ (short damper mode) and $\lambda = 0$ (long damper mode) requires some time to position the seal accurately at the optimal position that would give the necessary damping to decrease the high peak of vibration. This positioning time results in some oscillations that could be diminished if the damping on the sealing is increased, but because of the uncertainty of the amount of this damping in our test rig, we chose it to be quite low. We envision that the behavior will improve when the controller is tested on our test rig since the damping at the seals could be greater due to friction effects. Figure 8(c) shows quite a higher transmitted force in the controlled case than that in the uncontrolled case illustrated in Fig. 7(c). The increase in force is clear at the critical location where higher damping action is needed to attenuate excessive vibration.

(b) Control of Sudden Unbalance (e.g., Blade Loss). Rotating machinery may experience dangerously high dynamic loading due to the sudden unbalance associated with blade loss, for instance. Many cases of the destruction of turbomachinery were blamed on excessive bearing loads due to blade loss. Although considerable efforts are put into the steady-state vibration control, there are few methods applicable to transient vibration control of rotor-bearing systems (Palazzolo et al., 1989b).

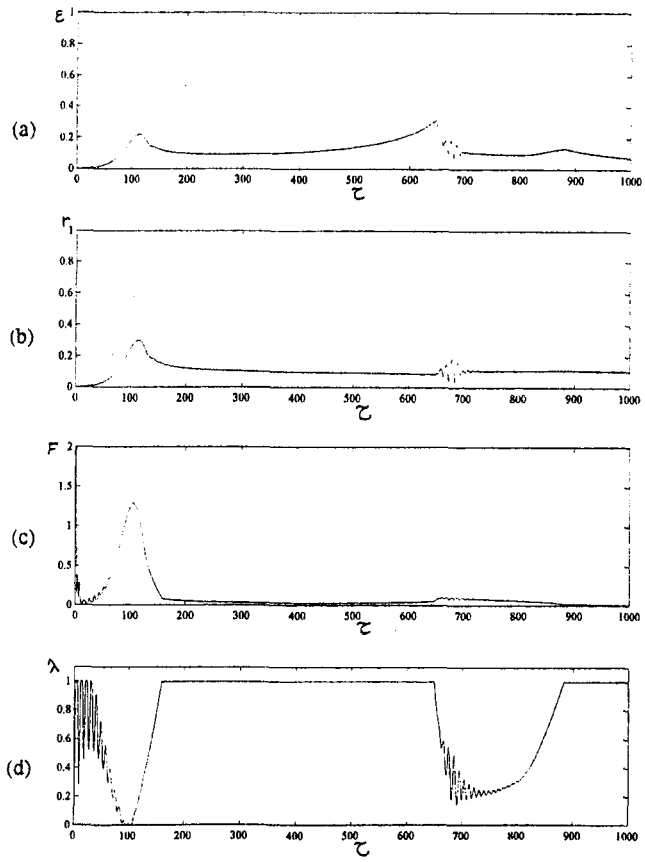

Fig. 8 Transient run-up of the controlled system

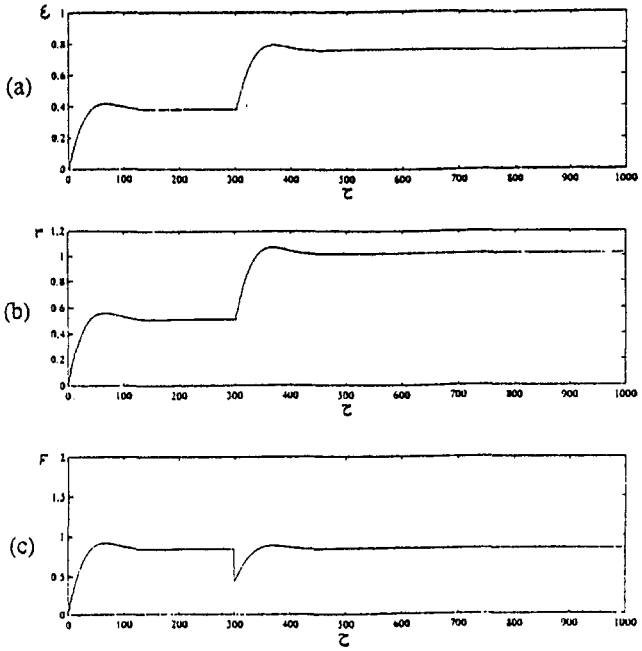

Fig. 9 Sudden unbalance response of the uncontrolled system

The objective of this research is to investigate the capability of the PI controller to suppress rotor vibrations caused by sudden mass unbalance.

The rotor is chosen to rotate at its normal working steady speed with an initial low unbalance of 0.05 at the disk. Then, suddenly at a nondimensional time of $\tau = 300$, the unbalance increases to a higher value equal to 0.1. For this case, we chose the normal working speed to be at $\Omega^* = 1$, which corresponds to the first critical speed of the rotor. This speed was chosen to investigate the performance of the controlled system under severe working conditions: sudden mass unbalance while the working rotational speed coincides with the first critical speed of the rotor. Figure 9 shows the behavior of the uncontrolled system to a sudden unbalance. The amplitudes of vibration of both the journal center ϵ and the disk center r have nearly doubled in magnitude due to sudden unbalance.

Figure 10 shows the closed-loop behavior. The behavior of the rotor is brought to its normal working condition through a transient overshoot, which persists for about 0.18 seconds. We can see clearly from Fig. 10(d) that λ is approximately positioned at a value of 0.6, which permits the HSFD to give exactly the right amount of damping to the rotor to return to its initial working condition. This implies that for higher unbalances, higher damping forces are needed to reach behaviors closer to the required working condition. This compensation is done with a higher signal from the controller to the servovalve, hence the sealing ring moves closer to the long damper mode (at $\lambda = 0$), with the penalty of increasing the transmitted damping force to the rotor, as shown in Fig. 11. This figure illustrates the behavior of the system to higher unbalances of 0.15 and 0.2 compared with the previous case where an unbalance of 0.1 was simulated. As discussed above, λ moves closer to $\lambda = 0$ (Fig. 11(d)) with higher unbalance forces acting on the rotor, and hence the HSFD produces higher damping forces (Fig. 11(c)) to attenuate excessive vibration and return its level as close as possible to the initial working condition of unbalance 0.05.

The excellent behavior of the HSFD in controlling sudden unbalance as shown in Figs. (10) and (11) should be qualified. It should always be remembered that the variable characteristics of the HSFD allowed the design of a large clearance damper (as high as 625 μm (25 mils)), which by default is a high load damper. This capability is the reason for good control of the

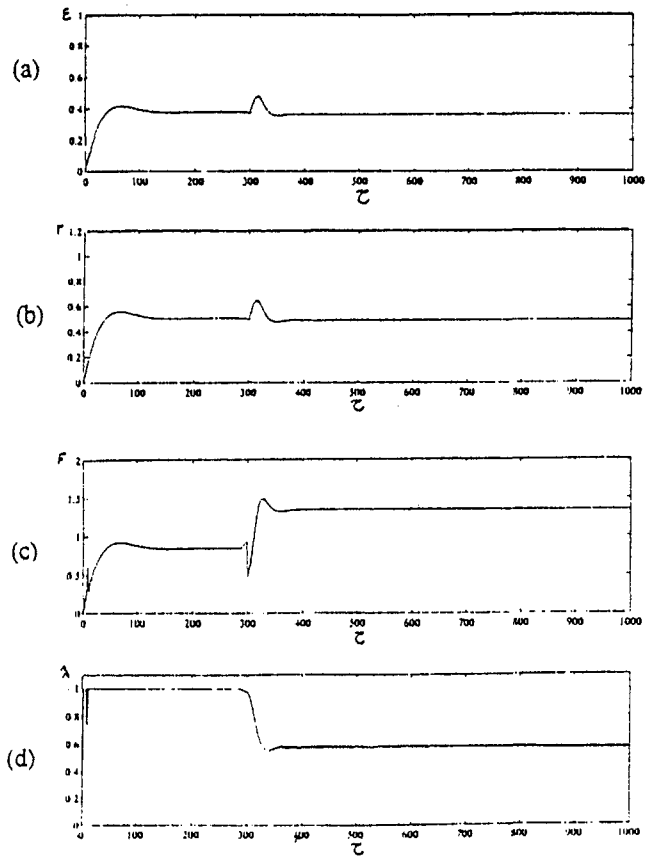

Fig. 10 Sudden unbalance response of the controlled system

blade loss, yet with still the ability of providing the appropriate damping to the rotor when needed. Nevertheless, there is a limit to the amount of control exercised by the HSFD on a blade loss. As shown in Fig. 11(d), an unbalance value of $U = 0.2$ gives the largest amount of damping ($\lambda = 0$) from the HSFD, consequently any larger unbalance the HSFD cannot be accommodated. This sets a further constraint on the design of the HSFD as to the required clearance in the HSFD versus the expected unbalance it is required to accommodate.

Gain Scheduling Technique for Enhancing the Closed-Loop Behavior

Conventional control theory, including the PI regulator, deals predominantly with linear systems having constant coefficients and fixed controller gains. However, linear control techniques can be quite efficient in controlling nonlinear systems, provided that such systems are regulated at fixed operating conditions. With moderate disturbances and a good control system, the deviations will be so small that the linear approximation is sufficiently good. This requires a thorough study of the plant to be controlled and a careful choice of controller gains. However, the linear coefficient approximation will not always be satisfactory when the operating conditions change significantly. Therefore, optimal gains would have to be tuned for different operating condition ranges. A solution for such cases would be the construction of a gain scheduling technique that will cope with the varying operating conditions in changing controller gains. Also, adaptive control techniques can be very useful for nonlinear systems with changing parameters and conditions. Investigations of such areas of modern control, and new algorithms applicable to this plant are within reach (Hathout, 1995). But, at this moment, the main interest is to study the full capabilities of the closed-loop system with PI control, including PI control with gain scheduling.

The PI controller is shown to be efficient in controlling the behavior of the system during run-up through critical speeds and sudden unbalance due to blade loss. However, the behavior of the closed-loop system while speeding up through critical speeds shows delayed control behavior while passing the first critical speed. To improve the control action through the first critical speed, we chose to incorporate the gain scheduling technique to the closed-loop system with the PI regulator.

The gain scheduling technique (GS) is viewed as a nonlinear feedback of special type: It has a linear regulator whose parameters are changed as a function of operating conditions in a preprogrammed way. GS is an open-loop compensation and can be considered as a system with feedback control in which the feedback gains are adjusted by feedforward compensation. The GS technique originated in connection with the development of process control and flight control systems and became a standard method in such applications. For example, in some flight control systems for supersonic aircraft, the Mach number greatly affects the response of the controller; therefore it is taken as an auxiliary variable, which is measured and used as the scheduling variable for varying the controller gains (Astrom and Wittenmark, 1989). This example is very close to the case in hand, since it can clearly be noticed that the characteristics of the system are related to the behavior of the rotational rotor speed, as illustrated in Fig. 7. Hence, the rotational speed, which can be easily measured in the test rig with a tachometer or a key phasor, can be considered as the appropriate scheduling variable for changing the regulator gains.

Unfortunately the design of the gain scheduling algorithm is far from being structured, since the gain scheduling technique is a nonlinear second level of control that requires both good judgment and trial and error simulations to obtain a good gain schedule. Good judgment was exercised in choosing the parameters to be scheduled. It was conceived that little can be added

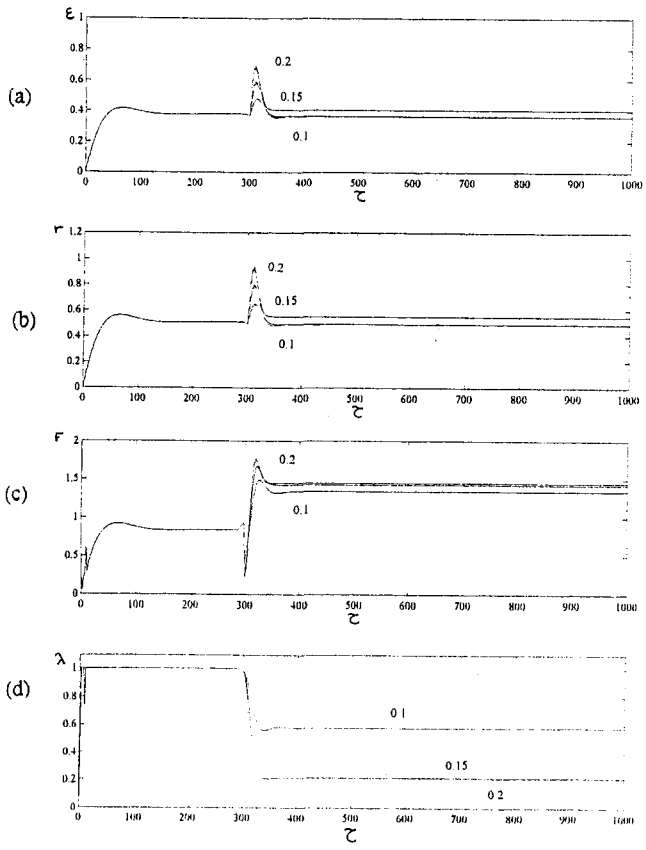

Fig. 11 Sudden unbalance response of the controlled system for different values of unbalances: −0.1, 0.15, and 0.2

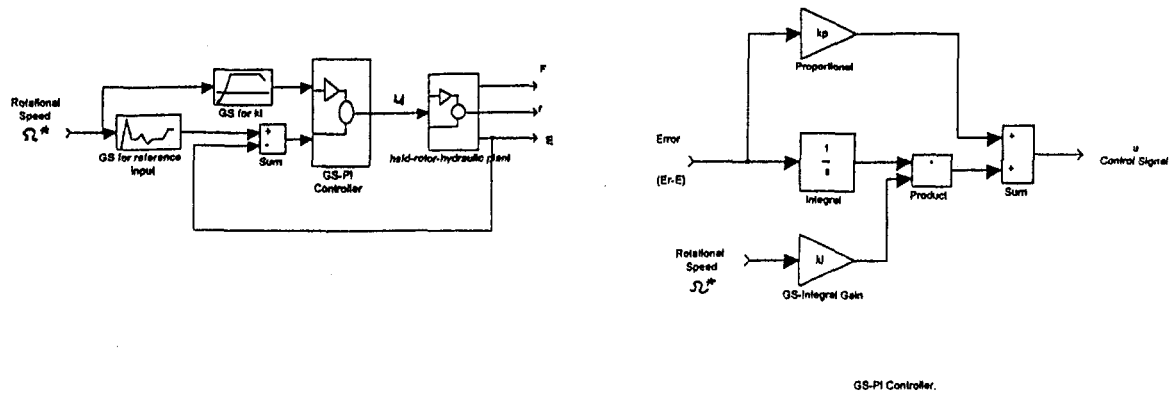

Fig. 12 Block diagram of the closed-loop system with GS–PI controller

by scheduling the proportional gain, and only the integral gain can be foreseen to provide better control when scheduled. In addition, good insight led to the important idea of scheduling the reference input and providing a speed schedule for the reference input. Only the integral gain required extensive trial and error simulations to schedule.

Figure 12 shows the closed-loop system with GS–PI controller incorporated. The scheduling of k_i with respect to the speed Ω^* is illustrated in Fig. 13. The choice of this schedule for k_i was designed by trial-and-error simulations until a satisfactory behavior was reached. It can be noticed that the gain is chosen negative from zero speed until overcoming the first critical; this was shown to be effective in forcing the HSFD to give maximum damping in this region of severe vibration. This can be explained from the fact that the corrective control action of the integral gain is slow toward the first peak of vibration, as explained before. This is because for a certain time at the beginning of the run-up the control input u_c is slightly negative due to a transient time delay caused by the integral action; this delay is known as integral windup (Van de Vegte, 1990). Integral windup causes the control input u_c (see Fig. 14(a)) to accumulate a large control signal with the same sign (negative in our case) of the error at regions of high disturbances, i.e., at the first critical, which is quite high. After the error becomes positive, and hence the controller is expected to activate the servovalve, the negative signal accumulated retards the wind-down to a value where the servovalve could be actuated. Hence, the negative value of the control input u_c is not capable of powering up the servovalve as soon as the peak arises, thus the HSFD is not activated. Gain scheduling of the integral gain in a manner that prevents this delay may be a good solution (Astrom and Wittenmark, 1989). Therefore, assigning a negative value to k_i for the region of the first peak rectifies the signal and this activates the servovalve. Figures 14(a) and 14(b) show the transient behavior of the control signal u_c for the PI controller alone and for the GS–PI controller, respectively. Also, it can be noted from Fig. 14(a) that u_c is undergoing integral windup in the negative direction after overcoming the second critical. GS of k_i corrected this behavior (Fig. 14(b)) by assigning lower values to the integral gain.

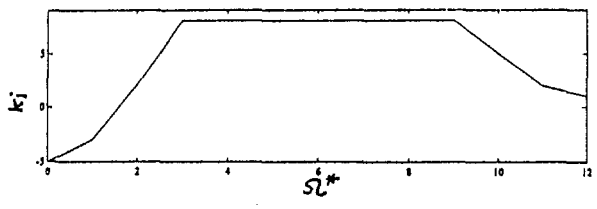

Fig. 13 Scheduling of K_I versus Ω^*

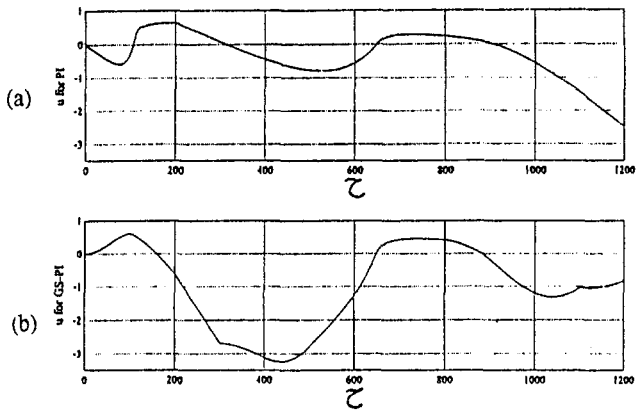

Fig. 14 Transient behavior of the control input u for both PI controller case (a), and GS–PI case (b)

A scheduling was also necessary for the reference input ϵ_r. For ϵ_r the scheduling variable is also taken as Ω^* since the reference input is affected by the speed of rotation. The relation between ϵ_r and Ω^* is shown in Fig. 15. The need of scheduling ϵ_r can be explained that for each speed range a certain value for the reference ϵ_r is the desired output. The schedule of ϵ_r with respect to Ω^* is designed to give the desired behavior for the eccentricity ratio ϵ at the journal. The amplitude of vibration is desired to be attenuated at criticals, hence the reference value ϵ_r is lowered at criticals. This will increase the error $(\epsilon_r - \epsilon)$, and thus the control signal u_c will increase (Eq. (11)) producing a current signal to the servovalve, which will produce the necessary pressure to push the sealing rings toward the long damper configuration and hence the HSFD dampens the vibration at criticals. On the other hand, ϵ_r is kept close to the short damper behavior (uncontrolled behavior) in regions of mild vibration where damping action is not needed, thus benefiting from the low transmitted damping force. Therefore, by scheduling the reference input in a manner that describes the behavior sought after, the more the integral action tends to minimize the error $(\epsilon_r - \epsilon)$, the closer the behavior of ϵ will resemble the behavior of ϵ_r through speed increase until coinciding with it when the

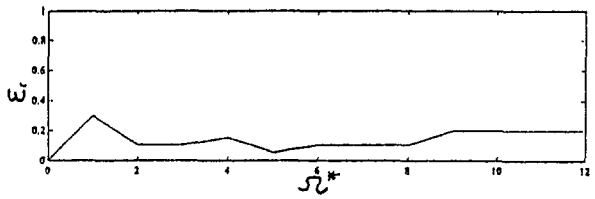

Fig. 15 Scheduling of ϵ_T versus Ω^*

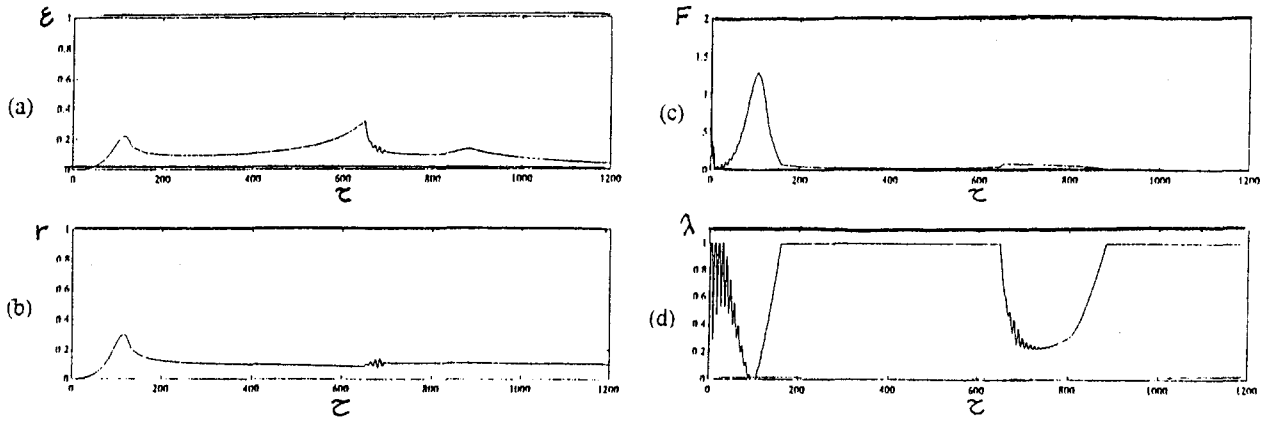

Fig. 16 Transient run-up of the GS–PI controlled system

error is minimized to zero, which is the advantage of integral control. The idea of ϵ tending to resemble ϵ_r can be quite noticed if Fig. 14 showing the schedule ϵ_r and Fig. 16(a) showing the eccentricity ratio ϵ transient response through controlled run-up are compared.

The transient closed-loop behavior of the system with GS–PI regulator while running-up the rotor through critical speeds is shown in Fig. 16. An improvement of the behavior is obvious when compared to Fig. 8, which describes the run-up behavior with PI control alone, especially in attenuating the amplitude of vibration of the first critical speed. Moreover, the transient chattering at the second critical is reduced. The GS–PI controller has the advantage of giving a well-behaved rotor run-up while maintaining the efficient controlled behavior to sudden unbalance of the PI regulator alone.

Gain scheduling enhanced the behavior of the closed-loop system since it has the advantage of changing the regulator parameters very rapidly in response to changes in the speed of the rotor. One drawback of this method is that the design of the integral schedule may be time consuming since the integral gain must be determined for many operating conditions, and the performance and stability of the closed-loop system with GS are typically checked by extensive simulations (Astrom and Wittenmark, 1989). Another consideration that must be noted while using GS is that this technique changes the regulator gains in open-loop in response to an auxiliary variable, which is the rotor speed in this case. This makes GS difficult to use unless the dynamics of the system are accurately known and the external disturbances well defined. This does not create a serious problem in this system, since usually elaborate studies of the rotor dynamics are done beforehand. In essence, sufficient knowledge of the rotordynamics is a prerequisite for the successful design of the gain scheduling technique. Yet the advantages of GS–PI, plus the experiences described in this paper, make it easy to justify the time spent in selecting the gain schedule.

Conclusion

In this paper, the PI control of hybrid squeeze film dampers (HSFDs) for actively controlling rotor-bearing systems is developed. A complete mathematical model of the HSFD-rotor-control system according to the currently existing control system of the test rig at Cairo University was implemented on a digital computer. The design of the PI regulator was described. Simulations show an overall enhanced closed-loop behavior for the transient run-up through critical speeds as well as for sudden mass unbalance at the disk (e.g., blade loss).

The controller was shown to react well with different sudden unbalances, and the damping induced by the HSFD to the rotor bearing system was directly proportional to the intensity of the sudden unbalance force. This is a very attractive issue since the control system is very sensitive to the severe forces produced by sudden unbalance change and produces the appropriate amount of damping necessary to improve the rotor behavior.

In addition, it was shown that while running-up through critical speeds, the PI controller showed some delayed behavior while overcoming the first critical due to the very rapid build-up of the vibration peak; nevertheless, the controller gave an overall enhanced behavior since it attenuated undesirable transient oscillations and reduced the peak. Moreover, the second vibration peak was well damped by the PI controller. Furthermore, the gain scheduling technique, as a second level controller, is incorporated in the closed-loop system with the PI regulator. This resulted in an improvement of the closed-loop system through run-up while maintaining the efficient control of the PI regulator to sudden unbalance. The most attractive issues of this control strategy are the simplicity and efficiency it provides, with a penalty paid in trial-and-error simulations to provide an appropriate integral gain schedule.

Acknowledgments

The authors would like to acknowledge fruitful discussions with Professor M. Elaraby, Dr. A. S. Zaki, and Mr. M. El-Hakim. The work presented in this paper was supported by EOARD, US Air Force Office of Scientific Research, Grant No. F49620-92-J-0512, Dr. Mark Maurice and Mr. John Schrand, program managers. This support is gratefully acknowledged. The U.S. Government has certain rights to this material.

References

Adams, M. L., and Zahloul, H., 1987, "Attenuation of Rotor Vibration Using Controlled-Pressure Hydrostatic Squeeze-Film Dampers," presented at the Eleventh Biennial ASME Vibrations Conference, Boston, MA, Sept.

Allaire, P. E., Mikula, A., Benerjee, B., Lewis, D. W., and Imlach, J., 1988, "Design and Test of Magnetic Thrust Bearing," presented at NASA Conference on Magnetic Suspension Technology, NASA Langley.

Astrom, K. J., and Wittenmark, B., 1989, *Adaptive Control,* Addison-Wesley Publishing Company.

Burrows, C. R., Sahinkaya, M. N., and Turkay, O. S., 1983, "An Adaptive Squeeze-Film Bearing," ASME Paper No. 83-Lub-23.

El-Shafei, A., 1990, "Unbalance Response of a Jeffcott Rotor Incorporating Short Squeeze Film Dampers," ASME JOURNAL OF ENGINEERING FOR GAS TURBINE AND POWER, Vol. 112, pp. 445–453.

El-Shafei, A., 1991a, "Unbalance Response of Jeffcott Rotor Incorporating Long Squeeze Film Dampers," ASME *Journal of Vibration and Acoustics,* Vol. 113, pp. 85–94.

El-Shafei, A., 1991b, "Hybrid Squeeze Film Damper for Active Control for Active Control of Rotors," U.S. Patent number 5,058,452, Oct.

El-Shafei, A., 1993, "Experimental and Analytical Investigation of Hybrid Squeeze Film Dampers," ASME JOURNAL OF ENGINEERING FOR GAS TURBINE AND POWER, Vol. 115, No. 2, pp. 353–359.

El-Shafei, A., and El-Hakim, M., 1995, "Development of a Test Rig and Experimental Verification of the Performance of HSFDs for Active Control of Rotors," ASME Paper No. 95-GT-256.

El-Shafei, A., El-Hakim, M., and Hathout, J.-P., 1993, "Control of Rotor Vibrations Using Hybrid Squeeze Film Dampers," Report MDP-EOARD-1/93, Cairo University.

El-Shafei, A., El-Hakim, M., Hathout, J.-P., and Youssef, R., 1994, "Control of Rotor Vibrations Using Hybrid Squeeze Film Dampers," Report MDP-EOARD-2/94, Cairo University.

El-Shafei, A., and Hathout, J.-P., 1995, "Modeling and Control of HSFDs for Active Control of Rotor-Bearing Systems," ASME JOURNAL OF ENGINEERING FOR GAS TURBINES AND POWER, Vol. 117, pp. 757–766.

Hathout, J.-P., 1995, "Active Control of Rotor Vibrations Using Hybrid Squeeze Film Dampers," M.Sc. thesis, Department of Mechanical Design and Production, Cairo University.

Hathout, J.-P., El-Shafei, A., and Youssef, R., 1997, "Active Control of Multi-Mode Rotor-Bearing Systems Using HSFDs," ASME *Journal of Tribology,* Vol. 119, pp. 49–56.

Holmes, R., and Dogan, M., 1985, "The Performance of a Sealed Squeeze-Film Bearing in a Flexible Support Structure," *Proc. I. Mech. E.,* Vol. 199, No. C1.

Keith, F. J., Williams, R. D., Allaire, P. E., and Schafer, R. M., 1988, "Digital Control of Magnetic Bearings Supporting a Multimass Flexible Rotor," presented at NASA Conference on Magnetic Suspension Technology, NASA Langley.

MATLAB, 1991, *MATLAB for Windows Users' Guide,* The Math Works Inc.

Palazzolo, A. B., Lin, R. R., Kascak, A. F., Montague, J., and Alexander, R. M., 1989a, "Test and Theory for Piezoelectric Actuator-Active Vibration Control of Rotating Machinery," ASME DE-Vol. 18-1, *Rotating Machinery Dynamics.*

Palazzolo, A. B., Lin, R. R., Kascak, A. F., and Alexander, R. M., 1989b, "Active Control of Transient Rotordynamic Vibration by Optimal Control Methods," ASME JOURNAL OF ENGINEERING FOR GAS TURBINES AND POWER, Vol. 111, pp. 264–270.

Palazzolo, A. B., Jagannathan, S., Kascak, A. F., Montague, G. T., and Kiraly, L. J., 1991, "Hybrid Active Vibration Control of Rotorbearing Systems Using Piezoelectric Actuators," ASME DE-Vol. 38-1, *Modal Analysis, Modeling, Diagnostics, and Control—Analytical and Experimental.*

Schweitzer, G., 1985, "Magnetic Bearings for Vibration Control," Bently Nevada Instability Seminar, Minden, NV.

Ulbricht, H., and Anton, E., 1984, "Theory and Application of Magnetic Bearing With Integrated Displacement and Velocity Sensors," I. Mech. E. Conf. on Rotordynamics, Paper No. C 299/84.

Van de Wegte, J., 1990, *Feedback Control Systems,* 2nd ed., Prentice-Hall, Englewood Cliffs, NJ.

Weise, D., 1985, "Active Magnetic Bearings Provide Closed Loop Servo Control for Enhanced Dynamic Response," *Proc. 27th IEEE Machine Tool Conf.,* Oct.

Zhu, W., Castelazo, I., and Nelson, H. D., 1989, "An Active Optimal Control Strategy of Rotor Vibrations Using External Forces," ASME DE-Vol. 18-1, *Rotating Machinery Dynamics.*

A Numerical Investigation of Premixed Combustion in Wave Rotors

M. R. Nalim
National Research Council.

D. E. Paxson

NASA Lewis Research Center,
Cleveland, OH 44135

Wave rotor cycles that utilize premixed combustion processes within the passages are examined numerically using a one-dimensional CFD-based simulation. Internal-combustion wave rotors are envisioned for use as pressure-gain combustors in gas turbine engines. The simulation methodology is described, including a presentation of the assumed governing equations for the flow and reaction in the channels, the numerical integration method used, and the modeling of external components such as recirculation ducts. A number of cycle simulations are then presented that illustrate both turbulent-deflagration and detonation modes of combustion. Estimates of performance and rotor wall temperatures for the various cycles are made, and the advantages and disadvantages of each are discussed.

Introduction

The wave rotor is a device that utilizes unsteady wave motion to exchange energy by direct work action between fluids, which may be chemically inert or reacting. It consists of a number of channels arranged about an axis; by rotation the ends of the channels are periodically ported to high and low-pressure ducts, which generate and utilize waves in the channels. Because the number of channels is large, the flow in the ducts is practically steady, and is directed to other steady flow components. An important feature is that as gases of a wide temperature range flow through the rotor, the mean channel-wall temperature is lower than the highest gas temperature. Rotational speed is low relative to turbomachines, and the geometry usually simpler, allowing greater strength and lower cost. For detailed descriptions of wave rotor principles and applications see Shreeve and Mathur (1985), Nalim (1994), and Welch et al. (1995).

A wave rotor acting as a pressure exchanger can be used (together with a conventional combustor) as a topping unit to enhance the performance of a gas turbine engine. Welch et al. (1995) have presented simulations based on validated codes, which indicate a substantial pressure gain possible between the compressor and the turbine. Similar pressure gain could also be obtained using an *internal-combustion* wave rotor. In this case, combustion occurs sequentially *within* the wave channels, each channel being periodically charged and discharged as it rotates past-properly-sized-and-timed inlet and outlet ports. Simplified combustion and wave processes are illustrated in the wave rotor sketch in Fig. 1. By accomplishing combustion on the rotor, the external combustor needed in a pressure-exchanger topping cycle is eliminated. So is the associated ducting, which might be long and unmanageably hot in some designs.

Combustion Modes. The implications of internal combustion and the feasible combustion modes are discussed in Nalim (1995). Rapid combustion is essential to minimize residence time and rotor size. The charge may be partially or fully premixed, and ignited by compression or other means. The feasible modes resemble combustion in various types of internal combustion (IC) engines. For relatively low inlet temperature (less than about 800 K for hydrocarbon fuel), premixing and sufficient turbulence are necessary to permit a high deflagration flame speed when ignited by a "spark" of residual or injected hot gas. With higher inlet temperatures, a detonation mode becomes likely in premixed gas, or a nonpremixed, turbulent "diesel" combustion mode may be used. Only *premixed* combustion is considered here.

Combustion Simulation Goals. This work is a step toward simulation of internal-combustion wave rotors. Numerical modeling of combustion is a challenging research area. There is a strong interaction between the energy release by chemical reaction and the dynamics of fluid motion. Localized energy release creates steep gradients in temperature and other properties, which drive transport of species, momentum, and energy. Fluid turbulence, when present, may interact with the reaction to the extent of dominating its rate. A wide range of time scales and length scales are important for different phenomena.

In an internal-combustion wave rotor, the large-amplitude nonsteady motion typical of wave rotors combines with intermittent combustion. This imposes a heavy computational burden, especially for multidimensional calculations. In the case of shock-induced reaction and detonation, the numerical problems typically associated with shock resolution and ensuring accurate shock-speed are compounded by the chemical reaction. Because chemical induction time is a sensitive function of temperature, it is a challenge to obtain accurate chemistry near a shock when there is locally poor accuracy for energy and temperature. In the case of turbulence-enhanced deflagration, the numerical representation of turbulence, as well as the choice of a combustion model that appropriately combines chemical kinetic and turbulence effects, are both difficult issues. The computation should properly resolve the flame thickness and the multiple time scales and length scales (acoustic, diffusion, and reaction). Ideally, adaptive gridding is needed to efficiently compute the flame propagation.

The present work attempts only the simplest, *one-dimensional,* representation of combustion that is compatible with an existing wave-rotor design and simulation code (Paxson, 1995a; Paxson and Wilson, 1995). This uniform-grid, one-dimensional code has already allowed much progress in designing pressure-exchange cycles, with rapid turnaround of computations on a single-processor workstation. It was desirable to create a similar tool for preliminary analysis and design of internal-combustion wave cycles. It is acknowledged that any one-dimensional representation of combustion processes will necessarily be rather crude, particularly when turbulence dominates. The intended approach is to select the model parameters to achieve simulation

Contributed by the International Gas Turbine Institute and presented at the 41st International Gas Turbine and Aeroengine Congress and Exhibition, Birmingham, United Kingdom, June 10–13, 1996. Manuscript received at ASME Headquarters February 1996. Paper No. 96-GT-116. Associate Technical Editor: J. N. Shinn.

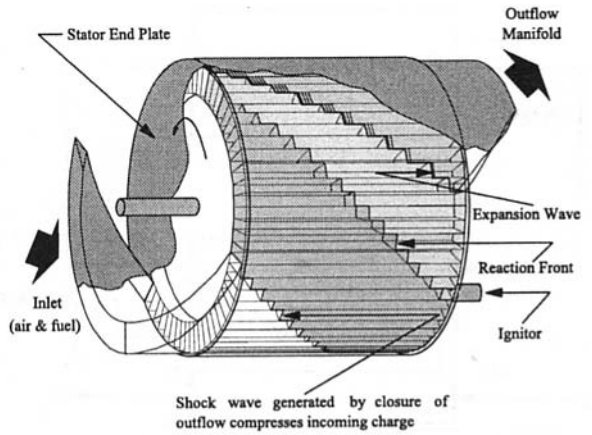

Fig. 1 Internal combustion wave rotor

of a desired combustion rate, and then estimate the required chemical and turbulence properties.

This paper is focused on the design of premixed-charge wave cycles, on understanding the flow dynamics relating the heat release to the pressure waves, and on estimating overall performance and material temperatures. The wave rotor model, governing equations for flow and combustion in the channels, and the numerical method used are described. A number of deflagration and detonation mode cycle simulations are then presented. The predicted pressure gains and wall temperatures are compared and the advantages and disadvantages of the various cycles are discussed.

Wave Rotor Model

The present model is based on a previous wave rotor simulation model for nonreacting gases (Paxson, 1992, 1995a). In this model, one-dimensional computation using a high-resolution CFD technique is performed for a single channel, neglecting interactions between channels. Losses due to the finite passage-opening time, leakage to the casing through the end gaps, heat transfer to the channel walls, and boundary layer viscous losses, are all treated by experimentally validated submodels (Paxson and Wilson, 1995). In addition to the CFD treatment of the flow in the channel, the cavities and the channel walls are treated by lumped-parameter models, and the ducts are modeled as steady, constant-area flows to obtain flow-homogenization losses. The overall pressure gain is calculated using averaged stagnation quantities computed from the absolute frame of reference, which takes the rotational speed into account.

Governing Equations for Channel Flow and Premixed Combustion. The present model assumes a calorically perfect gas, i.e., with a constant specific heat ratio (γ). The composition of the charge at any time and location is described solely by a reaction progress variable (z), which changes from 1 (pure reactant) to 0 (product) as combustion occurs, similar to Colella et al. (1986). Thus there will be one additional equation to be solved, besides the Euler equations of the nonreacting model. A simple representation of turbulence is included in the form of an eddy diffusivity.

The model numerically integrates the equations of motion in a single passage as it revolves past the ports and walls that comprise the ends of the wave rotor and establish the boundary conditions for the governing equations in the passage. Ports are specified by their circumferential location relative to some fixed point on the wave rotor casing, and by a representative pressure, temperature, and reactant fraction. With each time step the passage advances an angular distance specified by the angular velocity. If the flow is into the passage, the pressure and temperature are specified as stagnation values. If the flow is out of the passage, only the port pressure is required, and it is specified as a static value. Determination of the direction of the port flows at each time step is discussed in Paxson (1992).

The governing equations written in nondimensional form are:

$$\frac{\partial \underline{w}}{\partial t} + \frac{\partial \underline{F}(\underline{w})}{\partial x} = \underline{S}(\underline{w}) \tag{1}$$

where vectors $\underline{w}$ and $\underline{F}$ have the respective perfect-gas forms:

$$\underline{w} = \begin{bmatrix} \rho \\ \rho u \\ \dfrac{p}{\gamma(\gamma-1)} + \dfrac{\rho u^2}{2} + \rho z q_0 \\ \rho z \end{bmatrix} \tag{2}$$

$$\underline{F} = \begin{bmatrix} \rho u \\ \dfrac{p}{\gamma} + \rho u^2 \\ u\left(\dfrac{p}{(\gamma-1)} + \dfrac{\rho u^2}{2} + \rho z q_0\right) \\ \rho u z \end{bmatrix} \tag{3}$$

The nondimensionalization of pressure (p), density (ρ), and velocity (u) has been obtained using a reference state p^*, ρ^*, and the corresponding sound speed a^*. The distance has been scaled by the passage length, L. The time has been scaled using the nominal wave transit time, L/a^*. The heat of reaction of the reactant gas, q_0, is assumed to be a constant. An alternative formulation is possible, in which the heat of reaction is treated like an external heat source, and the chemical energy term is not used. Although this simplifies the algebra and coding, and the computations were checked to be equivalent, the given formulation is more consistent with the use of conservation variables, and can be extended to treat multiple species and real chemistry with variable q_0.

The source vector, $\underline{S}(\underline{w}, x)$ includes contributions from the chemical reaction rate, turbulent eddy diffusion, and viscous forces and heat transfer at the walls. A leakage term is also added for the end gas. Without leakage, the source term is

$$\underline{S}(\underline{w}, x) = \begin{bmatrix} 0 \\ \dfrac{\epsilon_t}{\mathrm{Re}^*}\dfrac{\partial^2 u}{\partial x^2} + \sigma_2 u |\rho u|^{0.75} \\ \dfrac{\epsilon_t}{\mathrm{Re}^*}\dfrac{\partial^2}{\partial x^2}\left(\dfrac{u^2}{2} + \dfrac{T}{(\gamma-1)\,\mathrm{Pr}_t} + \dfrac{z q_0}{\mathrm{Sc}_t}\right) \\ \qquad + \sigma_3 |\rho u|^{0.75}(T - T_{\mathrm{wall}}) \\ \dfrac{\epsilon_t}{\mathrm{Re}^* \mathrm{Sc}_t}\dfrac{\partial^2 z}{\partial x^2} - \rho z (1 - c_1 z)\begin{Bmatrix} K_0; T \geq T_0 \\ 0; T < T_0 \end{Bmatrix} \end{bmatrix} \tag{4}$$

The forms of the wall source terms for viscous stress and heat transfer and their coefficients σ_2 and σ_3 are based on semi-empirical correlations. The expressions and definitions for the combustion rate and eddy diffusion terms are discussed below.

Combustion Rate. In general, the rate of combustion at a given location in the flow will depend on the local composition, temperature, pressure, and turbulence properties. The mechanisms of combustion are quite different for turbulent deflagration and for detonation of premixed charges, and different forms of the rate equation are expected. In each case we represent combustion by a finite-rate, single-step reaction.

For the calculation of shock-ignited reaction and detonation, the rate (R) is assumed to be proportional to the reactant fraction, and to have an Arrhenius-type dependence on temperature. The rate coefficient is based on available single-step reaction kinetic models. Usually, a large activation energy is assumed, and ignition temperature kinetics are used, i.e., the rate coefficient is zero below a threshold (ignition) temperature (T_0), and is a constant (K_0) above it. This mode is activated by setting $c_1 = 0$ in Eq. (4).

For the calculation of turbulent deflagration, the turbulence model described in the next subsection is activated. Here also, ignition-temperature kinetics are used, but the rate is assumed to be proportional to both the reactant and the product fractions, i.e., $R \propto z(1 - z)$ by setting $c_1 = 1$ in the source vector, based on the suggestion of Magnussen and Hjertager (1976). This implies that the reaction can occur only at a propagating flame surface. The rate coefficient must be assigned phenomenologically, based on an estimate for the reaction timescale, which may be influenced by both chemistry and turbulence.

No special model is used for the ignition process to initiate a deflagration. In the cases considered here, initiation takes place by recirculation of hot combustion gas from leading channels, and by residual hot gas in the channel. Cavity leakage was also observed to initiate a flame in some simulations not discussed here. The one-dimensional treatment does not capture the penetration and vortex mixing effect of a jet of hot gas injected through an orifice smaller than the channel width.

Turbulence Model. The effect of turbulence is approximated by the use of an eddy diffusivity, which results in diffusive fluxes of z, energy, and momentum, proportional to their respective streamwise gradients. In Eq. (4), Re* is a Reynolds number based on the reference state ρ^*, a^*, and L; ϵ_t is the eddy viscosity scaled by the molecular viscosity. The formulation permits the use of different diffusivities for mass, momentum, and heat, by specifying the turbulent Prandtl number Pr_t and turbulent Schmidt number Sc_t.

Clearly, such a model has little predictive value, because the role of turbulence in flame propagation is much more complex than simply eddy diffusion. Within the constraints of a one-dimensional calculation, however, there is not much scope for worthwhile sophistication. It is comforting that the flame propagation rates calculated showed an appropriate sensitivity to the values for the model parameters, as discussed later. A more detailed model and multidimensional computations are needed to examine the real physics of turbulent flame propagation.

System Model and Wall Temperature Calculation. The system layout for wave rotor simulation is shown schematically in Fig. 2. Boundary conditions for the end or port regions of the channel flow are generally supplied as stagnation states. These are either provided directly by the user, as in the case of the port leading from the upstream compressor, or calculated by lumped-capacitance models of the rotor housing space and the recirculation passages. The space between the rotor and the housing, to and from which leakage occurs, is lumped as a single cavity. The pressure differences between the cavity and the channels, together with the specified gap between rotor and endwalls, govern the leakage flow via a source term in the first and last computational cells of each channel. The recirculation ducts are also lumped together as if they were a single cavity. A stagnation pressure loss proportional to the square of the mass flow is imposed on the flow going through the recirculation loop. The downstream turbine could also be modeled as a cavity and valve; however, in this study, the exhaust port pressure was held constant based on previous calculations for topping cycles (Paxson, 1995b). In this paper, the term lumped-capacitance implies that the kinetic energy of the flows in the components is neglected. Thus, they may be modeled using only mass and energy conservation equations.

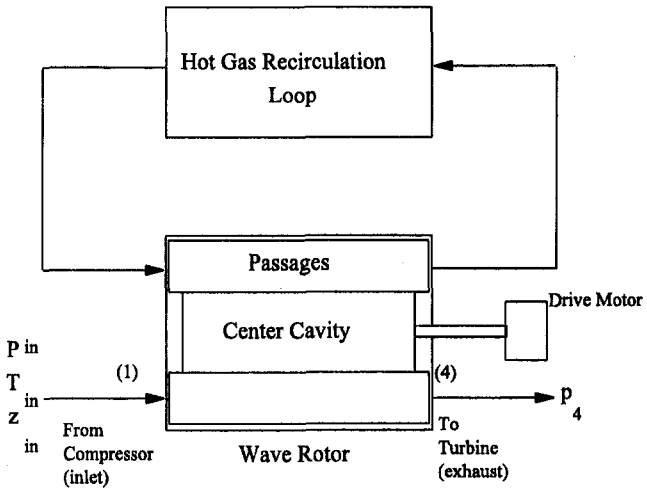

Fig. 2 System layout

The stagnation boundary conditions supplied by the user or component models are used by each channel in the CFD code to determine the state of the so-called image cell at the next instant of time. The code is capable of assessing whether a given condition will lead to inflow or outflow in a given channel. This allows robust operation of the simulation even in some off-design conditions where a portion of the flow in a given port may be into the rotor and a portion out of the rotor. For outflow conditions, only the boundary pressure is used, and it is treated as a static value. For inflow conditions some accounting is made if the flow in the duct is not aligned with the passage (i.e., shaft work into the system). For both inflow and outflow conditions accounting is made at the boundaries for the effects on the flow of those channels, which are only partially opened to a port: so-called finite opening effects. The ducts leading to and from the ports are assumed loss free (isentropic); however, a constant area mixing calculation is used in outflow ports to account for losses due to non-uniformities in the flow.

A lumped capacitance method is also used to track the wall temperatures, as described by Paxson (1995a), except that the channel side walls also contribute to the heat transfer, and are assumed to be at the same temperature as the upper and lower walls. Longitudinal conduction in the rotor is not allowed in order to obtain the worst case wall temperatures. Thus, each slice of the rotor that is in contact with a channel computational cell is treated as a separate lump. The computed steady-state wall temperature may be thought of as a time-averaged gas temperature, but weighted for heat transfer.

Numerical Method

Equation (1) is integrated numerically as follows:

$$\underline{w}_i^{n+1} = \underline{w}_i^n - (\underline{f}_{i+1/2}^n - \underline{f}_{i-1/2}^n)\frac{\Delta t}{\Delta x} + \underline{s}_i^n \Delta t \qquad (5)$$

where the numerical flux estimate is

$$\underline{f}_{i+1/2}^n = \frac{\underline{F}_{i+1}^n + \underline{F}_i^n}{2} - \frac{1}{2}\underline{\Phi}_{i+1/2}^{\mathrm{Roe}} + \frac{\Delta t}{4}([A]_{i+1}^n \underline{S}_{i+1}^n + [A]_i^n \underline{S}_i^n) \qquad (6)$$

and the numerical source term is

$$\underline{s}_i^n = \tfrac{1}{2}(3\underline{S}_i^n - \underline{S}_i^{n-1}) \tag{7}$$

The term $\underline{\phi}^{\text{Roe}}$ in Eq. (5) refers to the flux-limited dissipation based on the approximate Riemann solver of Roe (1986) for Eq. (1) without a source vector. The matrix $[A]$ is the Jacobian of the flux vector $\underline{F}$. The superscript n and subscript i are indexes for the discrete temporal and spatial steps, respectively. This scheme has the advantage of being formally second-order accurate in time and space when the flow is smooth yet maintaining the high resolution of Roe's method in the vicinity of shock waves. Furthermore, as the source strength approaches zero, the scheme becomes monotonic, which is physically correct.

There are additional requirements on the numerical scheme to preserve the physical meaning of z, which are not inherent in the governing equations: z should remain in the range from 0 to 1, and the combustion source term for the rate of change of z in Eq. (4) should be negative or zero. These are usually satisfied by the use of physically meaningful initial and boundary conditions, well-behaved source term discretization, and a stable numerical scheme with monotonic source-free behavior. A simple first-order stiffness scheme was created for the combustion source term, by dividing it by a factor $(1 + K_0\Delta t)$, to ensure positivity of z. In practice, this was found unnecessary because the time step for stability of the Riemann solution was always much smaller than the reaction time scale. There are situations, unrelated to the source term, in which numerical integration of the Riemann problem results in slightly out-of-range z, even with a monotonic scheme (Larrouturou, 1991); however, in the simulations to be presented, they did not arise.

Since the time constants associated with transients in the wall temperatures and cavity properties are much larger than a complete wave cycle, these quantities are treated as constants for each wave cycle, and then updated using simple Euler integration (Paxson, 1995a). The actual rotor thermal inertia and cavity volumes do not affect a steady-state solution. Hence, the smallest values that allow stable computation are used for rapid convergence to a periodic, zero-net-flux solution, and steady-state wall, cavity, and duct properties.

Test Cases and Grid Independence. A number of reaction-wave test problems were solved to ensure that the numerical scheme was stable and produced meaningful solutions. These included the development of detonations in various frames of reference. For a direct test of accuracy in computing detonation speed, the boundary and initial conditions were set up to match a steady Chapman–Jouguet (C–J) detonation in a perfect gas with $\gamma = 1.2$, and fixed heat release, $q_0 = 30$, where the reference state is that of the unburned gas. After a brief transient, due to the fact that the prescribed initial step profile neglects the thickness of the reaction zone, the detonation becomes steady with the propagation speed correctly matching the prescribed inflow speed. The classical Zeldovich–von Neumann–Doring (ZND) structure appears, with the computed von Neumann pressure spike within 3 percent of the theoretical value of 30.9 (with $\Delta x = 0.005$, $K_0 = 30.0$, $T_0 = 2.0T_1$). While the detonation speed was independent of reaction rate parameters and grid spacing, the pressure spike was underpredicted for coarser grids or lower T_0. Computations of overdriven and underdriven detonations were also qualitatively correct.

It is not equally straightforward to directly compare turbulent flame computations with any data or with realistic models, as the one-dimensional model rate parameters have limited physical meaning. In a sense, however, the inverse of K_0 can be related to the dominant reaction time scale, which is expected to be the turbulence time scale. It has been found experimentally (Heywood) that highly turbulent premixed flames, such as those found in IC engines, have flame speed (s_t) comparable to the turbulence intensity, u', which should imply

$$s_t \propto u' \propto \sqrt{\frac{K_0 \epsilon_t}{\text{Re}^*}} \tag{8}$$

In computations of flame propagation in a closed tube, this relationship was seen to be roughly preserved with a proportionality constant in the range of 1.0 to 1.2, for values of ϵ_t from 250 to 1000, and K_0 from 8 to 40, all other variables being fixed at typical values ($\text{Re}^* = 8.3 \times 10^6$, $\text{Pr}_t = \text{Sc}_t = 1.0$, $q_0 = 4.0$, $T_0 = 1.5$, $\gamma = 1.33$). The flame speeds computed are also sensitive to changes in q_0 and T_0. For this same range of variables, grid-independent solutions were achieved for values of Δx less than 0.005, i.e., 200 cells in a channel length. Coarser grids resulted in exaggerated, grid-dependent flame speed.

Deflagration Mode Wave Cycles

Several possible wave cycles using turbulent deflagration were simulated. Because it is likely that low-pressure-ratio engines will use this mode (Nalim, 1995), the simulations assumed a design similar to a throughflow pressure-exchange wave rotor optimized for a small engine with an upstream compressor pressure ratio of approximately 8 (Paxson, 1995b). The major design parameters for such a reference wave rotor, listed in Table 1, are retained in nondimensional form except as noted. The reference state for nondimensionalization of variables is the stagnation state of the inlet to the wave rotor. In all the simulations, $\text{Re}^* = 8.3 \times 10^6$, $\text{Pr}_t = \text{Sc}_t = 1.0$, $\gamma = 1.353$. The simulations are presented as space–time contour diagrams of gas density and reactant fraction, over a full rotor revolution, with positive time in the upward vertical direction. The port timings are indicated by the breaks in the side borders representing the end plates. It is noted that the gas dynamics of a pressure-gain wave rotor allows, in each cycle, only partial discharge of the combustion gas to the higher-pressure exhaust port, while fresh charge enters from the lower-pressure inlet port.

Fast-Burn Reverse-Flow Cycle. In this mode, the wave rotor is designed for opposed pairs of reverse-flow cycles, with the one inflow and one outflow port at each end of the rotor, as illustrated in the computed wave diagram of Fig. 3. With exact symmetry of the port placement and the resulting gas dynamics, there will be a resident layer of gas, which moves from side to side but does not leave the channel.

Each wave cycle is required to be completed in about the same half-revolution time as the corresponding pressure-exchange cycle. This requires very fast combustion, and almost instant ignition. The cycle is designed to provide hot gas recirculation from leading channels, via a transfer passage, to create a torch jet into the premixed charge. It is assumed that the hot residual gas, heated by combustion and repeated compression, also initiates a flame in the charge. The illustrated simulation was obtained by setting $K_0 = 28.0$, $T_0 = 1.5$, and $\epsilon_t = 1000.0$. The inlet mixture is uniform, and q_0 is 3.42 to provide an overall temperature ratio of 2.2. Based on Eq. (8), and examination of the simulation, the corresponding flame speed is estimated to be 25 m/s for the candidate engine operating at standard ambient

Table 1 Reference wave rotor dimensions and design performance

Mean Rotor Radius	8.15 cm.	(3.2 in.)
Rotor Length	15.24 cm	(6.0 in.)
Rotor Passage Height	2.18 cm.	(0.86 in.)
Rotational Speed	16800 rpm	
Cycles/Revolution	2	
Number of Passages	52	
Mass Flow Rate	≈2.3 kg/s	(5.0 lbm/s)
P_4/P_1 (Fig. 2)	1.23	
T_4/T_1	2.21	

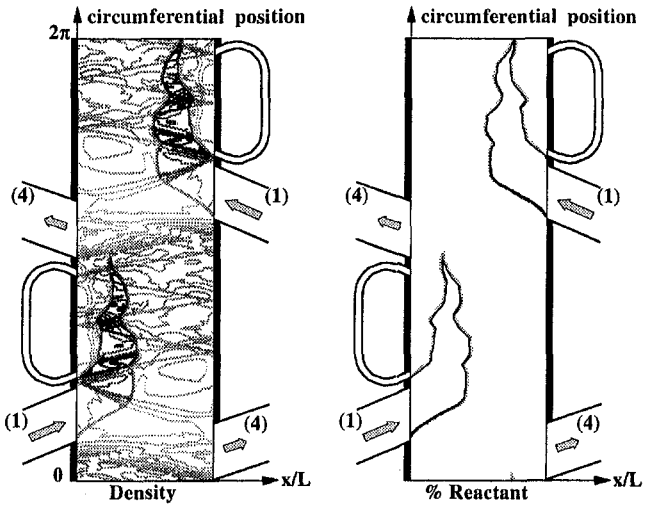

Fig. 3 Fast-burn reverse-flow cycle

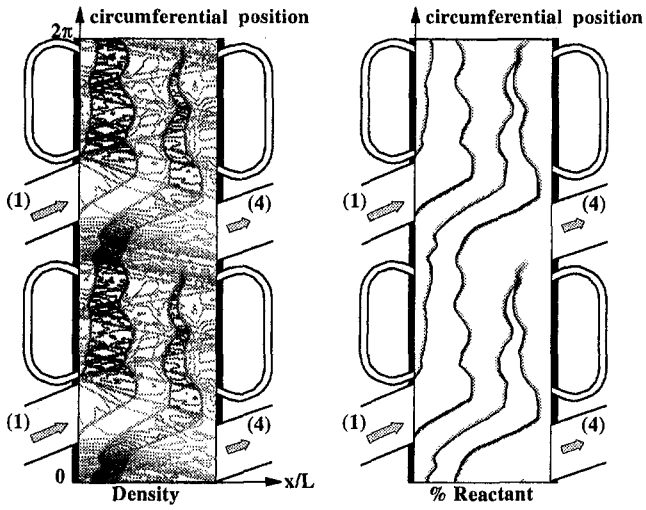

Fig. 5 Slow-burn throughflow dual cycle

temperature. This is at the high end of common IC engine experience, where 10 m/s might be more typical.

A fast-burn *throughflow* cycle, which completes combustion of the charge in each half-revolution, would be very similar to this reverse-flow cycle in flame pattern and performance.

Slow-Burn Throughflow Single Cycle. This design is intended for relatively slow-burning mixtures and conditions. It has only one cycle per revolution, with the inlet and exhaust ports on opposite ends. In the simulation illustrated in Fig. 4, the inlet charge is stratified so that the middle one-fifth of the air has no fuel ($z = 0$). Ignition is similar to the last case. Here, the flames have about thrice the time to complete combustion, and a fifth less distance to travel. Flame temperatures are higher, with $q_0 = 4.275$, to retain the overall temperature ratio of 2.2. The simulation shown used $K_0 = 6.0$, $T_0 = 1.5$, and $\epsilon_t = 500.0$, consistent with a flame speed about one-third that of the fast-burn simulation, based on Eq. (8). Combustion is completed before discharge and, at this level of diffusivity, some temperature stratification persists in the exhaust.

The mass flow rate in this wave rotor will be half that of the reference design, or conversely, a given flow rate will dictate double the rotor size. This may be a crippling penalty, and a solution to the problem is presented in the next case.

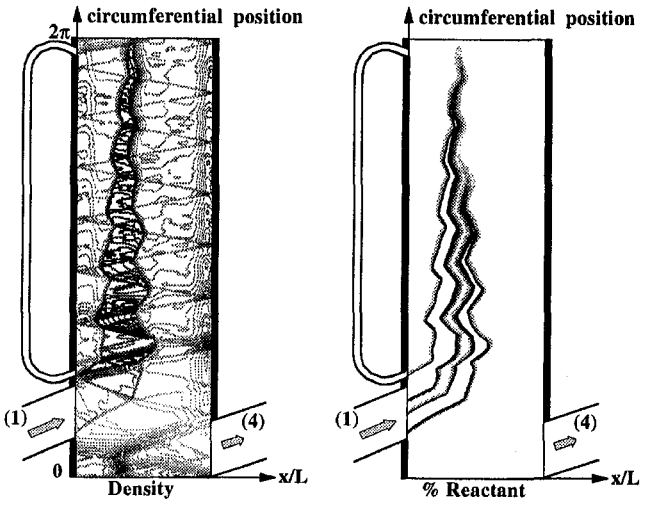

Fig. 4 Slow-burn throughflow single cycle

Slow-Burn Throughflow Dual Cycle. If combustion is very slow, combustion of a charge introduced in one cycle may not be completed before the next discharge process. In a two-port pressure-gain cycle, optimized for an overall temperature ratio of 2.2, only about 60 percent of the gas in the channel is discharged in each cycle. Therefore, a dual throughflow cycle may be envisioned, in which the fresh charge introduced at one end of the channel is burned over a period of two cycles, such that all the gas discharged at the other end has completely burned before final expansion. The throughput mass flow rate of the reference design is now recovered. The corresponding simulation, shown in Fig. 5, used $K_0 = 10.0$, $T_0 = 1.5$, and $\epsilon_t = 500.0$. Equation (8) implies flame speed about two-fifths that of the fast-burn case, which is roughly consistent with the relative combustion durations of the two cases, if it is noted that combustion is slowed during the low-pressure period. In this case, recirculation loops are provided at both ends to ensure quick ignition and complete combustion.

Detonation Mode Wave Cycles

The detonation mode is likely to be used for high-pressure-ratio engines with inlet temperature close to the autoignition temperature for the fuel used. For the purpose of this paper, however, most of the design parameters of the reference small-engine wave-rotor (Table 1) are retained in nondimensional form. We also keep $\mathrm{Re}^* = 8.3 \times 10^6$, $\mathrm{Pr}_t = \mathrm{Sc}_t = 1.0$, $\gamma = 1.353$. The throughput mass flow rate is approximately doubled relative to the reference design by doubling the number of cycles per revolution (to four) to take advantage of the rapidity of detonative combustion. The rotor speed is adjusted slightly to match the strong combustion-driven waves. The contour diagrams in this section cover only half a revolution, and temperature is shown instead of density because detonation involves only a slight change (increase) in density.

Throughflow Cycle. The throughflow cycle presented in Fig. 6 has a stratified inlet charge, with no fuel in the first one-fifth of the port duration to avoid the possibility of flashback or premature ignition of the nearly detonable charge. This buffers the fuel from the residual hot gas in the channel. To compensate and maintain the overall temperature ratio at about 2.2, the simulation uses $q_0 = 3.785$. The reaction rate used is $K_0 = 10.0$, with $T_0 = 1.2$ and $\epsilon_t = 100.0$. At this low level of diffusivity, the temperature stratification due to the buffer layer persists in the exhaust.

The detonation is initiated by coalescing compression waves generated by closing the exhaust port while there is still signifi-

cant flow velocity. The inlet port is closed just before the detonation wave arrives, and the exhaust port is designed to open at the time that the reflected detonation-generated wave reaches the opposite end, based on preliminary computations. This requires the rotor speed to be about 6 percent slower than the reference design, with four cycles per revolution. When a converged solution was obtained, however, it was found that the detonation wave timing had changed somewhat.

Reverse-Flow Cycle. The reverse-flow cycle of Fig. 7 also has a stratified inlet charge, but with fuel concentrated in the middle three-fifths of the port. While the leading buffer layer prevents pre-ignition as before, the trailing buffer layer is used to attempt to ensure that combustion is completed within the channel, and no unburned fuel reaches the exhaust port. This allows a finite land between the inlet and exhaust ports without weakening the detonation. The ideal timing is to open the exhaust immediately when the detonation-generated wave reaches the end wall, and the rotor speed in the simulation is adjusted to be about 12 percent faster than the reference design, to match the estimated timing. In practice, the time of initiation of the detonation varies from cycle to cycle, as seen in Fig. 7. Frequently, the detonation is late, and runs into the exhaust expansion, resulting in performance loss, or incomplete combustion, despite the buffer zone.

Another drawback of the reverse-flow cycle is that the residual gas, which never leaves the channel, becomes very hot due to repeated traversal by strong shock waves, resulting in increasing expansion of this gas and reduced room for fresh charge. In practice, the temperature of this gas will be limited by loss of heat to the walls (if cooled) and axial diffusion in the gas. It was found that convergence of this solution to the approximate steady state of Fig. 7 required an eddy diffusivity of $\epsilon_t = 1000.0$, with $K_0 = 20.0$, $T_0 = 1.2$, $q_0 = 5.0$.

Precise and repeatable timing of detonation initiation is difficult to ensure in any detonation mode. The sensitivity to charge conditions may be exaggerated because of the ignition-temperature kinetics used in the simulations, but will exist even with more realistic chemistry. Delayed initiation is less of a concern for the throughflow cycle, where there is adequate time for fuel burn-up. If the exhaust opening is timed without regard for the detonation-generated wave, a poor exhaust velocity profile and strong unsteadiness or nonuniformities in the outflow may result. *Delayed* exhaust opening, timed for later reflections of the wave, would throw away the fast-burn advantage of detonation, and increase the wall heat load and leakage.

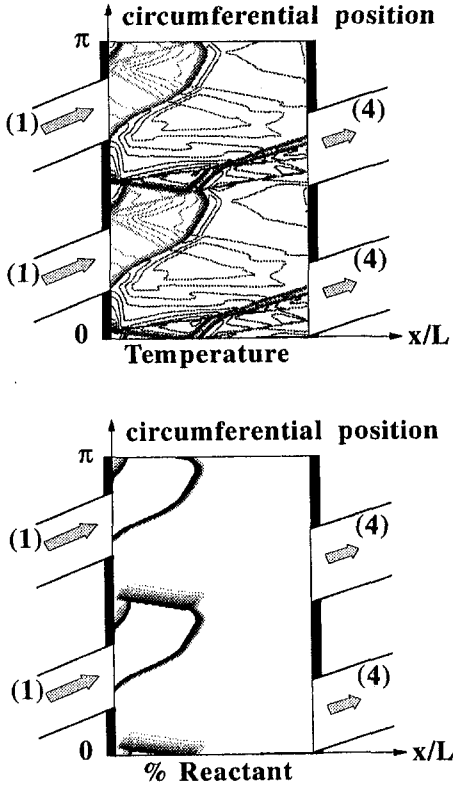

Fig. 6 Throughflow detonation-mode cycle

Comparison of Performance and Wall Temperatures

For all three cases of deflagration cycles, the pressure gain (averaged exhaust flow pressure over inlet pressure) was 1.20 ± 0.05. The slow-burn single cycle has a leakage coefficient set to half that of the other two to compensate for the increased time at high pressure, since it is not intended to examine the absolute effect of leakage here. It seems remarkable that the slow-burn dual cycle suffers very little from the fact that some combustion may occur at low pressure, when it is thermodynamically unfavorable for pressure gain. In the combustion model used, the rate of reaction is slowed during that time, as would be expected in reality. The pressure gain computed for the throughflow detonation cycle is 1.22. Pressure gain for the reverse flow detonation cycle is not reported because an acceptably steady solution with well-timed and complete combustion was not achieved.

For comparison, the equivalent throughflow pressure-exchanger wave rotor of Paxson (1995b) has a computed pressure gain of 1.23. It should be noted that no attempts were made to optimize any of the cycles for geometry, rotor speed, wave timings relative to port timings (except detonation, without success), correctness of duct angles for the velocity profiles, etc. The port durations for the hot gas recirculation loops are made greater than the channel width, due to the present limitation of the code for opening/closing calculations. This results in excessive recirculation flow (sometimes 20 percent of net flow), which may affect performance adversely. The waves generated by these ports also appear sometimes to cause strong nonuniformity in the exhaust. With good optimization of the cycles, improved performance is expected.

The steady-state wall temperature profiles of the simulations differ significantly, as shown in Figs. 8 and 9. Recall that longitudinal conduction in the wall is absent in these computations. The *mean* wall temperature is indicated by a horizontal bar for each case. This is an indicator of the rotor temperature when its conductivity is high. It may differ slightly from the temperature computed if a *uniform* wall temperature was assumed (infinite conductivity), since local heat transfer depends on the local temperature difference.

Converting the deflagration mode curves of Fig. 8 to absolute temperatures, assuming a turbine inlet temperature (TIT) of 1300 K, the peak wall temperature for the throughflow dual cycle is roughly equal to this TIT. For the reverse flow and throughflow single cycles, the peak wall temperatures are respectively about 110 K and 190 K higher than the TIT. The mean wall temperature for the throughflow dual cycle is *250 K lower than TIT,* whereas the mean temperature for the other two cycles are about equal, both 70 K below TIT.

For the detonative cycles (Fig. 9), conversion of temperature to absolute values based on same TIT and temperature ratio assumes a detonable fuel–air mixture at low inlet temperature. The throughflow cycle has a peak wall temperature close to TIT and a mean temperature 170 K below TIT. This is much cooler than the throughflow deflagrative single cycle, due to the relatively short time at high temperature, and the passage of the cold buffer layer. There are two curves for the reverse-flow cycle, one for a simulation with $\epsilon_t = 1000.0$ and the other with $\epsilon_t = 100.0$. These are intended only for a relative comparison, since the solutions were not sufficiently well converged for

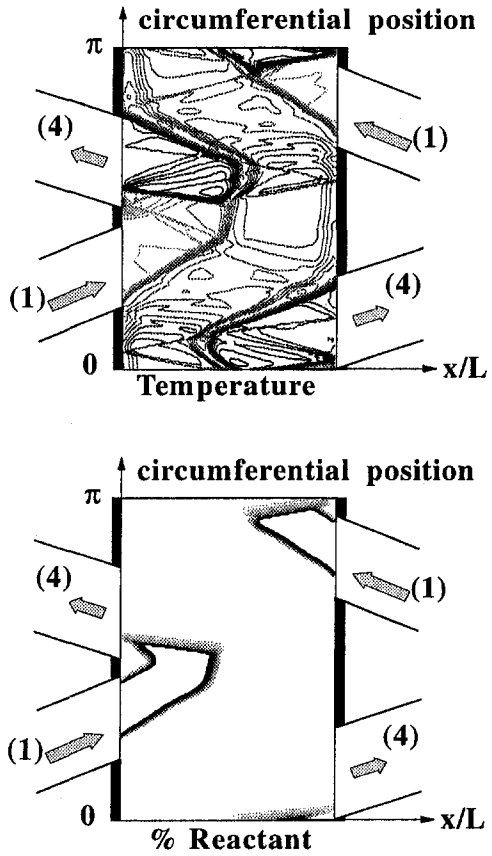

Fig. 7 Reverse-flow detonation-mode cycle

quantitative comparison. It is also noted that the heat transfer model validated for flow in channels may not be as accurate for flows involving detonations, which have structure and transverse oscillations that may substantially enhance heat transfer.

Concluding Remarks

A computational model for flow and premixed combustion in wave rotors has been developed that allows rapid simulation of deflagrative and detonative combustion mode wave cycles. The one-dimensional treatment of channel flow and combustion is coupled with validated models for loss mechanisms and external component interaction effects to provide realistic estimates of wave rotor performance and temperatures. The example simulations demonstrate that useful wave rotor cycles can be designed that can utilize a great range of combustion rates, depending on the fuel chemistry and turbulence properties provided. The highest throughput mass flow rates for a given rotor size can be achieved with detonative mode cycles. However, the sensitivity of this mode to port timing and boundary conditions is a significant issue. The throughflow detonative cycle is relatively well-behaved.

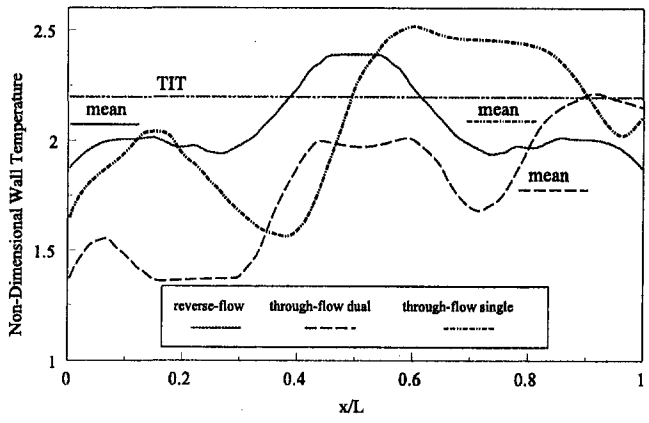

Fig. 8 Deflagration mode wall temperatures

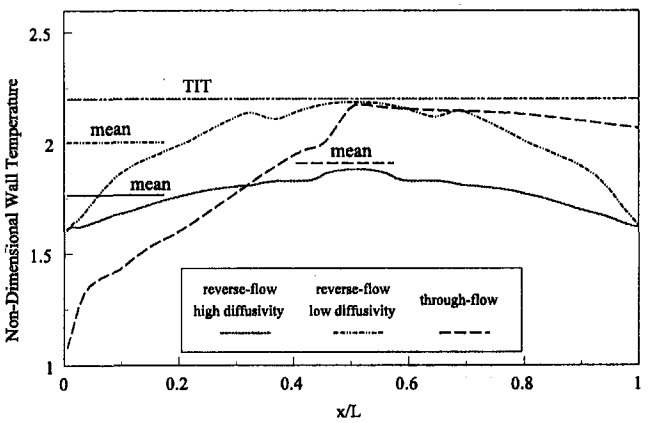

Fig. 9 Detonation mode wall temperatures

This exercise calls attention to the possibility that combustion within a wave rotor may have an inherent potential for instability, as the wave dynamics and combustion rates become closely coupled. Because combustion is naturally autocatalytic, perturbations that reduce the combustion rates may rapidly degenerate to a flame-out state. This may be the most significant drawback relative to an external-combustion pressure-exchange wave rotor. The use of hot gas recirculation for ignition of deflagration would seem to only add to the dependence on positive feedback. Nevertheless, the deflagration simulations appeared to be quite stable compared to the autoignited detonations. Further exploration of the sensitivity and stability issues for different combustion rate formulations and parameters is necessary.

Very high flame speeds will be needed for reverse- or throughflow deflagration mode cycles, which attempt to provide the same throughput mass flow rates as an equivalent equal-size pressure exchanger using an external combustor. Instead, it is possible to design a throughflow cycle that accommodates relatively slow flames, simply by allowing combustion of the charge to continue for the duration of two cycles. Since pressure-gain wave-rotor cycles always have incomplete purging, there is the opportunity for each particle of charge to complete combustion before expansion to exhaust. Injection of recirculated hot gas can be provided at both ends to ensure early ignition and complete combustion. In effect, this results in four flame sites during the confined pressure-rise combustion periods, while the naturally reduced reaction rates during the low-pressure periods helps to preserve the wave-rotor thermodynamic benefit.

An additional benefit of the slow-burn throughflow dual cycle is that it allows almost the full length of the channel to come in contact with fresh cold gas, resulting in a very favorable wall temperature profile. It may be possible to extend the dual cycle idea to multi cycles, where combustion of each charge continues for more than two cycles, if the exhaust expansion is weaker and a smaller fraction of combusted gas is exhausted per cycle. Throughput and pressure gain will be affected, and the optimal design will depend on the design wave-rotor temperature ratio.

It is evident from this discussion that there are many design possibilities for internal combustion wave rotor cycles. The development of the simulation code described here opens the door to further examination of such concepts.

Acknowledgments

This work was performed while the first author was a National Research Council–NASA Lewis Research Center Research Associate.

References

Colella, P., Majda, A., and Roytburd, V., 1986, "Theoretical and Numerical Structure for Reacting Shock Waves," *SIAM J. Sci. Stat. Comput.*, Vol. 7, No. 4.

Heywood, J. B., 1988, *Internal Combustion Engine Fundamentals,* McGraw-Hill, New York.

Larrouturou, B., 1991, "How to Preserve the Mass Fractions Positivity When Computing Compressible Multi-component Flows," *J. Comput. Phys.*, Vol. 95, pp. 59–84.

Magnussen, B. F., and Hjertager, B. H., 1976, "On Mathematical Modeling of Turbulent Combustion With Special Emphasis on Soot Formation and Combustion," *16th Symposium (International) on Combustion,* Combustion Institute, pp. 719–729.

Nalim, M. R., 1994, "Wave Cycle Design for Wave Rotor Engines With Limited Nitrogen Oxide Emissions," Ph.D. Thesis, Cornell University, Ithaca, NY.

Nalim, M. R., 1995, "Preliminary Assessment of Combustion Modes for Internal Combustion Wave Rotors," AIAA Paper No. 95-2801; NASA TM-107000.

Paxson, D. E., 1992, "A General Numerical Model for Wave Rotor Analysis," NASA TM-105740.

Paxson, D. E., 1995a, "A Comparison Between Numerically Modeled and Experimentally Measured Wave Rotor Loss Mechanisms," *AIAA Journal of Propulsion and Power,* Vol. 11, No. 5, pp. 908–914.

Paxson, D. E., 1995b, "A Numerical Model for Dynamic Wave Rotor Analysis," AIAA Paper No. 95-2800; NASA TM-106997.

Paxson, D. E., and Wilson, J., 1995, "Recent Improvements to and Validation of the One Dimensional NASA Wave Rotor Model," NASA TM-106913.

Roe, P. L., 1986, "Characteristic-Based Schemes for the Euler Equations," *Ann. Review of Fluid Mech.*, Vol. 18, pp. 337–65.

Shreeve, R. P., and Mathur, A., eds., 1985, *Proc. 1985 ONR/NAVAIR Wave Rotor Research and Technology Workshop,* Naval Postgraduate School, Monterey, CA.

Welch, G. E., Jones, S. M., and Paxson, D. E., 1995, "Wave Rotor Enhanced Gas Turbine Engines," AIAA Paper No. 95-2799; NASA TM-106998, ARL-TR-806.

A Numerical Investigation of the Startup Transient in a Wave Rotor

D. E. Paxson
NASA Lewis Research Center,
Cleveland, OH 44135

The startup process is investigated for a hypothetical four-port wave rotor, envisioned as a topping cycle for a small gas turbine engine. The investigation is conducted numerically using a multi-passage, one-dimensional CFD based wave rotor simulation in combination with lumped volume models for the combustor, exhaust valve plenum, and rotor center cavity components. The simulation is described and several startup transients are presented which illustrate potential difficulties for the specific cycle design investigated. In particular it is observed that, prior to combustor light-off, or just after, the flow through the combustor loop is reversed from the design direction. The phenomenon is demonstrated and several possible modification techniques are discussed that avoid or overcome the problem.

Introduction

The wave rotor is currently being investigated for use as a topping cycle for future gas turbine engines. The device, shown schematically in Fig. 1, uses gas dynamic waves to transfer energy directly to and from the working fluid through which the waves travel. Typically, it consists of a series of constant-area passages that rotate about an axis. Through rotation, the ends of the passages are periodically exposed to various circumferentially arranged ports, which initiate the traveling waves within the passages. The particular location of the ports determines the thermodynamic cycle of the working fluid. When used as a gas turbine topping cycle, the gas path is such that each passage of the wave rotor is periodically exposed to both hot and cold flow. The mean temperature of the rotor material is therefore considerably below the peak cycle temperature. This feature, combined with the relatively efficient nature of unsteady gas dynamic work transfer, and low rotational speed make the wave rotor a strong potential candidate for achieving high peak cycle temperatures and pressures without resorting to advanced materials. Steady-state simulations of the wave rotor, in a topping cycle environment, using validated numerical codes, have shown favorable performance both on and off-design (Welch et al., 1995). Promising experimental results have also been demonstrated by Klapproth (1960), Moritz (1985), and Thayer (1985). Unsteady simulations (i.e., time-dependent boundary conditions) have indicated that the wave rotor responds very rapidly to transient input, and is quite robust even when the magnitudes of the transient input perturbations are severe (Paxson, 1995a).

In most of the published analytical, numerical, and experimental literature, however, it is assumed that the wave rotor is already running. That is to say, the simulations (or experiments) are approximately centered about the design point. The question of how to actually start a wave rotor is an important one and is particularly relevant to the NASA Lewis Research Center, where a prototype four-port wave rotor is presently being fabricated for testing. It is not obvious what the wave patterns look like in the extreme off-design regime of startup, or even if a wave pattern can easily be established. In the literature on past wave rotor experiments, little has been written regarding the starting procedure; however, several publications suggest that it was not trivial. Klapproth (1960) mentioned the use of a propane pilot burner in order to accurately control the temperature in the combustor loop during startup. Zehnder et al. (1989) described a bypass valve for starting a diesel engine equipped with a wave rotor super-charging system. Moritz (1985) suggested that a wave rotor topped gas turbine may not start conveniently, although no explanation was given for this conclusion.

The present paper examines the starting process for a particular wave rotor using a numerical wave rotor simulation (Paxson, 1995a) as the test environment. It is noted that there are many conceivable wave rotor cycles for many types of applications and that the starting process may vary from one cycle to the next. The focus in this paper is on a hypothetical through-flow, four-port wave rotor, which would be used as a topping cycle for a small gas turbine engine. The term "through-flow" refers to the fact that the flow from the upstream compressor travels from one end of the wave rotor to the other before being sent to the combustor (Welch et al., 1995).

In the pages that follow, details of the wave rotor under investigation will first be presented. A brief description of the numerical simulation will then be given along with the associated simplifying assumptions. Following this, several hypothetical wave rotor start transients will be shown and discussed. The numerical results will show that starting scenarios exist where the flow in the combustor loop is reversed from the design direction. It will also be shown, however, that with careful control of fuel flow and rotor speed, or with some augmentation to the rotor design such as the addition of an injection valve in the combustor loop or modification of the timing in the port leading from the combustor, this phenomenon can be avoided or overcome.

Wave Rotor Description

The specific dimensions and design point operating performance of the wave rotor under consideration may be found in Table 1. The gas turbine engine it is intended to top has a compressor pressure ratio of approximately 8 at the design point. The wave rotor ducts are placed at angles to the axis of rotation that allow it to be self-driven under normal operating conditions; however, for the startup operations to be examined it is assumed that an independent drive motor is available. The rotor passages are aligned with the axis of rotation, and have constant trapezoidal cross section. The placement of the ports, their angles, and a computed design point wave pattern for this wave rotor may be seen in Fig. 2. This figure shows the time-averaged (averaged over the time required for one rotor passage

Contributed by the International Gas Turbine Institute and presented at the 41st International Gas Turbine and Aeroengine Congress and Exhibition, Birmingham, United Kingdom, June 10–13, 1996. Manuscript received at ASME Headquarters February 1996. Paper No. 96-GT-115. Associate Technical Editor: J. N. Shinn.

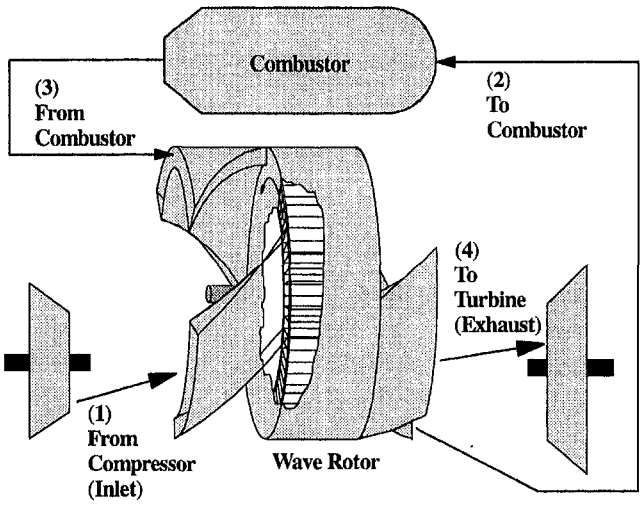

Fig. 1 Wave rotor schematic

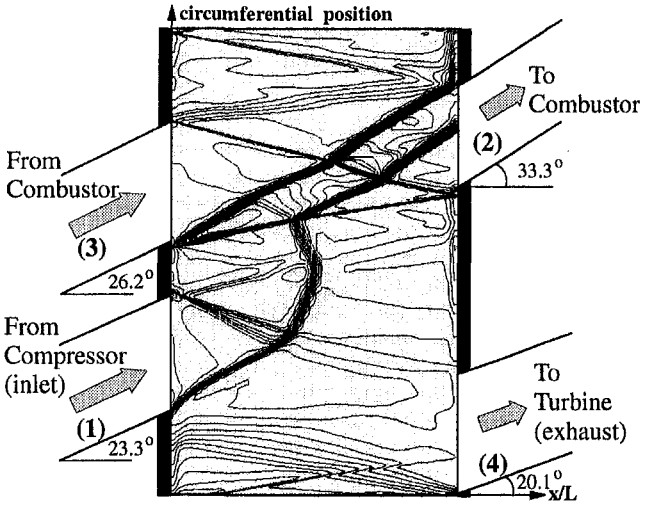

Fig. 2 Port placement and time-averaged design point wave pattern

to traverse a given point) contours of gas density in the passages for one cycle of the wave rotor. The contours were computed using a one-dimensional CFD simulation code, which follows a single passage of the wave rotor as it rotates past the various ducts (Paxson, 1995b, c). The numerical cell spacing in the passage was 2 percent of the length. The time step was set at 0.6 percent of the time required for a sound wave at the design point inlet stagnation temperature to travel from one end of a passage to the other. The throughflow nature of the cycle can clearly be seen in this figure by noting the movement of the inlet gas from left to right. It is interesting to note as an aside that this figure illustrates a recirculation of hot gas through the combustor at the design point. That is, for this four-port throughflow cycle, there is more gas traveling to and from the combustor than there is from the inlet.

Numerical Simulation Description

The wave rotor simulation used in this investigation has been described in detail elsewhere (Paxson, 1995a). As such, only a brief description will be provided here in order to maximize space for presentation of results and discussion. The simulation layout is shown schematically in Fig. 3. The gas dynamics in each passage of the wave rotor itself are modeled using a high-resolution one-dimensional, perfect gas CFD code, which integrates the Euler equations with a source term. The source term accounts for losses due to boundary layer viscous effects, heat transfer to and from the passage walls, and leakage to and from the center cavity inside the rotor housing. Boundary conditions for the port regions of the code are supplied as stagnation states. These are either provided directly by the user, as in the case of the port leading from the upstream compressor, or calculated by several lumped volume models of the external components.

Table 1 Wave rotor dimensions and design point performance

Mean Rotor Radius	8.15 cm.	(3.2 in.)
Rotor Length	15.24 cm	(6.0 in.)
Rotor Passage Height	2.18 cm.	(0.86 in.)
Rotational Speed	16800 rpm	
Cycles/Revolution	2	
Number of Passages	52	
Mass Flow Rate	2.3 kg/s	(5.0 lbm/s)
P_4/P_1 (Fig. 1 or 2)	1.23	
T_4/T_1	2.21	

These external components consist of the combustor, which couples two of the ports (ports 2 and 3), and the plenum linking the exhaust valve to the exhaust port (port 4). The rotor center cavity, to and from which leakage occurs, is also modeled as a lumped volume component. This cavity is comprised of the empty space inside the rotor housing that is not occupied by the rotor itself. The pressure difference between the cavity and the gas in the passages, together with the specified gap between rotor and endwalls, governs the leakage flow via a source term in the first and last computational cell of each passage. In this paper, the term lumped volume means that the kinetic energy of the flows in the components is assumed low. Thus, they are modeled using only mass and energy conservation equations. The energy equation for the combustor component contains a term that allows for external heat addition. This term simulates energy into the system, which is derived from burning the fuel. It is noted that such a model does not account for the added mass of fuel to the system, nor does it account for the delay between fuel injection and heat release. It does not seem likely, however, that either of these shortcomings will significantly affect the results to be presented. The rate of heat addition (i.e., simulated fuel flow), is assumed to be externally controlled. Additionally, the area of the exhaust valve, which simulates the downstream turbine, is assumed externally controlled; however,

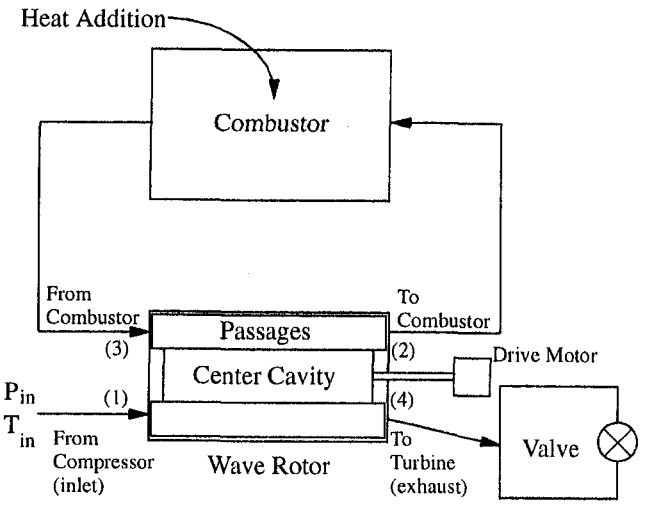

Fig. 3 Simulation schematic showing modeled components

in this study, the area was held constant at the value prescribed by the design operating point.

The stagnation boundary conditions supplied by the user, or component models are used by each passage in the CFD code to determine the state of the so-called image cell at the next instant of time. The code is capable of assessing whether a given condition will lead to inflow or outflow in a given passage. This allows robust operation of the simulation even in far off-design conditions where a portion of the flow in a given port may be into the rotor and a portion out of the rotor. For outflow conditions, only the boundary pressure is used, and although specified as stagnation, it is treated as a static value. For inflow conditions, some accounting is made if the flow in the duct is not aligned with the passage (i.e., shaft work into the system). For both inflow and outflow conditions, accounting is made at the boundaries for the effects on the flow of those passages that are only partially opened to a port: so-called finite opening effects. The ducts leading to and from the ports are assumed loss free (isentropic); however, a constant-area mixing calculation is used in outflow ports to account for losses due to nonuniformities in the flow and a stagnation pressure loss proportional to the square of the mass flow is imposed on the flow going through the combustor loop. No accounting is made for losses incurred due to the finite thickness of the passage walls.

In order to avoid undue demand on the computing resources, a rather large numerical spacing was used for the simulation results to be presented. Unless otherwise stated, each numerical cell of each passage in the wave rotor code was 10 percent of the length. The corresponding time step was set at 5 percent of the time required for a sound wave at the design point inlet stagnation temperature to travel from one end of a passage to the other. Such crude grid spacing obviously leads to inaccuracies in the results; however, given the extreme off-design conditions in which the code is running, the errors incurred from crude grid spacing are likely no worse than those that arise from several of the simplifying assumptions made in the model (i.e., one-dimensional flow, loss-free ducts, uniform static pressure across outflow ports, etc.) and none are sufficiently severe as to invalidate the results.

It is noted that the simulation described above does not include a model for the upstream compressor. The stagnation conditions in the inlet are simply specified. In reality, there would be a high degree of dynamic interaction between the compressor and the wave rotor, including possible system instabilities. Investigations into these sorts of interactions are planned.

Simulation Results

The results to be presented below are divided into several simulation scenarios, which illustrate various aspects of the starting process. Each scenario is labeled with a letter and a brief descriptor. In the subsequent discussion, the various scenarios are referred to by letter. Although many system variables are informative, only the port mass flow rates, plenum pressures, and controlled variables (i.e., rotor speed and heat addition rate) will be presented in the following time trace plots. The mass flow rates are normalized by the design point inlet mass flow rate. The pressures are normalized using atmospheric pressure. The rotor speed is shown as a fraction of the design point value. The data output interval from the simulations was short enough to capture fluctuations in system variables caused by passage opening and closing in the ports; however, the data shown in the time traces have been smoothed in order to eliminate this effect. For all of the simulation scenarios the pressure downstream of the exhaust valve was held at the standard atmospheric value.

Scenario A: Initial Spoolup Without Heat Addition. The initial phase of the start process establishes flow through the rotor with no heat added to the combustor. In an engine environment this would presumably occur by simultaneously spooling the upstream compressor and wave rotor up to some low speed. Figure 3 shows the simulated results of such a process. The spooling of the upstream compressor was simulated using a linear rise in the wave rotor inlet stagnation pressure from atmospheric to 30 percent above atmospheric over the first 1.0 second period of the simulation. After this it was held constant. The corresponding inlet stagnation temperature was calculated assuming a compressor efficiency of 0.7. The rotor was linearly accelerated from 1.8 to 32 percent of the design rotational speed (2.6–44 percent of the corrected rotational speed) over the initial 2.0 seconds of simulation time after which it was held constant. Figure 4 shows time traces of the four port mass flow rates, and the combustor and exhaust plenum pressures. Also shown for reference are the inlet pressure and the rotor speed schedules. The rotor acceleration was chosen to be slow enough such that all of the flow quantities were essentially in equilibrium. Thus, although the rotor speed was increasing, the flow quantities at any instant of time are essentially steady-state results. This may be seen by noting that the inlet and exhaust port mass flow rates are nearly coincident as are those leading to and from the combustor. Furthermore, it can be seen that after the initial 2.0 second rotor acceleration period the flow quantities do not change. The salient feature of this plot is the apparently cyclic oscillation between forward and reversed flow in the combustor loop. The waves that exist in the rotor are quite weak during the startup transient; however, examination of the computed wave diagrams indicates that these oscillations are related to the number of reflections, and their location relative to the ports leading to and from the combustor, of the weak shock generated by the closing of the exhaust port (port 4 in Fig. 3).

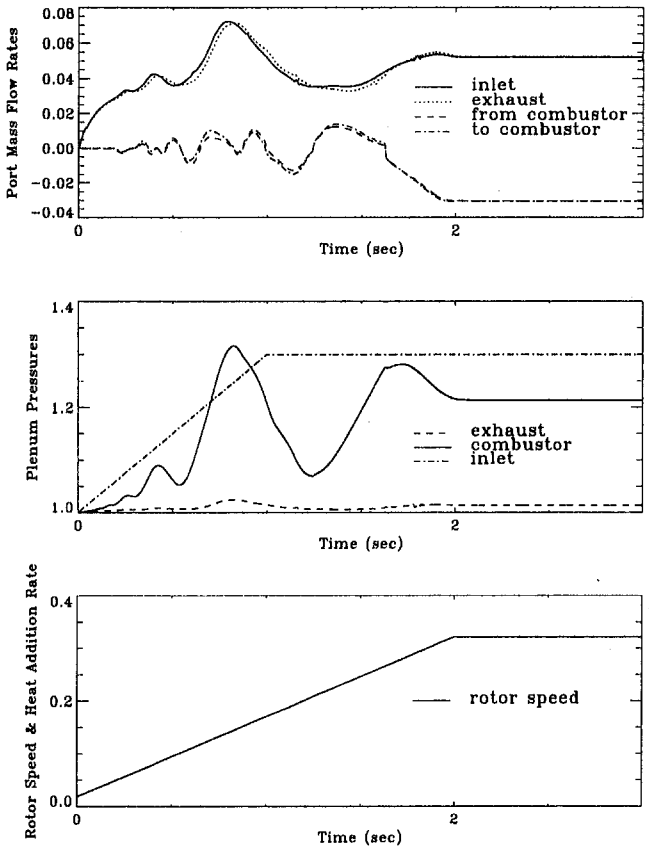

Fig. 4 Time traces of flow quantities for Scenario A: initial spoolup without heat addition

Scenario B: Continued Constant Rotor Acceleration Followed by Ramp Heat Addition Rate Increase. The rotor speed from Scenario A at which the largest forward combustor

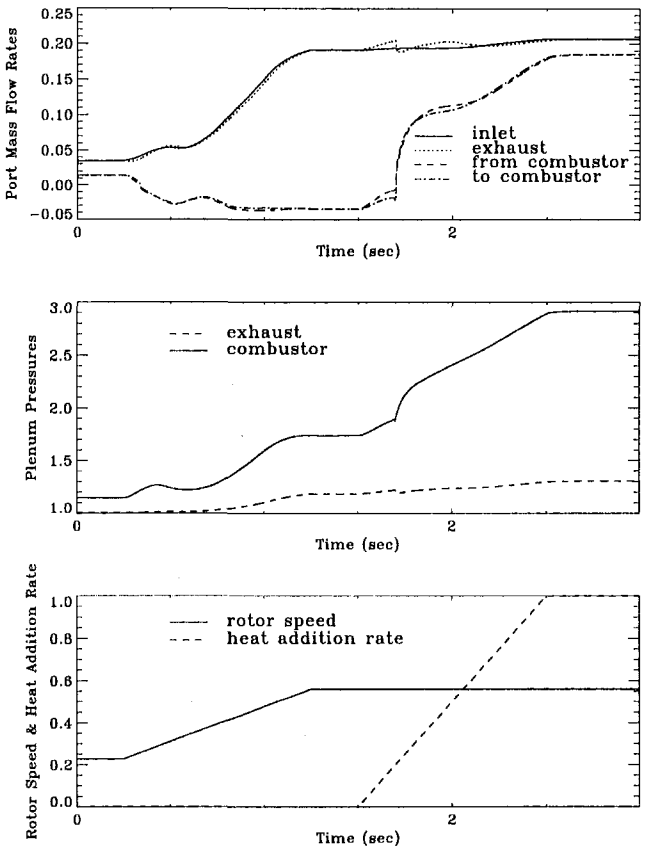

Fig. 5 Time traces of flow quantities for Scenario B: continued rotor acceleration followed by ramp heat addition rate increase

loop flow occurred was used as the starting point for all of the remaining simulations to be discussed. This speed was found to be approximately 23 percent of the design speed. The upstream compressor pressure ratio was maintained at 1.3. Figure 5 shows the results of a further constant rotor acceleration followed by combustor heat addition. The rotor speed was held constant for the first 0.25 s, then increased over a 1.0 second period to 56 percent of design speed, where it was maintained for the remainder of the simulation. At 1.5 s, the heat addition rate (i.e., fuel flow rate) was increased linearly from 0.0 to 4.9 percent of the design point value over a 1.0 second interval, after which it was held constant. The final values of rotor speed and heat addition rate were chosen because, at steady state, they result in a favorable idle position where there is zero net torque on the rotor (i.e., no drive motor necessary) and a pressure ratio across the wave rotor, P_4/P_1 slightly above unity. The plotted quantities of Fig. 5 are the same as those in Fig. 4, except the constant inlet pressure is not shown and the heat addition rate is presented as a fraction of the final idle value. It can be seen in this plot that, prior to the addition of any heat, further increases in rotor speed do not yield forward combustor loop flows. In fact, the flow through the combustor loop becomes more negative as rotor speed is increased above the 23 percent of design speed setting. It is interesting to note that prior to any heat addition, the inlet mass flow rate increases steeply with rotor speed. This is due to the establishing a favorable wave pattern (i.e., waves terminating and originating at port opening and closing positions) in the inlet and exhaust port section of the wave rotor. It is also interesting that, once the idle rotor speed has been reached, the inlet and exhaust mass flow rates are relatively insensitive to the subsequent and large changes in the combustor loop mass flow rates. As the heat addition rate is increased (from zero) it is seen that the combustor pressure rises and the flow through the combustor loop approaches zero. At approximately 1.7 seconds there is an abrupt change in flow direction, which is followed in turn with a rapid increase in the mass flow rate. Once forward flow has been established in the combustor loop, the system approaches the steady state idle in a smooth fashion.

For reference, the steady-state idle wave pattern is shown in Fig. 6 in the form of time-averaged density contours as was done for Fig. 1. Figure 6 was made using the same single passage (steady-state) code described for Fig. 1. The numerical grid spacing was again, 2 percent of the passage length. The time step was set at 0.1 percent of the time required for a sound wave at the design point inlet stagnation temperature to travel from one end of a passage to the other.

The starting sequence described above (rotor acceleration followed by heat addition) is undesirable due to the initially reversed combustor loop flow. It is not practical to light a conventional combustor with reversed flow. Thus, this scenario would require some sort of auxiliary pilot flame, or other heat source, in the combustor that would be insensitive to flow direction.

Scenario C: Simultaneous Constant Rotor Acceleration and Ramp Heat Addition Rate Increase. Although the results are not presented here due to space constraints, it was found that reversed flow in the combustor loop also occurred when heat was added to the system prior to rotor acceleration (e.g., essentially the opposite sequence of Scenario B). When both the rotor speed and the heat addition rate were simultaneously increased, however, it was found that the startup sequence proceeded without reversed combustor loop flow. The results are shown in Fig. 7. The rates and limits are the same as in Scenario B; however, both were initiated at 0.25 s. As with the previous two scenarios, the system appears to be operating in a nearly steady-state fashion throughout most of the simulation. This suggests that the four port, throughflow wave rotor may be started in general by coupling the heat addition rate (i.e., fuel flow) to the rotor speed, although the optimal relationship will not necessarily be linear as is shown here. It is doubtful, however, that conventional combustors have this sort of fine control capability in the very low fuel flow range of operation. Thus, it is probable that the start sequence described here would again require an auxiliary heat source.

Scenario D: Step Minimum Heat Addition Rate and Simultaneous Rotor Acceleration. A more appropriate representation for the heat addition rate during the early portion of startup would probably be a step increase to some fraction of

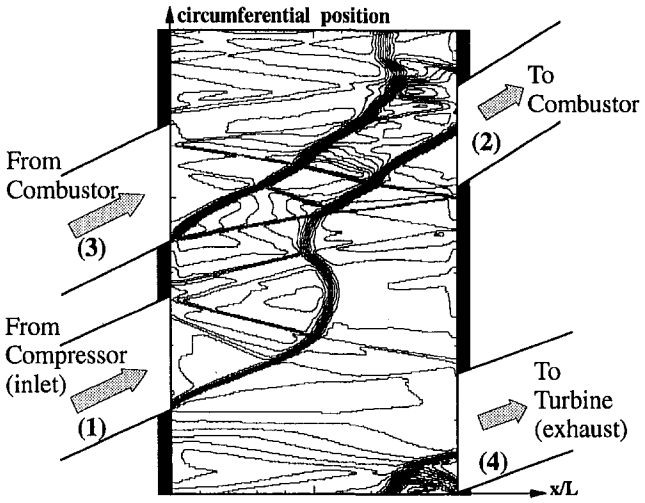

Fig. 6 Idle point time averaged wave pattern shown as contours of density

the idle value. This would simulate the initial combustor light-off. Following this would be a ramp increase (linear or otherwise) up to idle. Although the results are again not shown due to space limitations, it was found that, starting from the same steady-state operating point as Scenario B, without increasing the rotor speed, a step increase of the heat addition rate to less than 11 percent of the idle value (0.6 percent of design) was enough to cause flow reversal in the combustor loop. Presumably, there is some minimum fuel flow level required in order to establish a flame in the combustor and it is assumed here to be larger than 0.6 percent of design. For this study, a minimum value for the heat addition rate of 1.2 percent of design (25 percent of the idle value) was chosen for the initial step to simulate combustor light-off. What was sought was the minimum rotor acceleration that would maintain forward flow through the combustor. Due to the simplicity of the combustor model, no consideration was given as to whether the flow of fresh air was sufficient to maintain a flame. Assuming Fig. 7 to be essentially steady state (though not optimal), the final rotor speed was chosen, which corresponded to the 1.2 percent of design step heat addition rate. This rotor speed was found to be approximately 31 percent of design value. The wave diagram for this steady-state post-lightoff operating point is shown in Fig. 8 using the same technique as Fig. 6. A true minimization process would have involved many simulation runs. The objective in this paper is simply to demonstrate a concept. As such the rotor acceleration minimization process was considered complete when a value less than or equal to that used in Fig. 7 was obtained, which would maintain forward flow through the combustor loop. It was found that a constant rotor acceleration rate from 23–31 percent of design speed over a 0.49 second interval (292.7 rad/s^2) would fit this criterion. The results are shown in Fig. 9. The acceleration and step rise in heat addition were commenced simultaneously at 0.25 s. The plotted quantities are the same as in Fig. 7. An estimate of the torque required for the plotted rotor acceleration yielded a value of approximately 18.0 N-m (13.3 ft-lbf). This was obtained using an approximation for the rotor moment of inertia and an assumed material density of 7860 kg/m^3. The bearings were assumed frictionless and drag between rotor and housing was assumed negligible. The instantaneous power requirement of the starting motor during the acceleration was thus found to vary linearly from 7.3 to 9.8 kW (9.7–13.0 h.p.). These are large values for an engine of this size, particularly in light of what is already required by starter motor for the upstream compressor. As such, Scenario D would not be practical for an aircraft engine but may be acceptable in other applications.

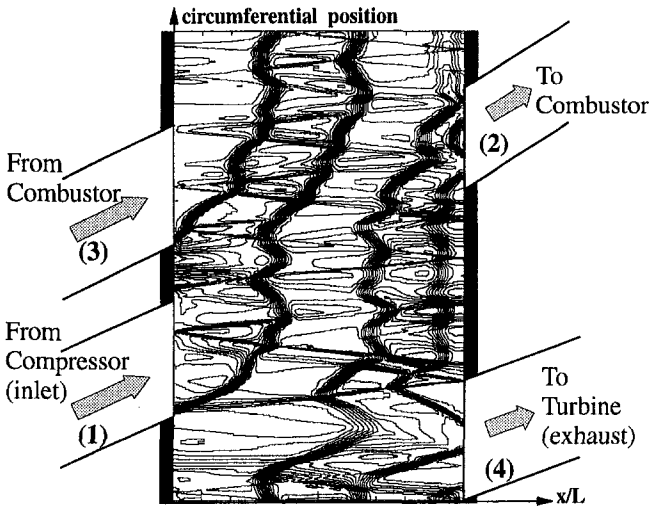

Fig. 8 Post-lightoff time-averaged wave pattern shown as contours of density

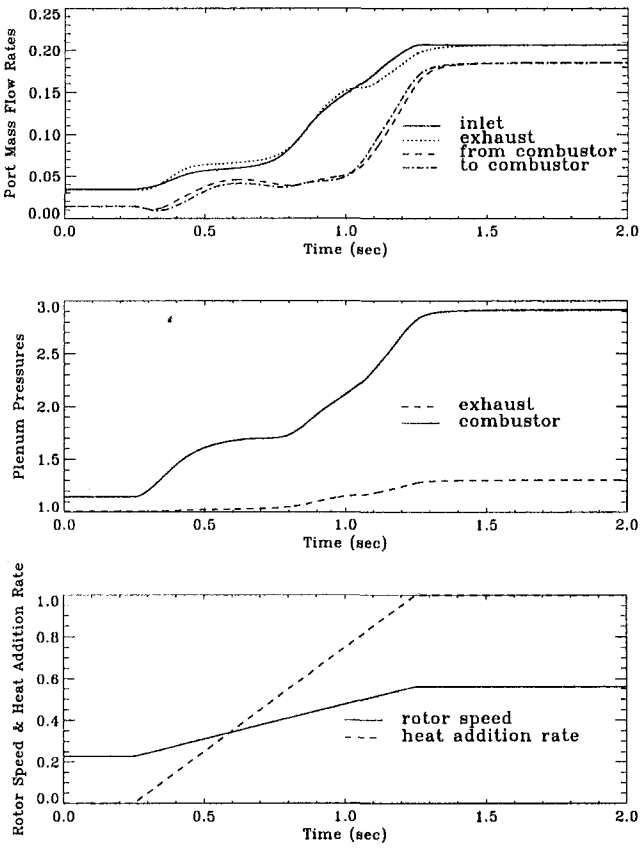

Fig. 7 Time traces of flow quantities for Scenario C: simultaneous constant rotor acceleration and ramp heat addition rate increase

Scenario E: Combustor Plenum Mass Injection. The investigation thus far has centered around starting methods, which do not require augmentation of the wave rotor other than providing a drive motor. It is worthwhile to consider now some simple augmentations to the wave rotor design, which might make the starting process somewhat more robust. One possibility is to add bleed and/or injection valves. Another possibility is to allow for small changes to the timing of one or several ports. These techniques will be explored in the following two scenarios.

For the injection or bleed technique, the valves could be placed either in plenum locations or strategically on the rotor endwalls. In the latter location, of course, they are essentially acting as extra ports and thus, the wave rotor is no longer a four-port device. In this paper, only the results of plenum injection will be presented. In particular, a valve was added to the combustor plenum, similar to the exhaust port valve, which had a source pressure that could be independently specified. The valve was designed as a check valve such that if the combustor pressure rose above the source pressure, the valve was closed. It is noted in passing that a similar bleed valve on the combustor was also investigated (e.g., flow from the combustor to atmosphere); however, the results did not indicate beneficial performance.

Before examining the combustor injection valve concept, it is instructive to examine briefly a shutdown type process from the steady-state idle condition. The reason for this is that the simulation results demonstrate a form of hysteresis, which suggests that combustor mass flow injection will be effective. Furthermore, the results give an idea of the source pressure required for the injector. Figure 10 shows time traces for such a shutdown procedure. The wave rotor was held at the idle state for 0.25 s, at which time the heat addition rate was abruptly set to zero.

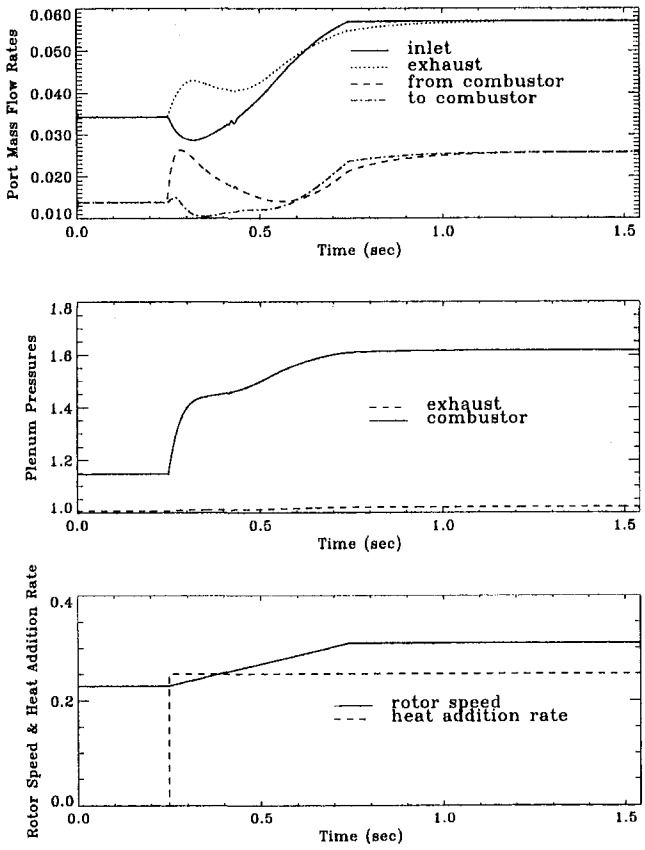

Fig. 9 Time traces of flow quantities for Scenario D: step minimum heat addition rate and simultaneous rotor acceleration

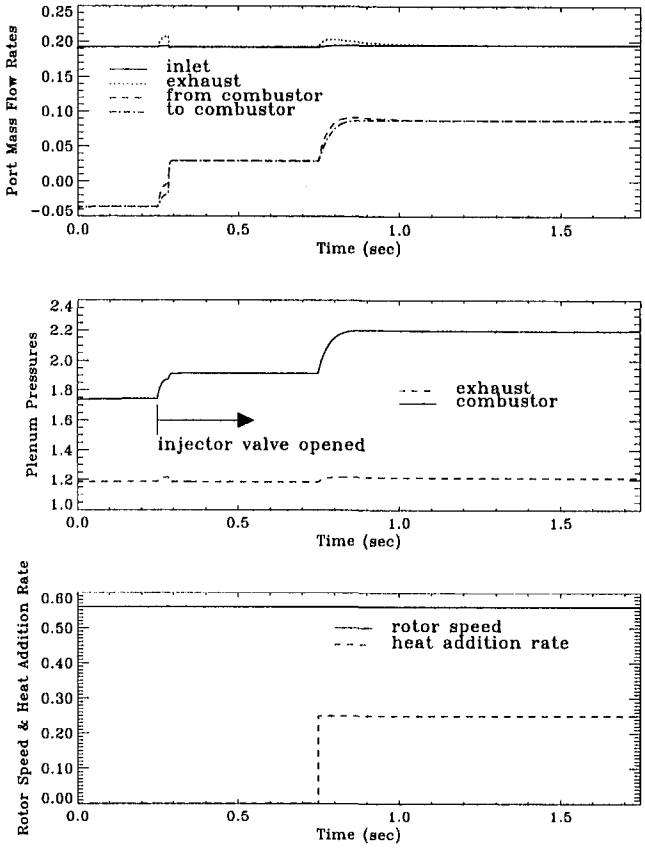

Fig. 11 Time traces of flow quantities for Scenario E: combustor plenum mass injection

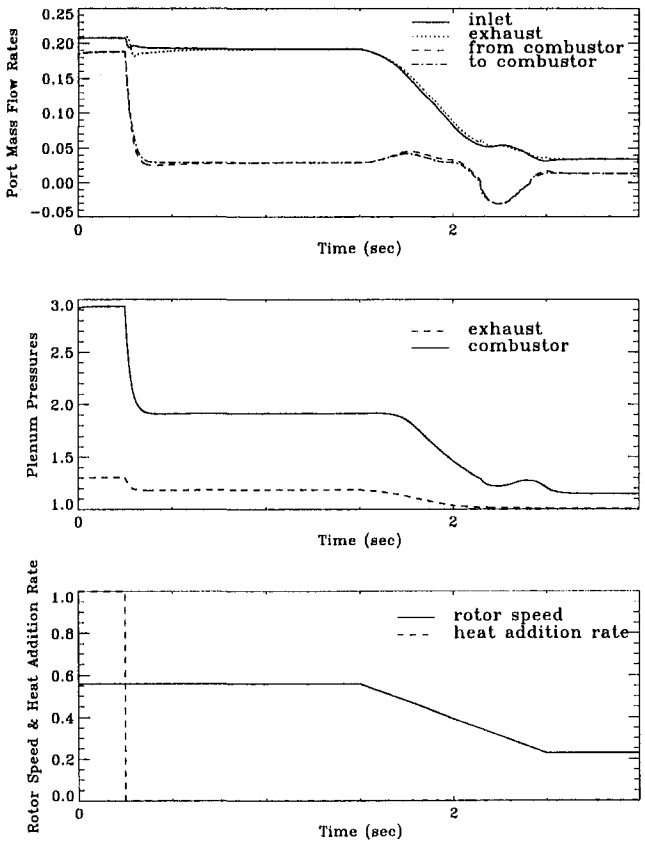

Fig. 10 Time traces of flow quantities for a shutdown from idle

After reaching steady-state operation, the rotor speed was slowly reduced from the idle value to the initial 23 percent of design value used at the start of Scenarios B, C, and D. The interesting feature of this figure is that at the idle speed, and even somewhat below, the combustor loop flow direction remains positive even without heat addition. This behavior should be compared to Scenario B (Fig. 5) where the combustor loop flow is in the reverse direction prior to any heat addition. Examining Fig. 10, it can be seen that during the interval where the combustor loop flow is in the forward direction, after the heat addition has been removed, the combustor pressure is higher at any rotor speed than the combustor pressure at the same speed in Fig. 5. Furthermore, the pressure is higher than the wave rotor inlet pressure. This observation suggests that the combustor loop flow might be induced to move in the proper direction during startup if the following procedure were employed. The rotor is first accelerated to the idle speed, as in Scenario B. The inlet pressure is assumed to be at the same value of 1.3 times atmosphere used in the other simulations. The combustor injector valve described above is then opened with an external source pressure corresponding to the combustor pressure in Fig. 10. Once the combustor loop flow is moving in the correct direction, the valve will shut and the combustor can be ignited. This process is illustrated in Fig. 11. The simulation commenced after the rotor had been accelerated to the idle speed of 56 percent of design and reached steady state. At 0.25 seconds the injector valve was instantaneously opened to a position such that the cross-sectional area was 16 percent of the exhaust valve area (3.6 cm^2). The source pressure for this injector was, from Fig. 10, approximately 1.91 times atmospheric. Since the injector valve was assumed to be a check valve, it was closed when the combustor pressure exceeded this value. The source temperature was chosen to be 289 K (520 R). At 0.75 s, the heat addition rate was stepped up from zero to the lightoff value of

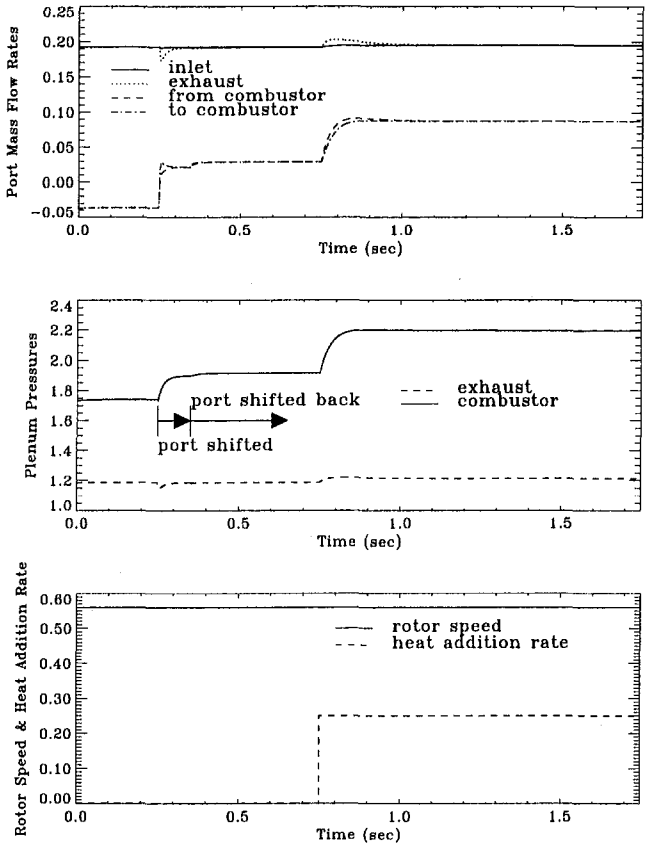

Fig. 12 Time traces of flow quantities for Scenario F: variable combustor port timing

1.2 percent of design (25 percent of idle). It is seen that the combustor injector did, indeed, induce forward combustor loop flow and that the subsequent lightoff process was smooth with forward flow maintained through the combustor. The calculated total mass flow through the combustor injector valve during this transient was 0.0024 kg (0.0052 lbm). This is a low value and could conceivably be supplied in an engine environment by a small tank of stored compressed air.

Scenario F: Variable Combustor Port Timing. Since the reversed combustor loop flow problem results from wave patterns established by the port locations, it is natural to consider solutions that modify their position. Although a systematic study of the flowfield sensitivity to the location of each port was not performed, it was found that changing the location of the opening for the port leading from the combustor could affect a change in the combustor loop flow direction. This is illustrated in Fig. 12. This simulation commenced with the same boundary conditions as Scenario E (i.e., 56 percent of design speed, inlet pressure 1.3 times atmosphere). At 0.25 seconds the position at which the port coming from the combustor opens was instantaneously shifted in the direction of rotation by 21.1 deg. At 0.35 seconds it was instantaneously shifted back to the original location. From there the combustor lightoff procedure was identical to Scenario D, with similarly smooth results. This lightoff procedure appears promising as long as the complexity associated with blocking off a portion of the port coming from the combustor is not prohibitive.

Concluding Remarks

The starting process for a four-port throughflow wave rotor was demonstrated using a multipassage, one-dimensional numerical simulation. It was found that, without augmentation to the configuration shown in Figs. 2 and 3, the wave rotor would exhibit reversed flow in the combustor loop. Once started, the flow reversal could be eliminated by increasing the heat addition rate to the system; however, this is undesirable since it necessitates an auxiliary flame source (conventional combustors cannot operate with reversed flow). It was found that the reversed flow scenario could be avoided entirely by accelerating the rotor as the combustor is ignited (i.e., at lightoff). Whether or not this is a practical starting scenario is unknown. If the combustor could deliver a highly controllable flame down to very small values of heat addition to the system, then such a technique could work. Given the current combustor technology, it is more likely that the lightoff process requires a minimum amount of heat addition, which is relatively substantial. In this case, it appears that such a technique requires a rather large motor in order to rapidly accelerate the wave rotor. Furthermore, it is unlikely that a required transient process is an acceptable procedure.

A more promising startup scenario was obtained when an injector valve was added to the simulation combustor plenum. In this case, forward flow could be induced in the combustor loop prior to lightoff and the lightoff could proceed without incident. The required driving pressure for this valve was higher than the 1.3 times atmospheric inlet pressure. In an engine environment, this would necessitate an external supply of air; however, the total valve mass flow necessary to establish forward combustor loop flow was quite small, suggesting that the external air supply could consist of a small pressure vessel, which would be recharged from compressor bleed during normal engine operation.

A second successful start scenario was obtained when the location of the opening for the port leading from the combustor was allowed to shift. Shifting it in the rotational direction induced forward flow through the combustor loop. Whether or not the mechanical difficulty associated with a movable port is practical is unknown.

It is recognized that there are many other modifications that could be considered in order to make this particular type of wave rotor start reliably. Furthermore, it is noted that other types of topping cycles (e.g., four-port, reverse-flow, five-port, etc.) may not exhibit combustor loop flow reversal, and hence may be inherently easier to start. The intentions of this paper were to demonstrate the potential problems that exist for a four-port, throughflow wave rotor, to describe some reasonable, preliminary solutions, and to illustrate the insight that may be obtained using a numerical simulation such as the one described.

References

Klapproth, J. F., 1960, "The Wave Engine Project," General Electric Quarterly Reports, R60FPD284, R60FPD419, & R60FPD585.

Moritz, R., 1985, "Rolls-Royce Study of Wave Rotors 1965–1970," Shreeve, R. P., and Mathur, A., eds., *Proc. 1985 ONR/NAVAIR Wave Rotor Research and Technology Workshop,* Report #NPS-67-85-008, Naval Post-Graduate School, Monterey, CA.

Paxson, D. E., 1995a, "A Numerical Model for Dynamic Wave Rotor Analysis," AIAA Paper No. 95-2800.

Paxson, D. E., 1995b, "Recent Improvements to and Validation of the One Dimensional NASA Wave Rotor Model," NASA TM 106913.

Paxson, D. E., 1995c, "Comparison Between Numerically Modeled and Experimentally Measured Wave-Rotor Loss Mechanisms," *AIAA Journal of Propulsion and Power,* Vol. 11, pp. 908–914.

Thayer, W. J., 1985, "Energy Exchanger Performance Measurements and Projections," Shreeve, R. P., and Mathur, A., eds., *Proc. 1985 ONR/NAVAIR Wave Rotor Research and Technology Workshop,* Report #NPS-67-85-008, Naval Post-Graduate School, Monterey, CA.

Welch, G. E., Jones, S. M., and Paxson, D. E., 1995, "Wave Rotor-Enhanced Gas Turbine Engines," Paper No. AIAA-95-2799.

Wilson, J., and Paxson, D. E., 1995, "Optimization of Wave Rotors for Use as Gas Turbine Engine Topping Cycles," SAE Paper No. 951411.

Zehnder, G., Mayer, A., and Matthews, L., 1989, "The Free Running Comprex," SAE Paper No. 890452.

Multidimensional Modeling of Combustion for a Six-Mode Emissions Test Cycle on a DI Diesel Engine

J. Xin
Research Associate.

D. Montgomery
Graduate Student.

Z. Han
Graduate Student.

R. D. Reitz[1]
Professor.

Engine Research Center,
Department of Mechanical Engineering,
University of Wisconsin—Madison,
1500 Engineering Dr.,
Madison, WI 53706

Numerical simulations of direct injection (DI) heavy-duty diesel engine combustion over the entire engine operating range were conducted using the KIVA code, with modifications to the spray, combustion, turbulence, and heat transfer models. In this work, the effect of the rates of species conversion from reactants to products in the combustion model was investigated, and a characteristic-time combustion model was formulated to allow consideration of multiple characteristic time scales for the major chemical species. In addition, the effect of engine operating conditions on the model formulation was assessed, and correlations were introduced into the combustion model to account for the effects of residual gas and Exhaust Gas Recirculation (EGR). The predictions were compared with extensive engine test data. The calculation results had good overall agreement with the experimental cylinder pressure and heat release results, and the multiple-time-scale combustion model is shown to give improved emissions predictions compared to a previous single-time-scale model. Overall, the NO_x predictions are in good agreement with the experiments. The soot predictions are also in reasonable agreement with the measured particulates at medium and high loads. However, at light loads, the agreement deteriorates, possibly due to the neglect of the contribution of SOF in the soot model predictions.

Introduction

Diesel engines are the primary heavy-duty power plant for both transportation and stationary use. Recently, the application of diesel engines has also been expanded to include automotive power sources, which used to be dominated by spark ignition (SI) engines. Due to the lean combustion associated with the nonhomogeneous combustion in diesel engines, diesel engines have superior energy efficiency and relatively low carbon monoxide emission. However, the nitric oxides (NO_x) and particulates emitted from diesel engines are pollutants of major concern. There are presently no efficient after-treatment methods to eliminate NO_x and particulates. Therefore, it is of interest to investigate measures to suppress NO_x and particulate formation within the combustion chamber.

The formation of NO_x and particulates depends on the mixing and combustion processes, which, in turn, are controlled by many engine design specifications, such as the injection pressure, nozzle hole sizes, combustion chamber geometry, induced swirl flows, and large-scale motion, as well as the running condition. It is very time consuming to explore new design concepts and to optimize design specifications experimentally. Therefore, there is a need to develop an accurate and efficient computer model to reduce the design-time cycle and cost, and to understand the mechanisms of mixing and combustion in diesel engine combustion chambers. A computer code for multidimensional chemically reacting flows (KIVA), initially developed by the Los Alamos National Lab (Amsden et al., 1989), has been used successfully in previous studies to predict heavy-duty diesel engine performance after many improved submodels were implemented (Rutland et al., 1994; Reitz and Rutland, 1995; Han and Reitz, 1995).

Although extensive computer simulations have been conducted, most of the previously mentioned numerical studies have been performed for a specific engine running condition, for instance, 1600 rpm, 75 percent load for a Caterpillar heavy-duty direct injection (DI) diesel engine (Rutland et al., 1994; Reitz and Rutland, 1995). As more and more stringent emission regulations are being introduced, newly developed diesel engines are expected to have low pollutant emissions over a wide range of running conditions in order to meet the emission standard under the federal transient test procedure. Thus, it is of extreme importance for a computer code to be capable of predicting engine performance over a wide range of operating conditions in order to be useful as an efficient tool for engine design and development. Objectives of the study were to evaluate the capability of the model to predict combustion and emissions of a DI diesel engine over its entire operating range, to provide more physical insight into the flow and combustion processes, and to identify where future model improvements are needed.

Experimental Setup

The test engine is an instrumented single-cylinder version of the Caterpillar 3400 series heavy-duty diesel engine. The engine is capable of producing 54 kW at a rated speed of 2100 rpm. Simulated turbocharging with intercooling is accomplished by metering compressed air into a temperature-controlled intake surge tank. An exhaust surge tank regulates the back pressure. Exhaust Gas Recirculation (EGR) was accomplished by a direct link between the exhaust and intake surge tanks. The back pressure was raised above the intake pressure to get the exhaust to flow into the intake surge tank when EGR was desired. Cooling of the recirculated exhaust gas was accomplished by installing a tube and shell heat exchanger.

The fuel system was an electronically controlled, common rail injector and its supporting hardware as described by Miyaki et al. (1991). This injection system is capable of single, double, triple, and quadruple injection schemes. Timing and duration

Contributed by the Internal Combustion Engine Division for publication in the JOURNAL OF ENGINEERING FOR GAS TURBINES AND POWER. Manuscript received at ASME Headquarters January 1997. Associate Technical Editor: W. K. Cheng.

could be varied independently for each injection pulse, providing a highly flexible injection system. The injector nozzle used has a 125 deg included spray angle. This spray angle has significant spray impingement on the piston crown, and has been shown to produce better emissions results than a nonimpinging 140 deg included-spray-angle injector nozzle (Pierpont et al., 1995).

Emissions data were calculated according to SAE J177 specifications. A sample of exhaust gas was routed through an ice bath, particulate filter, and a desiccant to remove particulate and water vapor before entering the gas analyzers. A full dilution tunnel designed following EPA 40CFR recommendations was used to measure total particulate. Testing was done at a baseline condition of 1600 rpm, 75 percent load as well as at six modes that constitute a six-mode federal transient procedure (FTP) simulation. The six running conditions (or modes) for the simulation chosen for this study are shown in Table 1. The running conditions were taken from the operating map of a six-cylinder production version of the Caterpillar 3400 series engine (435 hp 3406E). Further details of the experiments are given by Montgomery and Reitz (1996).

Model Description

The numerical calculations were performed using the KIVA-II code (Amsden et al., 1989) with improvements in the turbulence, gas/wall heat transfer, spray, ignition, combustion, NO_x, and soot models, as described by Han and Reitz (1995). The modified RNG $k-\epsilon$ model was used in the present study. It was assumed that the in-cylinder turbulent flow at intake valve closure is homogeneous; the initial value of k was assumed to be 160 percent of the kinetic energy based on the mean piston speed. Two initial k values (160 and 30 percent) were tested, and it was found that the effect of initial k values on combustion is negligible—the soot predictions differ by 10 percent. The initial value of ϵ was determined based on the assumed k and an assumed uniform length scale, which is 1.12 cm. The results were also found to be insensitive to the initial ϵ value. Diesel ignition and combustion are sensitive to the amount of residual gas present in the combustion chamber and the surrounding temperature (which depends on the initial temperature) of fuel sprays at the start of combustion. To account for these, modifications were introduced in the present study in the ignition and combustion models, as follows.

Ignition Model. In previous study by Kong and Reitz (1993), the Shell auto-ignition model (Halstead et al., 1977) was used with the introduction of generic molecular species. It was found that the formation rate of a labile intermediate species Q (Halstead et al., 1977) is the rate-limiting step in the kinetic path. The formation rate of Q is given by rate $= f_4 K_p$, where

$$f_4 = A_{f04} e^{-E_{f4}/RT} [O_2]^{x_4} [R]^{y_4} \tag{1}$$

Table 1 Engine conditions and measured engine-out conditions

running condition	mode 1 90/30MPa	mode 2	mode 3	mode 4	mode 5	mode 6	baseline 8BTDC/10BTDC
speed (rpm)	750	953	1074	1657	1668	1690	1600
% load	0	25	75	100	50	25	75
θ_{inj}	-6	0	6	6	0	-3	-6/-10
$\dot{m}_{fuel}$	0.5	2.0	6.4	10.2	5.4	3.2	7.7
$\dot{m}_{air}$	59.3	77.4	141.	324.	205.	168.	224.
T_{in} (K)	299	302	304	313	305	302	309
P_{in} (kPa)	100	108	168	239	164	132	183
T_{ex} (K)	401	549	887	906	700	573	812/787
P_{ex} (kPa)	100	112	144	220	164	143	159
NOx (g/kgfuel)	27.4/46.4	66.4	30.9	14.3	19.6	32.4	32.8/40.2
particulate (g/kgfuel)	10.1/1.6	0.39	1.09	1.41	2.1	0.733	0.62/0.54

and $E_{f4} = 3.0 \times 10^4$, $x_4 = -1$, $y_4 = 0.35$, and the rate K_p is given by Theobald and Cheng (1987) and Kong et al. (1995). The sensitivity of the ignition delay to the Q formation rate was investigated by Theobald and Cheng (1987) who found that the total delay is sensitive to the pre-exponential factor A_{f04}.

For the present six-mode engine simulations, the initial residual gas composition and temperature varies from one mode to another, and it is expected that the ignition delay depends on the gas composition. Therefore, the species Q formation rate was identified as an adjustable parameter. Accordingly, the constant A_{f04} was adjusted in each case such that the measured ignition delay was matched. The result of this procedure gave the A_{f04} values that are listed in Table 2. The results are adequately represented by the correlation

$$A_{f04} = \frac{446 - 1.25\, T_{ivc}}{P_{ivc}} \times 10^4 \tag{2}$$

where T_{ivc} and P_{ivc} are gas temperature and pressure at IVC, in K and bars, respectively. The initial chamber gas conditions (pressure, temperature, and residual gas mass fraction) at intake valve closure were calculated using a simplified computer code, which takes scavenging and back-flow effects into account (Senecal et al., 1996).

Combustion Model. Combustion was simulated by adopting a characteristic-time combustion model, initially developed for spark ignition engines by Abraham et al. (1985). Similar to the SI engine combustion model, the change rate of the partial density of species m is written as

$$\frac{d\rho_m}{dt} = -\frac{\rho_m - \rho_m^*}{\tau_{c,m}} \tag{3}$$

where ρ_m^* is the local and instantaneous thermodynamic equilibrium value of the partial density, and $\tau_{c,m}$ is the characteristic time to achieve such equilibrium. The computations were limited to the major chemical species whose inclusion is required for accurate predictions of combustion energy release (Reitz and Bracco, 1983). Previously, for simplicity, $\tau_{c,m}$ was assumed to be the same for the six species considered: fuel, O_2, CO_2, CO, H_2O, and H_2. The limitation of this assumption is obvious since it is likely that these species approach their equilibrium partial densities at different rates or characteristic times, depending on the nature of the reactions and mixing processes involved. In general, for the six species (C_nH_{2n+2}, O_2, H_2O, CO, CO_2 and H_2) and three atom (O, H, C) system, the characteristic time is a 3×3 matrix (Reitz and Bracco, 1983). In particular, if only the diagonal elements are nonzero, then three characteristic times for destruction of fuel, and H_2 and CO are to be specified. The conversion rates of other species can be calculated from the atom conservation equations. According to the characteristic time combustion model, the change rates of fuel, H_2, and CO are

$$\frac{d\rho_{\text{fuel}}}{dt} = -\frac{\rho_{\text{fuel}} - \rho_{\text{fuel}}^*}{\tau_{c,\text{fuel}}}, \quad \frac{d\rho_{\text{CO}}}{dt} = -\frac{\rho_{\text{CO}} - \rho_{\text{CO}}^*}{\tau_{c,\text{CO}}},$$

$$\frac{d\rho_{\text{H}_2}}{dt} = -\frac{\rho_{\text{H}_2} - \rho_{\text{H}_2}^*}{\tau_{c,\text{H}_2}} \tag{4}$$

and the change rates of CO_2, H_2O, and O_2 can be determined from the atom conservation equations.

In the standard implementation of the characteristic-time combustion model, the characteristic time $\tau_{c,m}$ is the same for all species and is composed of a turbulent-mixing time and a laminar chemical-kinetics time (Kong et al., 1995)

$$\tau_c = \tau_{c,m} = \tau_l + f\tau_t \tag{5}$$

Table 2 Model parameters used for six-mode test

mode	A,×10^{-12}	A_{f04}	C_{dis}	T_{ivc}, K	P_{ivc}, kPa	α
1	3.81	3.1×10^5	0.7/0.6	330	107	0.053
2	3.70	1.29×10^5	0.7	345	118	0.043
3	3.32	2.8×10^5	0.7	310	181	0.0073
4	3.26	1.0×10^5	0.7	337	265	0.002
5	3.62	6×10^4	0.7	346	186	0.035
6	3.80	5×10^4	0.7	350	149	0.052
baseline	3.39	2.9×10^5	0.7	312	196	0.014

In the present multiple-time scale combustion model, a similar formulation is used where the time scales for CO and H_2 conversion are assumed to be fractions of the fuel time scale, as described later. In Eq. (5), it is clear that the longer of the two times has more influence on the conversion rate. The laminar time scale is derived by Kong et al. (1995) based on single droplet auto-ignition experimental data

$$\tau_l = A[C_nH_{2n+2}]^{0.75}[O_2]^{-1.5}e^{E/RT} \quad (6)$$

where A is a model constant and equal to 1.625×10^{-11}, R is the universal gas constant, and E is the activation energy (30,000 cal/mole). Kuo and Reitz (1992) studied the effect of residual gas concentration on the laminar characteristic time in computations of two-stroke engine combustion with high EGR rates. They found that the laminar-kinetic time increases with increasing residual gas concentration. This effect was accounted for by modifying the pre-exponential constant, A, in Eq. (6), by dividing it by a correlation factor CF^2, where $CF = 1.27\ (1 - 2.1\alpha)$, and α is the residual mass fraction, $\alpha = m_r/m_t$, where m_r is the mass of residual gas and m_t is the total trapped mass. The modification was chosen to be consistent with Metghalchi and Keck's correlation (1982) between the laminar flame speed and the residual mass fraction given as

$$S_u = [B_1 - B_2(\phi - \phi_m)^2]T_u^a P_u^b(1 - 2.1\ \alpha) \quad (7)$$

where $a = 2.18 - 0.8(\phi - 1)$, $b = -0.16 + 0.22(\phi - 1)$, and ϕ is the equivalence ratio. The other constants, B_1, B_2, and ϕ_m, vary with different fuels. Equation (7) shows that a slower laminar flame speed results from the dilution of reactants by the residual gas.

In the present investigation, the values of A given in Table 2 were used in order to account for the residual gas effect. In this case, A is well represented by the correlation

$$A = \left(1 + \frac{10\alpha}{3}\right) \times 3.24 \times 10^{-12} \quad (8)$$

It should be noted that during the diffusion burn portion of the combustion, the turbulent time scale dominates the overall conversion time, and, hence, this correlation only influences the initial stages of combustion. The turbulent time scale τ_t is given by

$$\tau_t = \frac{C_2 k}{\epsilon} \quad (9)$$

where k is the turbulence kinetic energy, and ϵ is the turbulence dissipation rate, and C_2 is a constant equal to 0.1 (Kong et al., 1995). Similar to the delay coefficient introduced in SI engines, the coefficient f characterizes the degree of turbulent combustion, defined in the present study as

$$f = \frac{1 - e^{-\gamma}}{0.632} \quad (10)$$

where γ is the ratio of the amount of products (*excluding residual and* EGR *exhaust gas*) to that of total reactive species, i.e.,

$$\gamma = \frac{Y_{CO_2,R} + Y_{H_2O,R} + Y_{CO,R} + Y_{H_2,R}}{1 - Y_{CO_2,r} - Y_{H_2O,r} - Y_{N_2}}$$

where the subscripts r and R indicate "residual" and "reaction," respectively. The parameter γ indicates the completeness of combustion in a control volume. From Eq. (5), it is seen that combustion is dominated by the laminar time scale during the early stages of combustion. The effect of turbulence on combustion becomes important after combustion events have proceeded to a certain extent. In previous applications (Kong et al., 1995), γ was calculated using the total concentration of each species, that is, $\gamma = (Y_{CO_2} + Y_{H_2O} + Y_{CO} + Y_{H_2})/(1 - Y_{N_2})$. Therefore, the combustion products left from previous cycles are included in the combustion products in the current cycle. This introduces an error, which becomes significant as the residual gas fraction increases, such as in cases with high EGR.

Spray and Emissions Models. Spray atomization is a complicated physical phenomenon. The spray characteristics depend on fluid properties and ambient conditions as well as on the fuel injector nozzle design specifications and operating conditions. Spray atomization was modeled using the wave breakup theory (Reitz, 1987). In the model, droplet parcels containing a number of identical droplets are injected from the nozzle with sizes initially equal to the nozzle exit diameter. By using the wave breakup model, it is not necessary to define the initial droplet size distribution at the exit of the nozzle. Instead, the breakup drop sizes are computed by considering the most unstable wave's wavelength Λ, i.e., $r = B_0\Lambda$, where $B_0 = 0.6$, and the breakup time is $\tau = 3.726\ B_1 r_0/\Lambda\Omega$, where Ω is the most unstable wave's growth rate and B_1 is the breakup time constant, which was equal to 60 for all cases in the present study. With this model the prediction uncertainties resulting from specifying a droplet size distribution are eliminated. However, there are uncertainties in the breakup model and the model does not account for some important factors, such as the known effect of the nozzle internal geometry (Han et al., 1996).

It has been shown that the effective area of fluid flow is smaller than the geometric nozzle area due to flow contraction (Han et al., 1996). However, in the diesel injector nozzle, there are essentially two flow restriction areas: the nozzle exit, and the area at the location of the nozzle/needle seal ring. The latter is a function of engine operating conditions and injection pressure, among other parameters. Since the initial droplet velocities are calculated based on the fuel flow rate and the nozzle exit area, the discharge coefficient C_{dis} represents the bottleneck effect and the contraction effect. The values adopted in the present study are shown in Table 2, and were derived from measured data (Montgomery and Reitz, 1996).

The extended Zeldovich mechanism was used to compute NO formation (Patterson et al., 1994). The present NO_x model was found to overestimate experimental data slightly. Accordingly, a calibration factor of 0.85 was applied to all the computed NO_x results (Han and Reitz, 1995). An additional factor of 1.533 was used to convert NO to NO_x according to the EPA standard. The soot emission model considers the rate of change of soot mass equal to the rate of formation less the rate of oxidation:

$$\frac{dm_{soot}}{dt} = \frac{dm_{form}}{dt} - \frac{dm_{oxid}}{dt}$$

The soot mass formation rate is given by $dm_{form}/dt = A_f m_{fv} P^{0.5} e^{-E_f/RT}$, where $A_f = 130$, m_{fv} is the fuel vapor mass, P is the pressure in bar, and $E_f = 12{,}500$ cal/mole. The soot oxidation rate is adopted from the Nagle and Strickland–Con-

stable oxidation model. In this model, carbon oxidation occurs by two mechanisms whose rates depend on surface chemistry involving the more reactive A sites and the less reactive B sites. Three reaction equations are formulated to describe the oxidation process with the net rate as $dm_{oxid}/dt = 6W_c m_s R_{total}/\rho_s D_s$, where W_c is the carbon molecular weight (12 g/mole), ρ_s is the soot density (2 g/cm^3), D_s is the soot diameter (3×10^{-6} cm), m_s is the soot mass. Details of the net reaction rate R_{total} are described by Patterson et al. (1994).

Results and Discussion

In this study the simulation results are compared with experimental results obtained from the single-cylinder Caterpillar heavy-duty truck engine. The experimental emissions results are listed in Table 1 and a detailed discussion of the experimental results is given elsewhere (Montgomery and Reitz, 1996). The seven experimental engine conditions in Table 1 represent the six-mode cycle and a previously examined baseline (1600 rpm, 75 percent load) running condition. Because the combustion chamber geometry is symmetric, and the six-hole injector nozzle is installed perpendicularly at the center, the computational domain considered is only one-sixth of the chamber, and symmetric boundary conditions are applied at 0 and 60 deg, respectively, in the azimuthal direction. There were 20 cells in the radial direction, 30 cells in the azimuthal direction, and 18 cells in the axial direction, with 5 cells in the squish region at top dead center. This mesh resolution has been found to give adequently grid-independent results (Han and Reitz, 1995). The computations used tetradecane ($C_{14}H_{30}$) as the fuel due to its similar C/H ratio to diesel fuel.

In the baseline running conditions, the intake pressure is much higher than the exhaust pressure (see Table 1), and it is expected that the scavenging effect plays an important role on the gas compositions and temperature at IVC. The calculated initial temperature is 312 K based on the estimation that the residual gas fraction at IVC is 1.4 percent (Senecal et al., 1996). For the present comparison, the results from the single-characteristic-time combustion model (termed *single scale* in the following discussion) and multiple-characteristic-time combustion model (called *multiple scale*) are presented based on the same initial pressure. The initial temperature for the simulation using the single scale model is 342 K because the constants of submodels were previously calibrated based on this initial temperature (Han et al., 1996). The constants used for the present multiple-time scale model are listed in Table 2.

The predicted and measured cylinder pressure histories for the baseline running condition with 6 BTDC injection timing are shown in Fig. 1. The short dashed line represents the prediction using the same characteristic time for all six species (single-scale model), while the long dashed line represents a multiple-time-scale model prediction, which assumes relatively fast conversion rates for CO and H_2, i.e.,

$$\tau_{c,CO} = \tau_{c,H_2} = 0.2\,\tau_{c,\text{fuel}} \tag{11}$$

It should be noted that this equation only indicates the fastest CO and H_2 conversion rates; the actual conversion rates in each time step and each cell also depend on the availability of oxygen. It is seen that the predicted pressure history using the multiple scale model has excellent agreement with that measured. The single-scale model underestimates the measured peak cylinder pressure somewhat. The numerical results also show that the specification of the initial conditions is critical to the accuracy of the model predictions. Although the initial pressures are identical, the predicted peak pressure using the single-scale model is slightly lower than the measured result because more energy is lost through the cylinder wall when the higher initial temperature is assumed.

In order to examine the model sensitivity to the engine operating conditions, an additional calculation was conducted for the baseline case with 10 BTDC injection timing. The predicted cylinder pressure history using the multiple-time scale model is seen to have excellent agreement with the measured pressure history, as also shown in Fig. 1, which indicates that the code predicts the ignition and combustion, as well as mixing fairly well.

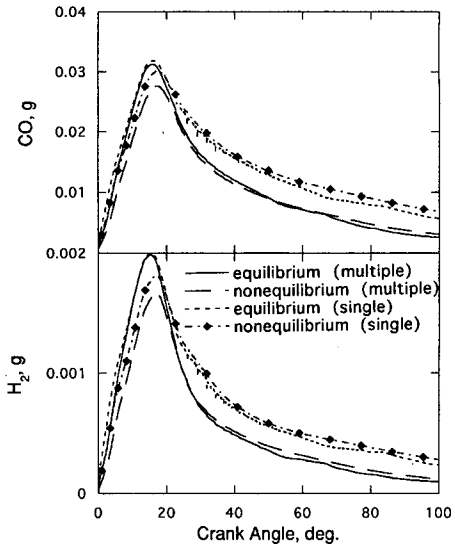

Fig. 2 Comparison of carbon monoxide and hydrogen predictions with the multiple and single-time scale combustion models

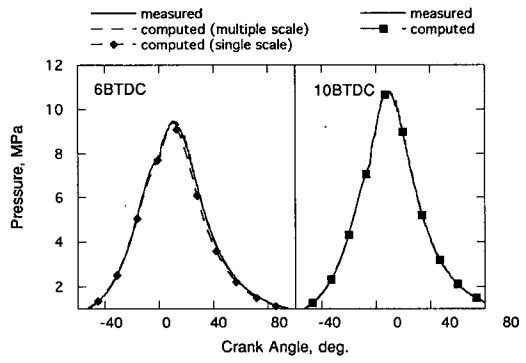

Fig. 1 Predicted and measured cylinder pressure histories for baseline cases with 6 BTDC and 10 BTDC injection timings

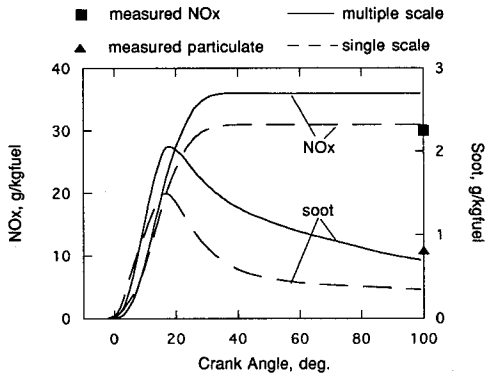

Fig. 3 Comparison of measured and predicted NO_x and soot variations for baseline case with 6 BTDC injection timing

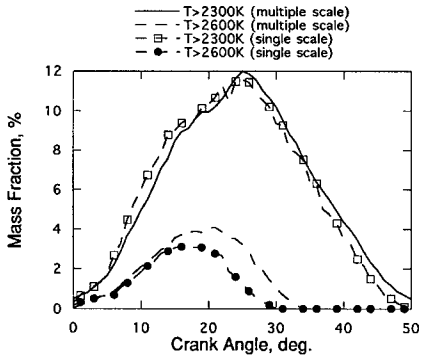

Fig. 4 Predicted mass fraction variations with temperatures greater than 2300 K and 2600 K for baseline case with 6 BTDC injection timing

Figure 2 presents the effect of the different characteristic time model formulations on total in-cylinder carbon monoxide and hydrogen mass variation with crank angle for the baseline case with 6 BTDC injection timing. The equilibrium mass in Fig. 2 represents the theoretical mass under instantaneous equilibrium conditions, i.e., the * values in Eq. (3), and the nonequilibrium mass indicates the actual transient mass. It is seen that the local species concentrations are always quite close to their local equilibrium values. The results show that the engine-out carbon monoxide mass (e.g., at 100 deg ATDC) decreases by 60 percent when the faster conversion rates of H_2 and CO are adopted. In addition, the presence of exhaust-out hydrogen is also significantly reduced. These results demonstrate that the predicted exhaust products and the completeness of combustion are sensitive to the details of the combustion model.

Figure 3 shows the predicted total in-cylinder NO_x and soot using the previous and present combustion models for the baseline case with 6 BTDC injection timing. It is interesting that although the initial gas temperature was reduced by about 30 K, the NO_x predictions from the single-scale combustion model and the multiple-scale combustion model are very close; the NO_x prediction from the multiple-scale model is slightly higher than that from the single-scale mode. The soot prediction from the multiple-scale model is also higher than that from the single-scale model, and has much better agreement with the experimental engine-out results. This phenomenon can be explained as follows: Due to the enhanced oxidation processes of H_2 and CO, the local mixture temperature increases significantly, as shown in Fig. 4. Compared with the single-scale combustion model results, there exists almost the same amount of mass with temperatures above 2300 K, and more mass with temperatures greater than 2600 K when using the multiple-scale combustion model, even though the cylinder gas temperature at intake valve closure was lower. Therefore, both models give similar NO_x predictions. It is known that the concentrations of CO and H_2 are high in the fuel-rich regions. On the other hand, soot particles are also formed mainly in the fuel-rich zones. Therefore, hydrogen, carbon monoxide and soot particles all compete for oxygen in the fuel rich zones. In Puri et al.'s study (1994) of laminar diffusion flames, they found evidence supporting the hypothesis that the observed strong correlation between soot and CO is a result of a competition between soot and CO for the oxidizing species OH. As a result, the predicted soot emissions increase as the conversion rates of CO and H_2 are enhanced.

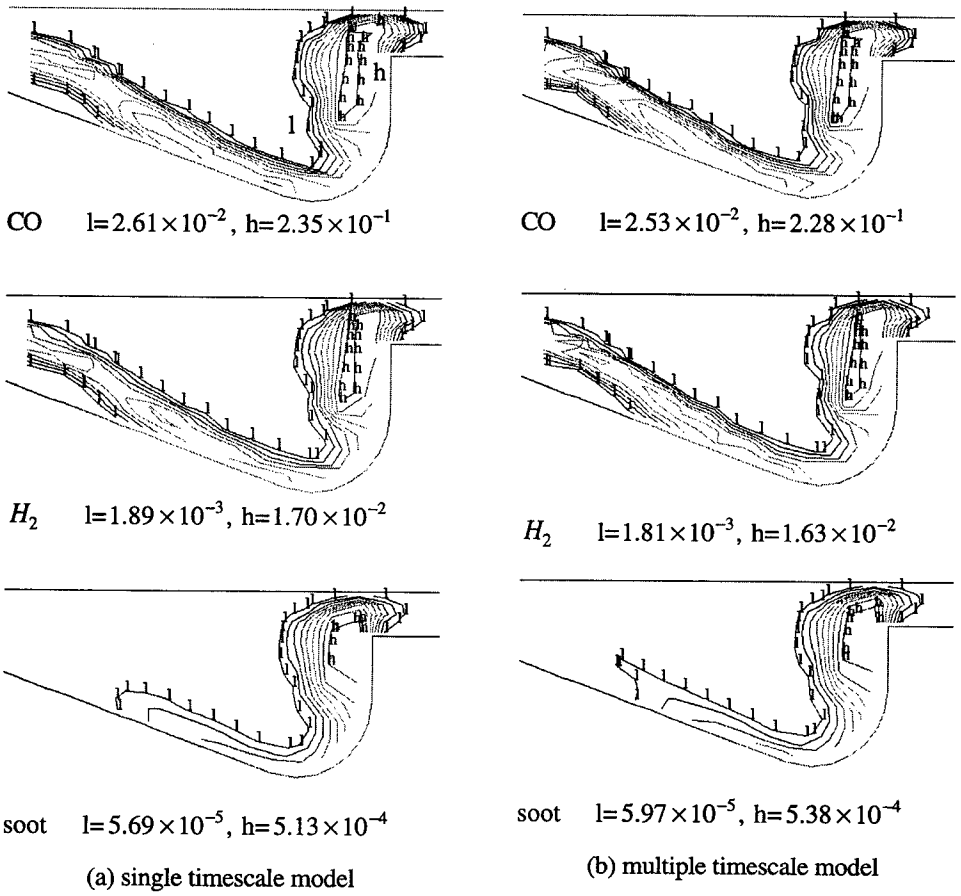

Fig. 5 Predicted CO, H_2, and soot concentrations at 9 ATDC with single-time scale and multiple-time scale combustion models

Figure 5 presents the instantaneous CO, H_2, and soot concentrations in a plane crossing the spray centerline and the cylinder axis. The results clearly show that the multiple-time scale combustion model predicts lower local CO and H_2 concentrations due to faster oxidation, and higher soot concentrations due to less oxygen being available.

Additional calculations were conducted using different conversion rates of CO and H_2 equal to 0.3 $\tau_{c,\text{fuel}}$, and 0.1 $\tau_{c,\text{fuel}}$ in Eq. (11), to examine the result sensitivity. The results differ only slightly from the simulations given above (within 10 percent). This indicates that the multiple-scale combustion model predicts combustion and emissions better, provided the species CO and H_2 reach their equilibrium states faster than the fuel conversion rate, but the precise time scale is not very important. The study of Turns and Bandaru (1993) indicates that the reaction rate of CO–air mixtures in the presence of H_2 is higher than that of hydrocarbon–air mixtures. This could also provide some additional out-of-engine justification for the present multiple-time scale model formulation.

In order to assess the effect of the combustion model alone on species conversion rates, two additional computations were performed using the two combustion models with the identical initial temperature (312 K). Similar results are obtained, i.e., the CO and H_2 concentrations become lower, while the soot concentration increases using the multiple-time scale combustion model. The predicted in-cylinder pressures using the two combustion models are almost identical. It should be noted that the in-cylinder pressure reflects the global averaged thermodynamic change; the NO_x and soot formations are very sensitive to local conditions. The increase of peak temperature in some cells due to the enhanced oxidation of H_2 and CO can result in substantial NO_x formation.

From these calculations, it is shown that the multiple-scale combustion model uses a lower (more realistic) initial temperature at the intake valve closure, and predicts emissions very well. Therefore, the multiple-scale combustion model was adopted for the remainder of the present study. The baseline results also demonstrate the capability to match experimental trends for the complicated chemically reacting, multiphase flows in diesel engines. In the following, the model is used to investigate the physical and chemical processes within the engine combustion chamber under the various running conditions of the six-mode tests.

Experimental results have shown that mode 1 (idle point) contributes as much as 41 percent of the total particulates in the six-mode cycle. By reducing the injection pressure from 90 MPa to 30 MPa, the particulate emission was significantly reduced to 6 percent (Montgomery and Reitz, 1996). The present multiple-scale simulation results for the two injection pressures

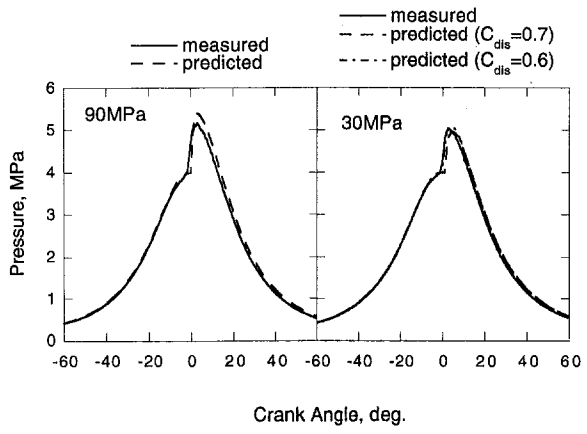

Fig. 6 Predicted and measured cylinder pressure history for mode 1 (idle) cases with injection pressure of 90 and 30 MPa

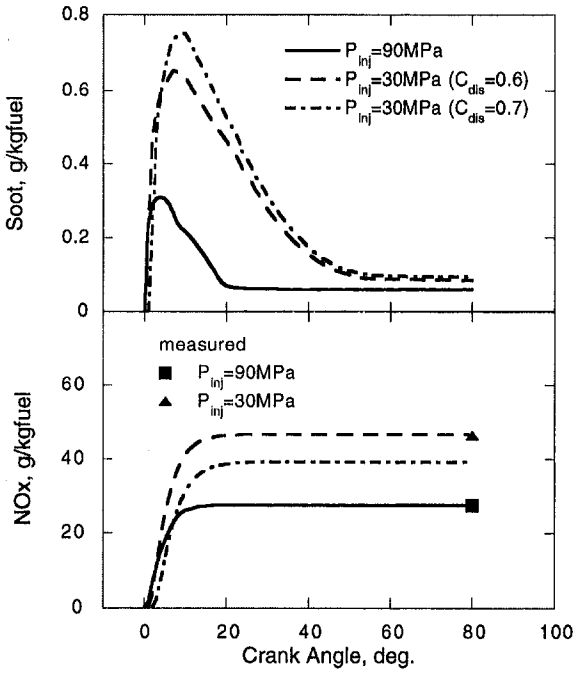

Fig. 7 Comparison of emission predictions for mode 1 with injection pressure of 90 and 30 MPa

(90 and 30 MPa) are shown in Figs. 6–8. As shown in Table 2, the nozzle discharge coefficient was reduced from 0.7 to 0.6 when the injection pressure was reduced from 90 to 30 MPa. This was done to explore its effect on the engine-out emissions. For the same flow rate and nozzle exit area, decreasing the discharge coefficient increases the injection velocity, which improves atomization and mixing. Figure 6 shows the in-cylinder pressure comparisons, and the numerical simulations have a reasonably good agreement with the experimental results for both injection pressures. The soot prediction is shown in Fig. 7. It is seen that the effect of discharge coefficient on in-cylinder pressure and soot emission is not significant, and the predicted soot with the reduced injection pressure is slightly higher than with 90 MPa injection pressure, which is opposite to the measured trend. In addition, the magnitudes are quite different, as can be seen by a comparison with the measured results presented in Table 1. This is probably because the measured particulate includes the Soluble Organic Fraction (SOF) contribution while the present soot model only considers "dry" soot. Experimental results show that the SOF portion of the particulate can be as high as 90 percent at low loads (Choi, 1995).

The effect of the fuel injection pressure on NO_x is shown in Fig. 7. The predicted engine-out NO_x emissions for both injection pressures agree well with the measured data, and the effect of the nozzle discharge coefficient is seen to be quite significant. In contrast to trends observed at high load conditions, NO_x is seen to be increased with decreasing fuel injection pressure for mode 1. It is known that NO_x is sensitive to the local mixture temperature, which, in turn, is affected by mixing (the equivalence ratio) and ignition delay, which are different when the injection pressure is reduced. When the injection pressure is reduced, the injection duration increases, and the initial droplet velocity decreases. Consequently, the spray penetration becomes short compared with the 90 MPa case, as shown also by the location of the spray droplets in the combustion chamber in Fig. 8. The reduced penetration prevents fuel from overmixing in this case of very low overall fuel/air ratio. For the 90 MPa injection pressure case, initial droplet velocities are high. Since the in-cylinder gas density is low at idle, the spray penetrates further during the ignition delay. Also, because of the

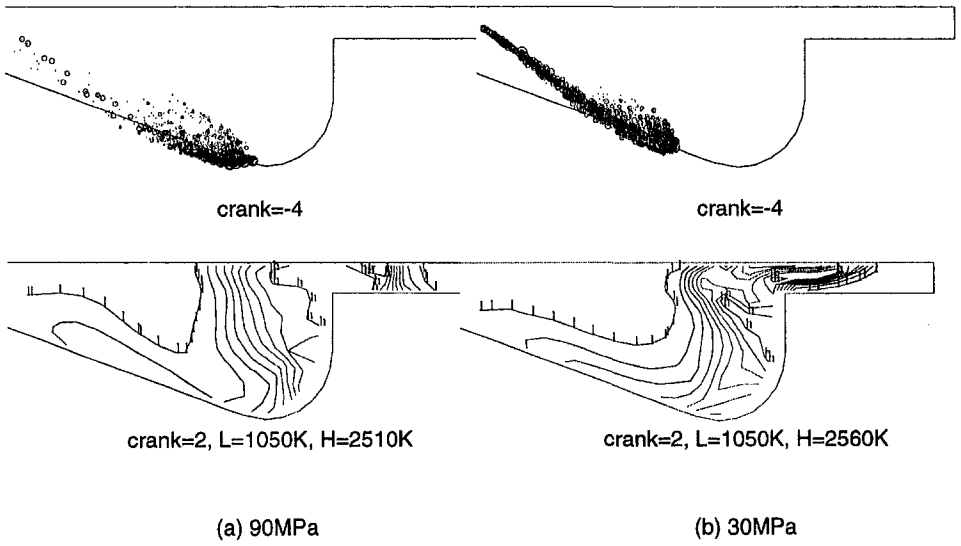

Fig. 8 Spray (top) and temperature (bottom) distributions within the combustion chamber for mode 1 with injection pressure of 90 and 30 MPa

shorter injection duration, liquid fuel droplets cluster together, and this reduces evaporation rates. When the mixture is ignited, some of fuel has reached the squish region, and the flammable mixture continues to move into the squish region. The high-temperature zones (combustion zones) are distributed along the combustion chamber head surface, as shown in Fig. 8(*a*) (2 deg ATDC). For the 30 MPa case, the spray is well distributed spatially within the piston bowl at the time of ignition. By 2 deg ATDC, some high-temperature zones are still within the piston bowl due to the slower movement of the flammable mixture. Therefore, for the 30 MPa injection pressure case, the combustion is confined within the piston bowl and there is less heat loss through the head surface, which tends to increase NO_x emissions and suppress soot formation.

Figure 9 shows comparisons of predicted and measured in-cylinder pressure histories for modes 2–6, while Fig. 10 summarizes the engine-out emissions comparisons of the six modes and the baseline case. Mode 2 is characteristic of low-load (25 percent), low-speed (953 rpm) engine operating conditions. The predicted results show fairly good agreement with the experimental pressure results. However, the predicted peak pressure is somewhat lower than that measured. The NO_x prediction agrees with the engine-out data very well. Because of the significant contribution of SOF to the measured particulate at low loads, it is expected that the present soot prediction should be low, and this is indeed found (see Fig. 10), as it is about 0.12 g/kg fuel compared with the experimental particulate measurement 0.39 g/kg fuel.

Mode 3 represents the high-load (75 percent) and low-speed (1074 rpm) engine operating condition. For this mode, the predicted in-cylinder pressure history has excellent agreement with the experimental result, as shown in Fig. 9. From the NO_x comparison with the experimental engine-out result shown in Fig. 10, it is seen that the simulation predicts slightly higher NO_x than that measured. The soot prediction is lower than that measured (measured particulate emission 1.09 g/kg fuel, predicted soot 0.82 g/kg fuel). It is believed that this discrepancy is attributed to SOF.

In the mode 4 case, the engine is operated at full load and high speed. The pressure traces of mode 4 are shown in Fig. 9, which indicates that the pressure history is predicted quite well. The numerical NO_x results show excellent agreement with the experimental engine-out results. The predicted engine-out soot emission is equal to 1.55 g/kg fuel, which is very close to the measured particulate value (1.41 g/kg fuel).

Mode 5 is characteristic of high engine speed and moderate load (50 percent). Figure 9 shows that there is very good agreement between the experimental and predicted pressure results. The predicted NO_x also agrees with the experimental engine-out result very well. However, the agreement of the predicted soot with the measured particulates again deteriorates as the engine load decreases. The predicted soot (0.98 g/kg fuel) is much lower than the measured engine-out particulates (2.1 g/kg fuel), again possibly because of the increased contribution of SOF to the total particulates at the reduced load.

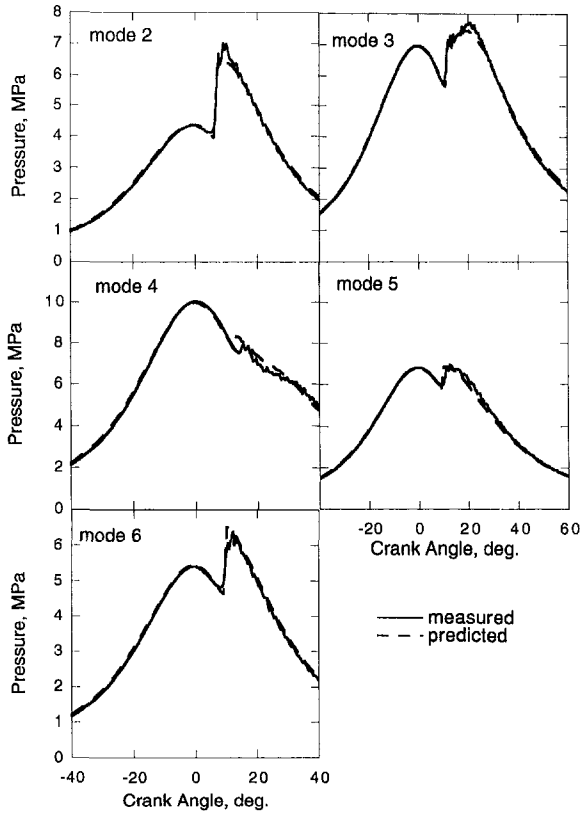

Fig. 9 Comparison of predicted cylinder pressure with measured pressure for modes 2–6

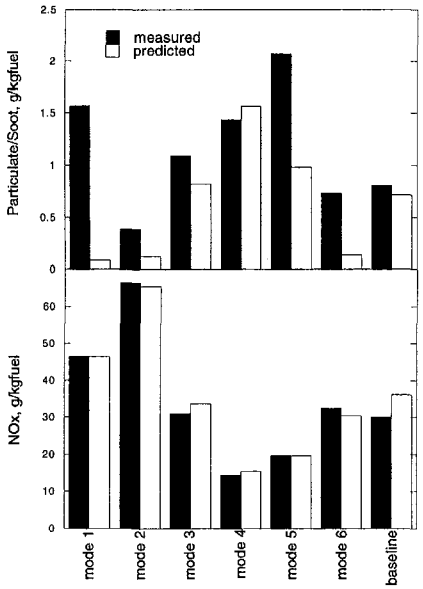

Fig. 10 Comparison of measured and predicted emissions for six-mode cycle and baseline

Mode 6 has a similar engine speed to mode 5, but the load is only 25 percent. As listed in Table 1, the exhaust pressure is higher than the intake pressure in this mode, and it is expected that a significant amount of combustion products tend to flow into the intake manifold during the valve overlap period. The estimated residual gas fraction is about 5.3 percent.

The predicted pressure history of the mode 6 case is in good agreement with the measured results, as shown in Fig. 9. The predicted engine-out NO_x also agrees very well with that measured (see Fig. 10). The predicted soot is lower than the measured particulate emissions, which is expected because SOF contributes a significant portion of particulates at low load conditions. This is in excellent agreement with recent measured data of Choi et al. (1997) taken at the same operating condition, which shows similar "dry" soot data to those predicted here.

From Fig. 10, it is seen that the overall NO_x prediction accuracy is satisfactory. There are larger discrepancies between the predicted soot and the measured particulates, probably because of the role of unburned fuel and lubricating oil in the SOF portion of the particulates under the various engine operating conditions. The results also show that the soot prediction accuracy for high and moderate load engine conditions is better than that for low-load engine conditions. The low-load cases feature longer ignition delays and dominant premixed-mode combustion. Therefore, mixing and evaporation play a more important role in low load modes, and the present results indicate that improvements may be needed in those models in order to improve the accuracy of the model predictions. This conclusion has also been reached by comparing model predictions with endoscope combustion visualization images. At light loads, significant discrepancies have been found between model and experimental results (Ricart and Reitz, 1996).

Conclusions

The present simulations of DI diesel engine combustion were carried out to predict the combustion and emissions over a wide range of operating conditions, which simulate the federal transient test procedure. The comparisons with the experimental engine-out data show that, with modifications to the ignition and combustion submodels, the model is capable of predicting diesel engine performance over the entire engine operating range.

The gas compositions and temperature at IVC vary significantly with the engine running conditions, and the increase of residual mass fraction reduces the laminar flame speed and results in a longer ignition delay. Correlations between the pre-exponential coefficient of the laminar time scale and the residual mass fraction, and between the pre-exponential coefficient of the ignition model intermediate species reaction rate and the initial gas temperature and pressure at IVC were introduced. In this study, it is found that the pre-exponential coefficient of the ignition model intermediate species reaction rate is required to vary from one mode to another in order to match the measured ignition delay. This indicates that the current ignition model needs improvements in order to model a wide range of engine operating conditions accurately. However, with the present empirical method, good levels of agreement with the experimental results were achieved.

A new multiple characteristic-time scale combustion model was implemented in this study. The assumption of using the same characteristic time for all species, which has been adopted in previous studies, was eliminated. In the modified combustion model, different characteristic time scales can be used based on knowledge of the combustion chemistry. By using the multiple-characteristic-time combustion model, the predicted engine-out CO and H_2 emissions are significantly reduced. In addition, the accuracy of the soot, NO_x, and cylinder pressure predictions is significantly improved. Overall, the NO_x predictions are in good agreement with the experiments. The soot predictions are also in reasonable agreement with the measured particulates at medium and high loads. However, at light loads, the agreement deteriorates, possibly due to the neglect of the contribution of SOF in the soot model predictions.

Acknowledgments

This work was supported by Caterpillar, Inc. Additional facilities and support were provided by the Army Research Office. The helpful comments of Caterpillar engineers are also appreciated.

References

Abraham, J., Bracco, F. V., and Reitz, R. D., 1985, "Comparisons of Computed and Measured Premixed Charge Engine Combustion," *Combustion and Flame,* Vol. 60, pp. 309–322.

Amsden, A. A., O'Rourke, P. J., and Butler, T. D., 1989, "KIVA-II: A Computer Program for Chemically Reactive Flows With Sprays," Los Alamos National Laboratory Report No. LA-11560-MS.

Choi, C., 1995, private communication, University of Wisconsin, Madison, WI.

Choi, C., Bower, G., and Reitz, R. D., 1997, "Effects of Biodiesel Blended Fuels and Multiple Injections on DI Diesel Engine Emissions," SAE Technical Paper No. 970218.

Halstead, M. P., Kirsch, L. J., and Quinn, C. P., 1977, "The Autoignition of Hydrocarbon Fuels at High Temperatures and Pressure-Fitting of a Mathematical Model," *Combustion and Flame,* Vol. 30, pp. 45–60.

Han, Z., and Reitz, R. D., 1995, "Turbulence Modeling of Internal Combustion Engines Using RNG $k-\epsilon$ Models," *Combustion Science and Technology,* Vol. 106, pp. 267–280.

Han, Z., Uludogan, A., Hampson, G., and Reitz, R. D., 1996, "Mechanisms of Soot and NO_x Emission Reduction Using Multiple-Injection in a Diesel Engine," SAE Technical Paper No. 960633.

Kong, S. C., and Reitz, R. D., 1993, "Multidimensional Modeling of Diesel Ignition and Combustion Using a Multistep Kinetics Model," ASME JOURNAL OF ENGINEERING FOR GAS TURBINES AND POWER, Vol. 115, pp. 781–789.

Kong, S. C., Han, Z., and Reitz, R. D., 1995, "The Development and Application of a Diesel Ignition and Combustion Model for Multidimensional Engine Simulation," SAE Technical Paper No. 950278.

Kuo, T. W., and Reitz, R. D., 1992, "Three-Dimensional Computations of Combustion in Premixed-Charge and Direct-Injected Two-Stroke Engines," SAE Technical Paper No. 920425.

Metghalchi, M., and Keck, J., 1982, "Burning Velocities of Mixtures of Air With Methanol, Isooctane, and Indolene at High Pressure and Temperature," *Combustion and Flame,* Vol. 48, pp. 191–210.

Miyaki, M., Fujisawa, H., Masuda, A., and Yamoamoto, Y., 1991, "Development of New Electronically Controlled Fuel Injection System ECD-U2 for Diesel Engines," SAE Technical Paper No. 910252.

Montgomery, D. T., and Reitz, R. D., 1996, "Six-Mode Cycle Evaluation of the Effect of EGR and Multiple Injections on Particulate and NO_x Emissions From a D.I. Diesel Engine," SAE Technical Paper No. 960316.

Patterson, M. A., Kong, S. C., Hampson, G. J., and Reitz, R. D., 1994, "Modeling the Effects of Fuel Injection Characteristics on Diesel Engine Soot and NO_x Emissions," SAE Technical Paper No. 940523.

Pierpont, D. A., Montgomery, D. T., and Reitz, R. D., 1995, "Reducing Particulate and NO_x Using Multiple Injections and EGR in a DI Diesel," SAE Technical Paper No. 950217.

Puri, R., Santoro, R. J., and Smyth, K. C., 1994, "The Oxidation of Soot and Carbon Monoxide in Hydrocarbon Diffusion Flames," *Combustion and Flame,* Vol. 97, pp. 125–143.

Reitz, R. D., and Bracco, F. V., 1983, "Global Kinetics Models and Lack of Thermodynamic Equilibrium," *Combustion and Flame,* Vol. 53, pp. 141–143.

Reitz, R. D., 1987, "Modeling Atomization Processes in High-Pressure Vaporizing Sprays," *Atomization and Spray Technology,* Vol. 3, pp. 309–337.

Reitz, R. D., and Rutland, C. J., 1995, "Development and Testing of Diesel Engine CFD Models," *Prog. Energy Combust. Sci.,* Vol. 21, pp. 173–196.

Ricart, L., and Reitz, R. D., 1996, "Visualization and Modeling of Pilot Injection and Combustion in Diesel Engines," SAE Technical Paper No. 960833.

Rutland, C. J., Eckhause, J., Hampson, G., Hessel, R., Kong, S., Patterson, M., Pierpont, D., Sweetland, P., Tow, T., and Reitz, R. D., 1994, "Toward Predictive Modeling of Diesel Engine Intake Flow, Combustion and Emissions," SAE Technical Paper No. 941897.

Senecal, P. K., Xin, J., and Reitz, R. D., 1996, "Predictions of Residual Gas Fraction in IC Engines," SAE Technical Paper No. 962052.

Theobald, M. A., and Cheng, W. K., 1987, "A Numerical Study of Diesel Ignition," presented at the ASME Energy-Source Technology Conference and Exhibition, Dallas, TX, Feb.

Turns, S. R., and Bandaru, R. V., 1993, "Carbon Monoxide Emissions From Turbulent Non-premixed Jet Flames," *Combustion and Flame,* Vol. 94, pp. 462–468.

Nonlinear Valve Train Dynamics Simulation With a Distributed Parameter Model of Valve Springs

J. Lee
Engine and Vehicle Research Division,
Southwest Research Institute,
San Antonio, TX

D. J. Patterson
The University of Michigan,
Ann Arbor, MI 48109

A simulation model of valve train dynamics was developed in order to investigate the vibrational behavior of a valve train under heavy normal load, especially for heavy-duty diesel engines. The nonlinear multi-degree-of-freedom model developed for this study uses input data resulting from the kinematic analysis. The valve spring was modeled as a distributed parameter system rather than a lumped mass system. The stiffness constants of each valve train component were theoretically obtained as nonlinear values. The partial differential equation describing the motion of the spring and the ordinary differential equations for other components, which were considered as a lumped mass system, were solved simultaneously without any iterations by using the numerical "Time Marching Step" method. The results of this simulation, which treated the elastic characteristics of each component as nonlinear, were more accurate than the previous studies that used simple linear elastic models.

Introduction

Valve train dynamic analysis is a necessary and useful tool for new valve train designs or component modifications. In response to the growing demand for higher speed and higher output engines, engineers have sought higher valve lift, and a more aggressive cam profile to drive the valve train. However, these changes conflict with the higher speed requirement, since these changes result in higher accelerations and greater forces applied to parts such as cam shaft, pushrod, rocker arm, etc. To comply with these requirements, a comprehensive model of the valve train that can provide a more complete understanding and more accurate prediction of valve train motion is required.

One of the earliest dynamic simulations of a cam/follower system was made by Hrones (1948) who used a simple spring-mass model with an analog computer. A few years later, Barkan (1954) developed a model including energy loss mechanisms. He used a single-degree-of-freedom model with an equivalent mass in which the energy dissipation is by both viscous damping and Coulomb friction.

In the 1960s, with the introduction of fast digital computers, it became easier to solve the equations for more complicated models. Hundal (1999) introduced equivalent viscous damping by lumping the various types of friction both linear and nonlinear. He also calculated the free motion of the valve train after a jump from the cam profile. A more detailed analysis of jump and bounce was made recently by Kurisu et al. (1991). Johnson (1999) included the effect of nonlinearities such as valve clearance, linkage separation, valve seating, and valve spring surge.

In the 1980s, the valve train engineer was confronted with a higher speed requirement for the engine. Consequently, he needed a more precise model to predict the behavior of the valve train. Pisano and Freudenstein (1983) developed a single-degree-of-freedom model with a distributed parameter spring model. He solved the coupled equations for the valve train elements including the spring by iteration. Later Chan and Pisano (1987) developed a model with six degrees of freedom. They included the effect of the hydrodynamic tappet and calculated the linear stiffness coefficients of each part based on Hertzian contact. Pisano (1984) also demonstrated the effect of friction on system response by considering the energy dissipation of the rocker arm pivot by Coulomb friction. Akiba and Shimizu (1981) used a two-mass model to forecast the valve train behavior, focusing on valve linkage separation. Several years later he improved the model with a five-degree-of-freedom system in order to determine the impulsive force acting on the valve (Akiba and Kakiuchi, 1988). Phlips et al. (1988) presented a model that included variable tappet stiffness with contact points and a distributed parameter model of the valve spring. However, he did not solve the coupled equations simultaneously but solved them through interpolation. Recently, Adam et al. (1990) used nonlinear stiffness coefficients of valve train parts, which were obtained by FEM analysis. They used a lumped mass model for the valve spring.

The valve train chosen for this research was from the exhaust valve of a Cummins L-10 engine as illustrated in Fig. 1. The valve train analysis includes a multi-degree-of-freedom model with nonlinear stiffness coefficients for each part and a distributed parameter model of a valve spring. Experimental data from the previous research were used to verify the modeling (Lee et al., 1994).

Dynamic Model of Valve Train

The actual valve train may consist of pushrod, follower, rocker arm, cam, valve, and springs. All of these have mass and elastic properties distributed throughout the system in accordance with their physical dimensions. A typical example is the automotive overhead valve gear system that is very common in diesel engines, like the subject engine of this research. In the dynamic modeling of a cam and follower system, the usual practice has been to reduce it to a simple mass, spring, and damper system by lumping the effective mass of each body. However, the simplification of the valve spring as a lumped mass system makes it impossible to get accurate dynamic behavior of the valve train. In this research the spring was modeled as a distributed parameter system to insure more close prediction of vibrational characteristics. A schematic diagram of the valve train model is shown in Fig. 2.

Contributed by the Internal Combustion Engine Division and presented at the Internal Combustion Engine Division Spring Technical Conference, Marietta, Ohio, April 23–26, 1995. Manuscript received at ASME Headquarters November 1996. Associate Technical Editor: W. K. Cheng.

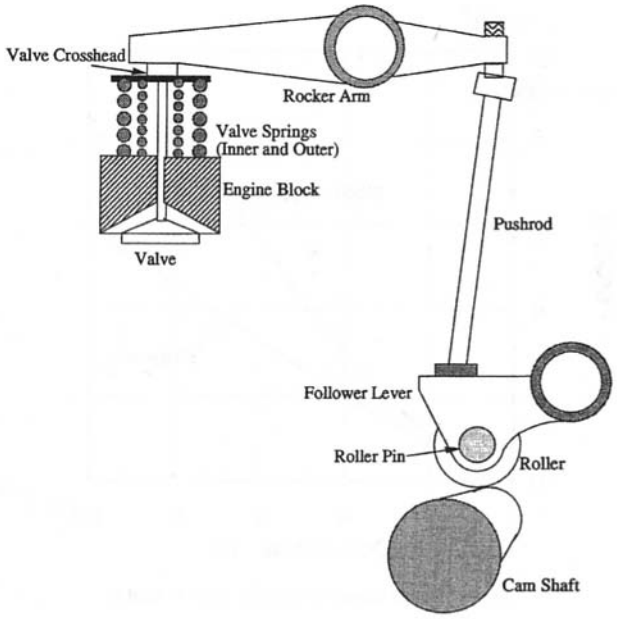

Fig. 1 Valve train schematic

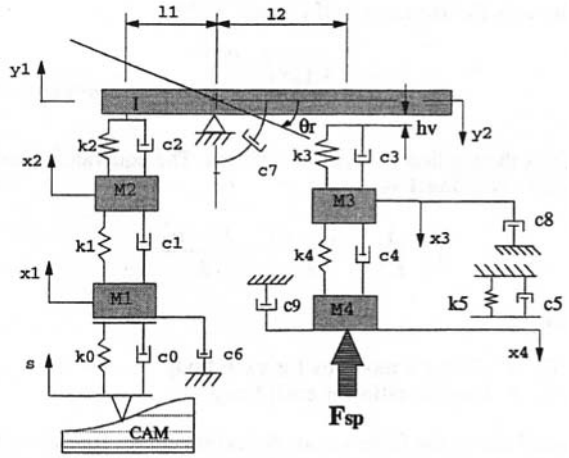

Fig. 2 Schematic of dynamic valve train model

It can be noted in Fig. 2 that the model consists of four masses ($M_1 \sim M_4$), one mass moment of inertia (I), six springs ($k_0 \sim k_5$), and ten dampers ($c_0 \sim c_9$). hv represents the valve lash located between the cross head and rocker arm. Note also that the model allows clearance between the cam and follower for valve jump. The reciprocating masses of the follower (M_1), pushrod (M_2), cross head (M_3), and valve (M_4) were directly measured. The mass moment of inertia of the rocker arm (I) was also measured. The mass of the roller follower lever is lumped into three masses: one for pushrod side, another for roller side, and the other for pivot side. Each reduced mass for the pushrod and roller sides is added to the mass of the pushrod and the roller themselves, in order to obtain the equivalent mass (Chen, 1982). The reduced mass for the lever pivot side may be ignored because this mass does not participate in the reciprocating motion.

The components of a valve train act as structural springs, which have stiffness coefficients according to their material properties and shape. Chan and Pisano (1987) applied the formulas for stress and strain developed by Roark and Young (1975), but used linearized values. Their formulas were derived based on Hertzian contact theory by using the equivalent radius of curvature (R). The following formulas, which were used in the current study, were also derived based on the formulas developed by Roark and Young (1975).

For the contact between the cam and roller, which are treated as two cylinders (R_1 = radius of curvature of a cam as a function of cam angle, R_2 = radius of roller follower):

$$k_0 = \frac{\pi E^* F}{2p(1-\nu^2)\left(\frac{2}{3} + 2\frac{R_1}{a} + \ln\frac{2R_2}{a}\right)}$$

Nomenclature

D = mean coil diameter
E = Young's modulus
F = applied load, N
I = mass moment inertia of rocker arm
L = total length of the spring = πDn
P = total force acting at distance x
R = equivalent radius of curvature = $R_1R_2/(R_1 + R_2)$
S = coordinate along the centerline of the spring wire
d = wire diameter
k = spring rate
n_a = number of active coils
P = pressure
s = cam rise
x = coordinate along axial line of the spring
y = deflection of the element "Q" from position when the spring is at rest
c' = damping coefficient per unit length
F_{sp} = spring force applied to valve
M_1 = equivalent mass of follower
M_2 = mass of pushrod
M_3 = mass of valve
M_4 = mass of crosshead
R_l = rocker arm pivot radius
c_0 = damping coefficient between cam and follower
c_1 = damping coefficient between follower and pushrod
c_2 = damping coefficient between pushrod and rocker arm
c_3 = damping coefficient between rocker arm and cross head
c_4 = damping coefficient between cross head and valve
c_5 = damping coefficient between valve and valve seat
c_6 = external damping coefficient at follower lever
c_7 = friction coefficient of rocker arm pivot
c_8 = external damping coefficient of cross head
c_9 = external damping coefficient of valve
k_0 = stiffness coefficient between cam and follower
k_1 = stiffness coefficient between follower and push rod
k_2 = stiffness coefficient between pushrod and rocker arm
k_3 = stiffness coefficient between rocker arm and cross head
k_4 = stiffness coefficient between cross head and valve
k_5 = stiffness coefficient between valve and valve seat
x_1 = displacement of follower
x_2 = displacement of pushrod
x_3 = displacement of cross head
x_4 = displacement of valve
y_1 = displacement of pushrod side of rocker arm
y_2 = displacement of valve side of rocker arm
l_2/l_1 = lever ratio of rocker arm
h_v = valve lash
δ = total deflection
γ = weight of the spring material per unit of volume
ν = Poisson ratio
θ_r = rotation angle of rocker arm

where a is the Hertzian half contact width:

$$a = 1.128\left(\frac{pR}{E^*}\right)^{1/2}$$

and p is the applied load per unit length. The equivalent elasticity (E^*) is defined as

$$\frac{1}{E^*} = \frac{1-\nu_1^2}{E_1} + \frac{1-\nu_2^2}{E_2}$$

where

E_1, E_2 = Young's modulus for each body
ν_1, ν_2 = Poisson ratio for each body

Figure 3 shows the force versus deflection curves for the contact between the cam and roller with two different values of cam radius of curvature.

For the contact between the pushrod and lever joint, treated as a sphere and a spherical socket (R_1 = radius of lever joint, R_2 = radius of pushrod bottom):

$$k_1 = 1.211(FE^{*2}R)^{1/3}$$

For the contact between the rocker arm and pushrod, treated as a sphere and a spherical socket (R_1 = radius of pushrod top, R_2 = radius of rocker arm joint):

$$k_2 = 1.211(FE^{*2}R)^{1/3}$$

Figure 4 shows the force versus deflection curves for the contacts between the pushrod and lever, and the pushrod and rocker arm. The stiffness coefficients of other components such as between the rocker arm and cross head, the cross head and valve, and the valve and valve seat are considered to be linear.

The energy dissipation in a valve train is assumed to arise from viscous damping because the relative motion between parts is very small. The viscous damping coefficients were taken to be 1.0 ~ 2.0 percent of critical damping. These values have often been chosen for viscous damping in valve train modeling (Chen, 1975). However, the energy dissipation at the rocker arm pivot is considered to be Coulomb friction because boundary friction is expected to occur under the high-load condition in the pivot.

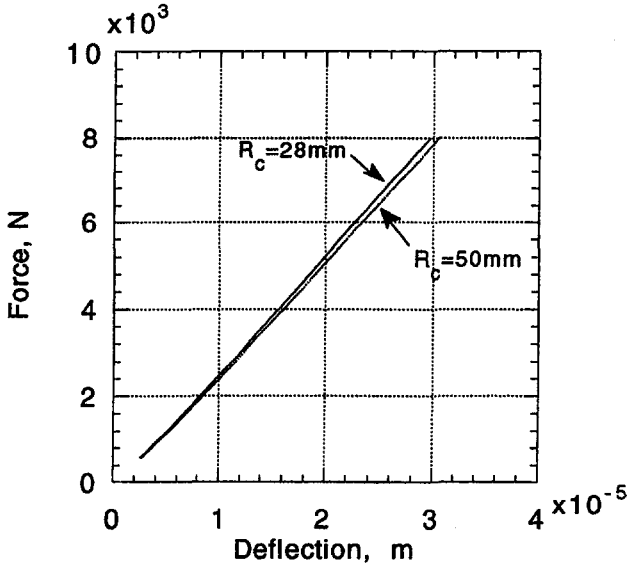

Fig. 3 Force versus deflection with k_0 (R_c = cam radius of curvature)

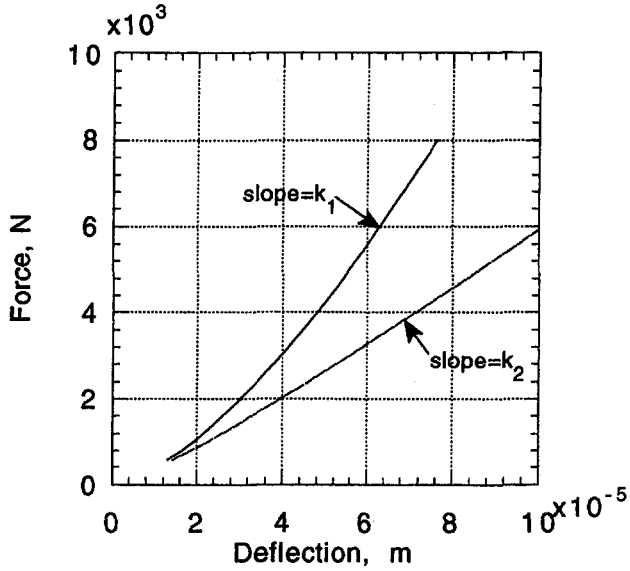

Fig. 4 Force versus deflection with k_1 and k_2

Equations of Motion

The model in Fig. 2 is based on a five-degree-of-freedom mass system to characterize the valve train elements, except the spring. The valve spring is taken to be a distributed parameter system. One mass is given to each of four parts such as the follower (M_1), pushrod (M_2), cross head (M_3), and valve (M_4), and one mass moment of inertia (I) is given to the rocker arm.

For the mass M_1 of the follower, the equation of motion is as follows:

(a) If jump does not occur

$$M_1\ddot{x}_1 + (c_0 + c_1 + c_6)\dot{x}_1 + (k_0 + k_1)x_1 - c_1\dot{x}_2 - k_1x_2 = c_0\dot{s} + k_0s \quad (1)$$

(b) If jump does occur

$$M_1\ddot{x}_1 + (c_1 + c_6)\dot{x}_1 + k_1x_1 - c_1\dot{x}_2 - k_1x_2 = 0 \quad (2)$$

For the mass M_2 of the push rod,

$$M_2\ddot{x}_2 + (c_1 + c_2)\dot{x}_2 + (k_1 + k_2)x_2 - c_1\dot{x}_1 - k_1x_1 - c_2\iota_1\dot{\theta}_r - k_2\iota_2\theta_r = 0 \quad (3)$$

For the mass moment of inertia I of the rocker arm,

(a) If y_2 ($=l_2q_r$) is smaller than the valve (h_v)

$$I\ddot{\theta}_r + c_2\iota_1^2\dot{\theta}_r + k_2\iota_1^2\theta_r - c_2\iota_1\dot{x}_2 - k_2\iota_1x_2 + u(\dot{\theta}_r)TF = 0 \quad (4)$$

where friction torque (TF) is:

$$TF = c_7R_\iota k_2(x_2 - \iota_1\theta_r)$$

(b) If y_2 is larger than the valve lash (h_v)

$$I\ddot{\theta}_r + (c_2\iota_1^2 + c_3\iota_2^2)\dot{\theta}_r + (k_2\iota_1^2 + k_3\iota_2^2)\theta_r - c_2\iota_1\dot{x}_2 - k_2\iota_1x_2 - c_3\iota_2\dot{x}_3 - k_3\iota_2x_3 - k_3\iota_2h_v + u(\dot{\theta}_r)TF = 0 \quad (5)$$

where friction torque (TF) is:

$$TF = c_7R_\iota[k_2(x_2 - \iota_1\theta_r) + k_3(\iota_2\theta_r - h_v - x_3)]$$

For the mass M_3 of the valve cross head,

(a) If y_2 is smaller than the valve lash (h_v)

$$M_3\ddot{x}_3 + (c_3 + c_8)\dot{x}_3 + k_4x_3 - c_4\dot{x}_4 - k_4x_4 = 0 \quad (6)$$

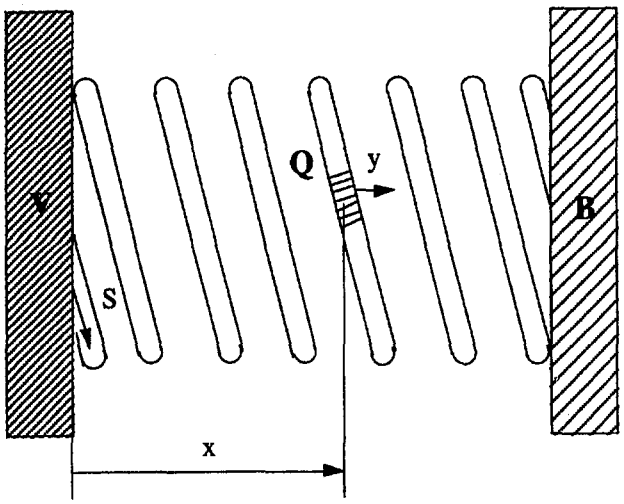

Fig. 5 Spring compressed between cylinder head and cross head

(*b*) If y_2 is larger than the valve lash (h_v)

$$M_3\ddot{x}_3 + (c_3 + c_4 + c_8)\dot{x}_3 + (\dot{k}_3 + k_4)x_3 - c_3\iota_2\dot{\theta}_r - k_3\iota_2\theta_r - c_4\dot{x}_4 - k_4x_4 + k_3h_v = 0 \quad (7)$$

For the mass M_4 of the valve,

$$M_4\ddot{x}_4 + (c_4 + c_9)\dot{x}_4 + k_4x_4 - c_4\dot{x}_3 - k_4x_3 + [1 - u(x_4)](c_5\dot{x}_4 + k_5x_4 - F_0) + F_{sp} = 0 \quad (8)$$

where:

unit step function $u(x) = 1$, when $x \geq 0$

$u(x) = 0$, when $x < 0$

F_{sp}: Spring force
F_0: Preset spring force

Note that the equations derived are nonlinear, since k_i ($i = 0, 1, 2$) is a function of x and these equations are required to be changed according to the conditions of valve jump, valve clearance, and so forth. These equations are simultaneously solved with the second order partial differential equation for the valve spring using a "Time Marching Step" scheme.

Valve Spring Model

The valve spring, which is a helical spring, is a key factor governing the high-speed dynamic motion of the valve train. Therefore, accurate study of valve spring behavior is required to predict the dynamic characteristics of a valve train system. The valve spring is now modeled as a distributed parameter system instead of a lumped mass system as in previous research.

In order to calculate the stress and deflection of a valve spring, it is first necessary to derive the differential equation of spring motion. The equation is derived including masses, springs, and dampers with assumptions as follows. The spring is considered to be closely wound and to have homogeneous material properties along its length. Nonlinear effects such as coil crash and end effects are neglected.

Consider an element "Q" of the valve spring sketched in Fig. 5.

The inertia force applied to each element is

$$dF_a = \frac{\gamma}{g}\frac{\pi d^2}{4}dS\frac{\partial^2 y}{\partial t^2} \quad (9)$$

The total axial deflection d is described as

$$\delta = n_a\Delta y = \pi Dn_a\frac{\partial y}{\partial S} \quad (10)$$

where Δy is the axial deflection for one complete turn.

The total force P will be $k\delta$, where k is the static spring rate.

$$P = k\delta = k\pi Dn_a\frac{\partial y}{\partial S}$$

The net force dF_b acting on the element can be derived from P as

$$dF_b = \frac{\partial P}{\partial S}dS = k\pi Dn_a\frac{\partial^2 y}{\partial S^2}dS \quad (11)$$

The damping force dF_d is given by

$$dF_d = c'\frac{\partial y}{\partial t}dS \quad (12)$$

where c' is a damping coefficient per unit length of wire.

From force equilibrium, we have

$$dF_a = dF_b - dF_d$$

$$\frac{\gamma}{g}\frac{\pi d^2}{4}\frac{\partial^2 y}{\partial t^2} + c'\frac{\partial y}{\partial t} = k\pi Dn_a\frac{\partial^2 y}{\partial S^2} \quad (13)$$

The objective differential equation is obtained by rewriting Eq. (13) as:

$$\frac{\partial^2 y}{\partial t^2} + c_{eq}\frac{\partial y}{\partial t} = a^2\frac{\partial^2 y}{\partial S^2} \quad (14)$$

where,

total helix length of spring, $L = \pi Dn_a$
density of spring material, $\rho = \gamma/g$
equivalent damping coefficient, $c_{eq} = (4gc'/\pi d^2\gamma) = (4c'/\pi d^2\rho)$
wave velocity, $a = \sqrt{4kL/\pi d^2\rho}$

This equation will be combined with the equations for other parts of the valve train, which was derived earlier.

The equivalent damping coefficient (c_{eq}) is calculated by establishing deviation from critical damping. First, we need to derive the natural frequency of the spring. For this, it is permissible to neglect damping. The first natural frequency is

$$\omega_1 = \frac{a\pi}{L} = \sqrt{\frac{4k\pi}{Ld^2\rho}}$$

Now, the equivalent damping coefficient (c_{eq}) can be calculated, based on critical damping. That is

$$c_{eq} = 2\xi\omega_1 = 2\xi\sqrt{\frac{4k\pi}{Ld^2\rho}}$$

where ξ is a viscous damping factor. c_{eq} will be for critical damping when $\xi = 1$.

For a valve spring, ξ is usually taken to be in the range of 0.02–0.03 (Pisano and Freudenstein, 1983), ξ is chosen as 0.02 for this study.

Numerical Solution

The ordinary differential equations describing the motion of valve train masses and the partial differential equation describing the motion of a valve spring were separately derived in the preceding sections as Eqs. (1)–(8) and (14). In order to accurately determine the vibrational behavior of the valve train, these equations should be solved simultaneously, not by itera-

tion. However, difficulty in solving these equations arises from coupling of the ordinary and partial differential equations.

In this study, a scheme called "Time Marching Step" is used to solve these equations simultaneously. The main idea of "Time Marching Step" is that the partial differential equations can be treated as a group of ordinary differential equations as a function of time (t), if we discretize the partial differential equation with respect to a space variable (S). Then those ordinary differential equations, including the converted equations from the partial differential equation, are solved using the "Runge–Kutta–Fehlberg" method. This method provides an estimation of the error as well (Gerald and Wheatley, 1989).

Equations (1)–(8) for valve train masses can be arranged in matrix form:

$$[M']\{\ddot{x}\} + [c']\{\dot{x}\} + [K']\{x\} = \{F'\} \qquad (15)$$

where mass matrix $[M']$, damping matrix $[C']$, and stiffness matrix $[K']$ are given by

$$[M'] = \begin{bmatrix} M_1 & 0 & 0 & 0 & 0 \\ 0 & M_2 & 0 & 0 & 0 \\ 0 & 0 & I & 0 & 0 \\ 0 & 0 & 0 & M_3 & 0 \\ 0 & 0 & 0 & 0 & M_4 \end{bmatrix}$$

$$[C'] = \begin{bmatrix} c_0 + c_1 + c_6 & -c_1 & 0 & 0 & 0 \\ -c_1 & c_1 + c_2 & -c_2\iota_1 & 0 & 0 \\ 0 & -c_2\iota_1 & c_2\iota_1^2 + c_3\iota_2^2 & -c_3\iota_2 & 0 \\ 0 & 0 & -c_3\iota_2 & c_3 + c_4 + c_8 & -c_4 \\ 0 & 0 & 0 & -c_4 & c_4 + c_9 \end{bmatrix}$$

$$[K'] = \begin{bmatrix} k_0 + k_1 & -k_1 & 0 & 0 & 0 \\ -k_1 & k_1 + k_2 & -k_2\iota_1 & 0 & 0 \\ 0 & -k_2\iota_1 & k_2\iota_1^2 + k_3\iota_2^2 & -k_3\iota_2 & 0 \\ 0 & 0 & -k_3\iota_2 & k_3 + k_4 & -k_4 \\ 0 & 0 & 0 & -k_4 & k_4 \end{bmatrix}$$

and

$$\{F'\} = \begin{Bmatrix} c_0\dot{s} + k_0 s \\ 0 \\ \pm TF \\ 0 \\ F_{sp} \end{Bmatrix}$$

This damping matrix and stiffness matrix need to be modified according to valve jump, valve clearance, and so forth. Those modifications are not shown here; however, they can be easily demonstrated referring to the Eqs. (1)–(8).

The partial differential Eq. (14) for the valve spring is partially discretized with respect to the space coordinate (S) in the form:

$$\frac{d^2y_j}{dt^2} + c_{eq}\frac{dy_j}{dt} = a^2\frac{y_{j+1}^n + y_{j-1}^n - 2y_j^n}{\Delta S^2}$$

$$n = 1, 2, \ldots, NT, \quad j = 1, 2, \ldots, NS \qquad (16)$$

where $t = n\Delta t$ and $S = j\Delta S$.

Boundary conditions are as follows:

$$y_1 = x_4$$

$$y_{NS} = 0$$

The spring force (F_{sp}) is calculated as

$$F_{sp} = kL\left.\frac{\partial y}{\partial S}\right|_{s=0} \cong kL\frac{y_1^n - y_2^n}{\Delta S}$$

Equation (16) can be arranged in the matrix form:

$$[M'']\{\ddot{y}\} + [C'']\{\dot{y}\} = \{F''\} \qquad (17)$$

where mass matrix $[M'']$ and damping matrix $[C'']$ are given by

$$[M''] = \begin{bmatrix} 1 & 0 & . & . & . & . & . & 0 \\ 0 & 1 & 0 & . & . & . & . & 0 \\ 0 & 0 & 1 & 0 & . & . & . & 0 \\ . & . & . & . & . & . & . & . \\ 0 & 0 & 0 & 0 & 0 & 0 & 0 & 1 \end{bmatrix}$$

$$[C''] = c_{eq}\begin{bmatrix} 1 & 0 & . & . & . & . & . & 0 \\ 0 & 1 & 0 & . & . & . & . & 0 \\ 0 & 0 & 1 & 0 & . & . & . & 0 \\ . & . & . & . & . & . & . & . \\ 0 & 0 & 0 & 0 & 0 & 0 & 0 & 1 \end{bmatrix}$$

and

$$\{F''\} = \begin{Bmatrix} f_1'' \\ f_2'' \\ . \\ . \\ f_{NS}'' \end{Bmatrix}$$

where

$$f_j'' = a^2\frac{y_{j+1} + y_{j-1} - 2y_j}{\Delta S^2}$$

Now Eqs. (15) and (17) are combined to obtain the objective matrix form:

$$[M]\{\ddot{q}\} + [C]\{\dot{q}\} + [K]\{q\} = \{F\} \qquad (18)$$

where displacement vector $\{q\}$, mass matrix $[M]$, damping matrix $[C]$, stiffness matrix $[K]$, and force vector $\{F\}$ are

$$\{q\} = \begin{Bmatrix} \{x\} \\ \hline \{y\} \end{Bmatrix} \quad [M] = \left[\begin{array}{c|c} [M'] & 0 \\ \hline 0 & [M''] \end{array}\right]$$

$$[C] = \left[\begin{array}{c|c} [C'] & 0 \\ \hline 0 & [C''] \end{array}\right]$$

$$[K] = \left[\begin{array}{c|c} [K'] & 0 \\ \hline 0 & 0 \end{array}\right] \quad \{F\} = \begin{Bmatrix} \{F'\} \\ \hline \{F''\} \end{Bmatrix}$$

The reduced equation (18) was solved by using the "Runge–Kutta–Fehlberg" method.

Results and Discussion

In order to verify the overall simulation accuracy, a correlation between the simulated and measured pushrod force was conducted. For a correlation, we focused on not only magnitude but also frequency. The simulation results and the experimental data for pushrod forces at engine speeds of 750, 1100, and

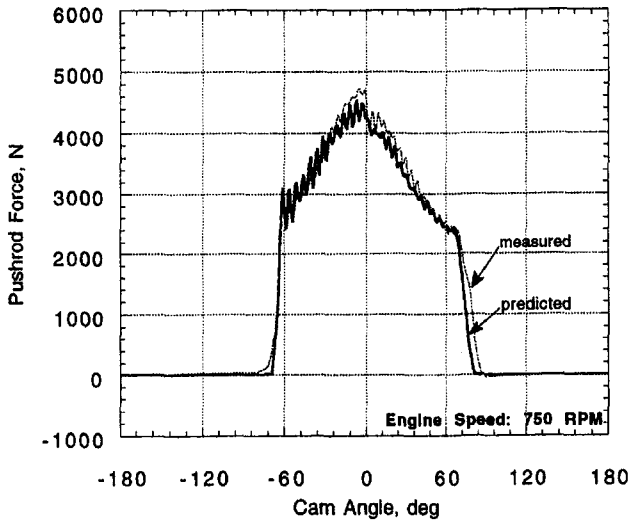

Fig. 6 Pushrod force at 750 rpm

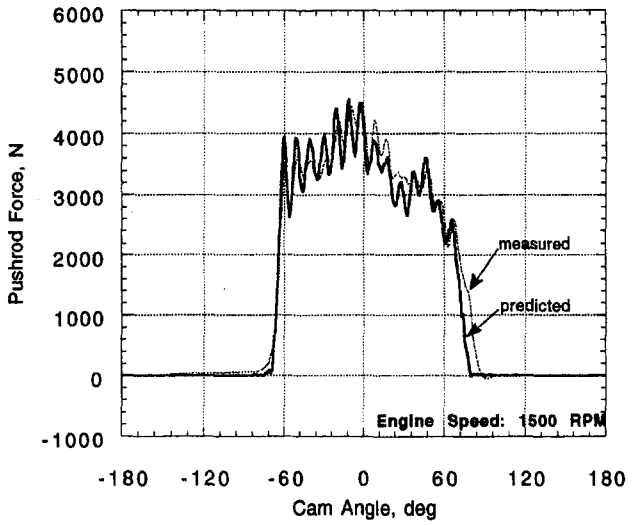

Fig. 8 Pushrod force at 1500 rpm

1500 rpm are shown in Figs. 6–8. The experimental work was presented in the previous research (Lee et al.). The calculated values of the pushrod force agreed very well with the experimental data both in magnitude and phase of vibration. In particular, the frequency of the simulated pushrod force vibration is very close to that of the experimental data. This model, which employs a distributed parameter model of a valve spring and nonlinear stiffness coefficients demonstrated better agreement with the measured value than previously published models, especially in terms of frequency. Valve jump and bounce were not seen in the simulations and our experiments, since the subject engine runs at relatively low speeds.

The energy losses during a cycle between the simulated and measured results were also compared for verifying the model regarding the friction loss. The energy loss factors included in the current model were viscous damping and Coulomb friction. Rocker arm pivot damping was considered as Coulomb friction since it operates under mixed lubrication due to high normal load. Upper valve train net friction over 360 deg of cam rotation was obtained by calculating the difference between the work flowing into the upper pushrod during valve opening and that recovered during closing. Figure 9 shows a comparison of upper valve train friction loss that includes rocker arm pivot, valve guide, etc., at each engine speed. The amount of friction loss between the simulated and calculated showed a good agreement. The measured friction loss was reduced as engine speed increased. However, the simulated friction loss showed an opposite trend. This opposite trend arises from the assumption that most of valve train components energy loss was considered as viscous damping rather than Coulomb damping. More detailed investigation of energy loss (damping) mechanism is left as a future study.

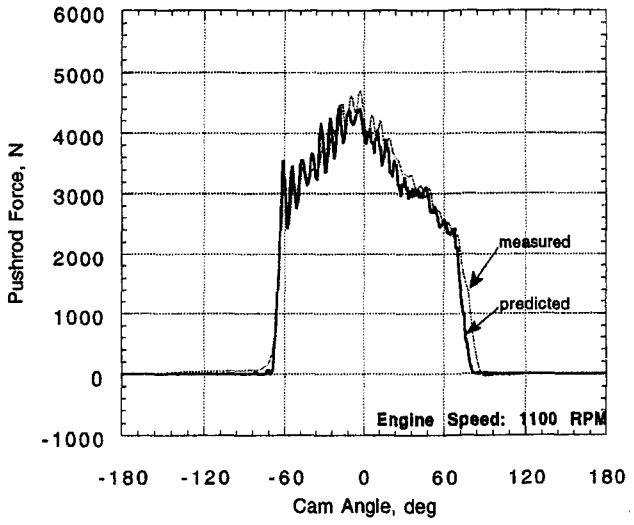

Fig. 7 Pushrod force at 1100 rpm

Conclusions

For the vibrational analysis of a valve train, a nonlinear five-degree-of-freedom model was developed and a valve spring was modeled as a distributed parameter system. The equations for a valve spring and other valve train components were solved simultaneously without any iterations. When compared with the experimental data, the dynamic model with the distributed parameter spring and the nonlinear stiffness coefficients provided an accurate simulation of the vibrational behavior of a valve train. Especially, the frequency of the simulated pushrod force was very close to that of the experimental data. It is critical to consider the stiffness of valve train components as nonlinear

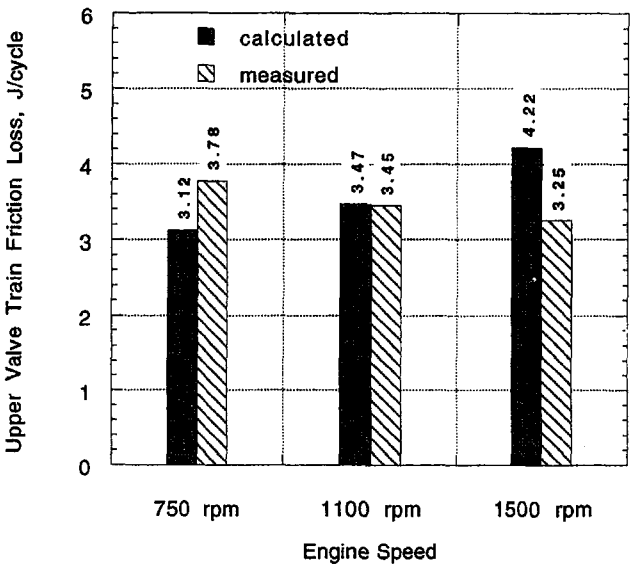

Fig. 9 Comparison of upper valve train friction loss (rocker arm, valve guide, etc., between pushrod and valve)

for improving the accuracy of a dynamic model, in particular, for a heavy-duty diesel engine since the valve train operates under heavy load. From the comparison of upper valve train energy loss, it was found that inclusion of Coulomb friction rather than viscous damping in a valve train model is necessary to improve the accuracy.

Acknowledgments

This research was partially supported by the U.S. Department of Energy. The authors wish to express our appreciation to Cummins Engine Co. for their technical support. We also thank SwRI for the permission to present this paper.

References

Adam, M., Bakaj, L., and Woyand, H. B., 1990, "Application of Numerical Simulation for the Analysis of the Dynamic Behavior of Valve Train Systems," *International Journal of Vehicle Design,* Vol. 11, No. 3, pp. 281–292.

Akiba, K., and Shimizu, A., 1981, "A Comprehensive Simulation of High Speed Driven Valve Trains," SAE Paper No. 810865.

Akiba, K., and Kakiuchi, T., 1988, "A Dynamic Study of Engine Valving Mechanisms: Determination of the Impulse Force Acting on the Valve," SAE Paper No. 880389.

Barkan, P., 1954, "Calculation of High Speed Valve Motion With a Flexible Overhead Linkage," *Transactions of SAE,* Vol. 61, pp. 687–700.

Chan, C., and Pisano, A., 1987, "Dynamic Model of a Fluctuating Rocker Arm Ratio Cam System," ASME *Journal of Mechanisms, Transmissions, and Automation in Design,* Vol. 109, pp. 356–365.

Chen, F. Y., 1975, "Dynamics of High Speed Cam-Driven Mechanisms," ASME *Journal of Engineering for Industry,* Vol. 97, pp. 769–776.

Chen, F. Y., 1982, *Mechanics and Design of Cam Mechanisms,* Pergamon Press, New York.

Gerald, C. F., and Wheatley, P. O., 1989, *Applied Numerical Analysis,* 4th ed., Addison-Wesley, Boston, MA.

Hrones, J. A., 1948, "An Analysis of the Dynamic Forces in a Cam Driven System," *Transactions of the ASME,* Vol. 70, pp. 473–482.

Hundal, M. S., 1999, "Aid of Digital Computer in the Analysis of Rigid Spring-Loaded Valve Mechanisms," *Applications of Computers in Valve Gear Design,* SAE, pp. 4–8.

Johnson, G. I., 1999, "Studying Valve Dynamics With Electronic Computers," *Applications of Computers in Valve Gear Design,* SAE, pp. 10–25.

Kurisu, T., Hatamura, K., and Omoti, H., 1991, "A Study of Jump and Bounce in a Valve Train," SAE Paper No. 910426.

Lee, J., Patterson, D. J., Morrison, K. M., and Schwartz, G. B., 1994, "Friction Measurement in the Valve Train With a Roller Follower," SAE Paper No. 940589.

Phlips, P. J., Schamel, A. R., and Meyer, J., 1988, "An Efficient Model for Valve Train and Spring Dynamics," SAE Paper No. 880619.

Pisano, A. P., and Freudenstein, F., 1983, "An Experimental and Analytical Investigation of the Dynamic Response of a High-Speed Cam Follower System: Parts I and II," ASME *Journal of Mechanisms, Transmissions, and Automation in Design,* Vol. 105, No. 4, pp. 699–704.

Pisano, A. P., 1984, "Coulomb Friction in High-Speed Cam Systems," ASME *Journal of Mechanisms, Transmissions, and Automation in Design,* Vol. 106, pp. 470–474.

Roark, R. J., and Young, W. C., 1975, *Formulas for Stress and Strain,* 5th ed., McGraw-Hill, New York.

Indicators of Fuel Maldistribution in Spark-Ignition Engines

A. C. Alkidas
Engine Research Department,
GM Research & Development Center,
Warren, MI 48090

Several exhaust-emissions-based parameters were experimentally found to be good indicators for fuel maldistribution (both in-cylinder and cylinder-to-cylinder) in spark-ignition engines. The quality of combustion greatly affected these indicators, thus possibly limiting their applicability. Corrections were developed to desensitize these indicators to the quality of combustion.

Introduction

Some degree of cylinder-to-cylinder fuel maldistribution is expected to exist in multi-cylinder port-fuel-injection (PFI) engines because of air-flow and fuel-injection unbalances. Recently, however, several studies (Arcoumanis and Enotiades, 1991; Baritaud and Heinze, 1992; Winklhofer et al., 1992), using optical techniques in PFI engines, have also shown the presence of significant in-cylinder mixture nonhomogeneities. Cylinder-to-cylinder fuel maldistribution and in-cylinder fuel stratification (air–fuel ratio nonuniformity) may cause an increase in emissions, primarily unburned hydrocarbons (HC), and carbon monoxide (CO), and a decrease in the fuel economy of the engine. In addition, the optimization of engine controls becomes exceedingly difficult.

To evaluate the degree of maldistribution (this term will be used to denote both cylinder-to-cylinder maldistribution and in-cylinder stratification unless otherwise specified), Eltinge (1968) introduced the parameter S_x, which physically represents the standard deviation of the fuel–air ratio distribution assuming that the distribution of fuel–air ratio is normal (Box et al., 1978).

The objective of the study is to evaluate the parameter S_x and other exhaust-emissions-based quantities as indicators of fuel maldistribution in spark ignition engines. A good metric for fuel maldistribution will facilitate the optimization of fuel delivery systems of engines.

Indicators for Fuel Maldistribution

Figure 1 shows computed equilibrium concentrations of the main exhaust gas species (CO, CO_2, H_2, H_2O, and O_2) as functions of the equivalence ratio of the reactants. Focusing our attention on the CO_2, CO, and O_2 species, the CO_2 concentration is highest at stoichiometric composition (equivalence ratio $\phi = 1$); as the stoichiometry of the reactants becomes leaner or richer the concentration of CO_2 decreases. The CO concentration is negligibly small for lean and stoichiometric mixtures ($\phi \leq 1$), and increases with increasing values of equivalence ratio for rich mixtures ($\phi > 1$). On the other hand, the O_2 concentration is negligibly small for rich and stoichiometric mixtures, and it increases linearly with decreasing values of equivalence ratio for lean mixtures.

These behaviors of the CO_2 and CO and O_2 exhaust concentrations with equivalence ratio allow us to use CO_2 and the linear combination of CO and O_2 as indicators of fuel maldistribution. The variations of the exhaust concentrations of CO_2 and of the combination CO + O_2 with equivalence ratio are highlighted in Fig. 2. At stoichiometric composition the CO_2 concentration attains a maximum value and the CO + O_2 concentration attains a minimum value. Furthermore, it is clear that a stoichiometric mixture that is nonuniform (has a distribution of equivalence ratios) will produce a lower exhaust concentration of CO_2 and a higher exhaust concentration of CO + O_2 than a uniformly distributed stoichiometric mixture. Thus, for stoichiometric mixtures, the exhaust concentration of CO_2 or the exhaust concentration of CO + O_2 may be employed as a measure of mixture nonuniformity.

Figure 3 shows the effects of the hydrogen–carbon ratio (H/C) of the fuel on the equilibrium values of CO_2 and CO + O_2 exhaust concentrations. These results show that CO_2 is moderately influenced by the H/C of the fuel throughout the range of equivalence ratio, whereas CO + O_2 is practically independent of the H/C of the fuel for the whole lean region and for rich compositions near stoichiometric; however, with progressively richer mixtures, the dependence of the CO + O_2 gradually increases.

The independence of the CO + O_2 exhaust concentration from the hydrogen–carbon ratio of the fuel for a large range of equivalence ratio makes this a very attractive indicator for fuel maldistribution.

The primary indicator for fuel maldistribution is the parameter S_x developed by Eltinge (1968) (see also Heywood, 1988). Assuming a normal distribution for the fuel–air ratio and complete combustion of the fuel, Eltinge computed the dry concentrations of CO, O_2, and CO_2 in terms of the fuel–air ratio of the mixture and the maldistribution parameter S_X, for a given value of the H/C of the fuel. The parameter S_X, as stated earlier, is the standard deviation of the fuel-air ratio distribution.

For ease of computation, Eltinge presented the following empirical equation of S_X in terms of the dry exhaust concentrations of CO and O_2:

$$\log S_x = a + b \log \mathrm{CO} + c \log \mathrm{O_2} + d(\log \mathrm{CO} * \log \mathrm{O_2}) \quad (1)$$

where log is the logarithm to the base 10, CO and O_2 are percent concentrations, and the constants a, b, c, and d, which are given in Table 1, are weak functions of the H/C of the fuel.

It is more convenient to consider equivalence ratio (stoichiometric value = 1) than fuel–air ratio. Therefore we defined S_ϕ as

$$S_\phi = S_x * \left(\frac{A}{F}\right)_{st} \quad (2)$$

where $(A/F)_{st}$ is the stoichiometric air–fuel ratio and S_ϕ is the standard deviation of the equivalence ratio distribution. Figure 4 shows the effect of S_ϕ on the equivalence ratio distribution with a mean value of unity (i.e., stoichiometric composition). One should note that a S_ϕ of, say, 0.05 means that the coefficient of

Contributed by the Internal Combustion Engine Division and presented at the Internal Combustion Engine 1995 Fall Technical Conference. Manuscript received at ASME Headquarters November 1996. Associate Technical Editor: W. K. Cheng.

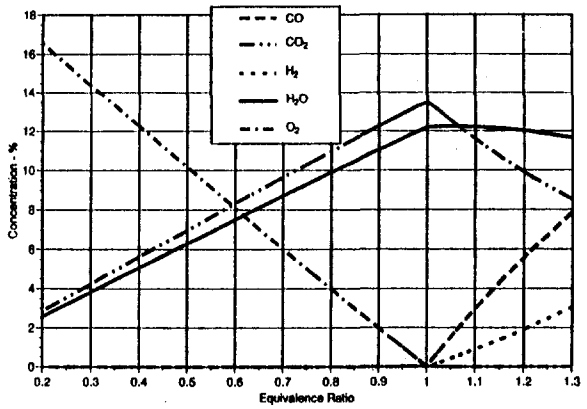

Fig. 1 Computed variations of the equilibrium wet concentrations of the main exhaust species with equivalence ratio

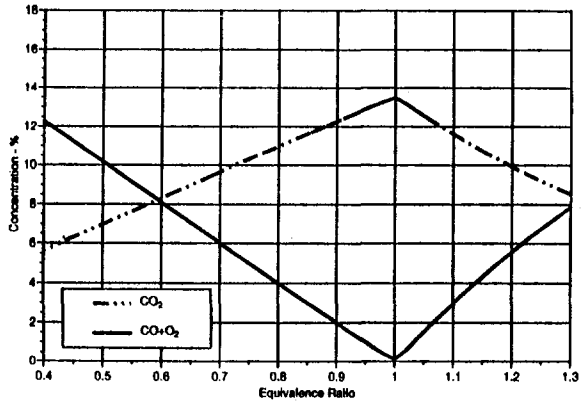

Fig. 2 Computed variations of the equilibrium wet concentrations of CO_2 and CO + O_2 with equivalence ratio

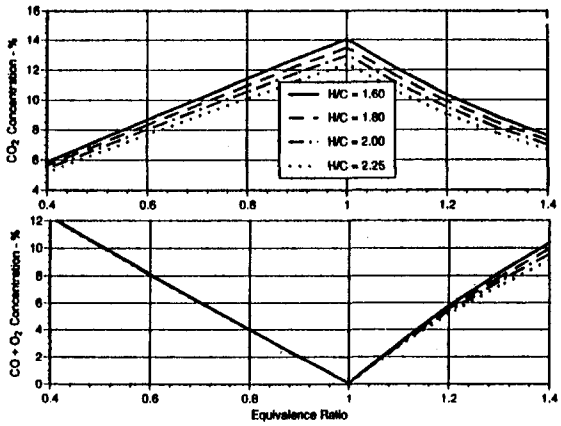

Fig. 3 Effects of the molar hydrogen–carbon ratio of the fuel on the equilibrium wet concentrations of CO_2 and CO + O_2

Table 1 Coefficients of the empirical equation for S_x

HC	a	b	c	d
1.14	-2.1311	0.3470	0.4126	-0.3320
1.80	-2.1463	0.3669	0.4227	-0.3424
1.90	-2.1492	0.3749	0.4312	-0.3498
2.00	-2.1503	0.3683	0.4208	-0.3480
2.25	-2.1537	0.3823	0.4241	-0.3470

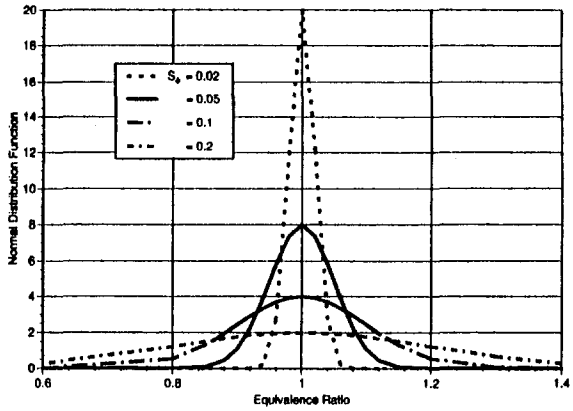

Fig. 4 Variations of the normal distribution of equivalence ratio with different values of the standard deviation, S_ϕ

Table 2 Engine specifications

Number of cylinders	4
Displacement (nominal), L	1.9
Compression ratio	9.5
Bore, mm	82
Stroke, mm	90
Connecting rod, mm	145
Pin offset, mm	0.8
Intake valve opening, deg	344
Intake valve closing, deg	592
Exhaust valve opening, deg	134
Exhaust valve closing, deg	374

0 deg corresponds to TDC (compression)

variation (COV)[1] of the equivalence ratio is 5%, a convenient measure.

Experimental Equipment and Procedures

Engine. The test engine was a Saturn 1.9L DOHC four-cylinder engine, which features pent-roof combustion chamber geometry, four valves per cylinder, and centrally located spark-plugs. The relevant specifications of the test engine are listed in Table 2.

Test Conditions. Baseline tests were run at two part-load conditions (test points B and D), which are described in Table 3. The lower part of this table lists the fluid temperatures, which were kept constant throughout this test series. Also, unless otherwise specified, injection timing, i.e., start of injection, was at TDCC (compression). The fuel used was Indolene (molar hydrogen–carbon ratio = 1.80, lower heating value = 42.28 MJ/kg, and stoichiometric air–fuel ratio = 14.5), the lubricating oil was Mobil 5W-30 and the coolant was a 50/50 mixture by volume of ethylene glycol and water.

To evaluate the above-discussed maldistribution indicators three types of comparative experiments were performed:

(A) *Variations of Operational Parameters:* The operational parameters and their ranges examined were equivalence ratio (0.935–1.074), injection timing (0–720 deg), exhaust gas recirculation (EGR) (0 and 8 percent), and coolant temperature (40 and 95°C).

[1] COV = 100 · (standard deviation/mean).

Table 3 Test points

Test Point	Test Conditions
B	1300 r/min, 330 kPa NMEP MBT spark timing
C	2200 r/min, 455 kPa NMEP MBT spark timing
D	2200 r/min, 650 kPa NMEP MBT spark timing

Outlet Coolant Temperature = 95 C
Outlet Oil Temperature = 95 C
Intake Air Temperature = 40 C

NMEP = BMEP + FMEP
where NMEP = net mean effective pressure
BMEP = brake mean effective pressure
FMEP = friction mean effective pressure
MBT = minimum spark advance for best torque

(B) *Premixed versus PFI Fuel Delivery Systems:* Using the identical test engine, the port fuel injection (PFI) production system was compared to a premixed, prevaporized fuel delivery system.

(C) *Cylinder-to-Cylinder Air–Fuel Ratio Variations:* The injection durations for cylinders #2 and 3 were adjusted such that the air–fuel ratios in the two cylinders were different (one leaner and the other richer) but the average air–fuel ratio of the exhaust stream sampled at the blowdown pipe (all four cylinders) remained constant, at stoichiometric.

Experimental Results

Effects of Operational Conditions. Figure 5 shows the variations of the parameter S_ϕ and of the exhaust concentrations of CO + O_2 and CO_2 with equivalence ratio, for the two part-load conditions examined, and for zero EGR and coolant temperature of 95°C. As expected from theoretical considerations, the CO_2 exhaust concentration exhibited a maximum and the CO + O_2 exhaust concentration exhibited a minimum at near stoichiometric composition. On the other hand, the S_ϕ parameter appears to have attained a minimum value in the lean region, roughly at 0.96 equivalence ratio. Furthermore, the S_ϕ parameter appears to have more data scatter and to be more influenced by the engine conditions than the CO + O_2 and the CO_2 emissions.

Figures 6 and 7 show the variations of the three maldistribution indicators with injection timing for the two engine test conditions, for air–fuel ratios of 14 and 15 (ϕ = 1.036 and 0.967), respectively. The intake valve opens at about 344 deg, and the durations of injection for test point B were 38.5 and 36.5 crankangle deg for the corresponding air–fuel ratios of 14 and 15. The corresponding injection durations for test point D were 113 and 118 crankangle deg.

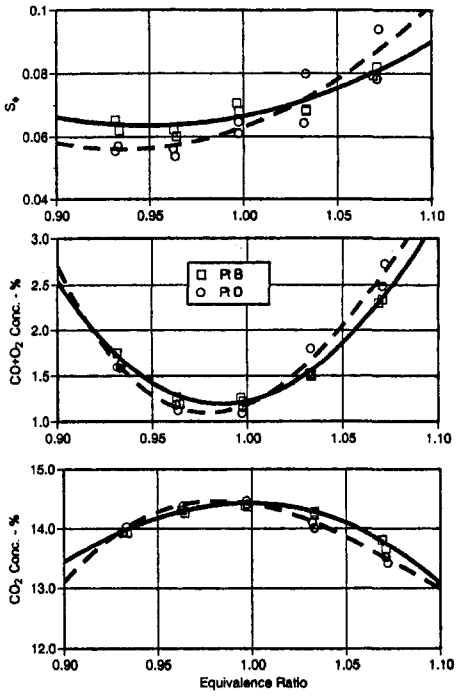

Fig. 5 Variations of the three fuel-maldistribution indicators with equivalence ratio for two engine loads

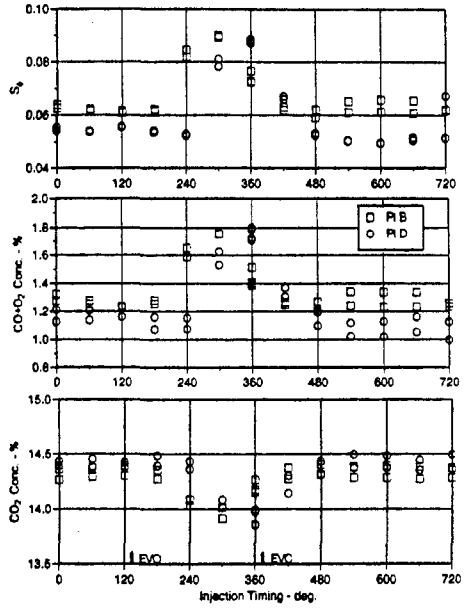

Fig. 6 Variations of the three fuel-maldistribution indicators with injection timing for two engine loads (air–fuel ratio = 14)

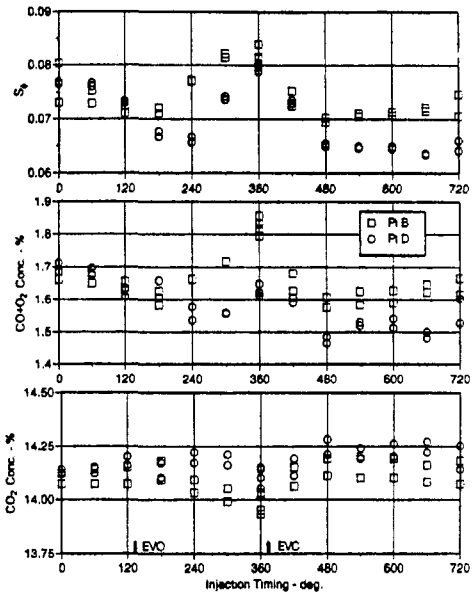

Fig. 7 Variations of the three fuel-maldistribution indicators with injection timing for two engine loads (air–fuel ratio = 15)

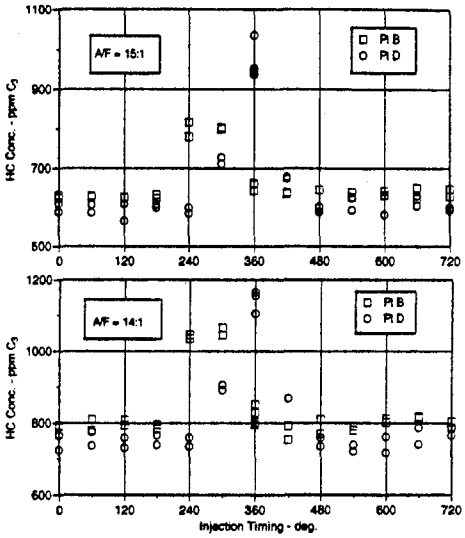

Fig. 8 Effects of injection timing on part-load engine-out unburned hydrocarbons for air-fuel ratios of 14 and 15

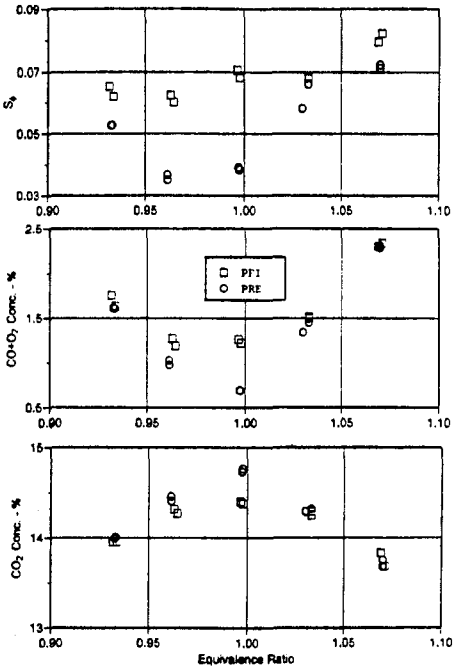

Fig. 9 The influence of fuel preparation (premixed, prevaporized system versus PFI system) on the three fuel-maldistribution indicators

These results show that within a range of injection timings, which is around the time for intake valve opening (IVO), S_ϕ and CO + O_2 attained maximum values and CO_2 attained a minimum value; outside this range, the values of these indicators were independent of injection timing.

Figure 8 shows the variations of the HC exhaust concentration with injection timing, which correspond to the conditions represented in Figs. 6 and 7. The overall trend of the variation of hydrocarbons with injection timing, exhibited in Fig. 8, is typical of other studies (Nogi et al., 1989; Yang et al., 1993; Alkidas, 1994). However, very remarkable is the similarity between the variations of hydrocarbons and the corresponding variations of the three maldistribution indicators.

The high HC emissions, which result when the injection timing is near IVO, are attributed to the incomplete vaporization of the fuel spray (Yang et al., 1993; Alkidas 1994). Thus, within a range of injection timings the fuel in the combustion chamber is not completely premixed and prevaporized, which causes an increase in the exhaust HC. Within this range, the parameter S_ϕ and the exhaust concentrations of CO + O_2 and CO_2 correctly predicted an increase in the fuel maldistribution.

PFI Versus Premixed. The influence of fuel preparation on the three potential indicators for fuel maldistribution is presented in Fig. 9, which shows the comparisons of the variations of these indicators with equivalence ratio for the test engine running with PFI and with a premixed fuel delivery system. Using the premixed, prevaporized fuel delivery system produced lower values of S_ϕ and CO + O_2 and higher values of CO_2 than using the PFI system. The differences in the values of the indicators using the two fuel delivery systems were highest near the stoichiometric condition. One should note that CO + O_2 and CO_2 exhaust concentrations are valid maldistribution indicators only at near stoichiometric conditions. Also, the parameter S_ϕ is accurate only near stoichiometric conditions (Eltinge, 1968).

Thus, all three indicators show that using a premixed, prevaporized fuel delivery system, instead of the production PFI system, resulted in a reduction in the fuel maldistribution.

Cylinder-to-Cylinder Air-Fuel Variation. To examine the sensitivity of the three indicators to cylinder-to-cylinder fuel maldistribution, the air–fuel ratios of cylinders 2 and 3 were intentionally varied, in such a way that the air–fuel ratios of the exhaust gases, which are normally sampled in the takedown (tkdn) pipe, did not change from their baseline value. Table 4 presents the values of air–fuel ratio of each cylinder, which were measured in appropriate locations at the exhaust manifold, their average value, the air–fuel ratio of the exhaust gases measured at the takedown pipe, and the coefficient of variation of the cylinder-to-cylinder air–fuel ratio. The first data column represents the unadjusted condition of the engine which has a COV of the cylinder-to-cylinder air–fuel ratio of 1.2 percent.

Figure 10 shows that as the COV of cylinder-to-cylinder air–fuel ratio increased, the S_ϕ and CO + O_2 increased and the CO_2 decreased. Furthermore, the variations of these indicators with the COV were linear. The exhaust concentration of CO + O_2 was most sensitive to changes in the COV of cylinder-to-cylinder air–fuel ratio followed by the parameter S_ϕ and least sensitive to the exhaust concentration of CO_2. A 100 percent change in the COV of cylinder-to-cylinder air–fuel ratio produced changes in the values of CO + O_2, S_ϕ, and CO_2 of roughly 27, 15, and −1.5 percent, respectively.

Thus, once more, the parameter S_ϕ and the exhaust concentrations of CO + O_2 and CO_2 correctly indicated changes in the fuel maldistribution.

Cylinder-to-cylinder variations in air–fuel ratio affect engine-out exhaust hydrocarbons. Figure 11 shows that the exhaust HC sampled at the exhaust manifold and at the takedown pipe increased significantly with increases in the COV of cylinder-to-cylinder air–fuel ratio. The higher values of HC sampled

Table 4 Cylinder-to-cylinder air–fuel ratio variations

Cyl #1	14.41	14.40	14.35	14.31
Cyl #2	14.69	15.31	15.96	16.87
Cyl #3	14.29	13.87	13.44	13.08
Cyl #4	14.69	14.72	14.74	14.72
AVG	14.52	14.58	14.62	14.74
TKDN	14.48	14.49	14.50	14.53
COV (%)	1.21	3.58	6.19	9.27

AVG = average of the four cylinders
TKDN = takedown pipe

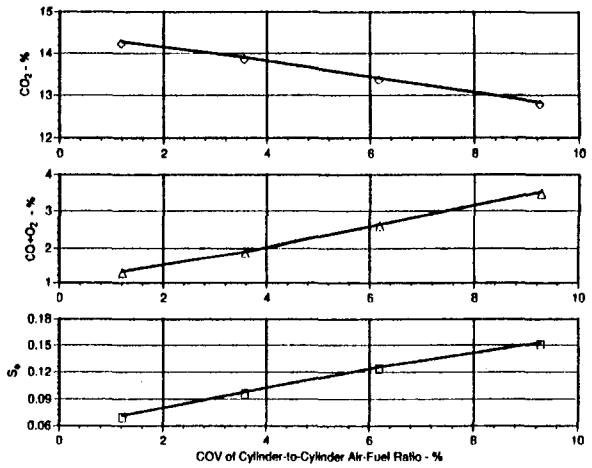

Fig. 10 Measured variations of the three fuel-maldistribution indicators with the COV of cylinder-to-cylinder air–fuel ratio

at the takedown pipe than those sampled at the exhaust manifold are thought to be due to the expected HC stratification at the exhaust manifold location. Normally one expects the HC concentration to decrease with increasing distance from the exhaust port because of HC oxidation.

Combustion Quality

The quality of the combustion process is expected to affect all exhaust emissions; consequently it is expected to affect the values of the three fuel maldistribution indicators, namely the exhaust concentrations of CO + O_2, of CO_2 and the parameter S_ϕ. Thus, a very important question remains to be answered. How do we correct for the effects of combustion quality in order that the values of the three potential indicators properly provide a measure of the fuel maldistribution? A further reason why one needs to consider the combustion of the fuel is that both the equilibrium calculations of the CO + O_2 and CO_2 exhaust concentrations and the analysis that led to the parameter S_ϕ assumed complete combustion of the fuel. However, in all engines, small but finite amounts of fuel escape the combustion process and exit the engine's cylinders as unburned hydrocarbons.

It is well known that below a certain level of manifold absolute pressure (ultra-light loads), the combustion process in an engine deteriorates and results in the emission of very high levels of hydrocarbons. Also, as the exhaust gas recirculation (EGR) increases, a point is reached beyond which the combustion process deteriorates, and consequently the brake specific fuel consumption (BSFC) and the exhaust hydrocarbons increase. The effects of manifold absolute pressure (MAP) at ultra-light loads and of EGR at a part-load condition on combustion quality were utilized to study the corresponding effects of combustion quality on the maldistribution indicators and to find ways to correct these indicators for combustion quality.

Corrections for the Presence of Unburned Hydrocarbons in the Exhaust. One way to correct for the presence of unburned hydrocarbons in the exhaust is to reduce the measured exhaust O_2 concentration by an amount equal to the amount needed to burn the exhaust unburned hydrocarbons completely, and to increase the measured exhaust CO_2 concentration by an amount equal to the amount of CO_2 produced by the combustion of the unburned hydrocarbons in the exhaust. Thus, the corrected O_2 concentration, $[O_2]_C$, and the corrected CO_2 concentration, $[CO_2]_C$, are given by

$$[O_2]_C = [O_2] - 0.0003\left(1 + \frac{y}{4}\right)[C_3] \tag{3}$$

$$[CO_2]_C = [CO_2] + 0.0003[C_3] \tag{4}$$

where $[O_2]$ and $[CO_2]$ are the measured O_2 and CO_2 concentrations in percent, $[C_3]$ is the measured concentration of unburned hydrocarbons in ppm C_3, and y is the molar hydrogen–carbon ratio of the fuel. Details of the derivations of all equations presented in this section are given in Appendix A.

Equations (3) and (4) are similar to those presented by Eltinge (1968) (see Appendix A), since they are based on the same reasoning. However, the magnitudes of corrections for both O_2 and CO_2 concentrations are much smaller in Eltinge's equations than for Eqs. (3) and (4). Because of absence of detail in the Eltinge study, the difference between the two sets of equations has not been resolved.

As discussed in Appendix A, another way to correct for the presence of unburned hydrocarbons is to assume that the amount of CO_2 present in the exhaust is proportional to the amount of fuel burned; then to use either the emission index of hydrocarbons, EIHC, or the combustion efficiency, η_C, to account for the unburned fuel. Thus one may derive the following equations for the corrected concentration of CO_2:

$$[CO_2]_C = \frac{[CO_2]}{\left(\frac{1 - \text{EIHC}}{1000}\right)} \tag{5}$$

and

$$[CO_2]_C = [CO_2] * \frac{100}{\eta_C} \tag{6}$$

One should note that Eqs. (5) and (6) are not equivalent equations. Using one or the other equation, one may also compute the corrected concentration of O_2 using the relation:

$$[O_2]_C = \left(1 + \frac{y}{4}\right)[CO_2]_C \tag{7}$$

The corrected concentrations of O_2 and CO_2, calculated by one of the above approaches, may be used to compute the maldistribution indicators: S_ϕ [Eqs. (1) and (2)] and exhaust concentrations CO + O_2 and CO_2.

Applications of the HC Corrections. At very light loads, because of the low pressures and temperatures and low turbulence levels in the combustion chamber, the quality of combustion in engines deteriorates with a significant increase in exhaust HC emissions. This is demonstrated in Fig. 12, which shows the variations of the emission indices of HC and NO and of the combustion efficiency with manifold absolute pressure (MAP), at ultra-light loads. As the MAP is decreased below about 28 kPa the combustion efficiency rapidly decreased and the HC

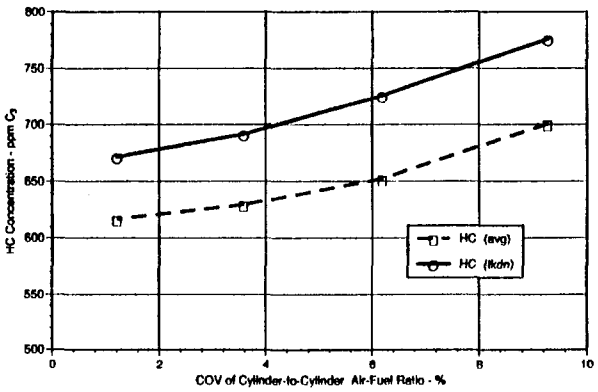

Fig. 11 Variations of the average exhaust-port HC concentration and the concentration measured at the takedown pipe with the COV of cylinder-to-cylinder air–fuel ratio

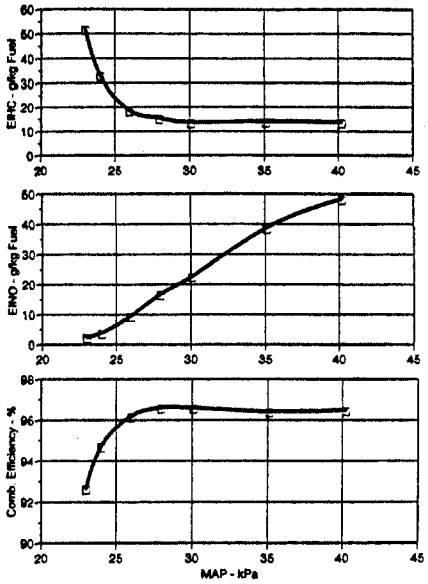

Fig. 12 Effects of manifold absolute pressure on the emission indices of hydrocarbon and oxides of nitrogen and on the combustion efficiency, for ultra-light-load conditions (1300 rpm, MBT spark timing)

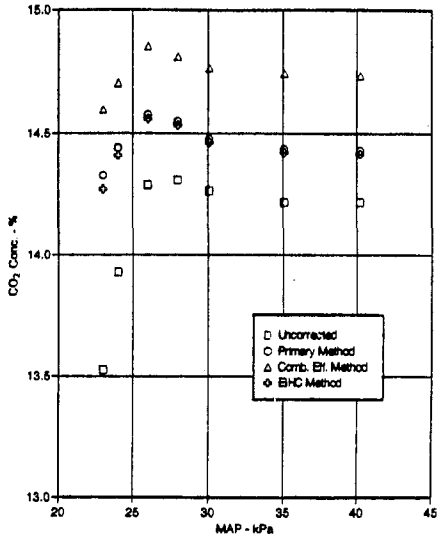

Fig. 14 Comparisons among three approaches for correcting the CO_2 concentration for the presence of unburned hydrocarbons in the exhaust

emissions rapidly increased. On the other hand, NO emissions appear to decrease linearly with MAP.

Figure 13 shows the corresponding variations of the three maldistribution indicators with MAP. The open-square symbols represent values calculated using the measured exhaust concentrations of CO, O_2, and CO_2, and the open-circle symbols represent values calculated using exhaust concentrations of O_2 and CO_2 corrected for exhaust hydrocarbons, using the primary method (Eq. (3) and (4)).

From the uncorrected values of the three indicators, it is apparent that as the quality of combustion deteriorates, both the parameter S_ϕ and exhaust concentration CO + O_2 increase, and the exhaust concentration of CO_2 decreases. Reducing MAP from 40 to 23 kPa resulted in percentage changes in the values of S_ϕ, CO + O_2 and CO_2 of roughly 60, 84, and −5 percent, respectively. Correcting for unburned hydrocarbons significantly reduced the sensitivity of these indicators to the combustion quality. Does it completely eliminate it? This is not clear because the changes in the indicator value, as the MAP is lowered, may be due to the effect of combustion quality, but it may also indicate an increase of fuel maldistribution with decreasing MAP for ultra-light loads.

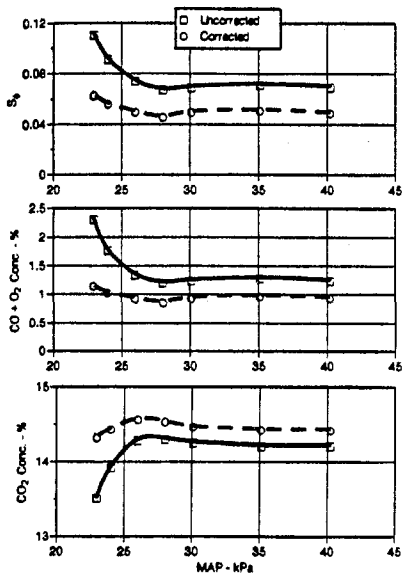

Fig. 13 Variations of the maldistribution indicators with manifold absolute pressure, for ultra-light loads. Comparison of HC-corrected and uncorrected indicators.

The effect of three types of hydrocarbon corrections on the exhaust concentration of CO_2 is shown in Fig. 14, which shows the variations of CO_2 concentration with MAP, for ultra-light loads. The open-square symbols represent the uncorrected CO_2 concentrations; the open circles, the open triangles, and the open crosses represent corrected CO_2 concentrations using the primary method, using the combustion efficiency, and using the emission index of HC, respectively. The correction method that utilizes EIHC appears to be equivalent to the primary method, whereas the combustion efficiency method resulted in much higher values of exhaust CO_2 concentration because it assumes that in addition to the unburned fuel the exhaust CO is also converted to CO_2. Nevertheless, the three "HC" correction methods produce similar behavior of CO_2 with MAP, and more importantly they desensitize the CO_2 emissions to the combustion quality.

The agreement between the two methods (primary and EIHC) suggests confidence in the corrections for combustion quality developed in this study. Consequently Eqs. (3) and (4) are to be preferred over the similar equations developed by Eltinge (1968), which result in much smaller corrections for both O_2 and CO_2 concentrations.

Turning our attention to the EGR experiments, Figs. 15 and 16, which correspond to test points B and C, respectively, show the deterioration of combustion efficiency and the corresponding dramatic increase in exhaust HC emissions when the EGR level was increased beyond a certain critical level. For the low-speed condition, this critical EGR level was about 12 percent, whereas for the high-speed condition this level was about 18 percent.

Figures 17 and 18 show the corresponding variations of the three maldistribution indicators with EGR for the two test conditions. In general, as EGR was increased the S_ϕ and CO + O_2 concentration gradually decreased and the CO_2 concentration gradually increased, until the critical EGR level was reached. Beyond this critical level, both the parameter S_ϕ and the CO + O_2 concentration rapidly increased and the CO_2 concentration rapidly decreased.

Thus, it is very clear that deterioration in the combustion quality results in increases of the parameter S_ϕ and in increases in the CO + O_2 concentration, and results in decreases in the CO_2 concentration. However, in order to utilize the parameter

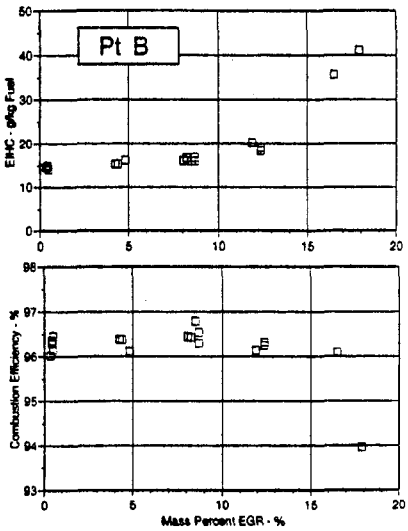

Fig. 15 The effects of exhaust gas recirculation on the hydrocarbon emission index and combustion efficiency at the part-load point B

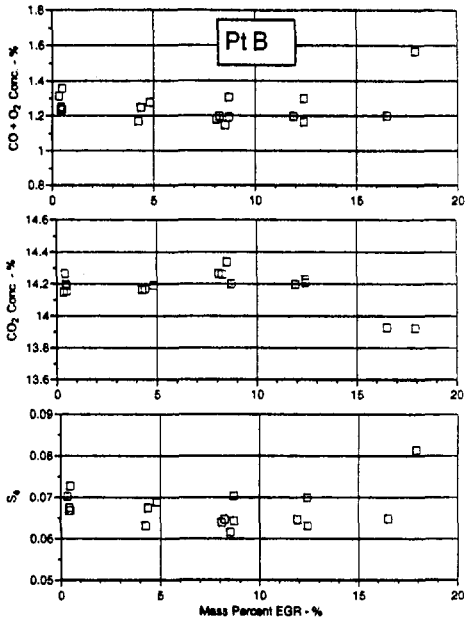

Fig. 17 Variations of the three fuel-maldistribution indicators with exhaust gas recirculation for the part-load condition *B*

S_ϕ and the exhaust concentrations of CO + O_2 and CO_2 as indicators of fuel maldistribution one needs to make two corrections to the results of Figs. 17 and 18. The first correction is the dilution effect of EGR on the exhaust concentration of CO and O_2, and the second correction is due to the presence of unburned hydrocarbons in the exhaust.

The corrected concentration of CO and CO_2 due to EGR dilution is given by:

$$[i]_C = \frac{[i]}{\left(\frac{1 - V_{EGR}}{100}\right)} \tag{8}$$

for i = CO, O_2, where $[i]_C$ is the corrected concentration of species i, $[i]$ is the concentration of species i, and V_{EGR} is the volume percent EGR. Details of the derivation of the Eq. (8) are given in Appendix B.

Figure 19 shows the variations of uncorrected S_ϕ and the corrected S_ϕ (both for EGR dilution and unburned hydrocarbons) with EGR for the two test points B and C. The correction for EGR dilution results in an increase in the CO and O_2 concentrations and therefore an increase in the value of S_ϕ. The hydrocarbon correction results in a decrease in the O_2 concentration and therefore a decrease in the value of S_ϕ.

Considering the variation of the corrected S_ϕ with EGR, in the case of test point B, S_ϕ remained constant up to an EGR level of about 12 percent; above this EGR level S_ϕ was significantly reduced. However, the data at the high EGR levels appear to be questionable. On the other hand, for point C, the corrected S_ϕ appears to decrease gradually with increasing level of EGR. The decrease in S_ϕ with increasing EGR level indicates that somehow increasing EGR decreases fuel maldistribution.

This trend is also predicted by examining the variations of the corrected concentration of CO + O_2 presented in Fig. 20 for the two test points. Once more, for point B, CO + O_2 remained constant up to an EGR level of about 12 percent; beyond this level the value of CO + O_2 appears to drop rapidly.

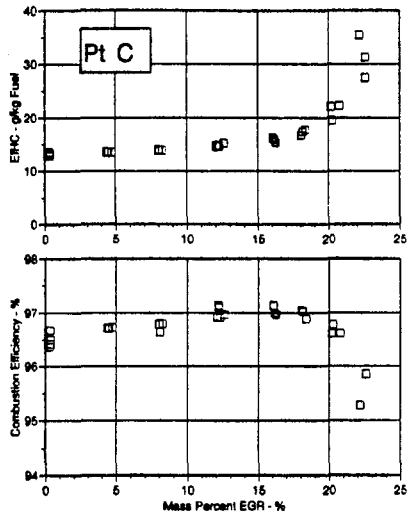

Fig. 16 The effects of exhaust gas recirculation on the hydrocarbon emission index and combustion efficiency at the part-load point C

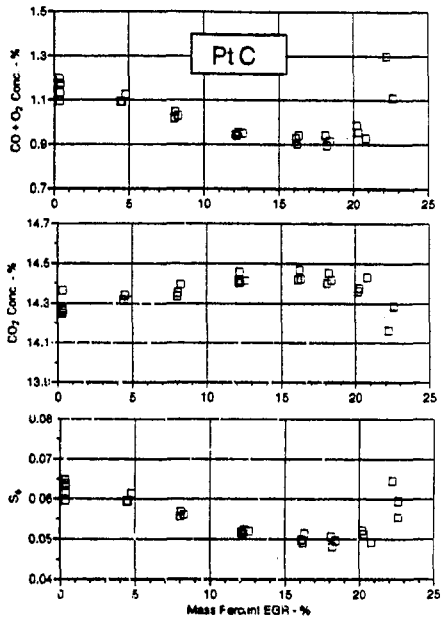

Fig. 18 Variations of the three fuel-maldistribution indicators with exhaust gas recirculation for the part-load condition *C*

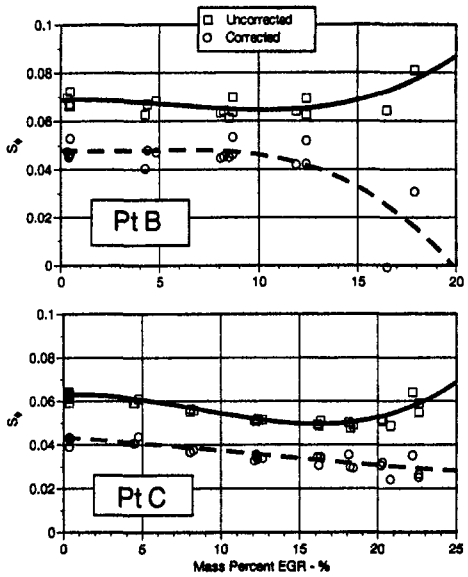

Fig. 19 Variations of S_ϕ and the combustion-corrected S_ϕ with exhaust gas recirculation for the two part-load conditions

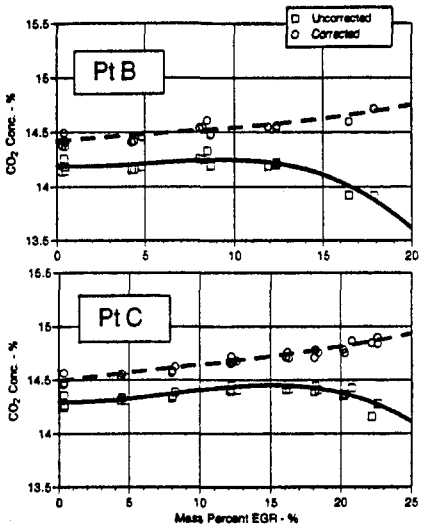

Fig. 21 Variations of CO_2 concentration and the combustion-corrected CO_2 concentration with exhaust gas recirculation for the two part-load conditions

On the other hand, for point C, the corrected concentration of CO + O_2 gradually decreased with increasing EGR level.

Figure 21 shows the variations of the corrected and uncorrected CO_2 concentrations with EGR for the two test points. Considering the corrected values, for both test points, the CO_2 concentration gradually increased with increasing EGR, indicating a progressive improvement in the fuel maldistribution with increasing EGR.

The behaviors of the parameter S_ϕ and the exhaust concentrations of CO + O_2 and CO_2 with EGR suggest that the fuel maldistribution is reduced with increasing EGR. Is this possible? Yes, although there is no evidence to corroborate this. A possible mechanism is that EGR augments the air temperature in the intake ports with the consequence of increasing the rates of evaporation of the fuel, which in turn improves the fuel distribution.

Discussion

The potential maldistribution indicators, which are based on exhaust emissions, are: CO_2, CO + O_2, and the parameter S_ϕ, which, in turn, is related empirically to the CO and O_2 emissions. Both the exhaust concentrations of CO + O_2 and of CO_2 are valid indicators of fuel maldistribution when the combustible mixture has stoichiometric composition. The parameter S_ϕ may have applicability for a wider range of air–fuel ratios; however, it too is most accurate for stoichiometric air–fuel mixtures (Eltinge, 1968; Heywood, 1988). Based on a number of tests, designed to vary the fuel distribution in the cylinder and the cylinder-to-cylinder fuel distribution, CO_2, CO + O_2, and S_ϕ, are good indicators of fuel maldistribution. The exhaust concentration of CO + O_2 is the most sensitive indicator to changes of the fuel distribution, followed with the parameter S_ϕ. The exhaust concentration of CO_2 has significantly lower sensitivity.

Figure 22 shows comparisons between the computed variation of equilibrium exhaust concentration of CO + O_2 with equivalence ratio and the measured variations of the exhaust concentration of CO + O_2 with equivalence ratio for several engines which include: the present study's four-cylinder, 1.9-L, Saturn engine utilizing both the production PFI system (Satrn-PFI) and a premixed, prevaporized fuel delivery system (Satrn-PRE), a single-cylinder, 2-L, Detroit Diesel Series 60 diesel engine (Ser. 60 diesel), a single-cylinder, GM Powertrain 3400 engine (3400 1-Cyl.) and a CFR engine, which utilizes a

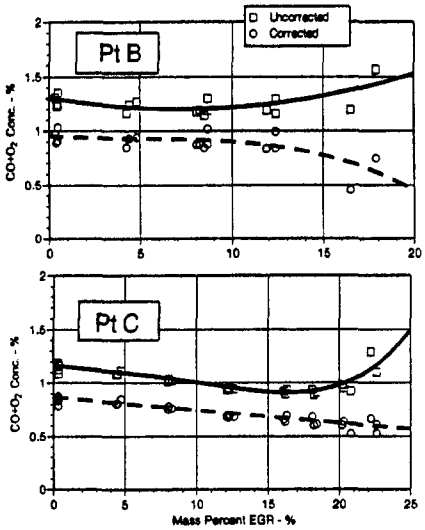

Fig. 20 Variations of CO + O_2 concentration and the combustion-corrected CO + O_2 concentration with exhaust gas recirculation for the two part-load conditions

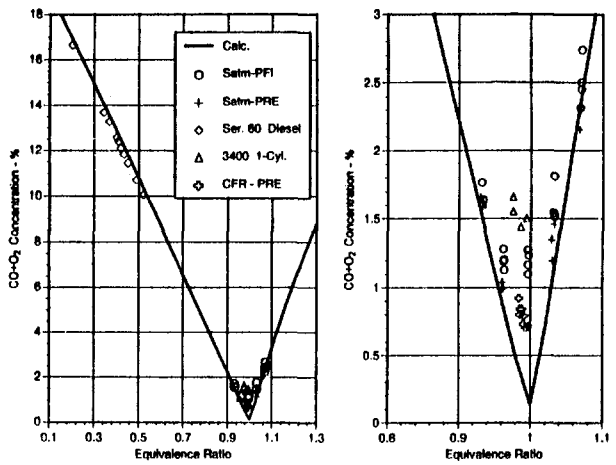

Fig. 22 Comparisons of the theoretical and experimental variations of the dry concentration of CO + O_2 with equivalence ratio

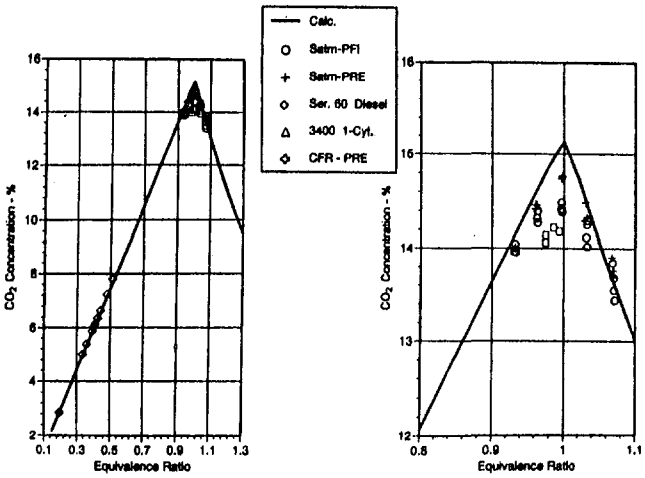

Fig. 23 Comparisons of the theoretical and experimental variations of the dry concentration of CO_2 with equivalence ratio

premixed, prevaporized fuel delivery system (CFR-PRE). The analytical results are represented by the solid lines. The left graph presents the data for a wide range of equivalence ratios (0.1 to 1.30), whereas the right graph magnifies the results at near stoichiometric composition (0.8 to 1.1). One must note that the computed equilibrium exhaust concentrations were converted to dry basis to be consistent with the measured exhaust concentrations.

Focusing at the near stoichiometric conditions where the CO + O_2 exhaust concentration may be used as a maldistribution indicator, the experimental CO + O_2 concentrations are significantly higher than the equilibrium concentrations. As expected, the lowest CO + O_2 concentrations were achieved by the engines utilizing premixed fuel delivery systems. These data were identified by crosses for ease of identification. At stoichiometric composition, the equilibrium CO + O_2 concentration is around 0.15 percent, the premixed engines resulted in values between 0.7 to 0.9 percent and the PFI engines produced CO + O_2 values of 1.1 percent and higher.

One should note that even for a perfectly uniform distribution of equivalence ratio the exhaust concentration of CO is expected to be in excess of its equilibrium value (Newhall, 1969). Furthermore, for the same equivalence ratio, it is independent of fuel type (Harrington and Shishu, 1973).

The corresponding comparisons between equilibrium values and measured exhaust concentrations of CO_2 (dry basis) are shown in Fig. 23. As expected, the equilibrium values are higher than the measured exhaust concentrations. At stoichiometric composition the equilibrium CO_2 concentration is around 15.1 percent, the premixed engines yielded a value of about 14.8 percent and the PFI engines produced values below 14.5 percent.

The applicability of the three fuel maldistribution indicators may be limited by the quality of combustion, which affects the three indicators in similar fashion to the fuel distribution. Thus, with increasing fuel maldistribution and/or deterioration in the combustion quality, the parameter S_ϕ and the exhaust concentration of CO + O_2 increase, and the exhaust concentration of CO_2 decreases. Alternatively, with decreasing fuel maldistribution and/or improving combustion quality, the parameter S_ϕ and the exhaust concentration of CO + O_2 decrease and the exhaust concentration of CO_2 decreases.

To minimize the effects of combustion quality on the three indicators for fuel maldistribution, simple equations were developed to correct the exhaust concentrations of O_2 and CO_2 for the presence of unburned hydrocarbons in the engine exhaust.

Conclusions

1 The parameter S_ϕ and the CO + O_2 and CO_2 exhaust concentrations are all good indicators of in-cylinder fuel stratification and cylinder-to-cylinder fuel maldistribution, for stoichiometric engine conditions. The exhaust concentration of CO + O_2 is the most sensitive indicator of fuel maldistribution, closely followed by the parameter S_ϕ.

2 Combustion quality significantly affects the three maldistribution indicators, thus possibly limiting their applicability. To minimize the effects of combustion quality on these indicators, simple equations were developed to correct the exhaust concentration of O_2 and CO_2 for the presence of unburned hydrocarbon in the engine exhaust.

References

Alkidas, A. C., 1994, "The Effects of Fuel Preparation on Hydrocarbon Emissions of a S.I. Engine Operating Under Steady-State Conditions," SAE Paper No. 941959.

Arcoumanis, C., and Enotiadis, A. C., 1991, "In-Cylinder Fuel Distribution in a Port-Injected Model Engine Using Rayleigh Scattering," *Experiments in Fluids*, Vol. 11, pp. 357–387.

Baritaud, T. A., and Heinze, T. A., 1992, "Gasoline Distribution Measurements With PLIF in a SI Engine," SAE Paper No. 922355.

Box, G. E. P., Hunter, W. G., and Hunter, J. S., 1978, *Statistics for Experimenters*, Chap. 2, Wiley, New York.

Eltinge, L., 1968, "Fuel–Air Ratio and Distribution From Exhaust Gas Composition," *SAE Transactions*, Vol. 77, pp. 425–450.

Harrington, J. A., and Shishu, R. C., 1973, "A Single-Cylinder Engine Study of the Effects of Fuel Type, Fuel Stoichiometry, and Hydrogen-to-Carbon Ratio on CO, NO, and HC Exhaust Emissions," SAE Paper 730476.

Heywood, J. B., 1988, *Internal Combustion Engine Fundamentals*, McGraw-Hill, New York, pp. 152–154.

Newhall, H. K., 1969, "Kinetics of Engine-Generated Nitrogen Oxides and Carbon Monoxide," *Twelfth Symposium (International) on Combustion*, The Combustion Institute, pp. 603–613.

Nogi, T., Ohyama, Y., and Yamauchi, T., 1989, "Effects of Mixture Formation of Fuel Injection Systems in Gasoline Engine," SAE Paper No. 891961.

Stivender, D. L., 1971, "Development of Fuel-Based Mass Emission Measurement Procedure," SAE Paper No. 710604.

Winklhofer, E., Fraidl, G. K., and Plimon, A., 1992, "Monitoring of Gasoline Fuel Distribution in a Research Engine," *Proc. Instn. Mech. Engrs., Part D, J. Automobile Engineering*, Vol. 206, pp. 107–115.

Yang, J., Kaiser, E. W., Siegi, W. O., and Anderson, R. W., 1993, "Effects of Port-Injection Timing and Fuel Droplet Size on Total and Speciated Exhaust Hydrocarbon Emissions," SAE Paper No. 930711.

APPENDIX A

Corrections for Exhaust Unburned Hydrocarbons

Primary Approach. Consider the chemical equation for the stoichiometric combustion of the fuel C_nH_{ny}:

$$C_nH_{ny} + n\left(1 + \frac{y}{4}\right)(O_2 + 3.773\ N_2) = nCO_2 + \frac{ny}{2}H_2O \quad (9)$$

where n is the number of carbon atoms in the fuel, and y is the molar hydrogen–carbon ratio of the fuel.

Thus, the relation between the oxygen concentration and the fuel concentration for stoichiometric combustion is

$$[O_2] = n\left(1 + \frac{y}{4}\right)[C_n] \quad (10)$$

where $[O_2]$ and $[C_n]$ are the concentrations of O_2 and of the fuel.

Similarly, the relations between the carbon dioxide concentration, $[CO_2]$, and the oxygen and fuel concentrations are

$$[CO_2] = \frac{[O_2]}{\left(1 + \frac{y}{4}\right)} \quad (11)$$

$$[CO_2] = n[C_n] \quad (12)$$

In the exhaust, the unburned hydrocarbons are measured in ppm C_3, and the concentrations of O_2 and CO_2 are measured

in percent. Thus the oxygen concentration required to consume the unburned hydrocarbons is

$$[O_2] = 0.0003\left(1 + \frac{y}{4}\right)[C_3]$$

and the corrected oxygen concentration is

$$[O_2]_C = [O_2] - 0.0003\left(1 + \frac{y}{4}\right)[C_3] \tag{13}$$

where $[O_2]_C$ is the corrected O_2 concentration in percent and $[C_3]$ is the unburned hydrocarbons in ppm C_3.

For a fuel of hydrogen–carbon ratio $y = 1.8$, the corrected O_2 concentration is given by

$$[O_2]_C = [O_2] - 0.000435\,[C_3] \tag{14}$$

From Eq. (12), the CO_2 concentration formed by the consumption of the unburned hydrocarbons is

$$[CO_2] = 0.0003\,[C_3]$$

and the corrected concentration of CO_2 is

$$[CO_2]_C = [CO_2] + 0.0003[C_3] \tag{15}$$

where $[CO_2]_C$ and $[CO_2]$ are the corrected and actual CO_2 concentrations expressed in percent.

Following similar reasoning, Eltinge (1968) suggested the following equations for correcting the O_2 and CO_2 concentrations:

$$[O_2]_C = [O_2] - 0.000190[C_3]$$

$$[CO_2]_C = [CO_2] + 0.000120[C_3]$$

One should note that the original Eltinge equations, which were expressed in terms of ppm hexane, were transformed to the equations by employing the relation $2[C_3] = [C_6]$. It is clear that Eltinge corrections of the O_2 and CO_2 concentrations for the presence of unburned hydrocarbons are significantly different than the corresponding Eqs. (14) and (15). The reason for this discrepancy is not clear, since Eltinge did not provide any details of the derivation of these corrections.

Other Approaches. Another way to correct for the presence of unburned hydrocarbons is to assume that the amount of CO_2 present in the exhaust is proportional to the amount of fuel burned. Thus, the ratio of actual mass of fuel burned to the total mass of fuel burned for complete combustion, y_C, is equal to the ratio of actual CO_2 concentration to the corrected CO_2 concentration. Then, the corrected concentration of CO_2 is given by

$$[CO_2]_C = \frac{[CO_2]}{y_C} \tag{16}$$

The ratio of the actual to the total mass of fuel burned, y_C, may be approximately expressed in terms of the emission index of hydrocarbons, EIHC ($= g$ of HC/kg of fuel), as

$$y_C = \frac{(1000 - \text{EIHC})}{1000}$$

Hence, the corrected concentration of CO_2 is given by

$$[CO_2]_C = \frac{[CO_2]}{\left(1 - \dfrac{\text{EIHC}}{1000}\right)} \tag{17}$$

The ratio y_C may also be approximately expressed in terms of the combustion efficiency, η_C, as

$$y_C = \frac{\eta_C}{100}$$

Hence, the corrected concentration of CO_2 is given by

$$[CO_2]_C = [CO_2] * \frac{100}{\eta_C} \tag{18}$$

The combustion efficiency is defined as (Stivender, 1971):

$$\eta_C = 100\left(1 - \frac{\Sigma\, n_i h_i}{h_f}\right)$$

where the n_i are the number of moles of CO, H_2, and HC per mode of fuel, respectively, the h_i are the molar enthalpy of combustion of these species and h_f is the molar enthalpy of combustion of the fuel.

To correct the O_2 concentration for the presence of unburned hydrocarbons, one may use Eq. (11). Thus

$$[O_2]_C = \left(1 + \frac{y}{4}\right)[CO_2]_C \tag{19}$$

APPENDIX B

Corrections for EGR Dilution

The main assumption for the development of the correction for EGR dilution is that the EGR gases do not contribute to the exhaust CO and HC emissions. That is, the products of incomplete combustion present in the EGR gases entering the chamber react with the available oxygen to form products of complete combustion prior to exiting the combustion chamber.

Let n_{CO} equal the moles of exhaust CO, then the CO exhaust mole fraction is

$$[CO] = \frac{n_{CO}}{(n_A + n_F + n_{EGR})}$$

Thus

$$\frac{n_{CO}}{n_A + n_F} = [CO]\left(\frac{1 + n_{EGR}}{n_A + n_F}\right) \tag{20}$$

Let V_{EGR} equal the volume percent EGR, i.e.,

$$V_{EGR} = 100 * \frac{n_{EGR}}{(n_A + n_F + n_{EGR})}$$

or

$$\frac{n_{EGR}}{(n_A + n_F)} = \frac{\dfrac{V_{EGR}}{100}}{\left(1 - \dfrac{V_{EGR}}{100}\right)} \tag{21}$$

Substituting Eq. (21) into Eq. (20) yields

$$\frac{n_{CO}}{(n_A + n_F)} = \frac{[CO]}{\left(1 - \dfrac{V_{EGR}}{100}\right)} \tag{22}$$

Similarly,

$$\frac{n_{HC}}{(n_A + n_F)} = \frac{[HC]}{\left(1 - \dfrac{V_{EGR}}{100}\right)} \tag{23}$$

Equations (22) and (23) are the EGR–dilution corrected mole fractions of CO and HC.

J. Y. Tu
Senior Computational Scientist,
Australian Nuclear Science and
Technology Organisation (ANSTO),
PMB 1, Menai, NSW 2234, Australia

C. A. J. Fletcher
Professor,
Centre for Advanced Numerical
Computation in Engineering &
Science (CANCES).

M. Behnia
Associate Professor,
School of Mechanical and
Manufacturing Engineering.
Mem. ASME

The University of New South Wales,
Sydney 2052, Australia

J. A. Reizes
Professor,
School of Mechanical Engineering,
University of Technology, Sydney,
P. O. Box 123 Broadway,
NSW 2007, Australia

D. Owens
Power Engineer.

P. Jones
Power Engineer.

Power Plant Engineering,
Pacific Power,
New South Wales 2001, Australia

Prediction of Flow and Erosion in Power Utility Boilers and Comparison With Measurement

Multidimensional simulations of both flue gas and fly ash (solid particle) flows with application to erosion prediction in the economisers of coal-fired power utility boilers are reported. A computer code specifically designed for power utility boilers, DS4PUB (Design Software for Power Utility Boilers), was used for the calculations. The major area of erosion often occurs at the economizer of the boiler and depends on the particulate velocity and concentration so that computational results include the economizer inlet distribution of the mean flue gas and particulate velocities, and fly ash concentration. The computer code was validated by comparisons with previously available experimental data and recently performed measurements for flue gas flow velocity, dust burden, and erosion rates at the inlet of economizers in large operating power stations. The results of the multidimensional simulations agreed reasonably well with the experimental measurements. An important finding of this study is that the transverse location of maximum erosion in the economizer tube bank strongly depends on the upstream geometric design of the boiler. For boilers with a shorter turning flow path, the maximum erosion is found to be close to the rear wall of the economizer because both the maximum particulate velocity and concentration occur in this region. For configurations with a long flow path, which includes a splitter plate, the maximum erosion region was found to be closer to the front wall of the economizer, mainly due to the high flow velocity in this region. A relatively high erosion area close to the side and rear wall was also found because of the high concentration of large fly ash particles in this area. Interesting features of fly ash flow in multidimensional complex boiler geometries such as concentration distributions for different fly ash particle sizes are also discussed.

Introduction

Burning pulverized coal for electricity generation creates products of combustion that contain small solid particles (fly ash). These particles are carried by the flue gas through the tube banks in power utility boilers. It is well known (e.g., Jones and Owens, 1995) that the transported fly ash can cause severe erosion to the boiler tubes, especially in the economizer, and the annual cost of erosion to a plant operator can be many millions of dollars (Pacific Power, 1995). A method of reducing erosion by appropriate modifications during the design stage of power utility boilers is crucial for their safe and more efficient operation. Many experimental and computational studies (Schweitzer and Humphrey, 1988; Schuh et al., 1989; Fan et al., 1991, 1992; Jun and Tabakoff, 1994) have contributed to understanding the role of the mechanism of solid particles eroding the material surface of an individual tube or two-in-line tubes.

There is very little reported work in which both global flue gas and fly ash flows in a full-scale boiler were simulated and the erosion distribution evaluated from the mean particulate velocity and concentration. The complexity of the flow generated within a power utility boiler (three-dimensional, two-phase, and turbulent) has compelled designers to make use of empirical information, often complemented by pilot plant experiments, in order to tackle problems associated with the erosion reduction (Bauver et al., 1984), and the design of new boilers (ECNSW, 1988; Jones and Owens, 1995). Such a design procedure is rather expensive and inefficient, and more importantly, it is often valid only for a very restricted parameter range. Available evidence suggests that the key to understanding the erosion caused by solid particle impact is the identification of a coupled and complex phenomenon including both fluid and particle motions (Humphrey, 1990). It is very important for designers to have information about the location of the maximum erosion rate and its causes. If this were available, erosion protection measures and new boiler configurations with lower erosion rates could be more readily developed. Thus, a computer code that accurately predicts the detailed flow and particulate distributions within power utility boilers under different operating conditions would be a desirable tool. Optimization of boiler configurations to minimize erosion rate could then also proceed in a cost-effective way.

The aim of the present investigation is to apply a specially written computational fluid dynamics (CFD) code for power

Contributed by the Power Division for publication in the JOURNAL OF ENGINEERING FOR GAS TURBINES AND POWER. Manuscript received by the Power Division January 1996; revision received November 1996. Associate Technical Editor: D. Lou.

utility boilers (DS4PUB), to investigate the flue gas and fly ash flows in two types of large boiler configuration (see Figs. 1 and 2), currently operating in the State of New South Wales, Australia. An attempt has been made to verify the computational results by using experimental data previously obtained at the Vales Point Power Station (total capacity 660 MW) (Platfoot, 1991; Benyon, 1991) and recent measurements performed for the validation of this program at the Wallerawang Power Station (total capacity 500 MW) (Pacific Power, 1995; Jones and Owens, 1995). Since erosion tends to be localized in particular areas of the boiler, failures have generally been experienced in the economizer (Benyon, 1991; Jones and Owens, 1995) where nonuniform flue gas and fly ash flow distributions occur (Platfoot, 1991; Pacific Power, 1995). Flue gas velocity, fly ash concentration, and tube wall thickness reduction (i.e., tube erosion rate) in the economizer were compared with calculated results.

Computational Approach

A brief description of the computer code used in this study is given in this section. The computational mesh and boundary conditions are also described.

DS4PUB Code. An advanced computer code specifically designed for power utility boilers, DS4PUB, is used to perform the computations. DS4PUB was developed mainly by the University of New South Wales, as part of a syndicate including Pacific Power (the State electricity generating company), Australian Nuclear Science and Technology Organisation (ANSTO), and the University of Sydney, to predict the flue gas flow and temperature and fly ash (particulate) behavior in large pulverized coal-fired boilers. The basic capabilities/methodologies in the DS4PUB code are presented in the appendix of this paper.

DS4PUB has undergone a considerable amount of systematic quantitative validation for both single and two-phase flows. Good-to-excellent agreement between benchmark experimental data and predictions has been shown (Guzman et al., 1994; Tu and Fletcher, 1994, 1995a, b; Zdravistch et al., 1995). In the present work, comparisons are presented of numerical predictions with measurements under operating condition in full-scale power station boilers.

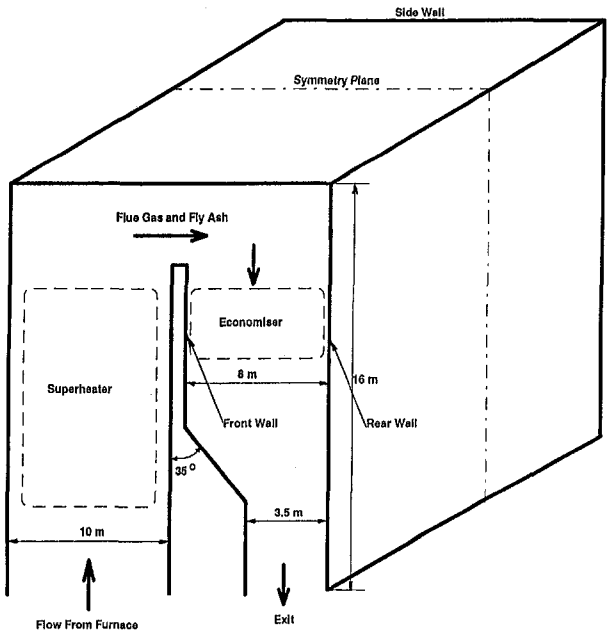

Fig. 1 Geometric domain for a typical power utility boiler (Vales Point Power Station boiler)

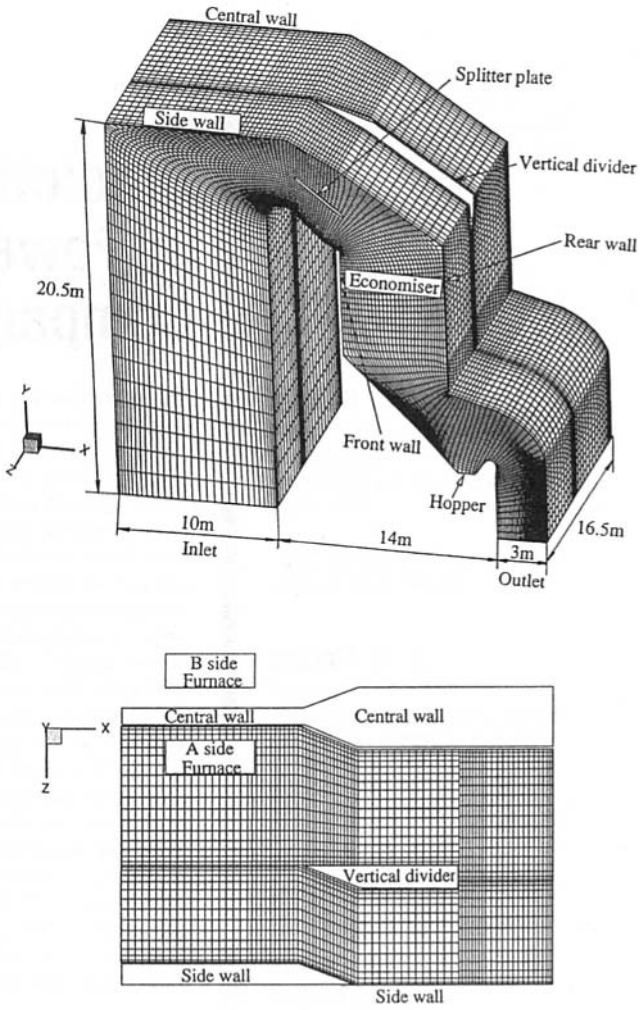

Fig. 2 Geometric domain and computational grid used for the Wallerawang Power Station boiler

Boiler Configurations and Computational Grids. Figure 1 illustrates a simplified arrangement of a typical power boiler with a 180 deg bend at the top. The flow characteristics of such a boiler configuration are that the flue gas and fly ash entrained into the economizer are thrown to the rear wall of the economizer due to centrifugal forces. The velocities of both flue gas and fly ash are highest in this region. One of the power boilers operating in Vales Point Power Station boiler has a configuration similar to Fig. 1 and measurements performed previously (Platfoot, 1991; Benyon, 1991) have been used for comparison with the present predictions.

In addition to there being a 180 deg bend in many power boiler configurations, some boiler designs present more complex flow paths, which entirely modify the flow characteristics of both the flue gas and the fly ash entrainment into the economizer. One example of such a boiler configuration is found at Wallerawang Power Station. Since this is a twin furnace boiler, it is symmetric about the central wall so that only one half of the boiler geometry need be used in the calculations. The computational domains are shown in Fig. 2. The flow passages from the superheaters are divided by several walls and plates before the flow enters the economizer. Because this increases the flow path from the superheater exit to the inlet of the economizer and the splitter plate in particular redistributes the flow, both the flue gas and fly ash are forced into the economizer near the front wall rather than the rear wall as in the previously discussed case. As a result, the erosion distribution in the econo-

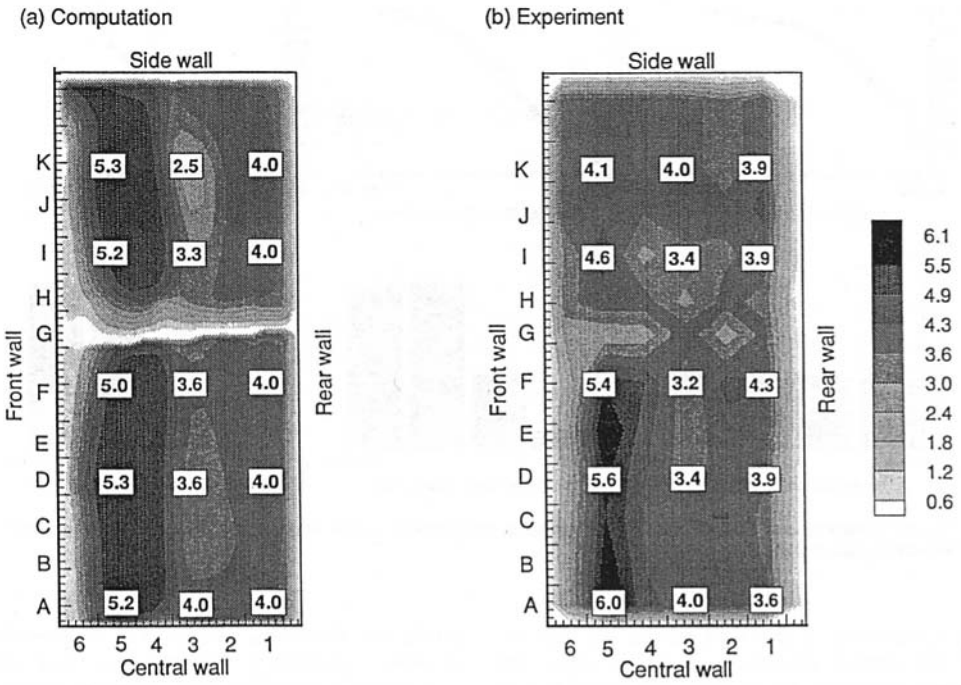

Fig. 3 Comparison of predicted gas velocity magnitudes at the economizer inlet with measurements

mizer tube bank for such a boiler configuration is quite different from the first configuration mentioned.

Here, body-fitted, nonuniform, nonorthogonal curvilinear coordinate grids for the configurations in Figs. 1 and 2 were generated using algebraic grid generation techniques with an elliptic grid smoother. The grid in Fig. 2 consists of 117,000 computational cells ($30 \times 130 \times 30$ in the I, J, K directions). Stretched grids are used to obtain an acceptable distribution of points near solid surfaces. Some solid cells (dead cells) are used for representing the splitter plate and the vertical divider within the boiler. The heat exchanger assemblies (such as superheaters and economizers) in the boiler are not modeled in this study.

Boundary Conditions. A uniform flow velocity and a uniform fly ash concentration distribution at the boiler inlet are assumed. The velocity distributions of the flue gas at the inlet of the boiler are specified to match the global flow mass conservation obtained experimentally at the inlet of the boiler. The fly ash velocity is assumed to be the same as the gas velocity at the inlet of the economiser. At the outflow the normal gradient of all dependent variables is set to zero. A "no-slip" boundary condition is employed for the gas velocity at solid boundaries. The boundary conditions on solid walls for the particulate phase are related to the mean restitution coefficients of particles interacting with the wall surface. The mean restitution coefficients of fly ash were obtained from experimental observations (Amoroso, 1990). Further details about the derivation and implementation of the Eulerian boundary conditions for the particulate phase can be found in Tu and Fletcher (1995a).

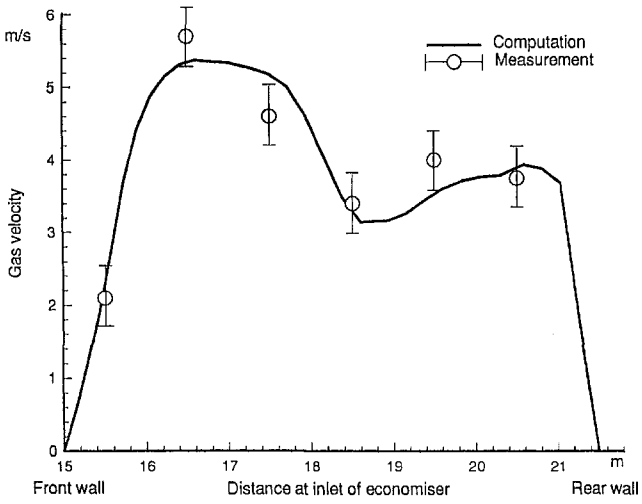

Fig. 4 Comparison of the gas velocity profile at Section D (see Fig. 3)

Results and Discussion

The following results include the flue gas and fly ash flow predictions together with erosion rate estimations. The numerical results are compared with experimental data wherever they are available.

Flue Gas Flow. Measurements, using cold air, of gas velocity distributions at the economizer inlet of the Wallerawang Power Station boiler (Pacific Power, 1995) were carried out specifically for the validation of the present computational modeling studies. Velocity measurements were taken on a grid of 6×11 points in each half of the economiser, 0.5 m above the top economizer tube bank. Velocity magnitudes ($|U| = \sqrt{u^2 + v^3 + w^2}$) were measured using a hand-held Kuiz velocity meter. For these measurements, both the induced and forced draft fans were operated at near their maximum flow conditions. Detailed description of flow conditions and measurement techniques can be found in the Pacific Power (1995) report.

Figure 3 shows a comparison of the measured and computed gas velocity at the economiser inlet. The results shown in Fig. 3 are present on a horizontal plane at the inlet to the economizer, which is just below the end of the vertical divider (Fig. 2). The numbers (1–6) and the letters (A–K) are used to define the location of the experimental velocity measurements. Section G (points G1 to G6) lies immediately below the end of the vertical divider. It can be seen from Fig. 3 that the distribution of gas velocity magnitude from the numerical prediction is generally in good agreement with the measurements.

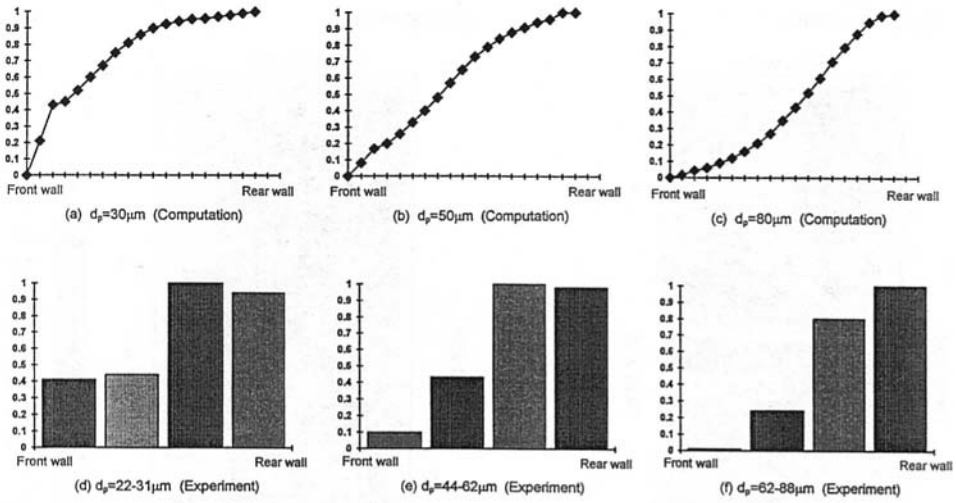

Fig. 5 Comparisons of particulate concentration distribution at the economizer inlet in the Vales Point Power Station boiler

Approximately 60 percent of the flow passes between the central wall and the vertical divider, so that this region has been called the main flow pass. In the main flow pass, a small recirculating zone near the front wall was observed in both the experimental and computational results. Although the region of peak velocity from the computation is slightly wider than the one in the experiment, in both cases the position of peak velocity is rather consistent, i.e., close to the front wall.

Under the end of the vertical divider (Section G), low-velocity magnitudes are predicted by the present computational model. However, the measurements are somewhat higher since a transverse flow from the main flow pass to the side flow pass (between the vertical divider and side wall) was observed in the actual boiler. It should be noted that in the main flow pass the mass flow rate is about 1.4 times higher than that in the side pass. Due to the resistance caused by the presence of the economizer tube bank assembly, part of the air flow in the main pass turned into the side pass through the one meter high gap between the vertical divider and the top tube rows of the economizer. This caused the flow in the side pass to be more turbulent than expected, which resulted in a considerable fluctuation in velocity magnitude and direction. It is noted that in these calculations we have not included the economizer tube bank and hence the transverse flow from the main pass to the side pass does not occur in the predictions. Thus, a peak velocity region near the front wall in the side pass is found from the computation; however, this is not as pronounced in the measurements.

Due to the influence of the splitter plate at the top of boiler, another small peak velocity occurs near the rear wall. This can be seen in Fig. 4, showing that the computed velocity profile from the front wall to the rear wall at Section D is in excellent agreement with the measured data. In our experience, the differences in flow measurements between physical scale models and full-scale boilers are often greater than 10 percent. Since the predictions obtained here are of the order within 10 percent when compared with full-scale measurements, the computer code DS4PUB has been shown to be a valuable tool for boiler designers at least as far as flow predictions are concerned.

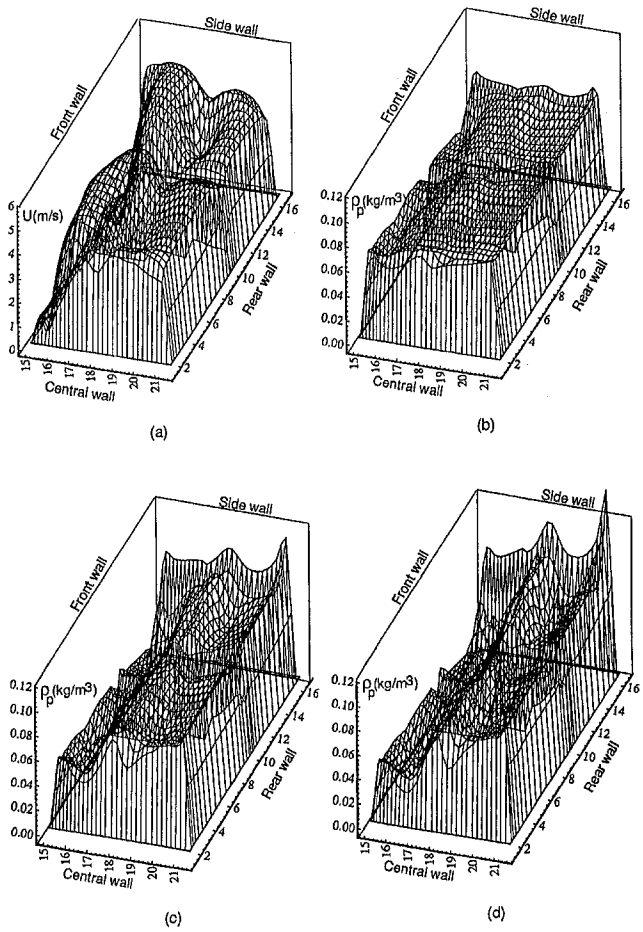

Fig. 6 Predicted fly ash flow fields at the economizer inlet: (*a*) fly ash velocity, d_p = 30 μm, (*b*) fly ash concentration, d_p = 30 μm, (*c*) fly ash concentration, d_p = 50 μm, (*d*) fly ash concentration, d_p = 80 μm

Fly Ash Flow. The fly ash particles are assumed to be spherical with a density of ρ_s = 1500 kg/m^3. The particle loading ratio is $m = \rho_p/\rho_g = 0.07$, where $\rho_p = \alpha\rho_s$ is the bulk density of the particulate phase, α is the volume fraction of the particulate phase, and ρ_g is the air density (1.17 kg/m^3). The total particle size range is from 2.5 to 120 μm (Platfoot, 1991). The results presented here are for 30, 50, and 80-μm-dia particles, which characterize the main particle size groups causing tube erosion.

Figure 5 shows a comparison of the computed fly ash concentration at the inlet of economizer with the measurement obtained by Platfoot (1991) in the Vales Point Power Station boiler. The coordinate in the vertical direction denotes the fly ash concentration normalized by dividing a maximum value for each group

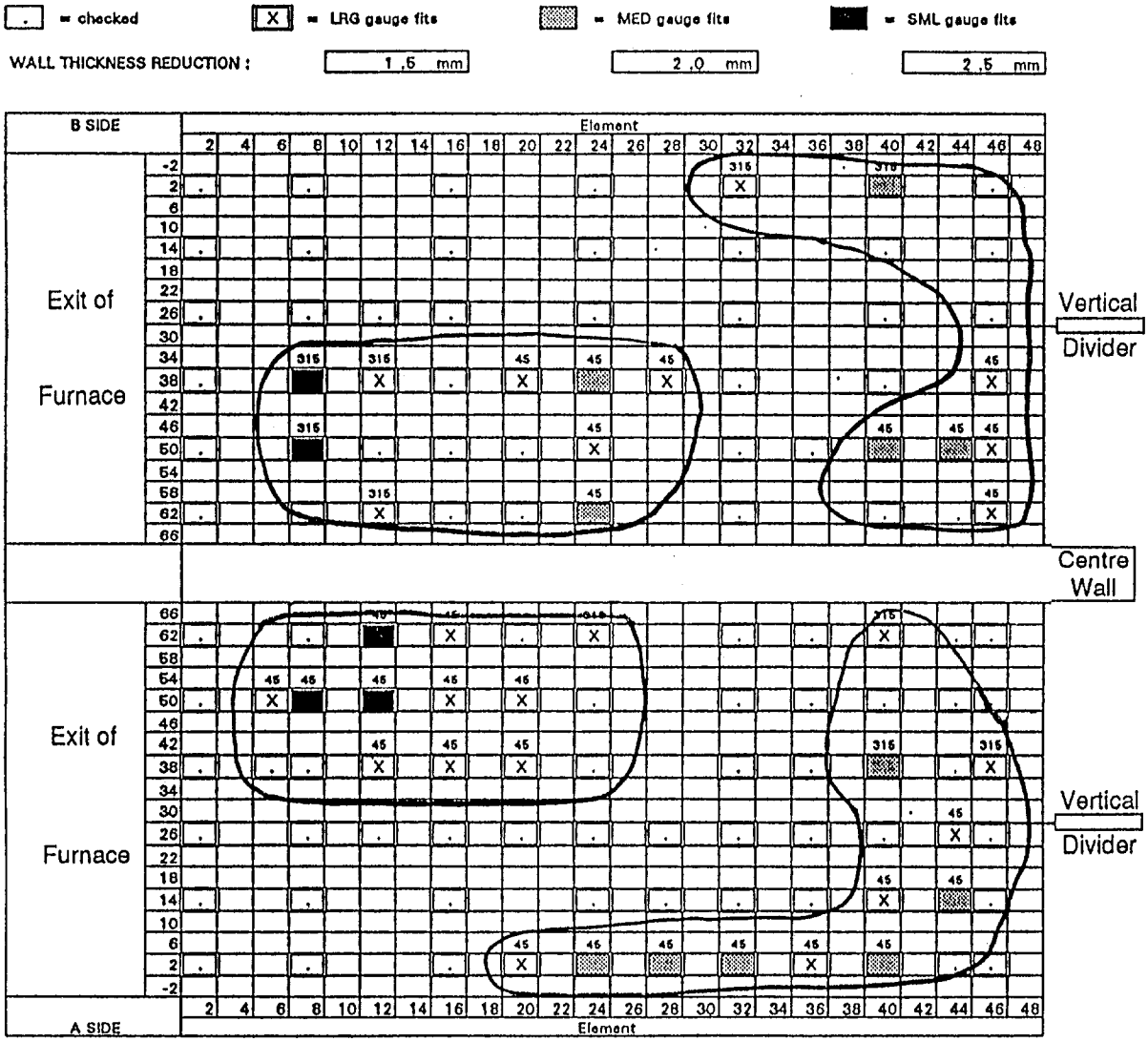

Fig. 7 Measured tubing wall thickness loss at the economizer inlet in the Wallerawang Power Station boiler

of particle sizes. Although not shown here, it is found in both the computations and measurements that the very small particles are uniformly distributed at the inlet of economizer. As the particle size is increased, the distribution is not uniform, with the maximum being shifted toward the rear wall. Fewer large particles are found near the front wall, while most particles move to the rear wall due to their high inertia. The computational results show very good agreement with the experimental measurements.

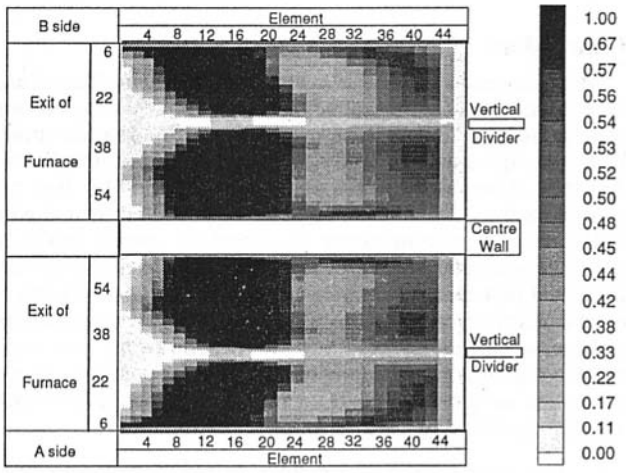

Fig. 8 Predicted erosion rate at the economizer inlet in the Wallerawang Power Station boiler

Figure 6 shows the fly ash flow prediction at the economizer inlet in Wallerawang Power Station, in terms of fly ash velocity (Fig. 6(a)) and concentration (Fig. 6(b–d)) for the same particle sizes as given above. The predictions indicate that the fly ash flow velocity distribution is only very slightly affected by particle size. However, the concentration distribution is clearly changed for different sizes. Because of the effect of the splitter plate at the top of boiler, not all larger particles can move toward the rear wall, so that a high concentration region is found after the splitter plate. This result is different from those calculated for the Vales Point Power Station boiler (see Fig. 5) in which there is no splitter plate at the top of the boiler.

Erosion Distribution. A survey of economizer tubing wall thickness using slip gages was performed at the Wallerawang Power Station (Jones and Owens, 1995) in order to determine the erosion rate. The erosion distribution at the top of economizer tube bank in terms of tube wall thickness reduction is shown in Fig. 7. The maximum value of tube wall thickness

reduction is over 2.5 mm; some tubes have lost between 1.5 and 2.5 mm while the remainder have lost less than 1.5 mm. Two main erosion areas can be identified on each side of the furnace, which seem to produce a symmetric distribution relative to the central wall. The maximum erosion was found at the area close to the front wall and the central wall. Another relatively high erosion area was found near the rear wall and the side wall.

Figure 8 shows the prediction of the distribution of the normalized erosion rate at the economizer inlet in Wallerawang Power Station, where the result of the B side economizer has been obtained by using a mirror image of the A side in order to compare with the measurement presented in Fig. 7. It is interesting to note that the region of the maximum erosion area is found computationally between the central and front wall of the economizer. This area corresponds reasonably well with the region as identified in the measurement (Fig. 7). The reason for the maximum erosion rate occurring in this region is the high velocity of both the flue gas and the fly ash particles (erosion rate is proportional to the velocity to a power of 2.4). Further, a relatively high erosion area has been predicted near the rear wall and the side wall, as was also found from the measurements (Fig. 7). This is due to the fact that more large fly ash particles move into this region, as can be seen from Fig. 6(*d*).

It should be noted that the additional erosion area at the side flow pass near the front wall of economizer was not clearly detected in the experiment, but is predicted by the current computational model. As pointed out earlier, the economizer tube bank has not been included in the computations, so that a high flow velocity is computed in this area. We expect that by introducing a model to represent the tube bank assemblies in the superheaters and economizers, the result would be improved.

In order to demonstrate further the capability of the DS4PUB code, a comparison of predicted and measured erosion rates (Benyon, 1991) at the first tube row of the economizer in the Vales Point Power Station is also presented in Fig. 9. A survey of tube erosion was carried out by using an ultrasonic inspection technique, which automatically measured the wall thickness of tubes. The coordinate in the vertical direction in Fig. 9 denotes the erosion rate normalized by a maximum value in each section for both the computational and measured results.

It can be seen from Fig. 9(*a*) that the maximum erosion at the symmetry plane of the economizer (see Fig. 1) occurs between the central position and the rear wall, which has been well predicted by the present computation. This erosion distribution in the Vales Point Power Station boiler is due to the fact that both the flue gas and fly ash particles tend to move toward the rear wall (see Fig. 5 for particulate concentration distribution). Note that two erosion peaks are found in both the prediction and measurement in the section near the side wall (Fig. 9(*b*)). This is because the two-dimensional flow character in the middle of boiler is modified by the constraining effect of the side wall, generating very complex fly ash velocity and concentration distributions (Tu et al., 1994). The discrepancy in the location of the maximum erosion rate in Fig. 9(*b*) between the prediction and measurement is probably due to the simplified erosion model, which does not include the effect of different particle sizes on the erosion rate, e.g., larger particles may cause a large erosion rate than smaller particles at the same velocity and material density. The economizer erosion rates are possibly inaccurate in terms of their absolute magnitudes of erosive wear. However, in a relative comparison they are of a considerable value for the purposes of design and maintenance in power stations.

In both cases presented in this paper the results for the boiler without tube bank assemblies are in good agreement with measurements from full-scale plants. It is thus possible to obtain a good indication of regions of high erosion rate without the need of modeling tube banks, thus greatly simplifying the calculations.

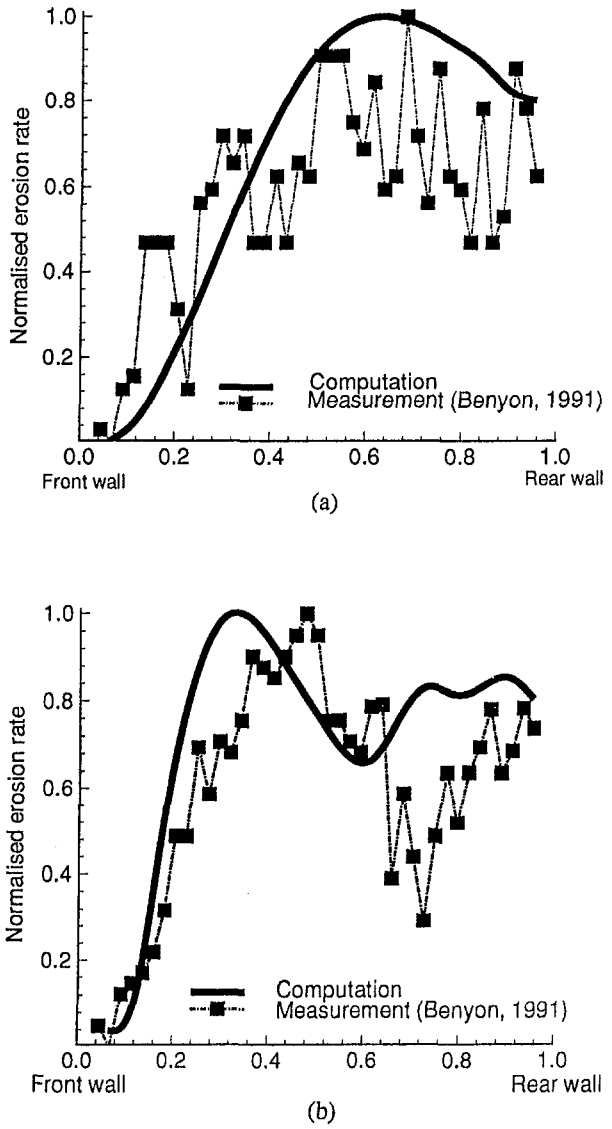

Fig. 9 Comparison of predicted erosion rate with the measurement in the Vales Point Power Station boiler: (*a*) symmetry plane, (*b*) near side wall

Conclusions

Multidimensional flue gas and fly ash flow calculations and measurements including surveys of economizer tube erosion were performed for two types of large coal-fired power utility boiler configuration, currently operating in New South Wales, Australia. Comparisons of numerical predictions for flue gas velocity and fly ash concentration at the economizer inlet with full-scale plant measurements show that the current model in the absence of tube bank assemblies has been able to capture the important flow features for both types of boiler. Comparisons of erosion distribution at the economizer inlet between predictions and measurements revealed that the location of the maximum erosion region at the economizer inlet can be predicted by the evaluation of erosion rate from the global flow calculations. The principal findings are as follows:

- The main feature of the flow in boilers with an empty 180 deg bend is that the flue gas and fly ash are directed toward the rear wall. This flow pattern can be modified

by inserting a splitter plate and providing a longer flow path at the bend. In this case the peak flow velocity is found near the front wall and not all the large fly ash particles move to the rear wall of the economizer.

- The present model predicts within engineering accuracy the global flow patterns of both flue gas and fly ash in different types of boiler geometries. The computed fluid velocity and fly ash concentration distributions for different particle sizes at the economizer inlet were in reasonable agreement with the measurements on full-scale plants.
- The estimate of erosion rate from the global flow solution indicates that the area of maximum erosion rate at the economiser inlet can be predicted with reasonable accuracy when compared with measurements of erosion rate on operational plants.

The quality of the solutions in boilers without tube banks is sufficient to provide an insight into the flow phenomena and erosion patterns within coal-fired boilers so that CFD codes may be employed in the future to generate designs in order to reduce the incidence of tube failures due to fly ash erosion.

It should be noted that there are three boiler templates built in the computer code library. These templates represent most of the power boiler configurations used in New South Wales, Australia. People can easily change the dimensions and have some modifications based on one of the templates. If one wants to build a completely new computational model for a particular boiler configuration, some typical components in the computer code library can be used for quick setup. This process may take approximately one week. The execution time for obtaining the flow solutions depends on the model complexity. As a guide, one flow calculation for the boiler configuration in Fig. 2 took one day on a HP735 workstation. This performance is quite reasonable since most of the user's time is spent performing analysis and modifying the configuration.

Acknowledgments

The work was undertaken as part of the DS4PUB project supported financially by DIST through Grant No. 16037. Appreciation is extended to the Pacific Power (Electricity Commission of New South Wales, Australia) for sponsoring the research program and releasing the data for publication. The first author also wishes to thank the Australian Research Council (ARC), Grant No. 9530335, for supporting his Research Fellowship when he was working at the University of New South Wales.

References

Amoroso, L. A. M., 1990, "Modelling Flow in Boiler Tube Banks," MEngSci. Thesis, School of Mechanical and Manufacturing Engineering, University of New South Wales, Sydney, Australia.

Bauver, W. P., McGough, T. C., and McGowan, J. G., 1984, "A Facility for the Characterization of Erosion of Heat Transfer Tubing," *Gas–Solids Flow,* ASME, pp. 115–122.

Benyon, P. J., 1991, "Economiser Erosion Investigation," BE Thesis, Department of Mechanical Engineering, The University of Sydney, Sydney, Australia.

Chieng, C. C., and Launder, B. E., 1980, "On the Calculation of Turbulent Heat Transport Downstream of an Abrupt Pipe Expansion," *Numerical Heat Transfer,* Vol. 3, pp. 189–207.

Cho, N.-H., Fletcher, C. A. J., and Srinivas, K., 1991, "Efficient Computation of Wing Body Flows," *Lecture Notes in Physics,* Springer, Vol. 371, pp. 167–191.

Christo, F. C., and Fletcher, C. A. J., 1992, "Erosion Modeling in Vales Point Power Station Using 'ECONEROS' Code," Technical Report, Department of Mechanical Engineering, The University of Sydney, Sydney, Australia.

ECNSW (Electricity Commission of New South Wales), 1988, "Liddell Power Station Unit 6: Boiler Rehabilitation," Specification and contract No. 3824.

Fan, J., Zhou, D., Jin, J., and Cen, K., 1991, "Numerical Simulation of Tube Erosion by Particle Impaction," *Wear,* Vol. 142, pp. 171–184.

Fan, J., Zhou, D., Zeng, K., and Cen, K., 1992, "Numerical and Experimental Study of Finned Tube Erosion Protection Method," *Wear,* Vol. 152, pp. 1–19.

Fletcher, C. A. J., 1991, *Computational Techniques for Fluid Dynamics, Vol. 2: Specific Techniques for Different Flow Categories,* 2nd ed., Springer, Heidelberg.

Fletcher, C. A. J., and Bain, J. G., 1991, "An Approximate Factorisation Explicit Method for CFD," *Computers and Fluids,* Vol. 19, pp. 61–74.

Guzman, M. M. de, Fletcher, C. A. J., and Hooper, J. D., 1994, "Computational Investigation of Cobra Probe Operation," *Int. J. Num. Meth. Heat Fluid Flow,* Vol. 4, pp. 425–445.

Hamed, A., 1992, "An Investigation in the Variance in Particle Surface Interactions and Their Effects in Gas Turbines," *Journal of Aircraft for Gas Turbines and Power,* Vol. 114, pp. 235–241.

Humphrey, J. A. C., 1990, "Review—Fundamentals of Fluid Motion in Erosion by Solid Particle Impact," *Int. J. Heat and Fluid Flow,* Vol. 11, pp. 170–195.

Jones, P., and Owens, D., 1995, "Wallerawang Power Station Units 7 & 8 Economiser Erosion and Replacement Investigation," Report No. pp/M/1266/1, Power Engineering Boiler, Fuel & Water Systems, Pacific Power, New South Wales, Australia, Apr.

Jun, Y. D., and Tabakoff, W., 1994, "Numerical Simulation of a Dilute Particulate Flow (Laminar) Over Tube Banks," ASME *Journal of Fluids Engineering,* Vol. 116, pp. 770–777.

Kitchen, A. N., 1990, "Flyash Erosion Prediction in Economisers," MEngSci. Thesis, Department Mechanical Engineering, The University of Sydney, Sydney, Australia.

Launder, B. E., and Spalding, D. B., 1974, "The Numerical Computation of Turbulent Flows," *Comp. Methods in Appl. Mech. and Eng.,* Vol. 3, pp. 269–289.

Orszag, S. A., Yakhot, V., Flannery, W. S., et al., 1993, "Renormalization Group Modeling and Turbulence Simulations," in: *Near Wall Turbulent Flows,* So, R. M. C., Speziale, C. G., and Launder, B. E., eds., Elsevier Science Publishers B. V., pp. 1031–1046.

Pacific Power, 1995, "Unit 7 Economiser Air Flow Test in Wallerawang Power Station," Technical Report No. MTT374, Pacific Power, New South Wales, Australia.

Platfoot, R., 1991, "Internal Flows in Coal Fired Boilers," PhD. Thesis, Department of Mechanical Engineering, The University of Sydney, Sydney, Australia.

Raask, E., 1988, *Erosion Wear in Coal Utilization,* Hemisphere Publishing.

Rhie, C. M., and Chow, W. L., 1983, "Numerical Study of the Turbulent Flow Past an Airfoil With Trailing Edge Separation," *AIAA J.,* Vol. 21, pp. 1525.

Schuh, M. J., Schuler, C. A., and Humphrey, J. A. C., 1989, "Numerical Calculation of Particle-Laden Gas Flows Past Tubes," *AIChE Journal,* Vol. 35(3), pp. 466–480.

Schweitzer, M. O., and Humphrey, J. A. C., 1988, "Note on the Experimental Measurement of Particle Flux to One and Two In-Line Tubes," *Wear,* Vol. 126, pp. 211.

Tu, J. Y., and Fletcher, C. A. J., 1994, "An Improved Model for Particulate Turbulence Modulation in Confined Two-Phase Flows," *Int. Comm. Heat and Mass Transf.,* Vol. 21(6), pp. 775–783.

Tu, J. Y., Fletcher, C. A. J., and Behnia, M., 1994, "Computation of Three-Dimensional Fly Ash Flow in Vales Point Power Station," DS4PUB Technical Report, No. 94-12, CANCES, University of New South Wales, Sydney, Australia.

Tu, J. Y., and Fletcher, C. A. J., 1995a, "Numerical Computation of Turbulent Gas-Solid Particle Flow in a 90° Bend," *AIChE Journal,* Vol. 41 (10), pp. 2187–2197.

Tu, J. Y., and Fletcher, C. A. J., 1995b, "Computational Analysis of Turbulent Gas-Solid Flows in In-Line Tube Banks," *Gas-Solid Flows,* ASME FED-Vol. 228, pp. 309–317.

Van Doormaal, J. P., and Raithby, G. D., 1984, "Enhancements for the SIMPLE Method for Predicting Incompressible Fluid Flow," *Num. Heat Transfer,* Vol. 7, pp. 147–163.

Zdravistch, F., Fletcher, C. A. J., and Behnia, M., 1995, "Numerical Laminar and Turbulent Fluid Flow and Heat Transfer Predictions in Tube Banks," *Int. J. Num. Meth. Heat Fluid Flow,* Vol. 5, pp. 717–733.

APPENDIX

A brief description of the basic capability and the numerical algorithm of the computer code and a brief presentation of the computational procedure for estimating erosion rates are given in this appendix.

The DS4PUB code can solve complex turbulent, two and three-dimensional flows, with the energy and the additional solid phase equations included to provide the temperature distributions and fly ash behavior. A two-fluid model (Eulerian approach), in combination with a newly developed particle-wall collision model and boundary conditions for the particulate phase, is employed (Tu and Fletcher, 1995a). The fluid turbulence is modeled by a standard $k-\epsilon$ model (Launder and Spalding, 1974) or an RNG-based $k-\epsilon$ model (Orszag et al., 1993) with a modification for confined two-phase flows (Tu and Fletcher, 1994). A two-layer wall function (Chieng and Launder, 1980) is used to avoid the need for very fine mesh distributions close to solid surfaces.

The code uses a finite volume discretization in conjunction with a nonstaggered generalized-coordinate grid. The grid-gen-

eration process is handled independently with the corner point locations read in from a separate database, which can be generated by users or from commercially available mesh generation package such as CAD packages. The convective terms are discretized at the faces of the control volumes with a generalized QUICK convective differencing method (Cho et al., 1991). Second-order derivatives are evaluated using three-point symmetric formulae. A velocity potential correction (Fletcher and Bain, 1991) is introduced to ensure that the continuity equation of the gas phase is satisfied and to upgrade the gas pressure using the SIMPLEC algorithm (Van Doormaal and Raithby, 1984). The stored values at the centroids of the control volumes are interpolated and modified to calculate the flux at faces of the control volumes using the moment interpolation method (Rhie and Chow, 1983). The governing equations for both the gas and particulate phases are solved sequentially at each iteration to obtain all the dependent variables. At every global step each equation is iterated, using a Strongly Implicit Procedure (Fletcher, 1991). This iteration process is continued until the equation residuals are sufficiently small—typically the mass should be conserved to approximately 0.001 percent. The complete solution is written to a data file, which can then be independently post-processed to generate graphic results.

The research on surface wear by particle impingement was recently reviewed by Raask (1988) and Humphrey (1990). The authors discussed mechanisms of erosion and clarified the roles played by the various contributing factors. Previous work (Kitchen, 1990, Christo and Fletcher, 1992) suggests that the location of the maximum erosion could be roughly estimated from a knowledge of the particulate velocity and flyash concentration profiles immediately upstream of the economizer. The evaluation of the relative erosion rate from different particle sizes can be obtained from:

$$E_{dp}(\mathbf{x}_i) = \rho_{dp}(\mathbf{x}_i) \cdot \delta_{dp} \cdot \{V_{dp}(\mathbf{x}_i)\}^n \quad (1)$$

where $\rho_{dp}(\mathbf{x}_i)$ and $V_{dp}(\mathbf{x}_i)$ are the local values of particle concentration and particulate velocity for one particle size range respectively. δ_{dp} is the relative weight of fly ash as function of particle size. $\mathbf{x}_i$ represents the coordinates at the plane at the economizer inlet. The velocity exponent, n, is between 2 and 4 for different target surface materials (Humphrey, 1990). Following the recent experiments of Hamed (1992) and its numerical application by Jun and Tabakoff (1994), the value of n in the present work is taken to be 2.4. The final erosion rate is calculated by summing the contribution for the various particle size ranges considered yielding,

$$E(x_i) = \sum_{dp} \{E_{dp}(x_i)\} \quad (2)$$

and the result is normalized by dividing the maximum value of $E(x_i)$.

Erosion-Oxidation of Carbon Steel in the Convection Section of an Industrial Boiler Cofiring Coal–Water Fuel and Natural Gas

J. J. Xie[1]

P. M. Walsh[2]

Fuel Science Program,
Department of Materials Science
and Engineering,
The Pennsylvania State University,
University Park, PA 16802

Walsh et al. (1994) reported measurements of erosion of carbon steel by fly ash and unburned char particles in the convective heat transfer section of an industrial boiler cofiring coal–water fuel and natural gas. Erosion was enhanced by directing a small jet of nitrogen, air, or oxygen toward the surface of a test coupon mounted on an air-cooled tube. Ash and char particles that entered the jet from the surrounding flue gas were accelerated toward the surface of the specimen. Samples were exposed for 2 hours with metal temperature at 450, 550, and 650 K (350, 530, and 710°F). Changes in shape of the surface were measured using a surface profiler. Time-averaged maximum erosion rates were obtained from the differences between the original surface height and the lowest points in the profiles. Erosion was slowest at the lowest metal temperature, regardless of the jet gas composition. When the oxygen partial pressure at the sample surface was very small, under the nitrogen jet, erosion increased with increasing temperature over the range of temperatures investigated. At the intermediate oxygen level, in the air jet, erosion was most rapid at the intermediate temperature. In the presence of the pure oxygen jet erosion was slow at all three temperatures. A model was developed by Xie (1995) to describe wastage of tube material in the presence of erosion by particle impacts and oxidation of the metal. The observed changes in erosion rate with temperature and oxygen concentration were consistent with a mechanism based upon the following assumptions: (1) Metal was eroded as a ductile material, at a rate that increased with increasing temperature. (2) Oxide was eroded as a brittle material, at a rate independent of temperature. (3) The oxide scale was strongly attached to the metal. (4) The erosion resistance of metal and scale was a linear combination of the resistances of the individual components. (5) Oxide formed according to the parabolic rate law, with a rate coefficient proportional to the square root of the oxygen partial pressure. (6) Erosion resistance from particles sticking to, or embedded in, the surface was negligible. Using the model and rate coefficients for metal and oxide erosion derived from the measurements, estimates were made of the erosion rate of a boiler tube as functions of impaction angle and gas velocity. Under the conditions of metal temperature, gas composition, particle size, particle concentration, and particle composition investigated, erosion of carbon steel is expected to be slower than 0.05 μm/h when the gas velocity in the convection section is less than approximately 8 m/s.

Introduction

A demonstration of coal–water slurry firing in an industrial boiler is being conducted by The Energy Institute at Penn State University for the United States Department of Energy/Federal Energy Technology Center at Pittsburgh and the Commonwealth of Pennsylvania (Miller and Scaroni, 1992; Miller et al., 1995). The purpose of the demonstration is to establish conditions under which slurry prepared using beneficiated coal containing less than approximately 4 wt% ash and 0.9 wt% sulfur can be burned in industrial boilers designed for oil firing, without adverse impact on boiler rating, maintainability, reliability, and availability. The project will also provide information on the requirements for new systems designed specifically to fire coal–water fuels. One of the components of this program is the measurement of erosion of heat exchanger tubes by ash and unburned carbon particles in the convective heat transfer section of a boiler. The objective of this work is to determine conditions of flue gas velocity, excess oxygen, metal temperature, coal ash content, ash composition, particle size, carbon conversion, and soot-blowing frequency under which coal–water fuel can be fired without significant deterioration of tube life or heat transfer in the convection section.

Results from field trials using slurry fuels and factors influencing erosion of heat exchangers by slurry–fuel ashes in boilers converted from oil firing were reviewed by Raask (1988). The ash content of the coal, quartz content of the ash, particle size, spray quality, unburned carbon, and gas velocity were

[1] Present address: National Semiconductor Corp., 2900 Semiconductor Drive, Mail Stop E120, Santa Clara, CA 95052-8090.

[2] Corresponding author. Present address: Energy and Environmental Research Corp., c/o Sandia National Laboratories, Mail Stop 9053, Livermore, CA 94551-0969.

Preliminary versions of this paper were presented at the Engineering Foundation Conference on the Impact of Ash Deposition on Coal Fired Plant, Solihull, Birmingham, UK, June 20–25, 1993; and at the 1993 International Joint Power Generation Conference, Kansas City, MO, October 17–20, 1993, Paper No. 93-JPGC-PWR-23. Manuscript received at ASME Headquarters January 1997. Associate Technical Editor: D. Lou.

among the fuel and boiler characteristics that Raask identified as most important. Raask noted that beneficiation of coal resulted in slower erosion, due to reductions in both ash concentration in flue gas and erosivity of the ash.

Hargrove et al. (1985) and Chow et al. (1992) measured erosion by fly ash from coal–water fuel combustion under conditions similar to those in boilers, using the technique of surface layer activation to detect material loss. The measurements were made in a high-velocity test section downstream from a test furnace, without alteration of gas or particle composition. The results indicated that excessive erosion should not be expected to occur in boilers firing the coal–water fuels investigated (Hargrove et al., 1987; Chow et al., 1992). Chow and co-workers (1992) also observed that beneficiation decreased the erosivity of ash, as well as the ash concentration.

A method for making in situ measurements of erosion by ash and unburned carbon particles in the convection section of an industrial boiler was described by Walsh et al. (1994). In these experiments a small jet of clean gas was used to accelerate the ash and unburned char particles suspended in flue gas, increasing the rate of erosion over a small area on a test coupon mounted on a probe. A model for interpretation of these measurements was developed by Xie (1995), including calculation of the trajectories of the particles in the jet, erosion of metal and oxide scale, and regeneration of the scale.

Experimental Measurements

The measurements were made in the convection section of a Tampella Keeler D-frame watertube boiler while cofiring coal–water fuel and natural gas. The boiler has a capacity of 6760 kg/h (14,900 lb/hr) of steam at 481 K (406°F) and 1.7 MPa (250 psig). Natural gas provided 31.5 percent of the heat input. The coal–water fuel was prepared using high volatile A bituminous coal from the Brookville Seam in Lawrence County, Pennsylvania. The moisture content of the fuel, as received, was 41.6 wt%, its higher heating value was 19.3 MJ/kg, and the median coal particle size was 23 μm. The proximate analysis of the coal was (weight percent, dry): ash, 3.6; volatile matter, 36.1; and fixed carbon (difference), 60.3; and the ultimate analysis was (weight percent, dry, mineral matter free): carbon, 82.8; hydrogen, 5.7; nitrogen, 1.6; sulfur, 0.9; and oxygen (difference), 9.0.

The flue gas contained (by volume, wet): H_2O, 14.3 percent; CO_2, 13.6 percent; O_2, 3.7 percent; CO, 190 ppm; SO_2, 430 ppm; NO_x, 570 ppm; and N_2, balance. Particles collected in the baghouse were 77 wt% combustibles and 23 wt% ash (dry). The ash composition was (weight percent, SO_3 free): SiO_2, 49.2; Al_2O_3, 35.6; TiO_2, 1.2; Fe_2O_3, 7.3; CaO, 2.7; MgO, 0.6; Na_2O, 0.5; K_2O, 1.3; and other oxides, 1.6. The apparent density of the particles was 870 $\pm$ 20 kg/m^3, determined from their settled volume, assuming a voidage of 0.42 (Mitchell et al., 1992). A volume-based size distribution of the baghouse catch is shown in Fig. 1. Assuming apparent densities of 2500 and 400 kg/m^3 for ash and char, respectively, the particles entrained in the flue gas were estimated to contain 95 percent combustibles by volume, so the size distribution shown in Fig. 1 is dominated by unburned char.

The erosion probe was placed in a cavity in the convection section intended for a small superheater, where the flue gas temperature was 850 K (1070°F), gas velocity was 4 m/s, and particle concentration was 2.7 g/m^3 (at flue gas temperature). Samples of carbon steel were cut from 25.4 mm outside diameter ASTM A179 tube having the following composition (weight percent): C, 0.08; Mn, 0.42; P, 0.027; S, 0.017; Si, 0.030; Al, 0.048; and Fe, balance. A flat area, 38 mm $\times$ 10 mm, was machined on the outside of each test piece, ground, and polished to roughness less than 0.05 μm. The samples were mounted in the opening formed by cutting an identical section from the air-cooled support. Temperature was controlled by adjusting the

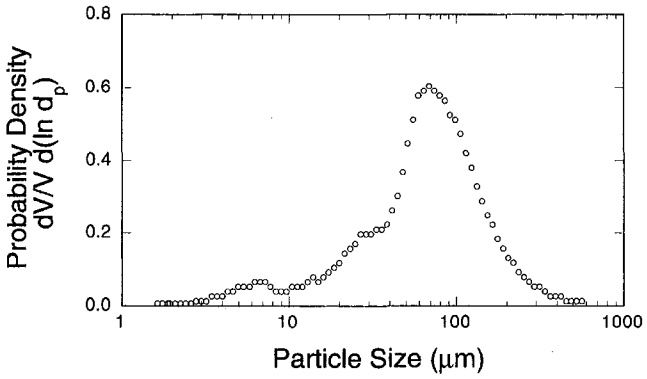

Fig. 1 Volume-based size distribution of particles collected in the baghouse, determined by laser diffraction using a Malvern Droplet and Particle Sizer. On the ordinate is plotted the fraction of sample volume, $\Delta V/V$, in the size interval between d_p and αd_p ($\alpha > 1$), divided by the width of the interval, ln αd_p − ln d_p = ln α.

cooling air flowrate. A small nozzle, 1.7 mm inside diameter, was supported on a sidearm attached to the probe and supplied with compressed gas. The jet issuing from the nozzle was oriented with its axis parallel to the flue gas flow and perpendicular to the surface of the sample. The average gas velocity at the jet orifice was 200 m/s. The jet entrains surrounding flue gas and particles, and accelerates them toward the surface. The conditions that were varied during the tests were metal temperature (450, 550, and 650 K) and jet gas oxygen content (3 vol ppm O_2 in N_2, 21 vol% O_2 in N_2, and 100 percent O_2).

Each sample was exposed to the effects of the jet, entrained flue gas, and particles for 2 hours. After a test, the shape of the surface of the sample was measured using a surface profiler (Snaith et al., 1987) and the erosion crater was examined using a scanning electron microscope. The profiles and electron micrographs of the entire set of samples may be found in a separate publication (Walsh et al., 1994). A representative example of the output from the surface profiler (Rank Taylor Hobson, Talysurf 10), obtained by traversing the erosion pattern along a path through its center, is shown in Fig. 2(a). Erosion predominates at the center of the pattern, near the stagnation point of the jet, and at distances from approximately 1 to 4 mm from the jet axis. In the region from approximately 0.5 to 1 mm from the axis, increases in height above the level of the original surface are due to ash deposits or expansion associated with oxidation of the metal. The presence of deposits was supported by EDAX analysis, which showed high concentrations of the ash constituents aluminum and silicon in this region. Ash deposition increased in importance with increasing temperature and oxygen concentration (Walsh et al., 1994).

The maximum erosion depths were identified on the right and left sides of the profile, for example at +1.7 and −1.3 mm from the jet axis in Fig. 2(a). The maximum depths were converted to time-averaged rates, assuming constant rate of material loss over the 2-hour exposure period. The averages of these maximum rates, with estimates of their uncertainty, are plotted as a function of temperature for each jet gas in Fig. 3.

Model for Erosion-Oxidation

The model is based on mechanisms of erosion-oxidation described by Levy (1982), Levy et al. (1985), Raask (1985, 1988), Wright et al. (1986, 1991, 1995), Kang et al. (1987), Sethi et al. (1987), Sethi and Wright (1989), Rishel et al. (1991), Sundararajan (1991a, b), and Kosel (1992). The oxidation of carbon steel and formation of oxide scale were assumed to occur at a rate inversely proportional to the thickness of the scale. Allowance was made for an oxygen concentration dependence of the rate, by including a power of the oxygen partial pressure as a factor in the rate expression:

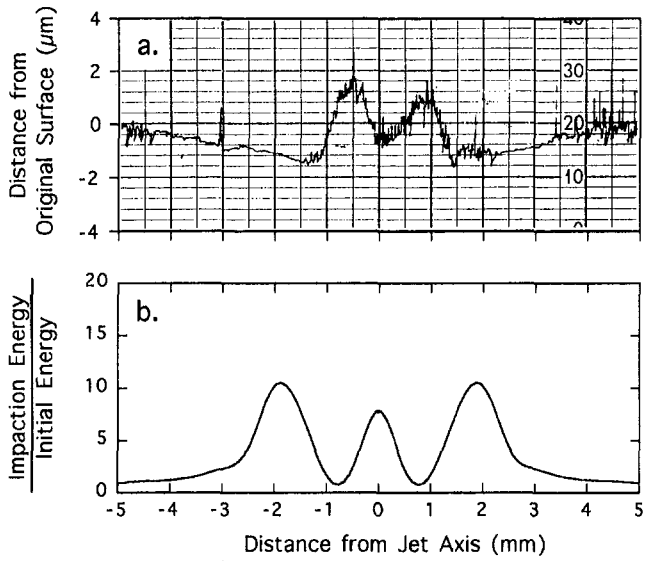

Fig. 2 Comparison of a profile of the eroded sample surface with the spatial distribution of energy brought to the surface by impacting particles: (*a*) profile of the surface of a carbon steel specimen after 2 hours of exposure to the high velocity jet, entrained flue gas, and particles. The metal temperature was 650 K and the jet gas was air. (*b*) Distribution of kinetic energy of impacting particles, relative to their approach energy, as a function of distance from the stagnation point of the jet.

$$\frac{dx}{dt} = \frac{k_o}{x} p_{O_2}^a \qquad (1)$$

where x is the thickness of scale, t is time, and p_{O_2} is the partial pressure of oxygen adjacent to the surface, in atmospheres. An estimate of the parabolic rate coefficient, k_o, was obtained by extrapolation of published work on iron in oxygen over the temperature range from 673 to 873 K, in the absence of particle collisions and erosion (Davies et al., 1951; Schmahl et al., 1958; Caplan and Cohen, 1966; Jansson and Vannerberg, 1971):

$$k_o = 1.6 \times 10^{-5} \exp(-19240/T) \quad \text{m}^2/\text{s}, \qquad (2)$$

in which T is the absolute temperature in Kelvin.

The composite erosion resistance of metal and scale was assumed to be a linear combination of the resistances of metal and oxide alone, weighted by their volume fractions in eroded fragments (Levy, 1982; Hovis et al., 1986; Conrad, 1987). The contribution from metal was described by the relations for ductile erosion (Finnie, 1958, 1960, 1980; Bitter, 1963a, b; Finnie et al., 1967; Neilson and Gilchrist, 1968; Engel, 1978), greatest at a collision angle of 30 deg, having a rate at normal incidence equal to 0.3 times the maximum (Shida and Fujikawa, 1985), and increasing with increasing temperature. The contribution from oxide was described by an expression for brittle erosion derived by Xie (1995), from the work of Sheldon (1970) and Evans et al. (1976). The rate of brittle erosion is proportional to the 3.4th power of the normal component of particle velocity, greatest at a collision angle of 90 deg, and independent of temperature (Levy, 1982; Conrad, 1987). Contributions to erosion resistance from deposits or isolated particles attached to the surface were neglected. The volume fractions of metal and scale in eroded fragments were determined from a material balance at steady state, in which the product of the collision frequency of the volume-weighted average size of particles and average volume of oxide removed per collision was equated to the rate of oxide formation. In this relation it is necessary to specify the area of oxide scale removed by a single particle impact.

Kinetic energies and collision angles of the impacting particles were needed to extract values for the adjustable parameters from the measurements of maximum depth in the erosion profiles. The trajectories of particles after entering the gas jet from the free stream were found from the equations of motion for the particles and gas in an axisymmetric, incompressible stagnation point flow, with the boundary condition of no slip at the target surface (Laitone, 1979a, b; Dosanjh and Humphrey, 1985; Schuh et al., 1989; Humphrey, 1990). The particles were subjected to mean and fluctuating components of gas velocity, with the standard deviations of the normally distributed fluctuating components proportional to the local mean axial and radial velocities. Additional information about the calculations may be found in other publications (Xie, 1995; Xie and Walsh, 1993).

Very large particles arrive at the target surface with velocities close to the approach velocity (4 m/s). Very small particles have velocities approaching zero at the surface, the boundary condition for the gas flow. The highest velocity at the surface was approximately 20 m/s, for 20 μm particles. Therefore, in spite of the fact that the velocity of the gas at the jet nozzle

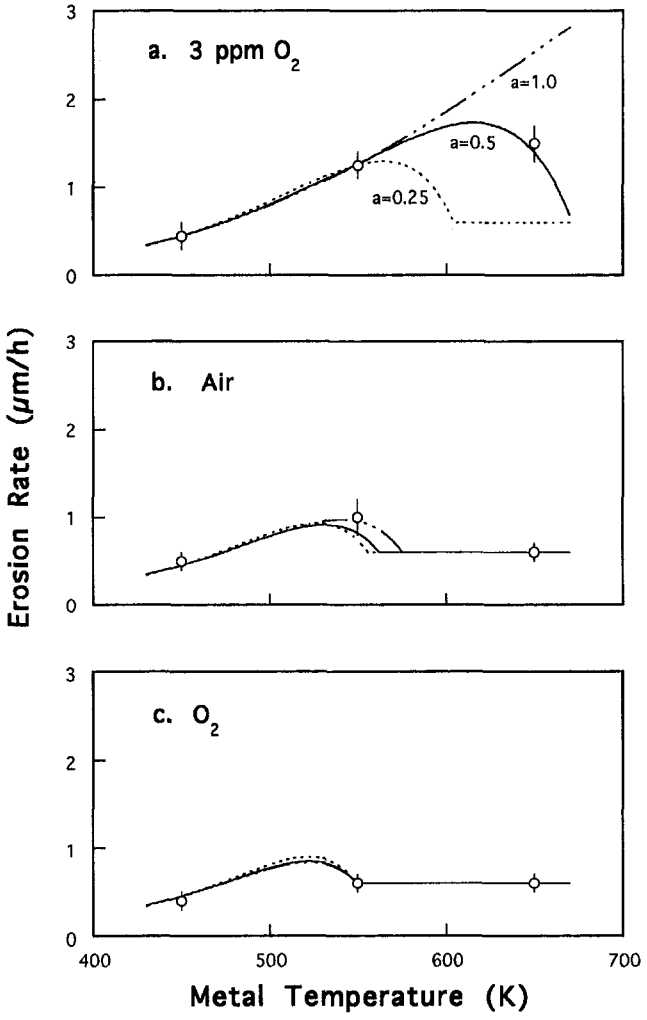

Fig. 3 Erosion rates of carbon steel as functions of temperature and the oxygen content of the gas jet used to accelerate the particles. The measured maximum rates (open circles) were determined from the low points in the surface profiles, assuming a constant rate of material loss over the two-hour exposure period. The curves are calculations for three values of the order, *a*, of the metal oxidation rate with respect to oxygen (Eq. (1)), using erosion rate coefficients determined from the measurements in the nitrogen and oxygen jets: (*a*) Nitrogen jet containing 3 vol ppm O_2 impurity. The metal erosion rate coefficient was determined from the measurements at 450 and 550 K. (*b*) Air jet. (*c*) Oxygen jet. The temperature-independent oxide erosion rate coefficient was determined from the measurements at 550 and 650 K.

was very high, the velocities with which particles impacted the surface were not excessive. However, the distribution of velocity with respect to particle size produced by the jet is different from the velocity-size distribution of particles colliding with a tube under normal convection section conditions, in the absence of the jet. The spatial distribution of the kinetic energy of particles at the sample surface is shown in Fig. 2(*b*). The average size and velocity of particles colliding with the target were calculated at a distance of 2 mm from the stagnation point of the jet, where the total kinetic energy of particles at the surface was a maximum. These particle properties were used in conjunction with the erosion-oxidation model to simulate the processes occurring at the locations on the surface where the erosion rate was a maximum. All particles were assumed to have the same erosivity.

Results and Discussion

At a distance of 2 mm from the jet axis, the integrated energy of impaction was 10 times the initial energy of particles suspended in flue gas, as shown in Fig. 2(*b*). The mean size of impacting particles at this location was 78 μm and their impaction efficiency was 0.64. The average impaction angle, weighted according to the size distribution and collision efficiency, was 83 deg. The collision frequency per unit area, based on the mean size of impacting particles, was 32×10^6 m^{-2} s^{-1}. The time interval between impacts removing the scale at a given location on the surface was 0.17 s.

As shown in Fig. 3(*a*), the erosion of carbon steel by ash and char in the presence of the nitrogen jet increased with increasing metal temperature. The effective ductile erosion rate coefficient k_d was determined from the measurements at the two lowest temperatures, assuming negligible thickness of oxide scale:

$$k_d = 2 \times 10^{-7} \exp(-2530/T) \quad \text{m}^3/\text{J}.^3 \qquad (3)$$

In the presence of the oxygen jet, erosion was nearly independent of temperature, as shown in Fig. 3(*c*). The rate coefficient for brittle erosion of oxide, k_b, was determined from the measurements at the two highest temperatures, assuming the scale was thick enough that only oxide was eroded under these conditions:

$$k_b = 3.5 \times 10^{-5} \quad \text{m}^2\ \text{kg}^{0.5}/\text{J}^{1.7}.^3 \qquad (4)$$

When the area of oxide scale removed by a single impact was adjusted to fit the data, the best fit was obtained using a value 25 times the cross-sectional area of the mean size of particles. An alternative was to set the area of scale removed per impact equal to the cross-sectional area of the mean size of particles, then adjust the parabolic rate coefficient for oxidation of the metal. When this was done, the parabolic rate coefficient giving the best fit was 25 times the value determined from the published data. The shapes of the curves fit to the measurements in Fig. 3 are not influenced by changes in the area ratio and parabolic rate coefficient as long as their product is kept the same. An increased metal oxidation rate in the presence of particle collisions and erosion was noted by Levy et al. (1986).

In earlier analyses of these data (Xie and Walsh, 1993, 1994) the dependence of the erosion rate on oxygen concentration was rationalized by suggesting that the composition of gas adjacent to the sample surface was influenced by mixing the jet with flue gas, the effect being most significant in the nitrogen jet. An alternative approach, taken here, was to assume that the oxygen content of gas adjacent to the surface was the same as in the jet at the nozzle, and fit the data by introducing an oxygen dependence into the scale formation rate, Eq. (1). Calculations for three values of the order, a, with respect to oxygen are shown in Fig. 3. The value of $a = 0.5$ gave the best fit to the measurements.

The dependence of erosion on temperature shown by the calculations in Fig. 3 arises from the model as follows. At the low end of the temperature range, the oxidation rate of carbon steel is slow, the oxide layer is thin, and the eroding material is metal, so the erosion rate exhibits the temperature dependence of ductile erosion, increasing with increasing temperature. Because the oxidation rate is slow, oxygen partial pressure has no effect on the erosion rate, as shown by comparison of the measurements at 450 K in nitrogen, air, and oxygen.

As temperature is increased, the oxidation rate increases, with corresponding increases in the steady thickness of oxide scale and contribution of oxide to eroded volume. Over most of the range of temperatures investigated (above approximately 475 K), the oxide scale is more resistant to erosion than metal; therefore, as the composition of eroded material approaches pure oxide, with increasing temperature or oxygen partial pressure, the erosion rate declines. The transition from metal- to oxide-dominated behavior gives rise to the maximum in the temperature dependence of the erosion rate.

When the oxidation rate is high, and the scale thick enough that erosion is confined to the oxide layer, the erosion rate becomes that characteristic of the brittle oxide, independent of temperature. This is the situation under the most strongly oxidizing conditions, on the right-hand sides of Figs. 3(*b*) and 3(*c*). Increasing oxygen concentration shifts the transition from the metal to oxide-controlled erosion regimes to lower temperature.

The objective was an estimate of the range of conditions under which acceptable erosion rates could be maintained in the convection section of the boiler. The trajectories of particles suspended in gas flowing around a tube, collisions of particles with the tube, and erosion of the tube surface were analyzed by Bauver et al. (1984), Schuh et al. (1989), and Fan et al. (1990). The calculation of characteristic erosion rates on a tube in crossflow was described by Rosner and co-workers for ductile (Rosner et al., 1995; Kho et al., 1996) and brittle (Khalil and Rosner, 1996) materials.

Material loss from a tube in the presence of both erosion and oxidation was calculated for typical conditions in the convection section of the boiler: gas temperature, 850 K; excess oxygen, 3.7 vol%; particle concentration, 2.7 g/m^3; particle size, 65 μm; particle density, 870 kg/m^3; metal temperature, 550 K; and tube diameter, 51 mm. The average impaction efficiency on the tube was obtained using the correlations of Israel and Rosner (1983) and Serafini (1954), as described by Walsh et al. (1988). The results of the calculations were unaffected by setting the area of oxide removed per collision equal to the particle cross-sectional area and increasing the parabolic rate coefficient by a factor of 25 or setting the area ratio equal to 25 and leaving the rate coefficient alone.

The erosion rates at impaction angles of 30 and 90 deg are shown as functions of convection section gas velocity in Fig. 4. At low velocity the erosion rate is low, and erosion occurs only from the oxide layer. Increasing the gas velocity increases the rate of oxide removal and decreases the steady thickness of the scale. At a critical velocity the oxide layer becomes thin enough that erosion removes both oxide and metal, and the rate increases markedly with further increase in gas velocity. The critical velocity is near 21 m/s at an impaction angle of 30 deg, but decreases to 13 m/s for impaction at 90 deg, the angle at which brittle erosion of oxide is expected to be most rapid. With further increase in gas velocity above the critical value, the scale becomes even thinner, and erosion tends toward the rate characteristic of bare metal. Because oxide is more resistant to erosion than metal at the temperature chosen for the calculation, and because metal erosion is greatest at 30 deg, while oxide erosion is greatest at 90 deg, the difference between the

[3] The values given for the coefficients in the pamphlet version of the paper (Xie and Walsh, 1993) were not correct.

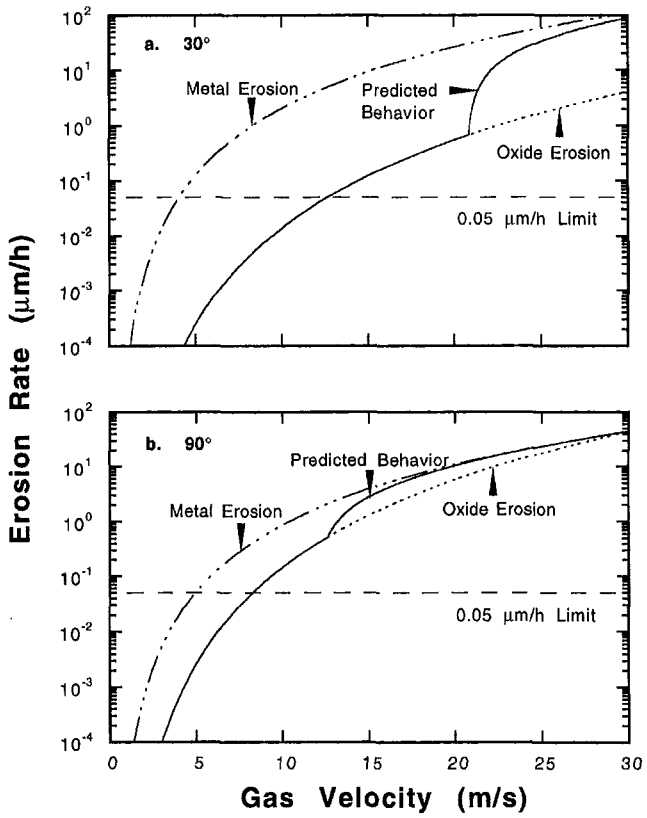

Fig. 4 Estimates of the erosion rate of a carbon steel tube by fly ash and unburned char from combustion of the coal–water fuel with natural gas, under the following conditions: gas temperature 850 K, excess oxygen 3.7 mol%, particle concentration 2.7 g/m^3, particle size 65 μm, particle density 870 kg/m^3, and metal temperature 550 K. The value of 0.05 μm/h is an estimate of the highest acceptable erosion rate (Raask, 1988): (*a*) angle of impaction of particles with the tube surface equal to 30 deg; (*b*) angle of impaction of particles with the tube surface equal to 90 deg.

metal and oxide erosion rates is greater at 30 deg than at 90 deg.

Raask (1988) considered 0.05 μm/h to be the highest acceptable rate of tube thickness loss. Erosion at an impaction angle of 90 deg, on the upstream stagnation line of the tube, is expected to be less than this rate at flue gas velocities below approximately 8 m/s, under the conditions of particle size, particle composition, particle concentration, metal temperature, and gas composition investigated. However, this estimate is highly uncertain because of the long extrapolation from the conditions of the accelerated erosion test, small number of data points, and large number of adjustable parameters in the model. The model is not so much a quantitative tool as a means of identifying where additional work is most needed. A few of the sources of uncertainty are: the effects of collisions and erosion on the metal oxidation rate, the dependence of the oxidation rate on oxygen concentration, the contribution to erosion resistance from particles attached to the surface, and differences in the erosivities of different types of particles, such as ash and char.

Summary and Conclusions

Erosion of carbon steel by ash and unburned char from combustion of coal–water fuel was measured in an accelerated test, as a function of metal temperature (450, 550, and 650 K) and the oxygen content of the gas used to accelerate the particles (3 vol ppm O_2 in N_2, 21 vol% O_2 in N_2, and 100 percent O_2). Erosion was slowest at the lowest temperature, regardless of the oxygen concentration, and slow under strongly oxidizing conditions, at high temperature and high oxygen concentration. Erosion was most rapid at high temperature in the presence of low oxygen concentration. These observations were consistent with a model having the following features: (1) Metal erodes according to the ductile mechanism, at a rate increasing with temperature. (2) Oxide erodes according to the brittle mechanism, at a rate independent of temperature. (3) The oxide scale is strongly attached to the metal. (4) The erosion resistances of the metal and scale are additive. (5) Oxide forms according to the parabolic rate law, at a rate proportional to the square root of the oxygen partial pressure. (6) There is negligible contribution to erosion resistance from particles sticking to the surface.

At low oxygen concentration or temperature, erosion was dominated by the ductile behavior of the metal, but, as conditions were made more oxidizing by increasing oxygen concentration or temperature, the steady thickness of oxide scale and influence of oxide on erosion behavior increased. The oxide was more resistant to erosion than the metal over most of the range of temperatures investigated (above approximately 475 K). Therefore, the transition from metal- to oxide-controlled erosion, with increasing temperature or oxygen concentration, was accompanied by a decrease in the erosion rate. Under the most strongly oxidizing conditions, when the scale was thick enough that metal made no contribution to eroded volume, the rate became independent of temperature, as for a brittle material.

Using experimentally determined erosion rate coefficients, the gas velocity dependence of erosion was calculated for a typical set of combustion and convection section conditions. The onset of the transition from oxide- to metal-controlled erosion, where the rate begins to increase rapidly, was predicted to occur at a velocity near 13 m/s for a collision angle of 90 deg (on the upstream stagnation line of the tube), and at a velocity near 21 m/s for collision at an angle of 30 deg. Erosion on the stagnation line is expected to be slower than 0.05 μm/h at gas velocities less than approximately 8 m/s, under the conditions of particle size, particle composition, particle concentration, metal temperature, and gas composition investigated. Further work is needed on the rate of scale formation in the presence of erosion, the oxygen concentration dependence of the scale formation rate, the erosivities of individual particle types, and the contribution to erosion resistance from particles attached to the surface.

Acknowledgments

This work was supported by the Commonwealth of Pennsylvania/Penn State Coal-Water Fuel Program, and by the United States Department of Energy/Pittsburgh Energy Technology Center under Cooperative Agreement No. DE-FC22-89PC88697, entitled: "Coal–Water Slurry Fuel Combustion Testing in an Oil-Designed Industrial Boiler." The Project Officer of the USDOE/PETC program was John C. Winslow. The authors thank Alan W. Scaroni, Director of The Energy Institute at Penn State; Bruce G. Miller, Associate Director of the Coal Utilization Center; Sarma V. Pisupati, Director of the Combustion Laboratory; and staff members Roger L. Poe, Carl J. Martin, Ronald T. Wincek, Ronald S. Wasco, and Scott A. Britton for their contributions to the work.

References

Bauver, W. P., Bianca, J. D., Fishburn, J. D., and McGowan, J. G., 1984, "Characterization of Erosion of Heat Transfer Tubes in Coal Fired Power Plants," ASME Paper No. 84-JPGC-FU-3.

Bitter, J. G. A., 1963a, "A Study of Erosion Phenomena, Part I," *Wear*, Vol. 6, pp. 5–21.

Bitter, J. G. A., 1963b, "A Study of Erosion Phenomena, Part II," *Wear*, Vol. 6, pp. 169–190.

Caplan, D., and Cohen, M., 1966, "Effect of Cold Work on the Oxidation of Iron From 400–650°C," *Corrosion Science*, Vol. 6, pp. 321–335.

Chow, O. K., Nsakala, N., Hargrove, M. J., and Levasseur, A. A., 1992, "Fireside Combustion Performance Evaluation of Beneficiated Coal-Based Fuels," ASME Paper No. 92-JPGC-FACT-1.

Conrad, H., 1987, "Erosion of Ceramics," *Proc. Conference on Corrosion-Erosion-Wear of Materials at Elevated Temperatures,* A. V. Levy, ed., National Association of Corrosion Engineers, Houston, TX, pp. 77–94.

Davies, M. H., Simnad, M. T., and Birchenall, C. E., 1951, *Trans. American Institute of Mining and Metallurgical Engineers,* Vol. 191, pp. 889–896.

Dosanjh, S., and Humphrey, J. A. C., 1985, "The Influence of Turbulence on Erosion by a Particle-Laden Fluid Jet," *Wear,* Vol. 102, pp. 309–330.

Engel, P. A., 1978, *Impact Wear of Materials,* Elsevier, Amsterdam.

Evans, A. G., Gulden, M. E., Eggum, G. E., and Rosenblatt, M., 1976, "Impact Damage in Brittle Materials in the Plastic Response Regime," Report No. SC5023.9TR, Rockwell International Science Center, Thousand Oaks, CA.

Fan, J., Zhou, D., Cen, K., and Jin, J., 1990, "Numerical Prediction of Tube Row Erosion by Coal Ash Impaction," *Chemical Engineering Communications,* Vol. 95, pp. 75–88.

Finnie, I., 1958, "The Mechanism of Erosion of Ductile Metals," *Proc. Third U.S. National Congress of Applied Mechanics,* R. M. Haythornthwaite, ed., ASME, New York, pp. 527–532.

Finnie, I., 1960, "Erosion of Surfaces by Solid Particles," *Wear,* Vol. 3, pp. 87–103.

Finnie, I., 1980, "The Mechanisms of Erosive Wear in Ductile Metals," *Corrosion-Erosion Behavior of Materials,* K. Natesan, ed., The American Institute of Mining, Metallurgical, and Petroleum Engineers, New York, pp. 118–126.

Finnie, I., Wolak, J., and Kabil, Y., 1967, "Erosion of Metals by Solid Particles," *Journal of Materials,* Vol. 2, pp. 682–700.

Hargrove, M. J., Levasseur, A. A., Miemiec, L. S., Griffith, B. F., and Chow, O. K., 1985, "Performance Characteristics of Coal–Water Fuels and Their Impact on Boiler Operation," *Proc. Seventh International Symposium on Coal Slurry Fuels Preparation and Utilization,* Coal & Slurry Technology Association, Washington, DC, pp. 855–872.

Hargrove, M., Kwasnik, A., Grinzi, F., and Romani, G., 1987, "Boiler Performance Predictions and Field Test Results Firing CWF in an Industrial Boiler," *Proc. Twelfth International Conference on Slurry Technology,* B. A. Sakkestad, ed., Coal & Slurry Technology Association, Washington, DC, pp. 393–399.

Hovis, S. K., Talia, J. E., and Scattergood, R. O., 1986, "Erosion in Multiphase Systems," *Wear,* Vol. 108, pp. 139–155.

Humphrey, J. A. C., 1990, "Fundamentals of Fluid Motion in Erosion by Solid Particle Impact," *International Journal of Heat and Fluid Flow,* Vol. 11, pp. 170–195.

Israel, R., and Rosner, D. E., 1983, "Use of a Generalized Stokes Number to Determine the Aerodynamic Capture Efficiency of Non-Stokesian Particles From a Compressible Gas Flow," *Aerosol Science and Technology,* Vol. 2, pp. 45–51.

Jansson, L., and Vannerberg, N.-G., 1971, "The Effect of the Oxygen Pressure and the Growth of Whiskers on the Oxidation of Pure Fe," *Oxidation of Metals,* Vol. 3, pp. 453–461.

Kang, C. T., Chang, S. L., Pettit, F. S., and Birks, N., 1987, "Synergism in the Degradation of Metals Exposed to Erosive High Temperature Oxidizing Atmospheres," *Proc. Conference on Corrosion-Erosion-Wear of Materials at Elevated Temperatures,* A. V. Levy, ed., National Association of Corrosion Engineers, Houston, TX, pp. 61–76.

Khalil, Y. F., and Rosner, D. E., 1996, "Erosion Rate Prediction and Correlation Technique for Ceramic Surfaces Exposed to High Speed Flows of Abrasive Suspensions," *Wear,* Vol. 201, pp. 64–79.

Kho, T., Rosner, D. E., and Tandon, P., 1996, "Simplified Erosion Rate Prediction Technique for Cylindrical Metal Targets in the High-Speed Cross-Flow of Abrasive Suspensions," *Powder Technology,* accepted for publication.

Kosel, T. H., 1992, "Solid Particle Erosion," *ASM Handbook, Vol. 18, Friction, Lubrication, and Wear Technology,* P. J. Blau, S. D. Henry, G. M. Davidson, T. B. Zorc, and D. R. Levicki, eds., ASM International, pp. 199–213.

Laitone, J. A., 1979a, "Aerodynamic Effects in the Erosion Process," *Wear,* Vol. 56, pp. 239–246.

Laitone, J. A., 1979b, "Erosion Prediction Near a Stagnation Point Resulting From Aerodynamically Entrained Solid Particles," *Journal of Aircraft,* Vol. 16, pp. 809–814.

Levy, A. V., 1982, "The Erosion of Metal Alloys and their Scales," *Proc. Conference on Corrosion-Erosion-Wear of Materials in Emerging Fossil Energy Systems,* A. V. Levy, ed., National Association of Corrosion Engineers, Houston, TX, pp. 298–376.

Levy, A. V., Yan, J., and Patterson, J., 1985, "Elevated Temperature Erosion of Steels," *Proc. International Conference on Wear of Materials,* K. Ludema, ed., ASME, New York, pp. 708–716.

Levy, A., Slamovich, E., and Jee, N., 1986, "Elevated Temperature Combined Erosion-Corrosion of Steels," *Wear,* Vol. 110, pp. 117–149.

Miller, B. G., and Scaroni, A. W., 1992, "Penn State's Superclean Coal–Water Slurry Demonstration Program," *Proc. 17th International Conference on Coal Utilization and Slurry Technologies,* Coal & Slurry Technology Association, Washington, DC, pp. 341–351.

Miller, B. G., Bartley, D. A., Poe, R. L., and Scaroni, A. W., 1995, "A Comparison Between Firing Coal–Water Slurry Fuel and Dry, Micronized Coal in an Oil-Designed Industrial Watertube Boiler," *Proc. 20th International Technical Conference on Coal Utilization & Fuel Systems,* Coal & Slurry Technology Association, Washington, DC, pp. 267–278.

Mitchell, R. E., Hurt, R. H., Baxter, L. L., and Hardesty, D. R., 1992, "Compilation of Sandia Coal Char Combustion Data and Kinetic Analyses: Milestone Report," SAND92-8208-UC-361, Sandia National Laboratories, Livermore, CA, pp. 28–31.

Neilson, J. H., and Gilchrist, A., 1968, "Erosion by a Stream of Solid Particles," *Wear,* Vol. 11, pp. 111–143.

Raask, E., 1985, *Mineral Impurities in Coal Combustion,* Hemisphere Publishing Corporation, pp. 361–396.

Raask, E., 1988, *Erosion Wear in Coal Utilization,* Hemisphere Publishing Corporation, pp. 393–456 and 547–554.

Rishel, D. M., Pettit, F. S., and Birks, N., 1991, "Some Principal Mechanisms in the Simultaneous Erosion and Corrosion Attack of Metals at High Temperature," *Proc. Conference on Corrosion-Erosion-Wear of Materials at Elevated Temperatures,* A. V. Levy, ed., National Association of Corrosion Engineers, Houston, TX, pp. 16-1 to 16-23.

Rosner, D. E., Tandon, P., and Labowsky, M. J., 1995, "Rapid Estimation of Cylinder Erosion Rates in Abrasive Dust-Laden Streams," *AIChE Journal,* Vol. 41, pp. 1081–1098.

Schmahl, N. G., Baumann, H., and Schenck, H., 1958, "Die Temperaturabhängigkeit der Verzunderung von reinem Eisen in Sauerstoff," *Archiv für das Eisenhüttenwesen,* Vol. 29, pp. 83–88.

Schuh, M. J., Schuler, C. A., and Humphrey, J. A. C., 1989, "Numerical Calculation of Particle-Laden Gas Flows Past Tubes," *AIChE Journal,* Vol. 35, pp. 466–480.

Serafini, J. S., 1954, "Impingement of Water Droplets on Wedges and Double-Wedge Airfoils at Supersonic Speeds," Report No. 1159, National Advisory Committee for Aeronautics, Washington, DC.

Sethi, V. K., Corey, R. G., and Spencer, D. K., 1987, "Wear Corrosion Synergism Studies," *Proc. Conference on Corrosion-Erosion-Wear of Materials at Elevated Temperatures,* A. V. Levy, ed., National Association of Corrosion Engineers, Houston, TX, pp. 329–344.

Sethi, V. K., and Wright, I. G., 1989, "Observations on the Erosion-Oxidation Behavior of Alloys," *Corrosion & Particle Erosion at High Temperatures,* V. Srinivasan and K. Vedula, eds., The Minerals, Metals & Materials Society, pp. 245–263.

Sheldon, G. L., 1970, "Similarities and Differences in the Erosion Behavior of Materials," ASME *Journal of Basic Engineering,* Vol. 92, pp. 619–626.

Shida, Y., and Fujikawa, H., 1985, "Particle Erosion Behavior of Boiler Tube Materials at Elevated Temperature," *Wear,* Vol. 103, pp. 281–296.

Snaith, B., Witton, J. J., and Wright, I. G., 1987, "Progress in Surface Topographical Analysis of Erosion Craters," *Proc. Conference on Corrosion-Erosion-Wear of Materials at Elevated Temperatures,* A. V. Levy, ed., National Association of Corrosion Engineers, Houston, TX, pp. 359–366.

Sundararajan, G., 1991a, "The Solid Particle Erosion of Metallic Materials at Elevated Temperatures," *Proc. Conference on Corrosion-Erosion-Wear of Materials at Elevated Temperatures,* A. V. Levy, ed., National Association of Corrosion Engineers, Houston, TX, pp. 11-1 to 11-33.

Sundararajan, G., 1991b, "An Analysis of the Erosion-Oxidation Interaction Mechanisms," *Wear,* Vol. 145, pp. 251–282.

Walsh, P. M., Beér, J. M., and Sarofim, A. F., 1988, "Estimation of Aerodynamic Effects on Erosion of a Tube by Ash," *Proc. Effects of Coal Quality on Power Plants,* EPRI CS-5936-SR, Electric Power Research Institute, pp. 2-19 to 2-34.

Walsh, P. M., Xie, J., Poe, R. L., Miller, B. G., and Scaroni, A. W., 1994, "Erosion by Char and Ash Particles and Deposition of Ash on Carbon Steel in the Convective Section of an Industrial Boiler," *Corrosion,* Vol. 50, pp. 82–88.

Wright, I. G., Nagarajan, V., and Stringer, J., 1986, "Observations on the Role of Oxide Scales in High-Temperature Erosion-Corrosion of Alloys," *Oxidation of Metals,* Vol. 25, Nos. 3/4, pp. 175–199.

Wright, I. G., Sethi, V. K., and Nagarajan, V., 1991, "An Approach to Describing the Simultaneous Erosion and High-Temperature Oxidation of Alloys," ASME JOURNAL OF ENGINEERING FOR GAS TURBINES AND POWER, Vol. 113, pp. 616–620.

Wright, I. G., Sethi, V. K., and Markworth, A. J., 1995, "A Generalized Description of the Simultaneous Processes of Scale Growth by High-Temperature Oxidation and Removal by Erosive Impact," *Wear,* Vol. 186–187, pp. 230–237.

Xie, J., and Walsh, P. M., 1993, "Erosion-Corrosion of Carbon Steel in the Convection Section of an Industrial Boiler Cofiring Coal-Water Fuel and Natural Gas," ASME Paper No. 93-JPGC-PWR-23.

Xie, J., and Walsh, P. M., 1994, "Erosion-Corrosion of Carbon Steel in the Convection Section of an Industrial Boiler," *The Impact of Ash Deposition on Coal-Fired Plants,* J. Williamson and F. Wigley, eds., Taylor and Francis, London, pp. 735–746.

Xie, J., 1995, "Erosion of Heat Exchanger Tubes in the Convective Section of an Industrial Boiler by Products of Coal Combustion," Dissertation, Department of Materials Science and Engineering, Pennsylvania State University, University Park, PA.

Numerical Investigation of the Grinding Process in a Beater Wheel Mill With Classifier

J. Anagnostopoulos

G. Bergeles

Department of Mechanical Engineering,
Laboratory of Aerodynamics,
National Technical University of Athens,
15700 Zografou—Athens, Greece

A numerical investigation is presented for a two-dimensional simulation of the gas flow field and of the dynamic behavior of lignite particles inside Beater Wheel mills with classifier, installed in large coal-fired plants. A large number of representative particles are tracked using Lagrangian equations of motion, in combination with a stochastic model for particle turbulent dispersion. All the important mechanisms associated with the particle motion through the mill (particle–surface collisions and rebounding phenomena, fuel moisture evaporation and erosion wear of internal surfaces) are modeled. A special model is constructed to simulate the fragmentation of impacting particles and to calculate the size distribution of the final mill product. The models are regulated on the basis of available data from grinding mills of the Greek lignite power stations. The numerical code is capable of predicting the locations of significant erosion and to estimate the amount of particle mass that circulates through the mill via the classifying chamber. Mean impact velocity and impingement angle distributions along all the internal surfaces are also provided. The results indicate remarkable differences in the extent of the erosion caused at different locations of the mill. Also, the significant role of the leading blades arrangement inside the classifier on its classification performance and efficiency is elucidated.

Introduction

One of the most important processes in large coal power plants is coal grinding. The fineness of pulverized coal drastically affects both the physical and chemical behavior of particles in the combustion chamber, determining the particle residence time in the flame and the total fuel area exposed to chemical actions. In addition, at the same time with grinding, the mill also accomplishes the drying process of the fuel, which may contain a high percentage of moisture (50–60 percent for the Greek lignite examined here).

In fluid-energy mills, which is the type installed in the Greek Public Power Corporation (PPC) stations, grinding is achieved via the impingement of coarse lignite particles on the blades of a fast rotating fan. This also acts as a suction pump and pneumatic conveyer for both the solid fuel and drying flue gas (Fig. 1). In contrast to the great progress attained during the last few decades regarding combustion efficiency, little effort has been spent on improvement of the grinding devices. A serious problem that reduces mill efficiency arises from the rapid deterioration of internal surface material, and especially of the fan blade surfaces. This damage is caused due to the wear propensity of abrasive mineral species (i.e., SiO_2) contained in the impinging lignite particle, and necessitates frequent replacement of blades, after only 2000 operating hours.

The quality of the supplied mineral fuel may vary with time, both in its composition and calorific value. Thus, the mill often has to operate under conditions different from the "nominal" ones, with unpredictable behavior. Another reason for variations in feed rate conditions is the unknown but important quantity of the largest particles that are captured in the classifying chamber and returned to the mill for further grinding.

The separation mechanism of bigger fragments within the classifier is based on gravity force action in combination with the downward motion, which is imposed on them as they pass through a row of sloping blades (Fig. 1). Due to their high inertia, the fragments eventually pass through the lower opening of the conical section of the classifier. In contrast, the aerodynamic drag force predominates over the foregoing actions for small particles. Thus, the main bulk of the gas flow sweeps them through the upper classifier exit to the burners.

A numerical investigation of the flow field inside the mill and the classifier could demonstrate the operational limits for an efficient operation and lead to useful suggestions for improved design of some parts, in order to minimize the erosion wear and lengthen the time between consecutive maintenance. The present work forms a first attempt to model the process of grinding inside a beater wheel mill with classifier, in a two-dimensional approach. The simulation of the various mechanisms governing the particle fragmentation and motion is the primary target of this work, instead of an exact calculation of the gas flow field, which can be done by standard CFD methods.

The problem can be considered as a two-phase, dilute flow of suspended solid particles, the numerical modeling of which has been developed and evaluated thoroughly in earlier works (Anagnostopoulos and Bergeles, 1992; Sargianos et al., 1993). The Eulerian approach is convenient for the continuous phase and is used through all these works, while a Lagrangian formulation for the particle motion is commonly adopted, as in the present study. The well known "$k-\epsilon$" turbulence model (Launder and Spalding, 1972) is used, because it has been found to provide realistic predictions for the range of the two-phase flow investigations undertaken by the authors.

The mechanisms and the parameters governing the particle rebound characteristics and the erosion wear caused by impinging particles have been extensively investigated in the past (Tilly, 1969; Laitone, 1983; Humphrey, 1990) and several calculation models can be found in the literature (Grant and Tabakoff, 1975; Beacher et al., 1982; Menguturk et al., 1983; Tabakoff et al., 1991; Hamed, 1992). However, most of these are confined to nonshattered particles. The significant effect of particle size and initial velocity on their trajectories is evident in all these works. However, the influence of gas turbulence on particle distribution and eroding behavior is taken into account

Contributed by the Power Division for publication in the JOURNAL OF ENGINEERING FOR GAS TURBINES AND POWER. Manuscript received by the Power Division April 1994; revision received March 1997. Associate Technical Editor: D. Lou.

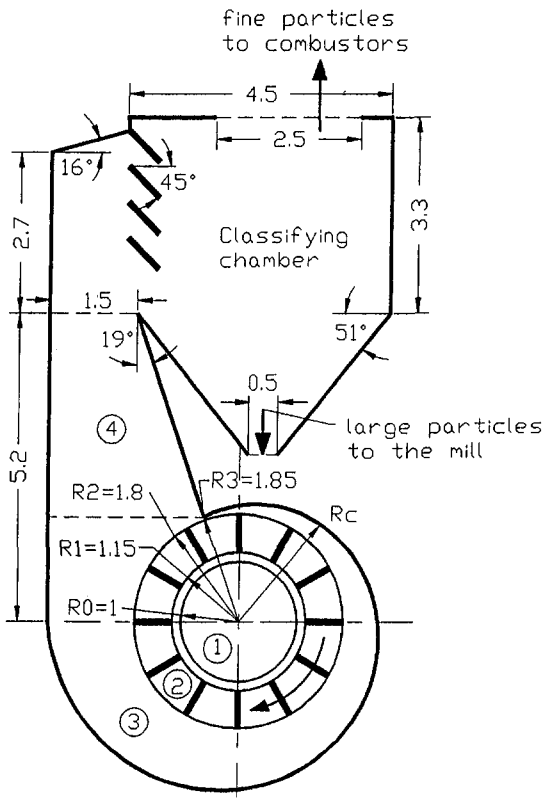

Fig. 1 Geometric configuration of the grinding layout

only in the predictions of Schuh et al. (1989) and Fan et al. (1991) for particle-laden flows past tube bundles, as well as by Founti et al. (1993) in their study of internal erosion of the distribution ducts that transfer pulverized fuel from the classifier to burners. Such turbulence effects are considered here too, using the stochastic model of Shuen et al. (1983).

Finally, a new model for the calculation of size distribution of fragments produced after a lignite-particle impact is presented here, based on the "breakage event" concept of Austin et al. (1984).

The computer code developed was applied to a certain PPC mill and several material-dependent parameters were calibrated for the particular lignite fuel type and operation conditions, to reproduce corresponding available measurements. The results demonstrate the particle fragmentation and motion through the grinding chamber and point out locations where excessive erosion wear occurs. Moreover, the role of the classifier design in its separation capability is analyzed in detail.

Mathematical Formulation

Test Conditions. A plane section of the geometric configuration of the considered mill is sketched in Fig. 1. The mill can pulverize about 100 tons of basic fuel per hour, consuming about 1000 kW and having a fan rotation speed of 450 rpm. The suction, transportation, and drying of lignite is achieved by an amount of the order of 170,000 Nm^3/h gas, which is a mixture of hot flue-gas recycling from the combustion chamber and of cold supplementary air drawn from the atmosphere. The cross section of the suction duct, which enters the mill perpendicularly, is the periphery R0 depicted in Fig. 1. The fuel is then delivered to twelve fan blades fixed on a circular ring that extends between R1 and R2. The mill is equipped with a classifying chamber, which captures the bigger fragments and leads them, through the conical base, back to the grinding chamber for further pulverization.

Gas Flow-Field Inside the Mill. In order to facilitate the development of a numerical algorithm, a global estimation of the gas flow-field inside the mill can be adopted at first, instead of an exact numerical solution; the latter would be easily embodied later into the numerical algorithm. The main assumptions made for this flow field can be summarized as follows: The interior of the mill is divided into four sections, as can be seen in Fig. 1. The gas motion resembles the solid body rotation behavior inside both sections 1 and 2, having constant angular velocity equal to the fan rotational speed. The flow field in section 3, between the blades and the spiral covering of the mill, can be well approximated as the superposition of two elementary fields formed around a linear source and a linear vortex, respectively, both placed along the axis of the fan. The velocity components of the resulting field can be expressed as follows:

$$v = Q/(2\pi r), \quad w = \Gamma/(2\pi r) \tag{1}$$

where v and w are the gas radial and circumferential velocity components, Q the volume flow rate of the source, Γ the vortex circulation, and r the radial distance. The magnitude of Γ can be determined from the relation:

$$\tan(a_s) = v/w = Q/\Gamma \tag{2}$$

where a_s is the expansion angle of the spiral casing.

The relations (1) are considered valid up to the entrance to the convergent section 4, that links the mill with the classifier (Fig. 1). The vertical velocity profile is taken as uniform through this last part of the mill, and the magnitude can be calculated from the given volume flow rate of the gas; the fuel moisture that has been evaporated is included. The horizontal velocity component is varied from zero on the left wall to a certain value on the right wall in order for the velocity vector to always be parallel to the adjacent boundary.

These assumptions, although resulting in some discrepancies between calculated and actual flow field, have only a minor effect on particle trajectories, at least within the most critical sections 1 and 2 where the high inertia of particles is the controlling trajectory parameter (mean initial diameter of the order of centimeter).

Finally, the gas temperature is calculated after an energy balance, assuming that gas and particles have acquired equal temperatures at the time they enter the mill. In sections 3 and 4 the energy balance equation accounts also for the heat absorbed during moisture evaporation, as well as for the different thermal capacity of the water vapor produced.

Gas Flow-Field Inside Classifier. The general form of the time-averaged, conservation equations describing the turbulent motion of steady, incompressible, particle-laden flows is written in two-dimensional, Cartesian coordinates as:

$$\frac{\partial}{\partial x}(\rho u \Phi) + \frac{\partial}{\partial y}(\rho v \Phi) = \frac{\partial}{\partial x}\left(\Gamma_\Phi \frac{\partial \Phi}{\partial x}\right) + \frac{\partial}{\partial y}\left(\Gamma_\Phi \frac{\partial \Phi}{\partial y}\right) + S_\Phi + S_{p,\Phi} \tag{3}$$

In this expression, replacement of Φ with the value 1 gives the continuity equation, whereas for $\Phi = u$ and v the corresponding momentum equations are obtained. Also, for $\Phi = k$ and ϵ, Eq. (3) results in the appropriate expressions for the turbulent kinetic energy (k) and its rate of dissipation (ϵ), dependent variables of the "$k-\epsilon$" turbulence model. Based on the latter model, an effective viscosity is computed in terms of the following relation:

$$\mu_{\text{eff}} = \mu + C_\mu \rho k^2/\epsilon \tag{4}$$

where μ is the dynamic viscosity and ρ the density of the gas,

Table 1 Turbulent diffusivities and source terms of Eq. (3)

Φ	Γ_Φ	S_Φ	$S_{p,\Phi}$
u	μ_{eff}	$-\frac{\partial p}{\partial x}+\frac{\partial}{\partial x}\left(\mu_{eff}\frac{\partial u}{\partial x}\right)+\frac{\partial}{\partial y}\left(\mu_{eff}\frac{\partial v}{\partial x}\right)$	$\sum(m_{in}u_{in}-m_{out}u_{out})$
v	μ_{eff}	$-\frac{\partial p}{\partial y}+\frac{\partial}{\partial x}\left(\mu_{eff}\frac{\partial u}{\partial y}\right)+\frac{\partial}{\partial y}\left(\mu_{eff}\frac{\partial v}{\partial y}\right)$	$\sum(m_{in}v_{in}-m_{out}v_{out})$
k	μ_{eff}/σ_k	$G-\rho\cdot\varepsilon$	$\overline{u}\cdot\overline{S}_{p,u}+\overline{v}\cdot\overline{S}_{p,v}-\overline{u}\cdot\overline{S}_{p,u}-\overline{v}\cdot\overline{S}_{p,v}$
ε	$\mu_{eff}/\sigma_\varepsilon$	$\frac{\varepsilon}{k}\cdot(C_1\cdot G-C_2\cdot\rho\cdot\varepsilon)$	$-2\cdot C_3\cdot\mu\cdot\frac{\varepsilon}{k}\cdot\left(\frac{\partial\overline{S}_{p,u}}{\partial x}+\frac{\partial\overline{S}_{p,v}}{\partial y}\right)$

$$G=\mu_{eff}\cdot\left[2\cdot\left(\frac{\partial u}{\partial x}\right)^2+2\cdot\left(\frac{\partial v}{\partial y}\right)^2+\left(\frac{\partial u}{\partial y}+\frac{\partial v}{\partial x}\right)^2\right]$$

$C_\mu = 0.09$, $C_1 = 1.44$, $C_2 = 1.92$, $\sigma_k = 0.9$, $\sigma_\varepsilon = 0.9$, $C_3 = 3$

subscripts in and out denote particle properties when it enters or leaves a cell.

while C_μ is a model constant. The turbulent exchange coefficient Γ_Φ, in Eq. (3) is defined as:

$$\Gamma_\Phi = \mu_{\text{eff}}/\sigma_\Phi \tag{5}$$

Values of the turbulent Schmidt/Prandtl number σ_Φ, along with the expressions of the gas source term S_Φ are summarized in Table 1. The additional source terms $S_{p,\Phi}$, which are also included in this table, represent the contribution of the particulate phase to gas phase quantities, at each computational cell. The effect of particles on the gas turbulence quantities ($S_{p,\Phi}$ for k and ϵ in Table 1) was simulated using the model of Shuen et al. (1983).

Particulate Phase

General Description. During its residence time inside the grinding chamber, a particle undergoes a series of changes, which have to be simulated. Several indicative particle trajectories inside the mill are plotted in Fig. 2. After its entry, a particle is centrifuged radially and soon enters the space between two rotating blades (section 2). Due to the high rotation speed of the fan, the bigger particles impinge on the blades almost immediately after entering the fan area. The resulting fragments are then centrifuged radially, and the normal component of their rebound velocity can be considered zero, due to the high rotational speed of the blade. The motion of the fragments along the blade surface is affected both by the aerodynamic drag and by friction forces. Fragments of different size acquire unequal velocities and leave the blade at different time instants (Fig. 2). After leaving the blade, the fragments pass through the spiral casing, where they encounter numerous successive collisions to the internal walls, with a continually declining impact angle (Fig. 2). Eventually, they enter the classifying chamber, through the convergent tube of section 4. There they acquire a downward or upward acceleration, depending on their inertia, which leads them toward either the recycling port or the exit to the burners.

During their way through the mill, the fragments lose the largest amount of their moisture content. Due to the large initial size, the rate of evaporation from a particle is negligible before its crushing (Mcintosh, 1976). Thus, it can be assumed that fuel moisture is released only in sections 3 and 4 of the mill (Fig. 1).

Particle Motion. The equations describing the motion of a solid particle inside a gas flow field can be expressed in two-dimensional, polar coordinates, as follows:

$$dv_p/dt = A\cdot(v - v_p) + w_p^2/r_p \tag{6}$$

$$dw_p/dt = A\cdot(w - w_p) - v_p w_p/r_p \tag{7}$$

$$d\vec{r}_p/dt = \vec{u}_p \tag{8}$$

where

$$A = \frac{3}{4}\frac{\mu}{\rho_p d_p^2} C_D \,\text{Re}_p \tag{9}$$

In these equations, ρ_p, d_p, and Re_p are the particle density, diameter, and Reynolds number, respectively, C_D is the drag coefficient, r_p the radial distance from rotation axis, and $\vec{r}_p$ the vector location of the particle. The subscript p denotes particulate-phase quantities.

The first right-hand term of these equations represents the force acting on the particle due to aerodynamic drag, while the last terms are the centrifugal and Coriolis force, respectively. All the other forces (i.e., Magnus, Basset, etc.) as well as particle–particle interactions can be ignored for the present flow conditions and loading.

The particle Reynolds number is defined as:

$$\text{Re}_p = \rho\cdot|\vec{u} - \vec{u}_p|\cdot d_p/\mu \tag{10}$$

and the drag coefficient C_D is expressed by empirical functions:

$$C_D = (1. + 0.15\,\text{Re}_p^{0.687})/(\text{Re}_p/24) \quad \text{for} \quad \text{Re}_p \le 1000$$

$$C_D = 0.44 \quad \text{for} \quad \text{Re}_p > 1000 \tag{11}$$

Gravity effects are ignored in sections 1 and 2, and they are not included in the preceding expressions. However, the gravity force is taken into account during particle motion computations in sections 3 and 4, as well as inside the classifier, where the Cartesian form of Eqs. (6)–(8) is used.

The stochastic particle dispersion model assumes that the flow field is comprised of eddies, whose characteristic length (L_e) and lifetime (T_e) are (Shuen et al., 1983):

$$L_e = C_\mu^{3/4} k^{3/2}/\epsilon \tag{12}$$

$$T_e = L_e/(2k/3)^{1/2} \tag{13}$$

A particle-eddy interaction lasts until the eddy's lifetime is terminated or the particle transverses the eddy, whichever happens faster. The instantaneous gas-phase velocities are calculated from the mean aerodynamic field plus a fluctuating quantity, which is randomly selected from a Gaussian distribution with standard deviation: $(2k/3)^{1/2}$.

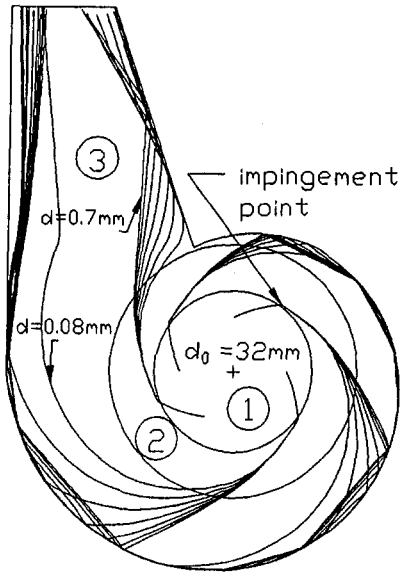

Fig. 2 Indicative particle trajectories calculated in the grinding chamber

Size Reduction. The detailed fragmentation mechanism of a particle impinging upon a solid surface has not yet been fully understood. In general, a colliding particle is subjected to a series of crushing events or breakage steps (Austin et al., 1984; Pauw, 1988), the number of which is analogous to the impact energy (or to the normal component of impact velocity). During each of these events, which for simplicity can be assumed sequential, all the particles in the top-size class are rebroken. Consequently, after n breakage events the mass fraction of the produced fragments falling in size class i is given as follows:

$$p_{i,n} = \sum_{j=1}^{n} (b_{i,j} p_{j,j-1}), \quad i > n \tag{14}$$

where the breakage function $b_{i,j}$ is the mass fraction of fragments of size class i in the products, after one breakage event of a particle of size class j. The $\sqrt{2}$ size interval rule is broadly used for the classification of the breakage products (Austin et al., 1984), and it is adopted in the present work. Based on that rule, several empirical expressions can be found in the literature, which correlate the breakage function with the material type, the impact energy, etc. (Austin et al., 1984; Pauw, 1988; Popplewell and Peleg, 1992).

An important feature of the analysis is the following simplifying assumption, based on experimental evidence (see, for example, Goodwin et al., 1969–70; Tasserie et al., 1992):

$$b_{i+1,j+1} = b_{i,j} \tag{15}$$

This expression signifies that the size distribution function of the produced fragments is the same, regardless of the size of the initial particle. Thus, the deduction of all finer size distributions after a given number of breakage events can be done by translation from the first size.

The number of breakage events should be reasonably dependent on both the material type and the impact energy. In order to take into account these effects in calculating the resultant fragment distribution after one particle impact, we introduce the following relation:

$$N = (V_{n1}/V_{\max})N_{\max} \quad \text{for} \quad V_{n1} > V_{\min}$$
$$N = 0 \quad \text{for} \quad V_{n1} \le V_{\min} \tag{16}$$

In the foregoing expression, N is the number of breakage events that happen after an impact, V_{n1} the normal component of the particle impact velocity, and $N_{\max}$, $V_{\min}$, and $V_{\max}$ adjustable constants. The coefficient $N_{\max}$ represents the number of breakage events produced for a relatively high particle impact velocity, $V_{\max}$. Moreover, no breakage occurs if the impact energy (or the impact velocity) is less than a threshold value, $V_{\min}$ (Goodwin et al., 1969–70). The cumulative product size distribution can be finally calculated from the equation:

$$P_{i,n} = 1 - \sum_{k=n+1}^{i} p_{k,n} \quad i > n \tag{17}$$

As can be observed in Fig. 2, fragmentation may occur also on the internal surface of the spiral casing, at least during the early collisions of larger fragments, where both impact velocity and angle are significant. This possibility has not been incorporated into the numerical code, for simplicity reasons. However, it will be taken into account indirectly, during the calibration of the model coefficients.

Restitution Coefficients. The bulk mass of the fragments produced at an impact is spread radially with relatively low velocity (40–50 percent of the impact speed), whereas only a small amount, consisted of finer fragments, is ejected with quite high radial velocities (170–400 percent of the impact speed, depending on material type; Tilly and Wendy, 1970; Uemois and Kleis, 1975). However, the subsequent motion of these finer fragments is strongly decelerated due to aerodynamic drag. On the basis of this concept, it can be accepted with no substantial error that there is an equal mean radial rebound velocity for all sizes produced after an impact on the rotating blades. The exact magnitude of that velocity is, however, unknown for lignite particles, and therefore needs regulation. Thus, we introduce the adjustable restitution coefficient R_t as follows:

$$V_{n2}/V_{n1} = 0, \quad V_{t2}/V_{t1} = R_t \tag{18}$$

where the subscripts 1 and 2 denote conditions before and after the collision, respectively, while the n and t signify normal and parallel to the surface velocity components.

The estimation of a particle's rebounding characteristics when it collides with the internal surface of the spiral casing or the classifier walls appears to be more difficult, since, to the authors' knowledge, no relevant experimental evidence exists for the lignite particles concerned here. Therefore, the polynomial functions of impact angle β_1, extracted by Grant and Tabakoff (1975) for 200 μm quartz particles impacting on aluminum target, are approximately adopted:

$$V_{n2}/V_{n1} = 0.993 - 1.76\beta_1 + 1.56\beta_1^2 - 0.49\beta_1^3 \tag{19}$$

$$V_{t2}/V_{t1} = 0.988 - 1.66\beta_1 + 2.11\beta_1^2 - 0.67\beta_1^3 \tag{20}$$

Erosion Wear. All the internal surfaces of the mill suffer from mechanical erosion and loose material, under the repetitive particle bombardment. The empirical model of Grant and Tabakoff (1975) is selected in the present work as one of the most reliable and advanced in the literature:

$$E = K_1 f(\beta_1) V_1^2 \cos^2 \beta_1 (1 - R_T^2) + f(V_{n1}) \tag{21}$$

$$R_T = 1 - 0.0016 V_1 \sin \beta_1 \tag{22}$$

$$f(\beta_1) = \{1 + C_K[K_2 \sin (90\beta_1/\beta_0)]\}^2 \tag{23}$$

$$f(V_{n1}) = K_3 (V_1 \sin \beta_1)^4 \tag{24}$$

where $C_K = 1$ for $\beta_1 \le 3\beta_0$, otherwise $C_K = 0$; $K_1 = 3.67 \times 10^{-6}$, $K_2 = 0.585$, $K_3 = 6.0 \times 10^{-12}$, and β_0 is the impingement angle causing maximum erosion (20 ÷ 30 deg for ductile targets).

The coefficients K_1, K_2, and K_3 depend largely on material type, and are fixed for quartz particles and aluminum alloy target. Therefore, their values must be re-adjusted for the lignite particles and surface material concerned here, and especially on the fan-blade surface, where a particle impact is coupled with fragmentation.

An additional material loss is caused on the blade surface due to abrasion of the parallel jet of sliding fragments. In order to quantify the extent of this erosion mechanism, we assumed that it can be directly related to the friction energy produced as the fragments are dragged along the blade surface. The friction force that acts on a fragment arises mainly due to Coriolis force, which is directed perpendicular to the surface. Thus, we can expect the correlation:

$$F_f = C_f \cdot (v_p w_p)/r_p \tag{25}$$

where F_f is the friction force and C_f the friction coefficient. A proportionality coefficient C_e has to be introduced in order to assess the fraction of friction energy C_e that is spent on material removal. This parameter must depend on the wear propensity of abrading fragments and on the wear-resistance characteristics of the blade surface (Raask, 1988). Hence the additional erosion wear per unit wall surface can be calculated as:

$$E_f = K_f \cdot \sum_i \left[\int_{l_i} (v_i w_i / r_i) ds \right] \tag{26}$$

where l_i is the path length of the fragment i along the surface, and $K_f = C_e C_f$ is an adjustable parameter.

Moisture Release. The rate of fuel moisture evaporation can be expressed by the following approximation (Mcintosh, 1976):

$$(MC) = (MC)_o \cdot e^{-nt} \tag{27}$$

where $(MC)_o$ is the initial and (MC) the final moisture content of a fuel particle (dry basis), after being dried at constant temperature for a time period t. The exponent n depends on temperature and fuel type and is also a function of particle size. On the basis of Mcintosh's data, the parameter n can be estimated from the relation:

$$n = C_v/d_p^2 \tag{28}$$

The parameter C_v has to be adjusted for the lignite fuel and should also stand for a global inclusion of the present drying conditions, where the gas temperature is gradually decreased toward the mill exit, as evaporation evolves.

Calculation Procedure and Boundary Conditions

Continuous Phase. The velocity field inside the mill is calculated from Eqs. (1)–(2). For the classifier region, the gas-phase differential equations are discretized via the "control volume" approach (Patankar and Spalding, 1972) and the "hybrid" difference scheme. The final general form of Eq. (3) becomes then:

$$a_P\Phi_p = \sum_i a_i\Phi_i + S_\Phi + S_{P,\Phi}$$

$$a_P = \sum_i a_i \quad i = E, W, N, S \quad \Phi = u, v, k, \epsilon \tag{29}$$

where a_i are coefficients of combined convective–diffusive flux through the i face of the control volume. The system of the equations is solved iteratively until convergence, using the SIMPLE algorithm and a TDMA solver (Patankar and Spalding, 1972; Patankar, 1980). Then the particles are tracked into the resultant flow field and the particle source terms are calculated and stored at every computational cell. The gas phase equations are solved again but with the new source terms, and this external iterative procedure is continued until simultaneous convergence of both phase's quantities is obtained.

The computational domain covers a two-dimensional cross section of the classifying chamber with a 45 × 60 nonuniform, Cartesian grid, shown in Fig. 3. The oblique parts of the boundary walls are simulated by a stair-step approximation that has been tested and verified in the past (Anagnostopoulos and Bergeles, 1992). The leading blades are represented by solidified cells at the corresponding grid nodes. The velocity profiles at the exit of the mill section 4 are used as inlet conditions for the classifier. Wall-functions boundary conditions (Launder and Spalding, 1974) are applied to all grid nodes that adjoin the internal surfaces, including the blades.

The small portion of gas issuing from the lower opening of the classifier is unfortunately not known. A broad estimation, based on geometric dimensions and on some pressure data given by PPC, gives a value of about 5 percent. It is worth noting, however, that the resultant flow field is not altered significantly if this portion is varied between 0 and 10 percent.

Particulate Phase. For the solution of the particulate phase, the numerical code calculates trajectories of a sufficiently large number of representative lignite particles. To perform this, the particle motion Eqs. (6)–(9) are integrated in time, during consecutive time intervals of 10^{-3} s.

Before its entrance into the mill, the lignite material is forced through a precrushing apparatus. The size reduction achieved there secures an upper limit of 4 cm for the exit particle diameters. Unfortunately, the exact distribution of the size classes thus produced is unknown. Hence, as for the inlet conditions at the mill entrance, a uniform weight fraction distribution is assumed to cover 30 consecutive size classes below 4 cm, following the $\sqrt{2}$ rule. The representative particles are ejected from 10 different radial positions along the radius of the inlet cross section. Their entrance to the blade section 2 is considered to happen through 100 uniformly distributed locations along the arc-line between two adjacent blades.

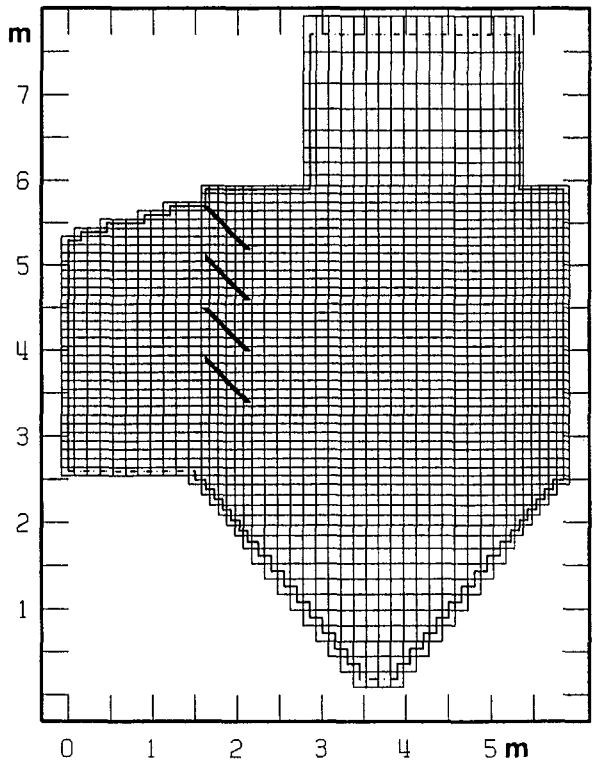

Fig. 3 Cartesian numerical grid arrangement

The fragments produced once a particle impinges on the blade surface are arranged in N_d consecutive size classes ($N_d = 1 \div 30$, depending on the number of breakage events). The trajectory of a representative fragment for each such class is then followed until it leaves the blade. The fragments move parallel to the blade surface and their radial velocity is computed from Eq. (6), which now includes the extra term of friction force (Eq. (25)). At the interface of sections 2 and 3 (Fig. 1) the fragments are re-classified into 30 size classes, thus producing a new frame of reference for the subsequent computations in section 3. Afterward, the trajectories of 30 particles of different size, launched from 360 starting positions allocated along the periphery R2, are followed through sections 3 and 4 up to the mill exit. The code also calculates the amount of moisture released from the tracked particle during each time step, using Eq. (27). As evaporation proceeds, the particle density is progressively reduced, while its diameter is kept constant.

At the classifier inlet, particles of all size classes obtained after the breakage into the mill are launched from 30 uniformly distributed locations. From each such location and for every size class, a great number of representative particles is followed. In total, about 400,000 trajectories are tracked in order to obtain accurate and smooth curves for the quantities of interest. The mean value and the standard deviation of the particle injection velocity are calculated on the basis of the numerical results at the exit of the mill section 4 (Fig. 1). For a better presentation of the particle behavior inside the classifier, it is convenient to classify the particles into three main categories, considering their inertia by the momentum equilibration number λ (see, for example, Humphrey, 1990):

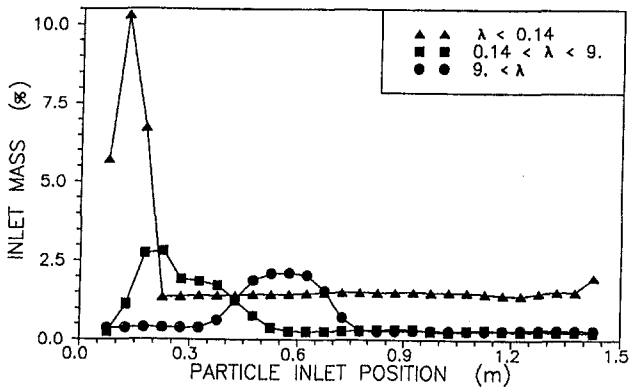

Fig. 4 Particle mass flux at the mill-classifier interface; x axis represents distance from the left wall

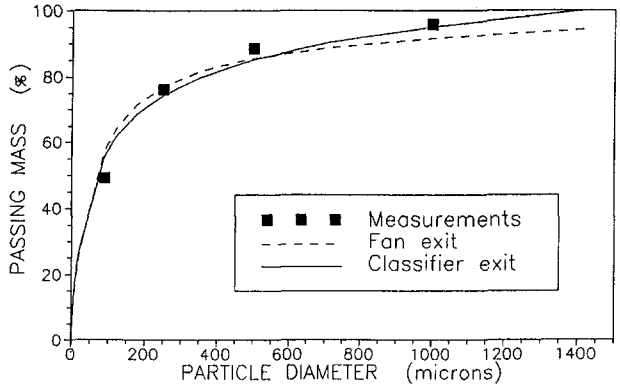

Fig. 5 Particle size analysis of the mill product

$$\lambda = \tau \cdot U_{\text{ref}}/L_{\text{ref}} \tag{30}$$

$$\tau = d_p^2 \cdot \rho_p/(18 \cdot \mu) \tag{31}$$

where τ is the particle response time and L_{ref}, U_{ref} a characteristic length and velocity of the flow field (length of the convergent section and mean gas velocity there, respectively, for the present case). As it is well documented in two-phase flow theory, particles having a value of λ much less than 1 closely follow the fluid streamlines. The greater portion of these particles, which is concentrated near the left edge of the inlet (Fig. 4), constitutes the outcome of the mass that slides along the spiral casing of the mill (Fig. 2). The peak in mass flux profile is displaced to the right as far as the biggest particles ($\lambda > 9$) are concerned. The latter, due to their high inertia, acquire and preserve significant normal rebound velocity component after impinging near the end of the spiral casing.

A prediction-correction recurrence technique (Diakoumakos et al., 1988) is applied to determine the exact impingement point of a particle that moves toward the surface of a blade or a wall. The exact particle impact and rebound angle and velocity, as well as the induced erosion wear of the internal surfaces are then calculated from Eqs. (19)–(20) and (21)–(24), respectively. Note that the actual slope of the oblique walls or blades is taken into consideration.

Results and Discussion

Calibration of the Adjustable Model Constants. Quite a few "runs" of the computer code have been performed in order to calibrate the various adjustable coefficients so that the numerical results match the measurements of PPC. The latter include mass flow rate, temperature and moisture content of gas, and pulverized fuel in the ducts beyond the classifier, where the size distribution of fuel particles is also provided and listed in Table 2. At the mill entrance only the fuel moisture percentage is measured, while the rest of the data of Table 2 have been evaluated by PPC with the aid of a mill energy balance. Moreover, some information is given concerning the shape of an eroded blade surface after about 2000 hours mill operation.

A brief description of the calibration method is given below: First of all, the size reduction model is regulated until the predicted particle size distribution beyond the classifier is thoroughly compared with the data of PPC in Fig. 5. These data reveal that almost all fragments in size classes above 1400 μm are captured in the classifier and returned to the mill. On the other hand, our model calculates the exact size distribution of fragments produced at the rotor exit (dotted line of Fig. 5); thus, the recycling mass is estimable and found to be about 1.5 kg/s, which corresponds to 5.8 percent of the total inlet fuel or to 11 percent of the dryed mass being transported to the burners. After subtracting the recycling mass from the dotted line, the continuous curve of Fig. 5 is obtained, which is comparable to the PPC data. Eventually, the evaporation parameter C_v is regulated in order to give 10.8 percent final lignite moisture content. This procedure is repeated a couple of times to achieve a fine tuning. The adjustment of the erosion-related parameters does not affect the previous calculations and will be presented later in the paper. All the parametric values obtained by the calibration procedure are summarized in Table 3.

Spiral Casing Erosion. According to Fig. 2, repetitive collisions of a particle upon the internal surface of the spiral casing occur, with an increasing frequency and smaller and smaller impact velocity and angle. As a result of this behavior, the total impacting mass increases gradually along the spiral expansion (Fig. 6), while the calculated mean (mass weighted) impact angle decreases at a rapid rate (Fig. 7). The mean particle impact velocity also exhibits similar reduction, plotted in Fig. 8, revealing an analogous decrease in mean impact energy. The latter is maximized at the early part of the casing, where the distance from the fan blades is minimum. The mean impact angle at that position is of the order of 25 deg, inside the highly eroding region for ductile materials (Humphrey, 1990). Consequently, despite the small impinging mass, the calculated erosion wear takes its highest value there, as can be seen in Fig. 9, which shows the erosion rate along the case walls. This result is in agreement with related observations made by the PPC. Erosion is being slowly reduced along the internal casing surface, as a result of the cumulative effect of the mean impact

Table 2 Mill operating conditions and grinding data

	Inlet conditions	Exit conditions
Gas Flow Rate (kg/s)	57.7	70.0
Gas Temperature (°C)	596	146
Fuel Flow Rate (kg/s)	26.0	13.7
Fuel Temperature (°C)	25	146
Fuel moisture (%, wet basis)	52.7	10.8
	Sieve size (mm)	**Passing Mass (%)**
Particle Size Analysis	1.00	95.85
	0.50	88.47
	0.25	76.10
	0.09	49.24

Table 3 Model parameters adopted in the numerical algorithm

$N_{max} = 8$, $V_{min} = 5$ m/s, $V_{max} = 50$ m/s, $R_t = 0.4$,
$K_3 = 9.0 \times 10^{-12}$, $C_f = 0.25$, $K_f = 1.875 \times 10^{-5}$, $C_v = 2.9 \times 10^{-7}$

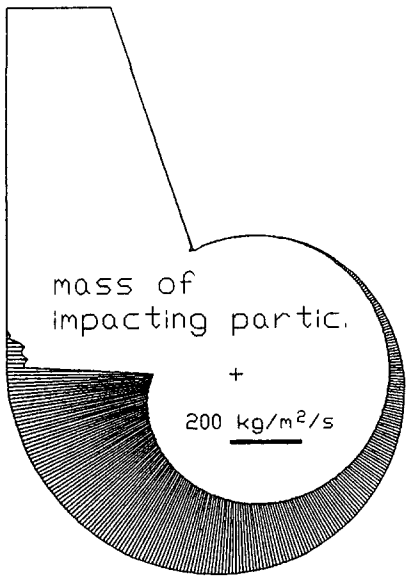

Fig. 6 Impact frequency on spiral casing internal surface

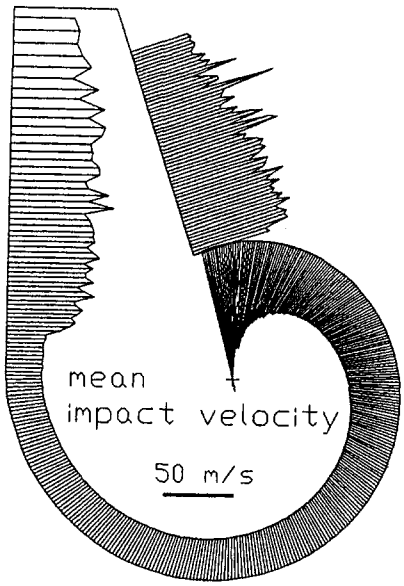

Fig. 8 Mean impact velocity on spiral casing internal surface

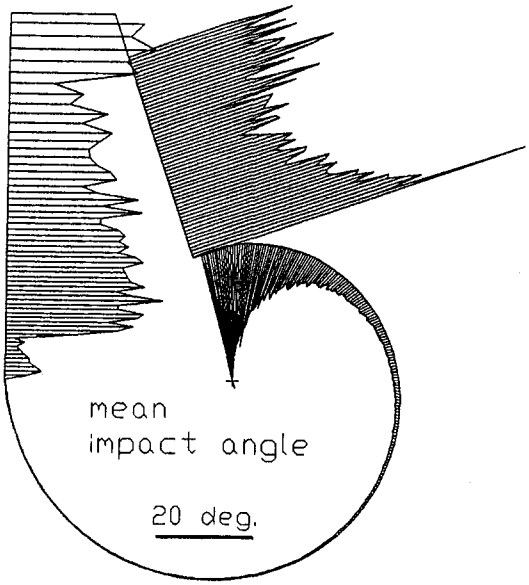

Fig. 7 Mean impact angle on spiral casing internal surface

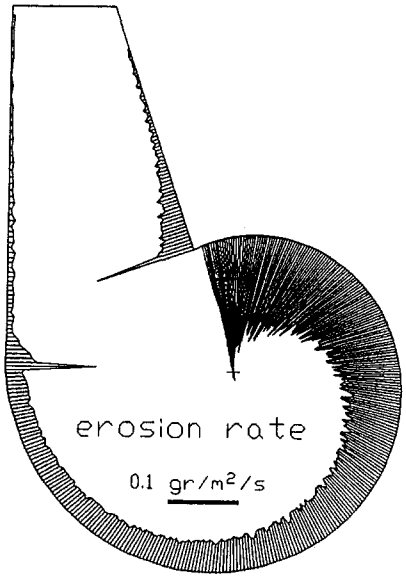

Fig. 9 Spiral casing surface erosion rate

angle and velocity and of the total impacting mass variations, mentioned above.

Two other regions of the casing that present extensive erosion wear are localized close to the lower edges of the vertical and inclined walls of the mill, as shown in Fig. 9. At the beginning of the vertical part, the abrupt change in casing curvature causes an analogous steep increase in mean impact angle of the almost sliding particles there. On the other hand, the lower part of the inclined wall is exposed to direct impingement of several fragments, which have left the fan a few degrees previously (Fig. 2) and are aimed at the wall with a considerable speed and angle (Figs. 7 and 8).

The number of striking particles is minimal toward the mill outlet, and thus the induced erosion becomes less important, although the corresponding values of both mean impact velocity and angle are significant all along this area (Figs. 6–9).

Blade Erosion. The larger portion of the inlet coal mass impinges on the front part of the blade surface. This portion consists mainly of the bigger lignite particles, the circumferential velocity of which is still very small compared to the blade rotation speed. On the contrary, the smaller particles are influenced by aerodynamic effects, which are reduced relative to the blade velocity (Laitone, 1979; Menguturk et al., 1983). Consequently, they penetrate deeper between two neighboring blades before eventually impinging, the latter occurring at a smaller angle and with a reduced impact velocity.

This behavior is in any case desirable, at least as far as the grinding efficiency of the mill is concerned, since the rotating blades offer more striking energy to the bigger particles and less to the smaller ones. However, at the same time it appears to be harmful to the blade surface resistance, since the eroding action of the particles is concentrated on a small area close to the blade leading edge, causing drastic material deterioration there. This effect is depicted in Fig. 10, along with numerical results for the additional wear caused by the abrading parallel jet of sliding fragments. The eroding action of the latter exhibits a gradual increase along the blade, as more and more fragments are produced.

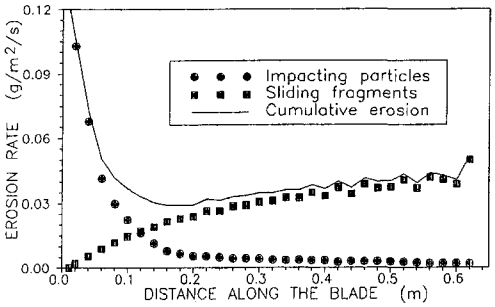

Fig. 10 Blade surface erosion rate

Erosion Model Calibration. The curves presented in Fig. 10 are obtained after previous calibration of the coefficients included in the corresponding erosion models of Eqs. (21)–(24) and (26). The calibration is performed with the aid of the sketch in Fig. 11, provided by PPC. The continuous line of this sketch represents a resultant average shape of the eroded blade surface, as it has been observed after about 2000 operation hours. In Fig. 10 it can be seen that the erosion pattern due to impacting particles and that due to sliding fragments become predominant over well-separated areas of the blade surface. Thus, the coefficient K_f can be adjusted independently of the parameters K_1, K_2, and K_3. Furthermore, according to the numerical results, the particles impinge almost perpendicularly close to the blade leading edge and therefore the total erosion magnitude there is determined mainly by the term of Eq. (24). Consequently, only the value of K_3 has to be fixed. The calibrated values of both parameters K_f and K_3 are included in Table 3.

Analysis of the Classifier Performance. The gas velocity field inside the classifier is demonstrated in Fig. 12. Initially, the flow is directed upward, but as it is forced through the inclined blades, it acquires a significant downward velocity component. A great portion of the gas passes through the blades, while only a small fraction flows beneath the lowest blade. A large vortex motion is established, occupying all the space of the conical section, while the smaller vortex that tends to be formed behind the upper blade is less important, since few particles reach there. In contrast, the large vortex formation that divides the right-wall area into two well separated parts, is decisive; the velocities are clearly rising in the upper part, whereas in the lower part the flow is directed toward the exit of the conical section.

The trajectories followed by the smaller particles ($\lambda < 1$) show, as expected, a great similarity with the gas streamlines. On the other hand, the motion of the very inert particles ($\lambda > 9$) is mainly determined by their inlet and rebound velocities. Thus, the indicative trajectories of 2828 μm particles drawn in Fig. 13 consist of almost rectilinear parts. The effect of the great inlet velocity standard deviation is evident in this figure, where all particles, after multiple successive collisions on the walls and on the leading blades, fall out of the lower opening, since the downward inert and gravity forces predominate. The trajectories of the medium-size particles are curved to a greater extent, as seen in Fig. 14. This enables some of the particles to

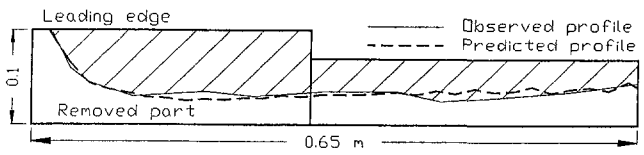

Fig. 11 Cross section of a fan blade after approximately 2000 operation hours

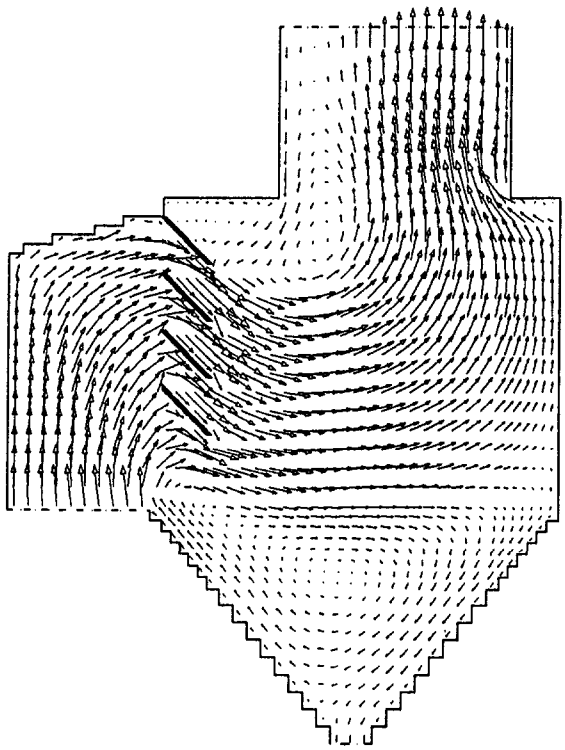

Fig. 12 Velocity vectors inside the classifier

pass through the upper two blades without impinging on any of them, and thus to reach the opposite right wall at elevated positions, where the upward gas stream is strong (Fig. 12). The aerodynamic drag forces that arise there eventually prevail over the particle's gravity, and the gas sweeps the particles toward the upper classifier exit. This analysis can explain the mechanism that allows an undesirable transport and insertion of relatively big particles into the combustion chamber.

The mass fraction of the pulverized fuel, which is being separated and eventually returns to the mill, is plotted in Fig. 15, in connection with the particle size and for several starting locations along the classifier inlet cross section. Almost all particles of diameter over 1400 μm recycle, in agreement with the PPC data mentioned previously. A significant fraction of big particles between 1400 and 400 μm escapes to the burners. An

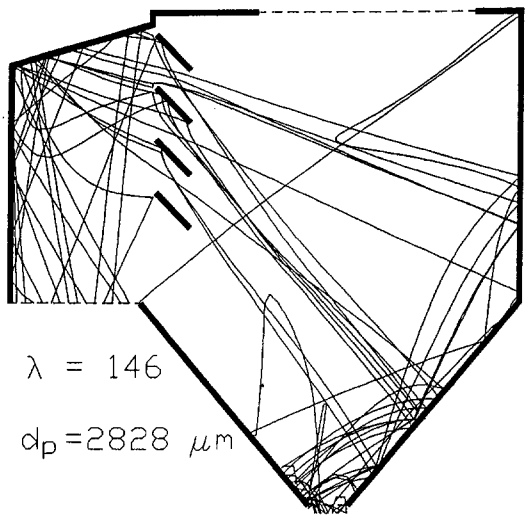

Fig. 13 Indicative trajectories of large particles

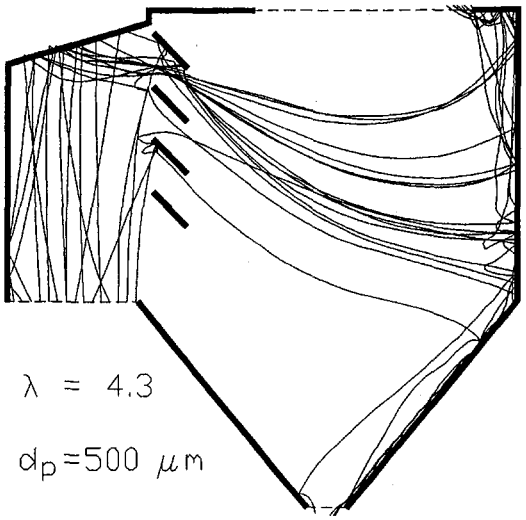

Fig. 14 Indicative trajectories of medium-size particles

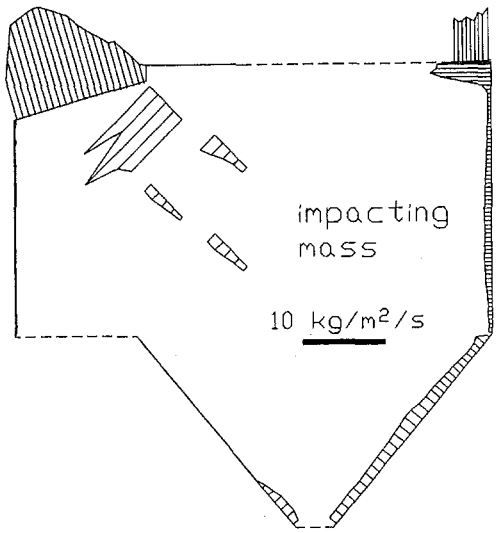

Fig. 16 Rate of particle impacting mass on the internal classifier surfaces

obvious size threshold is localized around 400 μm, below which there are no more particles returning to the mill. A noticeable exception can be observed concerning the right corner of the inlet section (x = 1.45 m); a significant part of even very small particles launched from that position drifts toward the mill, though no further size reduction is needed. This undesirable treatment is, however, insignificant, since the percentage of these particles in the total fuel mass is very small. The additional amount of recycling particles in size classes between 1400 and 400 μm is equal to 1.25 kg/s, increasing the cumulative recycling mass up to a value of 2.75 kg/s.

The Role of the Classifier Blades. The particle mass impact rate and the erosion wear caused on the classifier internal walls are shown in Figs. 16 and 17, respectively. The second and fourth blades are shifted to the right, in order to make the figures more readable. Inspection of Fig. 16 shows that a great fraction of particles impinges on the upper oblique internal wall. Although the mean impact velocity is considerable there, the mean impact angle is of the order of 50 deg, clearly outside the highly eroding region (20 ÷ 30 deg) and therefore the predicted erosion rate of the wall surface is moderate (Fig. 17). Of the same order of magnitude is the left-wall erosion rate, which is due to a different combination of particle characteristics; the impact angle is now inside the 20 ÷ 30 region and the impact velocity is higher, but only few particles impinge on this wall, as Fig. 16 reveals. This behavior has been observed also in practical classifiers, where the left and the upper oblique walls are reinforced internally with coatings of wear-resistant materials.

The first of the four leading blades receives the main load of the impinging particles, whereas the collision rate is considerably lower on the rest of the blades (Fig. 16). The combination of high impact velocities and moderate impact angles (20 ÷ 30 deg) toward the leading edges of the blades favors a drastic increase in the erosion wear there, which is more pronounced on the first blade surface (Fig. 17), due to the greater amount of impacting mass there (Fig. 16). This result is consistent with relevant PPC observations.

Suggestions for an Improved Design. A well-designed classifier should ensure the recycling of all the particles bigger than an upper permissible limit, and moreover must constantly preserve this prescribed size threshold, during long operation periods. The foregoing numerical results reveal that this particular classifier allows some relatively large particles to escape through its blades to the burners. Furthermore, the continuous erosion wear and deterioration of the blade leading edges is expected to aggravate the problem with the length of time of

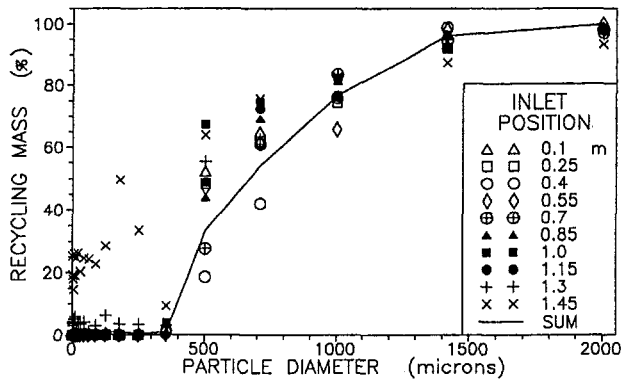

Fig. 15 Particle mass recycling to the mill

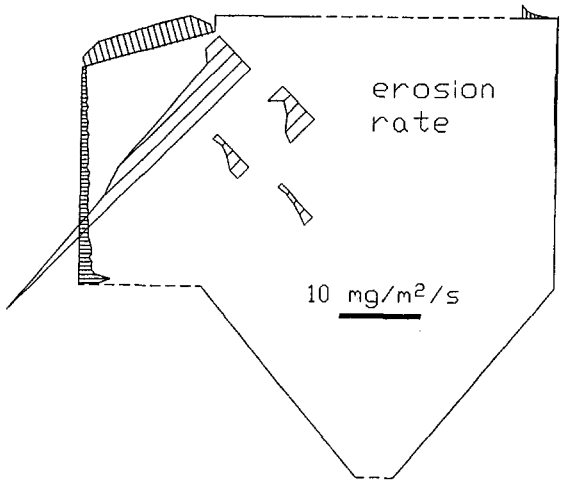

Fig. 17 Classifier internal surface and blade erosion rate

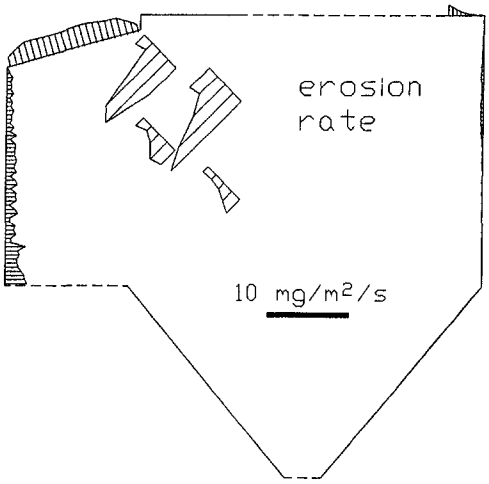

Fig. 18 Erosion pattern for a modified blade arrangement

the operation. Calculations were made assuming that 20 or 40 percent of the upper blade length has been removed due to erosion, and the predicted recycling mass has indeed been reduced to 2.3 kg/s and 1.95 kg/s, respectively. The first idea to deal with this problem could be an increase in the blade sloping angle, in order to eliminate the unwanted gap between two neighboring blades. Calculations with a 10 percent increased angle showed an analogous increase in recycling mass, from 2.75 to 3.05 kg/s. However, the destructive erosion pattern on the upper blade (Fig. 17) remains unchanged.

Another proposed modification concerns a different blade arrangement. The two upper blades are placed at a 33 percent closer distance, in order to achieve simultaneously two desirable results: the elimination of the unwanted gap and the sharing out of the impacting mass and consequently of the induced erosion wear among several blades. Calculations made with this modified design produced very encouraging results. As can be seen in Fig. 18, the eroding action of particles is now more uniformly distributed on both the two upper blade surfaces, reducing considerably the maximum erosion rate (compared to Fig. 17). In addition, the total recycling mass is augmented to 3.7 kg/s, and all particles above 700 μm return to the mill.

Conclusions

A two-dimensional numerical algorithm is developed and used to describe and investigate the gas flow field, as well as the particle dynamic behavior inside a coal beater wheel mill with classifier, utilized in large power plants. The particle motion, impingement, and rebounding characteristics, as well as the evaporation of the moisture content and the erosion wear caused on the internal mill surfaces, are simulated by appropriate models. A simple model is introduced to account for the erosion of the fan blades due to abrasion of coal fragments. Also, a new technique is proposed for an effective calculation of particle breaking after impact and of the size distribution of the produced fragments. All model constants were adjusted on the basis of available measurements, taken by the Greek PPC in a real, full-scale mill.

The fraction of particles captured in the classifier and recycled back to the mill for further grinding, which is a nonestimable quantity in real conditions, is numerically assessed and related to the particle inlet conditions and inertia. Careful analysis of various particle trajectories is performed, in order to demonstrate and explain possible inefficiencies of the classifier concerning the handling of certain particle size classes. Particle impact and erosion characteristics are provided at all the internal walls and blades. The results obtained point out the regions that suffer significant erosion wear, and are in agreement with the practical evidence. The important role of the classifier design and especially of its leading blades arrangement is elucidated. The mechanical erosion wear of the latter seems to be responsible for a fast and premature reduction of the classifier efficiency.

Finally, some preliminary applications of the computer code are made in an attempt to explore possible improvements in classifier design. Other modifications concerning either operation or design parameters of the entire grinding layout can be easily investigated by the developed numerical algorithm, avoiding the excessive cost that would be entailed by a trial-and-error procedure under real conditions.

Acknowledgments

This work was financially supported by the Greek Public Power Corporation and the General Secretariat for Research and Development.

References

Anagnostopoulos, J., and Bergeles, G., 1992, "Discrete-Phase Effects on the Flow-Field of a Droplet-Laden, Swirling Jet With Recirculation: a Numerical Study," *Int. J. Heat Fluid Flow,* Vol. 13, No. 2, pp. 287–301.

Austin, L. G., Klimpel, R. R., and Luckie, P. T., 1984, *Process Engineering of Size Reduction: Ball Milling,* Society of Mining Engineers, New York.

Beacher, B., Tabakoff, W., and Hamed, A., 1982, "Improved Particle Trajectory Calculations Through Turbomachinery Affected by Coal Ash Particles," ASME JOURNAL OF ENGINEERING FOR POWER, Vol. 104, pp. 64–68.

Diakoumakos, H., Anagnostopoulos, J., and Bergeles, G., 1988, "A Theoretical Study of Solid-Air, Two-Phase Flow," *Mathematical Modeling in Combustion and Related Topics,* NATO ASI Series E, C. M. Brauner and C. Shmidt-Laine, eds., Martinus Nijhoff Publishers, pp. 449–459.

Fan, J., Zhou, D., Jin, J., and Cen, K., 1991, "Numerical Calculations of Tube Bundles Erosion by Turbulent Particle-Laden Gas Flows," *Chem. Eng. Comm.,* Vol. 104, pp. 209–225.

Founti, M., Giannakopoulos, D., and Klipfel, A., 1993, "Transport Characteristics of Pulverised Coal and Erosion Wear in the Distribution Ducts From the Mills to the Furnace Burners in Large Power Plants," *Proc. 2nd International Conference on Combustion Technology for a Clean Environment,* Lisbon, Paper No. 28.5, Vol. II, pp. 34–39.

Goodwin, J. E., Sage, W., and Tilly, G. P., 1969–70, "Study of Erosion by Solid Particles," *Proc. Institution of Mechanical Engineers,* Vol. 184, pp. 279–292.

Grant, G., and Tabakoff, W., 1975, "Erosion Prediction in Turbomachinery Resulting From Environmental Solid Particles," *Journal of Aircraft,* Vol. 12, pp. 471–478.

Hamed, A., 1992, "An Investigation in the Variance in Particle Surface Interactions and Their Effects in Gas Turbines," ASME JOURNAL OF ENGINEERING FOR GAS TURBINES AND POWER, Vol. 114, pp. 235–241.

Humphrey, J. A. C., 1990, "Fundamentals of Fluid Motion in Erosion by Solid Particle Impact," *Int. J. Heat Fluid Flow,* Vol. 11, pp. 170–195.

Laitone, J. A., 1979, "Aerodynamic Effects in the Erosion Process," *Wear,* Vol. 56, pp. 239–246.

Laitone, J. A., 1983, "Characterization of Particle Rebound Phenomena in the Erosion of Turbomachinery," *Journal of Aircraft,* Vol. 20, pp. 275–281.

Launder, B. E., and Spalding, D. B., 1972, *Mathematical Models of Turbulence,* Academic Press, London.

Launder, B. E., and Spalding, D. B., 1974, "The Numerical Computation of Turbulent Flow," *Comp. Methods Appl. Mech. Eng.,* Vol. 3, p. 269.

Mcintosh, M. J., 1976, "Prediction of Performance of a Browncoal Mill System," *Braunkohle,* Vol. 12, pp. 433–448.

Menguturk, M., Gunes, D., Mimaroglu H. K., and Sverdrup, E. F., 1983, "Blade Boundary Effect on Turbine Erosion and Deposition," ASME *Journal of Fluids Engineering,* Vol. 105, pp. 270–276.

Patankar, S. V., and Spalding, D. B., 1972, "A Calculation Procedure for Heat, Mass and Momentum Transfer in Three-Dimensional Parabolic Flows," *Int. J. Heat Mass Transfer,* Vol. 15, pp. 1787–1806.

Patankar, S. V., 1980, *Numerical Heat Transfer and Fluid Flow,* Hemisphere Publishing Co., Washington, DC.

Pauw, O. G., 1988, "The Minimization of Overbreakage During Repetitive Impact Breakage of Single Ore Particles," *Powder Technology,* Vol. 56, pp. 251–257.

Popplewell, L. M., and Peleg, M., 1992, "Theoretical Kinetic Model for Particulates Disintegration Process That Result in Bimodal Size Distributions," *Powder Technology,* Vol. 70, pp. 21–30.

Raask, E., 1988, *Erosion Wear in Coal Utilization,* Hemisphere Publishing Corporation, New York.

Sargianos, N. P., Anagnostopoulos, J., and Bergeles, G., 1993, "Influence of Particle Diameter Distribution on the Downstream Particle Turbulence in a Two-Phase, Turbulent, Round Jet," *Int. J. Numerical Methods Fluids,* Vol. 16, pp. 287–301.

Schuh, M. J., Schuler, C. A., and Humphrey, J. A. C., 1989, "Numerical Calculation of Particle-Laden Gas Flows Past Tubes," *AIChE Journal,* Vol. 35, pp. 466–480.

Shuen, J. S., Chen, L. D., and Faeth, G. M., 1983, "Evaluation of a Stochastic Model of Particle Dispersion in a Turbulent Round Jet," *AIChE Journal,* Vol. 29, pp. 167–170.

Tabakoff, W., Hamed, A., and Metwally, M., 1991, "Effect of Particle Size Distribution on Particle Dynamics and Blade Erosion in Axial Flow Turbines," ASME JOURNAL OF ENGINEERING FOR GAS TURBINES AND POWER, Vol. 113, pp. 607–615.

Tasserie, M., Bideau, D., Troadec, J. P., Dodds, J., Laurent, Y., and Verdier, P., 1992, "Experimental Results on Fragmentation of a Brittle Material," *Powder Technology,* Vol. 73, pp. 61–66.

Tilly, G. P., 1969, "Erosion Caused by Airborne Particles," *Wear,* Vol. 14, pp. 63–79.

Tilly, G. P., and Wendy, S., 1970, "The Interaction of Particle and Material Behaviour in Erosion Process," *Wear,* Vol. 16, pp. 447–465.

Uemois, H., and Kleis, I., 1975, "A Critical Analysis of Erosion Problems Which Have Been Little Studied," *Wear,* Vol. 31, pp. 359–371.

Journal of Engineering for Gas Turbines and Power

Technical Briefs

Frequency Spectrum Analysis and Applications to Steam Turbine Vibrations

J. Ling[1] and Y. Cao[1]

Introduction

Bearing vibrations in turbogenerators are common failure modes. Identification of vibration failure during the operation of turbogenerators and the subsequent quick failure elimination in a short shut-down period are very important to turbine engineers. In this paper, a brief theoretical analysis of the characteristics of the frequency spectrum and the diagnoses of three typical vibration failures of steam turbines in power stations are presented. It is our hope that the results will be useful to turbine engineers who need to make correct judgments for the causes of turbine vibrations.

Application of the Frequency Spectrum Theory for Vibrations Caused by Misalignment of Shaft Centerlines

For a turbogenerator with rigid couplings, if the shafts of the turbine and generator have the misalignment with the parallel shaft centerline shown in Fig. 1(a), the two shafts must rotate synchronously because of the couplings. Therefore, the shaft system rotates around the same center, O, with the angular velocity, ω, and within radius of eccentricity e between the shafts of the turbine and generator. It also whirls around the center, O' of the shaft with the same rotating angular velocity, ω, as shown in Fig. 1(b).

Suppose that the deflection of the shaft system is negligible, and point P is an arbitrary mass point on the shaft. Point P whirls in the radius, r, and around the shaft center, O'. At the same time, point P also makes extra rotating movements around the center, O. At an arbitrary time, t, if the coordinate of point P is $P(x, y)$ and the whirling angle of the point P is ωt, the extra rotating angle of point P is also ωt. The axial projection of the rotating movement of point P is shown in Fig. 1(b). At time t, the displacements of point P in the x and y directions are:

$$x = e \cos \omega t + r \cos 2\omega t$$

$$y = e \sin \omega t + r \sin 2\omega t$$

respectively. According to these equations, the movement of arbitrary mass point P in the shaft system is not only a function of the angular velocity ω, but also a function of 2ω.

In general, the eccentricity, e, between the two shaft centerlines of the shaft system is much smaller than the radius, r. Therefore, the main harmonic component in the frequency spectrum may indicate the existence of the first harmonic component of the fundamental frequency. If the deflection of the shaft system cannot be neglected, these phenomena take place only near the couplings. While the ends of the shaft system still rotate around their shaft centerlines, the fundamental frequency component will be present in the frequency spectrum.

When the two shafts meet with an angle, α, there exists a bending moment in the coupling. The action of the bending moment tends to reduce the angle, α. The bending moment changes its direction per revolution, and the bending deformation caused by the bending moment also changes its direction per revolution. Therefore, the fundamental frequency component will be present in the frequency spectrum.

The analyses presented above were applied to a k116-50/20 steam turbine, which was connected with the generator by the rigid couplings as shown in Fig. 2. The first harmonic of the fundamental frequency was mainly present in the horizontal and vertical direction of bearings #2 and #3 during the operation of the steam turbogenerator. Based on the frequency spectrum theory, the misalignment with parallel shaft centerlines must have occurred, because the radius, r, was always much larger than the eccentricity in practice. During the shut-down period, it was found that the eccentricity, e, between two shaft centerlines was 0.212 mm, and the angle, α, was zero. Therefore, the diagnosis concerning the misalignment with parallel shaft centerlines was proven.

Application of the Frequency Spectrum Theory for Impinging Vibration of High-Pressure Oil in the Main Oil Pump

The main oil pump in the steam turbine is connected with the shaft of the steam turbine directly and installed in the front-bearing housing. Therefore, the periodic impingement and vibration in the main oil pump will take place if the high-pressure oil from the outlet of the main oil pump cannot flow into the guide vane and the shell of the main oil pump smoothly (Horlock, 1973). The vibration will be transmitted to the front bearing housing, because that is where the main oil pump is installed.

If the vibration of the front-bearing housing is measured, the high-pressure oil from every flow path of the main oil pump will impinge once in the direction of the measuring point when the pump rotates a turn. Thus, the vibration frequency of the

[1] Department of Mechanical Engineering, Florida International University, Miami, FL 33199.

Contributed by the Power Division of THE AMERICAN SOCIETY OF MECHANICAL ENGINEERS. Manuscript received at ASME Headquarters January 1997. Associate Technical Editor: D. Lou.

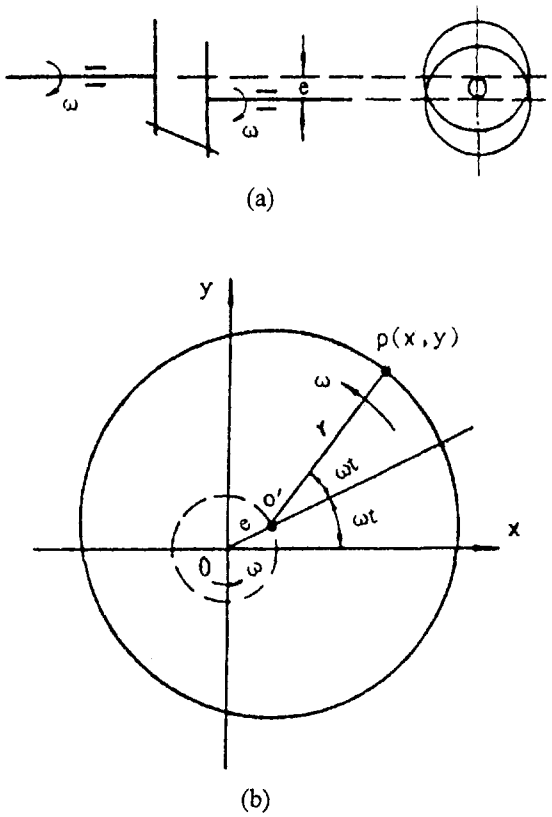

Fig. 1 Schematic representation of the misalignment with parallel shaft centerlines: (*a*) schematic of two shafts with parallel shaft centerlines; (*b*) axial projection of rotating movement of point *P*

measuring point must be equal to the rotating frequency of the pump times the number of the flow paths.

The frequency spectrum analysis was also applied to a K116-50/20 steam turbine. The front-bearing housing was installed in the front of the steam inlet of the steam turbine, as shown in Fig. 2. The rated revolution of the steam turbine was 3000 rpm. There were seven flow paths in the main oil pump. The vibration in the front bearing housing was measured during the steam turbine operation. The frequency spectrum is shown in Fig. 3. It is apparent that the highest harmonic component at seven times the fundamental frequency was caused by the impingement of the high-pressure oil. The harmonic components on both sides of the highest component were caused by the modulation of the fundamental frequency (Marole, 1987). Thus, the main cause for the vibration of the front-bearing housing was believed to be the impinging vibration from the high-pressure oil at the outlet of main oil pump.

After the problem related to the main oil pump was solved during a shut-down period, the measurement was made again at the same point of the front-bearing housing during the operation. All harmonic components at six, seven, and eight times

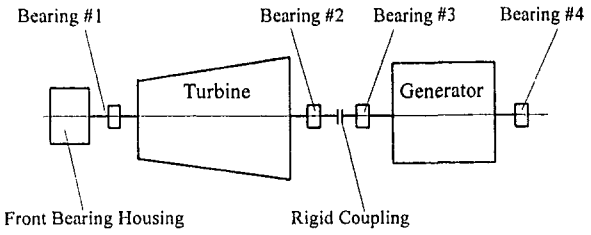

Fig. 2 Schematic of steam turbogenerator

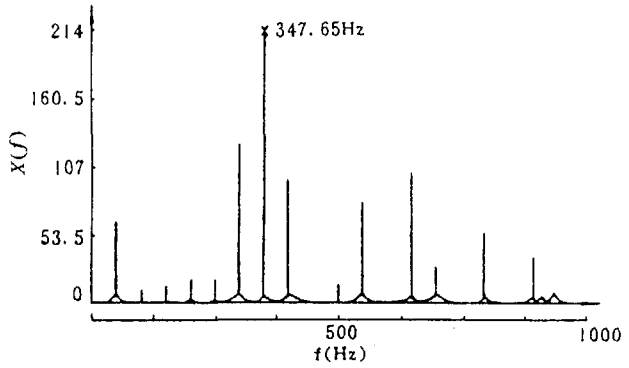

Fig. 3 Frequency spectrum of the vibration on the front bearing housing

the working frequencies were eliminated, and the vibration of the front-bearing housing was greatly reduced.

Application of the Frequency Spectrum Theory for High-Frequency Bearing Vibrations

In general, after the turbogenerator operates for a long period of time, the dynamic stiffness of the bearings will be weakened in some directions, the connection between the bearing foundation and foundation bolts will be loosened, and the compressive stress in the bearing housing will be reduced. Thus, the damping of the bearings will be changed (Goodwin, 1989; Ragulskis, 1989). Because of these reasons, the intrinsic vibration frequency of bearings in some directions may be possibly close to the integral times of the fundamental frequency of the turbogenerator. Therefore, high-frequency vibration of the bearings will be induced during the operation.

The vibration frequency spectrum on bearing #4 of the K116-50/20 steam turbine is shown in Fig. 4. It can be seen that there is a high harmonic component at ten times the fundamental frequency, in addition to the first harmonic of the fundamental frequency caused by the misalignment with parallel shaft centerlines in the vertical direction. Because there is no vibration at ten times the fundamental frequency of the other bearings, the possibility that the rotor exhibits an exciting force with ten times the fundamental frequency can be excluded. In addition, after analyzing the shape in the frequency spectrum, it was found that the shape of the frequency spectrum was similar to that of the resonance on the bearing. Therefore, it was certain that the high-frequency resonance in the vertical direction of bearing #4 had happened when the turbogenerator rotated in the fundamental frequency.

During the inspection of bearings after the steam turbine was shut down, it was found that there were six pads under the base of bearing #4. Because there were too many pads, it was be-

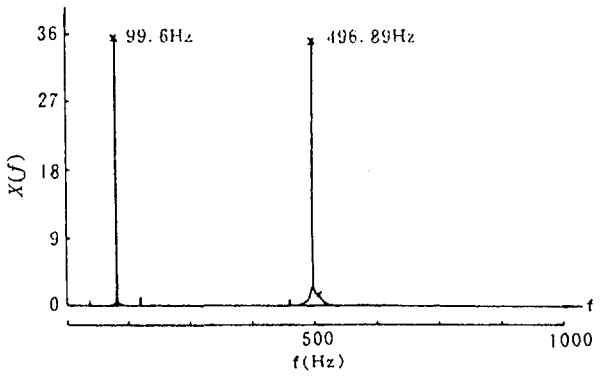

Fig. 4 Frequency spectrum of the vertical vibration on bearing #4

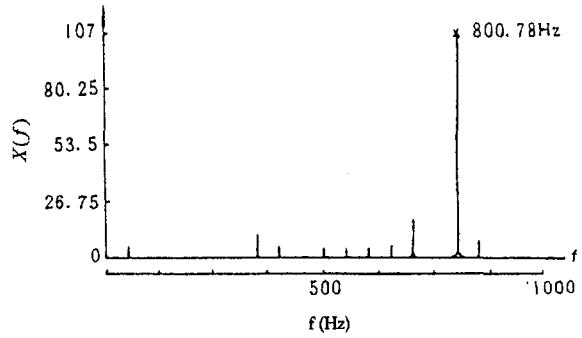

Fig. 5 Frequency spectrum of the vertical vibration on bearing #1

lieved that the compacting contact between the bearing foundation and base plate was destroyed. After the number of the pads was reduced to three, the vibration of bearing #4 in the vertical direction was decreased greatly, and the harmonic component at ten times the fundamental frequency was eliminated.

Similarly, the frequency spectrum in the vertical direction of bearing #1 is shown in Fig. 5. The frequency of the main vibration was 16 times the fundamental frequency of the turbogenerator. Because bearing #1 was located in front of the steam inlet of the steam turbine, it was subjected to a higher temperature, and the change of the compressive stress in the bearing housing was larger than that of the other bearings. During maintenance, the compressive stress of bearing #1 was increased to an upper-limit value based on the maintenance standard. The vibration in the vertical direction of bearing #1 was measured again. At this time, the harmonic component of the high frequency was weakened effectively and the vibration was decreased greatly.

Therefore, it was concluded that strengthening the compacting contact between the bearing foundation and base plate and increasing the compressive stress in bearing housing are effective methods that eliminate or weaken the high-frequency vibration on bearings.

Conclusions

The frequency spectrum theory and its application to industrial problems were successfully demonstrated, but improvements are still needed for the realization and identification of vibrations on the turbogenerator because of the complex nature of the vibration phenomenon. With further development in the frequency spectrum theory and the accumulation of practical experience, the frequency spectrum analyses will take a more and more important role in rotating machinery.

References

Goodwin, M. J., 1989, *Dynamics of Rotor-Bearing Systems,* Unwin Hyman, London.

Horlock, J. K., 1973, *Axial Flow Turbines,* Robert E. Krieger Publishing Company, Malabar, FL.

Marole, S. L., 1987, *Digital Spectral Analysis With Applications,* Prentice-Hall, Inc., Englewood Cliffs, NJ.

Ragulskis, K. M., 1989, *Vibration of Bearings,* Hemisphere Publishing Corporation, New York–Washington, DC.

Receptance Method for the Sensitivity Analysis of Critical Speeds to Rotor Support Stiffness

Chen-Kai Su[1] and Shyh-Chin Huang[2]

A rotor system can be studied via various approaches, e.g., FEM, the transfer matrix method, etc. The receptance method has been one of the methods used for frequency analysis of rotors. The authors, herein, have shown an application of the receptance matrix for sensitivity analysis. Examples of critical speed sensitivity to support stiffness were illustrated and a computing algorithm was developed. Numerical examples proved the approach to be valuable for rotor engineers in quick evaluation and understanding of the support effects.

1 Introduction

The dynamics of rotor systems have been studies for several decades. Owing to the demands of today's turbomachinery, the investigation of rotor dynamics has become more pressing in recent decades. In the present paper, the authors focus on the sensitivity analysis of a rotor to its support stiffness. Similar investigations were conducted by Rajan et al. (1986, 1987) with different methods. In the present studies, the receptance formulation is applied. The receptance method has been extensively used for eigenfrequency calculation. The paper will show that, in addition to the eigenfrequencies, the receptance matrix exhibits inherent advantages over parameters sensitivity analyses. The sensitivity analysis of rotor critical speeds to support stiffness is illustrated as an application of the receptance method. Although the present examples do not consider the bearing damping and support asymmetry, we can include these effects as well. The subsequent changes will be complex receptances, and finding of the roots becomes more time consuming.

2 General Concept

For the purpose of mathematical modeling, a rotor system can be divided into two main bodies, the rotor and the supports, as shown in Fig. 1. With the employment of the receptance method, the natural frequencies, or critical speeds, of rotor systems are realized via study of the rotor and support characteristics. The advantage of dividing the rotor system into components is to simplify the analysis process, which may become very tedious and inaccurate for a complex system when treated as a whole. In the present paper, the authors prove that the receptance matrix provides useful information, not only for frequency analysis, but also for sensitivity studies as well. A sensitivity matrix of critical speeds given as functions of support stiffness is then derived as an application.

2.1 Characteristics of the Rotor. The eigenfunctions, $\psi_n(Z)$'s, of a free rotor obtained from the modified transfer matrix (MTM) method (Chiau and Huang, 1989) are here employed as base functions of the rotating rotor in an assumed-modes method. The displacement functions then take the form:

$$\begin{cases} U(Z,t) = \sum_{n=1}^{N} \psi_n(Z) f_n(t) = \{\psi(Z)\}^T \{f(t)\} \\ V(Z,t) = \sum_{n=1}^{N} \psi_n(Z) g_n(t) = \{\psi(Z)\}^T \{g(t)\} \end{cases}, \quad (1)$$

[1] Graduate Student, Department of Mechanical Engineering, National Taiwan Institute of Technology, Taipei, Taiwan; email: cksu@vib2.me.ntit.edu.tw.

[2] Professor, Department of Mechanical Engineering, National Taiwan Institute of Technology, 43, Keelung Rd., Sec. 4, Taipei, Taiwan, 10772; email: huang@vib2.me.ntit.edu.tw.

Contributed by the International Gas Turbine Institute of THE AMERICAN SOCIETY OF MECHANICAL ENGINEERS. Manuscript received by the International Gas Turbine Institute April 8, 1996. Associate Technical Editor: R. E. Kielb.

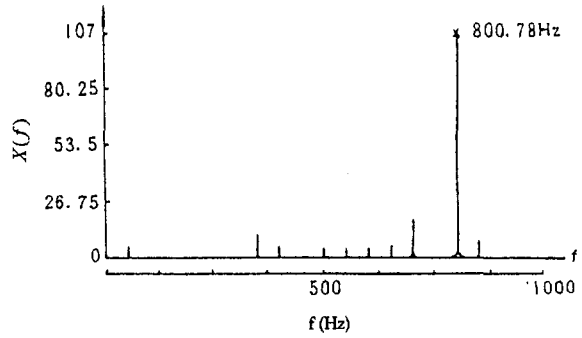

Fig. 5 Frequency spectrum of the vertical vibration on bearing #1

lieved that the compacting contact between the bearing foundation and base plate was destroyed. After the number of the pads was reduced to three, the vibration of bearing #4 in the vertical direction was decreased greatly, and the harmonic component at ten times the fundamental frequency was eliminated.

Similarly, the frequency spectrum in the vertical direction of bearing #1 is shown in Fig. 5. The frequency of the main vibration was 16 times the fundamental frequency of the turbogenerator. Because bearing #1 was located in front of the steam inlet of the steam turbine, it was subjected to a higher temperature, and the change of the compressive stress in the bearing housing was larger than that of the other bearings. During maintenance, the compressive stress of bearing #1 was increased to an upper-limit value based on the maintenance standard. The vibration in the vertical direction of bearing #1 was measured again. At this time, the harmonic component of the high frequency was weakened effectively and the vibration was decreased greatly.

Therefore, it was concluded that strengthening the compacting contact between the bearing foundation and base plate and increasing the compressive stress in bearing housing are effective methods that eliminate or weaken the high-frequency vibration on bearings.

Conclusions

The frequency spectrum theory and its application to industrial problems were successfully demonstrated, but improvements are still needed for the realization and identification of vibrations on the turbogenerator because of the complex nature of the vibration phenomenon. With further development in the frequency spectrum theory and the accumulation of practical experience, the frequency spectrum analyses will take a more and more important role in rotating machinery.

References

Goodwin, M. J., 1989, *Dynamics of Rotor-Bearing Systems,* Unwin Hyman, London.

Horlock, J. K., 1973, *Axial Flow Turbines,* Robert E. Krieger Publishing Company, Malabar, FL.

Marole, S. L., 1987, *Digital Spectral Analysis With Applications,* Prentice-Hall, Inc., Englewood Cliffs, NJ.

Ragulskis, K. M., 1989, *Vibration of Bearings,* Hemisphere Publishing Corporation, New York–Washington, DC.

Receptance Method for the Sensitivity Analysis of Critical Speeds to Rotor Support Stiffness

Chen-Kai Su[1] and Shyh-Chin Huang[2]

A rotor system can be studied via various approaches, e.g., FEM, the transfer matrix method, etc. The receptance method has been one of the methods used for frequency analysis of rotors. The authors, herein, have shown an application of the receptance matrix for sensitivity analysis. Examples of critical speed sensitivity to support stiffness were illustrated and a computing algorithm was developed. Numerical examples proved the approach to be valuable for rotor engineers in quick evaluation and understanding of the support effects.

1 Introduction

The dynamics of rotor systems have been studies for several decades. Owing to the demands of today's turbomachinery, the investigation of rotor dynamics has become more pressing in recent decades. In the present paper, the authors focus on the sensitivity analysis of a rotor to its support stiffness. Similar investigations were conducted by Rajan et al. (1986, 1987) with different methods. In the present studies, the receptance formulation is applied. The receptance method has been extensively used for eigenfrequency calculation. The paper will show that, in addition to the eigenfrequencies, the receptance matrix exhibits inherent advantages over parameters sensitivity analyses. The sensitivity analysis of rotor critical speeds to support stiffness is illustrated as an application of the receptance method. Although the present examples do not consider the bearing damping and support asymmetry, we can include these effects as well. The subsequent changes will be complex receptances, and finding of the roots becomes more time consuming.

2 General Concept

For the purpose of mathematical modeling, a rotor system can be divided into two main bodies, the rotor and the supports, as shown in Fig. 1. With the employment of the receptance method, the natural frequencies, or critical speeds, of rotor systems are realized via study of the rotor and support characteristics. The advantage of dividing the rotor system into components is to simplify the analysis process, which may become very tedious and inaccurate for a complex system when treated as a whole. In the present paper, the authors prove that the receptance matrix provides useful information, not only for frequency analysis, but also for sensitivity studies as well. A sensitivity matrix of critical speeds given as functions of support stiffness is then derived as an application.

2.1 Characteristics of the Rotor. The eigenfunctions, $\psi_n(Z)$'s, of a free rotor obtained from the modified transfer matrix (MTM) method (Chiau and Huang, 1989) are here employed as base functions of the rotating rotor in an assumed-modes method. The displacement functions then take the form:

$$\begin{cases} U(Z,t) = \sum_{n=1}^{N} \psi_n(Z) f_n(t) = \{\psi(Z)\}^T \{f(t)\} \\ V(Z,t) = \sum_{n=1}^{N} \psi_n(Z) g_n(t) = \{\psi(Z)\}^T \{g(t)\} \end{cases}, \quad (1)$$

[1] Graduate Student, Department of Mechanical Engineering, National Taiwan Institute of Technology, Taipei, Taiwan; email: cksu@vib2.me.ntit.edu.tw.

[2] Professor, Department of Mechanical Engineering, National Taiwan Institute of Technology, 43, Keelung Rd., Sec. 4, Taipei, Taiwan, 10772; email: huang@vib2.me.ntit.edu.tw.

Contributed by the International Gas Turbine Institute of THE AMERICAN SOCIETY OF MECHANICAL ENGINEERS. Manuscript received by the International Gas Turbine Institute April 8, 1996. Associate Technical Editor: R. E. Kielb.

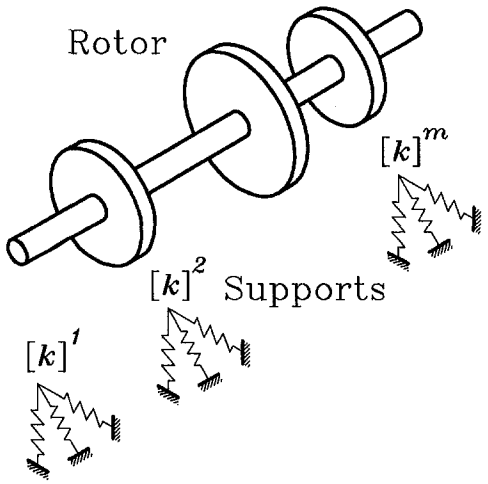

Fig. 1 Rotor and supports

where N is the number of modes deemed necessary for satisfactory convergence and accuracy, and $f_n(t)$ and $g_n(t)$ are the undetermined generalized coordinates associated with the nth mode. Subsequently, the Lagrange equations yield the discretized equations of motion of the free rotor:

$$\begin{bmatrix} [M]+[N] & 0 \\ 0 & [M]+[N] \end{bmatrix} \begin{Bmatrix} \ddot{f}(t) \\ \ddot{g}(t) \end{Bmatrix} + \begin{bmatrix} 0 & \Omega[P] \\ -\Omega[P] & 0 \end{bmatrix} \begin{Bmatrix} \dot{f}(t) \\ \dot{g}(t) \end{Bmatrix} + \begin{bmatrix} [K_1]-\Omega^2[K_2] & 0 \\ 0 & [K_1]-\Omega^2[K_2] \end{bmatrix} \begin{Bmatrix} f(t) \\ g(t) \end{Bmatrix} = \begin{Bmatrix} \{Q_1\} \\ \{Q_2\} \end{Bmatrix}. \quad (2)$$

The entries of the matrices $[M]$, $[N]$, $[P]$, $[K_1]$ and $[K_2]$ can be found in a previous paper (Huang et al., 1994). $[Q_1]$ and $[Q_2]$ are the generalized forcing vectors dependent on the external excitation. $[K_1]$, resulting from elastic deflection, predominates at lower rotation speed, yet $-\Omega^2[K_2]$, from the centrifugal effect, becomes more important at higher speed.

2.2 Receptance Method for Elastically Supported Rotor. A receptance is defined as the ratio of displacement response to a harmonic point loading. The reader may refer to Johnson and Bishop (1960) for detailed information. Now, consider a rotor with m intermediate elastic supports, as shown in Fig. 1. It is assumed that the ith support is located at Z_i and has stiffness constants k^i_{xx}, k^i_{xy}, k^i_{yx}, k^i_{yy} in X, Y, and their cross directions, respectively. The displacements of the rotor at the ith supporting point Z_i, due to harmonic point forces at the jth supporting point Z_j, are

$$\begin{cases} U(Z_i,t) = \sum_{j=1}^{m} \{\psi(Z_i)\}^T[D]\{\psi(Z_j)\}F_{Xj}e^{i\omega t} = \sum_{j=1}^{m} \alpha_{ij}F_{Xj}e^{i\omega t} \\ V(Z_i,t) = \sum_{j=1}^{m} \{\psi(Z_i)\}^T[D]\{\psi(Z_j)\}F_{Yj}e^{i\omega t} = \sum_{j=1}^{m} \alpha_{ij}F_{Yj}e^{i\omega t} \end{cases}, \quad (3)$$

where $[D] = [-\omega^2([M]+[N]) + \Omega\omega[P] + ([K_1] - \Omega^2[K_2])]$.

The receptances of the rotor and the supports are accordingly obtained:

$$\begin{cases} \alpha^{ij}_{xx} = \alpha^{ij}_{yy} = \{\psi(Z_i)\}^T[D]\{\psi(Z_j)\} \\ \alpha^{ij}_{xy} = \alpha^{ij}_{yx} = 0 \end{cases} \quad (4)$$

$$\beta^{ii}_{xx} = \frac{k^i_{yy}}{k^i_{xx}k^i_{yy} - k^i_{xy}k^i_{yx}}, \quad \beta^{ii}_{xy} = \frac{-k^i_{yx}}{k^i_{xx}k^i_{yy} - k^i_{xy}k^i_{yx}},$$
$$\beta^{ii}_{yx} = \frac{-k^i_{xy}}{k^i_{xx}k^i_{yy} - k^i_{xy}k^i_{yx}}, \quad \beta^{ii}_{yy} = \frac{k^i_{xx}}{k^i_{xx}k^i_{yy} - k^i_{xy}k^i_{yx}}, \quad (5)$$
$$\beta^{ij}_{xx} = \beta^{ij}_{xy} = \beta^{ij}_{yx} = \beta^{ij}_{yy} = 0, \quad \text{when} \quad i \neq j.$$

The frequency equation of the supported rotor is then derived:

$$R(\omega,\Omega) = \begin{vmatrix} [\alpha^{11}]+[\beta^{11}] & [\alpha^{12}] & \cdots & [\alpha^{1m}] \\ [\alpha^{21}] & [\alpha^{22}]+[\beta^{22}] & \cdots & [\alpha^{2m}] \\ \vdots & \vdots & \ddots & \vdots \\ [\alpha^{m1}] & [\alpha^{m2}] & \cdots & [\alpha^{mm}]+[\beta^{mm}] \end{vmatrix} = 0, \quad (6)$$

where

$$[\alpha^{ij}] = \begin{bmatrix} \alpha^{ij}_{xx} & 0 \\ 0 & \alpha^{ij}_{yy} \end{bmatrix}, \quad [\beta^{ii}] = \begin{bmatrix} \beta^{ii}_{xx} & \beta^{ii}_{xy} \\ \beta^{ii}_{yx} & \beta^{ii}_{yy} \end{bmatrix} \quad (7)$$

$[\alpha^{ii}]$ and $[\beta^{ii}]$ represent the receptance matrices of the rotor at Z_i and of the ith support, respectively. $[\alpha^{ij}]$ are the cross receptances of the rotor at Z_i and Z_j. $[\beta^{ij}]$ vanishes owing to the assumption that all the supports were fixed on a rigid stator, and therefore cause no mutual influence between supports. If the flexibility of a stator is considered, the cross receptances have values, and evaluation of those values requires some effort. The present discussion is focused on sensitivity analysis stemming from Eq. (6) and does not include the stator effect, for simplicity. The receptance matrices shown were of dimension two, representing the X and Y directions. If the supports are isotropic, the dimension of matrices is reduced by half.

3 Sensitivity Analysis

Equation (6) was customarily used for natural frequencies and critical speed analysis of rotor systems. The authors noticed that Eq. (6) has been a function of critical speeds and support stiffness. Therefore, it can be utilized for the sensitivity analysis of rotor natural frequencies or rotor critical speeds to support stiffness variations. This feature appears to be valuable in rotor dynamics. Although similar discussions could be seen in the literature (Rajan et al., 1986, 1987), application of the receptance matrix, to the authors' knowledge, was not seen in the literature. In the following, the authors introduce the derivation of sensitivity matrix of critical speeds. Subsequently, a computing algorithm is developed as well. Through the following derivation and discussion, the approach will prove itself a very efficient technique.

For critical speed analysis, we let $\omega = \Omega$ and rewrite Eq. (6) in the form

$$R(\Omega_{cri}, \mathbf{k}_j) = 0, \quad i = 1, 2, \ldots, n, \quad j = 1, 2, \ldots m, \quad (8)$$

where Ω_{cri} denotes the ith critical speed to be studied and $\mathbf{k}_j$ is the jth support stiffness allowed to vary. Note that each support $\mathbf{k}_j$ denoted four stiffness parameters. For numerical simplicity, we herein assume support symmetry and use only one radial stiffness, k_j. Mathematically, Eq. (8) represents a function of $n+m$ parameters, i.e., n critical speeds and m supports stiffness. Practically, Eq. (8) asks for possible solutions of adjusting (placing) n critical speeds via changing the m supports stiffness.

Table 1 Computing steps in example 1

Step	Critical speed, Ω_{cr} (rad/sec)	Sensitivity, $\frac{\partial\Omega}{\partial k_1}$	Stiffness, k_1 (N/m)
0	653.85	0.0000120	1.75×10^7
1	657.98	0.0000054	2.26×10^7
2	659.60	0.0000035	2.63×10^7
3	659.97	0.0000031	2.75×10^7
4	660.00	0.0000031	2.76×10^7 (57.7%)

It is realized that no solution exists for $n > m$, and there exists a possible unique solution for the case of $n = m$. For $n < m$, there are numerous solutions, and for such a case, an optimal scheme is usually required. To present the usage of the developed approach, the authors here focus on the case of $n = m$, and the optimal modification for more sophisticated rotors will be presented by the authors in a following paper.

Define the sensitivity coefficient as

$$S_{ij} = \frac{\partial\Omega_{\text{cri}}}{\partial k_j} = -\frac{\partial R}{\partial k_j}\Big/\frac{\partial R}{\partial\Omega_{\text{cri}}}, \quad \begin{matrix} i = 1, 2, \ldots, n \\ j = 1, 2, \ldots, m \end{matrix} \tag{9}$$

where S_{ij} represents the sensitivity of the ith critical speed (Ω_{cri}) to the jth support (k_j) at an existing state. Note that the sensitivity coefficients are obtained via forward calculations, i.e., no iteration is necessary, provided the current state has been solved. With the sensitivity matrix $[S]$, the relation between critical speed variations and support stiffness changes can be written as

$$\{\Delta\Omega_{cr}\} \cong [S]\{\Delta k\}, \tag{10}$$

where $\{\Delta\Omega_{cr}\} = \{\bar{\Omega}_{cr}\} - \{\Omega_{cr}\}$ denotes the variation vector of critical speeds, in which $\{\Omega_{cr}\}$ and $\{\bar{\Omega}_{cr}\}$ represent the current and the desired critical speed vectors, respectively. $\{\Delta k\} = \{\bar{k}\} - \{k\}$, in a similar fashion, denotes the required stiffness changes in order to move the current critical speeds to the desired ones. Prior to solving the equation, some comments concerning the sensitivity matrix $[S]$ need to be addressed. First, a zero entry in the matrix, e.g., $S_{ij} \approx 0$, means the ith critical speed being insensitive to the jth support, and any zero row indicates that the limit of that critical speed has been reached, i.e., any increase (decrease) of support stiffness imposes no more change of that critical speed. A zero column means a support has reached its extremum, usually approaching a rigid or a very flexible support. Thus, further increase (decrease) of stiffness has no more effect on all critical speeds. The sensitivity matrix therefore provides not only the sensitivities of critical speeds to support stiffness, but also the allowable ranges for critical speed adjustment. For instance, as $[S]$ approaches a singularity, a limit of one or more critical speeds are reached.

Table 2 Computing steps in example 2

Step	Critical speeds			Stiffness of support ($\times10^7$ N/m)		
0	653.85	873.24	1339.69	1.750	1.750	1.750
1	549.60	842.59	1397.83	1.399	3.625	0.918
2	602.14	887.43	1400.11	1.636	3.277	1.204
3	609.78	889.96	1400.01	1.650	3.205	1.256
4	610.00	890.00	1400.00	1.650 (-5.7%)	3.203 (83.0%)	1.258 (-28.1%)

Table 3 Sensitivities in each step in example 2

Step	Sensitivity ($\times10^{-5}$)								
	S_{11}	S_{12}	S_{13}	S_{21}	S_{22}	S_{23}	S_{31}	S_{32}	S_{33}
0	0.1206	0.1848	0.8593	1.7720	0. 4411	0.0498	0.0027	0.8234	1.1142
1	0.1807	0.0264	1.9993	1.8067	0.1190	0.2980	0.0192	0.6606	0.8648
2	0.1755	0.0440	1.5118	1.6996	0.1497	0.2344	0.0124	0.6866	0.9106
3	0.1802	0.0473	1.4343	1.6859	0.1591	0.2261	0.0108	0.6918	0.9204
4	0.1800	0.0472	1.4365	1.6862	0.1588	0.2263	0.0109	0.6917	0.9201

Provided the desired adjustment of critical speeds is reasonable, so that no zero row or column would occur in the subsequent calculations; then

$$\{\Delta k\} \cong [S]^{-1}\{\Delta\Omega_{cr}\} \tag{11}$$

We solve Eq. (11) for the required changes of support stiffness, $\{\Delta k\}$, in order to shift the critical speeds to the desired values. The calculated values are, however, just a prediction based on the sensitivity at the current state. The sensitivity coefficients vary continuously with the support stiffness. Therefore, a one-step calculation usually does not meet the final conclusion. A few steps are usually required. The computing algorithm is described as follows:

Steps:

1 Calculate the critical speeds of the original configuration from Eq. (6).
2 Calculate the sensitivity coefficients, from Eq. (9).
3 Check whether the $[S]$ matrix is singular. If the $[S]$ matrix approaches a singularity, the desired critical speed adjustment cannot be reached.
4 Solve Eq. (11) for $\{\Delta k\}$.
5 Configure the new support stiffness and calculate the new critical speeds. If the new critical speeds meet the desired values, end the iteration, otherwise go to step 2.

4 Numerical Examples

In the following, two examples are illustrated. A rotor system adopted directly from Rajan et al. (1987) is demonstrated. Details of the system configuration and material properties may be referred accordingly. The rotor assembly is assumed to be supported on a rigid foundation through isotropic undamped bearings with stiffness $k_1 = k_2 = k_3 = 1.75 \times 10^5$ N/cm. The first example shows a simple case, where support No. 1 is allowed to vary for the first critical speed adjustment. The first critical speed of the original system was 653.85 rad/s. Assume it is to be moved to 660.0 rad/s. Table 1 shows the iterations. It was seen that after four steps, the first critical speed was successfully shifted to the desired value. The result indicated that the first support should be changed from 1.75×10^7 to 2.76×10^7 N/m. The subsequent changes of sensitivity coefficient are also given in the table. It was seen that the value of sensitivity decreased in steps. It is hence expected a limit would eventually be reached if one wanted to move the critical speed further. Table 2 shows a more complicated example, where the first three critical speeds were to be moved from 653.85, 873.24, and 1339.69 to 610, 890, and 1400 rad/s. To have a possible solution, at least three supports must allowed to vary. Here, we let supports $1 \sim 3$ be adjustable and search for a solution. Table 2 shows excellent convergence and the illustrated final changes of the three supports. Table 3 shows the variations of sensitivities in steps. It is noticed that the first critical speed was domi-

nated by support No. 3, as that coefficient (S_{13}) was larger than the others. Similarly, the second critical speed was affected the most by support No. 1, and the third critical speed was dominated by supports 2 and 3.

5 Conclusion

An application of the receptance matrix for the sensitivity analysis of rotor critical speeds was introduced. The influence of bearing supports to the critical speeds was illustrated in examples. This derivation provides rotor engineers valuable information for rotor modification and design. This approach can be used for studying the sensitivities of eigen frequencies, unbalance responses, etc., support stiffness as well. Numerical examples also show excellent convergence in the solution process.

Acknowledgments

The authors are grateful to the National Science Council of Taiwan for the support of the research under grant No. NSC 83-0401-011-073.

References

Bishop, R. E. D., and Johnson, D. C., 1960, *The Mechanics of Vibration,* Cambridge University Press, England.

Chiau, S. W., and Huang, S. C., 1989, "On the Flexural Vibrations of Rotor Systems Using a Modified Transfer Matrix Method," *Proc. 6th Chinese Society of Mechanical Engineers,* pp. 1607–1618 [in Chinese].

Huang, S. C., Chang, C. I., and Su, C. K., 1994, "A New Approach to Vibration Analysis of Undamped Rotor-Bearing Systems," *Journal of the Chinese Society of Mechanical Engineering,* Vol. 15, No. 5, pp. 465–478.

Rajan, M., Nelson, H. D., and Chen, W. J., 1986, "Parameter Sensitivity in the Dynamics of Rotor-Bearing Systems," ASME *Journal of Vibration, Acoustics, Stress, and Reliability in Design,* Vol. 108, pp. 197–206.

Rajan, M., Rajan, S. D., Nelson, H. D., and Chen, W. J., 1987, "Optimal Placement of Critical Speeds in Rotor-Bearing Systems," ASME *Journal of Vibration, Acoustics, Stress, and Reliability in Design,* Vol. 109, pp. 152–157.